Crustal Accretion Near Ridge-Transform Intersections: Kane Fracture Zone, Mid-Atlantic Ridge.

by

N. Kate Lawson

A thesis submitted in partial fulfilment of the requirements for the degree of Doctor of Philosophy

Department of Geological Sciences

University of Durham

February 1996

VOLUME CONTAINS CLEAR OVERLAYS

OVERLAYS SCANNED SEPERATELY AND OVER THE RELEVANT PAGE.

CONTAINS

PULLOUT

This thesis is dedicated

to my family, friends and

the sunrise over

Durham Cathedral.

GLOSSARY

AMC	Axial magma chamber
ANGUS	Acoustically Navigated Undersea Survey
AVR	Axial volcanic ridge
CAMH	Central axial magnetic high
CD57	Charles Darwin cruise number 57
cpx.	clinopyroxene
DEVAL	Deviation from axial linearity
DSDP	Deep-sea drilling program
EPR	East Pacific Rise
FAMOUS	French American Mid-Ocean Undersea Study
GMT	Global Mapping Tool
GPS	Global Positioning System
HAM	High-amplitude magnetic
HREE	Heavy rare earth element
ICP-MS	Inductively-Coupled-Plasma emission Mass Spectrometry
IOSDL	Institute of Oceanographic Sciences and Deacon Laboratory
KFZ	Kane Fracture Zone
LILE	Large Ion Lithophile Element
LLD	Liquid-line-of-descent
LNB	Level of neutral buoyancy
LREE	Light rare earth element
Ma	Million (10^6) years
MAR	Mid-Atlantic Ridge
MARK	Mid-Atlantic Ridge at Kane
MARNOK	Mid-Atlantic Ridge north of Kane
mgal	milligal = 10^{-5} m s^{-2}
MOK	Mokuaweoweo
MORB	Mid-Ocean Ridge Basalt
N-MORB	Normal Mid-Ocean Ridge Basalt
NERC	Natural Environment Research Council
NTO	Non-transform offset
NVR	Neovolcanic ridge
NVZ	Neovolcanic zone
ODP	Ocean drilling program
ol.	olivine
PTDZ	Principal transform displacement zone
plag.	plagioclase
ppm	Parts per million (1 in 10^6)
REE	Rare Earth Element
RGB	Red-green-blue
RTI	Ridge-transform intersection
TAG	Trans-Atlantic Geotraverse
TFE	Transform effect
TOBI	Towed ocean-bottom instrument
TVG	Time-varying gain
UDIRL	University of Durham Industrial Research Laboratories
vol.%	volume percentage
WASP	Wide-angle survey photography
wt.%	weight percentage
XRF	X-Ray fluorescence spectrometry

ABSTRACT

Crustal Accretion Near Ridge-Transform Intersections: Kane Fracture Zone, Mid-Atlantic Ridge.

N. K. Lawson, University of Durham, 1996.

Two mid-ocean ridge spreading segments in the MARNOK (Mid-Atlantic Ridge north of Kane) area have been investigated with an integrated program of TOBI high-resolution sidescan sonar, WASP deep-tow photoanalysis and dredging. The MARNOK area is situated on the western intersection of the Mid-Atlantic Ridge with the Kane Fracture Zone at about 24°N and 46°20'W. It comprises two second order segments, which are offset by 1km at 24°22'N by a right-stepping, third order, non-transform offset (NTO). On the basis of their morphology, these two second order segments fall into the different groups defined by Sempéré et al. (1993). The segment adjacent to the transform is a group 1, narrowgate-type while segment 2 to the north is a group 2-type.

I establish a basis for the geological interpretation of TOBI sidescan sonar by identifying a wide range of textural terrains. The geological significance of these textural terrains is determined by correlation with deep-tow camera traverses, dredge localities, the 7.5kHz profiler and the submersible dives of Zonenshain et al. (1989). Volcanic terrains include hummocky ridges and mounds (comprising pillow flows), flat-topped seamounts, cratered cones, areas of tumescence, smooth-textured sheet flows and pillow fields. Tectonic terrains include fissures and different scales of faulting. Aligned hummocky ridges are thought to originate from fissure eruptions, but are often related to underlying faults and sometimes eruption occurs along a fault plane. Mass wasting of fault scarps and hemipelagic sedimentation can produce talus fans, erosional gullies, landslides, sediment slumps and debris flows. Very steep-sided mounds may be of hydrothermal origin but dredges from a steep summit cone, named Thatcher's Nose, recovered a lava with 40% accumulated plagioclase megacrysts. Here the steep sides are accounted for by the high viscosity of such a highly phyric lava.

The flat-topped seamounts are preferentially located at the ends of segments, often over faults or next to the median valley walls. Their parental magmas are distinct from nearby hummocky terrain. They have similar petrological and geochemical characteristics to shield volcanoes in Iceland and their morphologies are especially akin to the subglacial seamounts, which may be a consequence of the common presence of water in the two eruptive environments. I reject the hypothesis that the flat top is produced by a limiting magmatic head, because it is inconsistent with the variation in seamount height and morphology along-axis in the MARNOK area. I suggest a model for crustal plumbing at accretionary plate boundaries, whereby flat-topped seamounts erupt if crustal rifting occurs in the absence of an upper crustal magma chamber, while hummocky terrain arises from rifting over upper crustal magma chambers. Thus, seamount eruption should be characteristic of rifting in a relatively low magma-flux environment (e.g. segment ends), or after a period of magmatic starvation.

The effect of the transform extends for 26km along the southern half of segment 1. The stress regime at the RTI suggests there is flexural downbending of the lithosphere in response to the formation of the nodal basin. The transform median ridge shows evidence for serpentinite protrusions and related slope failure. There is no decrease in the degree of bulk mantle melting towards the transform, but there is a reduction in the magma supply resulting in a small (3-6km) length scale of petrological segmentation which correlates well with discrete volcanic edifices identified on the sidescan images. The relative lack of a magmatic transform effect suggests that transform segmentation is primarily of a tectonic origin.

The second order segmentation dominates the magmatic systematics. Primitive lavas occur at the centres of the segments and fractionated compositions at the ends. There is no variation in the bulk degree of melting along-axis, favouring melt migration rather than mantle upwelling as the primary control for along-axis variations in crustal thickness. Group 1 segment morphologies are thought to result from a relatively high melt-flux comprising regular injections of magma, strongly focused on the segment centre. This maintains a shallow brittle-ductile transition in the centre of the segment, resulting in a symmetrical median valley. These magmatic conditions will also promote the development of a relatively continuous, well-mixed magma chamber with low crustal residence times in the segment centre and thus accounts for the primitive compositions erupted at the axial-highs and the relatively long petrological segmentation (6-11km). With decreasing magmatic input, the brittle-ductile transition is lowered and the valley wall faulting becomes asymmetric, as for a group 2 morphology. Comparison with the 26°S segment (Grindlay et al., 1992; Niu & Batiza, 1994) suggests that if the degree of melting exceeds ~15.5% then the additional buoyancy provided by the increased melt fraction initiates 3D, focused mantle upwelling.

DECLARATION

I declare that this thesis, which I submit for the degree of Doctor of Philosophy at the University of Durham, is my own work and is not substantially the same as any which has previously been submitted for a degree at this or another university.

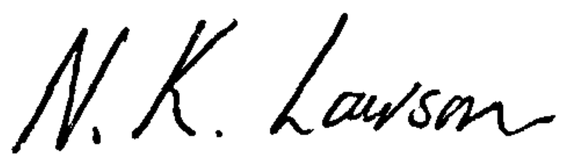

N.K. Lawson

University of Durham

Department of Geological Sciences
February, 1996

ACKNOWLEDGEMENTS

Firstly my thanks must go to my supervisors, Roger Searle and Julian Pearce, for initiating and organising the project in the first place and for their support throughout my time at Durham.

Secondly, a special thanks to Pam Kempton for her hard work on the isotope analyses, being a proficient teacher in good lab technique and her support and advice throughout the project. I am also indebted to Igor Browning for the electron probe analyses, carrying rocks, steeling my chocolate and coming up to Durham to discuss some of the finer aspects of ridge segmentation and Easter eggs. Likewise, I am grateful to the other ship-board scientists for discussions during and after the CD57 cruise: Simon Allerton; Catherine Mevel; Bram Murton; Robin Owens and Hans Schouten.

A mention should go to the technical staff and crew, especially Paul Burridge for steering a perfect question mark over the MARNOK area and letting me drive; Ian McGill for a awakening my taste for things with big engines that go fast, Gareth for aiding and abetting some of the finer moments of April 1st, Mike Conquer for flooding the hold and providing me with the rolls of WASP film, Nick Millard and Bob Kirk for managing not to crash TOBI into the inside corner high.

Chris McLeod has been a source of encouragement and an invaluable guide in the field in Cyprus. In addition he donated samples from the Eastern Limassol Forest, Cyprus for ICP-MS and isotope analysis and has been available for several useful discussions on boninites. Bram Murton provided samples from the Kapillio area and is thanked for his interest in the project.

I am grateful to Eddie McAllister for sending me the SeaBeam data (and I still owe him a pint) and Stephan Hussenoeder for providing me with the deep-tow magnetisation inversions.

I have enjoyed being a member of the BRIDGE and INTERIDGE communities which has given me several opportunities to discuss my work with many eminent scientists including Rodey Batiza, Brian Tucholke, Mike Perfit, Don Forsyth, Charlie Langmuir and Jo Cann, to name but a few.

Marty Kleinrock is thanked for skiing at Lake Tahoe, Graham Cocksworth for acting as chauffeur around California and Mark and Parky for allowing Boo to jump in for a bit of 'slap and tickle'.

Special thanks to my 'predecessor' and fellow 'cider-sister', Cherry Walker, for her faith, encouragement and advice in BRIDGE-related matters. Good luck with the gardening and married life, Chezza!
My thoughts also turn to my old lecturers at Cambridge who started me off on the path of geoscience, especially: 'Uncle Nig' Woodcock and Mike Bown who encouraged me to enter the 'heady world' of research; Martin Sinha for sparking my interest in ridges; Paul Browning for doing the same with ophiolites; and Dan McKenzie for his vote of confidence and willingness to lend his programs.

Moving on to those in the department in Durham: Dave Asbery will be remembered for being 'a true gent', Carol and Lynne for logistic support in the office, Ron Lambert for not minding too much when I took over his desk and computer, Julie and George for thin sections, Karen for advice on CorelDRAW, Dick Reeves for providing the magic spray for unseizing bike locks, Alan Carr for a very last minute photograph, George Ruth for mending computers, Mary for sweeping round my maps and Brenda for her advice on 'things hormonal' -B_6, Mg and evening primrose oil has worked wonders!
I am especially grateful to Gerry Dresser for the mammoth effort required to produce all the photographs of TOBI mosaics in this thesis, Ron Hardy for running the XRF and Dave Stevenson for his advice on many aspects of computing throughout the years.
Best wishes and thanks go to the members of staff in the geology department: my tutor Dick Swarbrick, for his support, offers of hospitality and encouragement when applying for jobs; Donny Hutton for confirming my thoughts on duplexes and other structural matters; Gill Foulger for an interesting and useful discussion on Iceland; Martin Bott for advice on numerical modelling; Bob Thompson for reference tips; Gilbert Larwood for 'housing'; Andrew Peckett for his efficiency and the offer of the America trip; and Chris Peirce for advice on thesis structure and conventions. A mention must also go to the post-docs: Neil Mitchell for his thoughts on sonar, Dimetri, Sally and Dave Peate for words of geochemical wisdom.

Cheers to the other postgrads who laughed and cried with me during the Durham 'learning experience', especially my office mates: Sue (a fellow sufferer and soul mate); Sarah (closet or maybe not so closet-wild-woman, who got me to the train on time on more occasions than I care to mention); Bole; Jon; and the shorter term residents, Eva and Affonso. The early days in Durham were spent with 'the Shincliffe Ravers': Jane, Marky-boy and Parky. Memhet is remembered for wild dancing at the Graduate Society and setting very high standards for the geochem boys, and Vicky for

trusting me with her car and lending a steady hand in a time of crisis. 'The lads' Mikey, Gary, Andy, Hunty, Steve, Tim, Si, Paul, Chris, Booler and Robin and the lasses: Ruth, Zoe and Charlotte are thanked for many good nights out on the town. The new generation 'lads' Wayne, Alun, Adam, Simon, Jonny Imber are thanked for providing access to their Red Dwarf collection, (not that they were in any state to remember or appreciate it!) and cooking me a juicy medium rare. Ziad is thanked for timely advice on viruses; Trevor for being good to tickle; Angus for being the latest addition to East Atherton Street. Debbie is thanked for lending me drawing office kit at a key moment and being a friendly presence next to the computer room. The Libyans, especially Fawzi and Khaeri will be remembered for late night cross-cultural discussions and Ismail for his medicine.
A mention must go to Darren Moore for his part in the Durham experience; for five minutes of glass picking, his impeccable timing and for the sea of stars in the Saharan Sabhka ('though it's just a memory, some memories last for ever...')
Alison McCann is thanked for requesting my services on the Cyprus fieldtrip for a second time and Guy Spence for covering for me when I was otherwise engaged.

My time at Durham has been considerably enhanced by my other friends in the university, including the Biology crowd: Helen Hooper (kindred spirit, wild woman and indie rocker), Bob (kindred spirit in a different way, who picked me up at a low ebb), Johan, Mark, Caroline and Tim. I mourn for the passing of the Rose Tree and have fond memories of the Slug. Also, the Chemistry crowd: Paddy 'the fiancé' (who took me to Chester via Leeds with the Mad Dog -ooh er! and who also has good timing), Fiona O'Carrol for her hospitality at Glenwood and a timely photocopy card and, of course, Pink Fiona and the guys in her lab.
A special mention must go to the night shift security men: Eddie, Frank, Billy Bob, John, Richard, Jeff and, last but not least, Lawrence (or is it Clarence) for services beyond the call of duty. They'll have no one to look after once I've gone!

There are many good friends form the B.S. group, Nicks and the Hockey club who are too numerous to mention, but I would especially like to thank Colin Darling (for safe cuddles), Francisco and Lourdes Astorga (for being inspiring and wonderful), the Gregory-Smiths (for Shipmates), Heather Robb (for melon and being an excellent housemate), George Moody (for his guitar and gentleness), Alison Verity (for prayers), Tracy West (for having been there before me), Onesimus (for a big smile) and Steve Lovell (for protection and self-defence lessons).

The companionship, support and help of Kevin Jesty over the last few months has been invaluable. He was there when I needed him the most! Christian Buchholdt is thanked for the lessons in punctuation, while David Dawes has been a great supplier of crisps and tips on inter-personal skills. I am indebted to Sarah for providing a roof over my head (though she still hasn't done the kitchen), for her care, cooking and company. Fiona and Adrian are thanked for their love and support, hospitality, flowers, chocolate and ménage à trois (well sort of). Similar sentiments with the exception of the latter for 'my sis' Emma, Nick and Emm, Miranda and Matthew, Alistair and Nancy, Ken and Eileen, Paul Groombridge, Kevin Jenkins, John Massey, Guido Barzini, Pete Webster, Kevin White, Alan Trewartha and John Williams. Reynold, Pete, Jeff, Sandra, Mike and Mikey are thanked for wild nights in Leeds and in Durham!

Dad, Karl Banzini, Jamie MacDonald and Kevin Jesty 'it's my baby' are thanked for their assistance in typing and sorting out references. Fiona Lough provided reviving company and demonstrated a remarkable ability in colour photocopying. Darling has truly lived up to his name by feeding me, labelling diagrams and generally coming to the rescue. Sarah is thanked for her prowess at cutting and sticking and Giles 'Mr Page Break' for his speedy proof reading and chapter formatting. I am also indebted to Pete, Vicky and Affonso and family for their help in other last minute bits and pieces.

Gary and Ruth are thanked for their hospitality in Holland and Mark for the tour round the rig. Thanks to Shell International for providing me with a job and hope for the future at an opportune moment.
Her Majesty's Government have provided my maintenance and funded this research via a NERC studentship, amongst other things!

Finally, I'm indebted to my family for their love, moral and financial support before and during my time at Durham.

"All things work to the good..."
Time to be "movin' on up now!..."

There's lots of ways to hit the ground,
Not many answers to be found,
We're faced with mysteries profound,
And this is one of the best ones...

Little round planet
in a big universe,
Sometimes it looks blessed,
Sometimes it looks cursed,
Depends on what you look at
obviously,
Even more it depends on
the way that you see.

Bruce Cockburn from 'Nothing but a burning light'

CONTENTS

Chapter 1: Introduction

Chapter 2: Methodology

Chapter 3: Interpretation of TOBI sidescan terrains

Chapter 4: Volcanology

Chapter 5: The transform and the RTI

Chapter 6: Segmentation

Chapter 7: Global comparisons

Chapter 8: Conclusions

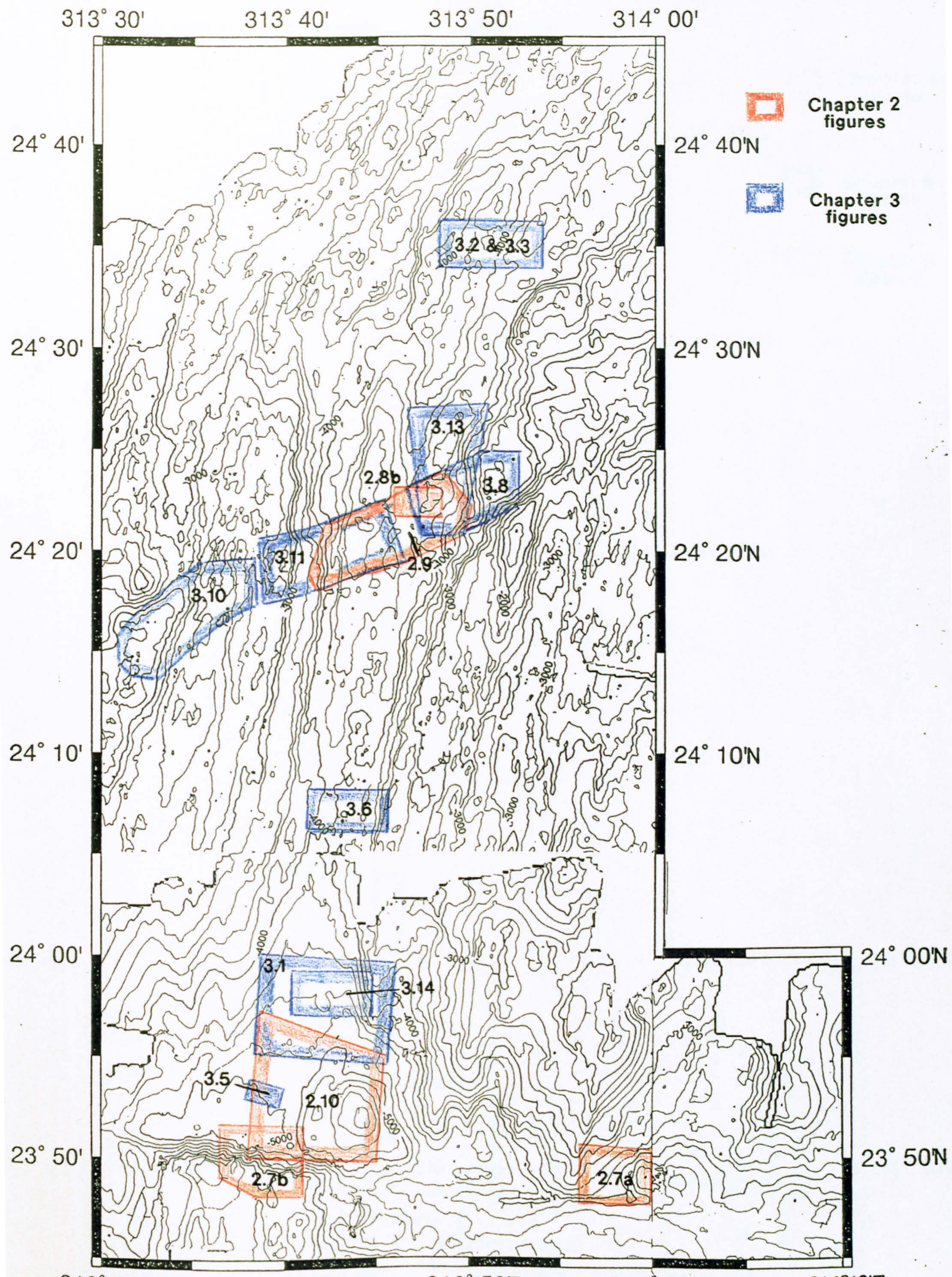

Locations of TOBI sidescan figures: chapters 2 & 3.

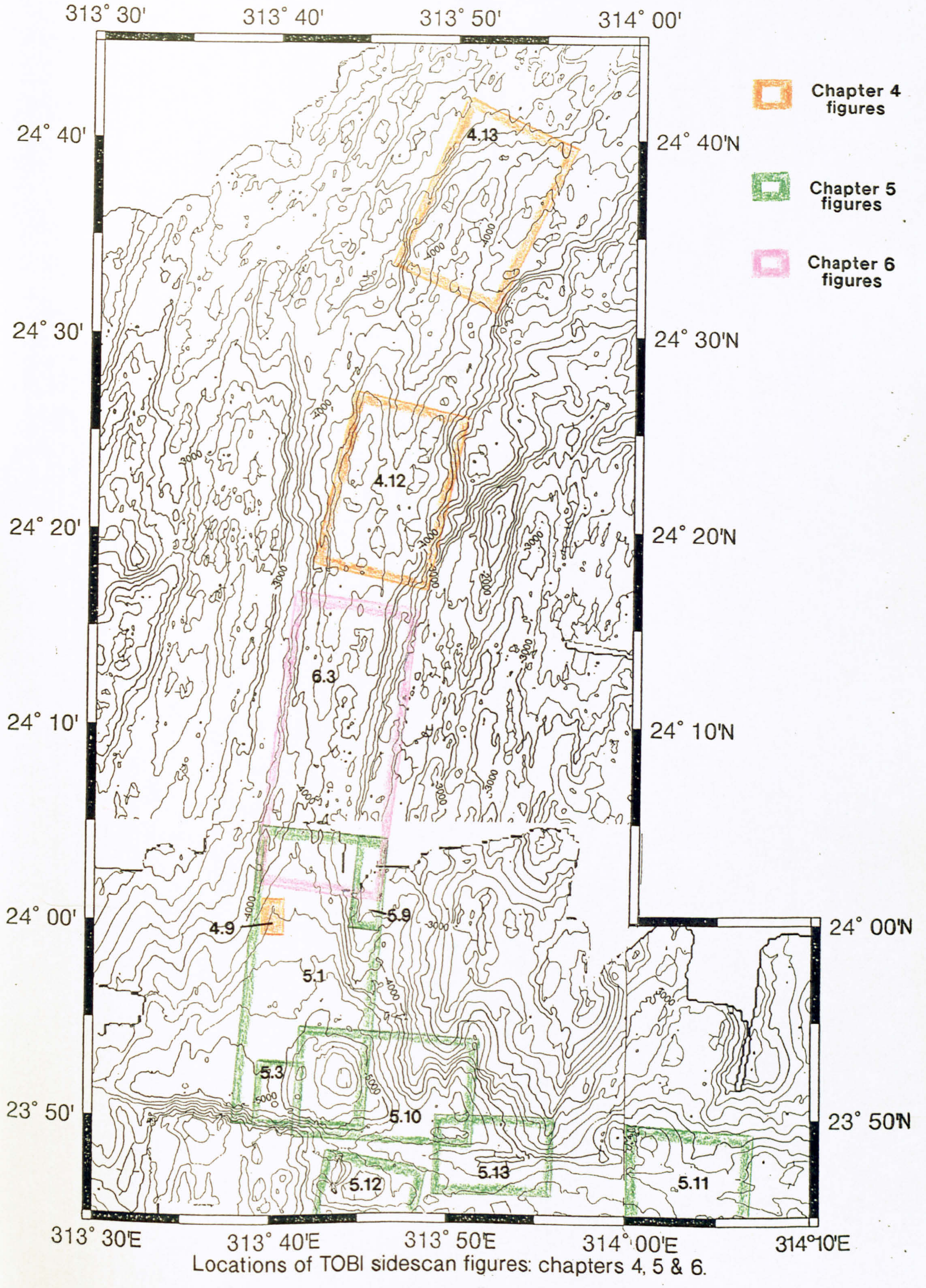

Locations of TOBI sidescan figures: chapters 4, 5 & 6.

Chapter 1

Introduction

Since leaving Tenerife the sea has been so calm that it is hard to believe it is the same element which tossed us about in the Bay of Biscay. This stillness is of great moment to the quantity of comfort which is attainable on ship-board. Hitherto I have been surprised how enjoyable life is in this floating prison....To enjoy the soft delicious evening of the tropics, to gaze at the bright band of stars, which stretches from Orion to the Southern Cross and to enjoy such pleasures in quiet solitude, leaves an impression which a few years will not destroy.

Charles Darwin, aboard HMS Beagle, 25th February, 1832.

Nearly 160 years after the young Charles Darwin himself left Tenerife on the start of his epic round the world voyage, the research vessel which now bears his name departed from Santa Cruz at the start of a 28 day cruise (CD57) to study ridge segmentation on the Mid-Atlantic Ridge north of the Kane transform fault. This thesis presents some of the results obtained as a result of this cruise.

1.1 Mid-Ocean Ridges as accretionary plate boundaries.

1.1.1 Studies of seafloor spreading on the Mid-Atlantic Ridge

It was just over 30 years ago when Hess (1962) proposed seafloor spreading as a unified model to explain the enigmas of basaltic volcanism and high heat flow along the seismically active rift zone on the crest of the Mid-Atlantic Ridge. The bilateral symmetry of magnetic anomalies found on other mid-ocean ridges (Vine & Matthews, 1963) elevated seafloor spreading to a widely accepted theory and led to the concept of global plate tectonics. The Mid-Atlantic Ridge (MAR) is the best studied example of a slow spreading accretionary plate boundary. It extends for over 12,000km from Iceland to the Bouvet Triple Junction, though scientific investigation has been focused onto certain areas (figure 1.1) including the FAMOUS area at 37°N (Heirtzler & Le Pichon, 1974; Ballard & Van Andel, 1977) and the nearby AMAR rift (Stakes et al., 1984, Frey et al., 1993), the MARK area at 23°N (Melson, Rabinowicz et al., 1978; Dmitriev, Heirtzler et al., 1978; Detrick et al., 1988; 1990), TAG at 26°N (Scott et al., 1974; Rona, 1980) and more recently the (24°N - 31°N) Kane-Atlantis section of ridge (Purdy et al., 1990; Lin et al., 1990; Sempéré et al., 1990, Smith & Cann, 1992). Less attention has been paid to the south Atlantic but, within the last few years, there

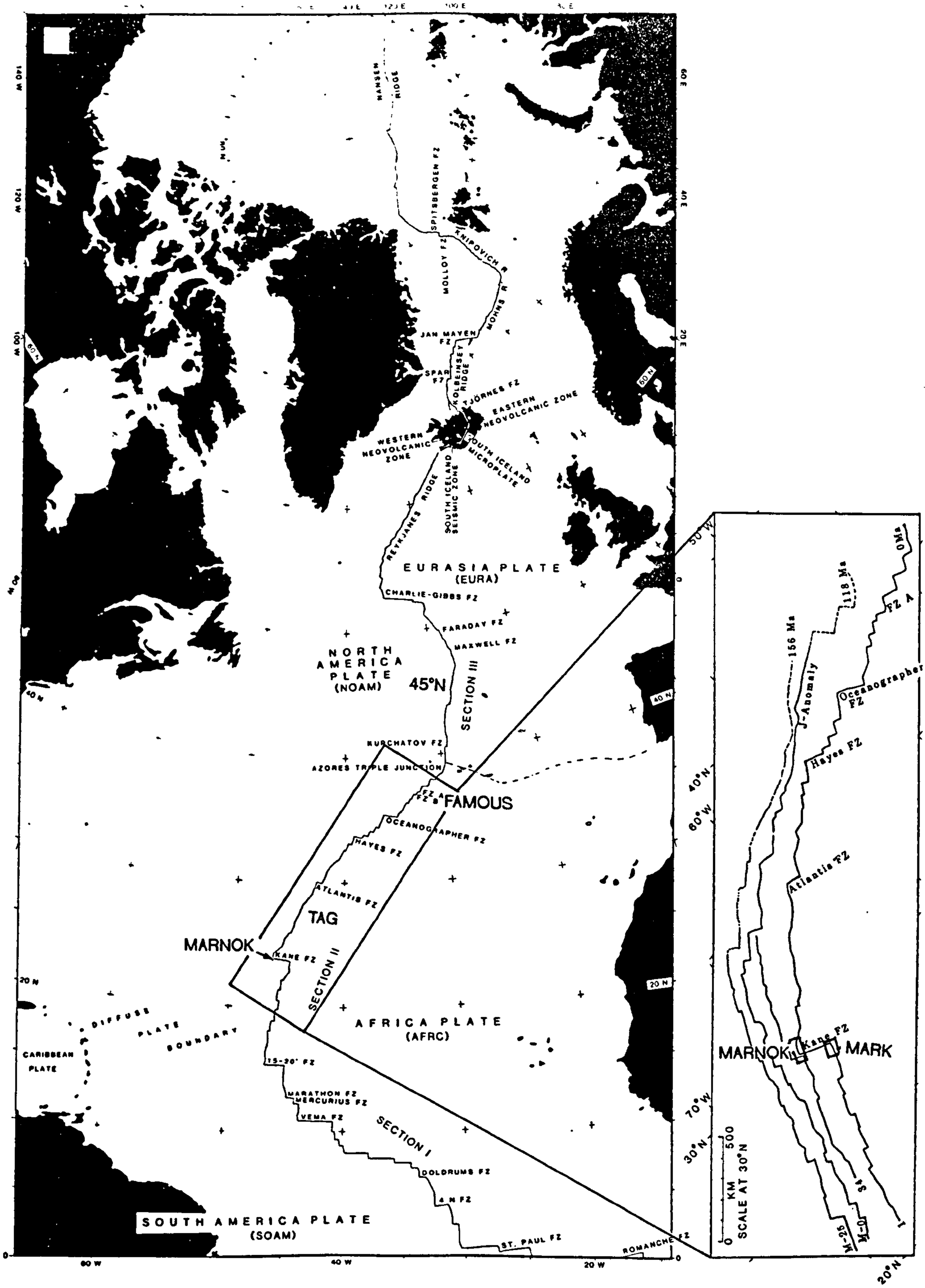

Figure 1.1 Location map showing the present plate boundary configuration of the north Atlantic. The study area is at the western intersection of the Kane Transform with the Mid-Atlantic Ridge. Other areas where research has been focused are also marked (adapted from Vogt, 1986).

have been integrated studies at 26°S and around 31°S (Carbotte et al., 1991; Fox et al., 1991; Grindlay et al., 1992; Niu & Batiza, 1994; Michael et al., 1994).

1.1.2 Morphology of the rift valley

The gross morphology of mid-ocean ridges seems to be controlled primarily by the spreading rate and the temperature of the upper mantle. At slow spreading rates (2-4cm yr^{-1}), away from the influence of plumes, the axis takes the from of a prominent median valley, 30-50km wide and 1-5km deep (Macdonald, 1986; Searle, 1992). The median valley is a nested rift with a series of normal faults separating near-horizontal terraces, stepping down towards the central graben of the inner valley. The inner valley varies in width from about 5-10km and comprises block faulted inner walls bounding the inner floor (Needham & Francheteau, 1974; Macdonald et al., 1975).

1.1.3 The neovolcanic zone

The focus of surficial volcanism which marks the accretion of the new oceanic plate occurs within the inner floor. The most recent expression of this volcanism is known as the neovolcanic zone (NVZ). There is no strict and rigorous definition of the NVZ as its boundaries depend very much on the information available and the interpretation of that information. In submersible, deep-tow camera and sampling studies, the fine scale sediment cover, the degradation and palagonitization of glassy ornamented pillow surfaces and the progressive coating of manganese are used to identify the most recent volcanism (Bellaiche et al., 1974; Ballard et al., 1975; Bryan & Moore, 1977).

In sidescan sonar studies, the recognition of the NVZ very much depends on the resolution of the instrument. In long-range sidescan surveys such as those produced by GLORIA, sites of recent volcanism are often imaged as moderate to high backscattering, diffuse, linear targets on the median valley floor (Laughton & Rusby, 1975; Searle & Laughton, 1977). As the resolution of the sonar instrument increases, the NVZ becomes defined by a high backscattering hummocky or smooth texture produced by the gross morphology of individual flows or groups of flows (Kappel & Normark, 1987; Kong et al., 1988). A large number of ridge crest studies are based on bathymetry data in which it is not always possible to distinguish between steep volcanic slopes and fault scarps. In the absence of sidescan sonar imagery or other groundtruthing information, the sub-linear locus of bathymetric peaks within the floor of the inner valley is usually interpreted as the NVZ (e.g. Sempéré et al., 1993).

On the MAR, the NVZ is often highly discontinuous and comprises a chain of volcanoes that are aligned approximately parallel to the spreading axis. A neovolcanic ridge (NVR) is formed where the volcanic features merge along-axis to form a relatively continuous constructional ridge within the inner valley floor. The NVZ will

often, but not always, lie along the crest of the NVR. Flanking marginal basins often occur either side of the NVR separating it from the inner valley walls.

1.1.4 The ridge flanks

Beyond the outer walls of the axial valley, the flanking topography of the rift mountains is rough and faulted, but becomes gradually smoothed by increasing sediment cover. Away from the axial valley the depth of the ocean floor and the inverse of the heat flow vary with the square-root of age until at ages greater than about 60Ma. there is a departure from the simple age-depth correlation and the depth decay becomes exponential towards a constant asymptotic value. These relations are consistent with the simple cooling of a plate with a heat flux to the base of the lithosphere preventing it from thickening beyond about 125km (Parsons & Sclater, 1977).

Comprehensive reviews of the volcanic and tectonic processes occurring at mid-ocean ridges are found in Sempéré & Macdonald (1987), Searle (1992), Phipps Morgan (1991), Klein (1991) and Smith & Cann (1993).

1.2 Observations of segmentation.

1.2.1 First order segmentation

The limited resolution of the widely spaced profiles available in the 1960s and 1970s initially gave rise to the view that mid-ocean ridges were essentially two dimensional linear structures, interrupted by first order segmentation in the form of transform faults (Heezen & Tharp, 1965; Wilson, 1965; Menard & Chase, 1970; Purdy et al., 1979). Fracture zones have been traced for thousands of kilometres between the continental margins on either side of the Atlantic (Johnson & Vogt, 1973; Philips & Fleming, 1978; Tucholke & Schouten, 1988) demonstrating the longevity and stability of this first order segmentation. Discontinuities in chemical composition occur across many transforms (Bougault & Treuil, 1980; Sigurdsson, 1981; Langmuir & Bender, 1984; Melson & O'Hearn, 1986; Schilling, 1986) although further work is required to clarify their temporal persistence and the resultant implications for mantle convection and heterogeneity. The style and distribution of transform faults varies with spreading rate, with an increase in the transform spacing as the spreading rate increases. On slow spreading ridges, transforms are found approximately every 200-400km, whereas on intermediate and fast spreading ridges they are spaced at 600-1000km (Sandwell, 1986), while very fast spreading centres (>145mm yr^{-1}) have no transform faults at all (Naar & Hey, 1989).

1.2.2 The transform effect

There is a deepening in the bathymetry by about 2km over several tens of kilometres as large offset transforms such as the Kane are approached (Karson & Dick, 1983; Fox & Gallo, 1984, 1986; Pockalny et al., 1988). The extreme deepening associated with the nodal basin is short-lived (Collette, 1986), but there is a persistence of the effect off-axis.

Whitmarsh & Laughton (1976) suggested that a perturbation of volcanic processes occurs towards the ridge-transform intersection (RTI) and seismic refraction studies have since confirmed the presence of anomalously thin crust (Detrick & Purdy, 1980; Cormier et al., 1984). In particular, layer 3, which is thought to be mostly cumulate, is diminished close to transforms, while layer 2 remains relatively constant (White et al., 1984; Mutter & Detrick, 1984; Minshull et al., 1991; Mutter & Mutter, 1993). The variations in crustal thickness take place within 20-30km of the transform, but very thin crust is found only in narrow strips which usually coincide with the fracture zone valley (Louden et al., 1986; Abrams et al., 1988; Forsyth, 1992).

These observations suggest that there is a reduction in the magma supply toward a transform, with very little ponding of magma in the lower crust to form gabbros. The upper layers of the crust are therefore likely to be emplaced through along-axis dyke injection as has been observed in Icelandic fissure swarms (Björnsson et al., 1977; Sigurdsson & Sparks, 1978; Brandsdottir & Einarsson, 1979; Einarsson & Brandsdottir, 1980).

Petrological effects observed in lavas erupted near transforms include cooler magmatic temperatures, a wider range of compositions, higher pressure fractionation and slightly smaller extents of melting (Hekinian & Thompson, 1976; Perfit et al., 1983; Bender et al. 1984; Langmuir & Bender, 1984). These systematic geochemical and geophysical changes associated with the proximity of a transform are known as the transform fault effect (TFE). Models explaining the TFE all predict a correlation between the magnitude of the edge effect and the age contrast of the plates juxtaposed at the RTI. Although a rough correlation exists between the maximum depth of a transform valley and the offset of the transform (Fox & Gallo, 1986), the geochemical TFE does not comply with this prediction (Langmuir & Bender, 1984; Le Roex et al., 1989).

1.2.3 Non-transform offsets

With the onset of higher resolution studies, smaller scales of segmentation became apparent. In the Atlantic, the discovery of zero offset transforms, where crustal thinning persists, started to switch the focus away from cold edge effects to

segmentation which involved individual spreading cells (Schouten & White, 1980; Schouten & Klitgord, 1982). A whole range of different non-transform offsets were classified on intermediate and fast spreading ridges with variations in morphology depending primarily on the size of the offset and the spreading rate of the ridge (see Macdonald et al. [1988] for a review). On the East Pacific Rise (EPR), the smallest form of discontinuity is the DEVAL (deviation from axial linearity) where there is a kink in the ridge axis without a loss of morphologic continuity. The discovery of magmatic edge effects at DEVALS, where tectonic 'cold edges' and depth anomalies are absent, has highlighted the dominance of along-axis systematics of upwelling, melt segregation and distribution over the thermal effect of a cold plate in causing the petrological manifestations of segmentation (Langmuir et al., 1986).

The full extent of segmentation of the Mid-Atlantic Ridge was first recognised during extensive surveys using multibeam swath mapping with SeaBeam (Sempéré et al., 1990; Grindlay et al., 1992), combined with gravity and magnetics (Kuo & Forsyth, 1988; Lin et al., 1990; Detrick et al., 1991, 1992; Deplus et al., 1992). The three dimensional variations were found to be more pronounced than those observed in the Pacific. A second order (non-transform) segmentation is defined by negative mantle Bouguer anomalies (of about 40 mGals) which tend to coincide with bathymetric swells at intervals of 50km to 100km along the ridge crest. Along strike variations in crustal thickness (thinner crust towards the ends of the segment) are thought to dominate over mantle density variations in contributing to these gravity anomalies (Lin & Phipps Morgan, 1992; Rabinowicz et al., 1993).

Microearthquake studies along the ridge crest have also contributed information on crustal structure. Kong et al. (1992) showed that there is a strong correlation between maximum hypocentral depths, along-axis velocity structure and ridge axis bathymetry. The shallowest sections of a ridge segment are underlain by hotter weaker crust, while the ends of a segment have a stronger more brittle lithosphere, implying that the magmatic heat input shapes the lithosphere thickness along the spreading centre. The fault pattern has also been observed to change along the length of second order segments. At the segment centres, the median valley bounding faults are long, linear, small-throw structures while towards the ends of the segments the faults have larger throws, are shorter in length, often curved and the abyssal hills are wider spaced. This suggests that amagmatic extension is also contributing to the crustal thinning near discontinuities (Shaw, 1992; Shaw & Lin, 1993).

The different sizes of discontinuity in the slow spreading North Atlantic have been characterised by Sempéré et al. (1993) while Carbotte et al. (1991) described the features of segmentation from the south MAR which falls in a transitional range

between slow and intermediate spreading rates. Second order discontinuities correspond to spatial offsets of 15-30 km and age offsets of 1-3 Ma. The associated depth anomalies are a couple of hundred metres and the offset is usually associated with minor changes (<10°) in the strike of the NVZ. The largest second order offsets have many features akin to transforms (such as basins on the inside corner). At slow spreading rates, the rigid plates at transforms constrain the shear into a narrow zone; as the age contrast between the segments decreases, the shear is distributed throughout discordant zones which correspond to along-axis depth lows. In the south Atlantic there is a temporal transition from the stable Moore transform to an oblique-trending second order discontinuity. This is accompanied by a period of rapid small-scale rift propagation which may be associated with the reduced age contrast in the lithosphere across the discontinuity (Carbotte et al., op. cit.). When the offset is greater than the width of the rift valley, but not large enough for the transitional transform morphology to develop, there is often a fault-bounded high separating the two rift valleys.

Off-axis magnetic anomalies, gravity and bathymetric traces left by non-transform discontinuities do not follow small circles about the pole of opening of the two plates (Macdonald et al., 1988). Instead they provide a record of the evolution of second-order segmentation, which is commonly characterised by along-axis migrations and a limited life span compared to the relative stability of nearby transforms (Sempéré et al., 1993; Carbotte et al., 1991). Studies out to 10Ma have established that there is temporal variation in second order segment length (Rommevaux et al., 1994; Gente et al., 1995), with V-shaped basins tracing the growth of some segments at the expense of others. Small offset discontinuities can be seen to initiate and diminish and adjacent segments often show independent histories in terms of the sense and degree of asymmetric spreading which results in changing offset lengths (Carbotte et al., op. cit.). However, in some areas (e.g. south of the Atlantis transform) more stable mantle Bouguer anomalies, which form linear features off-axis, show that focused upwelling has been maintained in approximately the same position for 10Ma (Sempéré et al., 1995).

Third order discontinuities are similar in many respects to second order discontinuities except that they do not have recognisable off-axis traces, which suggests that they may either be short lived features or be newly forming second order discontinuities. They have smaller lateral offsets (<10km) and small reorientations of the NVZ (<5°) which sometimes coincide with abrupt breaks or small horizontal deviations in the rift valley walls. For many third order discontinuities the offset is smaller than the width of the rift valley and is accommodated by extensional relay zones and/or linear volcanic constructions parallel or subparallel to the spreading axis. Fourth order discontinuities are minor offsets of the NVZ (<4km) which do not disrupt the continuity of the valley,

but may be related to small changes in the orientation of the NVZ (<10°). They have small (<200m) along-axis depth anomalies which bound short-wavelength undulations of the spreading centre corresponding to gaps between individual volcanoes or strings of volcanoes.

Sempéré et al. (1993) divide the spectrum of rift valley morphologies observed in the Kane-Atlantis transect into two primary groups. The first is characterised by a narrow, deep rift valley with a V-shaped cross-sectional profile and an hourglass morphology in plan view. The group 2 segments have a wide inner valley, with a U-shaped cross-sectional profile and a deep inner floor. The group 1 segments are associated with sharp, pronounced mantle Bouguer anomalies, thought to indicate strong focusing of the mantle upwelling and/or along-axis crustal variations. The gravity data obtained so far on the group 2 segments suggest that there are no well-defined mantle Bouguer anomalies, suggesting in turn that the along-axis variations in mantle upwelling and/or crustal structure are not so strongly focused.

These two end member segment morphologies have been interpreted in two ways. The first interpretation was in terms of a cyclic evolutionary model in which phases dominated by tectonism and volcanism alternate with time (Ballard & Van Andel, 1977; Karson et al., 1987; Eberhart et al., 1988). Sempéré et al. (1993) have made the alternative suggestion that the bimodal distribution of segment morphology represents longer term distinct types which reflect differences in the flow patterns, volume and temporal continuity of magmatic upwelling on a segment scale.

1.2.4 Variations in rift valley asymmetry

Across-axis variations in rift valley asymmetry occur along the length of segments, which are more symmetrical near their centres but develop a marked asymmetry approaching discontinuities. The inside corners (on the active transform side) are consistently more elevated than the non-active outside corners (Tucholke & Lin, 1994). The degree of asymmetry in inside/outside corner elevation correlates with the rift valley relief, but not with the magnitude of the offset or the spreading rate (Severinghaus & Macdonald, 1988). At RTIs, the formation of the nodal basin on the inside corner results in a much greater change in relief over the wall of the inside corner than that of the outside corner so the valley at an RTI is highly asymmetric. Positive residual gravity anomaly spikes, which have amplitudes of up to 20 mGal, often coincide with the major fault scarps across the inside corner suggesting that the crust is thinned by normal faulting (Escartin & Lin, 1995). The positive gravity spikes tend to be regularly spaced across-axis, consistent with the presence of successive large-offset, normal faults that originate episodically at the inside corners. The gravity peaks are statistically larger at transforms compared to non-transform offsets

indicating that the length of the ridge offset and its tectonic style may have a control on the amount of crustal thinning which can take place at the inside corner of the active discontinuity.

Serpentinites and lower crustal lithologies are more commonly sampled from the walls of inside corners than outside corners (Karson & Dick, 1983; Tucholke & Lin, op.cit.) suggesting that extreme thinning may be concentrated on the inside corner. This has been attributed to low-angle detachment faults that dip from the inside corner beneath the axis during phases of amagmatic extension, thus allowing the asymmetry to develop (Brown & Karson, 1988; Karson, 1990).

The elevation of the inside corner high tends to be greater than the normal crust age-depth predicted by Parsons and Sclater (1977), but within a few million years it can subside to more normal depths (Tucholke & Schouten, 1988; Severinghaus & Macdonald, 1988). There are also some cases where the crust maintains this anomalous elevation for tens of millions of years forming a transverse ridge adjacent to the transform (Collette, 1986). Gravity studies over transverse ridges (Robb & Kane, 1975; Louden & Forsyth, 1982) have shown that they are not isostatically compensated, so there is an element of dynamic, but non-buoyant support. Hence, there is a dynamic component causing inside corner uplift which may or may not be removed off-axis, but there may also be other non-dynamic mechanisms which contribute.

1.2.5 Crustal magma chambers

Seismic experiments on the East Pacific Rise have imaged a bright crustal reflector which coincides with a sharp interface between high crustal velocities above and low velocities below (Detrick et al., 1987; Harding et al., 1989; Vera et al., 1990). This is interpreted as a crustal magma chamber, 1-2 km deep, with typical across-strike widths of 1-1.5 km (Kent et al., 1990). The axial low velocity zone is roughly 6km wide, extends down to the Moho and is consistent with mafic or ultramafic rocks containing a small (<3%) melt-fraction (Burnett et al., 1989; Caress et al., 1992). In contrast seismic reflection studies on the Mid-Atlantic Ridge show no evidence for magma chamber reflectors suggesting that they must be transient, discontinuous features (Detrick et al., 1990). However, along-axis variations in velocity structure suggest there have been recent intrusions in certain areas, with generally more intrusion towards the segment centre (Kong et al., 1992).

1.3 Segmentation models.

1.3.1 Basic concepts

1.3.1.1 Magmatic or lithospheric origin

An ongoing and as yet unresolved theme of mid-ocean ridge research is whether segmentation has a magmatic or lithospheric origin. In models which advocate a magmatic origin, segmentation arises from the three dimensional nature of mantle flow and/or melt migration. Alternatively in tectonically-controlled models segmentation may primarily be a consequence of the way the lithosphere breaks under extensional stress. In this second scenario along-axis variations in mantle upwelling are a consequence, not a cause, of the plate boundary configuration. This includes the perturbation of mantle flow and the thermal regime by the juxtaposition of the 'cold edge' of an older plate against the truncated ridge axis. I will start in section 1.3.2 by discussing magmatic controls on segmentation and in section 1.3.5 I come to possible lithospheric causes.

1.3.1.2 Focused upwelling verses focused melt delivery

In magmatic models, the decrease in crustal thickness towards the ends of both first and second order segments requires a reduction in melt delivery towards the ends of a segment. This has been explained by two end member mechanisms of melt migration:

1) *focused mantle upwelling* along-axis which causes corresponding variations in the extent of decompression melting. It is the mantle flow which transports the melt from the large region of upwelling to the narrow region of crustal formation at the axis;

2) *focused melt migration* towards the ridge axis causes the main variations in crustal structure. Melt is generated in a broad region below the ridge as the mantle itself upwells relatively uniformly along-axis.

The end-member models of focused upwelling and focused melt delivery can be discriminated by the variations in the degree of partial mantle melting observed along the segment. The latter produces a uniform melting signature along-axis while the former should show a decrease in extent of melting towards the ends of the segment. One objective of this thesis is to test these two end-member models.

1.3.1.3 Central injection verses multiple injection

The spreading cell model, originally conceived by Schouten and Klitgord (1982) to describe transform-bounded ridge segments, has been adapted to explain second order segmentation. The spreading cell model proposes that magmatic injection centres are focused at regular spaces along the ridge axis, corresponding to the along-axis bathymetric highs. Within each individual ridge segment, the magma injection could

follow two end-member models: a single central injection point or a multiple central injection. Figure 1.2 illustrates the differences between these two model concepts.

For a single central injection (figure 1.2b), magma moves out from a single central magma chamber by lateral transport (probably dyke injection), along the ridge in a manner analogous to the observed rift eruptions in Iceland (Sigurdsson & Sparks, 1978). This idea has received support from bathymetric studies (Francheteau & Ballard, 1983), from the location of hydrothermal fields (Francheteau & Ballard, op. cit.; Crane, 1985), from the interpretation of multi-channel seismic results (Mutter, 1985) and from theoretical consideration of potential Rayleigh-Taylor instabilities during melt production beneath ocean ridges (Whitehead et al., 1984; Crane, op. cit., Schouten et al., 1985). In its simplest form, the central injection model predicts that the temperature of eruption of lavas should decrease regularly from a maximum at the bathymetric high at the centre of a spreading cell to lower temperatures at the boundaries (Thompson et al., 1985). The single open system magma chamber in the centre of the segment homogenises melt packets through magma chamber processes. With the exception of fractionation, there should be little geochemical variation within a segment, but subtle variations between segments may be preserved.

A contrasting, but not mutually exclusive idea, is that magma supply is not confined to a single centre for each segment, but that there are multiple injection centres distributed along the ridge (figure 1.2a). Less melt is injected near ridge offsets because of edge effects, which lead locally to cooler temperatures and possibly lower extents of melting (Bender et al., 1984; Perfit et al., 1983; Natland, 1980, Langmuir & Bender, 1984). The variable multiple injection model predicts less systematic long wavelength variations in temperature and chemistry along-axis, except in the vicinity of large offsets, where the cold edge effect leads to lower temperature lavas. At each injection site, the melt packets may evolve with minimal along-axis homogenisation, so that eruption events maintain some evidence of their distinct petrogenetic histories. This may include variations in fractionation, partial melting and small scale mantle heterogeneities, leading to greater diversity in geochemistry within a single segment than in the central injection model.

The remainder of section 1.3 goes into further detail about the wide range of physical and numerical models and the various underlying factors thought to control the different scales of ridge segmentation.

Segmentation Models

(a) Variable injection into the crust

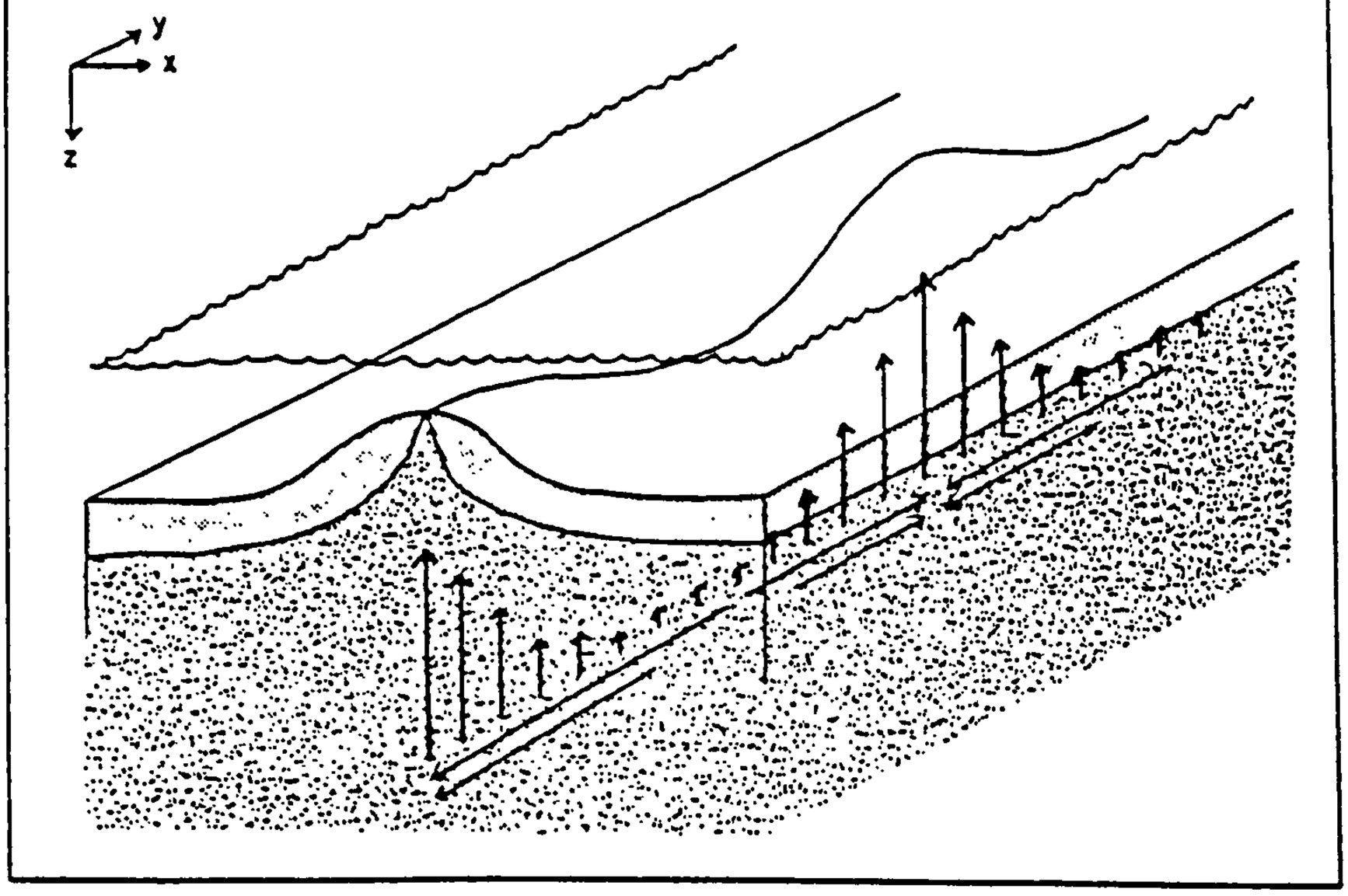

(b) Focusing into open system magma chambers

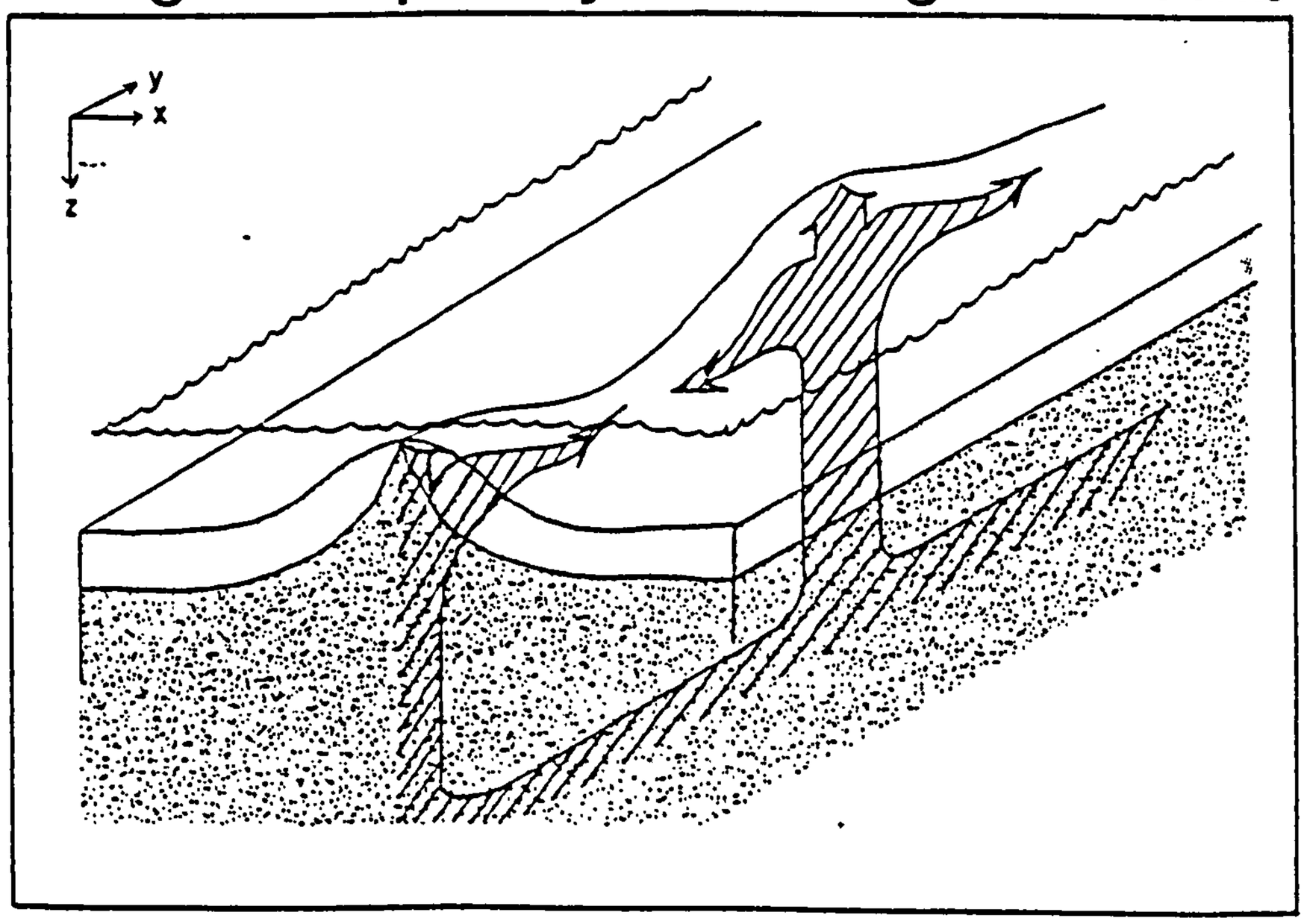

Figure 1.2 Sketch to illustrate the differences between a central injection model and a multiple injection model.

1.3.2 Magmatic controls on segmentation

1.3.2.1 Buoyancy forces -2D models

Buoyancy forces resulting from density differences can have important three dimensional effects on mantle flow beneath spreading centres. Three mechanisms have been proposed for creating buoyancy within the mantle. Firstly, thermal expansion was recognised early on as being a source of density gradients in the mantle (McKenzie & Richter, 1976; Parsons & Richter, 1981). Secondly, compositional buoyancy is a result of the low density of depleted mantle relative to primitive lherzolite and is enhanced if there is a high melt-filled porosity in the upwelling region. A number of two dimensional numerical models have investigated the modification of plate driven passive upwelling by compositional buoyancy (Scott & Stevenson, 1989; Sotin & Parmentier, 1989; Cordery & Phipps Morgan, 1992). These show a focusing of the mantle flow and the development of a strongly stratified mantle density structure with the most depleted mantle lying directly beneath the crust. The density stratification prevents convective overturn near the ridge axis and the total amount of upwelling and melting is limited by the rate at which plate spreading can carry away the previously melted mantle.

Thirdly, the importance of buoyancy created by melt-filled porosity has been the subject of some debate. The distribution and degree of melt present also has an effect on the thermal regime and the mantle viscosity. If melt is efficiently removed then the influence of the partial melt on the overall flow will be relatively small. Conversely, if the melt-fraction becomes greater than 5%, it is thought to be a significant source of buoyancy forces (Scott & Stevenson, 1989). The reduction in viscosity which accompanies the increase in the melt-fraction (Cooper & Kohlstedt, 1984) may result in an element of positive feedback modelled in a 2D scenario by Buck & Su (1989). Melt accumulation in the high production region lowers the viscosity and increases the buoyancy, leading to more concentrated upwelling which, in turn, will tend to enhance the accumulation. This mechanism can cause extreme focusing of the upwelling mantle. However there is much evidence to suggest that melt is very efficiently removed so the high porosities required for this model would not occur. Melt can segregate easily because of the interconnectivity of the melt along grain boundaries at low porosities (<1%) (Cooper & Kohlstedt, 1986; Daines & Richter, 1989) and its relative buoyancy with respect to the matrix. This results in efficient extraction by porous flow (McKenzie, 1984, 1985a,b; Ribe, 1985a,b; Scott & Stevenson, 1986; Ahern & Turcotte, 1979). Trace element studies on abyssal peridotites have demonstrated that they are residues of near fractional melting rather

than batch melting (Johnson et al., 1990) which is further evidence that the melt is rapidly segregated and is not able to reequilibrate with mantle assemblages.

1.3.2.2 Buoyant flow models with no imposed segmentation

While two dimensional models are useful in assessing the relative importance of buoyancy forces, three dimensional models are required to investigate the issue of segmentation. Models which assume a continuous ridge axis can be used to investigate whether the crustal thickness variations seen along segments and the offsets themselves can develop as a result of mantle flow patterns rather than as a response to a predefined lithospheric structure. Early laboratory experiments looked at the effect on buoyant thermal convection of varying the mode of heat supply, in a constant viscosity fluid under the influence of a moving upper plate (Richter & Parsons, 1975). When heating is from below, the flow stabilises after a time interval which corresponds to less than 10Ma with axis-parallel circulation and convective rolls aligned perpendicular to the spreading axis. When the heat source is uniformly distributed throughout the fluid an upper cold boundary layer develops, but there is no hot boundary layer at the base. This results in the formation of a similar flow pattern to that described above, but with strongly focused downwelling regions separated by more diffuse planar upwellings. The cylindrical convective rolls tend to have an aspect ratio of one in their transverse section. Thus if the distance between downwelling regions corresponds to the length of the segmentation along-axis, the depth of the convecting layer would be expected to be half the segment length.

Rabinowicz et al. (1993) produced numerical models of the experiments of Richter & Parsons (1975), but introduced a low viscosity upper layer to the mantle. When heated from below, the plate-forced flow becomes concentrated in the low viscosity layer which causes a decoupling between the plate and the higher viscosity mantle below. This results in an increase in the time required for longitudinal convective rolls to stabilise, to the extent that they are unlikely to develop beneath oceanic plates. Instead, a complex, time-varying, three dimensional flow of sheets and jets is likely to be present. As the plates are drifting and the ridges are not necessarily located over ascending convective plumes it seems likely that ridge segmentation is not related to the large scale convection induced by heat sources within the whole mantle (Houseman & McKenzie, 1982), but to transient convective circulation within the low viscosity zone.

When the flow is driven by the buoyancy forces within the low viscosity layer or by transient cooling of its upper interface, longitudinal rolls develop which are confined within this layer. However the rolls tend to develop at large distances from the axis unless there is a drastic viscosity contrast between the two layers of up to 3 orders of

magnitude. Then the mantle upwelling becomes segmented along the ridge axis, and the flow character becomes increasingly three dimensional with higher viscosity contrasts. Spreading rate can also influence the distance from the axis that the rolls initiate, with sub-axis rolls more likely to form at low spreading rates (Sparks & Parmentier, 1990). Rising plumes in the mantle below the low viscosity layer tend to prevent the initiation of this separate upper layer convective flow. This may be one explanation why the mantle Bouguer anomaly described by Searle et al. (1994) below the plume-influenced Reykjanes Ridge is so smooth compared to rest of the Mid-Atlantic Ridge. Thus Rabinowicz et al. (op. cit.) propose that variations in temperature and viscosity structure are responsible for the contrasting morphologies of fast and slow spreading ridges and that segmentation along ridge crests requires both strong viscosity contrasts and a lack of deep convective flow.

Rouzo et al. (1995) developed this model further by investigating the shear forces induced by the coupling of the buoyant flow and the diverging plates, but using a 60km thick constant viscosity model rather than a layered viscosity. The model starts from a situation of buoyant convective flow which produces randomly oriented rolls. The symmetric shear of the diverging plates acts to orient the convective rolls, but a degree of asymmetry is maintained in the convection cells because of the slow adjustment to the boundary conditions. This, in turn, produces an asymmetric stress field in the lithosphere which is calculated to be great enough to favour asymmetric breaking of the axial valley lithosphere. This accounts for the asymmetric spreading commonly observed to occur by both asymmetric tectonism on the valley wall faults and accretion which is not focused in the centre of the rift valley (Macdonald & Luyendyk, 1977; Karson & Dick, 1983; Karson, 1990). The ridge axis will tend to migrate towards the tensile stress maxima and so develops into separate segments (~50-150km long) with offsets of 10-100km. The temporal evolution of the flow also accounts for the along-axis propagation and shortening of some ridge segments. The geometry and evolution of the segmentation is strongly dependent on the initial convective field. When a ridge is initiated oblique to the spreading direction, the convective flow induces segmentation with offsets having the same sense, creating a pattern that is very similar to large stretches of the MAR. If this model is correct it implies that the dynamics of ridge segmentation is controlled by coupling of the oceanic lithosphere to small scale convection of the low viscosity layer underneath.

Parmentier & Phipps Morgan (1990) produce a 3D numerical model of the modification of 2D passive flow by compositional rather than thermal buoyancy forces, as compositional buoyancy is thought to be the more important of the two (Sotin & Parmentier, 1989). They found that given the same temperature and viscosity conditions, the spreading rate can be an important factor in determining whether the

flow has a two dimensional or three dimensional structure. At slow spreading rates the buoyancy forces are more important, resulting in a transition from an initial 2D structure to a 3D mantle flow with along-axis variations in upwelling and melting which would produce quasi-stable zero offset discontinuities. At fast spreading rates, the two dimensional structure does not undergo this transition. Jha et al. (1994) develop this model to include a degree of melt-retention buoyancy and introduce a viscosity-layered halfspace. This produces multiscalar convection with segmentation on two wavelengths. The longer wavelength is intrinsic to the melting region (at about three times the maximum depth of melting) and may correspond to the spacing of major fracture zones. The shorter wavelength variations in upwelling, comparable to the asthenosphere thickness, are likely to correspond to the spacing between gravity lows which define second order segmentation. The element of melt-retention buoyancy produces very focused upwelling at low spreading rates which would require a significant amount of along-axis transport to produce the variations in crustal thickness which are observed.

Sparks & Parmentier (1990) have included a combination of compositional and thermal buoyancy forces and as expected, the resulting flow is a combination of that seen from the models described above. The compositional density stratification suppresses the formation of thermally driven rolls near the axis, and when it is large causes the thermal rolls to become unstable, leading to time-dependent behaviour.

1.3.2.3 Fluid mechanical analysis of gravitational instabilities

The first explanations proposed for second order segmentation invoked gravitational Rayleigh-Taylor instabilities. These initiate in a low-viscosity, melt-rich region that underlies the spreading axis and produce regularly spaced protrusions of the partially molten zone. Laboratory analogues have shown how protrusions of less viscous material grow and eventually ascend as a spherical pocket of fluid fed by a conduit (Whitehead et al., 1984; Crane, 1985; Schouten et al., 1985). The upwelling conduits are found to consist of solitary waves (Whitehead, 1986) which are thought to be a mechanism of magma ascent during porous flow of compacting mantle (Scott & Stevenson, 1986). This provides a mechanism for the strong focusing of the melt delivery during segregation from the matrix, which results in pooling to form crustal magma chambers in the centres of segments. This lateral flow of melt towards the centre of individual ridge segments would inhibit the mixing of melt between ridge segments, but enhance the extent of mixing within a single segment. Consequently this model predicts that any heterogeneities in the mantle sampled beneath each segment may be preserved as variations in the average geochemistry of lavas between adjacent segments.

The major problem with the acceptability of this model is that there is little direct evidence for the existence of a continuous layer which is sufficiently rich in melt under ridge systems. The relatively high frequency of fracture zones found in slow spreading ridges will also tend to disrupt the continuity and thickness of the instability layer.

1.3.2.4 Melt migration and extraction at the ridge axis

Although there is considerable evidence that melt migration is rapid, it is important to understand how melt migrates as the 3D migration pattern may have a strong influence on the resulting crustal structure. However, little has yet been resolved in the quantification of the horizontal component of melt migration. Many models assume that melt delivery is entirely controlled by the focusing of mantle upwelling (e.g. Scott & Stevenson, 1989; Shen & Forsyth, 1992; Sparks et al., 1993). These porous flow models, which neglect compaction, result in melt migration in the vertical plane only, so crustal formation can never become more focused than the underlying distribution in extent of mantle melting. More sophisticated assumptions about the paths of melt migration will lead to different crustal distributions, but as the mechanism is not well understood it is difficult to quantify.

There is already considerable evidence that melt migration is non-vertical in the very narrow zone of crustal accretion which occurs at the ridge axis. There are two end member scenarios which can explain this observation. Either the melting must occur within a broad region beneath the ridge crest and be focused by melt migration, or the focusing is done by mantle upwelling. Although compositional buoyancy forces, thermal buoyancy forces and variable viscosity will cause a degree of focusing, only models which allow the feedback effect of melt-retention buoyancy can produce the extreme focusing required to explain the narrow NVZ (Rabinowicz et al., 1987; Buck & Su, 1989).

The pressure gradients induced by asthenosphic corner flow of a viscously deforming matrix will tend to produce some focusing of melt flow lines, but the effect is not very strong unless unreasonably high mantle viscosities are used (Spiegelman & McKenzie, 1987). A much stronger effect on the melt flow is produced by the anisotropic permeability variations resulting from the finite strain of mantle material in the upwelling region (Phipps Morgan, 1987). Anisotropic fabrics have been observed to converge in a three dimensional upwelling pattern in a number of ophiolites (Nicolas et al., 1988; Nicolas & Boudier, 1995). This convergence has been interpreted as a record of diapirs with sub-crustal and sometimes intercrustal flow away from the centres of upwelling, although Phipps Morgan (1991) suggests that the fabrics may just be the root zones of sub-axial volcanoes. Sparks & Parmentier (1991)

propose that the presence of a high porosity boundary layer beneath an impermeable cap of cooler solid mantle provides a mechanism for focusing the melt flow. Gravity tends to drive the melt in this layer towards the ridge axis thus providing another mechanism for the focusing of melt into a narrow region. Until a consensus on melt migration is reached it is impossible to rigorously relate the degree of partial melting inferred from basalt composition to the spatial distribution of melting processes occurring in the mantle below.

1.3.3 Perturbation of mantle flow by imposed segmentation

1.3.3.1 Passive mantle flow with transform segmentation imposed

None of the 3D models described above have a transform segmentation imposed as boundary conditions, yet variations in crustal thickness can also result from the effect on mantle flow of an imposed plate boundary. At a RTI, the juxtaposition of a colder, thick edge of lithosphere against the truncated ridge axis is thought to have implications with regard to both the thermal regime and the 3D geometry of mantle upwelling (Fox et al., 1980; Fox & Gallo, 1984). The deepening of the rift valley toward the transform was first explained as a dynamic effect resulting from viscous flow (Sleep & Biehler, 1970; Parmentier & Forsyth, 1985). However, the persistence of this deepening off-axis is an indication that some process other than dynamic viscous head loss is operating. The first quantitative models of passive mantle upwelling with a constant mantle viscosity found that upper mantle conductive cooling from the 'cold edge' is only a very weak factor and suggested that the perturbation of mantle upwelling and melt migration are stronger controls (Forsyth & Wilson, 1984; Phipps Morgan & Forsyth, 1988). Passive upwelling models with temperature and pressure dependent viscosities (Shen & Forsyth, 1992) or a thickening rigid lithosphere (Blackman & Forsyth, 1993) produce a stronger, more focused TFE with greater temperature gradients near the transform induced by the stronger, narrower upwelling zone. These models are more consistent with the scale of the geophysical observations of crustal thickness variations near transforms.

1.3.3.2 Three dimensional buoyant flow with transform segmentation imposed

Sparks et al. (1993) modelled the three dimensional effects of thermal and compositional buoyancy on convection beneath a thermally defined rigid lithosphere with a transform segmented plate boundary imposed. For reasons discussed earlier (in section 1.3.2.1) they neglect the buoyancy forces due to the presence of melt. They use a uniform low-viscosity asthenosphere to which convection is confined, overlying an upper mantle half-space with much higher viscosity (100 times more viscous than the low viscosity layer) that does not convect, but flows in response to plate spreading. The asthenospheric layer is 200km thick at the axis, but decreases in thickness off-

axis as conductive cooling penetrates deeper into the mantle and depleted mantle becomes locked into the lithosphere. They found that the buoyant flow amplifies the along-axis variations seen in the 3D passive models with reduced upwelling occurring near the transform. The relative magnitudes of the buoyant and plate-driven components of mantle flow are controlled by the spreading rate and the asthenospheric viscosity. The mantle flow pattern becomes three dimensional as the buoyant contribution becomes greater at lower spreading rates. This is an explanation for the fundamental differences in morphology between fast and slow spreading ridges.

As in the two dimensional models, the density stratification produced as a result of compositional buoyancy prevents convective overturn near the ridge axis, but thermal buoyancy drives convective rolls away from the ridge crest. These align perpendicular to the ridge crest with a preferred along-axis wavelength of twice the thickness of the asthenosphere. The distance from the axis that the rolls form increases as spreading rate, viscosity and amount of melting in the garnet field all increase. Hence slow spreading ridges are more likely to have convective rolls that form near or even under the axis. The position and stability of the rolls are also influenced by the temperature gradients which develop as a result of the transforms. In most cases the geometry of the lithospheric segmentation prevents a stable configuration of the rolls in which case time-dependent flow develops. In a limited number of special cases a stable roll geometry develops. One of these occurs when the transform spacing is four times the asthenosphere thickness. Then there is upwelling in the centre of the segment and the downwelling of the rolls is aligned with the transform.

The buoyant upwelling creates along-axis variations in bathymetry and partial melting that are not just confined to the region near the transform, but produce predicted mantle Bouguer anomalies which are similar to those observed at slow spreading rates. Neglecting along-axis melt migration, the along-axis gradients in temperature and melting are predicted to result in crustal thinning by as much as 3-5km towards a transform which results in isostatic deepening by 500-1500m and gives mantle Bouguer anomalies of 30-100 mGal. These modelled values fall within the range of observed anomalies at different spreading rates as recorded by Lin & Phipps Morgan (1992).

A similar 3D model by Rabinowicz et al. (1993) also includes a low viscosity layer above a high viscosity upper mantle, but the mantle flow due to plate motion is confined to the upper 200m and only thermal buoyancy forces are considered. Transform segmentation is imposed by upper boundary conditions which do not include a thickening lithosphere. An important feature of this model that differs from that of Sparks et al. (1993) is the strong localised downwelling that occurs beneath the

transforms. It also predicts a toroidal mantle flow pattern that shifts the plumes away from the ridge crests creating an asymmetry about the axis, which would lead to a greater tendency for ridge jumps to occur. This flow pattern has implications for the formation of the inside corner high as will be discussed later. Sparks et al. (op. cit.) suggest that these differences occur because of the inclusion of compositional buoyancy which suppresses downwelling near the axis in their models.

1.3.4 Models explaining rift valley topography and asymmetry across-axis.

1.3.4.1 Rift valley formation

There have been several hypotheses proposed to explain the formation of a median valley at slow spreading ridges. The first was a viscous-flow induced pressure drop caused by the asthenosphere ascending up a narrow sub-ridge conduit formed by the lithosphere (Sleep, 1969; Lachenbruch, 1973; Sleep & Rosendahl, 1979). However this model has been increasingly questioned in recent years because the predicted near ridge thermal structure would not be able to generate the variations in lithospheric strength required to form such a conduit, and also because such a dynamic mechanism does not account for the existence of fossil median valley topography which is preserved on abandoned spreading centres (Phipps Morgan et al., 1987; Lin & Parmentier, 1990; Chen & Morgan, 1990a).

Tapponnier & Francheteau (1978) originally suggested that necking caused by extension of the relatively strong, slow spreading lithosphere may be the mechanism that generates axial topography. This idea has been refined by Phipps Morgan et al. (1987) who showed that the median valley could be formed by moments due to lithospheric stress in the thickening plate. Lin & Parmentier (1990) develop a similar model of extension of an idealised elastic/plastic plate while Chen & Morgan (1990a & b) introduce a strong degree of coupling between the brittle plate and the ductile mantle flow beneath. Although there may be minor problems with some of these models, the extension of a lithosphere which is at least several kilometres thicker at a slow spreading ridge than fast spreading ones seems to account for the differences in topography between the two. These models also provide solutions for the aspects of ridge topography which the viscous-head model could not explain. Variations in the magmatic input will control the thermal structure of the lithosphere and the amount of amagmatic extension which is likely to occur. A consequence of this is along-axis variations in faulting style, with large throw faults supported by the strong lithosphere at the ends of the segments and small throw faults at the centre (Shaw & Lin, 1993) There is increasing evidence that the large throw faults at the ends of the segments are low-angle detachments (Karson, 1990; Tucholke & Lin, 1994; Escartín & Lin, 1995).

1.3.4.2 Asymmetry near axial discontinuities

Collette (1986) proposed that the viscous drag exerted by the parting lithosphere on the asthenosphere could cause asymmetry of the flow pattern at the RTI. Numerical models have shown that asymmetric mantle flow can develop as a result of the interaction of a diverging plate and buoyant flow, which in turn can trigger asymmetric lithospheric extension (Rouzo et al., 1995). When a transform boundary is imposed, the active transform segment becomes the favoured location for locally descending currents (Rabinowicz et al., 1993). The convergence of flow lines towards the active transform promotes the development of compressive shear stresses up to several tens of kilometres from the intersection. The lithospheric deformation which results from these compressive stresses will be concentrated in the youngest portions of the plate at the RTI, where they could develop to high enough values to support 1km of uncompensated topography (Rabinowicz et al., op. cit.). This mechanism may explain, at least in part, the enhanced elevation of the inside corner high.

The driving forces which cause the formation of the median valley and the uplift of the ridge flanks, are likely to produce enhanced uplift of the inside corner because of the very low mechanical strength of the active discontinuity (Severinghaus & Macdonald, 1988). The enhanced elevation of the inside corner may partly be a result of serpentinization which will lead either to diapirism or isostatic uplift (Bonatti, 1976). Isostatic rebound of the depressed nodal basin crust, which is predicted to be greater on the inside corner than the outside corner, may also be a contributing factor. Nonlinear viscoelastic rebound can be generated by purely horizontal motion typical of active discontinuities (Bercovici et al., 1992). This can cause inside corner uplift and also maintain the uplift allowing transverse ridges to form.

1.3.5 Lithospheric causes of segmentation

The very close spacing of transforms in the equatorial Atlantic coincides with the dramatic change in the orientation of the continental margin round the west coast of Africa and the east coast of South America (figure 1.1). This, and the persistence of fracture zone traces right across the ocean basin suggests that transform initiation may well have been a Eularian response to the way continental rifting originally occurred (Wilson, 1965). Collette (1974) and Turcotte (1974) suggest that the lateral cooling and contraction of the oceanic lithosphere may, in fact, be the root cause of transform faults and fracture zones. Haxby and Parmentier (1988) propose that fracture zones form in response to bending stresses as opposed to thermal contraction, because there is no segment length dependence on the magnitude of the contraction stresses and hence thermal contraction cannot control the spacing of transform faults.

The role of half-graben development and detachment faulting in creating segmentation as a whole as well as across-axis asymmetry is presently being debated, in the light of observations that continental rifts extend by forming a chain of alternating sense half-grabens (Rosendahl, 1987).

Mutter & Karson (1992) present a radically alternative hypothesis for the origin of segmentation on slow spreading ridges. They highlight the importance of mechanical deformation on crustal formation at slow spreading centres and suggest that segmentation is mechanically controlled by detachment faults and intervening accommodation zones where extensional strain is transferred from one detachment to another. In their model, the mantle upwelling is a consequence not a cause of the plate boundary configuration, affecting only the thermal structure of segments in terms of the local pattern of brittle ductile deformation.

1.3.6 Summary

Crustal thickness variations of the order observed along-axis can be explained by mantle flow models with and without imposed transform segmentation. Although 3D mantle flow models with no imposed lithospheric structure are coming close to mimicking the features observed along ridge crests, there is also a renewed emphasis on the role of half-graben development at slow spreading ridges. The configuration of the initial continental rift almost certainly had a strong influence on the present plate boundary, and especially the position of the large-offset fracture zones. However, the subsequent evolution of these boundaries may have a mantle control. The transient nature of second order segmentation suggests that this is more likely to have its origins in the dynamics of mantle and magmatic processes, and certainly on fast spreading ridges there are very small offset discontinuities which have magmatic edge effects but very little manifestation in the tectonics. However at slow spreading ridges, where tectonic effects are more important, a primary tectonic origin has certainly not been ruled out. An along-axis study of basalt petrogenesis might help to distinguish between melt migration and mantle convection, as mechanisms for causing varying crustal thickness. However, it is always difficult to assess the redistribution of melt within the crust. Ideally such work should be combined with seismic studies, like those carried out on Iceland, to assess the importance of along-axis dyke injection. Future models, which will attempt to evaluate the causes and consequences of ridge segmentation, will certainly benefit from the constraints provided by rigorous, detailed geophysical and petrological observations both on-axis and off-axis.

1.4 The MARNOK study area

The MARNOK area (Mid-Atlantic Ridge North of Kane) is situated on the western intersection of the Mid-Atlantic Ridge with the Kane Fracture Zone at about 24°N and 46°20'W (figure 1.1). It was chosen for a combined geophysical and petrological study of ridge segmentation because there is a large range in offset length and segment style. In addition, the area is relatively simple, having orthogonal spreading and being a sufficient distance from any mantle plume influence. The MARNOK area (figure 1.3) comprises two second order segments to the north of the fracture zone which are separated at 24°22'N by a 3rd order discontinuity corresponding to a right-stepping, ~1km offset of the NVZ. On the basis of their morphology, these two second order segments fall into the different groups defined by Sempéré et al. (1993). The segment adjacent to the transform is a group 1-type while segment 2 to the north is a group 2-type.

1.4.1 The Kane Transform

The Kane Transform is located at ~24°N on the MAR and is a typical long-offset transform, accommodating dextral strike-slip motion of about 30mm yr^{-1} (figure 1.1). It strikes at approximately 098° with a present offset of 150km (Pockalny et al., 1988). The age offset at the western intersection is about 9.5Ma which differs from that at the eastern intersection (11.5Ma) because of asymmetric spreading (Tucholke & Schouten, 1988). At the western intersection, magnetic anomaly picks show that, at present, the half spreading rate is 13mm yr^{-1} to the west, but to the east the half rate varies from 8mm yr^{-1} at the RTI to 13mm yr^{-1} in the north of the area (Hussenoeder et al., *in prep*). Hunter and Kempton *(in press)* discuss new data on the isotopic discontinuity across the Kane Fracture Zone which was first recognised by Machado et al. (1982).

The Kane is well-known in mid-ocean ridge research because the MARK area, at its eastern intersection, is one of the most intensively studied sections of ridge in the Atlantic. The western intersection has been less thoroughly studied, but there is SeaBeam bathymetry coverage of both the transform (Pockalny et al., 1988) and a 50km wide band centring on the ridge crest (Purdy et al., 1990), which reveals the nature of the second order segmentation.

1.4.2 Segment 1: the narrowgate

The segment immediately north of the fracture zone (segment 1) is 57km long, trends ~010°, and has a narrowgate-type morphology, where the V-shaped inner valley narrows as the floor shallows towards a bathymetric saddle point (3950m deep) near 24°06'N (figure 1.3). The rift valley is symmetric at the saddle point, where the

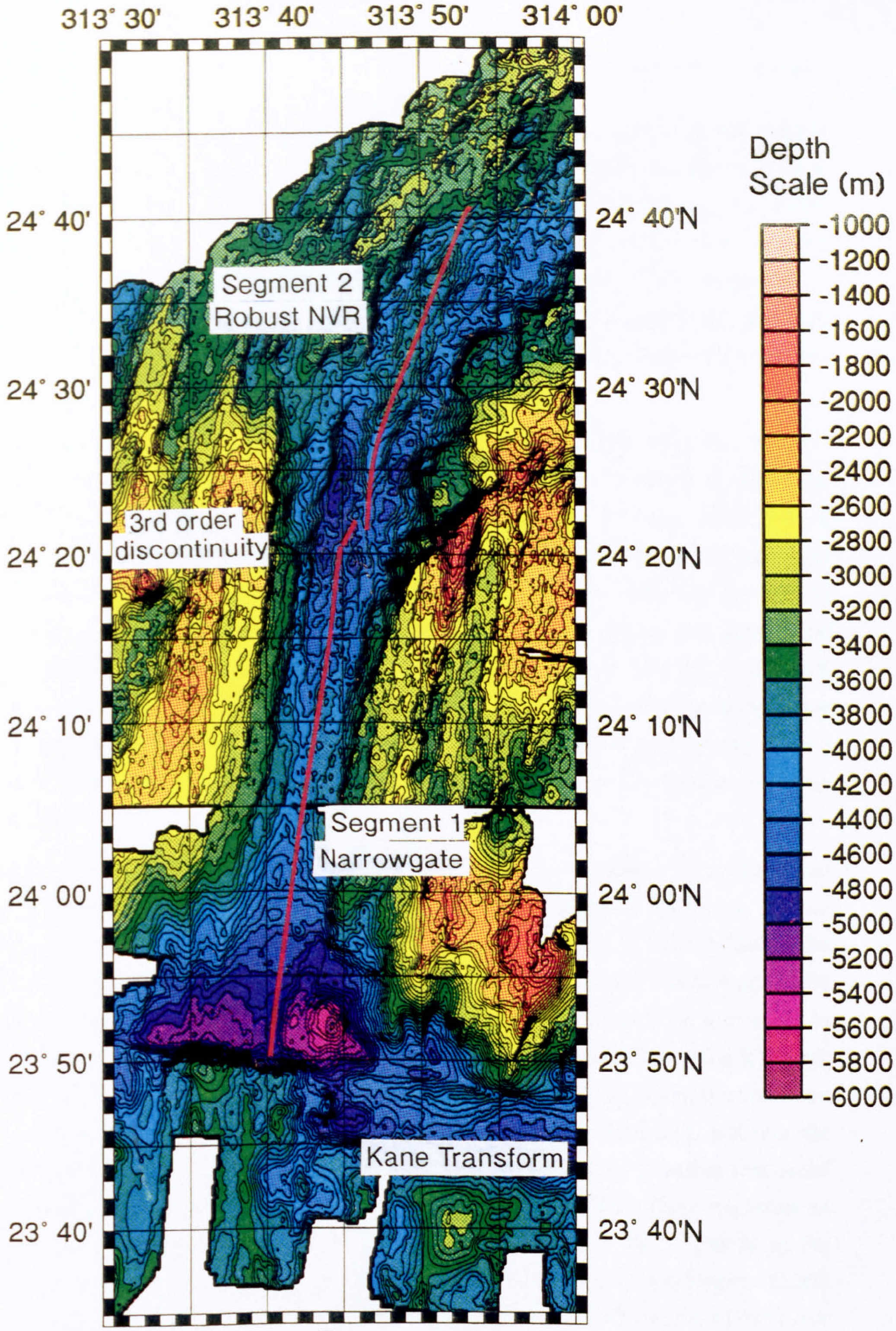

Figure 1.3 Bathymetric map of the MARNOK area (Mid-Atlantic Ridge North of Kane). The area comprises two second order segments to the north of the large offset, dextrally-slipping Kane Transform. These are labelled by continuous red lines running along the strike of the axis. The segments are separated at 24°22'N by a 3rd order discontinuity corresponding to a right-stepping, ~1km non-transform offset of the NVZ. On the basis of their morphology these two second order segments fall into the different groups defined by Sempéré et al. (1993). The segment adjacent to the transform is a group 1 'narrowgate' type while segment 2 has a wide U-shaped valley and a robust neovolcanic ridge. The spreading direction is orthogonal to the strike of the axial valley, except along the northern half of segment 2 which lies within an oblique portion of the MAR.

cumulative tectonic strain is lowest (~10%), but becomes increasingly asymmetric to the north and south (Allerton et al., 1995). As the valley deepens towards the ends of the segment, the relief of the eastern wall increases. At the point of maximum asymmetry near the 24°22'N discontinuity, a strain of ~25% is calculated by Allerton et al. (1995) for an area 20km either side of the ridge axis. This difference in cumulative strain between the centre and ends of segment 1 is probably compensated for by additional magmatic accretion at the segment centre according to the magma budget concept (Harper, 1985).

The strike of the eastern wall swings round slightly from 020° near the 24°22'N discontinuity to about 007°, just south of the narrowgate. To the north of the nodal basin, the strike of the eastern wall becomes approximately N-S and at the RTI it achieves 3km of elevation in an almost continuous slope between the nodal basin and the inside corner high. A submersible study by Zonenshain et al. (1989) up the wall of the inside corner, found outcrops of foliated greenstone after gabbro and greenstone breccia which they interpreted as fault zones spaced at 2.5km intervals, each with ~500m throw. As there is heavy sedimentation and no active mass wasting, they conclude that tectonic activity has ceased on the inside corner and moved to the western wall of the nodal basin, where they speculate that a new inside corner is beginning to grow.

In contrast the western wall of the median valley comprises a number of well-defined terraces, each block being 1km-2.5km wide and having 200m-400m throw. To the north of the narrowgate the strike of these is relatively constant at 012°, while to the south of the narrowgate they deviate to 020°. The throw on the fault terraces gradually diminishes towards the transform and those immediately adjacent to the axis seem to all but die out. This causes a considerable widening of the inner valley at the RTI with a broad basin, 15km wide and somewhat shallower than the nodal basin, occurring on the non-transform side of the NVZ. Karson & Dick (1983) found that, whereas the nodal basin is filled with sediment and rubble, this western basin contains numerous well preserved, variably sedimented coherent pillow flows which have experienced only moderate tectonic disruption, and is thus continuous with the volcanics of the NVZ. The NVZ itself is poorly developed to the south of the narrowgate saddle forming a string of discontinuous edifices (Karson & Dick, 1983), while to the north of the saddle there is a more integrated but still discontinuous ridge with 50m -150m elevation.

1.4.3 Segment 2

Segment 2, defined by Sempéré et al. (1993), stretches from 24°22'N to 24°39'N and is quite a dramatic contrast from segment 1 in terms of the morphology of the NVZ

and the rift valley. This segment is only 35km long (compared with 57km for segment 1) and its northern half lies within an oblique portion of the MAR which trends at 57° from 24°30'N to 25°00'N (45° to the average strike of the ridge between Kane and Atlantis as defined by Argus et al., 1989). With the exception of the RTI area, the inner valley of segment 2 is slightly wider than that of segment 1 and the NVZ takes the form of a robust NVR, 400-600m high, which is continuous for the entire length of the segment. The gross morphology of the NVR is rather like an upturned keel, broadening towards the centre and tapering at the ends, with marginal basins separating the ridge from the inner walls. It reaches its shallowest depth of 3550m towards the northern end of the segment near 24°37'N. The strike of the NVR crest is N-S at its southerly end and bends round to 020° in the north, where it terminates on the older crust of the oblique trending flanks as there is no well developed wall fault at this point.

Preliminary results of Fujimoto et al. (1994) imply that there has been southward propagation of both ridge segments over the past 7-8Ma, as suggested by seafloor topography and magnetic anomalies. This is most clearly apparent in segment 2 where the propagation rate is 1cm yr^{-1}, slightly slower than the half spreading rate. The axial valley corresponding to the southern half of segment 2, between 24°20'N and 24°30'N, is highly asymmetric and on the western flank the faults are continuous with those of segment 1 (Allerton et al., 1995). At 24°24'N, 313°44'E, the axial valley reaches the local deep in a trough which is co-linear with the NVR of segment 1, and approximately corresponds to the maximum elevation on the flanks. North of this, the flanking rift mountains plunge steeply into a row of off-axis basins at about 24°32'N, which probably mark the earlier position of the discontinuity, now 10 minutes further south. If this is the case, then propagation has taken place within the last million years only, that is within the life time of the present inner valley.

A submersible transect at 24°23'N, across the southern tip of the NVR of segment 2, found younger lavas on the central and upper part of ridge outcropping above the older, heavily sedimented flows of the flanks, suggesting that the NVR built up in a relatively symmetrical manner (Zonenshain et al., 1989). The sediment cover on the older flows is greater than 1m thick, suggesting an age of about 100,000 years assuming a sedimentation rate of 1-2cm/1000years (Marks, 1981). However, even the flows on the crest cannot be considered as recent, as the glass is palagonitised, they are covered by a thin iron manganese film and the sediment cover is up to 0.5m thick. An axial fracture 3km long and 100m deep runs along the crest of the ridge and both younger and older basalts are cut by numerous open fissures and fractures. Zonenshain et al. (1989) suggest that eruptions ceased about 10,000 years ago and that this part of the NVR is in a tectonic phase corresponding to a dying magmatic cell. These

submersible observations are perhaps not what would be expected from a recently propagating tip, although the NVR is not so old that the propagation hypothesis is unviable.

The valley wall faulting is further complicated by the right-lateral oblique zone, which opens up the valley on its eastern side and causes the development of two intersecting trends of valley wall fault (figure 1.4). These intersecting faults lead to the uplift of lens-shaped terraces which are rounder on the inside corner (eastern flank) where the strain partitioning is more pronounced and the angle between the two sets of faults is greater. At the southern end of the segment, faults with trends of N-S and 057° intersect on the eastern wall, while towards the centre of the segment a bounding fault appears to curve from 033° to 078° as the oblique character becomes more dominant. On the western wall and flanks, there is also a fault trend of approximately 033° but this is cut by faults striking at 013°, continuous with the trend of the narrowgate segment. Allerton et al. (1995) interpret the oblique cross faults as transfer faults that are a kinematic necessity of the differential extension. The elevation of the flanks adjacent to the oblique section of ridge average about 800m lower than the flanks of segment 1, which may reflect a reduction in the total magma budget over the oblique zone.

1.4.4 Crustal structure

Unfortunately there have been no seismic refraction studies nor published gravity surveys over the MARNOK area to provide information on crustal thickness and structure. Seismic lines have been shot across the Kane transform at the eastern RTI (Purdy & Detrick, 1986; Cormier et al., 1984) and across the eastern end of the fracture zone (Detrick & Purdy, 1980; Cormier et al., op. cit; Abrams et al., 1988). These provide the closest indication of how the crustal structure in the present day MARNOK area might vary although the lines actually show crust accreted at the western RTI, between 11.5 and about 30 million years ago.

The seismic surveys have shown that anomalous crust is consistently formed symmetrically around the transform. This ribbon of crust is, on average, 2-3km thick, although there are large variations in crustal thickness and/or velocity structure along the length of the fracture zone. There is gradual crustal thinning up to several tens of kilometres approaching the fracture zone, but the very thin crust is confined to the transform valley itself (~10km from the plate boundary). It is characterised by low compressional wave velocities, the absence of a normal layer 3 reflector and is inferred to consist of a few hundred meters of extrusives overlying 2km of intrusives (Detrick & Purdy, op. cit.; Cormier et al., op.cit.; Abrams et al., 1988). A transverse ridge appears on the older lithosphere opposite the eastern RTI, and extends to the east

Mid-Atlantic Ridge North of Kane Structure

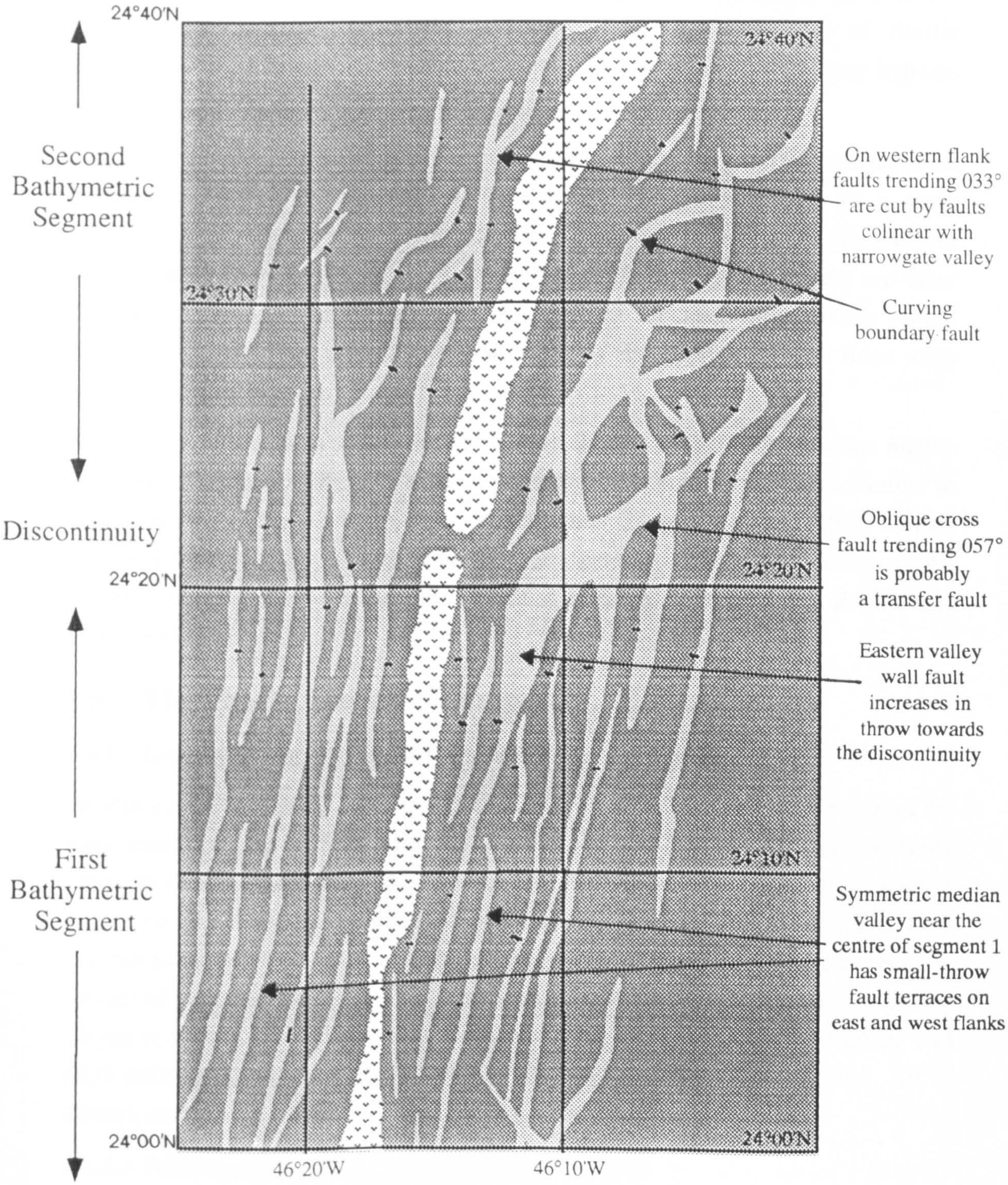

Figure 1.4 Structural map showing normal faults (light shading) mapped from SeaBeam bathymetry and TOBI sidescan data. The v-shading shows the extent of the non-tectonised volcanic terrain as defined by the TOBI sidescan textures (adapted from Allerton et al., 1995).

along the northern edge of the fracture zone (Tucholke & Schouten, 1988; Abrams et al., op. cit.). All the seismic lines described above were shot across areas of the fracture zone with a transverse ridge. There is no transverse ridge of similar dimensions at the western intersection near the MARNOK area, which may indicate that these two settings are not strictly comparable.

The 30km long ridge segment that abuts the transform in the MARK area has a crustal thickness of 4-5km and is separated from normal crust to the south by a sharp discontinuity (Purdy & Detrick, 1986). However, the anomalous crust of this segment may not necessarily be related to the proximity of the transform, as there are other unusual features, such as the non-coincidence of the median valley and the central magnetic anomaly, that suggest that local tectonics and perhaps a recent ridge jump may be responsible.

Preliminary results of a recent gravity survey show weak, broad, negative mantle Bouguer anomalies centred over several ridge segments north of the Kane, similar to those found elsewhere between Kane and Atlantis (Fujimoto et al., 1994). Crustal thickness variations are thought to be the main factor contributing to similar mantle Bouguer anomalies (Kuo & Forsyth, 1988; Lin & Phipps Morgan, 1992; Rabinowicz et al., 1993).

1.5 The Charles Darwin 57 cruise.

1.5.1 Geophysical surveying and dredging

Prior to the CD57 cruise, the sampling of the ridge near the western intersection of the Kane transform had been very limited (Bryan et al., 1981). The only sidescan sonar coverage over the area was a single width GLORIA swath along most of segment 1 and two overlapping swaths along the transform fault (Roest et al., 1984). This is in contrast to the MARK area at the eastern intersection of the Kane, which has been the subject of high resolution sidescan sonar (Kong et al., 1988) and extensive sampling (Bryan et al., 1981, 1994; Reynolds & Langmuir, *in press*), including four DSDP and ODP drilling legs (Melson, Rabinowicz et al., 1978; Dmitriev, Heirtzler et al., 1978; Detrick et al., 1988, 1990).

1.5.1.1 TOBI survey

Cruise CD57 successfully completed a high resolution survey with the deep-tow geophysical package, TOBI (Towed Ocean Bottom Instrument). The survey covered nearly 100km of the median valley floor, with two ridge parallel sidescan swaths and three oblique trending passes which extended up to 25km out onto the ridge flanks (figure 1.5). There are also four transform-parallel swath widths covering the RTI area and two of these swaths extend 50km along the transform valley.

1.5.1.2 WASP phototraverses

Two traverses, 26W and 28W, across the inner valley floor by the WASP (Wide-Angle Survey Photography) deep-tow camera system were designed to compare the tectonic and volcanic condition of the centres of the two segments (figure 5.1), and to groundtruth TOBI's high resolution sidescan sonar.

1.5.1.3 The dredge localities

Thirty dredge stations were completed during the CD57 cruise, 28 of which were in the MARNOK area (figure 1.5; Table 1.1). The first two localities were to the east of the MARNOK area on the southern transform wall at about 24°N 45°20'W. There were two stations sited on major faults, one being on the southern transform wall (D27) and the other up the eastern inner valley wall at the 24°22'N discontinuity (D22). The remainder of the dredge stations targeted the inner valley floor.

There are 12 stations on the NVZ south of the narrowgate with spacings of about 1km in the south and averaging 4 km further north. Of these D12 and D4 targeted flat-topped seamounts, D13 a composite seamount with steep summit cones, named Thatcher's Nose, and D11 a flatter, brightly backscattering area of the NVZ. Two dredges in the nodal basin, D7 and D10, respectively sampled the relict NVZ on the western wall of the nodal basin and a smooth-textured, poorly backscattering sediment pond.

North of the narrowgate there are five dredge stations sampling the poorly developed, but uniform, hummocky NVR of segment 1 with an average spacing of 5km. D29 targeted the flat-topped "nested" seamounts which occur just beyond the northern tip of this ridge at the discontinuity between segment 1 and segment 2. The sampling is more sparse over segment 2 with a total of only six stations over the NVZ with the spacing ranging from 3km to 11km. Of these, D30 is at the 24°22'N discontinuity and D32 is the northern-most station across the highest point of the NVR at 24°37.5'N. There was almost no recovery from D25 which was in the slight depression just to the south of the large crestal seamount at 24°36.5'N on the NVR of segment 2.

1.5.2 Objectives of this study

The main objectives of this integrated study were to assess the volcanic, tectonic, petrological and geochemical variations along two contrasting second order segments, bounded by a first order transform discontinuity. A geological map was constructed of the area using the TOBI sidescan sonar. The volcanology and structure revealed by this imaging has aided the interpretation of the geochemical data. In the light of these

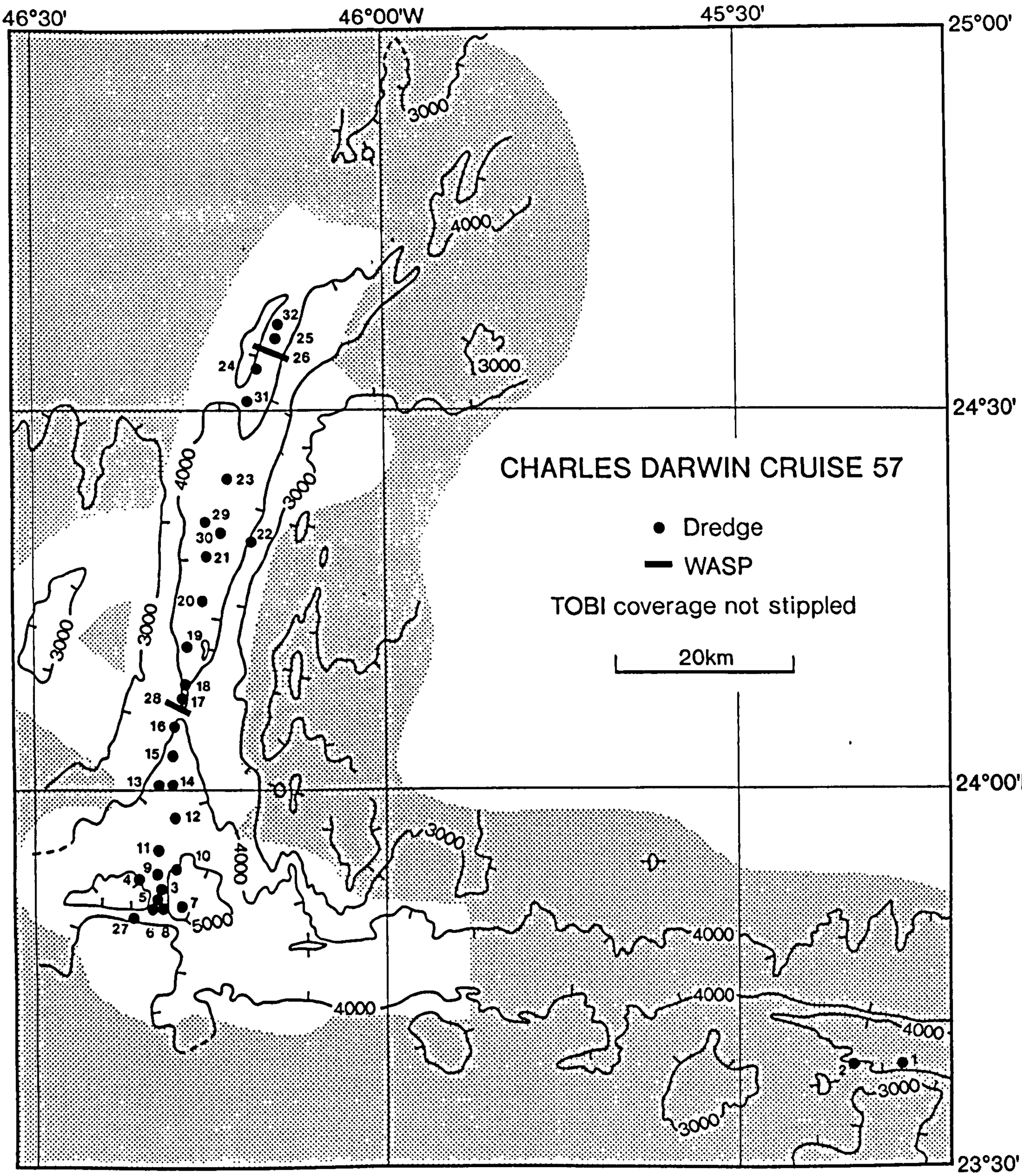

Figure 1.5 Location of the CD57 high resolution survey. Non-shaded areas show TOBI coverage, while dots indicate dredge localities (with station number) and heavy lines the WASP camera tracks. Contours are at 1000m depth intervals.

TABLE 1.1: STATION POSITIONS

Number	Type	Location	Start[a] Time	Latitude	Longitude	Depth	End[a] Time	Latitude	Longitude	Depth
CD57/1D	Dredge	Foot of transform S wall	080/0710	23° 38.6'N	45°16.4'W	4399	0819	23° 38.2'N	45° 15.7'W	4290
CD57/2D	Dredge	Foot of transform S wall	080/1324	23° 39.1'N	45° 20.5'W	4067	1454	23° 38.0'N	45° 20.0'W	3544
CD57/3D	Dredge	RTI NVR[b], Seg 1a	081/0555	23° 52.7'N	46° 19.6'W	4828	0716	23° 52.4'N	46° 19.0'W	4759
CD57/4D	Dredge	RTI seamount, W of NVR	081/1348	23° 53.4'N	46° 21.6W	4960	1546	23° 52.9'N	46° 20.6'W	4835
CD57/5D	Dredge	RTI NVR, seg 1a	081/2230	23° 51.9'N	46° 19.9'W	4900	0017	23° 51.6'N	46° 19.5'W	5000
CD57/6D	Dredge	RTI NVR, seg 1a	082/0435	23° 51.3'N	46° 20.6'W	4985	0810	23° 50.9'N	46° 19.4'W	4900
CD57/7D	Dredge	W flank of nodal basin	082/1350	23° 51.3'N	46° 18.0'W	5255	1439	23° 51.0'N	46° 17.4'W	5514
CD57/8D	Dredge	S. tip of NVR in RTI	088/1256	23° 50.5'N	46° 19.8'W	4920	1348	23° 51.2'N	46° 19.9'W	4914
CD57/9D	Dredge	Slightly oblique NVR, seg 1a	088/1833	23° 53.3'N	46° 19.5'W	4895	1957	23° 54.4'N	46° 19.8'W	4778
CD57/10D	Dredge	Volcano NW of nodal basin	089/0226	23° 53.6'N	46° 17.9'W	5030	0338	23° 54.4'N	46° 17.9'W	4944
CD57/11D	Dredge	Flat area,W of NVZ, seg1a	089/0935	23° 55.4'N	46° 19.3'W	4715	1040	23° 56.3'N	46° 19.3'W	4740
CD57/12D	Dredge	Large seamount,centre seg.1a	089/1623	23° 57.1'N	46° 17.9'W	4600	1735	23° 58.0'N	46° 18.1'W	4482
CD57/13D	Dredge	Axial smt.(Thatcher's Nose)	089/2225	24° 00.2'N	46° 19.4'W	4244	2345	24° 01.0'N	46° 19.4'W	4272
CD57/14D	Dredge	NVR axial graben, seg.1a	090/0439	24° 00.2'N	46° 18.2'W	4360	0601	24° 01.0'N	46° 17.7'W	4317
CD57/15D	Dredge	Seg.1a NVR	090/1113	24° 02.4'N	46° 18.2'W	4118	1323	24° 03.3'N	46° 17.9'W	4080
CD57/16D	Dredge	N. tip of segment 1a	090/1815	24° 04.6'N	46° 18.5'W	3970	1936	24° 05.4'N	46° 17.5'W	3948
CD57/17D	Dredge	S. tip of segment 1b	091/0015	24° 06.8'N	46° 17.9'W	4030	0155	24° 07.2'N	46° 17.2'W	3900
CD57/18D	Dredge	SE margin of seg.1b	091/0615	24° 08.0'N	46° 17.1'W	3900	0724	24° 08.5'N	46° 16.6'W	4000
CD57/19D	Dredge	Centre of segment 1b	091/1226	24° 11.1'N	46° 16.9'W	4100	1350	24° 11.8'N	46° 16.3'W	3855
CD57/20D	Dredge	Broad NVZ, seg.1b	091/1835	24° 14.6'N	46° 15.9'W	4179	2000	24° 15.1'N	46° 15.1'W	4177
CD57/21D	Dredge	N tip of segment 1b	092/0123	24° 18.4'N	46° 15.8'W	4390	0245	24° 18.4'N	46° 14.9'W	4447
CD57/22D	Dredge	Major scarp on W MV wall	092/0719	24° 19.7'N	46° 12.2'W	4150	0950	24° 19.5'N	46° 11.0'W	3455
CD57/23D	Dredge	S tip of seg.2, broad NVR	092/1523	24° 24.6'N	46° 13.7'W	4250	1745	24° 24.5'N	46° 12.8'W	4445
CD57/24D	Dredge	Centre of seg.2, broad NVR	092/2332	24° 33.4'N	46° 11.1'W	3787	0057	24° 33.1'N	46° 10.0'W	3731
CD57/25D	Dredge	Segment 2 axis	093/0628	24° 35.7'N	46° 09.8'W	3782	0717	24° 35.7'N	46° 09.0'W	3765
CD57/26W	WASP	Across segment 2 NVR	093/1258	24° 35.1'N[c]	46° 11.1'W	4220[c]	1818	24° 34.6'N[c]	46° 08.4'W	4180[c]
CD57/27D	Dredge	S wall of W FZ limb	095/2159	23° 50.3'N	46° 22.2'W	5160	2400	23° 50.0'N	46° 21.1'W	4600
CD57/28W	WASP	Across 'narrowgate'	096/0635	24° 07.3'N[c]	46° 18.6'W	3920[c]	1333	24° 06.3'N[c]	46° 16.4'W	3880[c]
CD57/29D	Dredge	Nested smts at N tip of seg.1b	096/1859	24° 21.5'N	46° 16.0'W	4545	2035	24° 20.8'N	46° 15.0'W	2577
CD57/30D	Dredge	Between segments 1b & 2	097/0157	24° 22.5'N	46° 13.9'W	4490	0308	24° 20.0'N	46° 14.0'W	4405
CD57/31D	Dredge	Centre of seg.2, broad NVR	097/0921	24° 30.6'N	46° 11.4'W	3688	0126	24° 29.8'N	46° 11.7'W	3640
CD57/32D	Dredge	N end of seg.2, NVR & smt.	097/1457	24° 37.8'N	46° 08.2'W	3570	1700	24° 36.4'N	46° 08.8'W	3695

[a] Ship position when instrument on/off bottom.
[b] NVR = neovolcanic ridge.
[c] Instrument position when on and off bottom
seg.1a = southern half of segment 1
seg.1b = northern half of segment 1
smt. = seamount

observations I assess the volcanic and tectonic processes that contribute to the morphology of the ridge axis and the transform and their subsequent modification by mass wasting processes. A combination of the volcanological and geochemical results will help to constrain the different mechanisms proposed for decreasing crustal thickness towards the segment boundaries.

The large variations in the segment offset lengths in the MARNOK area allow the contribution of the TFE to be compared with the edge effects that are associated with a very small discontinuity. Variations in mantle source within and between segments may clarify whether there is extensive mixing within segments, combined with isolation of the flow between segments, as predicted by the model of Whitehead et al. (1984), discussed above. The systematics of mantle melting observed within a second order segment will help to discriminate whether focused upwelling or focused melt delivery is the primary cause of second order crustal thickness variations. In addition, I assess processes which are occurring in the crust, including the length scales of petrological segmentation as defined by the spatial distribution of NVZ lavas with common parents; this may reflect the scales and organisation of crustal plumbing and the possible role of lateral dyke injection.

1.6 Related work and presentation of this thesis.

This thesis will concentrate on the fine detail of the inner valley floor and the volcanic and tectonic systematics along-axis. It is intended to complement Allerton et al. (1995), which focused on tectonic aspects and the large-scale morphological variation of the segments, and Hussenoeder et al. (*in prep.*) which will present the results of the TOBI deep-tow magnetics.

The geochemistry of the MARNOK area was undertaken as a group project. My part in this work was the major and trace element whole-rock analyses (see appendices 3, 4 and 5). The probe work was performed by Paul Browning, the isotopes by Pam Kempton, the peridotite petrology by Catherine Mével, while peridotite geochemistry was done by Julian Pearce, who also co-ordinated the team effort. As the combined results of this team effort need to be considered in an integrated synthesis, the reader is referred to the unpublished cruise report (associated with NERC grant GR3/7340) by Pearce et al. (1993).

Chapter 2 presents the methodology of the multi-disciplinary approach, which not only includes descriptions of the different techniques used, but reviews the way these data sets can be combined to enhance the interpretation of the study area. I highlight the particular uses of each data set, describe the methods of interpretation and comment on any relevant pitfalls.

Chapter 3 takes, as its basis, the different textural terrains that have been identified in the TOBI sidescan images. Volcanic, tectonic and mass wasting features are described, and an attempt is made to provide a basis for their geological interpretation. In order to do this I use information from this and other cruises.

Output from the 7.5kHz sub-bottom profiler has been well-characterised on deeply sedimented areas of ocean floor, but with the exception of Francis (1987) there is little previous work on the nature of their returns from a rocky ridge crest. I discovered different types of return from the median valley floor, walls and variably sedimented ridge flanks and compared these with the sidescan records. They are used to add weight to the interpretation of features such as sediment slumps on the valley walls. The characteristics of the profiler returns are then analysed by using general considerations of the interaction of the incident ray with different surface textures found near a ridge axis.

Chapter 4 focuses on the volcanology of the area, starting with a comparison of the WASP traverses across the centres of the two segments. I use the volcanic and tectonic characteristics and relative age variations across the two NVZs to deduce their respective life cycles. I then relate this to the thermal and mechanical structure of the lithosphere, and the causes of variations in flow rate are assessed. This is followed by an analysis of some notable aspects of the WASP surveys, namely the relationship of pillow flow front breccia to syn-magmatic tectonism and the first comprehensive description of sheet flow morphologies from a slow spreading plate boundary. The mechanisms acting to produce sheet flow transformations in the deep-sea environment are discussed and compared with the findings of laboratory simulations (Gregg & Fink, 1995). The focus then switches to an analysis of some of the more unusual volcanic morphologies on the sidescan data, including a hummocky seamount chain with distinctive summit cones, named 'Thatcher's Nose', and some unique flat-topped seamount morphologies that have proved particularly useful in subsequent interpretations. I go on to use seamount statistical data to test a model for seamount construction and provide additional information to aid the interpretation of the different sidescan volcanic morphologies. The origins of hummocky ridges and flat-topped seamounts are discussed in the final two sections.

Chapter 5 features the RTI area in the south of segment 1, the nodal basin and the transform. I relate the volcanic, petrological and geochemical diversity within the transform domain to the magmatic plumbing system The orientation of structures on the median valley floor and walls are discussed in terms of the variation in the stress regime towards the transform. I describe and interpret features in the nodal basin and

the transform valley, including the PTDZ and the median ridge, and discuss the role of serpentinite diapirism combined with transtensional tectonics.

This chapter focuses on aspects of second order segmentation. It starts with the presentation of a geological map of the MARNOK area and a description of the volcanic, tectonic, hydrothermal and relative age variations seen along the ridge axis. The contrast between the east and west valley walls and brief descriptions of the ridge flanks are also included. The remainder of the chapter brings together data from the whole of segments 1 and 2, including the transform domain in the southern half of segment 1, so that the relative importance of second order and first order segmentation can be assessed. Petrological and geochemical systematics with segmentation are presented. This includes along-axis variations in extent of fractionation, melting, mantle source, and petrological (fourth order) segmentation. The deep-tow magnetic inversions performed by Hussenoeder et al. *(in prep.)* are discussed to assess the primary cause of the variations in magnetization in the MARNOK area. The relative contributions of the first and second order segmentation are assessed.

These observations are then discussed in terms of mid-ocean ridge dynamics, including the episodicity and focusing of volcanism, the crustal residence time in the magma chamber, and the factors controlling the brittle-ductile transition. Finally, a model of segment accretion is developed.

Chapter 7 presents a comparision of the MARNOK area with some other areas of the ridge system, focusing on Iceland, and particularly an analogy between the flat-topped seamounts and Icelandic shield volcanoes. I then go on to discuss seamount volcanism on the Reykjanes Ridge and in the Pacific. Finally I return to segmentation and present a comparison of the morphological, petrological and geochemical characteristics of the MARNOK segments with another transform-bounded segment at 26°S (one of the few segments on the MAR with a similar data coverage to MARNOK). This enables me to extend the MARNOK segmentation model and suggest possible root causes of global variations in segmentation at slow spreading ridges.

A summary of the main conclusions of this study is presented in chapter 8.

BLANK IN ORIGINAL

Chapter 2

Methodology

A few observations and much reasoning lead to error,
many observations and a little reasoning to truth.

Alexis Carrel

2.1 Introduction to the multi-disciplinary approach.

Studies of ocean ridges in recent years have shown that a combination of geophysical, geological and petrological information provides the best approach for constraining the processes of crustal accretion at ocean ridges. This study presents an interweaving of many types of data, each with a different resolution, which together are used to address outstanding issues of oceanic crust formation, evolution and segmentation.

TOBI (Towed Ocean Bottom Instrument), developed and built by the Institute of Oceanographic Sciences, was the main geophysical tool used to map the MARNOK area. It carried a 30-32 kHz sidescan sonar, a 7.5 kHz sub-bottom seismic profiler, a triaxial fluxgate magnetometer, a thermistor probe and vehicle status sensors giving heading, speed, pitch, roll and hydrostatic pressure. We also used the WASP camera system, which includes a 35.5kHz near bottom echo sounder and pressure sensor which were used in the construction of high resolution bathymetric profiles. These WASP profiles and previous studies with other deep-tow camera systems and submersibles (Karson & Dick, 1983; Zonenshain et al., 1989; Fujimoto et al., 1994) were used to systematically ground-truth the TOBI sidescan sonar. The SeaBeam bathymetry (Purdy et al., 1990; Pockalny et al., 1988), dredge samples and the 7.5 kHz TOBI sub-bottom profiler provide further information for characterising the geological significance of textural terrains on the sidescan sonar.

While the SeaBeam bathymetry, sidescan sonar, and camera system provide information about the surface of the seafloor, the magnetic data and the 7.5 kHz sub-bottom profiler can be used to assess properties of both the surface and sub-surface. The samples collected during dredging provide direct information on the rock types, ages and lava

morphologies on the surface, but also can be used to infer information about crustal and sub-crustal magmatic processes through the tools of petrology, mineral chemistry and geochemistry.

A description of the methods used in collecting, processing and interpreting these different data types follows.

2.2 SeaBeam bathymetry.

2.2.1 Instrument specifications

SeaBeam is a multi-narrow-beam echo-sounder which can ensonify a swath of seafloor with a width of ~3/4 of the water depth. The bathymetry maps of the MARNOK were produced by combining the data set over the transform and the RTI area south of 24°05'N (Pockalny et al., 1988) with that of Purdy et al. (1990)—a 50km wide band, centred on the ridge axis, north of 24°05'N. The lateral resolution of the instrument is 100-200m and the vertical resolution (over rough topography) is about 10m (Tyce, 1986). The SeaBeam data sets are gridded at approximately 150m intervals in keeping with the lateral resolution. The Global Mapping Tool package (Wessel & Smith, 1992) was used to generate the plots. Typical shell scripts and the colour scales devised for various contour intervals and plotting mediums are included in Appendix 1.

2.2.2 Sources of error

Navigation is unquestionably the primary source of error in the bathymetry maps. The Global Positioning System (GPS), which has an accuracy of several tens of metres, was used whenever possible, but was only available for approximately 8 hours a day during the collection of the transform data (Pockalny et al., 1988) and about 3 hours a day for the Kane-Atlantis data set (Purdy et al., 1990). When GPS was not available the navigation system consisted of dead reckoning by Doppler log and gyro compass between Transit satellite fixes. During the Kane-Atlantis survey there were periods of 4-6 hours, during which substantial course changes occurred without a usable Transit satellite fix. No quantitative measure of the final uncertainties is possible, though a qualitative estimate of the maximum navigational uncertainty is 0.5nm or about 925m (Purdy et al., op. cit.). This caused some discrepancy when attempting to correlate high resolution bathymetry with the SeaBeam maps, to provide a navigational constraint for the WASP traverses (as discussed further in Appendix 2).

2.2.3 Use in segmentation studies

The SeaBeam bathymetry maps are the primary source revealing the nature and scale of segmentation on the ridge crest. Analyses of geomorphology based on bathymetric data have previously interpreted very steep slopes with sub-linear strikes as faults and the sub-linear locus of peaks within the rift valley floor as volcanoes of the NVZ (Ballard & Van Andel, 1977; Sempéré et al., 1993). However in the absence of sidescan sonar imagery it is difficult to distinguish volcanic slopes and fault scarps from SeaBeam alone. Nevertheless, the SeaBeam bathymetry remains a great aid in the interpretation of the TOBI sidescan images and other data sets, as will become apparent in this and other chapters.

2.2.4 Using bathymetry to calculate volcano shape statistics

In this study seamounts were identified on 20m contoured SeaBeam maps plotted at the same scale as the shipboard sidescan mosaics (80"/degree at the equator). For each seamount fitting the criteria described below, the latitude and longitude were recorded (to the nearest minute) and the dimensions were measured, allowing the shape of each seamount to be defined.

Only seamounts on the floor of the median valley are included in this analysis, the edges of the valley being defined by the first scarp greater than 200m in height. These scarps are identified on bathymetry and confirmed on the sidescan images. Edifices on the walls of the nodal basin are also excluded. The results of this study are presented and discussed in chapter 4.

2.2.4.1 Criteria defining seamounts

The criteria for recognising subaqueous seamounts were originally defined for the EPR (Batiza, 1982) and continued for studies on the MAR (Batiza et al., 1989; Smith & Cann, 1990). A seamount is a topographic high, having a relief greater than 50m on all sides and approximately equant plan shapes (aspect ratios of up to 2 are included, although Batiza et al. (op. cit.) restricted their study to aspect ratios of 1.5). The term does not distinguish between a central volcano which is fed by a pipe vent and volcanoes fed by an elongated conduit.

2.2.4.2 Methods for estimating shape parameters

There have been two methodologies used for estimating the shape parameters of seamounts from bathymetry data. Both approximate seamount shapes to truncated, right circular cones. Jordan et al. (1983) used cross-sectional profiles with the flat top defined

by a line which grazed the maximum height. If a seamount was significantly acircular the values from two or more profiles were averaged. Smith and Cann (1992) used a plan view fitting method where a closed curve was drawn round the shallowest point of the break in slope at the seamount's base and also around the near-summit break in slope, if present.

2.2.4.2.1 Method One

The first method used to characterise seamount dimensions adhered to the strict criteria of Batiza (1982), that more than 50m of relief is required on all sides (table 4.4). Hence, when working from the 20m contour maps only those features defined by three or more closed contours were selected. The basal diameter was defined by the lowest closed contour and summit diameter by the upper break in slope. Both maximum and minimum diameters were recorded so that the aspect ratio could be calculated. If the aspect ratio was greater than 1.2 then the azimuth of the long axis of the base was also noted. The depth of the base and summit were taken as the lower and upper closed contours, while the depth of the summit plateau is the depth of the upper break in slope.

This method will systematically underestimate the height of the seamount (sh), as the maximum height is always fractionally above the maximum contour and the lower break in slope is below the lower closed contour. There are some seamounts which may fit the criteria and be between 50m and 60m high, which have been excluded from the compilation because it cannot be proved on a 20m contour map that their heights are above 50m. It should also be noted that this method is quite different from that used by Smith and Cann (1990; 1992) as will be discussed later.

2.2.4.2.2 Method Two

The second method is similar to that described by Smith and Cann (1992) and is thought to provide more realistic values of seamount diameter and height. The major disadvantage of the method is that it can be accurately used for only circular steep sided seamounts, but is little use for the more gently inclined fissure mounds.

The steep flanks of many flat-topped seamounts can be identified as concentric arcs in the contours and this provides the basis for the second data compilation. Instead of the basal and summit diameters being constrained by closed contours, radial concentric arcs are used to estimate the upper and lower break in slope (for examples of method 2 in use see figure 4.14). Cross checking with the sidescan images confirms the presence of seamounts which are defined in this way. As the methodology assumes approximately radial symmetry, no values for aspect ratio or azimuth are included in the second data compilation (table 4.5) and values for the average radii are given.

2.2.4.3 Shape parameters

The measurements taken directly from the bathymetry were used to calculate a number of shape parameters, following Jordan et al. (1983); Smith and Cann, (1992) and Scheirer and Macdonald, (1995). These include the summit height (sh = depth of base - depth of summit); the cone height (ch = depth of base - depth of plateau); average basal and summit radii (rb & rs); the flatness (=rs/rb); ξ (=h/rb); ε (= ch/(rb-rs)); ϕ, the angle of the right circular cone (=$\tan^{-1}\varepsilon$) and the volume v, (= $^1/_3\pi(rb^2H-rs^2(H-ch))$ where H is the height of the untruncated cone (= rb x ε).

2.3 WASP deep-tow camera system.

2.3.1 System specifications

The WASP camera system was towed near to the bottom of the seafloor. Its altitude was monitored by a near-bottom echo sounder (NBES) trace on the hard copy output of a Waverley linescan recorder. The wire out was adjusted to maintain the optimum distance for photographic exposures (~8m). The pressure was also monitored to give a measure of the water depth and each exposure (or flash) was marked by a tick at the edge of the linescan trace. An example of the WASP hard copy output is shown in appendix 2 (figure A2.1).

WASP produced 35mm black and white photographs, each labelled in a data chamber at the corner of the frame with the time and the altitude at which it was taken. The clearest exposures were taken when the altitude registered between 7 and 10m. Above 10m the backscatter progressively obscured the images. The full viewing angles are 35°x50° (I.O.S.D.L. system report), so for an optimum towing altitude of 8m, the resulting frame has dimensions of 7.5m x 5m. Frames were taken at 30s intervals to produce a near continuous swath at an average speed of 0.5 knots (7 to 8m separation between centres of adjacent photographs). I found that the figures recorded in the data chamber were not always reliable, as photographs which were obviously taken from different altitudes sometimes had the same altitude values recorded in the data chamber (e.g. figure A2.4 in appendix 2). Hence the scaling of the photographs has an element of uncertainty.

Many sections of the film are very dark due to the intermittent operation of the flash, especially after camera crashes and as power failed towards the end of a run. Inability to maintain operating altitudes over the sharply dipping scarps caused auto shut-off and further data gaps on a number of occasions. There is often overlap between adjacent frames, but the wide variation in the altitude of the camera over the rough topography

cause the dimensions of the photographs to vary considerably. Mosaicing of the frames is difficult in such areas but is possible over flatter terrains, for instance sheet flows.

2.3.2 High resolution profiles

The 35.5kHz near bottom echo sounder mounted on the WASP has a range of 7 to 80m and a resolution of 10cm (I.O.S.D.L. system report). During the survey it produced a good clear signal on a Waverley linescan recorder, allowing the construction of high resolution bathymetric profiles of the traverses. The depth of the instrument can be deduced from its pressure sensor, which has a resolution of 1m and an accuracy of +/- 1m. Details of the pressure transducer calibration can be found in appendix 2 (section A2.3). No digital recordings were made of data so the pressure and altitude traces on the Waverley linescan hard copies had to be digitised by hand. The digitising process and the programs used to convert the traces to sea depth and generate the profiles are also described in appendix 2. The profiles are plotted against time (as recorded on the hard copy output of the 35.5kHz echo sounder) as this facilitates correlation with the photographs.

The values of seafloor depth plotted in the high resolution profiles were calculated by summing the depth of the instrument and its contemporaneous altitude. Interpretations of these profiles, plotted with approximately no vertical exaggeration are shown in figures 4.1, 4.2, 4.3, and 4.4, while the 'expanded' versions used to record the initial photoanalysis are presented at the end of appendix 2.

A clock battery problem during the traverse over segment 2 caused the time figures in the data chamber to be very dim and for most of the run they appear to be completely absent. Where a time value was not available, the frames were positioned with respect to the profile by counting the flash ticks on the hard copy output and assessing the local trend of the topography with respect to the high resolution profiles.

2.3.3 Instrument position

For a first estimation, the maximum horizontal distance of the camera with respect to the ship was determined using Pythagoras' theorem on the depth of the camera (calculated from the pressure) and the wire out (assuming a straight, diagonal trajectory between ship and instrument). The WASP path was constructed along a line parallel the ship's track, so that the SeaBeam bathymetry, at the calculated horizontal distance from the ship, best matched the calculated depth at the instrument. Later, the high resolution profiles were correlated with the SeaBeam bathymetry to provide an additional navigational constraint (see Appendix 2.5; figures A2.2 and A2.3).

The overlaps between adjacent frames were useful for deducing the relative orientation of the instrument at approximately 30 second intervals and hence the local direction of movement of the camera. At the start of the traverses, the overlaps between adjacent frames reveal a period of drifting with rotations of up to 60° between frames. Bottom currents probably caused the camera to drift in this way before the instrument gathered momentum in response to the acceleration of the ship. Subsequently, the relative orientation of the frames showed that the camera moved in a straight line which seems, from the high resolution profiles, to be parallel to the ship's track.

2.3.4 Photoanalysis

The reader is referred to Table II of Barth et al. (1994) for a summary of the definitions used in seafloor photoanalysis, a guide to related terms and prior usages and a comprehensive reference list of published examples. Lava morphologies, tectonic features and sediment cover were systematically described in frame description logs. Appendix 2 contains examples of the different flow morphologies, flow contacts and tectonic features. At the end of appendix 2, I also present the detailed results of the frame description logs recorded on 'expanded' high resolution profiles.

2.3.5 Using lava morphologies to estimate flow rates

The temperature dependant viscosity and pseudoplastic behaviour of the lava leads to different growth mechanisms and hence different lava morphologies at different flow rates. Although each flow commonly comprises several lava morphologies, there is often a dominant form that reflects the average flow rate. The flow rates in turn are governed by the conditions of extrusion (effusion rate, eruption temperature and slope) and the rheology of the magma—viscosity and crystallinity (Ballard et al., 1979; Luyendyk & Macdonald, 1985; Bonatti & Harrison, 1988).

Submarine flows are typically classified as pillowed, lobate or sheet flows on the basis of their morphology (e.g. Fox et al., 1987). Pillow lavas, analogous to subaerial tube-fed pahoehoe are thought to result from low effusion rates, where a high degree of channelisation is established. Sheet flows are considered to be the submarine equivalent of surface fed pahoehoe and compared with pillow flows they represent a phase of activity where delivery rates are faster and there is little or no channelisation (Ballard et al., 1979; Luyendyk & Macdonald, 1985). The lobate surface is classed as an intermediate between the sheet and pillow flow types.

The first attempts at quantitative modelling of submarine flow morphologies involved the injection of hot wax into a tank of water (Griffiths & Fink, 1992a). These experiments

have revealed four distinct flow regimes, of which one is thought to be equivalent to pillow flows, the other three are sheet flows, and lobate morphologies occur as a transitional form. These regimes are characterised by specific ranges of a dimensionless parameter. This parameter incorporates the key physical properties of both the extruding material and its environment, including factors such as the volume flux, the eruption temperature and the viscosity at the vent. Of these, the extrusion rate is thought to be the primary determinant of flow morphology. Bulbous outgrowths (analogous to pillows) form at effusion rates of <1 m^3s^{-1}; sheet flows occur above this value, while lobate flows are an observed transitional morphology.

Within the major categories of pillow and sheet flow, there exists a wide variety of surface shapes and textures, which occur under specific flow conditions, and hence add a further subdivision to the categorisation of flow rates. Pillow morphologies include varieties such as knobby, bulbous, elongate, phallic, elephant trunk, trapdoor and toothpaste pillows (Ballard & Moore, 1977). Subaqueous sheet flows also come in many forms: jointed, lineated, ropy, whorly, wrinkled, rifted, jumbled and hackly sheet flows have been reported, mainly from fast and intermediate spreading ridges (Ballard et al., 1979; Lonsdale & Spiess, 1980; Embley et al., 1990).

2.3.5.1 Pillow morphologies formed at slow flow rates

At slow flow rates subaqueous lavas progress by spreading mechanisms, where the chilled skin periodically ruptures, forming a surface textured with crenulations and fault slivers (Moore, 1975; Moore & Lockwood, 1978; Walker, 1992b). Ballard and Moore (1977) estimated that crenulations in bulbous pillows occur when they spread at rates of the order of 5 cm s^{-1}, while fault slivers are generated at much slower spreading rates (of the order of 0.2 cm s^{-1}). Breadcrust cracks can form where the thick crust parts a small amount in the final phase of growth (Ballard and Moore, op. cit.). Other pillow morphologies formed by spreading include trapdoor, elephant trunk and toothpaste pillows, which are usually found in the flows where bulbous pillows are common. The slow asymmetric spreading which forms a strongly crenulated surface, characteristic of toothpaste pillows, is envisaged to operate on lavas of higher viscosity (Yamagishi, 1985; Walker, 1992b).

2.3.5.2 Pillow morphologies formed at faster flow rates

Stretching as opposed to a spreading mechanism implies rapid growth and requires a chilled skin which is thin and has a low enough viscosity to deform in a plastic manner. The characteristic feature of knobby pillows are the abundance of small protuberances,

known as buds and fingers, which cover the parent pillow. The smooth, surface of these buds and fingers imply that they grow by a uniform stretching mechanism (Walker, 1992b). Small areas of chilled skin expand to accommodate the injected lava, until the buds reach a couple of centimetres in diameter, when they freeze quickly because of their high surface area to volume ratio. In contrast, the parent pillows commonly have a patchy crenulated surface, generated by periods of spreading between the highly localised episodes of rupture and bud formation. Hence knobby pillows are formed in a regime which is transitional between spreading and stretching.

Lobate flows have a smooth surface free from striations, which implies formation when local effusion rates are similar to crustal growth rates, resulting in stretching over the entire crust. This is confirmed by laboratory observations using wax extruded into sucrose solution which show that lobate flows form in a manner similar to pillow flows, but the crust swells without cracking to accommodate additional lava (Gregg & Fink, 1995). The classification of the lobate surface as an intermediate between a sheet and pillow type flow is confirmed by the morphological transitions observed within single flows. Lobate sheets transform into pillows at the distal ends of the flow, and sometimes a slight increase in gradient can induce a change to knobby pillows from a lobate form. Occasionally the reverse transformation occurs as a steeply dipping pillow tube reaches a flatter, smoother surface and spreads into more unconstrained lobes.

Whereas the lobate morphology occurs when a flow is relatively unconstrained, networks of branching lava tubes develop as a rapidly moving flow matures and channelisation becomes established. Compared with pillows, lava tubes exhibit little closure and branches can be easily traced. The surfaces of tube are smooth and relatively free of crenulations and fault slivers, showing that crustal stretching is more significant than during pillow formation. However, shallow breadcrust cracks show that late stage spreading sometimes occurs.

2.3.5.3 Sheet morphologies formed at fast flow rates

A wide range of submarine sheet flow morphologies have been described from fast and intermediate spreading ridges, but whereas the formation of pillow lava has been observed off the Hawaiian coast (Moore and Lockwood, 1978), the extrusion of subaqueous sheet flows has not yet been directly observed. As a result, surprisingly little has been established about their emplacement parameters and the mechanisms of their formation.

Within the literature 'jumbled' and 'hackly' lavas are used as synonymous terms. However, from submersible dives, Ballard et al. (1979) recognised two subtypes of 'aa-like' surface which, although they differ in their origins, are often indistinguishable in photoanalysis. The first is gradational with more coherent folded surfaces like the jumbled lava described above and the second appears to be a highly vesicular friable glassy mass.

In this study, the flows described as 'hackly' have a dominance of granular clots and fine gravelly surfaces. The rubble covering the hackly surface ranges from granular fragments up to pebble size, equant, jagged lumps. Hackly flows sometimes form seafloor which is rough on a scale of meters as well as centimetres and can look superficially like a breccia. Flows referred to as 'jumbled' have a surface structure which dominantly resembles disrupted folds and chaotically oriented blades. Broken clasts which have ropy morphologies, or a platy internal structure are commonly associated with this type of flow. Although a division of the two terms has been specified here, their synonymous usage in other studies is also justified, as usually flows are found with a range of the characteristics described above.

The formation mechanisms for these deep water flows are a subject of current debate, but a number of authors have commented on the close resemblance between the jumbled/hackly surfaces and the clinkery brecciated texture of subaerial aa (Ballard et al., 1979; Griffiths & Fink, 1992a; Gregg & Fink, 1995). Observations of subaerial aa have shown that their formation occurs by widespread crustal failure and slow crustal healing (Kilburn & Lopes, 1991; Kilburn, 1993). The ropy clasts of jumbled flows are evidence that they may evolve from folded flows which undergo increased shearing or crustal fracture. Griffiths and Fink (1992a) suggest that jumbled sheet flows are analogous to the lêvéed flows of their wax experiments. These correspond to the flow regime with the highest effusion rates (>3000 m^3s^{-1}), where flow velocities are so great that crustal formation is prevented, except at the margins.

Ropy flows, with their characteristic swirls and folds, are subaqueous forms of sheet-fed pahoehoe, thought to be analogous to the cross-stream folds which form in the wax experiments at 100-3000 m^3s^{-1} (Griffiths & Fink, 1992a). Rifted plates are the third sheet flow regime observed in these experiments at effusion rates of 1-100 m^3s^{-1}. These contain flow-parallel crustal stringers which cause differential solidification of the flow surface, possibly resulting in the formation of grooves on the solidifying surfaces. Similar flow-parallel striations occur on lineated sheet flows (Embley & Chadwick, 1994), which may be the submarine equivalent to these rifted flows (Griffiths & Fink, op. cit.; Gregg and Fink, 1995).

The experimental predictions of Griffiths and Fink (1992b) seem to hold with observations from the fast spreading Galapagos Rift, where Ballard et al. (1979) report a characteristic sequence of sheet flow morphologies corresponding to a decreasing flow rate with increasing distance from the eruptive vent. An intensely folded and rubbly jumbled flow marks the axis of eruption. This becomes a more gently folded and lineated flat morphology which grades into a hummocky lobate sheet as it descends into the marginal basin.

Another type of submarine sheet flow takes the form of fractured polygonal blocks, named paving stone lava, and has been observed on the EPR (Lonsdale & Spiess, 1980) and the Afar Rift (Tazieff, 1972). The regular polygonal fractures resemble desiccation cracks implying formation by thermal contraction of the surface. This morphology is not mentioned by Griffiths and Fink (1992a) in their analogue experiments, but Bonatti and Harrison (1988) comment that the partial fragmentation of the lava upon eruption implies that it is an intermediate form between a quiet and reactive eruption product. This style of eruption is associated with a volumetrically smaller discharge of lava per unit time, a lower temperature and higher viscosity of the lava on eruption.

2.3.5.4 Effect of local flow conditions

Local flow conditions commonly control local morphologies, so caution must be exercised when interpreting isolated views of seafloor lavas. A single lava flow may comprise a number of different morphologies which reflect a change in the effusion rate from high near the vent, to low at the margins. The dominant flow morphology is thus used as a measure of the average effusion rate, although a knowledge of the three dimensional nature of the flow is necessary to comprehensively achieve this.

The underlying slope and the resulting variation in flow rate due to gravitational acceleration must also be taken into account. The effect of slope on lava morphology can be quite dramatic. When a flow surface is horizontal, pillows have a short and rounded form, but on gently dipping flows they become elongated in the downslope direction, with aspect ratios of up to 5. The formation of pillow buds is also affected by the slope. Elongated pillows with a large number of small rounded buds tend to occur on gently dipping flows. At moderate gradients, buds form as elongated fingers which often protrude out of the end of pillows. On steeper slopes bud formation tends to be suppressed and highly elongate pillows, sometimes with surface bulges, result. The slight variations in the cylindrical diameter have been labelled a 'neck-and-knob' profile by Ballard and Moore (1977). The most strongly elongate pillows at the steep edges of the

flow front have a fairly smooth surface texture indicating their formation by uniform or localised stretching mechanisms (Walker, 1992b).

Steep pillow fronts form as the advance of the feeding lobe is dammed at its front and the flow continues to build out by progressive draping of foreset-bedded pillows (Ballard & Moore, 1977). The highly elongate pillows which occur almost exclusively at flow fronts aren't particularly related to the effusion rate of the flow as a whole and if anything an inverse relationship exists (steeper fronts are generated by slower flows). Hence flow fronts are ignored when estimating the flow rate using the lava morphology.

2.3.6 Estimation of flow type from degraded and sedimented surfaces

The flow morphology of lava surfaces in varying degrees of degradation can be recognised from the characteristics of the spall which collects on their surfaces. Knobby pillows rapidly shed their delicate extrusive ornamentation, and can be recognised by the loose buds and fingers which collect as pockets of rounded pebble breccia. The rims of bulbous pillows fracture in a conchoidal manner to produce slightly curved platy spall and bread crust texture produces tabular and blocky spall-rubble. On highly sedimented terrain where the lava surface is concealed by hemipelagic cover, flow morphologies are revealed by the cross-sectional view on the edge of fissures and faults.

2.3.7 Mapping contacts between flows

It is necessary to establish the contact relationships and hence the extent of individual flows in order to make estimates of their effusion rate and relative age. Given that each WASP traverse essentially comprises a data strip 5-6km long by 5m wide, there are difficulties in relating features such as flow contacts and flow directions in three dimensions. A single flow may impinge on a traverse several times, and each time it would be mapped as a different unit. This leads to an over estimation in the number of flows along a traverse, but contacts may also be obscured by sediment cover, tectonic disruption, dark indistinct frames and data gaps.

The presence of a steep flow front with a frontal breccia provides one of the most obvious ways of demarcating adjacent pillow flows. The flow foot breccia is thought to be material which has avalanched down the steep pillow flow fronts, both during eruption and afterwards as the result of post volcanic processes (Ballard & Moore, 1977). Features which discriminate between flow front breccia and fault talus are described in section 2.3.9 The steep flow fronts can reach inclinations of 70° (locally they can be near vertical), and comprise foreset-bedded, narrow, elongated pillows with aspect ratios of up to 15.

Flow contacts can be easy to identify when neighbouring flows have different morphologies, but care must be taken that the change in morphology is not the result of a morphological transition within a single flow. When a sheet flow onlaps a steeply dipping pillow flow there is clearly a contact, but a dramatic change in morphology across a sheet flow surface is often due the transformation in flow mechanics within a single unit, rather than the presence of a contact. To complicate matters further, the sediment cover on sheet flows is notoriously deceptive, so a morphological transition can be accompanied by an apparent change in relative age because of systematic differences in sediment cover with morphology. Smooth flat surfaces are almost invariably obscured by sediment dusting, while nearby jumbled or hackly surfaces appear to be free of sediment. The suddenness of the morphological change is used to discriminate between a flow contact (which should be completely abrupt) and a morphological transition (which may occur over a very short distance, but nevertheless shows some gradation between morphologies).

Because of systematic differences in sediment cover and the considerable evidence for sediment redistribution on the MAR (Van Andel & Komar, 1969; Macdonald & Luyendyk, 1977; Marks, 1981), only the most striking changes in sediment cover can be used to define flow contacts. Plate A2.6d illustrates a contact where slightly elongate, phallic and knobbly pillows of a younger flow (relative age scale 1.6, see section 2.3.8) gently onlap highly sedimented terrain (relative age scale 3.0). The low aspect ratios of the onlapping pillows and the gentle inclination of the onlapping surface suggest that this contact is at the lateral edge of a flow, rather than an advancing front.

The most tenuous way of identifying a contact is from the topography and direction of flow of the pillows. Contacts are marked where pillows flow down from opposite directions into a local depression. Although it would be impossible for lavas to flow uphill, the inability to correlate eruptive units in the third dimension makes it possible that such scenarios are lobes belonging to the same main body or adjacent tumuli-like cones which have erupted above the same main feeder flow.

2.3.8 Age estimations from sediment cover

2.3.8.1 The relative age scale

The ages of pillow flows can be estimated by using the extent of degradation of the surface and the amount of hemipelagic sediment cover. In order to compile a relative age scale, frames were selected with the whole spectrum of sediment cover. They were arranged in relative order and assigned values on the relative age scale to correlate as closely as possible with the sketches of Ballard et al. (1981). Plate 2.1 shows a sample

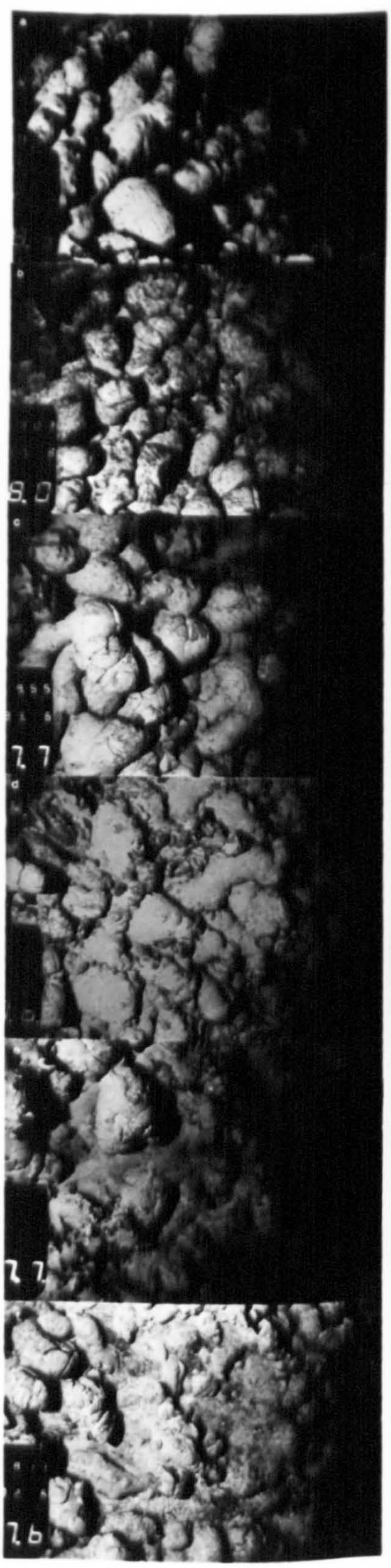

1.0

No sediments; specular reflections from very glassy pillows with pristine crustal texture.

1.2

Very light dusting of sediments, but with no accumulation of small pockets. Pillow surface has become dull, but surface texture is still clear.

1.3

Very light dusting of sediments with occasional small pockets forming in depressions between pillows. Surface texture still shows no degradation.

1.5

Sediment dusting is heavier and in places obscures surface ornamentation. Small isolated pockets also occur. Buds and pillow crust may start to spall off.

1.7

Pockets of sediment grow larger and become more numerous. The majority of these pockets remain isolated. Patches of pebble breccia may start to develop on knobby flows.

1.9

Most pillows are surrounded by sediment pockets but only about half of these are interconnected.

2.0

Sediment forms a network of almost entirely interconnected pockets. Note how much of the fine ornamentation has been preserved on these knobby pillows.

2.3

Smaller pillows become covered with drapes of sediment, but larger features still stand proud from sediment blanket.

2.5

Sediments dominate with isolated lava forms protruding through the cover.

3.0

Blanket of sediment completely covers pillows, but surface still has an undulating form reflecting the flow surface beneath. Here there is a flow of relative age 3.0 (right) contacts against a flow of relative age 1.5.

3.5

Smooth sediment surface with occasional pillow form protruding. (Note: in some cases outcrop may occur as a result of tectonic activity :-The line of breccia here is probably related to a fissure.

3.9

Planar smooth sediment surface with virtually no rock visible. Note the pale squiggly trace of the feeding trail.

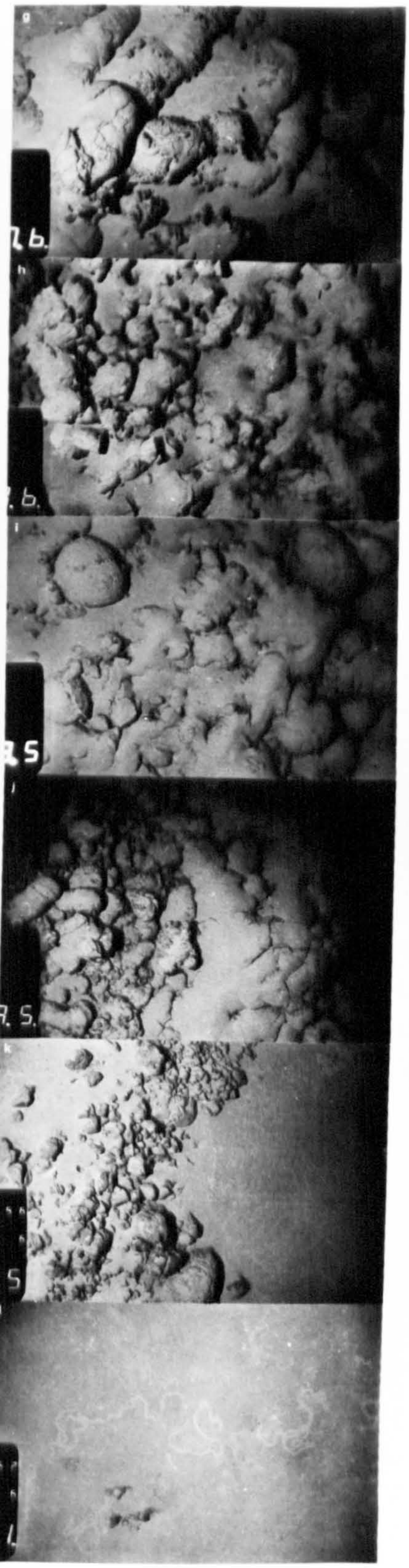

Plate 2.1 Relative age scale for pillow lava flows based on sediment cover (adapted and extended from Ballard et al., 1981).

from this relative age scale. During the systematic frame logging, each frame was assessed by visually matching against this scale. It is difficult to assess errors for such a conjectural qualitative method but repeat analysis of several sections of film gave a maximum variation of 0.4 on the relative age scale.

2.3.8.2 Problems in making consistent estimates of sediment cover

The difficulties involved in obtaining consistent estimations of sediment cover fall into two main categories. The first result from the limitations of deep-sea photography and associated artefacts, while the second are a consequence of the variability in the characteristics of flow surfaces. The presence of a light sprinkling of sediment is determined by the contrast of pale ooze against dark basalt and the clarity of the surface architecture of the pillows. Hence variabilities in contrast of the photographs can produce inconsistencies in the assessment of sediment cover. The flash operation was rather inconsistent following vehicle crashes on the seafloor. (These occurs during both traverses: at 16:50 on the segment 2 traverse and at 07:50 on the segment 1 traverse.) The damaged flash system resulted in a very low contrast in many of the frames and the occasional over exposure. Over exposure causes the lava to look anomalously fresh by generating the intense black colour and apparent reflective qualities of pristine glassy basalt. Surfaces usually appear smoother and more sedimented when viewed from a distance compared with the photographs taken at much shorter ranges. The obscuring effect of the water column causes a loss in resolution of the surface architecture and a reduction in contrast which both contribute to an apparently smoother more highly sedimented texture.

Consistent comparisons between the relative ages of different flow morphologies can be difficult because of variable manner that sediment settles on the different microtopographies. For example, sediment on the surface of knobby pillows tends to stand out more clearly than that on smooth, or only lightly crenulated surfaces, because of the strong contrast between the dark glassy buds and the pale hemipelagics. The problem is compounded on sheet flow surfaces where many authors have commented on the deceptive nature of sediment cover. Ballard et al. (1979) suggest that sediment deposited on rougher flows may collect in small crevices and depressions and thus, is less visible than the sediment deposited on a featureless flat surface. Alternatively the flow regime of the bottom currents may be affected above the rougher surfaces so that less deposition occurs on them. A histogram analysis of the association between lava type and sediment cover on Axial Volcano, Juan de Fuca Ridge is presented by Embley et al. (1990; figure

11). This provides a method of directly comparing the percentage cover on a pillow flow with that on various sheet flow surfaces.

In addition to variations in the microtopography of different flows, the mode of sediment cover itself can vary, draping in some areas and ponding in others. When draping occurs, the same volume of sediment has a greater percentage of areal cover than when the hemipelagics pond into crevices and pits in the lava surface. Hence, assessing the degree to which the mode of sediment cover varies is an important part of the interpretation—a process which is easier when the sediment cover is light.

2.3.8.3 Relative ages of flows

Once the relative age of individual frames have been assigned, these must be collectively appraised to achieve relative ages for separate flow units. The extent of sedimentation can vary considerably over a single flow and is especially dependent on the local gradient. Steep pillow flow fronts have very low relative age scale values (usually between 1.2 and 1.4) whereas the apparent sedimentation on the gently inclined top of a single flow (excluding the flow front) can vary by as much as 1.5 points on the relative age scale. The redistribution of sediments has been widely reported on the MAR (Van Andel & Komar, 1969; Macdonald & Luyendyk, 1977; Barth et al., 1994) and results in systematically less sediment on the topographic highs and ponding in lows, especially into fault controlled depressions. In a detailed study of sedimentation over the FAMOUS area, Marks (1981) concluded that downhill transport occurs on all scales, the most significant mechanism being extensive bioturbation leading to the resuspension of fine material and gentle gravity transport. She suggested that considerable redistribution can occur in all areas, not just those affected by strong bottom currents and/or a high level of microearthquake activity.

Although sediment redistribution is obviously significant, relative age determinations of lithologic units on the ridge axis are routinely made on the basis of sediment accumulation (Needham & Francheteau, 1974; Ballard et al., 1981; Embley et al., 1990). Macdonald (1986) supports the use of sediment cover for age estimates on pillow flows where the roughness of the lava surfaces helps to shield local sediment pockets from bottom current erosion. Macdonald and Luyendyk (1977) show that, despite highly erratic variations in sediment cover on a local scale, thickness generally increases with distance from the axis in a predictable manner. Hence gross variations in sediment should provide meaningful relative age estimates. Most authors now seem to recognise that although

there are considerable pitfalls, the technique is usable as a rough first order estimate of age.

It is clear that the effective use of sediment cover to determine age estimates is critically dependent on how the representative sample for a single flow is chosen. Compensation must be made for local variability, given the way the sediments in a particular area are likely to be redistributed.

The extent of sediment redistribution itself depends on the age of a flow. There is some degree of local ponding along flow tops of all ages, suggesting that redistribution must occur, to a small extent, even on the younger flows. Sharp contrasts in sediment cover marking the contact between two flows, can only be preserved if the time scale at which sediment moves laterally is large compared with the age of the more recent eruption. Such sharp contrasts in sediment cover are observed at shallow contacts between flows, as well as those where the accompanying change in gradient is likely to be the dominant cause of an abrupt change in sediment cover (e.g. a steep flow fronts downlapping onto a gently dipping flow top). This suggests that for younger flows (relative ages of less than 2.0), sediment transport between adjacent flow units is limited and hence a reasonable estimation of the relative age of a single flow unit can be achieved by averaging values along the respective flow top. The flow ages obtained by this method can be checked to ensure that they are consistent with the contact relationships observed in the photoanalysis.

For the older flows (relative ages greater than 2.0), the local topography of a wider area should be taken into account. Sediment is transported down the flanks of a robust NVR (such as that occurring in segment 2), resulting in a systematic increase in extent of sediment cover towards the lower flanks and the marginal basin. However a similar sediment distribution is predicted from standard models of seafloor spreading and volcanic construction, where intrusion and extrusion are thought to focus at the centre (and peak) of the NVR. Consequently, it is very difficult to separate the effect of sediment redistribution from that of expected age variation on a robust NVR.

When the NVZ occupies the topographic low, as in the saddle area of segment 1, sediment will tend to be transported from the higher fault terraces towards the axis and so sediment redistribution is acting in the opposite direction to variations resulting from age gradation. Thus, it is possible to assess the relative importance of these two factors, by considering the sediment profile over the narrowgate traverse. Age variations were found to be the dominant factor compared with sediment redistribution. Hence, the method

adopted for obtaining relative age of the older flows is the same as that used for the younger flows, although it is recognised that the errors are greater because of the longer time available for sediment redistribution between flows.

In the previous section, the difficulties in determining a consistent relative age estimate of a sheet flow surface, when using a scale derived from pillow flows, were discussed. The data set for individual flows can be made internally consistent by a number of means. Relative age estimates for sheet flows with pillowy margins should be based on the cover on the pillowy area. Values for other sheet flows can be constrained by the ages of adjacent flows, where a clear contact relationship is observed, and by comparison with the sheety areas of the transitional flows mentioned above.

2.3.8.4 Absolute age estimates

An early attempt by Luyendyk and Macdonald (1977) to relate the areal sediment cover observed during photoanalysis to the absolute age of pillows, gave anomalously low sedimentation rates of 0.2 to 0.3 cm/1000 yrs. Large errors were introduced by model approximations of the flow surfaces to closely packed cylinders. More recently, Lichtman et al. (1984) attempted to create a curve of percentage of apparent sediment cover on a pillow flow versus absolute age. They use a model for calculating sediment volumes constructed with ANGUS photographs which assumes that the ponded sediment comes from gravitational downslope transport from the immediately surrounding pillows. They use a sedimentation rate for their area of the EPR of 1.5cm/1000 yrs (Goldberg & Koide, 1962) which is similar to that estimated by Marks (1981) of 1-2cm/1000 yrs for the centre of the North Atlantic. They estimate that a terrain of pillows averaging 1m in diameter will be half covered in 600 years and completely obscured in 40,000 years.

Using the curve of Lichtman et al. (1984), all flows of relative age 2.0 and less are younger than 500 years and those less than 1.7 are younger than 100 years. The latter estimate seems remarkably low. It is apparent from the exponential nature of the curve, that the slight errors in the percentage sediment cover for the young end of the age spectrum can cause dramatic variations in the age obtained. Errors induced by the assumptions of the model will also be most apparent for very small amounts of sediment cover. The model assumes complete sediment ponding into the inter-pillow pockets and yet observations show that draping of pillows with sediment also occurs and is perhaps the dominant mode of rest on a young flow, where a light sprinkling of sediment coats the whole surface. A model that disregards sediment draping will consistently underestimate the ages of flows.

Hence it is necessary to reassess the estimates of absolute age discussed earlier, bearing in mind that there are large errors associated with the visual estimates. I do this by interpolating between smooth sediment cover of a pillowed surface at 40,000 years old and the first indications of slight sediment cover at 1.2 years. I estimate that flows with relative ages of 1.2 should be no more than 100 years old; 1.5 suggests several hundred years while 1.7 may be about 1000 years. A flow of 2.0 relative age must be several thousand years old, 2.5 probably indicates about the 10,000 year mark, while 3.0 must be at least 20,000 years. I propose that even this rough visual estimate provides a more accurate assessment of age, than the method of Lichtman et al. (1984), which is based on assumptions that do not apply to the pillow lavas on the MARNOK traverses.

Very young flows which have only the lightest sprinkling of sediment and well preserved surface architecture, but don't have the very intense black shade or highly reflective surfaces of very fresh glass are deemed to be in the order 10s of years, consistent with estimates from submersible dives from the EPR (Macdonald et al., 1988; Haymon et al., 1991).

2.3.8.5 Age estimates of tectonised crust.

The sediment cover over tectonised crust reflects the age of active faulting rather than the age of the crust itself. Fault scarps have diminished sediment cover because of their steep slopes, while any sediment falling on fault-related talus ramps tends to filter down through the loose blocks. Composite faults, where narrow terraces separate steep scarps, produce a strongly fluctuating sediment profile, as the sediment progressively accumulates on the lower ledges.

The ages of fissures are reflected by the extent of infilling rubble and sediment. Rubble collects within a fissure, mostly during its formation, but also as a result of subsequent erosion of the vertical scarps. Once a fissure becomes inactive, hemipelagic sediment settles on top of the rubble and, with time, can completely fill a fissure until only two faint parallel ridges mark its edge. The time taken for sediment infilling to occur depends on the sediment cover of the surrounding flow and the extent to which redistribution from the surrounding flow contributes to the process. Small fissures which have recently formed on highly sedimented areas are demarcated by ridges of broken pillows protruding slightly out of the sediment.

When attempting to estimate crustal ages from sediment distribution, fissures faults and their related talus accumulations should be discounted from the averaging process.

2.3.9 Discriminating flow front breecia from fault talus

Several authors have commented on the similarity between fault talus and pillow flow front breccias (Luyendyk & Macdonald, 1977; Ballard & Moore, 1977). In addition, it has been suggested that steep flow fronts actually mask fault scarps (Bellaiche et al., 1974; ARCYANA, 1975). If this is the case then flow front breccia and fault talus may be one and the same. It was nearly impossible to keep the WASP within a useful range when descending a steep drop and, unlike other camera systems, it was not designed with a horizontal incidence capability. Hence, many easterly facing sub-vertical slopes were not photographed, since our camera runs were from west to east. The talus at their bases can, however, provide a clue to the nature of the steep slope above. The high resolution bathymetry can also help in this matter, as faults have a sharp, angular cut off, while flow fronts tend to have a more rounded cross-section.

It is easy to recognise a fault talus when dealing with larger mature faults, like those which bound the inner valley. In addition to the associated fault scarp, the talus ramps can contain large, 1-2m blocks of massive basalt which have fallen from the exposed scarps of massive basalt (Luyendyk & Macdonald, 1977). Fault zones can also contain welded breccia, where fine grained talus has become lithified in a matrix of hemipelagic sediment. Ballard and Moore (1977) suggest that welded breccias are commonly seen on fault scarps, as faults often occur on reactivated fissures; the breccia being the lithified fissure infill.

The task is harder when dealing with faulting of pillow flows in the NVZ. The throws of the faults on the NVZ are not likely to be large enough to expose massive basalt, which occurs relatively deep in the lava section (Luyendyk & Macdonald, 1977). Hence the broken lava forming the fault talus will comprise ubiquitous broken pillows which are similar in size and nature to the pillow front breccia. It should be possible to discriminate flow front breecia, formed by constructional over-steepening, from fault talus, by an abundance of cylindrical fragments which originate from the elongate pillows outcropping on the steep flow front. Towards the top of a talus ramp the breccia itself becomes finer grained and less well sorted, allowing areas of the underlying lithology to protrude. This will be unbroken elongated pillows at flow fronts and fractured bulbous pillows on fault scarps.

2.3.10 Assessing fault dip

The dip angle of faults on the MAR is a topic relevant to a number of current issues, ranging from calculating the composite strain across the axis to the contribution made by

low angle faulting to axial morphology. From bathymetric maps, the valley wall faults often seem to dip at 30°-60° yet high resolution surveys have shown that they actually comprise composite zones where vertical scarps are separated by narrow terraces (Macdonald, 1986). A combination of high resolution bathymetry and photographs from the WASP are used to determine the true dip of faults within the inner valley. Fault scarps which are steep, but non-vertical, tend to collect loose rubble and sediment on the fractured basalt surface, whereas vertical scarps will remain relatively free of debris.

2.3.11 Assessing backtilting of flow surfaces

The importance of tectonic backtilting and its role in the subsidence of old volcanic edifices within the inner valley is an unresolved issue. Minor rotations of around 5° about a horizontal axis have been associated with fault planes dipping at about 60° in the inner valley (Ballard & Van Andel, 1977; Kong et al., 1988). In contrast, Hall (1979) proposed a model based on palaeomagnetic and ophiolite studies where volcanic constructions are dismembered by tectonic rotations of up to 40°. Large tilts acquired during crustal formation are also aspects of models proposed by Cann (1974) and Atwater (1979). These large degrees of rotation need not necessarily be related to faulting, but can also be achieved by intrusion combined with subsidence due, perhaps, to magma chamber collapse.

It is often difficult to determine whether a rough pillow flow terrain has been tilted, since there is usually no obvious reference surface. Direction of flow can be determined by pillow tapering, branching and the blunt round terminations of elongate pillows (Ballard & Moore, 1977). This gives some indication of the palaeoslope of older flows which can be useful in assessing whether constructional terrain has been tilted subsequent to its formation. Unfortunately, by the time the crust is old enough to have been faulted and tilted, the flow surface is usually considerably degraded and sedimented. Flow fronts should dip in the down-slope direction and the degree of elongation of pillows should be consistent with the gradient of the flow surfaces. For example, round bulbous pillows on a steep slope or highly elongated pillows on a horizontal surface are strong indications of post-formation backtilting.

2.4 TOBI sidescan sonar.

2.4.1 TOBI and the principle of sidescan sonar

TOBI (Towed Ocean Bottom Instrument), developed and built by the Institute of Oceanographic Sciences, was the main geophysical tool used to map the MARNOK area.

It carried a 30-32 kHz sidescan sonar, a 7.5 kHz sub-bottom seismic profiler, a triaxial fluxgate magnetometer, a thermistor probe and vehicle status sensors giving heading, speed, pitch, roll and hydrostatic pressure.

The vehicle is ballasted so it is slightly positively buoyant in water and is attached to the armoured coaxial tow cable via a 600kg depressor weight and a 200m neutrally buoyant umbilical. This has the effect of stabilising the instrument as the heavy mass largely decouples the vehicle from the vertical motions of the ship which would otherwise cause distortion to the image. The amount of tow cable deployed is about 1.5 times the water depth. This is required to maintain the vehicle at operating altitudes of about 400m above the seafloor and it is the drag from the cable which limits the survey speed to 1.5 - 2 knots (Murton et al., 1992). The two 3m, linear transducer arrays operate at slightly differing frequencies: 30.37 kHz - starboard and 32.15 kHz - port (Flewellen et al., 1993), to minimise the cross talk between the two sides. They generate a sonar beam either side of the vehicle which is wide enough to illuminate a swath width of about 6km with an along-track angle of 0.8° (figure 2.2).

The transmit-pulse is 2.8 ms long, repeated every 4s, with the return analogue backscatter signal digitally sampled at a frequency of 1kHz. This gives 8000 pixels per 6km swath (a nominal across-track display resolution of 0.75m). With an average towing speed of 1.75 knots, the along-track display resolution will be 3.6m, (the distance travelled by the ship between pings). However, it is the acoustic beam width and pulse length which primarily govern the true resolution of the instrument and define the size of the acoustic footprint.

As the width of the beam on the seafloor increases with distance from the tow fish, the along-track and across-track resolution also vary with range (figure 2.3). Equations for calculating the size of TOBI's insonified footprint are given in Flewellen et al. (1993). Near the nadir, the footprint size is 3.5m along-track and 8m across-track, whereas at the far range of 3km, the dimensions change to 43 x 2.1m (Blondel & Parson, 1994). Hence an across-track display resolution of 0.75m is unnecessary and results in files which are virtually unmanageable because of their large size. Subsampling the data by a factor of 8 and averaging across-track not only reduces data acquisition to a manageable rate but also considerably increases the signal to noise ratio (Le Bas, 1993). The resultant 1000 pixels per swath gives an across-track display resolution of 6m which is closer to the size of the insonified footprint, though some ultrafine detail across-track is smoothed. Nevertheless, TOBI has an order of magnitude better resolution than the previous GLORIA sidescan sonar survey of the Kane transform (Roest et al., 1984).

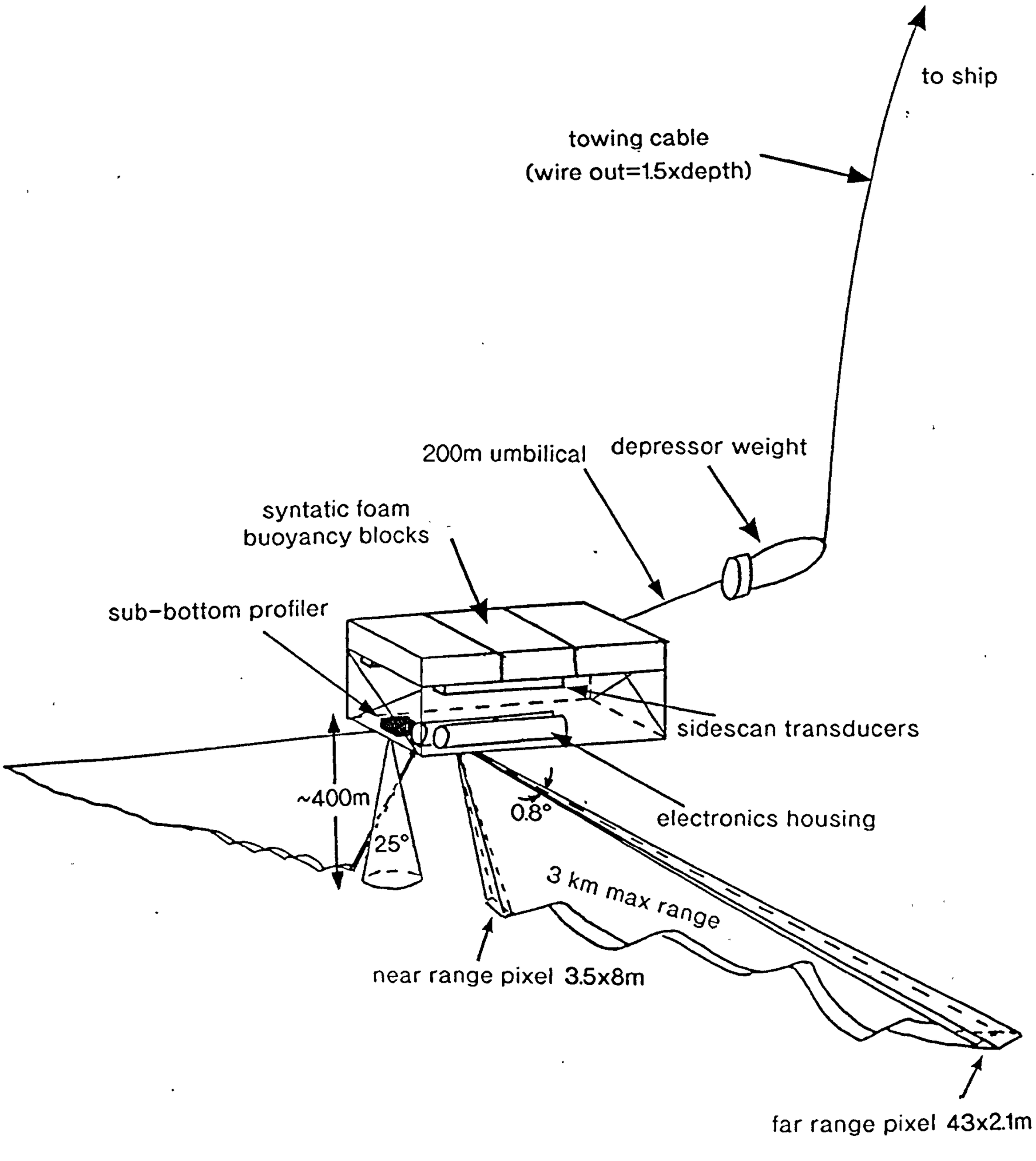

Figure 2.2 Schematic diagram of TOBI showing towing conditions and beam dimensions (adapted from Flewellen et al., 1993).

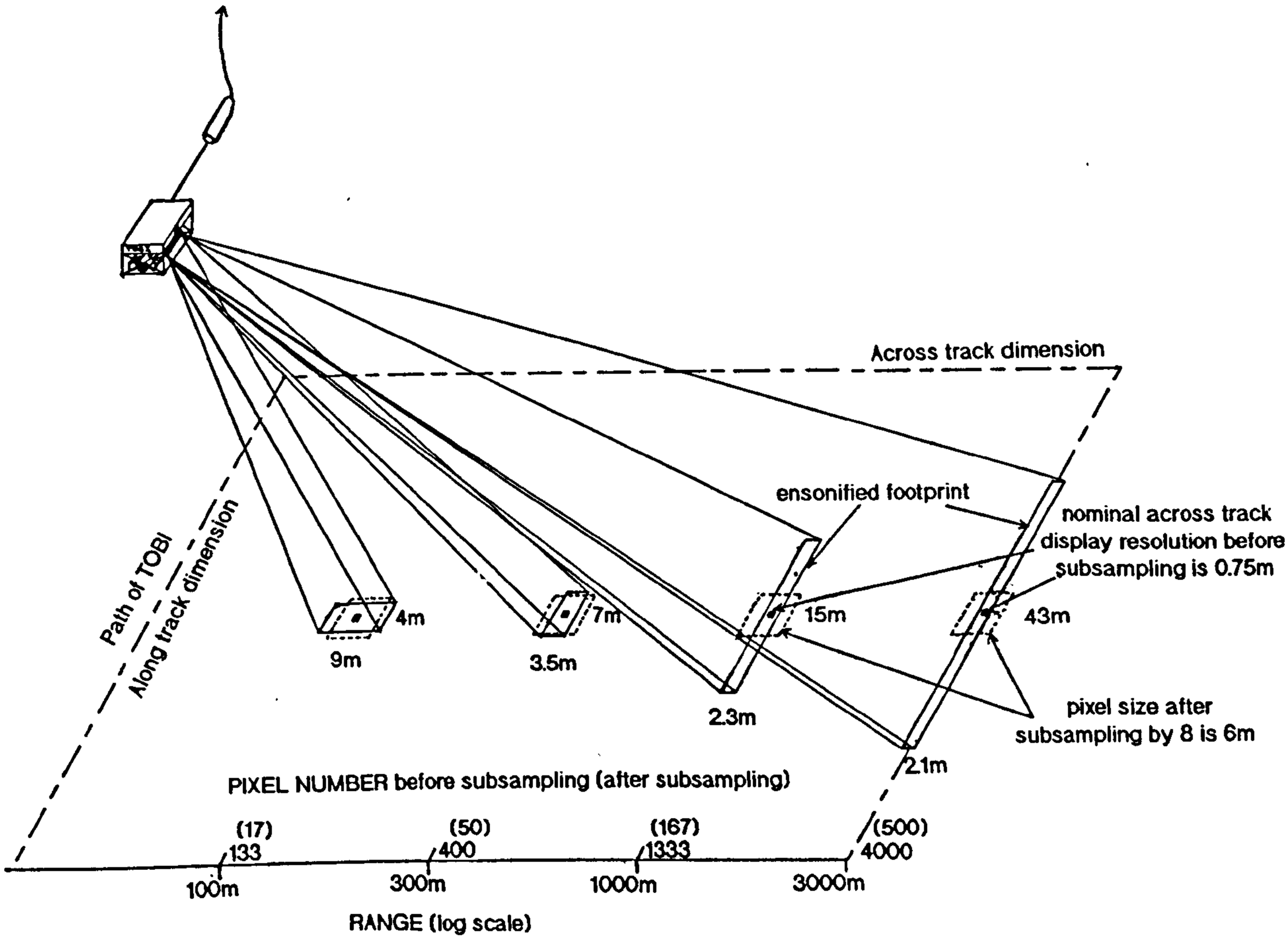

Figure 2.3 Diagram showing the relationship between the display resolution (pixel size) and the instrumental resolution (footprint size). Adjacent pixels have large areas of both along- and across-track overlap. Subsampling of the data set eliminates most of this redundant data (adapted from Johnson & Helferty, 1990).

Much of the transmitted energy is lost in direct planar reflections away from the transducers. The acoustic return at the receiver is a variable combination of backscattered (diffracted) sound and specularly reflected sound (as if from tiny mirrors) from the seafloor (Johnson & Helferty, 1990). The two main factors in determining the amplitude of the return signal are the acoustic impedance contrast between the seawater and the surface media and the different scales of topography on the seafloor. A high degree of surface roughness causes a greater reverberation of energy than a smoother area of the same acoustic impedance (defined as density x sound velocity). This is maximised where the wavelength of the microtopography and the incident sound are comparable, and where the diffraction and reradiation of sound is in the direction of the transducers; the return signal being stronger where there is a high angle of incidence of the sonar beam. Hence

the general direction of slope is important in dictating whether useful backscatter returns can reach the receivers (figure 2.4).

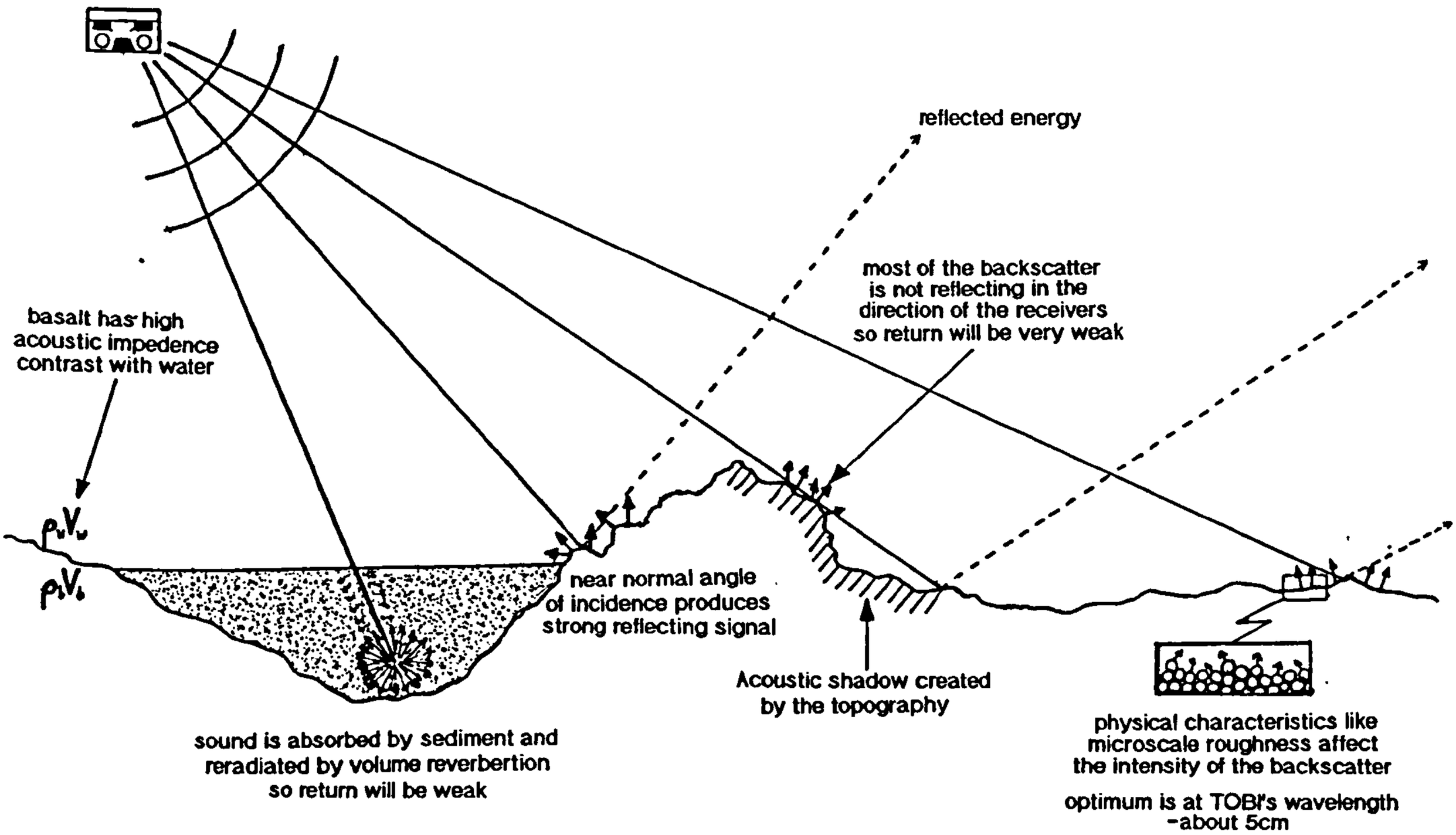

Figure 2.4 Diagram showing the interaction of acoustic energy with the seafloor in the generation of sidescan images (adapted from Johnson & Helferty, 1990).

Figure 2.4 also illustrates how acoustic shadows are generated behind areas of positive relief where the signal cannot penetrate. When there is sediment present a lower amplitude return occurs because of acoustic penetration of subsurface. The sound interacts with and is absorbed by the volume of sediment before being reradiated in all directions in a phenomenon known as volume reverberation (Johnson & Helferty, 1990.). Estimates vary for the maximum depth of penetration of a 30kHz acoustic signal. Barone and Ryan (1990), when working on the 30kHz *SeaMARC I* data, estimate the ages of terrains assuming that the signal will not penetrate more than 1m of sediment; a figure based on work by Urick (1979). In contrast, penetration depths of up to 5m were suggested for the TOBI system in discussions at a recent BRIDGE sidescan sonar workshop (N. C. Mitchell pers. comm.).

The TOBI sidescan images are displayed as a pixel greyscale swath with high amplitude returns as bright pixels and low amplitude dark, so acoustic shadows are cast as black areas.

2.4.2 Preprocessing and mosaicing of the TOBIgrams.

2.4.2.1 Digital preprocessing

Preprocessing corrections are made to generate an image which is to the first order spatially correct and has the correct amplitude values. A time-varying gain (TVG) is applied during the signal acquisition to compensate for the progressive reduction in sound intensity with cylindrical spreading and absorption through the water column (at about 3.65dB/km (Flewellen et al., 1993). Although this TVG should ideally be a smooth function, 1.5dB steps are inherent in the digital amplifier and sometimes these background 'contours' can be detected in the final image. Le Bas et al. (1995) have developed an algorithm to correct for this effect, but in the MARNOK survey the effect is only apparent when there is a shadow at far range, and does not seem to hinder any geological interpretation.

A water column correction ensures that the processor doesn't start the construction of the image until the sound from the bottom has reached the receiver and suppresses the near nadir pixels which contain the high amplitude bottom bounce.

The slant range correction is the trigonometric correction necessary to convert the actual "slant range" distance into the horizontal distance along the seafloor assuming a flat bottom. This uses the altitude data obtained from the first return of the 7.5kHz sub-bottom profiler. The slant range times for given horizontal distances are calculated and the pixel intensity at the appropriate slant range is returned in order to achieve a continuous series of pixels across the full horizontal range without gaps forming. As the required sampling rate for the slant range correction near the nadir is greater than the actual subsampled data frequency, some pixels are replicated to avoid gaps, which can give the near range image a blocky appearance.

Variations in vehicle speed are compensated for in the display process by the anamorphic correction. Rows of pixels are duplicated or removed to produce an image where the along-track and across-track scales are the same. In this data set the anamorphic corrections were chosen so that features on the sidescan best matched the bathymetric maps.

2.4.2.2 Mosaicing and vehicle positioning

The positioning of TOBI used a similar method to that previously described for WASP in section 2.3.3. The water pressure from the vehicle sensor could be converted to give instrument depth. This and the wire out were used to calculate hypothetical maximum and minimum instrument positions, corresponding to the two end member configurations for the towing wire (figure 2.5). The images were then mosaiced by hand using the ship's track and hypothetical maximum and minimum instrument positions as a guide, but the final positions of the mosaiced pieces were decided by the best match with features from the bathymetry. This usually involves an adjustment of a few hundred metres from the maximum hypothetical instrument position. The final vehicle position usually falls in the maximum quarter of the hypothetical range suggesting that a model cable position is close to a straight diagonal line from ship to instrument. When the ship increases speed the vehicle tends to rise and the horizontal range increases whereas hauling in the wire with the ship moving at constant velocity has the effect of decreasing the horizontal range as well as the vehicle depth.

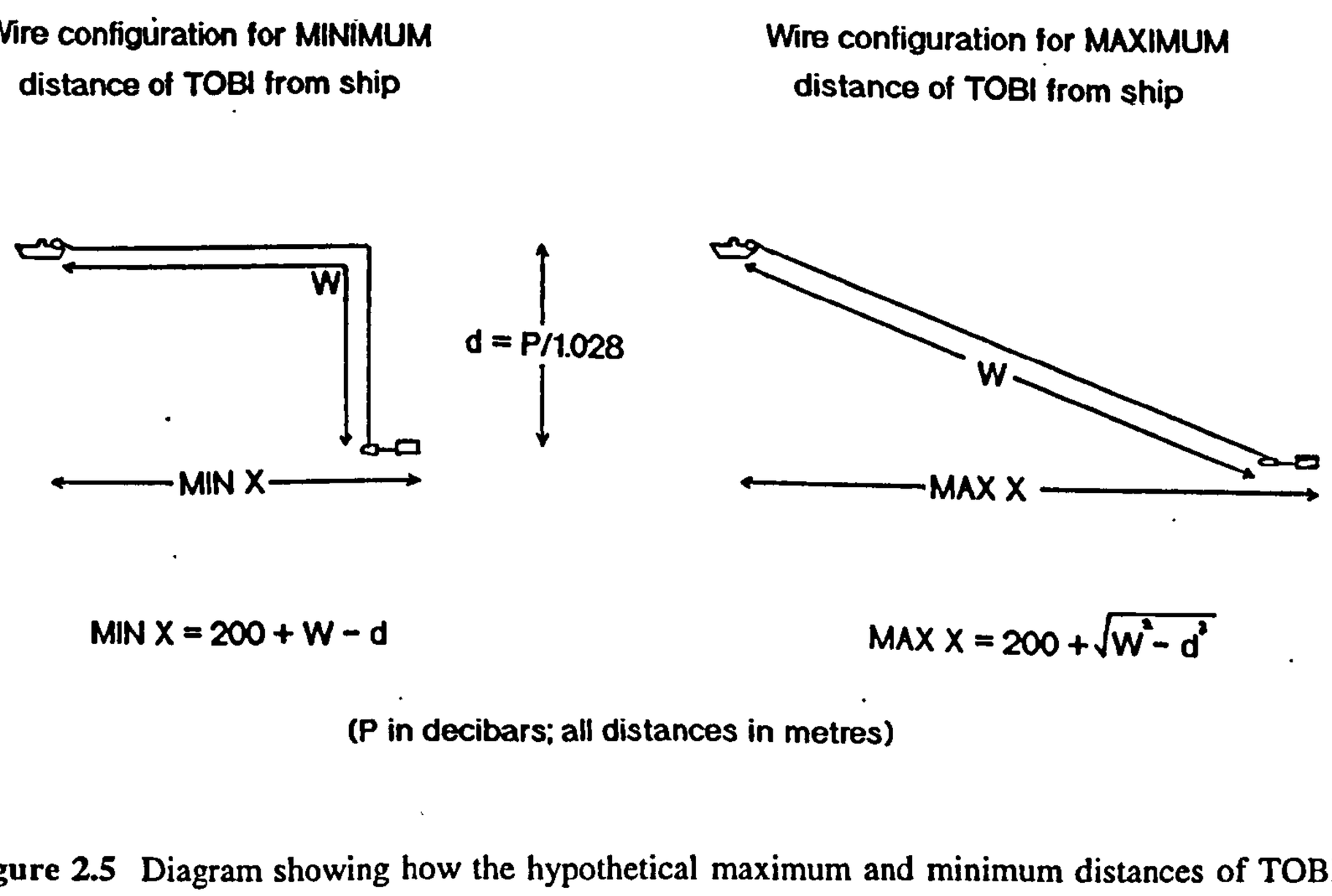

Figure 2.5 Diagram showing how the hypothetical maximum and minimum distances of TOBI from the ship were calculated.

Le Bas (1993) attempted to constrain the position of the vehicle using a profile matching technique, where the profile from the 10.5kHz ship board echo sounder was compared with that constructed from TOBI's sub-bottom profiler and pressure sensor. He found that

the profiles matched very well which adds credence to the assumption that the vehicle follows the path of the ship closely. Exceptions to this occur when there is a major alteration in course or when bottom currents push the vehicle sideways. Le Bas (op.cit.) suggested that errors of up to 2km on vehicle position have been experienced in such situations. In this data set some apparent movement of the vehicle either side of a straight ship's track can be accounted for by a layover effect caused by distortions from the topography (see 2.4.3.3).

2.4.3 Artefacts and considerations in the interpretation of the images

2.4.3.1 Errors resulting from vehicle positioning and tow path

The substantial distance between the instrument and the ship in a deep-towed system (~6-7km) presents a degree of uncertainty in the location of the instrument and subsequent image. However, for most of the survey, vehicle positioning did not pose a major problem because of the excellent constraint given by matching features in the sidescan images with the variable topography of the seafloor. Over more uniform areas, such as the western basin at the RTI, there may be location errors of up to 500m.

The ship completed several turns in the transform and off-axis oblique coverage. During these turns the instrument is estimated to have deviated no more than 750km from the ship's track along a path which falls inside the curve followed by the ship. The swath on the inside of the bend over samples the area so that point sources are drawn out into lines, while the coverage on the outside of the bend is incomplete.

2.4.3.2 Effects of spurious altitude values

When the vehicle was towed over high relief terrain such as the transform zone occasionally the profiler would temporarily loose lock on the bottom. This resulted in a time when spurious altitude data were recorded causing errors in the slant range correction and construction of the image with characteristic 'balloons' of deficient data symmetrical about the nadir. An extreme example of this occurs over the nodal basin where a 'black hole' occupies most of the swath width and virtually no useful data are present. At such times operator intervention was required to manually rectify the problem. The same effect occurs on a much less drastic scale throughout the data set as the altitude output from the bottom detector algorithm tends to oscillate around the correct altitude, varying by about 40m over a period of 60s (Le Bas et al., 1995).

2.4.3.3 Layover and effects of bathymetric variation

Over the mid-ocean ridge and fracture zone where the topography is quite rugged, the flat floor assumed in the slant range correction is not adequate for ensuring that there is no distortion in the image positioning. Layover is the term given to the geometrical distortions where features are shifted from their true positions by topographic deviations from the horizontal datum assumed in the slant range correction (Reed and Hussong, 1989). Where the seafloor slopes upwards from the nadir the target will appear closer than it really is and where the bottom slopes down the target appears further away. It is difficult to correct for layover without co-registered swath bathymetry. This is not yet available on TOBI so errors in the across-track positioning of acoustic targets are to be expected. Figure 2.6 demonstrates how acoustic targets over the ridge and transform can be displaced by as much as 300m. Linear features on slopes have been found to be rotated by 10°. Figure 2.6 also illustrates how, on such sloping terrain, the actual first return may not be from the seafloor directly below the tow body, but from that part of the slope closest to the receivers. Where parallel tracks with opposite look directions overlap, the same topographic features will be displaced in opposite directions resulting in difficulties in co-registration.

Towards the far range of the swath the relief commonly rises above the acoustic beam resulting in an effective "shadow" which approximately follows the contours (figure 2.6). Care must be taken not to confuse this with a true shadow which would occur where the relief decreases rather than increases. Figure 2.7 illustrates some cases where these effective shadows are easily recognised by their size, shape and location (at the edge of a swath during imaging of a steep slope). However, many occurrences of this artefact are considerably more subtle and can lead to misinterpretation and the obscuring of sizeable features.

Figure 2.8 demonstrates a case in question, where an area of the NVR of segment 2 imaged by TOBI has also been studied in detail using bathymetric mapping, dredging, piston coring and a submersible dive. (Zonenshain et al., 1989). The high resolution bathymetry reveals a narrow, linear depression, 300m wide and 100m deep, running along the 46°14'W longitude line and cutting through a circular seamount. This axial fracture consists of two vertical scarps of 70m and 30m which downthrow the western flank in an asymmetrical manner.

The corresponding sidescan image comprises a mosaic of two swaths (figure 2.8b). The two crestal scarps should be imaged as sharp, bright lines on the western swath, while

313° 56' 313° 57' 313° 58' 313° 59' 314° 00'

23° 50' 23° 50'

-4300

-4500

23° 49' 23° 49'

-3500 -3600 -3700 -3800 -3900 -4000 -4100 -4200

23° 48' -4000 -4100 -4200 -4300 -4400 23° 48'N

313° 56' 313° 57' 313° 58' 313° 59' 314° 00'E

313° 37' 313° 38' 313° 39' 313° 40'

23° 51' 23° 51'

-5100 -5000 -4900 -4800 -4700 -4600 -4500 -4400 -4300 -4200 -4100 -4000 -3900 -3400 -5000

23° 50' 23° 50'

23° 49' 23° 49'N

313° 37' 313° 38' 313° 39' 313° 40'E

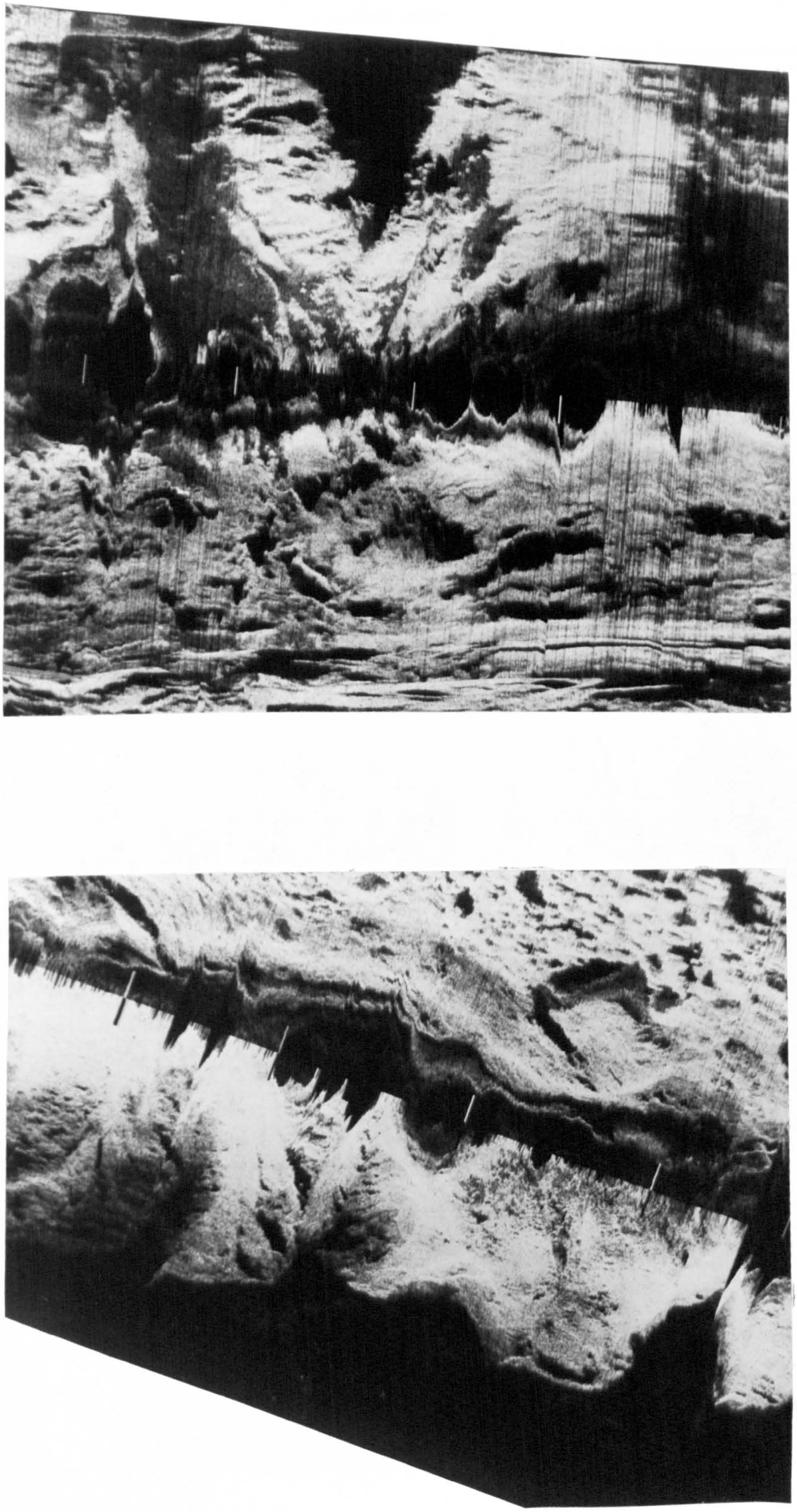

Figure 2.7 TOBIgrams illustrating the effective shadow that is generated at the edge of the swath when the relief rises above the acoustic beam. Note how the shadow follows the contours of the steep slope and is not due to a crest which has lower relief terrain in shadow behind it.

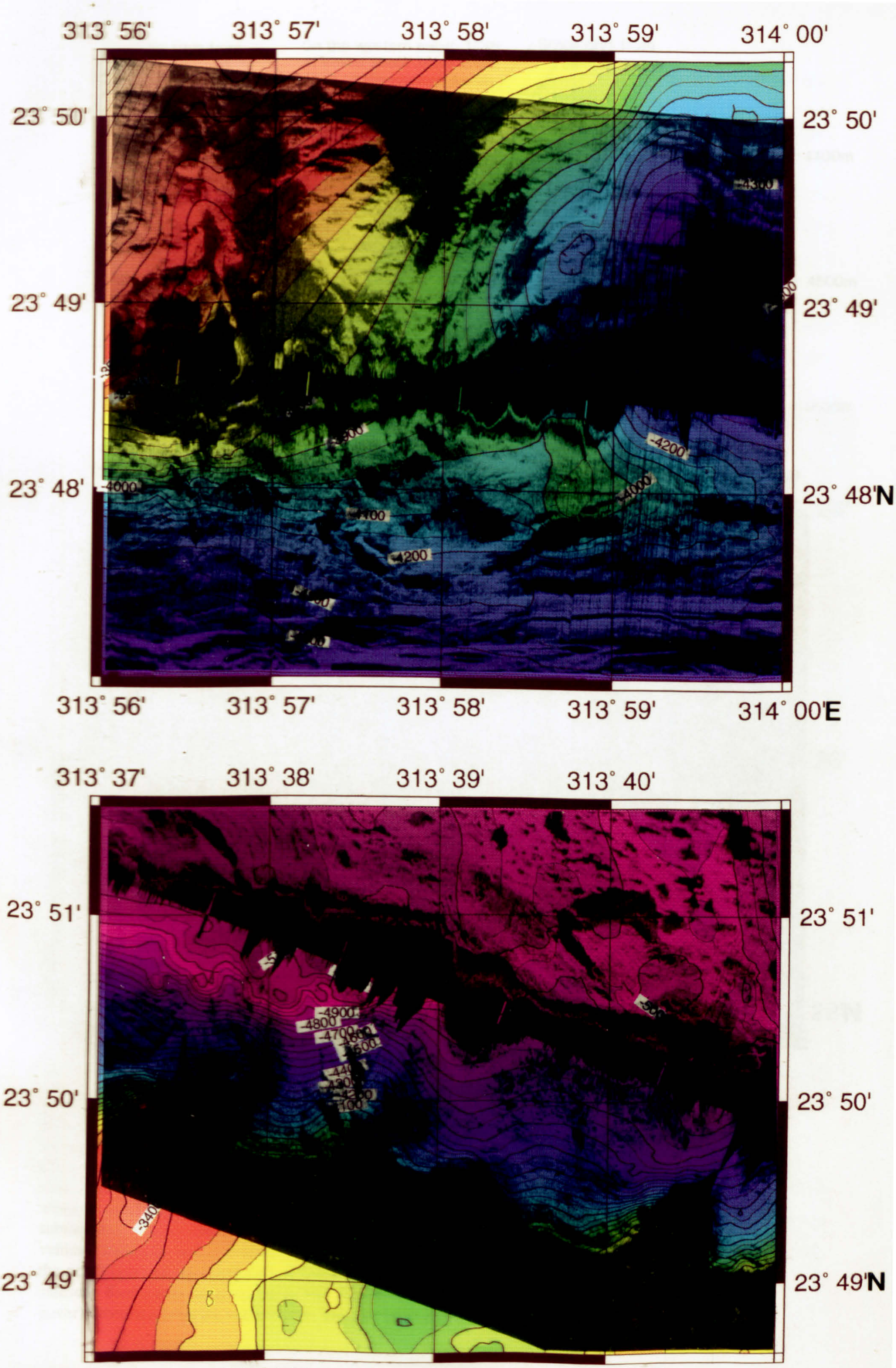

Figure 3.7 3DBIgrams illustrating the effective shadow that is generated at the edge of the swath when the relief rises above the acoustic beam. Note how the shadow follows the contours of the steep slope and is not due to a crest which has lower relief terrain in shadow behind it.

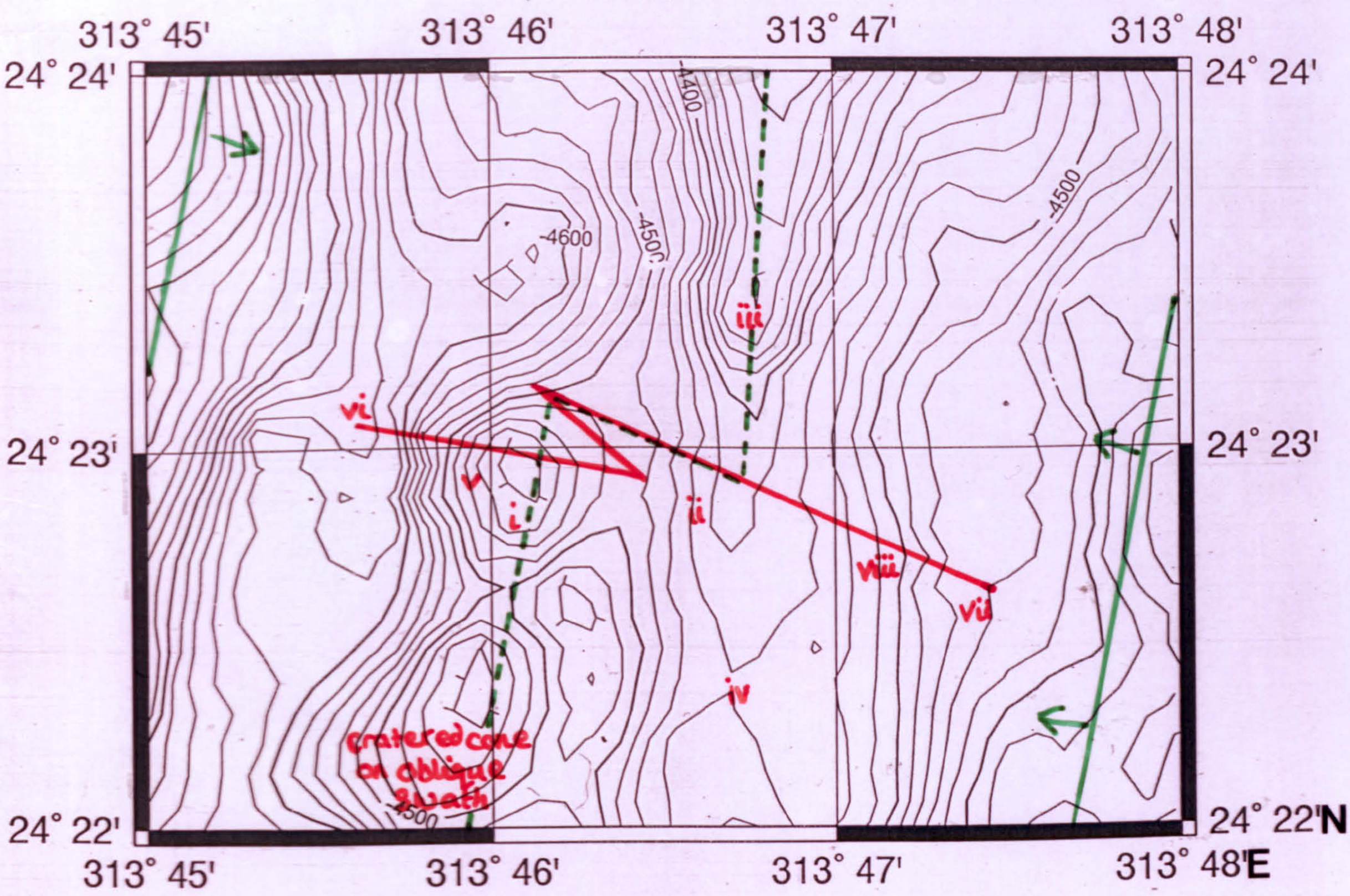
313° 45'
313° 46'
313° 47'
313° 48'
24° 24'
24° 23'
24° 22'
-4400
-4500
-4600
-4500
-4500
i
ii
iii
iv
v
vi
vii
viii
crater ed cone
on oblique
south
-4500
313° 45'
313° 46'
313° 47'
313° 48'E
24° 22'N

(a)

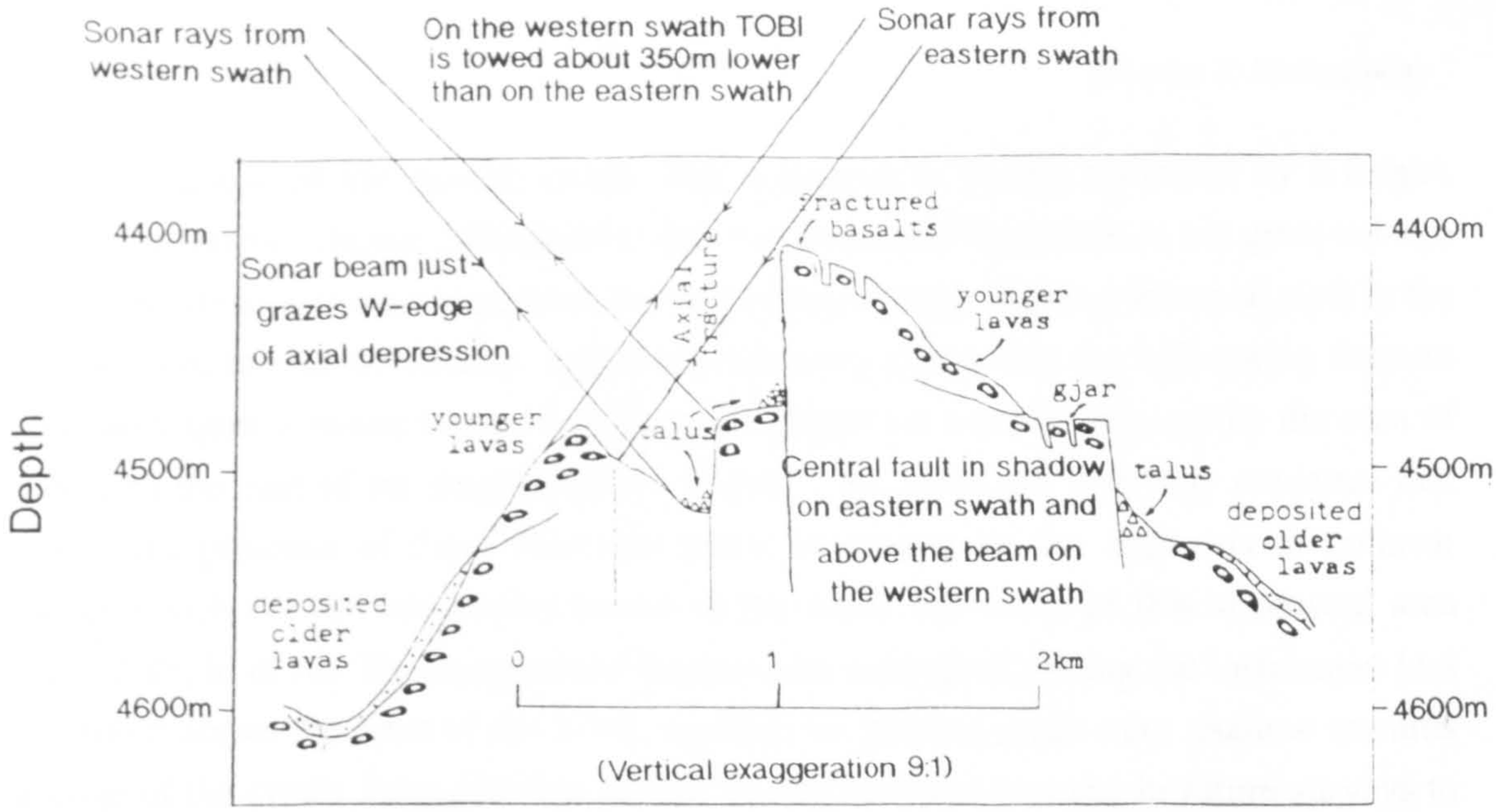

(b)

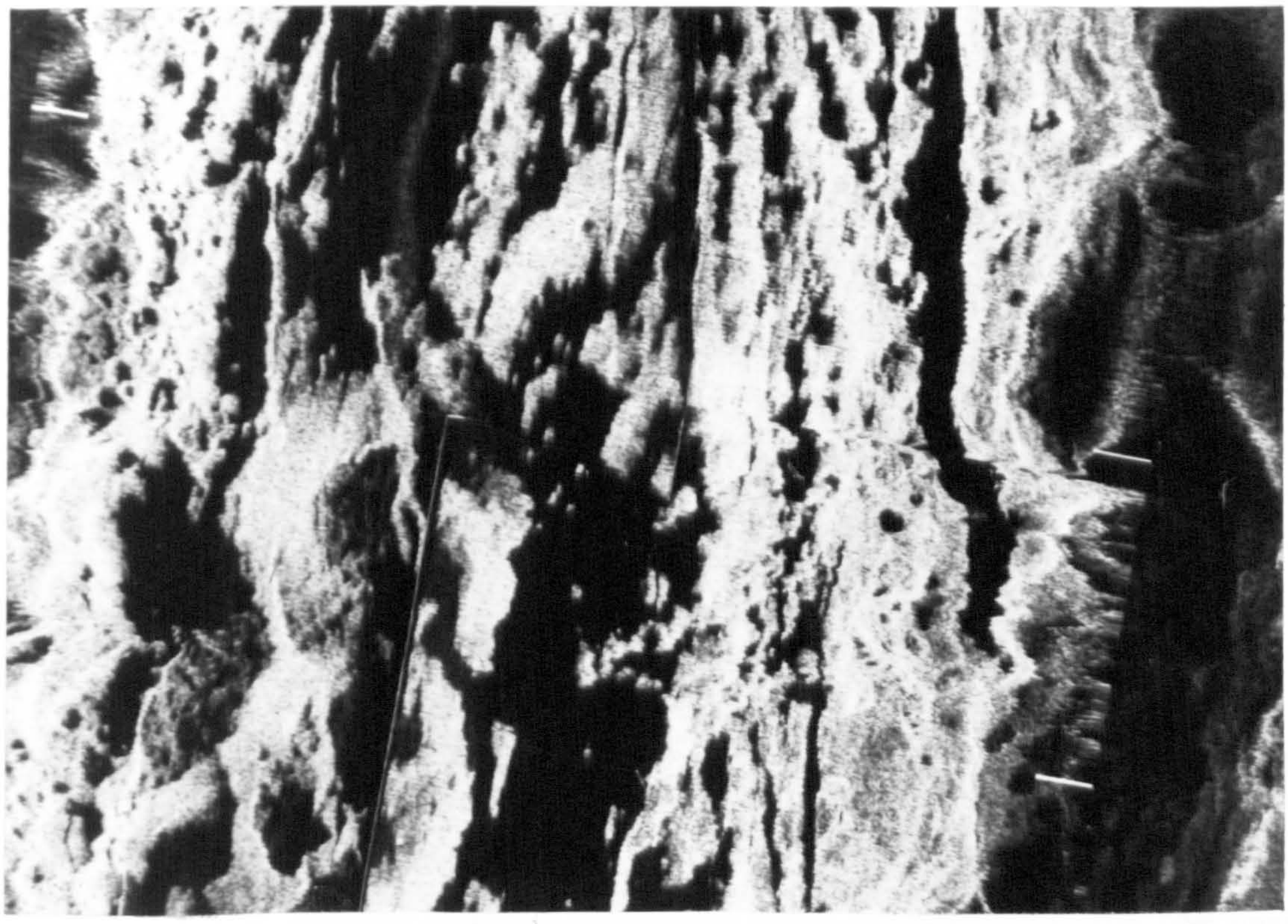

Figure 2.8 (**a**) Transect 4 of Zonenshain et al. (1989) based on the MIR-1 submersible dive profile through the inner floor along 24°23'N. (**b**) TOBI sidescan mosaic at same horizontal scale as (a), showing location of transect 4 (red line). This section of mosaic is composed of two swaths, joined along green dashed line. Nadir of swaths marked by unbroken green line with insonification direction shown by arrows. A bifurcating fracture (i) dissects a flat-topped seamount (v). To the east of (i) the western swath is in shadow and the large crestal west facing scarp which is prominent in the submersible transect (a) is not imaged. This is thought to be a result of the low towing altitude of the vehicle. The scarp is also in shadow in the easterly swath shown here (ii), but the fault can be traced to the north (iii) and the south (iv) of shadowed area. At the ends of the traverse the amplitudes of the sidescan backscatter decrease (vi & vii). This correlates with the older lavas (with > 1m of sediment cover) identified from the submersible. The gjar (viii) are also identified from the submersible.

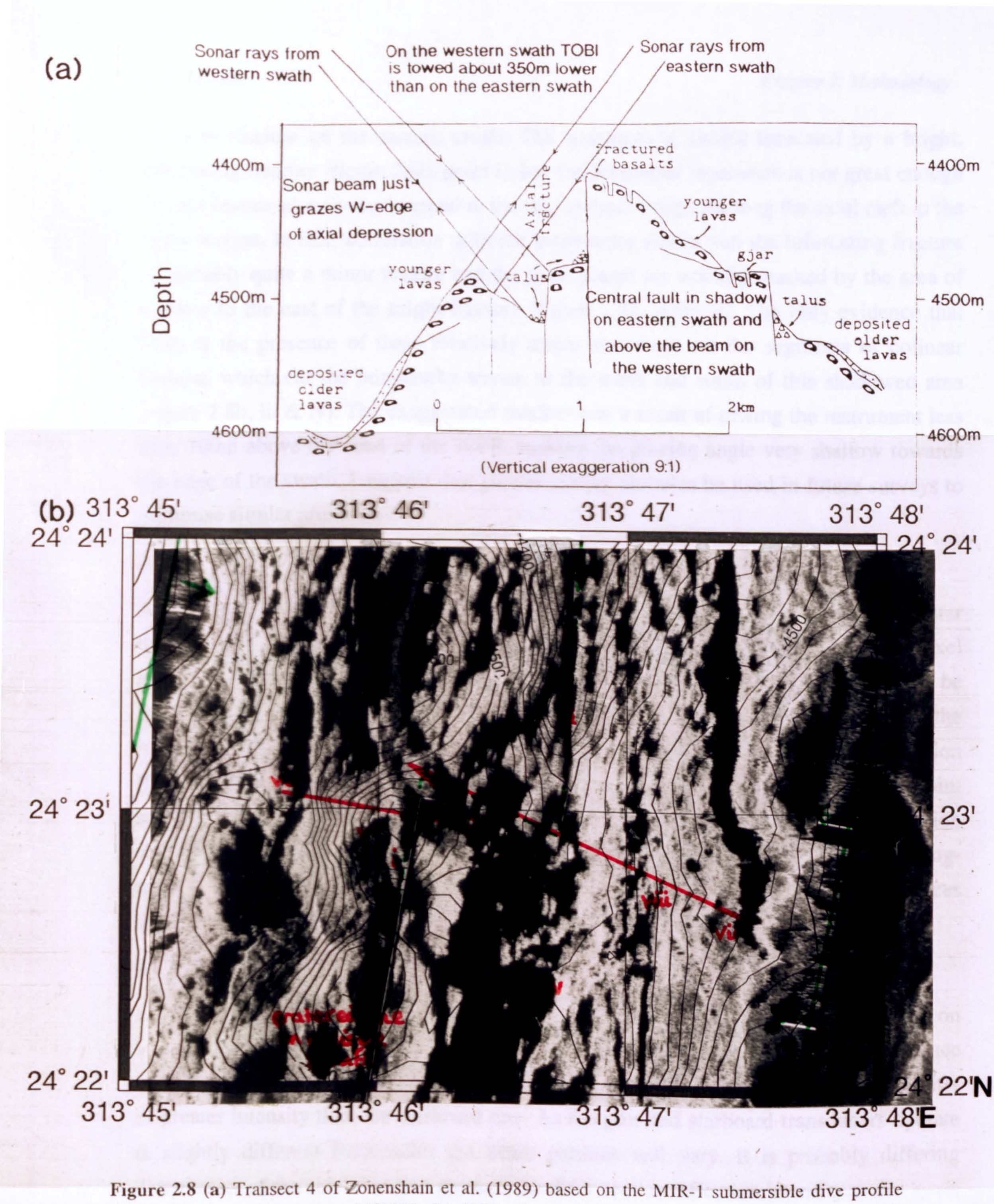

Figure 2.8 (**a**) Transect 4 of Zonenshain et al. (1989) based on the MIR-1 submersible dive profile through the inner floor along 24°23'N. (**b**) TOBI sidescan mosaic at same horizontal scale as (a), showing location of transect 4 (red line). This section of mosaic is composed of two swaths, joined along green dashed line. Nadir of swaths marked by unbroken green line with insonification direction shown by arrows. A bifurcating fracture (i) dissects a flat-topped seamount (v). To the east of (i) the western swath is in shadow and the large crestal west facing scarp which is prominent in the submersible transect (a) is not imaged. This is thought to be a result of the low towing altitude of the vehicle. The scarp is also in shadow in the easterly swath shown here (ii), but the fault can be traced to the north (iii) and the south (iv) of shadowed area. At the ends of the traverse the amplitudes of the sidescan backscatter decrease (vi & vii). This correlates with the older lavas (with > 1m of sediment cover) identified from the submersible. The gjar (viii) are also identified from the submersible.

being in shadow on the eastern swath. The seamount is clearly truncated by a bright, bifurcating fracture (figure 2.8b, point i), but the horizontal separation is not great enough for this feature alone to correspond to the two vertical scarps forming the axial cleft in the cross-section. In fact, correlation with the bathymetry shows that the bifurcating fracture is probably quite a minor feature and the main scarps are actually masked by the area of shadow to the east of the bright fracture (figure 2.8b, point ii). The only evidence that hints at the presence of these relatively major structures are the segments of colinear features which cut the hummocky terrain to the north and south of this shadowed area (figure 2.8b, iii & iv). The exaggerated shadow was a result of towing the instrument less than 100m above the crest of the NVR, making the grazing angle very shallow towards the edge of the swath. I suggest that greater towing altitudes be used in future surveys to minimise similar artefacts.

2.4.3.4 Point migration

As the beam footprint at virtually all slant ranges has an along-track dimension greater than the inter-ping spacing, any isolated strong reflectors less than the nominal pixel length will be insonified several times by adjacent pings causing the point source to be drawn out into a linear feature on the image. This effect increases with range as the insonified footprint gradually becomes more elongated in the along-track dimension (figure 2.3). At the far range of 3000m the along-track footprint is 43m and so any point source will be imaged by at least 7 pixels (as display resolution is 6m). In addition strongly reflecting areas will be expanded by several pixels on either side in the along-track direction. The effect is similar to that seen in seismic data where point sources spread into hyperbolic reflectors (Reed, 1987).

2.4.3.5 Sea surface reflections

Lines of high intensity pixels which run symmetrically about the ship's track are seen on some of the oblique swaths across the ridge. These are reflections from the sea surface which appear when the vehicle is towed above 2600m. The port reflection is consistently of greater intensity than the starboard one. As the port and starboard transducers operate at slightly different frequencies the beam patterns will vary. It is probably differing directivities of the sidelobes that produce the difference in reflection intensity.

2.4.3.6 Noise

Two kinds of noise are apparent in the TOBI sidescan - dropouts, (swath lines with anomalously low intensity) and speckle (sharp single pixel peaks or troughs). The speckle is caused by ambient noise in the water column. When the speckle occurs symmetrically

about the ship's track, the origin of the noise may be from the vehicle itself, for example squeaking of the slip rings (Le Bas, 1993).

Line dropouts occur frequently in the data especially where the towing conditions of the vehicle are altering. It is possible that changes in the vehicle pitch, roll or direction during a ping may reduce the sensitivity of the receiver array to the returning signal. Data may also be lost in the encoded signal whilst being transmitted up the cable, but this is relatively rare.

2.4.3.7 Data lost in the nadir

The nadir is the region directly under the sidescan tow body from which there are no useful backscatter returns. The nadir region is usually about 1.5 km across and a considerable amount of information can be lost within it. Figure 2.9 compares two swaths from a 30km^2 area at the junction between segment 1 and 2. The three nested seamounts imaged on the oblique swaths are almost entirely lost under the nadir region of the ridge-parallel swath. If the oblique swath over this region hadn't been available, then the extent of this constructional feature may have been missed. This is a cause of some concern when attempts are made to estimate the number of seamounts over the study area from the TOBIgrams. Examination of the bathymetry over the same area also gives an indication of the presence of seamounts and demonstrates how interpretation of these images is always best accompanied by careful consideration of the bathymetry. In the nadir region, the bathymetry and the sub-bottom profiler are the best clues to the kind of morphology that may be present.

2.4.3.8 Direction of swath

Sidescan sonar is fundamentally an anisotropic imaging technique. Because of the variations in the size and shape of the insonified footprint, resolving power is both range dependent and orientation dependent. Small-scale features parallel to track lines may be resolvable in the image while features perpendicular may not. This can mean that important boundaries may not be imaged if the swath is in an unfavourable direction.

The directionality of the beam also tends to cause shadows to be cast which highlight the fabric in a swath-parallel orientation. As a result of this, the same area of seafloor can look quite different in swaths with different orientations. This is demonstrated in figure 2.10 where the appearance of the fabric over the nodal basin varies considerably between the ridge and transform-parallel swaths. Consequently the directional bias from the orientation of the swath should be considered in the interpretation. Care must be taken

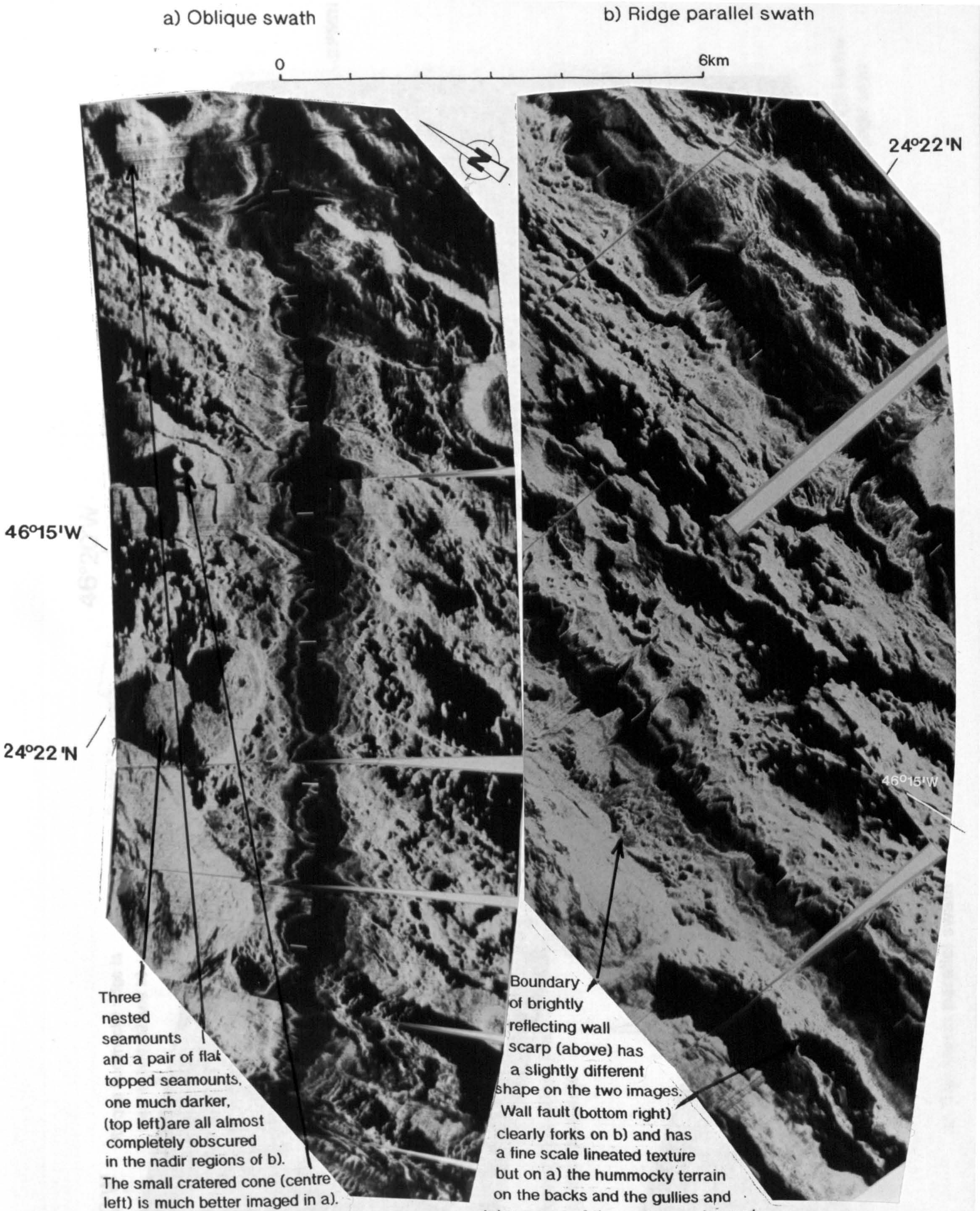

Figure 2.9 (a) Oblique and (b) ridge-parallel swaths over the same area at the junction between segment one and two. More seamounts are identifiable in the oblique swath including the three nested seamounts which are lost in the nadir of the ridge-parallel swath. Note also how layover, point migration and directional bias cause slight differences in the shape and nature of different textural domains. The bathymetry over the same area gives an indication of a constructional edifice but the nature of the nested seamounts is not apparent.

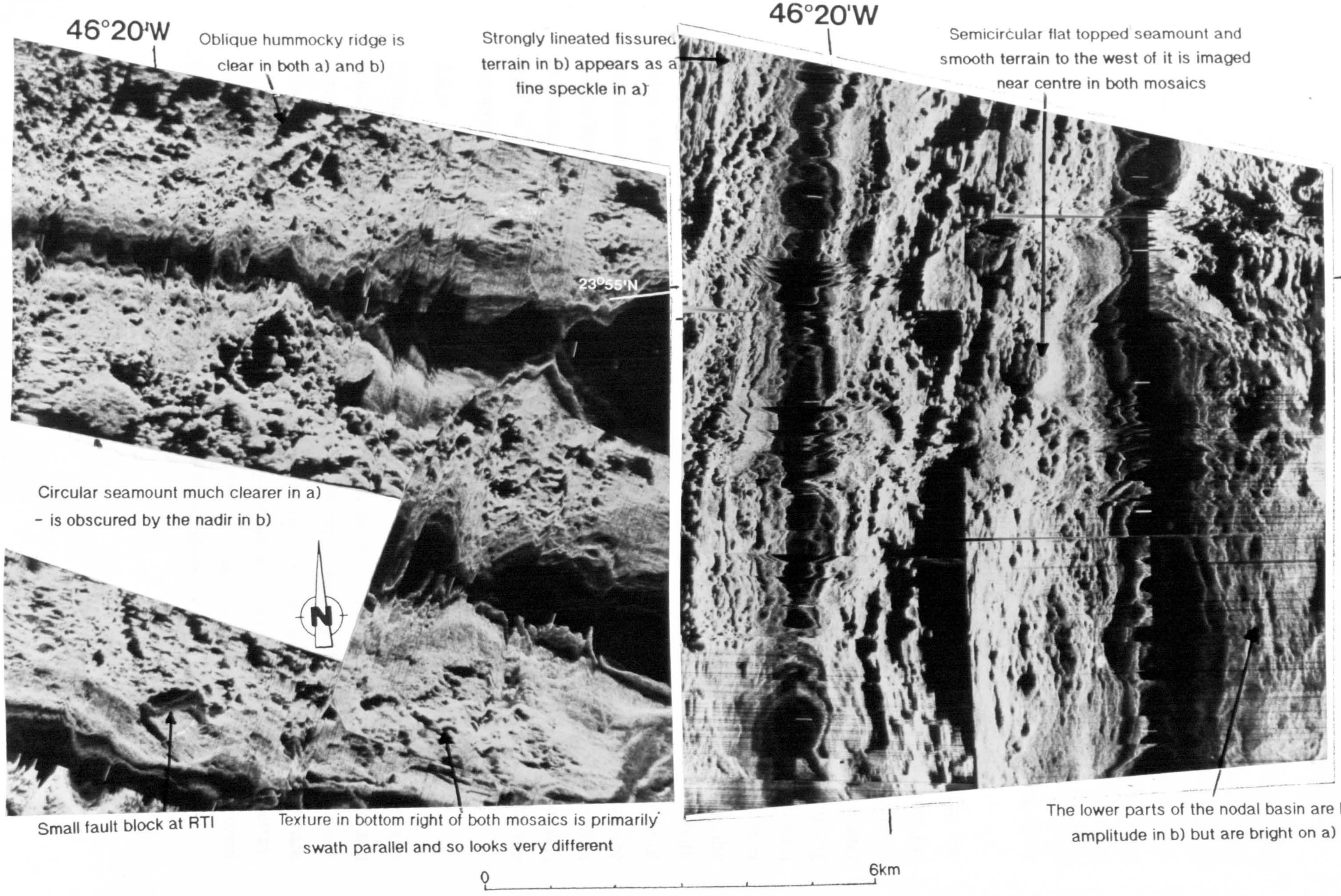

Figure 2.10 (a) Transform-parallel and (b) ridge-parallel swaths over the same area to the west of the nodal basin. Note how the features highlighted tend to be in a swath-parallel orientation, so the same area of seafloor can look quite different under different illumination directions.

when assigning a swath-parallel orientation to features which are only viewed from that one illumination direction and are not resolvable from the bathymetry. For example, the identification of ridge-parallel, hummocky neovolcanic ridges from ridge-parallel swaths should be treated with a certain amount of caution. In this study area, where ridge-parallel and transform-parallel features are present, track lines laid at 45° to the spreading direction will optimise the imaging potential of these perpendicular fabrics and compensate for the anisotropic resolution. However, oblique swaths are an inefficient strategy for obtaining complete coverage of the axial valley and the amount of time spent turning is considerably increased.

The angle of insonification can also affect the intensity of the backscatter. On the transform-parallel swath, there is a slight decrease in the backscatter intensity over the descent into the nodal basin, and even the terrain in the bottom of the basin has a relatively strong backscatter. In contrast, there is a strong decrease in the backscatter amplitude towards the bottom of the basin, which would seem to reflect increasing sediment cover (figure 2.10). The tow heights for TOBI were fairly similar for both passes over the nodal basin so the lack of agreement in backscatter variation is best explained by the topographic variation with respect to the beam orientation. As the instrument descended into the nodal basin on the transform-parallel run, the relief on both sides of the swath was roughly equal. In contrast, on the ridge-parallel swath the angle of incidence on the upper half of the basin will always be greater than the angle of incidence on the lower half, leading to lower amplitude returns from the latter. Hence, the variation in amplitude of the backscatter, which might be interpreted as increasing sediment cover, may be largely an artefact induced by the interaction of the swath orientation with the topography.

2.4.4 Groundtruthing the sidescan

Groundtruthing is the process by which an area of known geology is imaged by a remote sensing technique to establish a useful correlation between the actual physical nature and particular characteristic returns of the remote sensing technique. With the sidescan sonar this is achieved by comparing individual sidescan textures with data on the surface geology obtained from camera traverses, submersible dives, and dredge recoveries. Further information relevant to the interpretation of a particular area can also be gained from other remote sensing techniques, such as sub-bottom profilers and bathymetry.

2.4.4.1 Terrain categorisation

The process of groundtruthing assumes that the sidescan can be categorised into textural 'acoustic' terrains which have a geological significance. Ideally there could be a one to one correspondence between the sidescan texture and geological features, but this is not always the case. The nature of the sidescan texture depends very much on the local topography and character of the shadows it casts. Features such as lava flows may have similar gross relief, but may differ considerably on a scale which is below the resolution of the instrument. For example, flat lying pillow fields may be indistinguishable on a sidescan swath from jumbled sheet flows, while the texture of an area of pillow mounds is completely different from that of a pillow field.

Groundtruthing can also establish to what extent TOBI can be used to resolve variations in the relative age of crust, as indicated by contrasts in sediment cover. The relationship between backscatter amplitude and sediment cover can be ambiguous as amplitude also depends on a number of other factors as discussed in section 2.4.3. For example, a flat-lying sheet flow with virtually no sediment cover may have a lower backscatter amplitude than a sedimented talus ramp, because the difference in the angle of incidence is dominant over the variation in sediment cover.

2.4.4.2 Sources used in groundtruthing.

Data sources from both the CD57 cruise and previous studies in the MARNOK area were used to establish the character of the seafloor in various areas and thus enable groundtruthing. Data from CD57 include the deeptow WASP traverses, the dredging and the 7.5kHz sidescan sonar.

Added to this were the two transects (numbers 4 and 5) of Zonenshain et al. (1989), the high resolution investigation of the RTI by Karson and Dick (1983) and some preliminary results of Fujimoto et al. (1994). Transect 4 of Zonenshain et al. (1989) extends for about 4km across the southerly extent of the NVR of segment 2, at 24°23'N 46°14'W (figure 2.8). It was constructed from bathymetric mapping, dredging, piston coring and a submersible dive. Transect 5 comprised a high resolution bathymetric profile across the rift valley, nodal basin and inside corner high with additional piston coring and two submersible dives up the eastern wall of the nodal basin (figure 5.2). Karson and Dick (1983) used ANGUS photographs and the manned submersible ALVIN while the dive survey of Fujimoto et al. (1994) covers the RTI and the area of the transform immediately to the east.

The groundtruthing techniques will be used in chapter 3 where the geological interpretation of the TOBI sidescan terrains are put forward.

2.5 The 7.5kHz profiler.

Output from the 7.5kHz sub-bottom profiler has been well-characterised on deeply sedimented areas of ocean floor, but Francis, (1977) provides the only previous analysis of echo character from a rocky ridge crest. During my examination of the profiler records I noticed that different types of return from the median valley floor, walls and variably sedimented ridge flanks corresponded with certain terrains on the sidescan records. In an iterative process I first used the the sidescan textures to confirm that the echo character of the profiler was varying with sediment cover, but I then went on to use the profiler returns to add weight to the interpretation of some ambiguous features on the sidescan (such as sediment slumps on the valley walls). I labelled the echo character type as I, II and III, with increasing sediment cover. In chaper 3 the echo character of the profiler returns are analysed by applying general considerations of the interaction of the incident ray with different types of surface found near a ridge axis. Hence, I include below a summary of some of the general principles applied in these interpretations.

2.5.1 General principles of interpretation

When attempting to understand and interpret the profiler records it is necessary to first consider the nature of the incident ray and the way the sound energy will interact with the types of seafloor; then view these results in the light of additional information such as the SeaBeam bathymetry and the sidescan images.

With a beam width of 25°, the diameter of the insonified area (assuming a flat bottom) is 177-266m for altitudes of 400-600m respectively. If the first direct reflections back from the centre and the edge of the beam are recorded the difference in the two way travel distance for these two paths would be 19m and 29m respectively for the above altitudes. With variable topography and returns from the subsurface a more prolonged return would be expected.

2.5.2 Generation of hyperbolic echos

There are three main mechanisms that generate hyperbolic echoes: diffractions, specular reflections and small-scale quasi-sinusoidal elements (Flood, 1980). Diffractions occur when the radius of curvature of the incident surface is less than the curvature of the wavefront of the sound (~20cm for the 7.5kHz profiler), while specular reflections are generated when the radius of curvature is several times larger. Specular reflections will be

stronger than diffractions as the sound is returned from a larger area (Hilterman, 1975). Hyperbolic echoes may not be observed if the width or spacing of the seafloor topographic diffraction points is much smaller than the first Fresnel zone (Sheriff, 1977). For the 7.5kHz echosounder, the first Fresnel zones for spherical waves will be 12.6m and 15.5m at towing altitudes of 400 and 600m respectively. Given the above information it is possible to speculate about the formation of the different echo types from different types of seafloor geology.

2.6 Deeptow Magnetics.

The magnetic inversion results of Hussenoeder et al. (1995) have been used in this study to compare with the geochemical, tectonic and age variations in the MARNOK area. Each of these three aspects can have an effect on the intensity of magnetization. The purpose of the comparison is to assess which, if any, are dominant.

2.6.1 High resolution inversion method

Hussenoeder et al. (1995) performed a magnetic field inversion along TOBI's oblique tracks across the ridge axis using the Equivalent Source method of Pilkington and Urquhart (1990). The magnetization was calculated by direct inversion of the equivalent source, which preserved the high resolution signal better than conventional methods of reduction to a horizontal plane prior to inversion (e.g. Guspi, 1987). Hussenoeder et al. (1995) show that this technique is especially suitable for near bottom surveys such as this one, where the instrument follows a path which drapes the topography. This is because the skewing induced by the geometrical consequences of the equivalent surface is negligible, but the increase in resolution is substantial.

2.6.2 The effect of crustal thickness variations on magnetization

The magnitude of magnetization obtained from the magnetic inversions also depends on the layer thickness. The inversions have used a constant layer thickness throughout the area, but the crustal thickness is expected to vary with segmentation as discussed in chapter 1. If the magnetic layer thickness varies, then the assumption of constant layer thickness will tend to produce higher values of inferred "magnetization" where the layer is thicker.

2.6.3 Using magnetics to map relative age of axial volcanism

The deep-tow magnetic data can be used to define the neovolcanic zone by mapping the maxima in the axial magnetization. The zones of most recent volcanism tend to be marked by very high magnetizations because the basaltic rocks have not yet been exposed

to the extensive low-temperature oxidation that tends to reduce magnetization (Irving et al., 1970). The narrower peaks, produced by the increased resolution of the above method, allow the most recent eruptions on the neovolcanic axis to be located very precisely, in a way which can not always be done by observation from the sidescan sonar.

The method of using the magnetization peak to map the most recent volcanism should be treated with a degree of caution and whenever possible verified by other means, as there are instances where it has been deceptive. Examples include the well defined central anomaly over the MARK area which was found to lie partly over a serpentinite body (Schulz et al., 1988; Karson, 1990) and variable degrees of maghemitization at depth in the NVR in the FAMOUS area (Prévot et al., 1979)

Because the intensity of the magnetization varies with the extent of alteration, it has been used in previous studies to gain a rough estimate of the age of the basalt source. Inversion of near bottom magnetic anomalies and direct measurements of the FAMOUS and AMAR areas (Van Wagoner & Johnson, 1983; Johnson & Atwater, 1977; Macdonald, 1977) show that recent lavas have magnetizations of 20 up to 80 Am^{-1} compared with 2 to 10 Am^{-1} for basalt older than 0.5Ma.

The rocks sampled during the CD57 cruise have not yet been measured directly for magnetization. As the magnitude obtained from the magnetic inversions depends on the layer thickness, it can not be used as a comparison with the direct measurements from the FAMOUS area. In their magnetic field inversions, Hussenoeder et al. (1995) account for the variation in crustal magnetization with age by fitting an exponential decay curve. The time constants of this exponential decay can be used to estimate variations in crustal age or tectonic destruction across-axis. The values obtained can then be compared with the FAMOUS area and relative age variations obtained from the WASP traverses.

There is likely to be a discrepancy between the age variations across the valley floor calculated from the magnetics and those estimated from the WASP phototraverse, because the deep-tow magnetization level is a crustal average, while the flows observed on the surface are merely a veneer of the most recent volcanism and do not represent the age of the total thickness of crust. Flows lower down in the stratigraphy will almost certainly be older and thus the average age assessed by the deep-tow data is likely to be greater than values assessed from the surface geology.

2.6.4 Effect of composition on magnetization

The concept of magnetic telechemistry (Vogt & Johnson, 1973; Vogt, 1979) proposes that the magnetic anomaly amplitude can be used to infer the degree of Fe-Ti enrichment

in crustal basalts. The magnetization of basalts increases with the degree of fractionation as highly fractionated rocks have higher values of Fe and Ti and so will also have greater abundances of titanomagnetite. This relationship has been found to be particularly strong at the highly fractionated tips of propagating rifts on intermediate spreading ridges such as the Galapagos and the Juan de Fuca Ridge (Vogt & de Boer, 1976; Vogt & Byerly, 1976).

However, more detailed geochemical surveys have shown that the level of differentiation decreases at the very tip of the propagating rifts even though the magnetic anomaly amplitudes remain high (Sinton et al., 1983). This suggests that magnetic telechemistry is limited and can only be truly predictive when other factors, such as magnetic layer thickness, are taken into account.

2.6.5 Tectonism of magnetic source layer

Faults and fractures enhance the destruction of the magnetic layer over and above the decay produced by crustal ageing. In fact, the magnetic layer may be completely destroyed during the formation of the large median valley wall faults. At the very least the magnetic source layer will be thinned creating a linear magnetic low along the strike of the fault. as modelled by Tivey et al. (1993).

2.7 Sampling.

2.7.1 Selecting dredge localities

The sidescan sonar was a considerable aid in selecting the sites for dredging, as particular features within a known geological context could be targeted. Although a wide range of sidescan textures were sampled, the emphasis was on sampling fresh material to gain a good coverage of the NVZ. Sample spacing is closer near the transform as the petrological variation caused by the 'transform effect' is likely to be greatest in this area. (See figure 1.5 and section 1.5 for a more detailed description of individual localities.)

2.7.2 Dredging precision

As the relationship between the geochemistry and the sidescan morphologies is an important aspect of this study, the spatial accuracy of the dredging is an important factor. The high resolution WASP profiles matched very well with their expected position, as calculated from the wire-out and the ship's position. The discrepancy between the wire-out and the seafloor depth is greater for the dredge sites implying that the wire deviated from vertical. Given the two end member configurations of wire position, the horizontal distance of the dredge from the ship must be in the range 300m - 1.5km. Ultimately the

accuracy of any work which is based on bathymetric maps is constrained by the errors associated with those maps, as discussed in section 2.1.

Location errors of greater than 1km are considerable when dealing with a high resolution survey. However, the pinger attached to the dredge invariably showed the expected topographic variation along the station giving a greater degree of confidence that the accuracy of the dredge locations are considerably better than this.

2.7.3 Unit Classification

For each dredge recovery the rocks were sorted into lithological units on the basis of hand-specimen identification. Basalts were divided into units on the basis of their phenocryst content, morphology and age (using the criteria of Bryan and Moore, 1977). The size of each unit was recorded in terms of approximate quantity of boulders, cobbles, pebbles, glassy chips and any sediment. This was followed by systematic hand-specimen descriptions including aspects such as alteration, morphology, surface appearance, vesicularity, modal mineralogy and phenocryst sizes. Each unit was given a number which was prefixed by the dredge station (e.g. the 3rd unit from dredge 22D is 22D-3). At least one sample was taken from most of the units. Each rock sampled was assigned a number and if more than one sample was taken from an individual rock then they were subdivided by letters (e.g. third specimen taken from the second rock sampled from unit 23D-1 is 23D-1-2c).

Appendix 4 contains a summary of the lithological units from each station and the hand-specimen descriptions of all the samples taken for whole-rock analysis.

2.7.4 Use of dredge results in groundtruthing

The contents of the bag and pipe dredges can be used to provide groundtruth information on sidescan terrains. In this study they have been particularly used to establish whether flat-topped seamounts comprise sheet or pillow flows, whether a dominance of a certain flow type correlates with a specific sidescan texture and to what extent variations in sediment cover can be recognised. Dredge recoveries also provide useful information on age variations along axis and distribution of hydrothermal activity.

2.7.4.1 Lava types

The dredge results can be used to assess the range of the flow types present in an area. The recovery of small pillow buds (such as the 'berlingots' of Needham and Francheteau, 1974) indicates that knobby pillows are present. The rubble produced from pillow flows comprises angular, broken blocks, mostly equant and of pebble and cobble size, with a

distinct radial fracture. Fragments from sheet flows tend to have a tabular appearance, with the original morphology of the lava cooling surface sometimes preserved on one side. Care must be taken not to confuse tabular sheet flow fragments with those from hollow pillows (Ballard et al., 1975), which are especially susceptible to collapse. The tabular plates of the latter can be recognised by their slightly curved appearance, having a glassy convex upper surface and concave underside, sometimes exhibiting drip marks.

Hollow pillows are produced when lava drains out of a pillow after the formation of the outer crust. Collapse pits form in a similar way by the draining of areas of sheet flow and the subsequent collapse of the surface crust. The magma either drains back into the subsurface plumbing system or downslope into a network of lava tubes. Either way, the formation of hollow pillows is often related to a sudden cessation of the eruption, where magmastatic pressure rapidly drops (Ballard et al., 1979).

2.7.4.2 Fault throw and intensity

As the throw of a fault becomes greater, increasingly lower levels of the crust become exposed and the corresponding lithologies collect in the talus at the base. A dredge over a talus ramp is bound to have a large recovery because of the loose nature of the blocks. The range and relative proportions of lithologies recovered gives an indication of the composition of the scarp above. Gabbros and greenschist facies dolerites indicate that throws are great enough to expose lower crustal lithologies, while boulders of massive lava and pillow beccias suggest smaller throws confined to the upper crust. Intense shearing in a well established fault zone is reflected by the presence of cataclasites (low temperature) and mylonites (higher temperature and deeper).

2.7.4.3 Age and sediment cover

The relative ages of the basalt can be assessed from the thickness of the glassy margins, the extent of palagonitisation of the glass, the surface encrustations of grey/black Mn-Fe oxides and the alteration of the interior. Water penetrates through cracks and joints in the rock, causing surface alteration and in some cases the precipitation of yellow sulphide minerals. Alteration fronts can be recognised by the colour change they produce: basalt turns from dark blue to having a greenish tinge; olivine phenocrysts alter from olive green to rusty brown; and plagioclase phenocrysts from white to dirty yellow. The alteration fronts permeate into the fresh interior from altered surfaces and the distance these fronts have penetrated is related to the age and porosity of the sample. Some of the older samples no longer have an unaltered interior and successive waves of alteration fronts can be mapped at varying distances from the surface. A thin, iron-manganese surface results

from the slow precipitation of Mn, Fe and other constituents from seawater as part of the normal ageing process (Bryan & Moore, 1977).

If sediment is present, it is recovered in the pipe dredge. It is assumed that the proportion of sediment to rock recovered roughly reflects the proportions on the seafloor. This can be used as a measure of relative age, as in the WASP traverses.

2.7.4.4 Hydrothermal activity

Intense 'sooty' coatings of Fe-Mn hydrothermal deposits suggest the proximity of a hydrothermal vent, which may be presently active or have only recently become extinct. The extent of the hydrothermal precipitation should decrease with distance from the vent source, so trends in the thickness of the black manganese coating can be used to constrain a likely location for the vent. Other evidence for hydrothermal activity includes the recovery of hydrothermal quartz which usually precipitates in veins with other minerals associated with alteration (e.g. quartz-epidote-chlorite veins).

2.8 Petrology and Mineral Chemistry.

Evidence about the history of a sample - alteration, crystallisation on eruption, crystallisation with a magma chamber, episodes of magma mixing and crystal accumulation - are all accessible from the thin section description. Petrology is a useful accompaniment to geochemistry as it reveals information necessary for sample selection and the accurate interpretation of the whole-rock, glass and mineral chemistry data. The mineral chemistry compliments the petrological and geochemical data set by enabling the extent of crystal equilibrium (or disequilibrium) to be assessed and the conditions of fractionation to be roughly quantified.

2.8.1 Identifying alteration and making age estimates

It is essential that the extent of alteration of a sample is known before it is selected for geochemical analysis as this knowledge will affect the interpretation of the geochemical results. The handspecimen and thin section assessments of alteration can vary, as the former enables a general assessment of alteration for the whole specimen, while the latter provides a very localised view, usually of an area within the centre of the rock sample adjacent to a chip used for geochemical analysis. Thus the petrographic identification of alteration is more useful for assessing potential element mobility in the geochemical analysis. However, thin sections taken from the very edge of a relatively fresh glassy rock

can provide a precise estimate of age by using the thickness of palagonite crust and Mn-Fe oxide coats[1] (Bryan and Moore, 1977).

From the particular alteration assemblage present, the degree of alteration can be assessed and a rough estimate for temperature of alteration can be made. This aids awareness of potential element mobility and enables the freshest samples to be selected for analysis. The stages of progressive low-temperature alteration of basalts have been well documented (Cox et al., 1979; Bryan & Moore, 1977).

Firstly, the fresh glassy crust develops a thin layer of palagonite, which is essentially a leaching and oxidation process. As the thickness of palagonite increases, some of the glass is replaced by clays and in the groundmass there are signs of secondary assemblages, such as low-temperature hydrous and oxidised minerals. At low temperatures, olivine alters to high birefringence green micaceous products, which concentrate along the curved cracks, while at higher temperatures marginal iddingsitation can take place (serpentine minerals and accompanying finely-divided opaques are also a higher temperature alteration assemblage that are not commonly observed in lavas). Plagioclase alters to a white mica called sericite, sometimes with accessory epidote. Clays, carbonates and zeolites (if the temperature is high enough to reach zeolite facies) are precipitated as amigdiodal phases in vesicles.

2.8.2 Identifying fractionation

The phases and modal proportions of phenocrysts give a rough indication of the extent of fractionation of a sample. The size and morphology of the crystals indicates whether they have been formed within a magma chamber or during eruption. Within the low-pressure basaltic system, olivine, ±Mg-Cr spinel and plagioclase are usually the first phases to crystallise, followed by clinopyroxene and then Fe-Ti oxides (e.g. Bryan & Moore, 1977; Bryan et al., 1981; Bryan, 1983). The Mg-Cr spinel phase is common in olivine-rich basalts, but rare in plagioclase-rich samples, and usually occurs as tiny inclusions within olivine.

The order of crystallisation can usually be determined by the inter-crystal relationships, such as one phase being consistently included within another. Miyashiro et al. (1969) showed that the order of crystallisation of the first two phases was dependant on the composition of the magma. Low-alumina tholeiites follow the order olivine⇒plagioclase

---

[1] Mn-Fe oxide accumulation occurs at a rate of 20μm/1000yrs, and palagonite thickness increases at about three times this rate (Bryan and Moore, 1977).

⇒clinopyroxene, while high-alumina tholeiites fractionate plagioclase before the olivine. Michael and Chase (1987) suggest that the order of crystallisation reflects not only a differing major element chemistry, but is strongly dependent on the H_2O content of the magma (high H_2O promotes early fractionation of plagioclase).

2.8.2.1 Crystallisation on eruption

Crystals which have formed during the drop in temperature and pressure associated with eruption have distinctive quench morphologies. Plagioclase commonly occurs as accicular microlites (figure 2.11) or in bow-tie intergrowths. Olivine microphenocrysts sometimes have skeletal forms (figure 2.11) which were confirmed by Donaldson (1976) to form as a result of quenching rather than resorption. Distinct skeletal morphologies relate to specific cooling rates and amounts of supercooling.

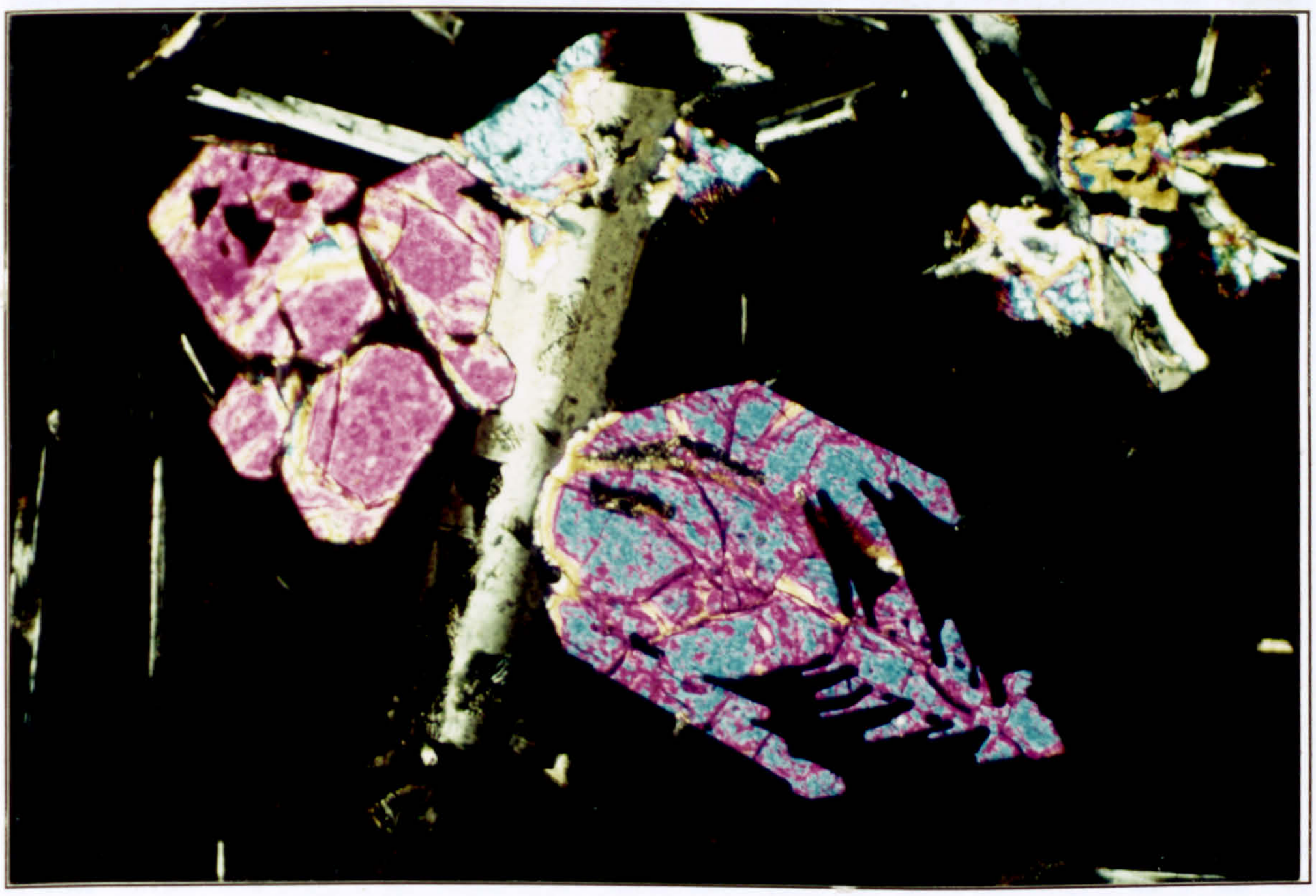

Figure 2.11 Example of quench textures in MORB. Olivine has a skeletal form or occurs as tiny subheadral microphenocrysts. Plagioclase forms accicular microlites. In the upper right these microlites radiate in a cluster with olivine. Note small field of view compared with following photomicrographs. Field of view is 1.3mm x 0.77mm —sample 6D-1-1b.

If large crystals are already present in the magma prior to eruption, the quench growth may occur by heterogeneous nucleation onto the edge of a previous phase. This results in

microphenocrysts clustered round the margins of the host phenocrysts and included within the quench rim (figure 2.12).

Crystal settling and accumulation are usually insignificant in the quench stage of crystal growth because of the small size and rapid growth of the phases. Hence, a whole-rock analysis of a basalt which only contains quench growth is essentially equivalent to a liquid composition. However sometimes crystal growth which occurs in conduits prior to the actual eruption of the lava can produce microphenocrysts which are capable of being concentrated by processes such as flowage differentiation, and crystal settling within a flow. If this is the case then, whole-rock compositions can deviate from that of true liquids, but the effect is likely to be small.

Figure 2.12 Euhedral plagioclase phenocryst is an intratelluric phase. It has a quench rim (grey) enclosing smaller olivine and plagioclase phenocrysts which have used the large phenocryst as a site for heterogeneous nucleation. Field of view is 3mm x 1.9mm —sample 6D-2-1b.

2.8.2.2 Intratelluric crystallisation

The intratelluric environment refers to processes that have taken place in a reservoir, prior to eruption. (Cox et al., 1979). In general, intratelluric crystals may grow to be large, euhedral phenocrysts (figure 2.12), but some, such as opaque minerals, may be small. Intratelluric phenocrysts can also form glomerophyric clusters of varying sizes (figure

2.13). Fractionation in a magma reservoir is thought to take place through crystal settling and boundary layer growth, thus separating the phenocrysts from the magma in which they formed. Hence, if a rock contains intratelluric crystals, the whole-rock analysis does not necessarily represent a liquid composition as some phases may have been preferentially removed or added by magma chamber processes.

Figure 2.13 Intratelluric glomerophyric cluster of plagioclase and olivine. Note the size difference between crystals in the cluster and the microlites in the quenched groundmass. Field of view is 6mm x 3.7mm — sample 21D-2-1b.

2.8.2.3 Closed-system fractionation

Closed-system fractionation occurs when a magma chamber evolves without interaction with other melts. Phenocrysts crystallise in the intratelluric environment from liquids that are represented by their groundmass composition after eruption. The petrographic evidence of a closed-system magma chamber includes the euhedral form of the crystals and zoning in a normal sense (as the composition of the crystalline phase remains in equilibrium with the evolving melt). The first formed crystals of a particular phase will tend to have a different composition to those formed later.

Under certain circumstances in closed systems, such as stratified magma chambers, phenocrysts can develop disequilibrium textures. These arise when crystals formed at the cooler top of the chamber settle through progressively hotter magmas of more refractory compositions. Disequilibrium textures will be discussed further in the section below.

2.8.3 Open-system processes—identifying magma mixing and assimilation

Strictly speaking, a system is classed as open when material is allowed to pass into or out of it. Using this strict definition, most MOR magma chambers must be open system as material is removed to form the layers of dykes and lavas in the crust. However it is more useful to discriminate magma chambers in terms of open or closed-systems by whether they experience multiple injection events and some assimilation of wall rocks (open-system) or evolve as a single batch with little or no interaction with the surrounding crust (closed system).

The likelihood of ridge basalt magma batches mixing during their uprise beneath spreading centres depends on the lateral and temporal permanency of subaxial magma chambers. Evidence for magma mixing comes from both petrographic and chemical studies of lava suites, though Donaldson and Brown (1977) point out that two sets of mutually incompatible crystals should occur in a sample before it can be claimed that magma mixing has definitely occurred. The petrographic implications of open-system process are discussed below.

2.8.3.1 Disequilibrium textures

After two magmas have mixed, the crystals that formed in one of the original magma batches are unlikely to be in equilibrium with the subsequent liquid composition. This will result in a reaction between the phenocryst with the magma to produce a variety of disequilibrium textures. Although disequilibrium textures should be common in mixed magmas, they are not diagnostic of an open system, as mentioned for the case of stratified magma chambers above.

When a phenocryst which usually has a euhedral form appears as a rounded form, perhaps with embayed margins it has almost certainly been corroded as a result of disequilibrium (figure 2.14). This occurs when a crystal is introduced into a magma which is more primitive than the one in which it was formed. If a phenocryst is undergoing active resorption when it erupts, a serrated and sometimes almost vermicular, texture is preserved along the rim (figure 2.15, figure 2.17).

The development of resorptional features when an influx a primitive magma is injected into a crystal rich magma chamber is by no means a foregone conclusion. Depending on the kinetics of the situation, the crystallisation of a more refractory composition onto the pre-existing phenocrysts may result in the formation of a mantle which isolates the 'core' from the magma. This is known as reverse zoning. In plagioclase, reverse zoning is often accompanied by a sharp break in the optical continuity of the crystal with more sodic (low anorthite) compositions in the core surrounded by more calcic (high anorthite) compositions (figure 2.15). If refractory phenocrysts suddenly find themselves surrounded by a magma of a relatively fractionated composition, a sodic mantled reaction rim forms round a calcic core.

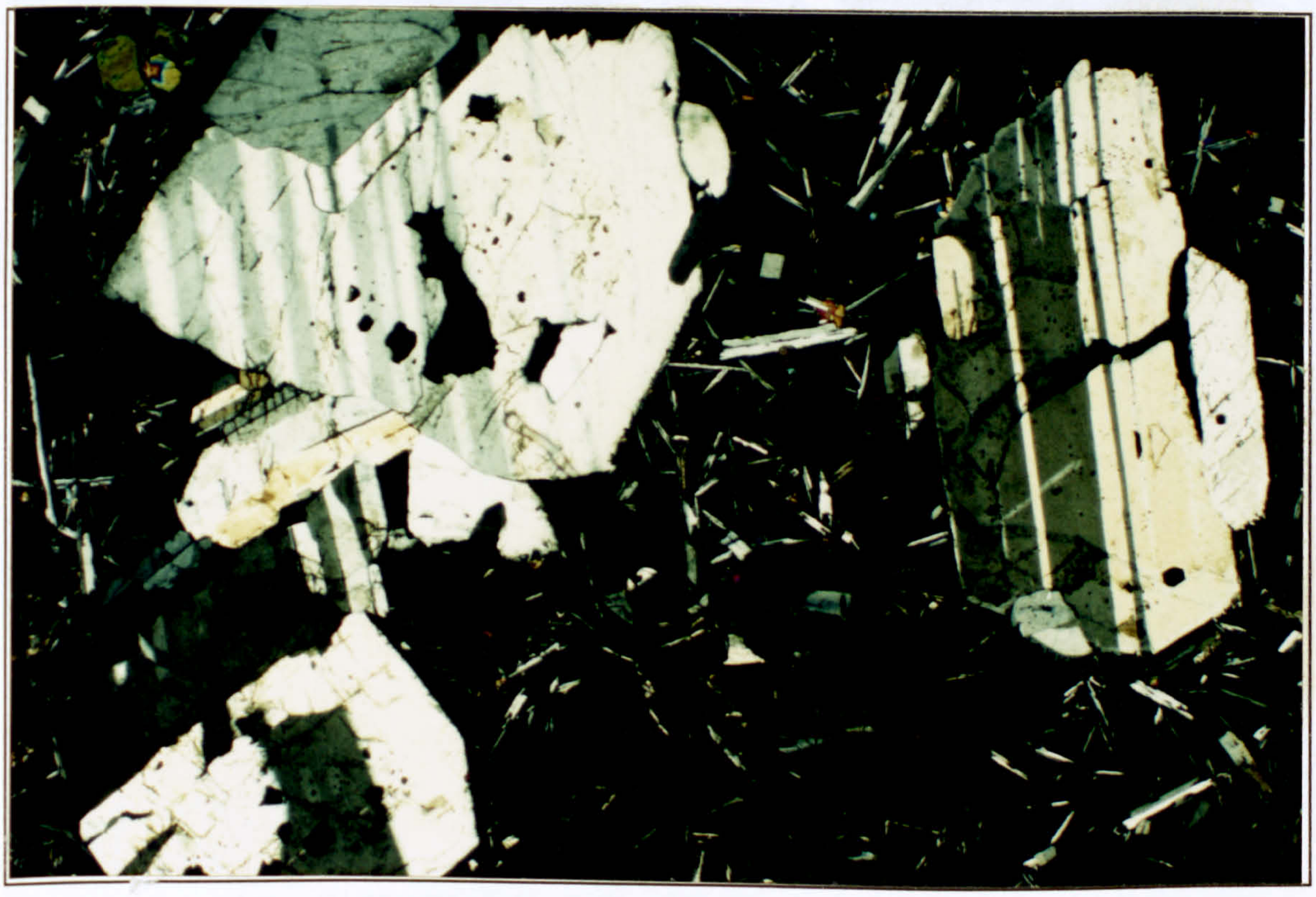

Figure 2.14 Example of intratelluric crystal textures. The large plagioclase phenocryst (right) is subhedral, the ragged margin at the top indicates that there may have been some disequilibrium. The phenocryst is surrounded by a slim quench rim. On the left a glomerophyric cluster of plagioclase contains some crystal with rounded and slightly embayed margins, indicative of resorption. Field of view is 6mm x 3.7mm — sample 21D-2-1b.

2.8.3.2 Xenocrysts

The term xenocryst is used to describe crystals accidentally incorporated into a magma from a foreign source. Xenocrysts in MORB can come form conduit/chamber walls

(Wilkinson, 1982), may be accidental mantle fragments, or may be high-pressure phenocrysts carried up by rising liquids into an open system magma chamber (Donaldson & Brown, 1977). Typically, xenocrysts are in disequilibrium with the host basalt, though disequilibrium by itself is not evidence of a xenocrystic origin. Crystals can form in disequilibrium with their parent magma, though in plagioclase oscillatory zoning is a sign of this (Loomis, 1982).

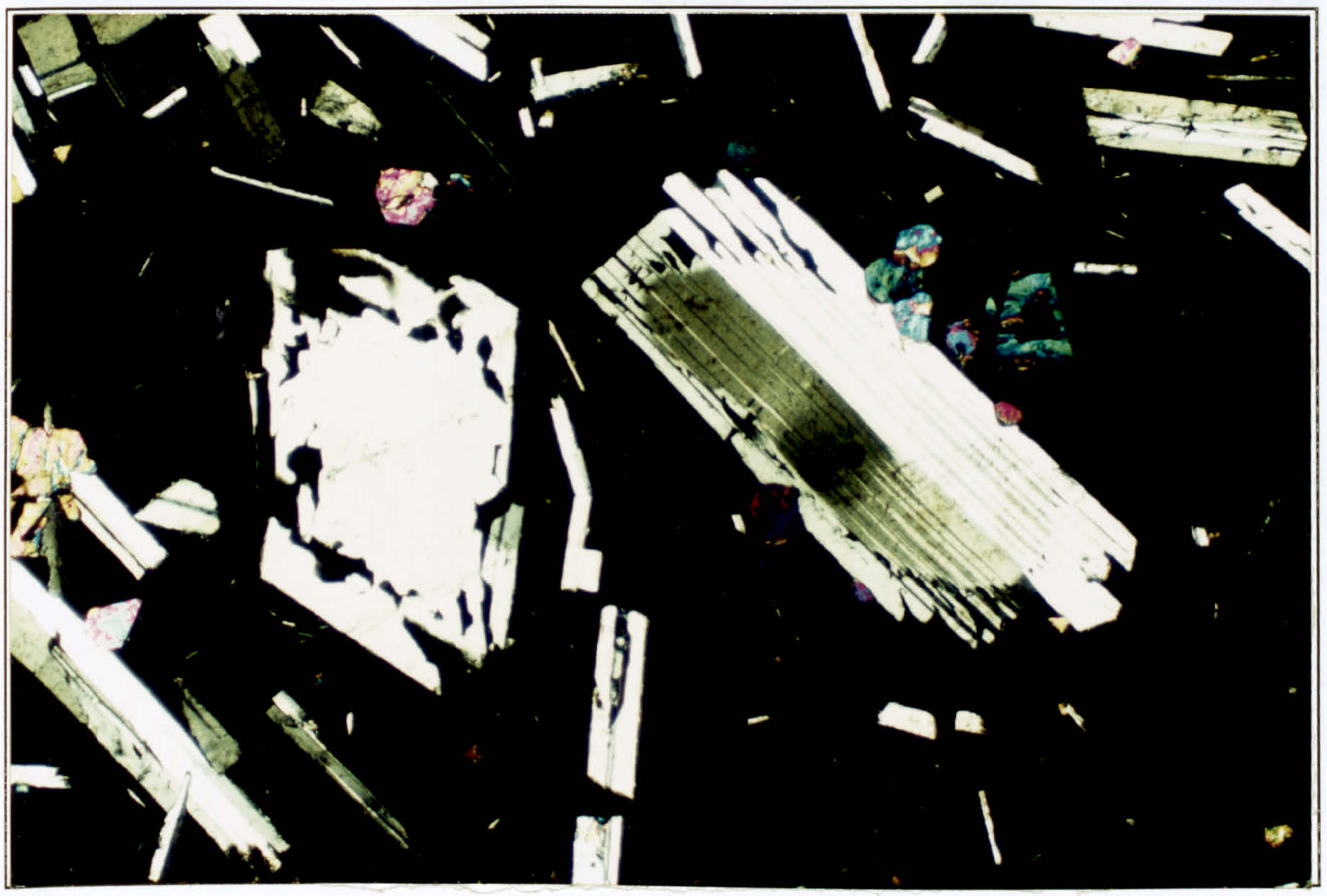

Figure 2.15 Plagioclase phenocryst showing discontinuous reverse zoning between the core and the rim (centre right). The rim of the phenocryst has been resorped along cleavage planes because there is disequilibrium between the fractionated magma (now glass) and the anorthitic rim. The resorption appears to halt at the zone boundary as the albitic core is in probably in equilibrium with the magma. Field of view is 3mm x 1.9mm —sample 6D-1-3c.

Xenocrysts in Atlantic MORB commonly take the form of olivine and/or plagioclase megacrysts (Aumento, 1968; Melson & Thompson, 1971; Donaldson & Brown, 1977; Dungan & Rhodes, 1978; Kuo & Kirkpatrick, 1982). The criteria for recognising megacrysts, as put forward by Donaldson and Brown (op. cit.) includes large (1-3mm), rounded, subequant form with broad, unzoned cores surrounded by a mantle and a narrow rim. Walker (1992b) found similar megacrysts in Iceland, but these were up to 10mm in diameter and some had a tabular form. The mantle should be the same composition as the coexisting phenocrysts and the rim is a quench feature, of the same composition as the

groundmass crystals. The cores of the megacrysts are usually refractory (An 80-92 for plagioclase and Fo 89-91 for olivine) and they can contain abundant melt inclusions (figure 2.16).

It is important to establish whether phenocrysts are xenocrystic in origin as they may cause deviations in the whole-rock geochemical and isotopic trends.

Figure 2.16 Plagioclase megacryst with rounded resorped margins and a large concentration of melt inclusions in core (centre right). Some of these melt inclusions are aligned along the cleavage, while others are amorphous blebs. The plagioclase megacryst on the left encloses a phenocryst of olivine. Note the larger field of view compared with other photomicrographs. Field of view is 12mm x 7.2mm —sample 6D-2-1b.

2.8.3.3 Xenoliths

Xenoliths are 'foreign bodies' which have become incorporated into the magma. Like xenocrysts, they can come from plutonic or mantle sources, but they are evidence that the magma has interacted with solid material (and not just mixed with another fractionating magma). They are almost always in disequilibrium with the host magma and so can show similar textural features to xenocrysts. The resorption of plutonic xenoliths (figure 2.17) is a form of wall rock assimilation which is often thought to accompany fractionation. The latent heat released during crystallisation can provide sufficient thermal energy to

consume wall rock in the process known as assimilation and fractional crystallisation (AFC) (Bowen, 1928).

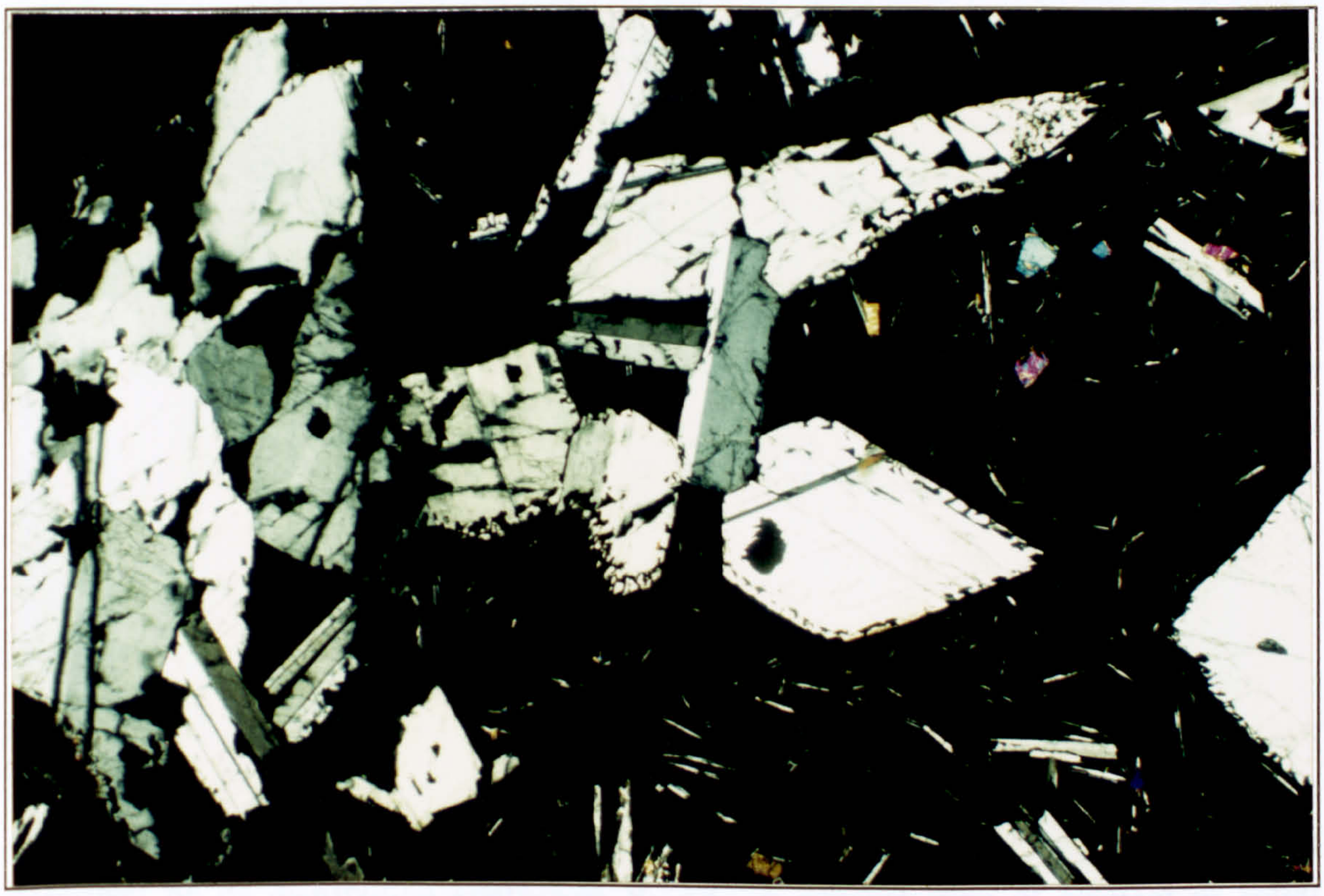

Figure 2.17 Small plutonic xenolith (xenocrystic clot) in disequilibrium with host basalt, comprises an agglomeration of plagioclase phenocrysts. The resorped margins have a serrated, vermicular texture. The clot has partially broken up, so single xenocrysts with similar textures are found elsewhere in the sample. Field of view is 6mm x 3.7mm —sample 21D-2-1b.

2.9 Geochemistry.

Variations in the composition of primary mantle melt are essentially a result of melting processes and source heterogeneity. Before eruption or intrusion near the surface, a primary mantle melt can undergo fractional crystallisation (at high or low pressure), magma mixing, crystal accumulation and crustal assimilation. When a rock solidifies at, or near the surface, it may be affected by hydrothermal alteration and surface rocks will undergo weathering.

Starting with alteration, the geochemical effects of each of these processes must be stripped away until the original source of the magma is revealed. For each stage, the geochemical evolution of the basalt must be identified, and if possible quantified, in order to ascertain the petrogenesis of a suite of samples.

2.9.1 Analysis

Geochemical analysis was carried out on 94 whole-rock samples. All the samples are basalt lavas, with the exception of one (1D-1-1b) which is a dolerite from the transform. Analysis of the whole-rock powders for major element oxides (using glass beads) and trace elements (using powder pellets) took place on the Durham University XRF spectrometer. A subset of 26 samples was analysed for rare earth elements (REE) and a wide range of trace elements on the ICP-MS at Durham (UDIRL). The analytical methods and error analysis are discussed at length in Appendix 3 and the whole-rock data set is presented in Appendix 5. Major element analyses of basalts glasses and phenocrysts were done on the electron microprobe at Bristol university by Paul Browning. Pamela Kempton analysed a selection of MARNOK samples for Sr, Nd and Pb isotopes at NERC Isotope Geosciences Laboratory, Keyworth.

2.9.2 Plots used in geochemical analysis

The geochemical signature left by both melting and crystallisation processes is caused by the differential partitioning of elements between crystals and melt. *Incompatible elements* are partitioned into the melt and *compatible elements* are partitioned into the crystals. The degree of compatibility shown by a *trace* element for a particular mineral phase is described by its distribution coefficient K_D (K_D = concentration of element in solid/ concentration of element in liquid). When $K_D<1$ trace elements are incompatible while compatible trace elements have $K_D>1$. Many of the plots used to interpret geochemical data rely on this concept of compatible and incompatible elements.

2.9.2.1 Bivariate variation diagrams

Bivariate variation diagrams are scattergrams on which two selected geochemical parameters are plotted (usually a trace element or major element oxide). They usually have a fractionation index on the x-axis which is specifically selected to arrange the data in evolutionary order, maximise the display of the geochemical variability or to study features of particular interest (Cox et al., 1979). The y-axis then shows how the concentration of a chosen parameter varies during the evolution of the parental melt.

The extraction or addition of a particular phase will cause a progressive trend in the liquid (glass) compositions respectively away from or towards the plotted composition of the phase. When a new mineral phases began to crystallise, there is an inflection in a liquid trend as the bulk fractionating composition changes (figure 2.18). Trends on variation diagrams using whole-rock phyric data rather than glasses will show more scatter because of the preferential loss or accumulation of particular phenocryst phases.

An important property of variation diagrams is the applicability of the Lever Rule for mass balance (Cox et al., 1979). This enables a graphical calculation of changes in liquid composition as a particular mineral phase is removed or a particular contaminant is added. It can also be used inversely to calculate the relative proportions of fractionating phases, given a coherent liquid trend and the compositions of the phenocrysts. The reader is referred to an igneous petrology/geochemistry text book (e.g. Cox et al., 1979; Wilson 1989; Rollinson, 1993) for further details about the procedure of lever rule calculations.

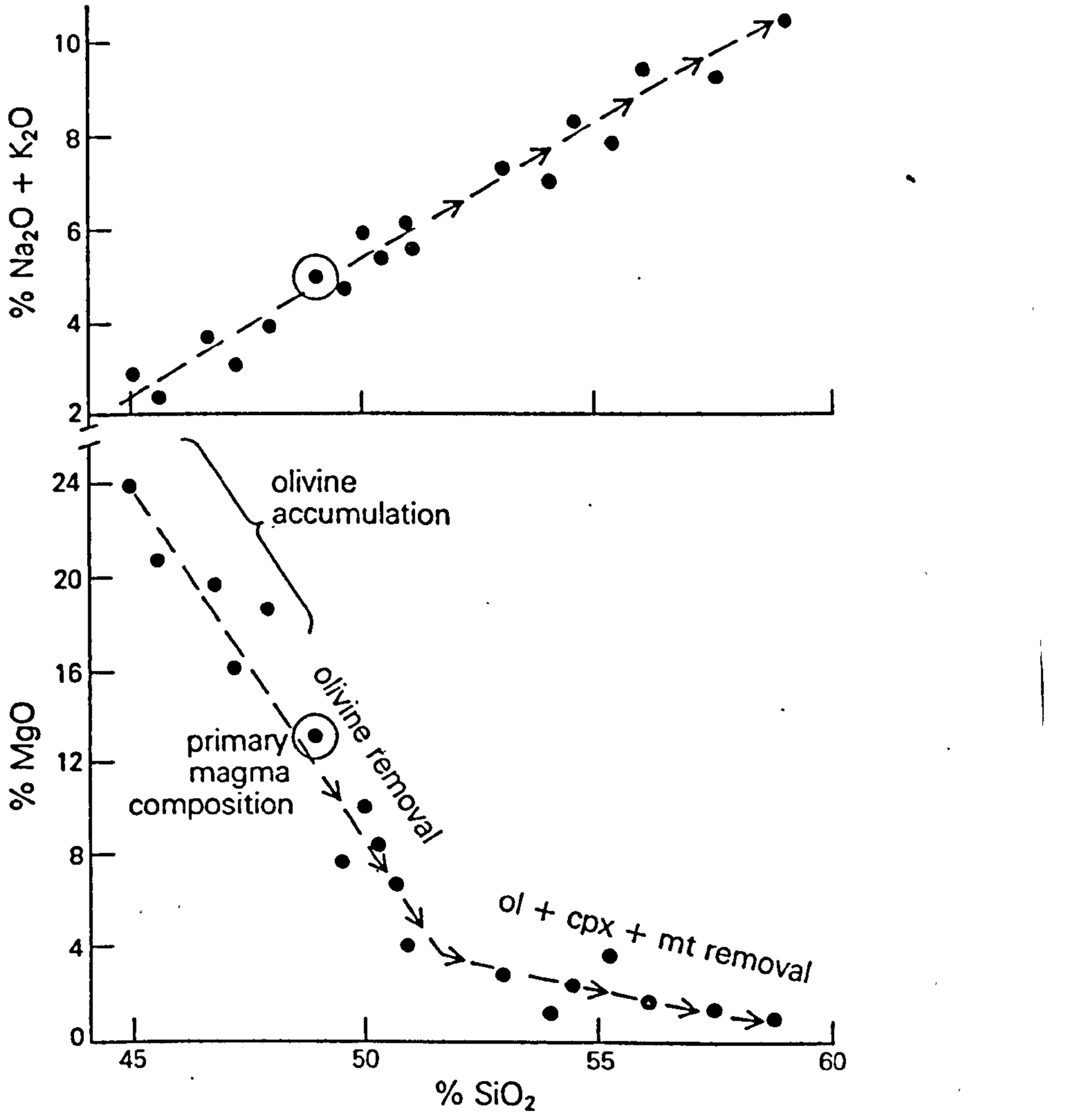

Figure 2.18 Bivariate variation diagram of wt.% Na_2O + K_2O and wt.% MgO versus wt.% SiO_2 for a suite of cogenetic volcanic rocks related by fractional crystallisation of olivine, clinopyroxene and magnetite. Mineral fractionation governs the liquid line of decent (marked by arrows), which trends from the parental composition, in a direction away from the bulk composition of the fractionating phases. An inflection in the liquid line of decent is the result of a change in the fractionating assemblage. This occurs when there is as change in the vector angle between the bulk composition of the phenocrysts and the glass, and so is only seen on plots of certain relevant elements. The basalts with MgO > 12wt.% may have accumulated olivine. Crystal accumulation causes a trend in whole-rock analysis, towards the accumulated mineral composition and should be evident from the petrography (i.e. the samples will be highly phyric). Figure taken from Wilson (1989—figure 2.1).

2.9.2.2 Plots using trace element ratios

Trace elements, whose preference is for the melt phase rather than the mineral phase, are known as incompatible elements. In contrast compatible elements partition into a mineral phase. Incompatible element ratio plots are a form of variation diagram which are commonly used to try to correct for fractionation, so that melting and source variations stand out more clearly. When this is the objective, the denominator of the element ratio is a highly incompatible element, such as Zr or Ti. These particular plots are useful when examining a suite with a large number of samples and are especially good for identifying geochemical trends.

2.9.2.3 Chondrite-normalised REE plots

The display of trace element data on multi-element plots is a particularly useful way of comparing a large number of elements at once and allowing broad conclusions to be drawn from their combined behaviour. The disadvantage of this type of plot is that only a small number of samples can be viewed on one diagram as they quickly become cluttered and confused (Rollinson, 1993).

The REE are arranged in order of atomic number, and also decreasing incompatibility, along the x-axis. The elemental abundances are normalised to a C1 chondrite composition, using values of Boynton (1984), and are plotted on a log scale up the y-axis. Normalising compensates for the Oddo Harkins effect to produce smooth trends of relative abundance, despite large variations in the absolute concentrations. The shape of the REE profile essentially relates to partial melting processes and source composition as described below in section 2.9.6.

2.9.2.4 MORB-normalised extended element plots

Extended element diagrams have a similar basis to REE plots in that elements are arranged in order of decreasing incompatibility along the x-axis. The log scale on the y-axis enables peaks of relative enrichment or depletion of elements to be compared between samples despite some large variations in normalised abundance. The Normal MORB (N-MORB) values of Sun and McDonough (1989) are used as normalising values for extended element plots as they form a coherent set of values for a large number of elements. These diagrams show clearly the scatter of certain elements affected by hydrothermal alteration, and like REE plots they can also be used to investigate subtle variations in mantle melting.

2.9.3 Effect of seafloor alteration

2.9.3.1 Element mobility during seafloor alteration

Potential element mobility must be taken into account prior to any attempt to study igneous processes using elements liable to be affected by alteration. Element mobility is more significant in high-temperature, hydrothermal alteration than low-temperature seafloor alteration. However, some degree of element mobility is almost inevitable in any suite of rocks that has been subject to seawater alteration.

The chemical effects of alteration are particularly marked in large ion lithophile elements (LILE), such as Rb, K, Cs and U together with the water content and Fe^{2+}/Fe^{3+} ratio (e.g. Humphris & Thompson, 1978a; Morrison & Thompson, 1983). These elements are mobile and with increasing seafloor weathering, Ba and Sr, also become mobile. In addition, there can be a decrease in major elements such as Na, Ca, Mg and Si (Pearce, 1976). In addition, the transition metals Mn, Zn and Cu tend to be mobile, particularly at high temperatures (Seewald & Seyfried, 1990).

The high field strength (HFS) elements, such as Sc, Y, Th, Zr, Hf, Ti, Nb, Ta and P are usually immobile (Pearce, 1983), as are the transition metals Co, Ni, V and Cr (Humphris & Thompson, 1978b). The REE, which are particularly relevant to this study, are traditionally regarded as immobile and included in the list of HFS elements. However Humphris (1984) shows that REE immobility can not be guaranteed, and sometimes the light rare earth elements (LREE), such as La, Ce and Nd, can become mobilised from basaltic glass. When alteration is intense, only Zr, Hf, Nb and Ta can be guaranteed to be immobile (Bienvenu et al., 1990).

Element mobility also has consequences for isotope systems. The high $^{87}Sr/^{86}Sr$ ratio of seawater relative to MORB and the mobility of Sr means that seawater alteration can relatively easily produce quite dramatic effects on $^{87}Sr/^{86}Sr$, even in young MORB. In contrast, the immobile Nd is insensitive to seafloor alteration, and thus $^{143}Nd/^{144}Nd$ is a good discriminator of source variations (see below). Two comparable studies of seawater contamination in the Pb isotope system produced contrasting results. Vidal and Clauer (1981) found that seawater contamination has no effect on Pb isotope ratios, whereas Spooner and Gale (1982) showed that it did. Hence, Pb isotopes should be regarded with a degree of caution as they are not particularly predictable.

2.9.3.2 Recognising alteration in geochemical plots

Element mobility as a result of alteration will tend to result in a incoherent scatter in bivariate plots. The geochemical effects of alteration are best assessed on extended element plots where it is possible to view the combined behaviour of a large number of elements. A knowledge of the petrology of the sample gives a idea of the expected spidergram pattern and alerts the interpreter as to what degree of element mobility should be expected. On the extended element plots, the mobile LILEs are plotted on the left-hand side. Element mobility is recognised by anomalous spikes in these elements, while the less mobile elements form a coherent trend.

An example of an extended element plot for sample 15D-2-1b is seen in figure 2.19. The petrography showed that this sample is relatively fresh, with only minor palagonitisation of the glass, yet Rb, Ba, Pb and U are all mobile, as shown by the enrichment spikes for these elements. Sr also forms a prominent enriched spike, which may partly be an effect of seawater alteration, but is probably a result of plagioclase accumulation (see section 2.9.5). For reasons of element mobility, the extended element diagrams in chapters 4 to 6 are truncated at Nb.

2.9.4 Effects of fractionation

2.9.4.1 Liquid lines of decent and parental magmas

Much of the chemical variety observed within MORB is the result of fractionation of a parental material (Cox et al., 1979). Fractional crystallisation is best studied by using variation diagrams (figure 2.18) to show the liquid line of decent (LLD). This is the path taken by residual liquids as they evolve through the differential withdrawal of minerals from the magma (Bowen, 1928). On a variation diagram, a group of glass analyses related together by fractional crystallisation from a common parent should fall on a coherent trend (the LLD). Scatter on a glass variation diagram, which is beyond that caused by analytical error may be a result of several different parental magmas, evolving in a similar manner to produce parallel liquid lines of descent.

2.9.4.2 Major element variations with fractionation

MgO is a well-established index of basalt fractional crystallisation as it is an important component of olivine and pyroxenes (phases in equilibrium with mafic melts). It shows good correlation with other major element oxides as they are enriched or depleted in residual liquids. The most primitive MORBs contain about 10-11wt% MgO; this decreases with olivine fractionation to about 8.0-8.4 wt% MgO, when clinopyroxene

joins olivine in removing MgO (Stakes et al., 1984; Bryan, 1983). Plagioclase joins the liquidus at ~9wt% (Bryan, op. cit.). The MgO values in the MORB fractionating sequence do not commonly fall below 5%. Table 2.2 shows some of the key major element oxides and the phases they are partitioned into.

The extent of fractionation and proportions of phases can be approximated using the lever rule, but more accurate estimates can be obtained by numerical approaches such as least squares analysis (Wright & Doherty, 1970) and other fractionation-specific algorithms (e.g. Weaver & Langmuir, 1990).

Oxide	Mineral Phase
MgO	olivine (forsterite), clinopyroxene (diopside)
Fe_2O_3T[2]	olivine (fayalite), clinopyroxene (hedenbergite), Ti-magnetite, ilmenite
Al_2O_3	feldspar, spinel
CaO	feldspar (anorthite), clinopyroxene (diopsidic augite)
Na_2O	feldspar (albite)
TiO_2	Ti-magnetite

Table 2.2 The compatible major element oxides and the mineral phases into which they are preferentially partitioned.

2.9.4.3 Trace element variations with fractionation

Incompatible trace elements can also be good fractionation indices, especially Ti, Zr and the REE, which show a considerable spread in concentration throughout the basalt spectrum and are usually unaffected by secondary alteration. Ti becomes compatible at evolved compositions when Ti -magnetite starts to fractionate. Table 2.3 shows the main crystallising phases within MORB and their respective compatible trace elements.

The REEs are incompatible during the fractional crystallisation of a basaltic magma. Eu is less incompatible in plagioclase than the other REEs, as in reducing conditions it has a

---

[2] Fe_2O_3T = Total (FeO + Fe_2O_3) expressed as Fe_2O_3.

+2 valency and so is able to readily substitute with Sr. The effect of fractional crystallisation is to increase the relative abundance of all the REE in the residual melt, resulting in parallel REE profiles. If plagioclase is fractionated, Eu will increase in concentration less than the other REEs producing a negative Eu spike in the REE profile of the residual melt. During extreme fractional crystallisation the ratios between the LREE and HREE may be slightly increased, though such large degrees of fractionation are not observed in this data set.

Crystallising phase	Compatible trace element
olivine	Ni, Co
plagioclase	Sr, Eu
clinopyroxene	Sc, Co, Ni, V
chrome-spinel	Cr
Ti-magnetite	V, Ti

Table 2.3 List of the major phases involved in the crystallisation of MORB and their compatible trace elements.

2.9.5 Effects of crystal accumulation

2.9.5.1 Accumulation in MARNOK samples

Plagioclase accumulation is almost ubiquitous within the MARNOK data set. Only 7 of the samples selected for whole-rock ICP-MS analysis are essentially aphyric (<1% modal plagioclase) and even these will have the odd phenocryst or megacryst. The whole-rock analyses of aphyric basalts are essentially comparable to basalt glass as they represent a true liquid composition, unaffected by the relative abundances of phenocrysts. In contrast phyric whole-rock analyses show to varying degrees the effects of selective accumulation of phenocrysts. The modal percentage of plagioclase phenocrysts and megacrysts in the samples analysed by ICP-MS, are recorded in Table 2.4 below.

Modal plagioclase(%)	**Samples selected for analysis by ICP-MS**
aphyric (<1)	1D-1-1b, 15D-1-2b, 17D-1-2a, 19D-1-2a, 21D-1-1b, 29D-3-2c, 32D-1-2c
~1	4D-1-1b, 5D-1-2b, 20D-1-1b
2 - 5	22D-2-1b, 7D-1-3b, 24D-1-1b, 30D-1-2c, 9D-1-2b, 12D-1-1b, 27D-1-1b
5 - 10	16D-1-1b, 3D-1-1c, 11D-1-1b
10 - 15	31D-1-2c, 8D-1-1b;
~20	6D-2-1c, 23D-2-3c;
~40	13D-1-1b.

Table 2.4 Modal plagioclase in samples selected for analysis by ICP-MS

2.9.5.2 Geochemical consequences of crystal accumulation

In order to accurately interpret the geochemical data, it is essential that the geochemical effect of this accumulation is quantified. On major and trace element bivariate diagram, accumulation causes a trend from the (liquid) glass composition towards the phenocryst composition (figure 2.18). A comparison between glass probe data and the whole-rock XRF and ICP-MS data from the same sample should show the effects of accumulation by a greater scatter on geochemical plots.

Subtle variations in trace elements can have important petrogenetic consequences. Hence it is necessary to quantify the effects of crystal accumulation for trace elements and particularly REEs. Figure 2.19 shows the results of some mixing calculations which model the progressive addition of plagioclase to a whole-rock basalt sample (15D-1-2b)[3]. As the modal percentage of plagioclase increases, the incompatible trace element

---

[3]Plagioclase compositions are calculated using the partition coefficients of McKenzie & O'Nions (1991) using the basalt composition of sample 15D-1-2b. (Concentration of element in plagioclase = concentration of element in basalt x K_D). The trace element compositions of plagioclase calculated in this manner will be higher than those of the accumulated megacrysts, as the megacrysts are refractory (i.e. they have fractionated from a primitive magma with lower incompatible trace element abundances). Hence these mixing calculations are maximum estimates. The bulk analysis of the accumulated compositions are calculated using a simple mass balance mixing equation between plagioclase and sample 15D-1-2b.

abundances in the whole-rock analysis decrease. The exception is Sr, which is compatible with plagioclase, and so with increasing accumulation, the whole-rock concentration of Sr increases. Eu forms a positive spike in the subparallel trace element profile but its concentration still decreases slightly as it is slightly incompatible. Hence, the effect of plagioclase accumulation on Eu is the opposite to that described for plagioclase fractionation.

Figure 2.20 shows the results of the same modelling of plagioclase accumulation, but in the form of a chondrite-normalised REE plot. The Eu spike has already been explained in previous paragraph. The remainder of the REEs form essentially parallel trends, except there is a very slight convergence of the lines towards the LREEs (the left-hand side). This is because the partition coefficients of the REEs for plagioclase decrease slightly with increasing atomic number. Figure 2.21 uses REE ratios to focus in on this convergence. The La/Sm ratio is a measure of the gradient of the REE profile across the left-hand half of the plot, while the Sm/Yb ratio describes the gradient on the right-hand side of the plot. Both La/Sm and Sm/Yb increase with accumulation, but the analytical error for these two ratios is about 0.3 (2σ), which is greater than increase caused by even 40% plagioclase accumulation.

In summary, plagioclase accumulation causes dilution of the REE concentrations and the development of a Eu spike, but even large amounts of plagioclase accumulation cannot affect the shape of the REE profiles beyond analytical error.

2.9.6 Variations in partial melting

Primary N-MORB comprises the pooled melt-fractions produced by polybaric incremental melting during adiabatic decompression over a pressure range of 5-25 kbars (McKenzie & Bickle, 1988; Johnson et al., 1990; McKenzie & O'Nions, 1991). This parental material is formed during partial melting of the mantle. The composition of the primary MORB depends on both the degree of bulk melting and the compositions of the increments which pool together to form the final batch (Plank & Langmuir, 1992; Devey et al., 1994).

2.9.6.1 Using major elements—correction for low-pressure fractionation

The major element contents of the parental magmas reflect the pressure, temperature and bulk degree of melting (Klein & Langmuir, 1987), yet the main spread in major element data comes from low-pressure fractionation. Hence, in order to study variations in mantle melting using major elements it is first necessary to correct for this low-pressure fractional crystallisation.

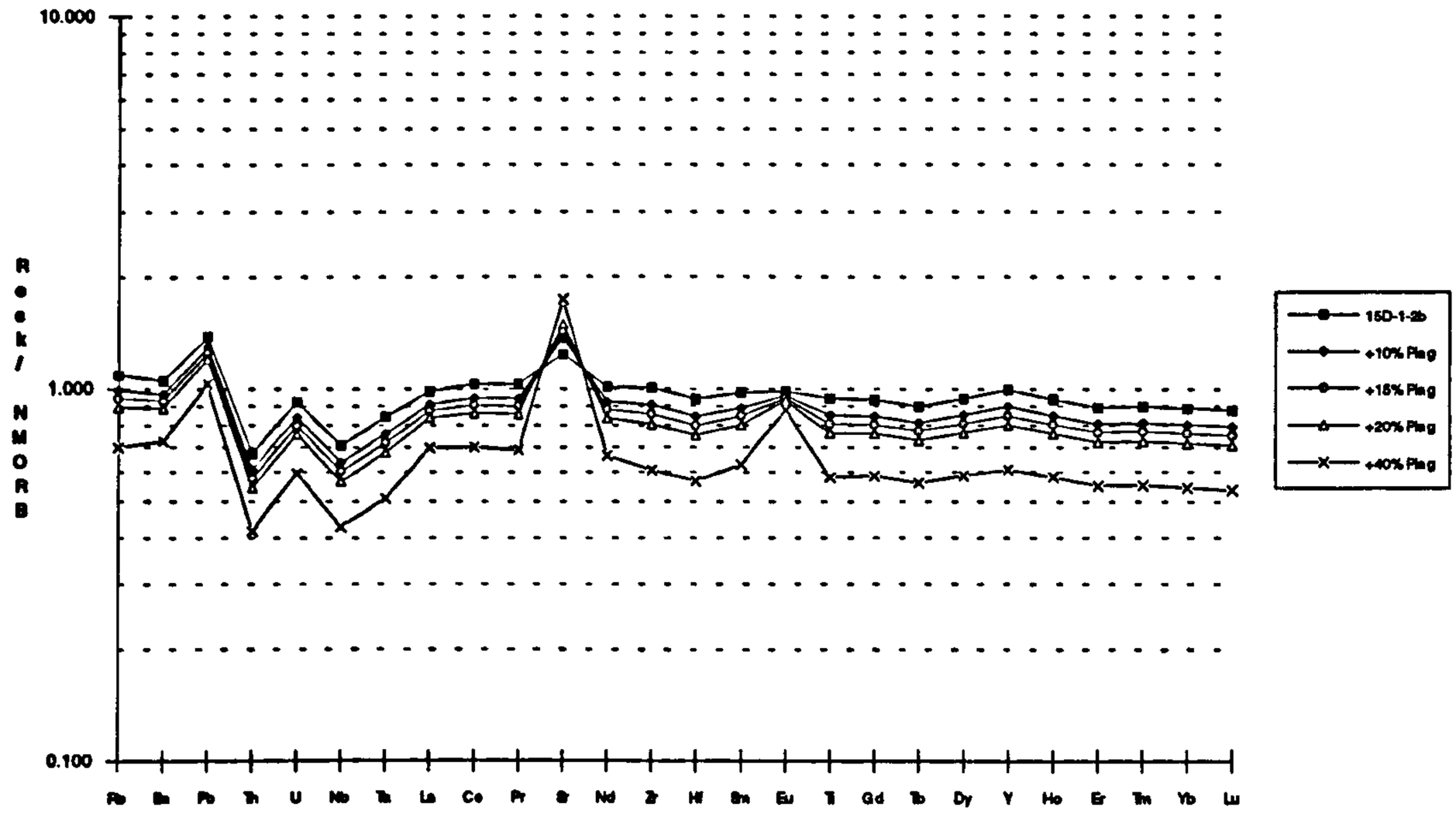

Figure 2.19 MORB-normalised extended element plot showing the effects of plagioclase accumulation on the whole-rock trace element patterns. The trends are subparallel except for Sr and Eu which form positive spikes compared to the other trace elements. The concentration of Sr actually increases because it is compatible in plagioclase. The concentration of Eu decreases, but only slightly, as Eu is only slightly incompatible in plagioclase (Sr $K_D = 2.0$; Eu $K_D = 0.73$—McKenzie & O'Nions, 1991.)

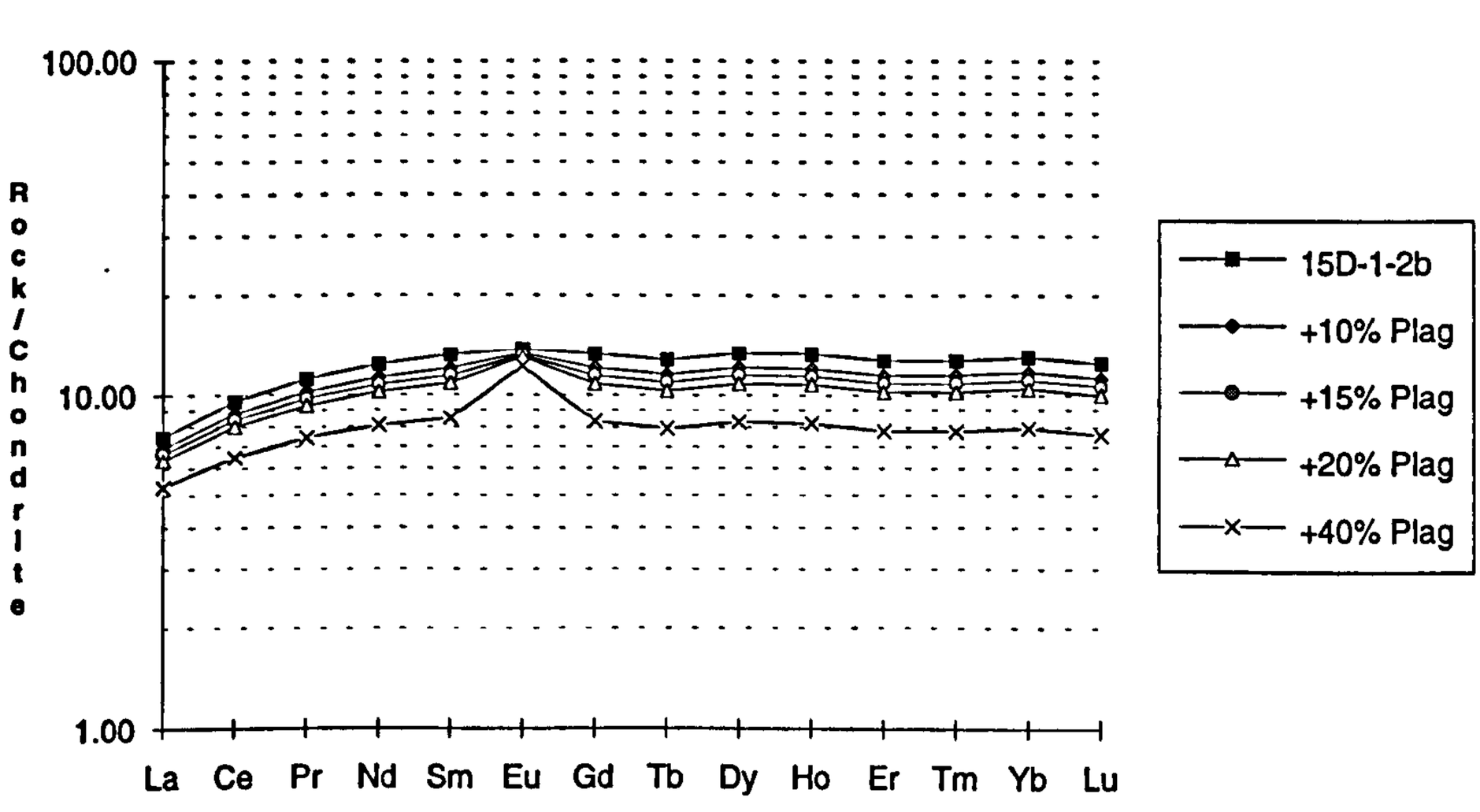

Figure 2.20 Chondrite-normalised REE plot showing the effects of variable degrees of plagioclase accumulation. In addition to the diluting effect on the REE concentrations and the development of a Eu spike, there is a slight convergence in the profiles towards the left-hand side of the plot caused by the increase in K_D for decreasing atomic number.

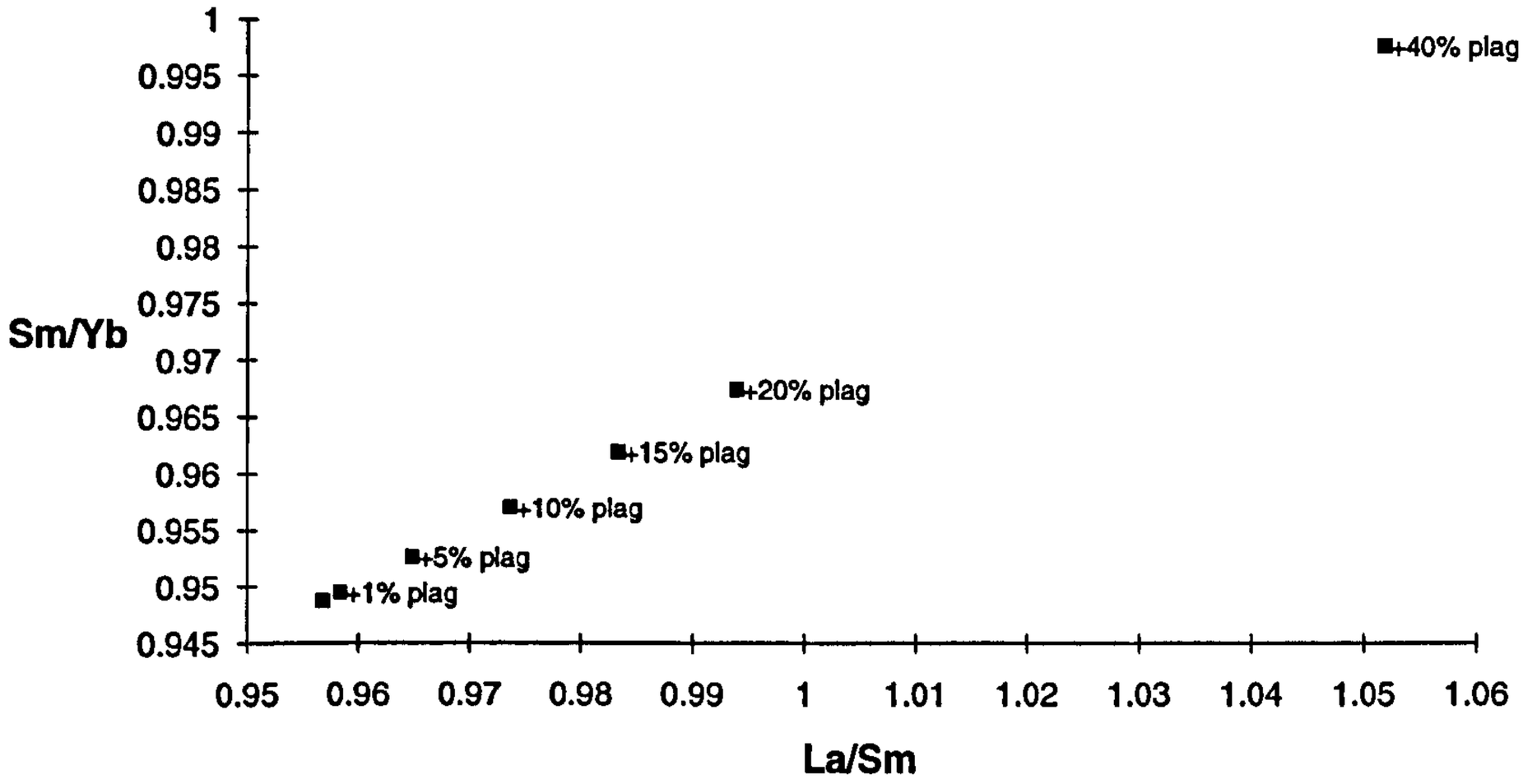

Figure 2.21 The effect on REE ratios of plagioclase accumulation. Both La/Sm and Sm/Yb increase (the former more than the latter) as the modal percentage of plagioclase increases, but these increases are less than analytical error, even for large degrees of accumulation.

The approach first proposed by Klein and Langmuir (1987) corrects individual oxide abundances in suites of multiply saturated basalts to a comparable level of MgO. This process involves firstly the calculation of liquid lines of decent for low pressure fractionation of olivine, plagioclase and clinopyroxene using the algorithm of Weaver and Langmuir (1990). An oxide is then corrected by projecting along a line parallel to the liquid line of decent to find the equivalent oxide composition at a fixed reference value of MgO (usually 8.0 wt.% MgO is selected). An oxide value corrected in this manner is usually referred to by a numbered subscript indicating the wt.% reference value of the MgO. Hence, Na_2O which has been corrected for fractionation to 8.0 wt.% MgO is written as $Na_{8.0}$. The differences in $Na_{8.0}$ within a suite of rocks reflect variations in the Na_2O contents of the parental magmas.

$Na_{8.0}$ is a measure of the extent of partial melting, with higher $Na_{8.0}$ values indicating lower degrees of bulk melting (Klein & Langmuir, 1987). Plank and Langmuir (1992) provide one of the most recent parameterisations of the $Na_{8.0}$ equation which accounts for the steepening of the Na/Mg liquid line of decent as a function of the Na concentration:

$$Na_{8.0} = [Na_2O + 0.115(8\text{-}MgO)]/[1+0.133(8\text{-}MgO)] \qquad [1]$$

2.9.6.2 Using trace elements to study melting processes

Normal MORB (N-MORB) are the products of melting a mantle depleted with respect to bulk earth in incompatible elements (Sun et al., 1979). In the mantle source, the degree of depletion of an element increases with increasing incompatibility. In a REE plot this is shown by the fact that the LREEs are more depleted than the HREEs, causing the REE pattern to slope to the left.

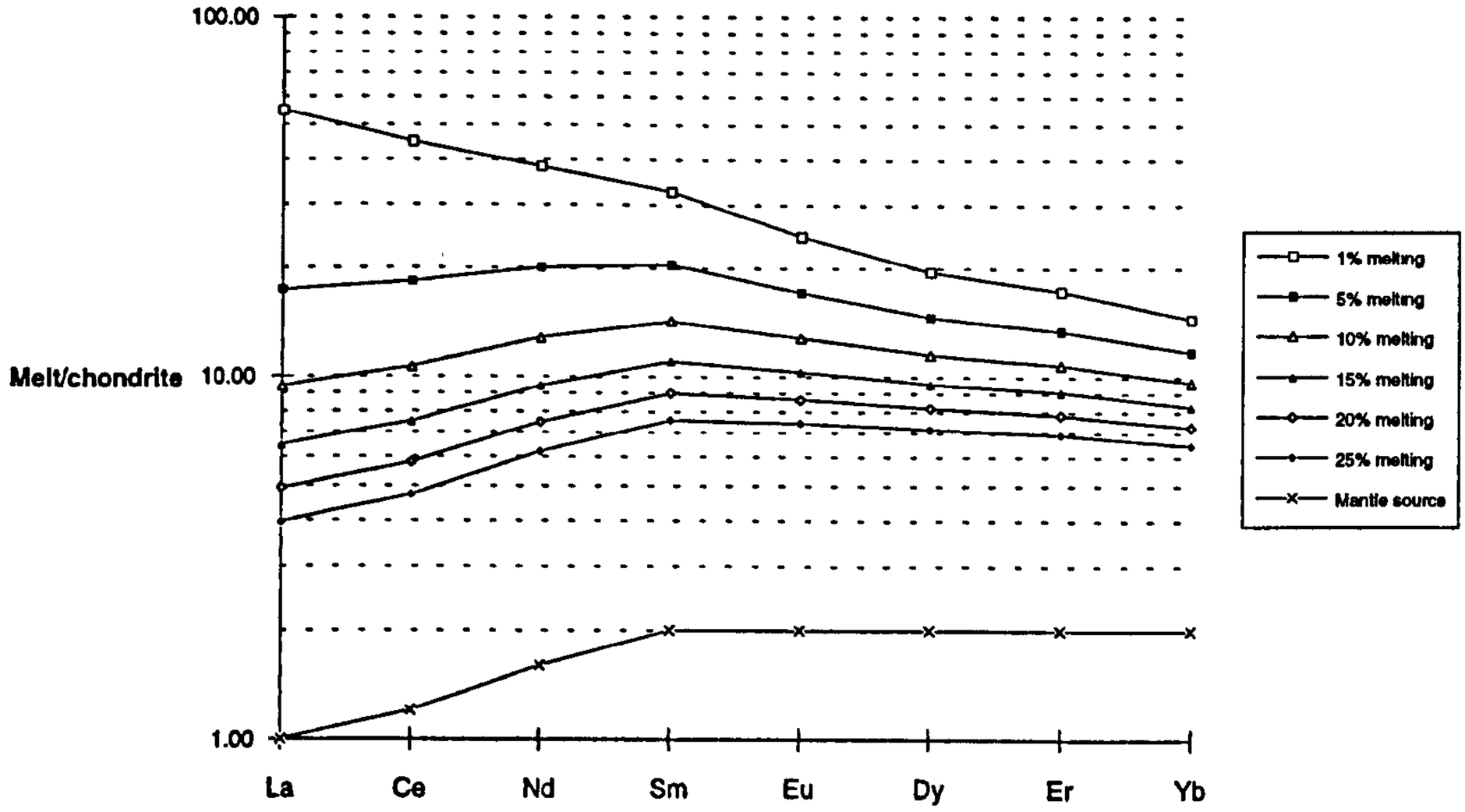

Figure 2.22 Chondrite-normalised REE plot showing progressive degrees of bulk melting of a depleted lherzolite mantle source[4]. Further details of the parameters (including partition coefficients) and the programs used to generate these melting curves are given in Appendix 6.

At very small degrees of melting, the incompatible LREE are preferentially partitioned into the melt giving a profile which dips down towards the HREE (see 1% melting on figure 2.22 above). As the degree of melting increases, the profile may flatten out and then become depleted, approaching the source composition (see 10-25% melting on figure 2.22). The degree of enrichment or depletion of LREE relative to HREE may be assessed using a ratio such as $[La/Yb]_n$ (subscript n denotes that these are chondrite-normalised values). Values below units are depleted in LREEs. Hence the degree of partial melting affects both the absolute concentration of the incompatible elements (higher concentrations are lower degrees of partial melting) and the shape of the plot. If

---

[4]In melt modelling calculations the depleted lherzolite mantle source has starting composition of 60% olivine, 25% orthopyroxene and 15% clinopyroxene. Clinopyroxene is melted out after 25% melting to leave a harzburgite residue which is 70% olivine and 30% orthopyroxene.

the REE patterns of two samples cross, they must come from different parental magmas with different melting histories. Crossing REE patterns can also result from differing mantle sources, so this possibility should first be discounted (by studying isotopic compositions —section 2.9.7) before assuming that variations in REE patterns are a result of melting.

Trace elements can be corrected for the effects of fractionation in a similar manner to major elements by projecting to a common reference level of MgO. For example, Plank and Langmuir (1992) use the following equation to calculate $Ce_{8.0}$ (note fractionation plots of major elements verses trace elements have an exponential form):

$$Ce_{8.0} = 10^{[\log Ce - 0.11(8-MgO)]} \quad [2]$$

2.9.6.3 Calculating degree of melting

Plank and Langmuir (1992) have compared the melting systematics of moderately incompatible major elements (such as Na_2O) with highly incompatible trace elements (such as the LREEs) using $Na_{8.0}$ and $Ce_{8.0}$ respectively. Using simple batch melting equations (which have virtually the same net effects as more realistic incremental melting equations) they find that the global spread of $Na_{8.0}$ corresponds melt-fractions to between 4% and 17%, which they name the melting base line (figure 2.23). The degree of bulk melting can be calculated by comparing calculated $Na_{8.0}$ with this melting baseline.

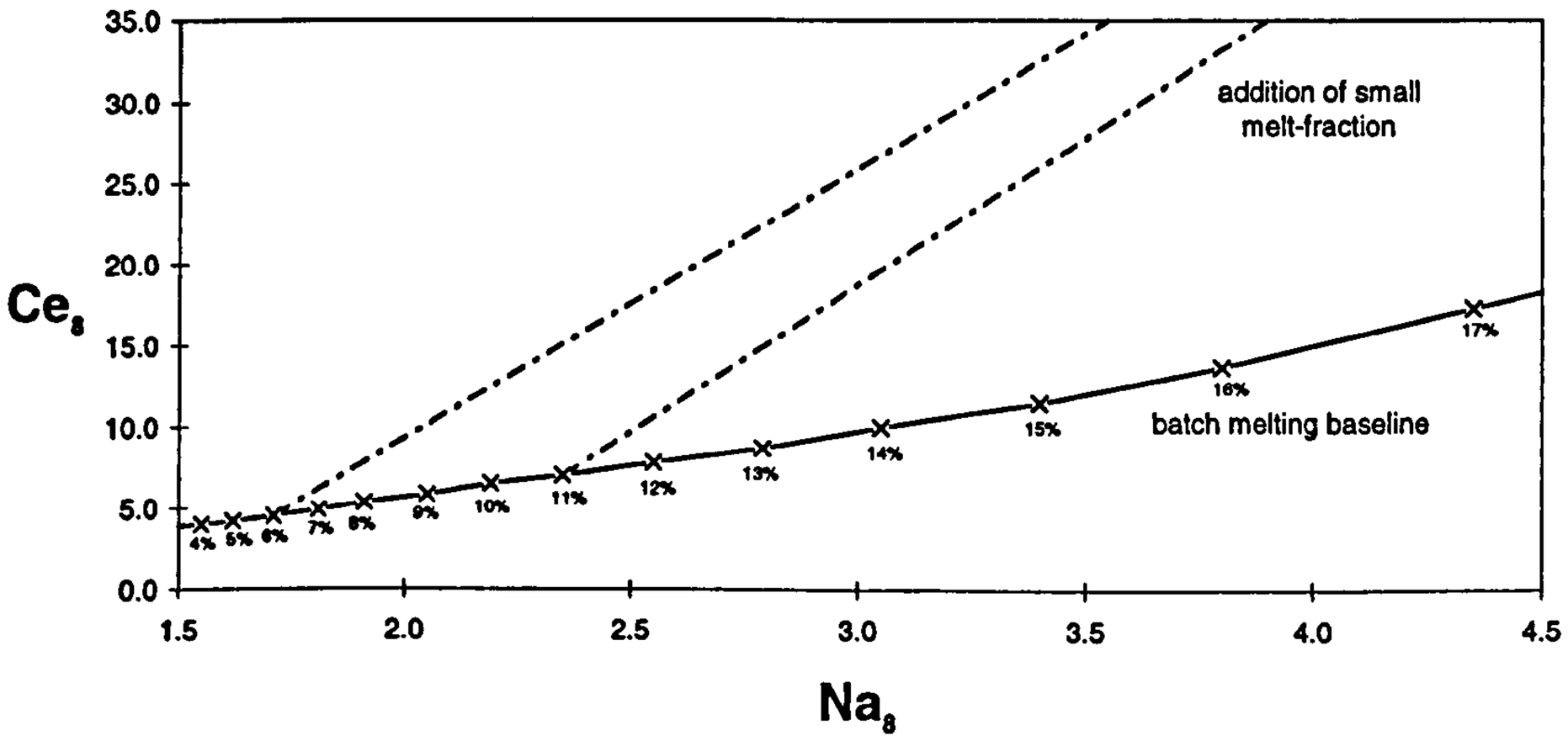

Figure 2.23 Plot of $Na_{8.0}$ verses $Ce_{8.0}$, adapted from Plank & Langmuir (1992). The degree of bulk melting can be estimated from $Na_{8.0}$ by matching with values along the melting baseline. The spread in $Ce_{8.0}$ reflects the variable addition of small melt-fractions. (Plotted trajectories are for mixing between baseline melts and a 0.5% melt of the same mantle source.)

The same batch melting variations can change the Ce concentrations by a factor of 4, but the observed spread in Ce is much greater than this. Similar discrepancies between $Na_{8.0}$ and the highly incompatible trace elements have been noticed elsewhere (Devey et al., 1994), and are attributed to dynamic melting processes. Plank and Langmuir (1992) modelled the variation in $Ce_{8.0}$ by the variable addition of small degree melts which are rich in incompatible elements. These are formed at the volatile-present solidus at the base of the melting column. MORB incompatible element patterns are very sensitive to melt addition to the source, while the moderately compatible $Na_{8.0}$ is robust and better reflects the bulk melt-fraction. On figure 2.23, the trajectories trending up from the melting baseline show the effect of mixing between the baseline melts and a 0.5% melt of the same mantle source.

2.9.7 Effects of mantle source heterogeneity

Isotope studies form a fundamental part of petrogenetic interpretation as they help to identify mantle source variations. Variations in radiogenic isotopic ratios reflect long-lived fractionation of the parent and daughter elements. Radiogenic isotope ratios ($^{87}Sr/^{86}Sr$, $^{143}Nd/^{144}Nd$, $^{206}Pb/^{204}Pb$, $^{207}Pb/^{204}Pb$, $^{208}Pb/^{204}Pb$) are not fractionated by processes such as mantle melting and fractional crystallisation. Hence the isotopic ratios of a MORB sample reflect the isotopic composition of its mantle source, provided the magma does not become contaminated by interaction with isotopically distinct wall rocks (see section 2.9.8) or other batches of magma.

2.9.8 Effects of assimilation

The effects of assimilation of oceanic crust can be quite difficult to recognise in MORB, because the composition of the assimilated material is very similar to the composition of the melt itself. A fresh MORB which has assimilated the hydrothermally-altered walls of a magma chamber will have similar geochemistry to a slightly hydrothermally altered basalt which has not undergone any assimilation. However assimilation can be identified by the discrepancy between the petrographic extent of alteration and that implied by the geochemistry. Another method involves the chemical removal of alteration products by acid leaching. If a sample still shows the geochemical signature of alteration (e.g. high $^{87}Sr/^{86}Sr$) when all the altered material has been removed then that 'alteration signature' is a magmatic in origin and wall rock assimilation is a likely cause.

BLANK IN ORIGINAL

Chapter 3

Interpretation of TOBI sidescan terrains

'Speak to the earth, and it shall teach thee.'

Job 12 vs 8.

3.1 Introduction.

The sidescan images were interpreted by demarcating the boundaries between different textural terrains. The geological significance of these textural terrains is established by correlation with deep-tow camera traverses, submersible dives, dredge localities and the 7.5kHz profiler. This is the first time anybody has assessed critically the interpretation and groundtruthing of TOBI. This chapter describes the textural terrains identified and discusses their geological interpretation. Many of the terrains discussed below are illustrated in figure 3.1a, an area of sidescan mosaic from the northern edge of the RTI region in segment 1. The interpretation in terms of different sidescan terrains follows in figure 3.1b.

3.1.1 The WASP traverses used in groundtruthing

The areas of median valley floor crossed by the WASP traverses were particularly useful for detailed groundtruthing of the sidescan textures. The northern WASP traverse (26W) is covered by two directions of TOBI swath, one ridge-parallel (figures 3.2) and one oblique (figure 3.3). These two sidescan orientations highlight different aspects of the seafloor. The oblique swath is the most useful for correlating with the eastern half of the camera run, as it shows a greater contrast in acoustic terrains and less of the image is obscured by acoustic shadows. The western end of the WASP traverse is better imaged by the ridge-parallel swath because a considerable amount of data are lost in the nadir of the oblique swath. The southern WASP traverse (28W) has TOBI coverage from the ridge-parallel mosaic only (figure 3.6).

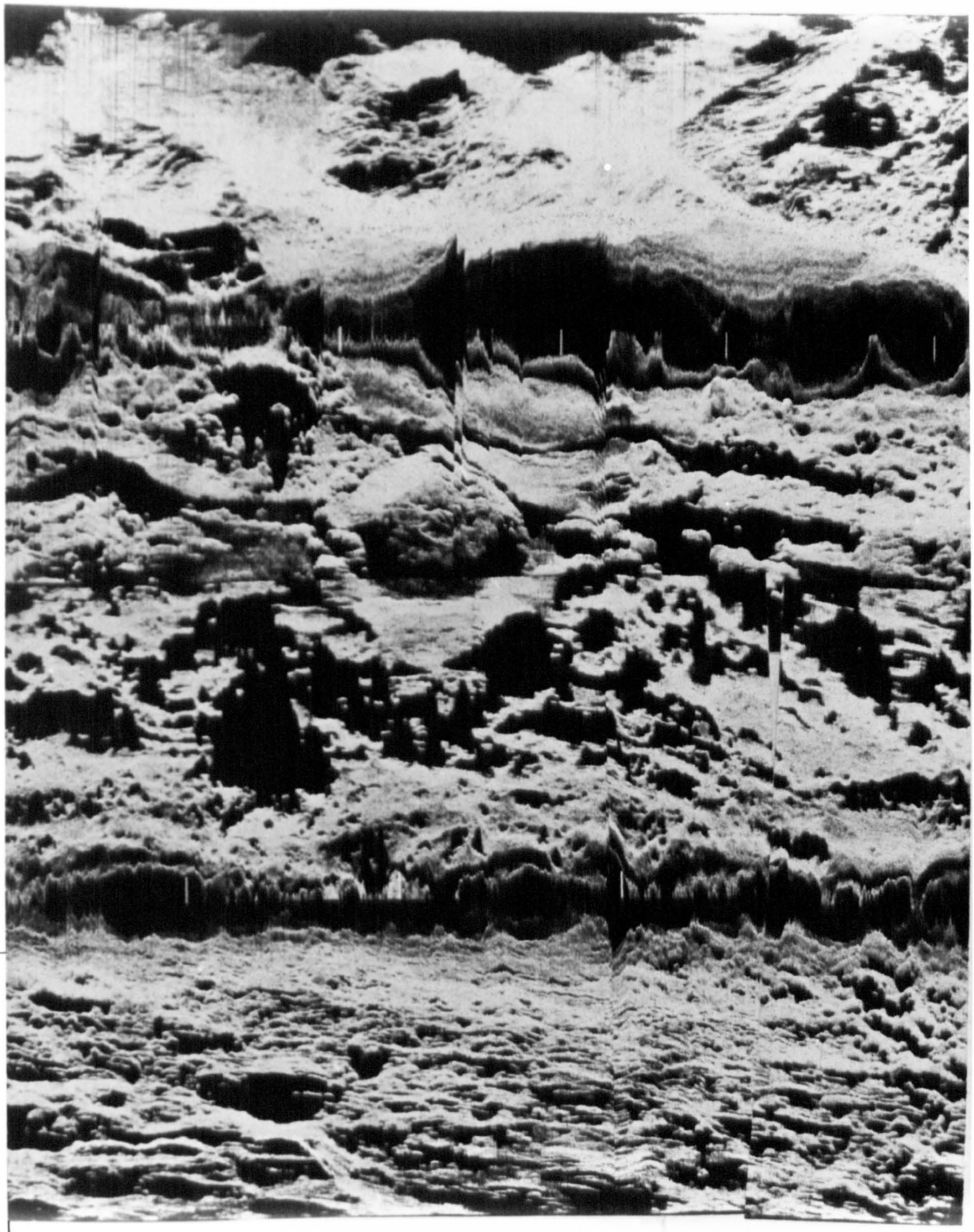

Figure 3.1a Sidescan mosaic of inner valley floor from near 24°N, the northern edge of the RTI, showing a wide variety of sidescan terrains.

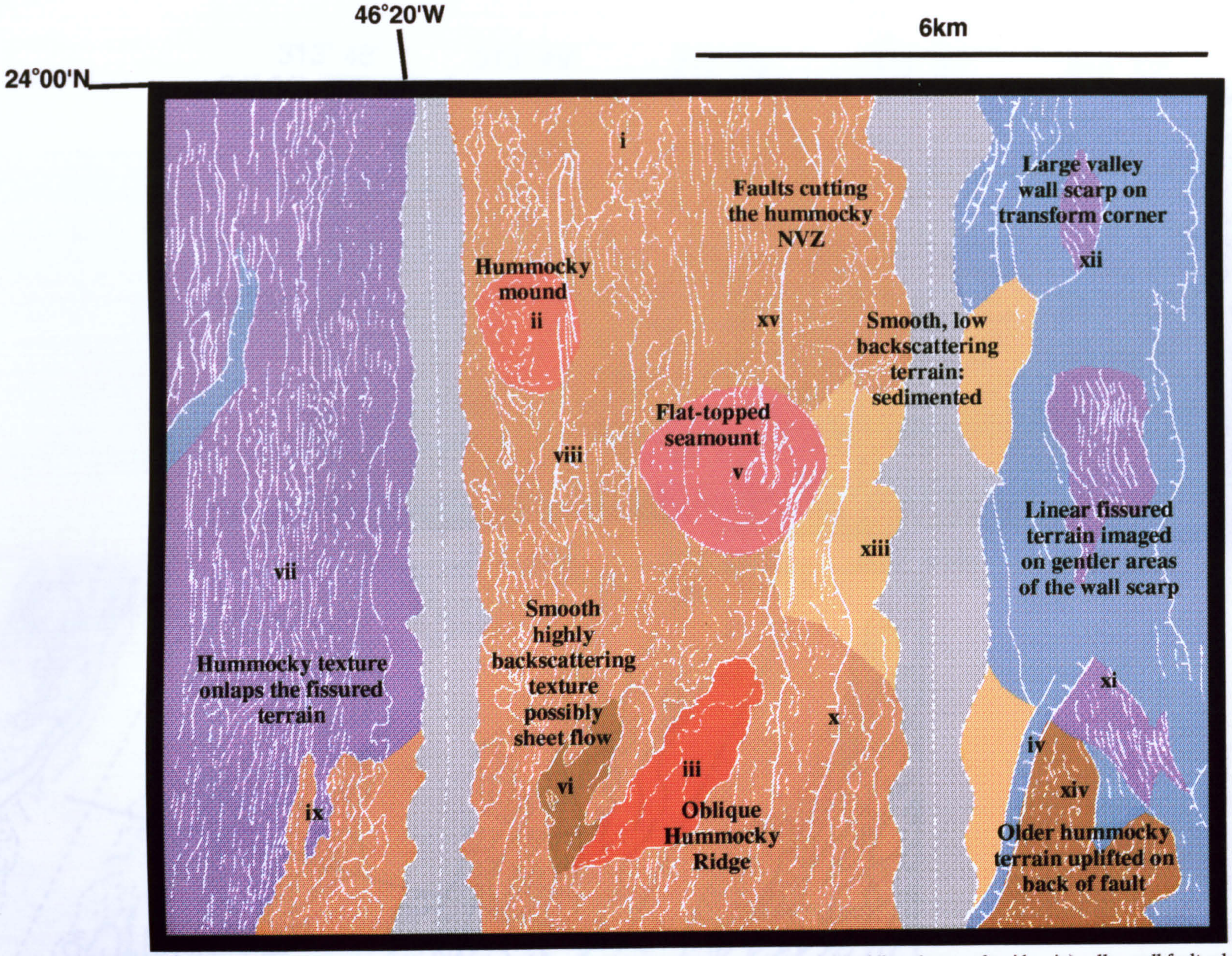

Figure 3.1b Interpretation of figure 3.1a. Sidescan terrains: i) hummocky neovolcanic texture; ii) hummocky mound; iii) oblique hummocky ridge; iv) valley wall fault splay with same trend as (iii); v) flat-topped seamount with summit depression and small faults and/or fissures across the summit plateau; vi) brightly backscattering smoother areas with faintly dabbled texture; vii) fissured terrain with some small angle normal faults; viii) patch of fissured crust between volcanic constructions; ix) fissured terrain is onlapped by thin hummocky ridges; x) faults cutting through NVZ, blend in with hummocky terrain to the south and peter out in smooth textured terrain to the north; xi) linear fissured terrain is stranded on gentler areas of the wall scarp between forks and splays on the main fault; xii) small fault horse with tectonised fabric on large throw valley wall scarp xiii) smooth, low backscattering sedimented terrain xiv) Older hummocky terrain uplifted on back of fault.

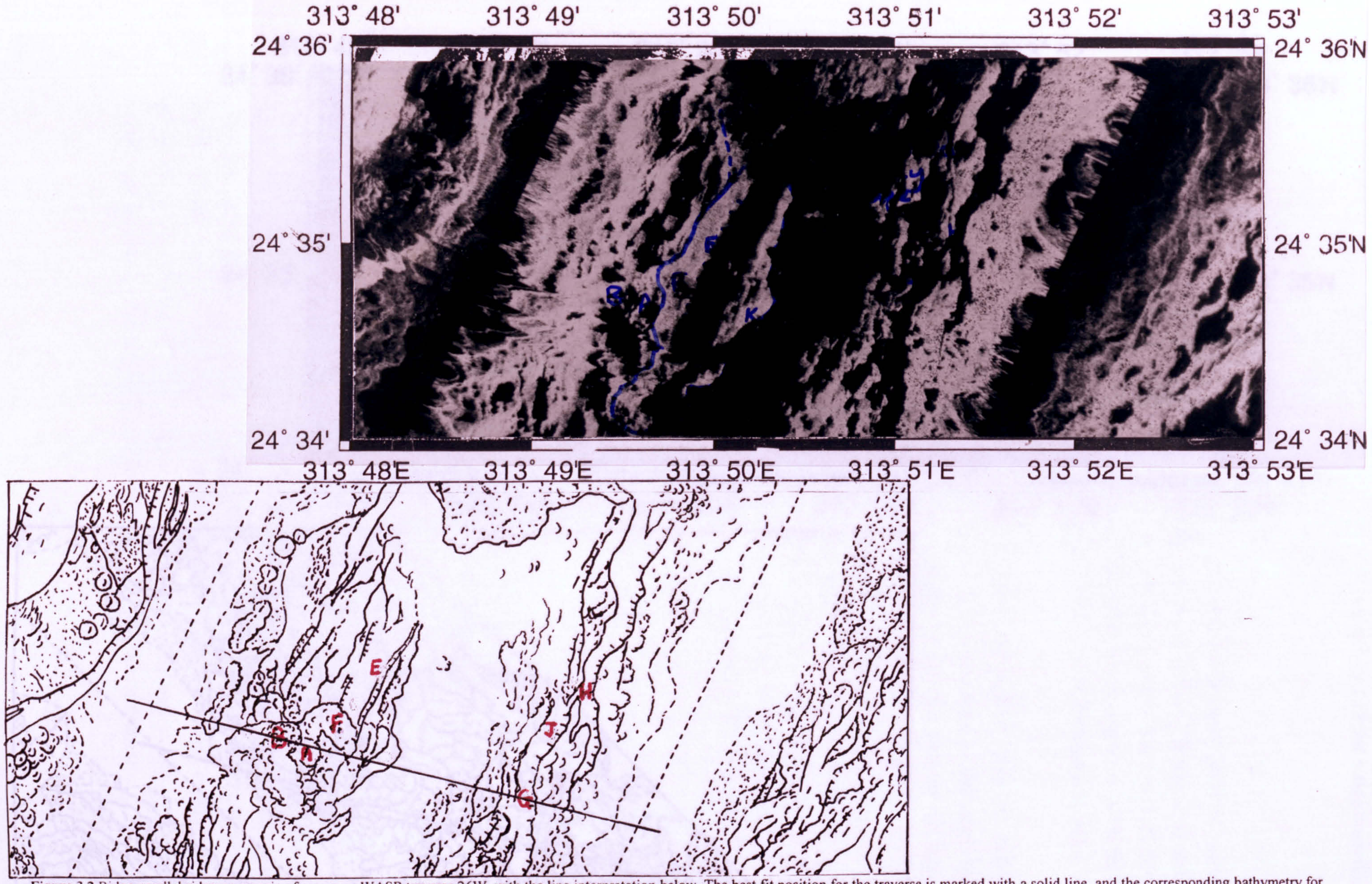

Figure 3.2 Ridge-parallel sidescan mosaic of area near WASP traverse 26W, with the line interpretation below. The best fit position for the traverse is marked with a solid line, and the corresponding bathymetry for the area is shown in figure 4.1. In the interpretation, low intensity backscatter terrain is stippled; fault scarps are lines with ticks on the down faulted side; fissures have across-line ticks; dashed lines mark the crests of hummocky ridges and the position of the nadir. Areas in shadow, such as the central depression of the NVR, are left blank. The texture of the pillow flows is highlighted by traces of the individual hummocky shadows, which are a reflection of the gross morphology of the flows, as discussed in the text. Short rounded flows with steep fronts correspond to single hummocks with strong arcuate shadows (A), while extensive moderately dipping flows comprise a cluster of small hummocks, resulting from their undulating surfaces (B). Other lettered labels (E, F, G, H, J and K) refer to discussion in the text.

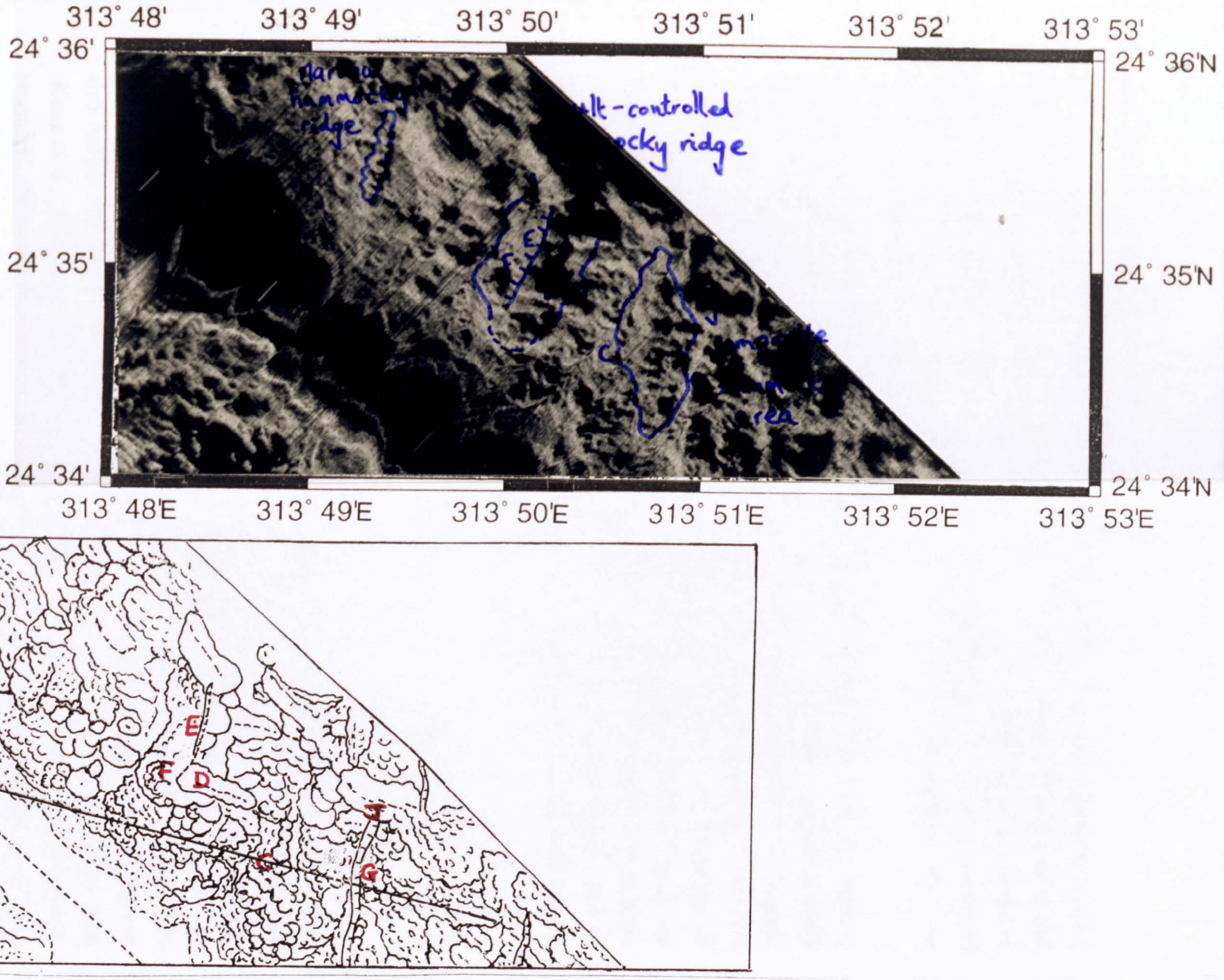

Figure 3.3 Northern oblique swath of the same area shown in figure 3.2 and with similar line interpretation. Note how this swath images the flows of the central depression (such as C) that are largely in shadow on the ridge-parallel swath. It also tends to highlight features in a swath-parallel orientation such as the flow down from the western crest which is elongated downhill (D). Labels E, F, G and J correlate to the same points marked in figure 3.2 and are discussed in the text.

3.1.2 The 7.5kHz profiler

The 7.5kHz profiler trace shows very little sub-bottom structure in the MARNOK survey, as a whole, and over the median valley the returns are very uniform. The lack of useful sub-bottom structure makes it seem unlikely that the 7.5kHz profiler will prove useful in quantifying sediment thickness or dip. However, the vehicle was towed at altitudes of 500-600m during this part of the traverse and better results may be obtained when the profiler is nearer the seafloor.

The descriptions included in this chapter concentrate on the profiles from the oblique swaths, as variations in the returns are more common with the increase in sediment cover off-axis. The oblique traverses did reveal some changes in the character of the signal, which can be correlated with the sidescan. As previously mentioned in chapter 2, the echo character types, I, II and III, are associated with increasing sediment cover. Examples of these different types are labelled in figures 3.7 and 3.12. The profiler traces are accompanied by the segments of the oblique sidescan swath to which they relate (figures 3.8 and 3.10 respectively). The ship time of the vehicle passage, which form the x-axis to the profiler traces, are marked on the sidescan swaths of figures 3.8 and 3.10 for the purpose of cross correlation.

3.2 Constructional terrains.

3.2.1 Pillow flows and mounds

3.2.1.1 Hummocky neovolcanic texture

The hummocky terrain comprises a conglomeration of myriad, circular mounds, whose diameters range from a few tens of metres to about 500m (figure 3.1i). The geometry of the shadows indicates that they are usually less than 50m high, have rounded summits and no summit craters. TOBI data from the Reykjanes Ridge show a similar terrain comprising large areas of the axial volcanic ridges (AVRs) (Parson et al., 1993; Murton et al., 1993, Searle et al., 1994). SeaMARC I, which has a similar frequency to TOBI, has also imaged hummocky terrain both on the MAR and elsewhere [e.g. the MARK area (Kong et al., 1988), the EPR (Kastens et al., 1986) and the Juan de Fuca Ridge (Kappel & Normark, 1987; Barone & Ryan, 1988; Appelgate, 1990)]. The groundtruthing with the WASP traverses show that the hummocky terrain on the sidescan images corresponds to pillow flows of varying sizes and shapes. The dredge sites over hummocky, neovolcanic terrain also invariably recovered pillow lava, confirming this interpretation.

3.2.1.2 Camera traverses over hummocky terrain

Groundtruthing using the deep-tow camera traverses showed that each hummock usually, but not always, corresponds to an individual pillow flow. The gross morphologies of the flows (revealed by the WASP high resolution bathymetry eg figure 4.1) and the corresponding shadowing in the sidescan govern the character of the hummocks in the image. I have divided the hummocky texture into four subtypes: A, strongly rounded; B, fine-scale hummocky cluster; C, diffusely hummocky and D, strongly elongate (see corresponding points on figures 3.2 and 3.3).

Individual pillow mounds with steep fronts, known as haystacks, form short, well defined hummocks with *strongly rounded* shadows (see figure 3.2, point A). In some cases individual hummocks do not correspond to separate flows. Instead, a *fine scale hummocky cluster* of shadows can result from the undulating surface of a single, gently inclined flow (figure 3.2, point B). The fine-scaled, composite appearance of such a flow is strongly dependent on the angle of incidence of the sonar beam. The contacts between gently undulating flows can sometimes be determined by the continuous (and usually sinuous) line of higher backscatter from the flow front. This can prove difficult when the margins of the flow unit are gently inclined compared with the rest of the surface as in the *diffusely hummocky* area (e.g. figure 3.3, point C), but becomes easier when flow fronts are relatively steep. Point D (figure 3.3) is a well-defined feature which is probably a *elongated* flow. Both the lateral margins and the front of this flow are probably steeply dipping, as indicated by the strong shadow defining this feature. It is distinct from the hummocky ridges described in section 3.2.2 because its elongation is in a downslope flow direction, rather than defining a small ridge crest (for bathymetry of the area see figure 4.1).

The camera traverses were also used to investigate whether different lava morphologies are associated with particular gross flow shapes (as characterised by the subtypes of hummocky texture, described above). Steep fronts of strongly elongated pillows are features common to the discrete, rounded hummocks (like figure 3.2, point A), while the tops of these flows tend to be relatively fast flow types such as lobate and knobby morphologies. Long, gently undulating flows (e.g. figure 3.2, point B) largely comprise knobby pillows. Bulbous pillows (suggesting slower flow rates) can also form quite extensive flows, but tend to have more strongly undulating surfaces and better defined flow fronts. A variety of pillow types from phallic tubes to broken bulbous pillows occur at subtype C. A larger data-base of flow types and sidescan textures would be required to corroborate the tentative correlations of this small data set.

3.2.1.3 Pillow volcanoes: composite hummocky domes

Hummocky cones or domes, reminiscent of cauliflower hearts (figure 3.1ii), are rare in this data set, though these composite mounds (up to 1.5km across and 50 - 150m high) are a common feature in the Reykjanes Ridge (Parson et al., 1993). The example in figure 3.1 is surrounded by hummocky terrain and is faulted on its eastern side, but it is unclear whether it had an underlying linear constructional phase before the radial symmetry developed.

3.2.2 Hummocky pillow ridges

Often the hummocks have a strong linear arrangement implying that the pillow flows are arranged as constructional ridges. These can take the form of a narrow row of connected mounds or a broad composite pile (see overlay of figure 3.3). Typically these hummocky ridges are several kilometres long and 100m to 2km wide, often arranged in closely-spaced parallel rows, thus building up the NVZ. Composite hummocky ridges occur where a number of flows have piled up on top of each other. In places the hummocky terrain has no distinct, strong linear shadowing, but the gross alignment of the resulting NVZ is still ridge-parallel.

The elongation in the constructional ridges is apparent in non-ridge-parallel swaths (compare figures 3.2 and 3.3), confirming that they are not an artefact of the directionality of the sidescan. In the GLORIA survey of the area, the hummocky ridges were barely resolved as a strong backscattering, subtly-striated band on the median valley floor (Roest et al., 1984).

3.2.2.1 Structural control on orientation

The alignment of the hummocky ridges is usually normal to the spreading direction suggesting that they are closely controlled by the stress regime. The control of the stress regime on the orientation of hummocky ridges is demonstrated in the NVZ at the RTI, where the hummocky ridges adopt an oblique trend (figure 3.1iii), paralleling other structural features in the area (e.g. figure 3.1iv). The origin of this oblique orientation is discussed later in chapter 6.

Well-defined, individual ridges may occur where the volcanism is focused on a single, dominant fissure or fault. In contrast, the broad, composite hummocky areas probably form where there is no single controlling structure, but coalescence of flows from a large number of eruptive conduits.

3.2.2.2 Relationship between pillow ridges and faulting

The groundtruthing showed that many hummocky ridges are intimately associated with faults. A fault is often present when the crest of a hummocky ridge has a sharp linear character. Sometimes the fault scarp (figure 3.2, point E) is overlapped by the dappled, hummocky texture of a flow, indicating that the faulting is syn-magmatic (figure 3.2, point F). The same features (points E and F) are recognised on the oblique swath (figure 3.3), though the image looks quite different, as a result of the oblique insonification.

In the previous example the fault itself is imaged by the sidescan as a sharp truncation of the hummocky crest coupled with the brightly backscattering line of the scarp. A relation between faulting and constructional ridges can also be demonstrated when the presence of a fault is not immediately obvious. Descending into the transform valley, at the at the southern tip of segment 1, the NVZ comprises a strongly continuous ridge, where individual hummocks merge along strike to form a 'pinch and swell' profile (figure 5.3). Karson and Dick (1983) report very steeply oriented, elongated lavas draped over pre-existing scarps in this area of the NVZ. The dives of Fujimoto et al. (1994) also confirm that recent synmagmatic deformation has taken place. I suggest when a hummocky ridge has a high aspect ratio and sharp, strongly-continuous nature, a pillow flow may have flowed over the top of a scarp.

3.2.3 Flat-topped seamounts

Isolated seamounts with relatively smooth-textured, broad summit areas form a distinctive volcanic morphology on the sidescan records (figure 3.1v). They are rare compared with the hummocky volcanic terrain, occupying less than 5% of the NVZ. On the sidescan they appear to have flat tops, but in fact the bathymetry often suggests there is a very slight doming to the summit plateau. They have a circular form, with steep, strongly backscattering rims and are 1-2km wide and 50m to 200m high. The volumes of lava comprising individual edifices are estimated to be between 0.05 km^3 and 0.5 km^3. The dimensions of these seamounts are in keeping with studies from wider areas of the MAR (Batiza et al., 1989; Smith & Cann, 1990; 1992). They are also similar in shape to those reported from near the axis of the EPR (Searle, 1983; Fornari et al., 1987b), but fall at the lower end of the size spectrum for Pacific seamounts.

Often there are circular areas of shadow, probably small pit craters (50-100m in diameter) directly in the centre of the of the circular summit. Figure 3.1v shows a larger central collapse structure 600m in diameter in the centre of a flat-topped seamount. Some later small fractures trending ridge-parallel and at ~020° also cross-cut the summit plateau of

this seamount disrupting the radial structure. A summit depression must be larger than 1km in diameter to be classed as a caldera (Batiza, 1982). None of the pit-like collapse structures in this data set are large enough to qualify, although TOBI sidescan from elsewhere on the MAR show seamounts which do have calderas (e.g. the breached caldera of W-seamount described by Cann et al., 1992a).

The radial symmetry and central depressions of these seamounts are strong indication of the presence of central pipe feeding conduits.

3.2.3.1 Groundtruthing flat-topped seamounts: submersible dives

One of the aims of the groundtruthing is to discern whether flat-topped seamounts comprise distinctive flow morphologies compared with the hummocky ridges. The smooth sonar texture of the summit plateaux implies that they may be primarily composed of sheet, rather than pillow flows. Serocki Volcano in the MARK area has a very similar surface texture to many of the flat-topped seamounts in the MARNOK area. Submersible dives across it found that although summit plateau was extremely flat with less than 5m of relief, it consists of bulbous and elongate, knobby pillows with only the occasional sheet flow (Humphris et al., 1990).

The transect 4 submersible dive of Zonenshain et al. (1989) crosses a flat-topped seamount on the western flank of the MARNOK NVR, near the southern tip of segment 2 (figure 2.8b, point v). The dive track marked in figure 2.8b just clips the northern margin of this seamount, covering the steep flanks, but possibly missing the summit plateau altogether. The geological transect suggests that the smooth-textured, steep flank of the seamount comprises sedimented pillows, with younger pillow lavas near the summit.

The talus which occurs within the axial fracture of the NVR (figure 2.8a) is related to the fault scarps and is not responsible for the uniform texture of the summit plateau. There is no evidence from this submersible dive that sheet flows are any more common on flat-topped seamounts than within the hummocky terrain, as the same pillow lavas are reported on both the western and eastern flanks, although their sidescan textures are quite different.

However, it should be noted that there is no location error cited for the transect of Zonenshain et al. (1989). The submersible possibly traversed a larger area of summit plateau, to the south, but alternatively it may have crossed the hummocky terrain to the north. Indeed, the reported bathymetric profile (figure 2.8a) is perhaps more in keeping with the latter location.

Submersible studies across the flanks of some larger Pacific seamounts have identified hyaloclastites as well as the products of mass wasting (Lonsdale & Batiza, 1980). However, as the seamounts on this part of the MAR are formed in water at greater than critical pressure, hyaloclastite formation is likely to be inhibited.

3.2.3.2 Groundtruthing flat-topped seamounts with dredging

Dredge stations 4, 12, and 29 targeted flat-topped seamounts. Pillow lavas were the most common morphology recovered from these dredge stations, although a small quantity of sheet flow fragments were found in D4 and D12. A slab of ropy, folded pahoehoe crust 40 x 25 x 3cm in size, indicates the presence of sheet flows at D4 (figure 3.4). Unfortunately there is incomplete sidescan coverage of the area dredged in D4. The crusts of hollow pillows were also recovered in this dredge haul suggesting that there may have been a sudden drop in magmastatic pressure at the end of the eruption.

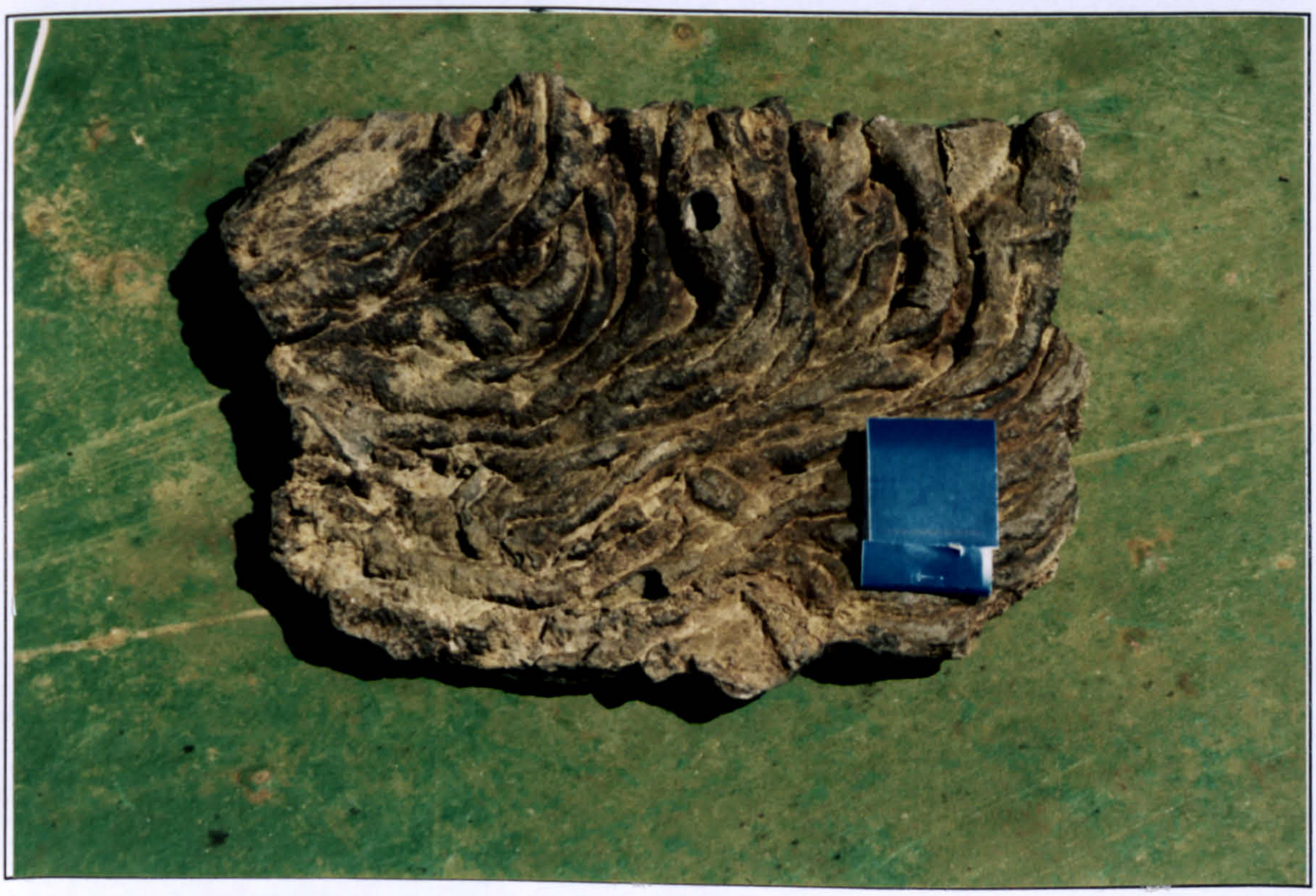

Figure 3.4 Slab of ropy pahoehoe basalt recovered in dredge 4 over a circular, flat-topped seamount. The blue match packet for scale is 8cm long.

One of the units from D12 comprises tabular samples a few centimetres thick. These have a thick, glassy margin on the upper surface and a thinner one on the lower surface. The lower surface is generally smooth in contrast to the upper surface, which shows the

conchoidal fracture of the glass. To have a quench on upper and lower surfaces these must be very thin sheet flows, and are likely to be similar to the ribbons reported by Ballard and Moore (1977). Ribbons are small areas of sheet flow found within much larger pillowed units. Tabular morphologies similar to those described above were recovered in a number of dredge hauls over hummocky terrain throughout the study area, suggesting that they are not especially associated with flat-topped seamounts.

No hyaloclastite samples were recovered during the whole sampling programme. This supports the suggestion in the previous section that hyaloclastite formation on the steep flanks of these seamounts is unlikely, although recovery may have been inhibited by the low preservation potential of hyaloclastites.

To summarise, there remains an element of ambiguity in the type of lava flows that form the 'flat-topped' seamounts, but submersible and dredging evidence from this study confirms the findings from Serocki Volcano in the MARK area that flat-topped seamounts comprise a mixture of low relief pillow flows, and sheet flows (Humphris et al., 1990).

3.2.4 Cratered cones

The cratered cone (labelled in figure 2.9a) is about 60m high and is located in the NTO. It has neither the flat top of the smoother seamounts, nor the elongation or composite flow morphology which is usually associated with the hummocky terrain. The well developed summit crater is about 600m in diameter and implies that the edifice is vent fed. The edge of the cone itself has a slightly dappled texture which suggests that its outer walls comprise low relief pillow flows. This cratered cone is imaged by both ridge-parallel and oblique swaths as shown in figure 2.9. (The ridge-parallel swath is seen at a larger scale in figure 2.8b—bottom left.) Although a cone-like form seems clear on the oblique swath, ridge-parallel and oblique faults are the primary features imaged on the ridge-parallel swath, and the crater is an ambiguous form at the edge of the swath.

3.2.5 Lava tubes and tumuli

Lava tubes and channels are a common feature of subaerial volcanism, and in recent years have been increasingly recognised in the subaqueous environment. For example, within and around the Lamont Seamounts in the Pacific, lava tubes are thought to act as conduits, transporting lavas for large distances across the seafloor. Some seem to have initiated at the caldera rim, but more commonly they emanate from small volcanic cones and domes in the satellite provinces (Fornari et al., 1984; Fornari, 1986).

Figure 3.5 shows a long thin feature 150m wide and at least 700m (and possibly 1.5km) long stretching between the steep-sided eastern flank of a flat-topped seamount and an area of hummocky volcanism and possible tumescence. This feature closely resembles the lava tubes of the SeaMARC 1 images near the Lamont Seamounts, although it is not as sinuous and has a relatively low length/width ratio compared with many subaerial lava tubes, which are commonly less than 50m wide, but can be several kilometres long (Peterson & Swanson, 1974, Peterson et al., 1994).

The broad shield shape of many subaerial basaltic provinces are reflections of the tube mechanism that acts to distribute lavas to great distances from the source vent (Peterson & Swanson, 1974). In figure 3.5, the tube seems to be relatively continuous with the edge of the flat-topped seamount to the west. However, the tube cannot have flowed from the flat-topped seamount in an easterly direction as the bathymetry shows this is uphill.

Instead, a more plausible scenario involves the eruption of magma from the large cones situated on the local high to the east of the seamount, with the resulting tubes flowing to the east and west. The westward tube follows a relatively straight trend, but is not elongated in the direction of the steepest gradient (as assessed from the bathymetry). Fornari (1986) suggests that many lava tubes are developed in pre-existing troughs and this one may have its orientation controlled by the lows between adjacent pillow flows and cones, or alternatively by a pre-existing transform-parallel structure such as a fissure or small fault scarp.

The flow to the east descends a steeper gradient and then levels out, becoming a bulbous lobe about 600m long and 400m wide. The bulbous character of this feature compared with the adjacent tubes and cones may indicate that inflation processes have been operating. Flow inflation is a relatively recently recognised process in submarine volcanism. Tumuli and inflated lava flows have been identified by submersible and on SeaMARC 1 images of Axial Volcano, Juan de Fuca Ridge (Appelgate & Embley, 1992), while Serocki Volcano in the MARK area is thought to be a flat-topped megatumulus (Humphris et al., 1990). Serocki Volcano has been found to be geochemically and petrographically related to a lava flow which originated from an adjacent cone located above the megatumulus (Bryan et al., 1994). The possibility of a similar origin for the flat-topped seamount to the west of the lava tube will be discussed in chapter 4.

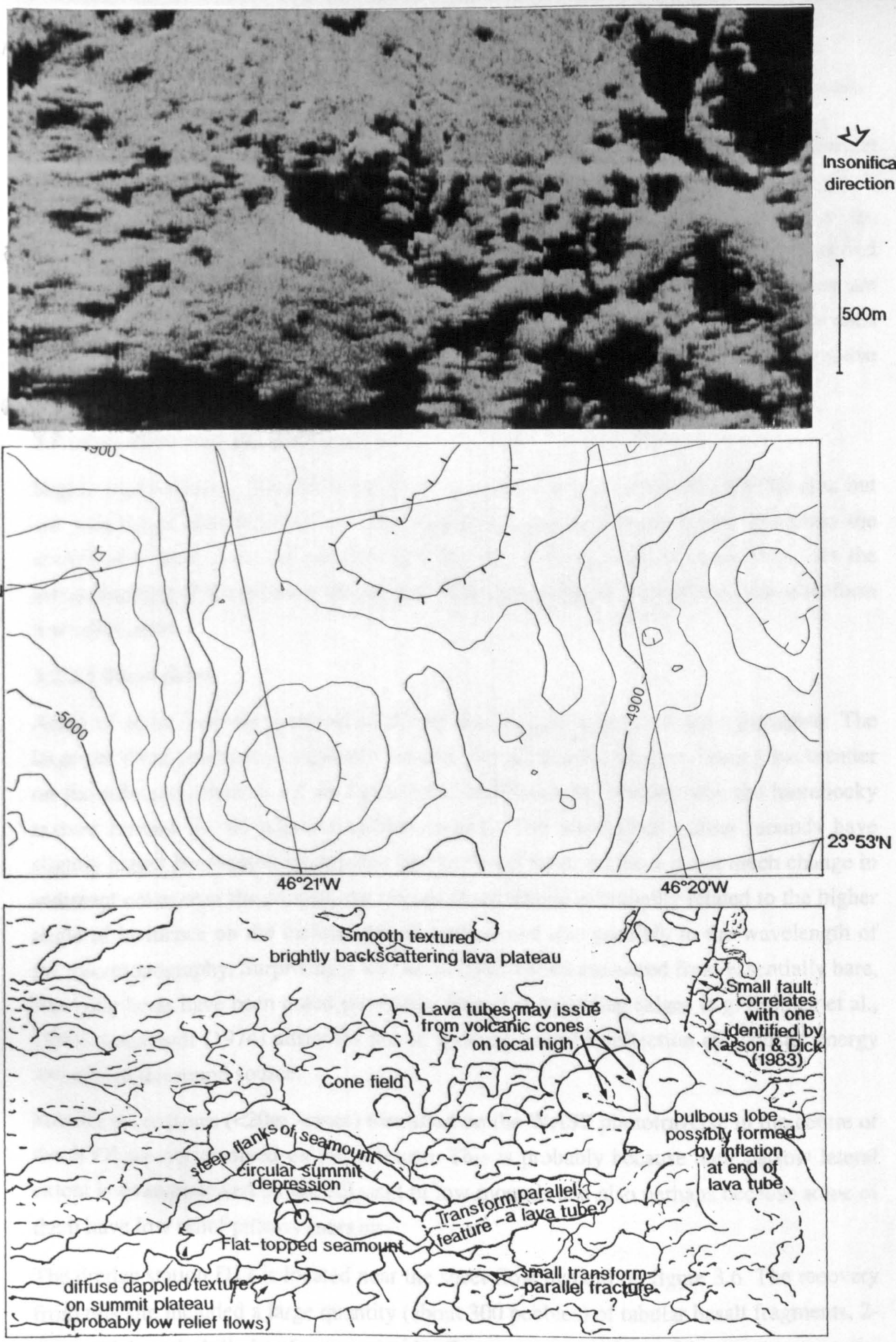

Figure 3.5 Transform-parallel feature in the NVZ near the RTI is probably a lava tube emanating from the volcanic cones on the edge of the lava plateau. A flat-topped seamount is imaged to the west of this transform-parallel feature. The oblique fault in the upper right correlates with one identified by Karson & Dick (1983).

The main difference between the bulbous lobe identified here and the tumuli studied in detail on the Juan de Fuca Ridge is the lack of surficial tension fractures which form in the crust as a result of the uplift and expansion during inflation (Appelgate & Embley, op. cit.). Although they are common, these cracks are not always present on areas identified as probable sites of tumescence. It is possible that tension fractures are present, but are too small to be resolved on the TOBI sidescan images. The main criteria which are used by Appelgate and Embley (op. cit.) to recognise the products of inflation are the positive relief and steep flanks of bulbous plateaux and their connection to sinuous ridges.

3.2.6 Smoother neovolcanic terrains

Highly backscattering, smoother flat areas are relatively rare in the MARNOK area but are sometimes observed between the hummocks and seamounts which dominate the neovolcanic zone. It is tempting to interpret all of these areas as sheet flow, yet the groundtruthing of the smooth, flat-topped seamounts suggests that pillows can also form low relief areas.

3.2.6.1 Sheet flows

Areas of sheet flow were identified during the WASP traverse of the narrowgate. The larger of these produced completely smooth, flat areas of moderately strong backscatter on the sidescan (marked 's.f' on figure 3.6), which sharply contrast with the hummocky texture formed by the adjacent pillow mounds. The steep-sided pillow mounds have slightly higher backscatter amplitudes than the sheet flow. As there is not much change in sediment cover over the contact, the change in amplitude is probably related to the higher angle of incidence on the inclined pillow surface and also possibly to the wavelength of the microtopography. Surprisingly low backscatter values measured from essentially bare, flat-lying lavas have been noted previously from fast spreading ridges (e.g. Embley et al., 1990). Leenhardt (1974) attributes this to forward specular reflection of acoustic energy away from the sound source.

Smaller sheet flows (<20m across) identified on the WASP phototraverse in the centre of the NVZ are not resolved on the sidescan. This is probably because their narrow lateral extent is overshadowed by the adjacent pillow mounds and also perhaps because some of them have low relief pillowy margins.

The dredge station D17 is located near the sheet flow marked on figure 3.6. The recovery from this site included a large quantity (about 300 pebbles) of tabular basalt fragments, 2-3 cm thick and chilled only on one side. Some specimens have drip structures on the lower surface indicative of a hollow cavity underneath. This and the relatively large

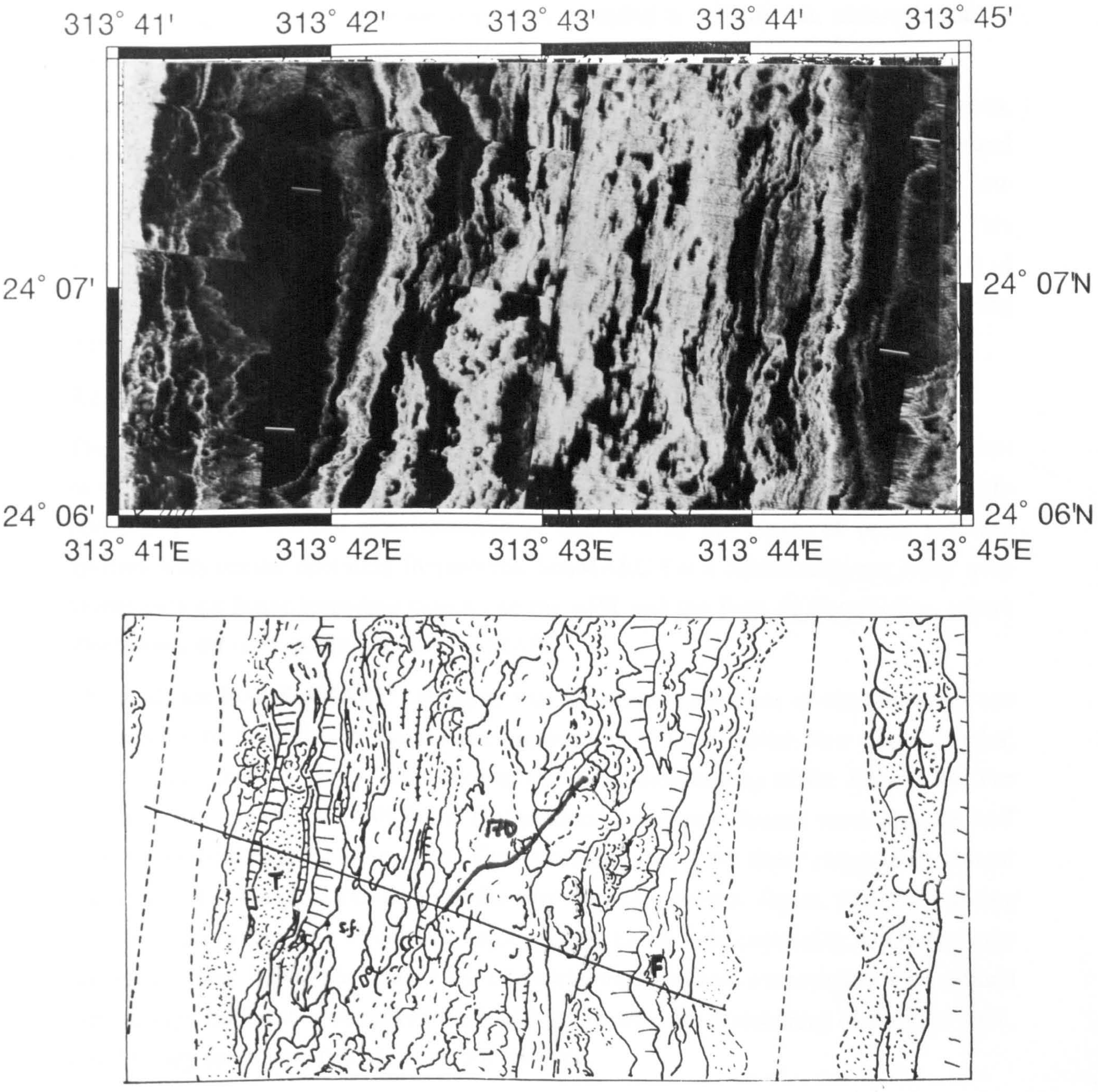

Figure 3.6 Ridge-parallel sidescan mosaic of area near WASP traverse 28W with the line interpretation below. The best fit position for the traverse is marked with a solid line, and the corresponding bathymetry for the area is shown in figure 4.2. See figure 3.2 for key to features in the interpretation. In addition, the smooth bright texture of sheet flow is indicated by 'sf', the sedimented western terrace by 'T', and the sedimented eastern fault block by 'F'.

recovery suggests that the dredge may have sampled a collapse pit, although such a feature is not resolved in the sidescan image.

With the exception of the pahoehoe basalt recovered from the flat-topped seamounts, small fragments of folded sheet flow were also recovered from two other stations, D9 and D20. Station D9 targeted a hummocky ridge, but to the west of it there is a smooth, low relief area with exactly the same texture as the sheet flow identified in figure 3.6. This area is within the precision error for the dredging location and so is perhaps the origin of the pahoehoe. There is no similar smooth texture near the locality for D20, confirming that some patches of pahoehoe sheet flow are not resolved in the sidescan.

3.2.6.2 Resolution of sheet flow morphologies

The WASP groundtruthing was used to discern whether different sheet flow morphologies can be resolved by textural changes in the TOBI sidescan image. TOBI's potential for this textural discrimination is indicated by the limits of other sidescan systems with similar operating frequencies. SeaMARC I is a 30kHz sidescan sonar used extensively on faster spreading ridges like the EPR and the Juan de Fuca Ridge, where sheet flows are more prevalent than the MAR.

The evidence from SeaMARC I suggests that sidescan instruments of this frequency are not capable of providing a visual discrimination of different sheet flow morphologies, except when there is also a difference in the gross morphology of the flow units. For example, Embley et al. (1990) found that jumbled flows near fissure vents provide well defined acoustic targets on the sonar. This is because they form linear ridges with several meters of relief which stand out from the surrounding smoother sheets. However, during the same survey they also observed a large jumbled basalt field containing patches of ropy and lobate sheet flows. The SeaMARC I sidescan record shows a reasonably well defined area of high backscatter in approximate agreement with the dimensions of the lava field, but the ropy and lobate patches were not resolved.

In the MARNOK study area, the different morphologies, which were clearly identified during the photoanalysis are not resolved on the TOBI sidescan (see figures A2.7 for photographs of sheet flow morphologies, figure 4.2 for location of sheet flow morphologies on traverse and figure 3.6 's.f' for the corresponding TOBI texture). This is not very surprising, given the small lateral extent of the different morphologies (about 10m - 80m along the photo-traverse). Although the larger areas should be within the resolution limit of the instrument, it seems unlikely that variations in the textural pattern of the backscatter could be discerned on this small scale. Thus, although the evidence to

date is negative, the discrimination of different morphologies might be possible over larger expanses of sheet flow.

3.2.6.3 Low relief pillow fields

Other high backscattering, low relief areas are not completely smooth but have a faintly dappled texture. A dredge station (D11) traverses one of these areas (figure 3.1vi), which was originally thought to be the location of a sheet flow. However, rounded pillow fragments were the only morphology recovered in the dredge. Hence, this may be the texture produced by a low relief pillow field. Alternatively the dredge may have only recovered material from the surrounding hummocky terrain which should have a higher recovery potential than a smooth sheet flow.

3.2.7 Profiler over fresh volcanic terrain

Figure 3.7a shows a typical profile from the NVZ, labelled a type I return. The signal has a moderate amplitude and is very diffuse in nature, with usually only a slight focusing of the backscatter into the first part of the return. The reverberation from the rough surface of the fresh basalt and the highly variable nature of the topography results in a relatively long return echo comprising diffuse, superimposed diffraction hyperbolae. These have variable vertex elevation and although the curves sometimes overlap, more often the hyperbolae are not focused enough to show up as a strong reflection beyond the first return. The result is a prolonged, structureless, fuzzy signal with a poorly defined seafloor surface.

Within the median valley floor, a marked increase in the sediment cover detected on the sidescan images is not always accompanied by a corresponding change in the character of the profiler trace. This is illustrated in the oblique swath (figure 3.8 i) where there is a strong decrease in the amplitude of the sidescan image, and a marked increase in smoothness near the base of the inner wall fault at about 094 15:20. The profiler record at figure 3.7b shows that the seafloor is flatter and consequently has a better defined and slightly stronger, more focused return. The diffraction hyperbolae are also less noticeable on this low relief topography. This difference in the thresholds of response of the two instruments will be discussed further in section 3.4.1.

3.2.7.1 Interpretation of the type I return

The unsedimented lava flows are irregular on a number of scales, from surface ornamentation to overall flow morphology, but features with spacings of less than 10m would not produce distinct hyperbolic diffractions but a prolonged fuzz (see section

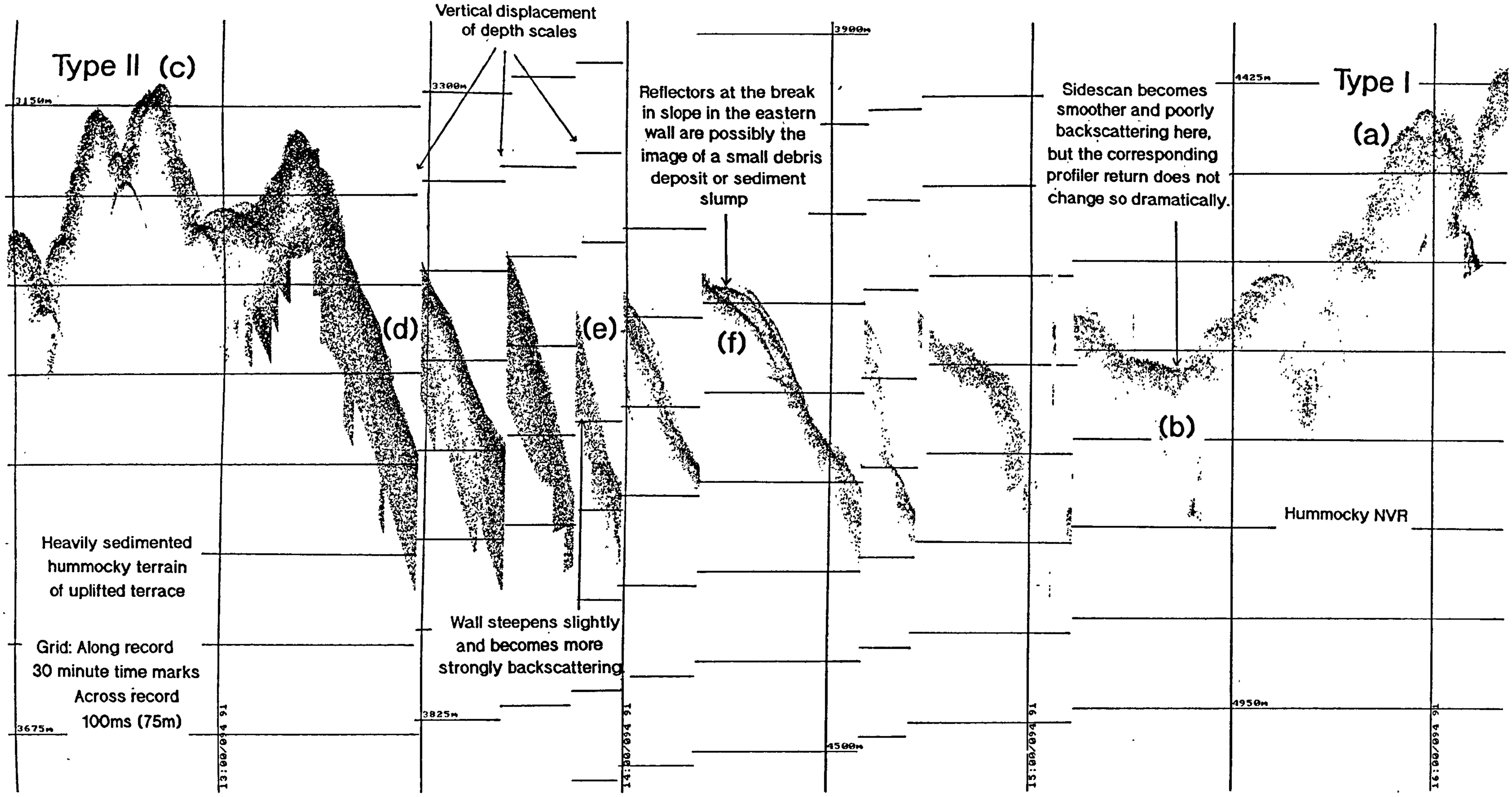

Figure 3.7 Record from the 7.5kHz profiler from central oblique swath extending from an uplifted terrace down the eastern wall to the middle of the inner valley. a) Type I return from the fresh hummocky terrain of the valley floor. b) Position on the sidescan image where the amplitude decreases markedly and the texture becomes smoother. There is no corresponding sharp change in the character of the profiler return. c) Type II return from the more sedimented hummocky terrain of the uplifted fault terrace. d) Return from upper part of the eastern wall fault where the sidescan indicates there is a moderate amount of sediment cover. e) Return from just above the break in slope of the valley wall where the sidescan becomes more strongly backscattering. f) Well defined reflectors at the break in slope which corresponds to the convex bulge outlined in red on figures 3.8 and 3.13. The very low intensity of the corresponding sidescan and the sharp character of the profiler trace (which is similar to the type III return in figure 3.12) indicates that there is a considerable.thickness of sediment. The wedge shape may correspond to the deposit from a sediment slump.

313° 46'
313° 47'
313° 48'
313° 49'
313° 50'
313° 51'
313° 52'
313° 53'
24° 25'
24° 24'
24° 23'
24° 22'
24° 21'
24° 25'N
24° 24'N
24° 23'N
24° 22'N
24° 21'N
313° 46'E
313° 47'E
313° 48'E
313° 49'E
313° 50'E
313° 51'E
313° 52'E
313° 53'E

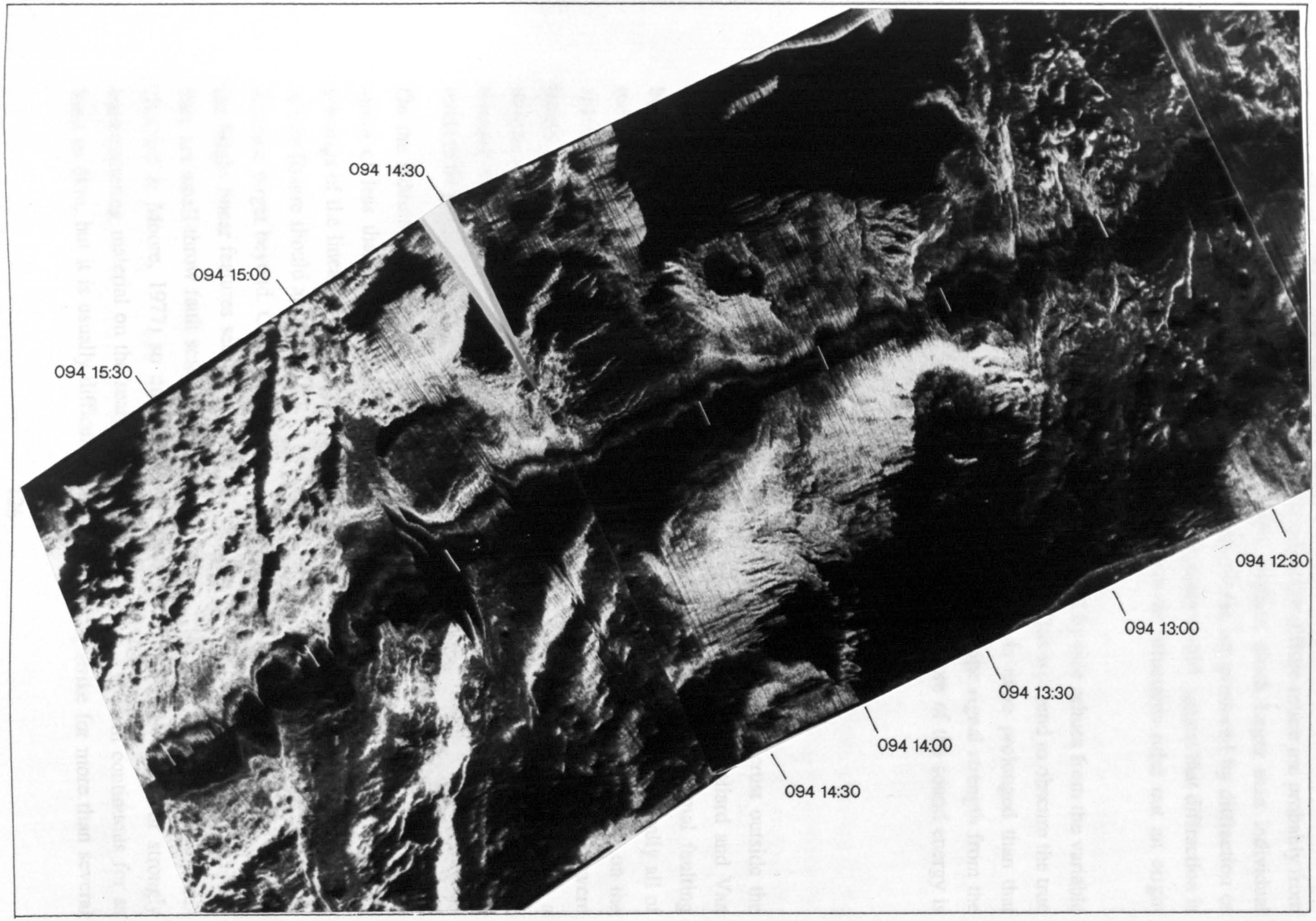

Figure 3.8 Oblique swath and bathymetry overlay over the eastern wall corresponding to the profile in fig 3.7. The sidescan can be related to the profiler trace using the time ticks. The convex bulge in the bathymetry of the wall is outlined in red and may be the deposit from a sediment slump.

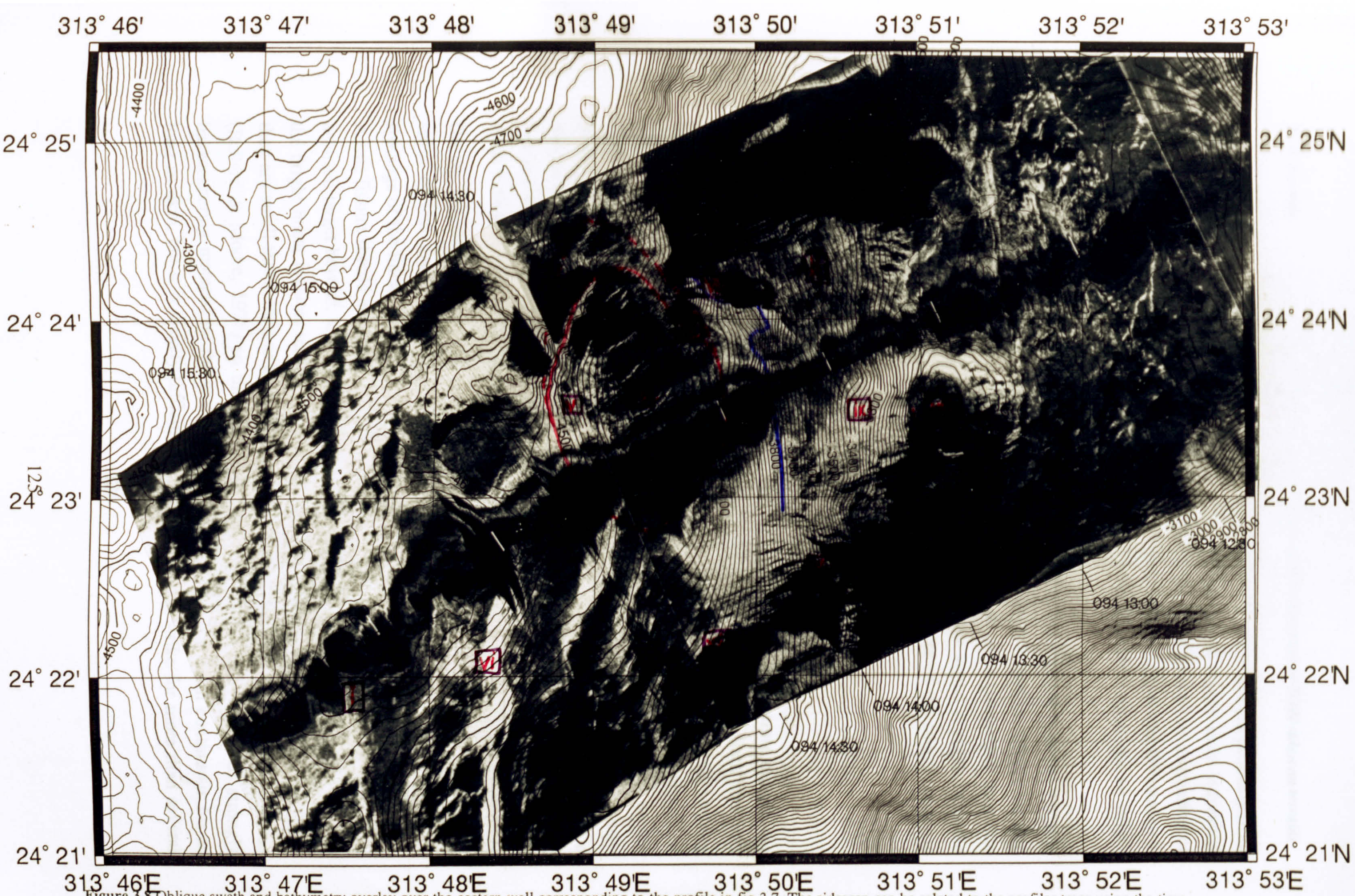

Figure 3.8 Oblique swath and bathymetry overlay over the eastern wall corresponding to the profile in fig 3.7. The sidescan can be related to the profiler trace using the time ticks. The convex bulge in the bathymetry of the wall is outlined in red and may be the deposit from a sediment slump.

2.5.2). Hence, the hyperbolae that are resolved within the diffuse return are probably from cones, flow fronts and undulations of the flow surface, much larger than individual pillows. It is impossible to say whether these hyperbolae are produced by diffraction or specular reflection, although the low amplitudes of many would suggest that diffraction is a dominant mechanism. The general absence of bow-tie structures rules out an origin from small-scale quasi-sinusoidal elements.

The variable vertices of the hyperbolae may be generated by side echoes from the variable topography within the insonified area (about 30,000m^2). This will tend to obscure the true shape of the seafloor and lead to an echo character that is more prolonged than that expected from a direct reflection off a flat bottom. The average signal strength from the fresh hummocky terrain is relatively low probably because more of the sound energy is scattered in directions which do not produce useful returns.

3.3 Tectonic sidescan terrains.

3.3.1 Fissured terrain

The strongly lineated terrain which characterises the older tectonised crust outside the NVZ (figure 3.1vii) was first identified in early studies of the MAR. Ballard and Van Andel (1977) described a zone of intense fissuring and small throw normal faulting between the distal edges of the NVZ and the inner walls of the rift valley. Virtually all of the fissures observed during the WASP traverses were too small to be identified on the sidescan. Some of the widest fissures (7-8m wide) on the narrowgate traverse (28W) were barely resolved, indicating that features comprising the 'fissured terrain' must be a minimum of about 5m wide (most are probably considerably wider). On the whole, the fissured terrain was imaged near the centre of the swath where the across track resolution tends to be greater (between 2m and 10m).

On the sidescan images, the tectonic fabric is closely spaced with a separation across strike of less than 50m for those features large enough to be imaged. The range in spacings of the lineations within the fabric extends right down to the limit of resolution. A true fissure should always have a shadow on the nadir side coupled with a bright linear acoustic target beyond. Closer examination of the 'fissured terrain' reveals that many of the bright linear features seem to be lacking a coupled shadow on the nadir side. Either they are small-throw fault scarps, or they are fissures which have been infilled by talus (Ballard & Moore, 1977) so that there is no change in relief, but a line of strongly backscattering material on the seafloor. Individual features can seem continuous for as long as 6km, but it is usually difficult to trace them along strike for more than several

hundred metres, as they easily become obscured by the shadowing from other features. Fissures can be seen splaying and joining again, sometimes with fluctuations in horizontal separation along their length, although they rarely cross as most are aligned subparallel to the ridge trend.

3.3.1.1 Delineating the edge of the NVZ

The outer edge of the neovolcanic zone on the median valley floor can be delineated by tracing the contact between the 'fissured terrain' and the hummocky texture. This contact is often very sharp and clearly defined, but there are a few places where it seems more gradational and marked by a progressive increase in the number of fissures, or by fissures in the areas between volcanic constructions (e.g. figure 3.1viii). Sometimes the contact is highly sinuous where the fractures and fissures are clearly onlapped by younger neovolcanic terrain (figure 3.1ix).

The sinuous nature of the contact suggests that the edge of the NVZ is controlled by the availability of eruptable magma within the crust. A wide gradational zone between the neovolcanic and tectonic areas will develop when a fracture sometimes taps magma, but sometimes does not. Such a scenario will arise when the zone of magma is discontinuous in space and time and/or the size and geometry of the fractures is such that only some intersect the magma chamber. Where the limit of the NVZ is sharp and well defined, the stages of volcanism and tectonism probably have a longer time period of episodicity, with voluminous volcanic episodes separated by periods of considerable tectonic dismemberment. Variations in the nature of the volcanic/tectonic contact will be discussed further in chapters 5 and 6 and they will be used to discuss the degree of magmatic focusing and the relative extent of volcanic and tectonic episodes along-axis.

3.3.2 Faults within the median valley

Faults cut through the surrounding terrain with sharply defined sub-parallel edges and a strong degree of linear continuity. They are usually strongly backscattering because their steeply inclined surfaces present a high angle of incidence to the sonar beam and allow minimal accumulation of sediment cover. Within the NVZ, some faults act as a focus for volcanism and can be closely associated with hummocky linear ridges (see section 3.2.2.3).

3.3.2.1 Faults in the WASP traverses

Faults identified on the WASP traverses range in size from a couple of centimetres displacement to large composite zones, several hundred metres across. The smaller faults

have near vertical scarps, expose cleanly broken pillows and usually lack talus accumulations at the base. They are often related to fissures or are antithetic to larger faults. The largest single fault observed has a throw of about 100m, but the large composite fault at the E end of the 28W traverse has a total throw 250m. It has an overall dip of 35°, but is in fact made up of at least 7 smaller, steeper dipping faults and has an extensive talus ramp which causes the topography to shallow towards the base (figure 4.4 11.6 -12.1 hours).

The older steep scarps sometimes have accumulations of fine fault gauge which contrast with the pale ooze because of its darker colour. Welded breccia, where fine grained talus has become lithified in a matrix of pale ooze, is another feature of these maturer fault zones. Ballard and Moore (1977) suggest that welded breccias are commonly seen on fault scarps as faults often occur on reactivated fissures; the breccia being the lithified fissure infill.

3.3.2.2 Groundtruthing faults within the median valley

On the WASP traverses, all the faults which were large enough to appear on the high resolution profiles could be correlated with features on the sidescan images. In the 26W traverse, the 60m throw fault on the eastern flank (figure 4.3 16.85 hours) stands out clearly on both the ridge-parallel and oblique swaths (point G, figures 3.2 and 3.3), although it is in shadow on the former and forms a brightly insonified lineation on the latter. These groundtruthing observations are confirmed by the many faults observed in the 28W traverse (figure 3.6).

Only a small number of the structures recorded in the ANGUS phototraverse of Karson and Dick (1983) can be correlated with features in the sidescan images. The oblique fault seen in the upper right-hand corner of figure 3.5 is one of these, although it is quite a subtle feature owing to its strike, which is almost parallel to the incidence of the insonifying beam. The majority of structures noted by Karson and Dick (op. cit.) are probably below the resolution of TOBI. The minimum scarp height I have known TOBI to image is about 15m.

3.3.2.3 Ambiguity with hummocky ridges

Care must be taken when interpreting linear shadowing in the NVZ, as faults can be confused with hummocky ridges if the fault scarp itself is in shadow. Figure 3.1x shows an example where two faults cut through the hummocky terrain but their southern ends closely resemble linear constructional edifices. In this case, the northern ends of these features are unmistakably the lines of faults, as their sharp linear shadows cut through the

smooth-textured terrain and can be traced for a number of kilometres before they gradually peter out.

Another ambiguity arising when a fault scarp is in shadow, involves the merging of the fault shadow with the shadow from constructional features. If this occurs along strike it creates the impression that the fault extends further than it really does. An example of this is seen in figure 3.2 (ridge-parallel swath), where the fault labelled G appears to have its northern termination at H. In fact the oblique swath shows that the northern termination is actually at point J, where the fault is truncated by a small group of pillow mounds. It is the shadow from the pillow mounds which makes the fault seem longer.

3.3.2.4 Faulting as a measure of crustal age

Figure 3.9 shows data from the WASP traverses over the central sections of the median valley floor which indicate that there is a rough correlation between the amount of faulting and the age of the crust. The first histogram (figure 3.9a) is of cumulative fault throw for categories of crustal relative age as measured from sediment cover estimated in the photoanalysis. The cumulative throw is calculated by summing the throws of all the faults in a particular relative age range. The individual fault throws are measured from the high resolution profiles for the larger faults (>10m) and estimated from the photoanalysis for the smaller ones.

There is a positive correlation between the cumulative fault throw and the relative age of the crust up to relative age values of 2.5. Faults with throws exceeding 20m are only found in crust of relative age greater than 1.6. The drop off in cumulative throw above age values of 2.5 is due to lack of data. Sections of crust with relative ages greater than 2.5 account for less than 15% of the total distance traversed.

In figure 3.9b an attempt is made to compensate for the uneven age coverage, which biases the values of cumulative flow in favour of those age categories which are most common in the WASP traverses. This is done by calculating the distance traversed over each age category as a percentage of the total distance and dividing the cumulative fault throw by the respective percentile values to give the normalised cumulative throw plotted in figure 3.9b. The positive trend of figure 3.9a is replaced by a dramatic jump in the normalised cumulative throw for relative age values greater than 1.5. This suggests that when crust reaches a certain age it becomes susceptible to the development of relatively large throw faults. This period of rapid faulting may be related to the subsidence and volcano collapse recognised elsewhere on the ridge system (e.g. Ballard & Van Andel, 1977; Hall, 1979; Atwater, 1979) and/or the tectonic dismemberment of the crust at the

edgeof the NVZ. Volcano collapse will be discussed further in chapter 4, and chapter 6 will include a comparative study of the faulting in the two traverses.

The WASP traverses and submersible dives confirm that the age of the median valley floor roughly correlates with the number and size of faults. Variations in relative age which are easily identifiable from direct observation do not readily show up as changes in the amplitude of the sidescan backscatter over hummocky terrain, but they do roughly correlate with the degree of tectonism of the crust. Thus extent of faulting could perhaps be used as a more sensitive age marker on the hummocky terrain than backscatter amplitude. However, this hypothesis must be treated with a degree of caution as factors other than age (such as availability of magma) are likely to cause variations in the extent of tectonism seen along and between segments.

On the Reykjanes Ridge the reduction in backscatter does correlate with the degree of faulting (Parson et al., 1993). This is probably because the sedimentation rate is faster on the Reykjanes Ridge.

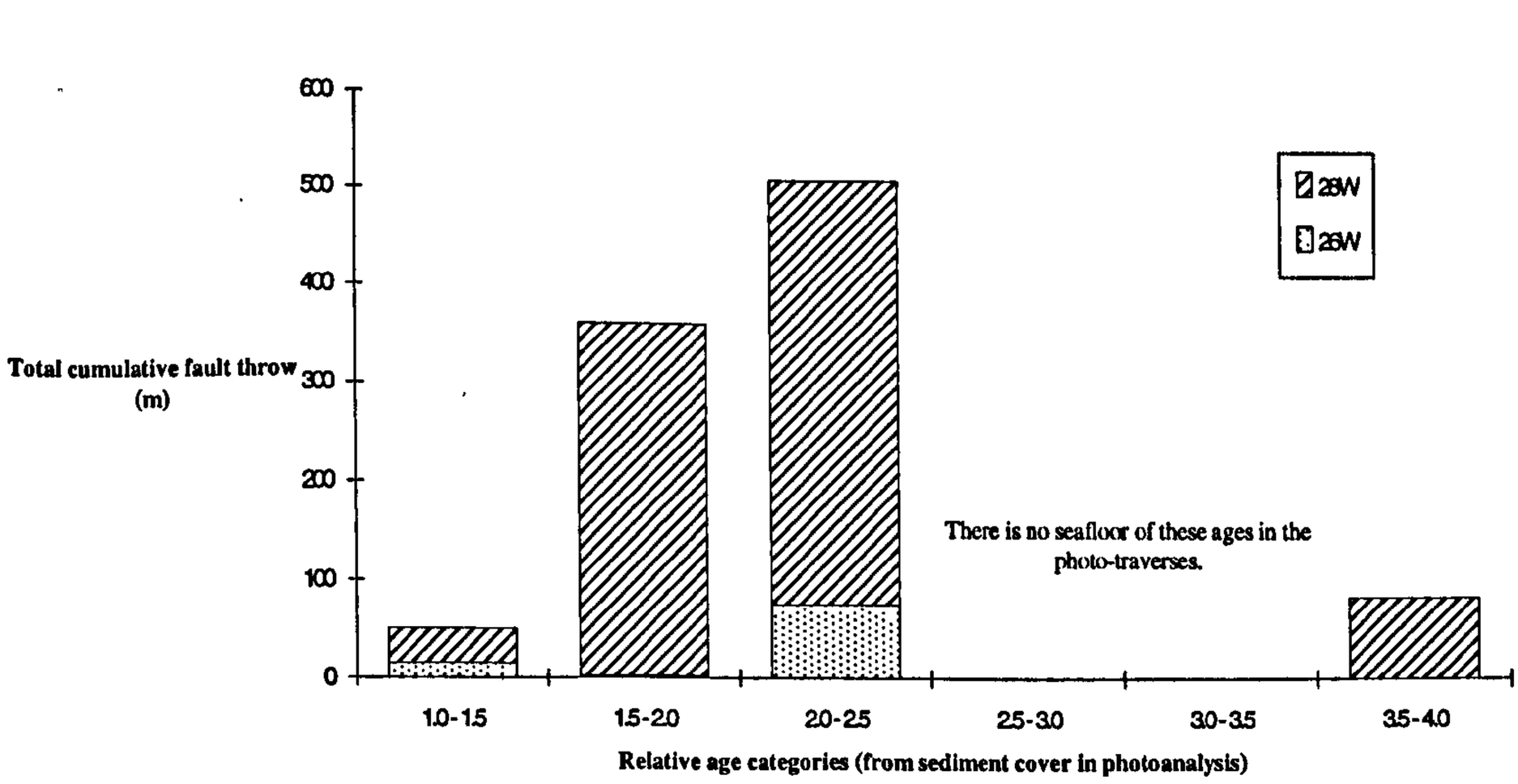

Figure 3.9a Histogram of cumulative fault throw for categories of crustal relative age, as measured from sediment cover. The cumulative throw is calculated by summing the throws of all the faults recorded for a particular relative age range. Data are taken from the photoanalysis and the high resolution profiles from the two WASP traverses.

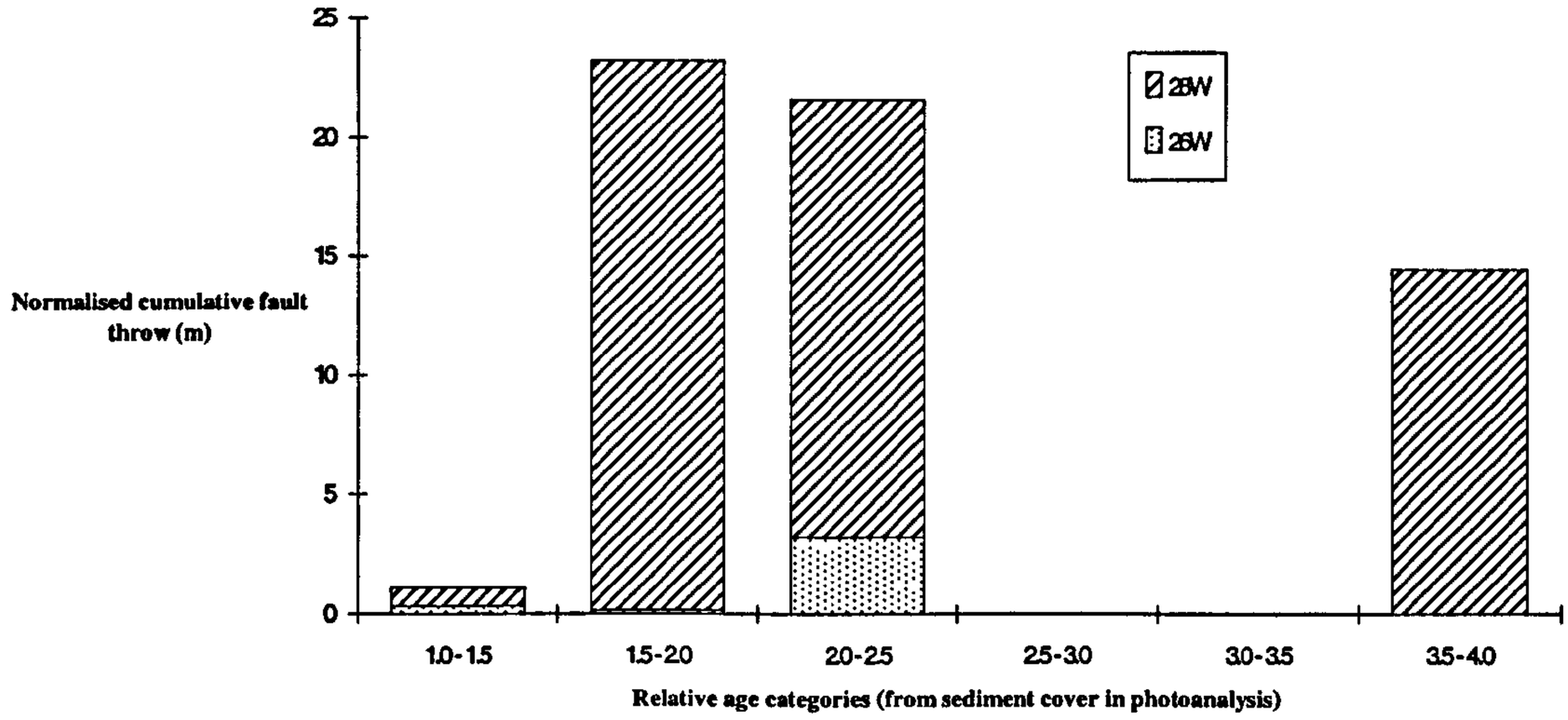

Figure 3.9b Histogram using the same data as figure 3.9a, except that the cumulative fault throw has been normalised in an attempt to compensate for the variations in extent of crust traversed in each age category. The distance traversed over each age category is calculated as a percentage of the total distance and the cumulative fault throw is divided by the respective percentile values[1].

3.3.3 The valley wall faults

The valley wall faults are unmistakable as broad bands of high backscatter running along the edges of the median valley. On medium resolution sidescan sonars, such as GLORIA (Laughton & Searle, 1979; Roest et al., 1984) and SeaBeam bathymetry, which has lateral resolution of 100-200m (Purdy et al., 1990), the inner walls of the median valley generally appear as single scarps. The TOBI sidescan reveals a detailed structure which has previously been observed on submersible dives (Macdonald & Luyendyk, 1977; Ballard & Van Andel, 1977) and on other high resolution sonars (Kong et al., 1988).

Only where the bathymetry is steepest do the valley wall faults seem to form a continuous bright scarp. As the gradient of the wall decreases the complexity and composite nature of the wall scarp is revealed. Small perched terraces of tectonised fabric are stranded on the median valley wall as the main scarps fork and splay (figure 3.1xi). Bridges connect steeper sections of the scarp which relay in a slightly en-echelon manner (figure 6.3 i). These sometimes result in horse blocks which have a crudely lensoid form and taper as the fault tips curve to link with adjacent scarps. The higher terraces of these horse blocks also tend to have a strong tectonic fabric (figure 3.1xii), while those at, or near, the base of the wall can be quite heavily sedimented (figure 4.13 i). A more detailed analysis of

---

[1] Total distance covered in both WASP traverses is 10km. Of this distance 46% is over crust of relative ages 1.0-1.5; 16% is 1.5 - 2.0; 24% is 2.0 - 2.5; 9% is 2.5 - 3.0; 0% is 3.0 - 3.5 and 5% is 3.5 - 4.0.

the faulting patterns recognised in TOBI and the development of the median valley wall faults is given in McAllister and Cann (in press).

3.3.3.1 Dredges from median valley and transform walls

The dredge with the largest recovery in the survey (over 200kg) was D22 at the base of the western valley wall fault in the NTO. Most of the haul consisted of irregular brecciated pillow, but massive lava, tectonic beccias and pelagic ooze were also present. This is consistent with recovery from talus and sediment ramps, such as those observed in the FAMOUS area (Ballard and Moore, 1977).

Dredge 27 from the southern transform wall contained similar material with the addition of greenschist facies cataclasites, reflecting the greater intensity of faulting in the transform. There is also evidence for hydrothermal activity with quartz-epidote-chlorite veins and a slight black manganese coating on the surfaces of the clasts.

3.3.4 Profiler over median valley wall faults

The 7.5kHz returns from the valley wall faults generally have higher amplitudes than those of the valley floor, though there is considerable variation within the data set. The large-throw eastern wall fault at the NTO is shown in figure 3.7 (d, e & f), and the corresponding sidescan swath is in figure 3.8.

The top half of this scarp produces a strong, homogenous, very prolonged reflection (truncated in figure 3.7), (figure 3.7d). There is a slight focusing in intensity towards the start of the return, which blends in with the type II return from the sedimented hummocky flanks. The high amplitude, diffuse speckle persists for a considerable time after the first return (for longer than the type II). There are also no hyperbolic diffractions, so in this respect the character of the signal is quite unlike that produced by the hummocky terrain or in the sedimented basin. The remainder of the discussing on the profiler coverage over the median valley wall (figure 3.7 e & f) is included in section 3.5.4 on sediment slumping.

3.3.4.1 Interpretation of the profiler records from the valley wall

The character of the return from the upper inner valley wall can be reasonably explained in terms of the relief and the nature of the surface. Compared to a horizontal plane, a conical beam over a slope will have a more prolonged surface reflection. For a conical beam angle of 25°, incident on a slope of 25° from an altitude of 600m, there is a maximum difference of 260m in the distance travelled for the ray paths of direct surface reflections (two way travel). This is compared to 100m for a 10° slope and 30m for a

horizontal surface for the same altitude. Hence, it is not surprising that the profiler record over the steep upper part of the wall fault is relatively prolonged.

However, this can not be the only factor contributing to the prolonged character, as the 25° - 30° inclination of the fault plane is no greater than the angles seen on the hummocky volcanic terrain. The structureless form is almost certainly due to considerable scattering by the debris and broken rock, and the lack of hyperbolae confirm that their origin on the hummocky terrain was from the general morphology of the flows rather than smaller scale edges of pillows and broken basalt. The high amplitudes are reminiscent of those from the type II return, and a similar focusing of the signal occurs over part of this upper section of the wall. This ties in with the moderate sediment cover indicated from the sidescan (figure 3.8 ii).

3.4 Ageing and Sedimentation of volcanic terrains.

The relationship between sedimented surfaces and low backscatter intensities has been demonstrated in many sidescan studies, particularly SeaMARC 1 (Kappel & Normark, 1987; Barone & Ryan, 1988; Embley et al., 1990). Not only do sedimented areas have lower backscatter amplitudes, but the textures are smoothed, owing to the ponding and draping of the hemipelagics.

The strong attenuation of the sidescan can be related to depth of sediment drape. There is an error of at least 50% in such estimates as the attenuation properties of deep sea sediments are not well known (Mitchell, 1993). To attenuate the backscatter return by more than 20dB the sediment would have a minimum 2m - 5m draped thickness (using a penetration angle of 30° and an attenuation coefficient at 30kHz of 1-3dBm^{-1}; Mitchell, pers. comm.). However, more than 2m - 5m of sediment is required to produce an entirely smooth sonar texture over pillow mounds, owing to the fact that sediment will pond into depressions in the irregular hummocky surfaces.

Sedimentation and mass wasting become increasingly dominant with distance from the axis, and there is a particularly strong contrast on the sidescan between the median valley floor and the fault terraces beyond the inner valley walls. The deepest sediment cover in the MARNOK survey occurs in the off axis basin shown in figure 3.10

313° 30' 313° 31' 313° 32' 313° 33' 313° 34' 313° 35' 313° 36' 313° 37'

24° 17' 24° 17'N

24° 16' 24° 16'N

24° 15' 24° 15'N

24° 14' 24° 14'N

313° 30'E 313° 31'E 313° 32'E 313° 33'E 313° 34'E 313° 35'E 313° 36'E 313° 37'E

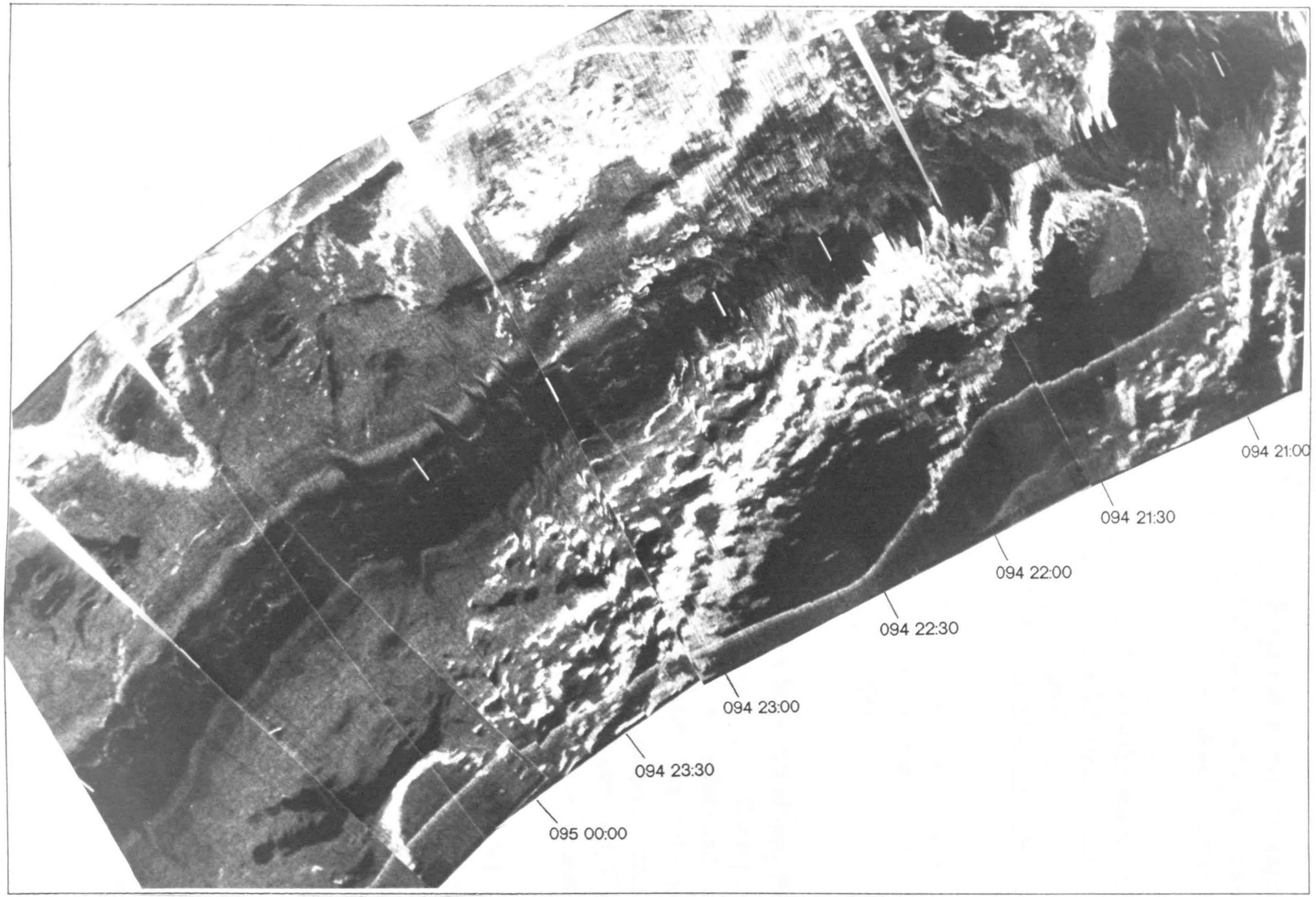

Figure 3.10 Oblique sidescan swath and bathymetry overlay of the walls and bottom of the off-axis basin. The sidescan can be related to the profiler trace of figure 3.12 by the time ticks. The transformation at point (a) in figure 3.12 to the type III return occurs in the basin bottom where the sidescan image has extemely low backscatter compared with the walls (point iv). Towards the southern edge of the swath the circular profile of a seamount demonstrates that constructional terrain is at least partly preserved in the depths of the basin (point ii). The bright linear feature protruding from the wall to the west (point vi) may be a fault block with an anomalous orientation. Note the difference in texture between the eastern wall, which seems more volcanic in character, and northern wall of the basin which is steeper with a texture similar to the reactivated southern wall of the transform.

313° 30' 313° 31' 313° 32' 313° 33' 313° 34' 313° 35' 313° 36' 313° 37'

24° 17' 24° 17'N

24° 16' 24° 16'N

24° 15' 24° 15'N

24° 14' 24° 14'N

313° 30'E 313° 31'E 313° 32'E 313° 33'E 313° 34'E 313° 35'E 313° 36'E 313° 37'E

Figure 3.10 Oblique sidescan swath and bathymetry overlay of the walls and bottom of the off-axis basin. The sidescan can be related to the profiler trace of figure 3.12 by the time ticks. The transformation at point (a) in figure 3.12 to the type III return occurs in the basin bottom where the sidescan image has extemely low backscatter compared with the walls (point iv). Towards the southern edge of the swath the circular profile of a seamount demonstrates that constructional terrain is at least partly preserved in the depths of the basin (point ii). The bright linear feature protruding from the wall to the west (point vi) may be a fault block with an anomalous orientation. Note the difference in texture between the eastern wall, which seems more volcanic in character, and northern wall of the basin which is steeper with a texture similar to the reactivated southern wall of the transform.

3.4.1 Low relief areas

The deep-tow photography showed that less than 1m thickness of sediment was required to cover horizontal pillow fields and sheet flows to form a planar surface of hemipelagics. This generated a smooth sidescan texture with moderate to low backscatter (figure 3.6, label T)

The results of the WASP groundtruthing are confirmed by the dredge recovery from D10—a smooth, low backscattering area on the edge of the NVZ (figure 3.1xiii). The pipe dredge returned from D10 full of pale brown ooze, though the morphology of the underlying basalt could not be determined from the few palagonitised fragments also recovered.

Many areas immediately adjacent to the nadir often have lower amplitudes and appear relatively smooth. Examination of cross-tracks shows that this is often an artefact of the beam pattern, rather than a reflection of the true surface morphology.

3.4.2 Hummocky terrain

As high relief, hummocky pillow flows become older and are transported off-axis, their hummocky nature becomes less pronounced (figure 3.1xiv and figure 3.11). This is partly a result of tectonic dismemberment and partly sediment cover. As the hummocks are progressively covered by hemipelagic sediments, the steep rounded edges of the flow remain brightly backscattering, but the size and number of the bright patches are reduced as the poorly backscattering, interstitial sediment ponds increase in thickness and lateral extent. The overall effect is both one of smoothing and average reduction in backscatter over the hummocky terrain.

Over a very thick pond of sediment, such as that seen in the bottom of the off-axis basin (figure 3.10), the sidescan texture is smooth and very low amplitude. The sound is not completely absorbed by the thick sediment as the smooth surface can still be distinguished from zero amplitude acoustic shadows (e.g. figure 3.10 i). The profiler traverse across the basin shows that there is still some topographic variation which would cause these acoustic shadows.

3.4.3 Flat-topped seamounts

The flat-topped seamounts in the MARNOK area show a wide range of relative ages as demonstrated by their textural characteristics. This is demonstrated by comparing the flat-topped seamount in figures 3.6 (which has a relatively young morphology) with the older seamount of figure 3.1v and the fractured seamount of figure 2.8b (which is probably one

6km swath width

24°20'N

Slide scar

Strongly backscattering area with incoherant striated texture downlapping (with lobate margins) onto median valley floor. This is interpreted as a landslide covering the fault terraces at the non-transform offset.

46°20'W

Further off-axis, sediment cover increases and hummocky volcanic texture becomes smoothed.

Well developed gullies and rock buttresses are highlighted by the oblique insonification direction.

Talus downlaps onto back of fault terrace with a sinuous margin.

Diffuse hummocky texture of volcanics on back of uplifted fault terrace.

Figure 3.11 The fault terraces on the western flank of segment 1, near the NTO.

of the oldest on the median valley floor). Figure 3.10 ii and iii shows two flat-topped seamounts on the ridge flanks, which are preserved almost intact on the edges of faults. These are about 1.5Ma older than the flat-tops on the median valley floor.

Relatively young seamounts have a strongly backscattering summit plateau with a faintly dappled texture (suggesting the summit lavas are unsedimented) and also have slightly irregular margins as would expected from fresh lavas or volcaniclastic flows. The steep-sided flanks either cast a crescent-shaped shadow or have a slightly sinuous base that tends to blend in with the surrounding hummocky terrain.

With increasing age the summit plateau becomes progressively more poorly backscattering as sediment accumulates. The edges of both the summit plateau and the base become smoother and more sharply defined as mass wasting degrades the steep constructional slope to produce a very uniform highly backscattering flank. The steep flanks of older seamounts contrast strongly with the summit plateau and downlap onto the adjacent seafloor. Older seamounts are sometimes dissected by faults. Much older seamounts outside the median valley are identified by the strongly backscattering, arcuate form of the steep flanks, which stand out against the darker circle of the sedimented summit (figure 3.10 ii, iii).

3.4.4 Instrument sensitivity

Although the reduction in backscatter amplitude by acoustic absorbance in sediment is a fundamental principle, the sensitivity of sidescan instruments (i.e. the thickness of sediment required to produce a noticeable reduction in backscatter) and the precise relationship between the age of crust and the amplitude of backscatter are not well established.

Embley et al. (1990) found boundaries in the backscatter images which did not seem to be related to distinct age contrasts in the photographic data. This implies that the sidescan data were more sensitive to the presence of a recently erupted flow than a direct visual assessment. However, in the high relief terrain of the MAR median valley, the angle of incidence of the sonar seems to be the primary control on the amplitude of the sidescan images. If variations in the angle of incidence can be discounted, amplitude variations with sediment cover may be more readily discernible. The following paragraphs look at examples of when the sidescan can detect variations in sediment thickness and when not.

3.4.4.1 Hummocky terrain—WASP traverse 26W

The WASP traverse across the NVR of segment 2 (26W) shows that the eastern flank (relative age ~ 2.7) is considerably more sedimented than the NVR crest and western flank (relative ages ~1.5), yet there was no apparent contrast in the amplitude of backscatter between these areas. (Contrast figure 3.2, points A and B on the west flank with point G on the east flank.) In fact, this is an example where the angle of incidence is the primary control on the amplitude of the sidescan. On the ridge-parallel swaths, the amplitude decreases towards the NVR crest as the grazing angle becomes shallower. On the oblique swath (figure 3.3), the vehicle was flown at a higher altitude, which reduces this effect at far range.

3.4.4.2 Hummocky terrain—WASP traverse 28W

The issue is complicated by the amplitude variations over the narrowgate WASP traverse (28W). Here the far eastern end of the traverse has a fine-scale, diffusely hummocky appearance (figure 3.6, point F), which has on average a lower backscatter than the pillow flows of the NVZ. However, the estimated relative age of this area is ~ 2.2, which is younger than the brightly backscattering, eastern flank in the 26W traverse. Although the two have a similar angle of slope, the former seems generally more degraded and covered in rubble, while the latter has a thicker sediment cover.

3.4.4.3 Hummocky terrain—submersible dive, transect 4

The submersible transect of Zonenshain et al. (1989) provided direct observations of an older section of NVR at the southern end of segment 2. Here the age of the NVR is symmetrical across-axis. This can also be seen in the sidescan images, which have smoother, poorly backscattering terrain on the flanks (figure 2.8b vi & vii). These low backscattering areas correlate with pillow flows having >1m of sediment cover. The lavas near the crest of the NVR are younger than the flanks, but still have up to 0.5m of sediment cover and no glass remaining. The backscattering amplitude and texture of this crest is very similar to that seen on the eastern flank of the 26W traverse. (Note the presence of several open fissures and step faults—figure 2.8b viii).

3.4.4.4 Low relief terrain—WASP traverse 28W

The instrument is more sensitive to variations in sediment cover over flat, low relief areas, where the incidence variations have little effect. This is demonstrated in 28W, where the western terrace (<1m of sediment cover) shows a considerable reduction in amplitude compared with the adjacent sheet flows (compare figure 2.6, point T with sf).

The reduction in amplitude is greater than that seen in the submersible transect described above, although there is greater sediment cover over the pillow flows of the latter.

3.4.4.5 Discriminating age variations

This evidence suggests that pillow mounds on the NVR are about 100,000 years old (>1m of sediment cover) before they show a clear change in texture compared with younger flows, but on flat lying terrain there is a marked effect on the backscatter at <40,000 years. However it may be possible to discriminate hummocky terrain >10,000 years old from younger flows by the smoothing effect of tectonic degradation which may reduce the backscatter amplitude in some cases. The presence of faults and fissures can be an indication that the crust is ~10,000 years when there is no discernible reduction in backscatter.

3.4.4.6 Non-linear response

There is some evidence that the backscatter amplitude does not decrease linearly with sediment cover, but there is a critical sediment thickness at which the backscatter is significantly reduced. This seems to happen when the cover over pillow flows exceeds approximately 1m, corresponding to the thickness required to almost completely cover the lava surface.

3.4.5 Profiler over moderately sedimented terrain

There is a strong contrast between the character of the profiler signal from inside the inner valley and that from the hummocky terrain beyond the valley wall scarp. The latter, labelled type II, is less prolonged and has a higher amplitude concentrated in the first part of the return (figure 3.7c). Despite the suggestion of considerable sediment cover from the sidescan images there is no sub-bottom structure visible in the profiler record. The diffraction hyperbola have similar sizes and shapes to the type I return but, in some places, the energy is concentrated resulting in a well defined curve. At the bathymetric lows, where the hyperbolae are not masked by the noisy first part of the echo, there is clear overlapping of the curves, but there are no bow-tie reflections joining the crests and troughs. The range of apex depths is relatively small compared to type I causing them to line up to form a continuous surface.

The type II return is not restricted to the ridge flanks, but is also occasionally seen within the inner valley itself. One of these exceptions occurs near the narrowgate, where the WASP photo-traverses showed low-lying terraces almost completely covered in sediment. Here, a rapid transition from type II to type I corresponds to the edge of the

highly sedimented fault terrace on the bathymetry. This dramatic transition on the profiler is not matched by an equivalent sudden reduction in amplitude of the sidescan image, but there is a gradational change.

It seems that the 7.5kHz profiler and the 30 kHz sidescan both show transitions in character which relate to increasing sediment cover, but these transitions do not correspond together precisely. This is perhaps because there are different thresholds in response due to the different frequencies and beam patterns of the instruments.

3.4.5.1 Interpretation of the type II returns

The WASP profiles suggest the type II return occurs when the pillow surface is almost completely covered in sediment. The difference in character between type I and type II must be related to uniformity and smoothness of planar sediment surfaces. The higher amplitude of the type II compared with the type I produces a paradox, as seafloor with greater sediment cover might be expected to absorb more sound. The higher type II amplitudes may be a result of the focusing effect of the thin sediment cover which will reduce the amount of energy scattered in directions which do not produce useful returns. In addition there will be less variation in the 1st Fresnel zone and so less destructive interference. The signal may also be more concentrated because of the reductions in topographic variability created by the smoothing effect of the sediment ponding in depressions. This will reduce the prolonged nature of the return and also result in less variation in the vertices of the hyperbolae. Although more focused, the similarity in size and shape of the hyperbolae to the type I echo character suggests that they have similar origins in diffractions and reflections from pillow fronts and hummocks.

3.4.6 Profiler over deeply sedimented terrain

The type III return (figure 3.12) is associated with the largest sediment thicknesses in the MARNOK survey. It is relatively weak but the energy is strongly focused into sharp well defined hyperbolae. Compared to the type I and II returns, the type III hyperbolae appear more numerous and the overlap between adjacent hyperbolae is more pronounced. This effect may be a result of the better defined nature of the curves as the fuzzy prolonged returns of the two former echo types may mask many of the diffraction hyperbolae.

As with the type I to II transition, the change in character of the return is very sudden (figure 3.12a). The apex heights of the hyperbolae vary considerably at any one point, with 15m delay not being uncommon (figure 3.12b, inset). This can give the impression that there are secondary sub-bottom returns from depth, but an equally likely cause is side reflections from the variable topography. The majority of hyperbolae seem to be unrelated

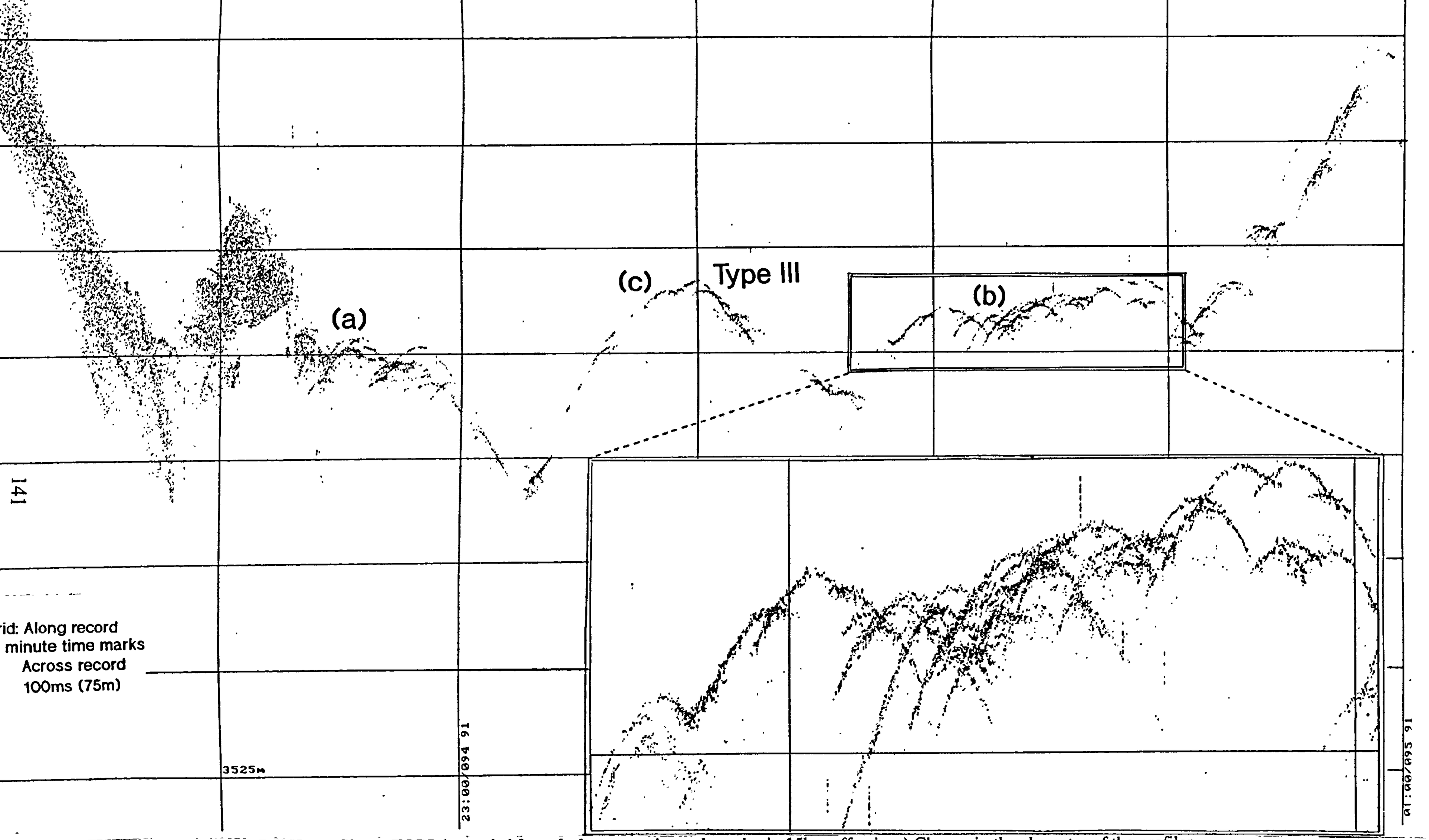

Figure 3.12 Record from the 7.5kHz profiler as TOBI descended from fault terraces into a large basin 15km off-axis. a) Change in the character of the profiler return at the basin floor. This corresponds to a transition in the sidescan to consistently very low amplitudes. b) Considerable overlapping of type III, well defined hyperbolae. There is 15m variation in apex height at one point which may be the result of side echoes. c) The shape of this topography differs from that of the axial hummocky terrain, with shallower angles and more triangular peaks. This may be due to the small scale faulting, degradation and sedimentation of remnant constructional terrain or alternatively the triangular high may be a small rotated fault block.

in a fairly random fashion. Some overlapping hyperbolae seem very symmetrical or have tangential curves reminiscent of bow-tie structures, but no clear cut examples of these were found.

The point (a) on figure 3.12, where the profiler signal changes in character, corresponds to a transition in texture in the sidescan (figure 3.10 iv) which occurs as TOBI reaches the bottom of an off-axis basin about 20km from the axis (at 094 22:45). The walls contrast quite sharply with the floor of the basin where the sidescan return becomes almost completely attenuated.

3.4.6.1 Interpretation of the type III returns

The lower amplitudes of the type III returns compared with the type II is consistent with energy absorption during the passage of the sound through the hemipelagics.

Hyperbolic returns from thick sequences of undeformed relatively flat-lying sediments beneath the seafloor are common and are usually attributed to erosional/depositional bedforms, often current induced (Damuth, 1980). In this case the hummocky nature of the underlying topography should also be taken into consideration. As there remains considerable variation in the height of the vertices of the hyperbolae, it is plausible that there is still sufficient topographic roughness to generate reflections and diffractions. This suggests that although there may have been ponding of sediment into the basin from the surrounding slopes, there is also a degree of draping which maintains some irregularities in the surface. Alternatively the irregular surface may be a result of mass wasting processes such as landslides or sediment slumps.

The type III hyperbolae are distinctive enough to be quantified. The number per unit length is found to be comparable with the frequency of bright patches which make up the dappled texture of the basin's lower eastern wall (figure 3.10 v). These bright patches are outcrops which are standing proud from the surrounding sediment ponds. Features such as these, covered in a thicker drape of sediment may be responsible for the hyperbolae of the type III return.

The absence of sub-bottom reflections from the deeply sedimented basin is a matter worthy of some discussion. It is possible that the sediment cover in the basin is thicker than maximum penetration depth (<20m, for 7.5kHz at near normal incidence—N. Mitchell *pers. comm.*). However, this would require a very dramatic increase in sediment thickness in order to explain the sudden changes in the character of the signal. This is unlikely, even in an off-axis basin.

Instead the answer may lie in the consequences of surface scattering. Previous echo character studies have noted that scattering at the surface severely reduces acoustic penetration, usually to near zero (Damuth, 1980). It seems probable that no coherent sub-bottom reflections are observed in this study for similar reasons. Consequently, the type III hyperbola may be diffractions and/or reflections from the sediment surface including a very thin layer of the subsurface, and do not originate from the full thickness of the deep sediment pond. The type II returns will also have experienced this small degree of penetration, but some sound may still reflect from the irregular basalt which has only a thin sediment coating.

3.5 Mass wasting and debris deposits.

3.5.1 Talus

Talus forms uniform and smooth, highly backscattering areas at the base of fault scarps or other steeply dipping surfaces, such as pillow fronts. Small patches of talus amongst hummocky terrain can look identical to sheet flows in the sidescan images (e.g. figure 3.2, point K). Bathymetry is the best means of discriminating the two. Talus associated with fault scarps is much easier to identify. In contrast to the brightly backscattering, sometimes striated appearance of the fault scarp, the talus forms a slightly duller, smooth-textured band at the base of the fault. Sometimes the talus forms an obvious fan which has prograded out to form a convex-curved or scalloped front (figure 4.13 ii).

3.5.2 Erosional gullies

Mass wasting of the exposed upper areas of the scarp produce erosional gullies which form shadowed depressions in-between the brighter streaks and knobbles of rock buttresses. This gives the top of the fault scarp a crenulated appearance with the gullies occurring approximately every 100m-200m along strike (figure 3.11). The talus fans often seem to emerge from the base of the gullies suggesting the degraded material has focused down them. McAllister et al. (1993) have studied the progressive change in fault morphology off axis and concluded that tectonic activity, either on or close to a fault, is the dominant degrading mechanism forming these erosional gullies.

3.5.3 Debris slides

Karson and Dick (1983) have observed loose rock fragments forming curvilinear trails, hundreds of metres long, down steeply-dipping walls (figure 5.10vi). They interpret these as debris slides. The debris slides correlate with streaks of high backscatter which trend downslope on the smooth-textured talus.

3.5.4 Sediment slumping

The criteria for recognising slumps (and landslides) includes the identification of paired deposits and slide scars. A combination of the bathymetry and the 7.5kHz profiler was a great aid to the sidescan in the identification of one particular sediment slump on the eastern wall at the NTO. The following section will describe the feature and discuss the lines of evidence that led to this conclusion.

3.5.4.1 The slump deposit

The slump produces a convex bulge in the slope of the valley wall, which extends for about 2km along strike (outlined in red on the overlays of figures 3.8 and 3.13) The shape of this bulge is similar to that of the landslide deposit reported by Tucholke (1992), but it is much smaller.

The sidescan from this area includes the oblique swath (figure 3.8) collected simultaneously with the profiler data of figure 3.7 and a ridge-parallel swath (figure 3.13) which extends about half way up the valley wall to the top of the bathymetric bulge. The additional data provided by the ridge-parallel swath are especially useful for interpreting the nature of the nadir region which is sampled by the profiler during the oblique pass.

The top of the convex bulge causes a break in slope on the wall scarp from 25° to 10°. At this break in slope there is a sudden decrease in the amplitude of the backscatter accompanying the decrease in gradient (figures 3.8 iii and 3.13 iii). The more gently dipping top of the convex bulge has very low backscatter amplitude, (figure 3.13 iv), which is crossed by a number of very thin, wispy, bright lineations on the oblique swath (figure 3.8 iv). This implies there is thick sediment cover over the top of the bulge, but the origin of the wispy lineations is ambiguous. They are not parallel to the local trend of the slope, but are approximately parallel to the overall direction of motion of the slide. Hence, they are likely to be depositional features (e.g. lines of pebble chutes) formed during the mass flow, rather than erosional features formed subsequently.

In contrast the steep front of the bulge is quite strongly backscattering. On the ridge parallel swath it has a disrupted, finely lineated texture (figure 3.13 v) while on the oblique swath it has a fuzzy diffuse character (figure 3.8 v). Both these textures contrast with the sharply defined fault scarps along strike to the south (figures 3.8 vi and 3.13 vi), and emphasise the disrupted nature of the material. The slump deposit has buried the two small fault scarps which can be seen emerging from the south of the bulge. The presence of these scarps underlying a thin coating of debris may be partially responsible for the steeping front of the deposit and its higher amplitude.

313° 47'
313° 48'
313° 49'
313° 50'
313° 51'
24° 27'
24° 26'
24° 25'
24° 24'
24° 23'
24° 22'
24° 21'
24° 27'N
24° 26'N
24° 25'N
24° 24'N
24° 23'N
24° 22'N
24° 21'N
313° 47'E
313° 48'E
313° 49'E
313° 50'E
313° 51'E
-4500
-4600
-4700
-4200
-4300
-4400
-4100
-4000
-3900
-3800
-3700
-3600
-3500
-3400
-3300
VIII
iii
iv
v
vi
vii
nadir of oblique swath

Figure 3.13 Ridge-parallel sidescan swath and bathymetry overlay over the lower half of the eastern median valley wall and adjacent inner floor at the southern end of segment 2. The convex bulge in the wall, which may be the deposit from a sediment slump, is outlined in red on the bathymetry overlay. The nature of the image beneath the nadir region of the oblique swath (marked on the overlay) can be examined using this swath. The strongly backscattering, diffusely hummocky area of wall to the north of the area outlined may be a larger landslide.

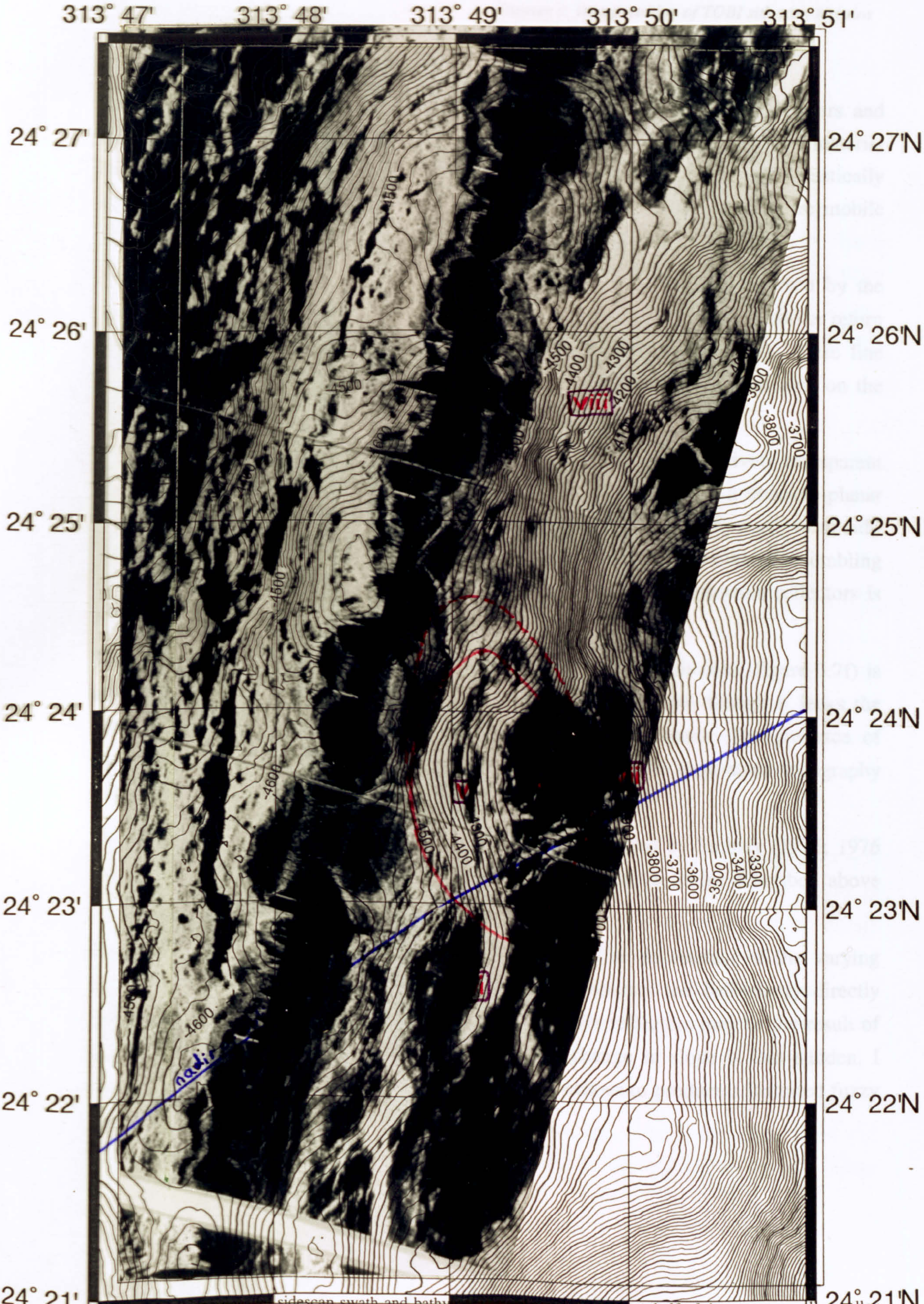

Figure 3.13 Ridge parallel sidescan swath and bathymetry overlay over the lower half of the eastern median valley wall and adjacent inner floor at the southern end of segment 2. The convex bulge in the wall, which may be the deposit from a sediment slump, is outlined in red on the bathymetry overlay. The nature of the image beneath the nadir region of the oblique swath (marked on the overlay) can be examined using this swath. The strongly backscattering, diffusely hummocky area of wall to the north of the area outlined may be a larger landslide.

3.5.4.2 Profiler over the slump deposit

Embley (1975; 1976 and 1980) has described criteria for recognising slide scars and debris deposits from high frequency echograms. The appearance of the displaced material depends on the degree of lithification during the mass movement. Diffuse, acoustically transparent lenses which lack internal reflectors are a common feature of more mobile unlithified flows, especially soft sediment slumps.

The convex bulge in the valley wall which is described above was traversed by the profiler across its southern extent. At the break in slope (about 4100m) the profiler return focuses into distinct line reflectors for about 100m of relief (figure 3.7f). These line reflectors correspond to the topographic bulge and the heavily sedimented area on the sidescan, described above.

The upper and lower line reflectors together form a lens-shaped, relatively transparent wedge. The lower reflector curves down from the break in slope in a concavo-planar manner at an average of 5°. while the upper surface curves, convex-upward, from sub-horizontal to 15°. Its upper truncation is against the break in slope in a manner resembling an onlapping contact. The maximum distance between the top and bottom reflectors is about 20m.

The strong attenuation and focused return of the profiler from this area (figure 3.7f) is also similar to the type III return indicating thick sediment cover, though it lacks the multiple superimposed hyperbolae observed in the off axis basin. The presence of continuous reflectors, rather than hyperbolae, indicates that the large-scale topography (>10 - 15m) is smooth compared with the off axis basin.

The similarity of this transparent lens to the deposits described by Embley (1975; 1976 and 1980), in addition to the sidescan textures and bathymetric bulge described above provides a strong case for a sediment slump.

However, it is also possible that the wedge is formed as an artefact of the varying topography along strike. The convex upper reflector mirrors the bathymetry directly below and to the north of the instrument, while the lower reflectors may be the result of side echoes from the scarp to the south where the change in slope is less sudden. I discount this hypothesis because I would expect side echoes to produce a distorted fuzzy return, rather then the discrete reflectors observed.

3.5.4.3 The slide scar

The second criterion used to identify slumps is the presence of a slide scar, though in this case the required feature is somewhat elusive. The best candidate for a slide scar occurs about one third of the way down the valley wall, immediately above the deposit. There is an increase in amplitude of the backscatter which must be the result of a steepening of the slope and/or a decrease in the sediment cover (see blue line traced on overlay of figure 3.8). This forms an oblique scarp to the north of the nadir between 3600m and 4000m (figure 3.8 vii) which is probably the slide scar. On the ridge-parallel swath this slide scar is moderately backscattering and seems to form the edge of a block with a finely lineated ridge-parallel texture (figure 3.13 vii).

3.5.4.4 Profiler over the slide scar

Slide scars usually produce strong images on the echograms, but not in this case. The slope immediately above the deposit, which probably corresponds to the slide scar (figure 3.7e) has a low amplitude diffuse character, showing similarities to the type I return, but with hyperbolae absent. This agrees with the reduction in sediment cover noted on the sidescan, and the steepening slope in the bathymetry. (Compare figure 3.7e with figure 3.7d, from higher up the wall, which is similar to type II.)

The scar may not be very obvious, as the volumes of material forming the slump are relatively small. In addition the examples described by Embley are all from very heavily sedimented continental margins, whereas the prolonged nature of returns from a basalt scarp may reduce the potential for producing a clear image of a slide scar.

3.5.5 Landslides

Landslides are common features on the median valley walls (figure 3.11; figure 3.13 viii) and in the transform, particularly on the median ridge. They create an irregular texture of moderately backscattering, diffuse, low amplitude domes and downlap with an abrupt lobate contact onto the terrain below. The landslips deposit in figure 3.11 has a striated internal structure which, although quite disrupted, is not entirely dissimilar to that of the wall fault itself. The associated scar is in shadow striking obliquely to the trend of the fault terraces.

The texture of the landslide deposit depends on both the material from which it is formed and the degree of consolidation of the debris. Fine grained, unconsolidated material will form a relatively smooth texture which may have a gently undulating surface. Large

consolidated blocks give the deposit an irregular texture with areas of well defined, internal structure.

Cruise CD65 produced TOBI images of nine landslides (Cann et al., 1992b), the largest of which was the major landslide described by Tucholke (1992). Sampling from these landslide sites has recovered a range of material. Some consists of basalt blocks and mud, while others yielded serpentinite and gabbro as well as basalt and metabasalt. It has been suggested that the latter were flows from serpentinite diapirs which have risen along the median valley bounding faults (Cann et al., 1992a).

3.5.6 Slump folds

I predict that the elongated undulations in heavily sedimented basins (e.g. figure 5.11 ii) are sediment slump folds, though there is no groundtruthing information available to confirm this.

3.6 Ageing of fault scarps.

3.6.1 Textural evolution of fault scarps

Allerton et al. (1995) have compiled a fault scarp evolutionary model based on the changing character of the valley wall fault with distance off-axis and the similar changes which occur in subaerial settings. With increasing tectonic activity, the talus ramp at the base of the fault becomes more extensive and mass wasting of the scarp becomes more pronounced with the formation of erosional gullies, stone shoots and debris flows. This is accompanied by a change in shape of the base of the fault which is sharp and linear in the immature stage, but develops a more cuspate and sinuous toe as the debris fans increase in size. The measured angle of dip also reduces with age as the original scarp becomes eroded and the talus ramp becomes more extensive. When a fault becomes inactive, fresh talus no longer accumulates so the backscatter becomes progressively weaker as a sediment drape forms. When this sediment becomes thick enough then sediment slumps can occur.

3.6.2 Reactivated faults

Reactivated faults have brightly backscattering fresh talus deposits on top of the old sediment covered ones. The extent of these fresh deposits depends on the intensity of the fault reactivation, and accompanying mass wasting. The debris ramps often have a speckled appearance which is just resolved on areas where the intensity of the backscatter is lower (e.g. figure 2.7b 23°50'N 313°39.5'E). The ANGUS traverse across these speckled areas showed reactivated debris slides which contain blocks of consolidated

talus from older deposits (Karson & Dick, 1983). The specks result from individual larger blocks within the debris, which are more likely to occur if deeper crustal levels are exposed or consolidated older deposits are broken up.

Small landslips are also common on reactivated faults. Angular shadows up to 500m long which are elongated oblique or subparallel to the strike of the fault are probably created by large consolidated masses of material which have detached but remained coherent as they slid a short distance down the slope (e.g. figure 2.7b 23°50'N 313°38.5'E). A more uniform distribution of lumps and shadows may reflect the blocky surface of a semiconsolidated landslip (e.g. figure 2.7b 23°50.5'N 313°37.3'E).

3.7 Hydrothermal features.

3.7.1 Hydrothermal supermounds

Very steep-sided mounds were identified in the transform domain of segment 1 (figure 3.14). Murton and German (1992) hypothesise that steep-sided bell-shaped mounds imaged by TOBI on the Reykjanes ridge are hydrothermal in origin. The Reykjanes supermounds are up to 190m high, with basal widths of between 90m and 160m giving maximum slope angles ranging from 54° to 71° (+/-6°). They are distinguished from purely volcanic mounds by the steep flank angles, and are higher than the hydrothermal mounds previously reported at Snake-pit (50m) and TAG (100m) (Karson & Brown, 1988; Thompson et al., 1988).

The supermounds in the MARNOK area form a short ridge about 1.5km west of the valley wall and 1km NE of a flat-topped seamount. They cast three adjacent spire-like shadows which are highly elongated despite their close proximity to the nadir (figure 3.14). Using simple trigonometry the features which create the shadows can be shown to have heights of 220m, 195m and 160m (+/-20m) above the seafloor. The sharp ridge on which they sit is about 1km long and has a slopes along its axis by ~10°. The basal diameters of the steep cones are 250m, 150m and 100m respectively and allowing for the varying height of the basal ridge this gives flank angles of 50°, 60° and 58° (+/-8°) respectively.

These are comparable sizes and slopes to the supermounds reported by Murton and German (1992) but the shadows are slightly more pointed than the rounded, bell-shaped summits of the Reykjanes supermounds. The steep angles of the mounds favour a hydrothermal origin, but evidence for extensive hydrothermal activity which should be

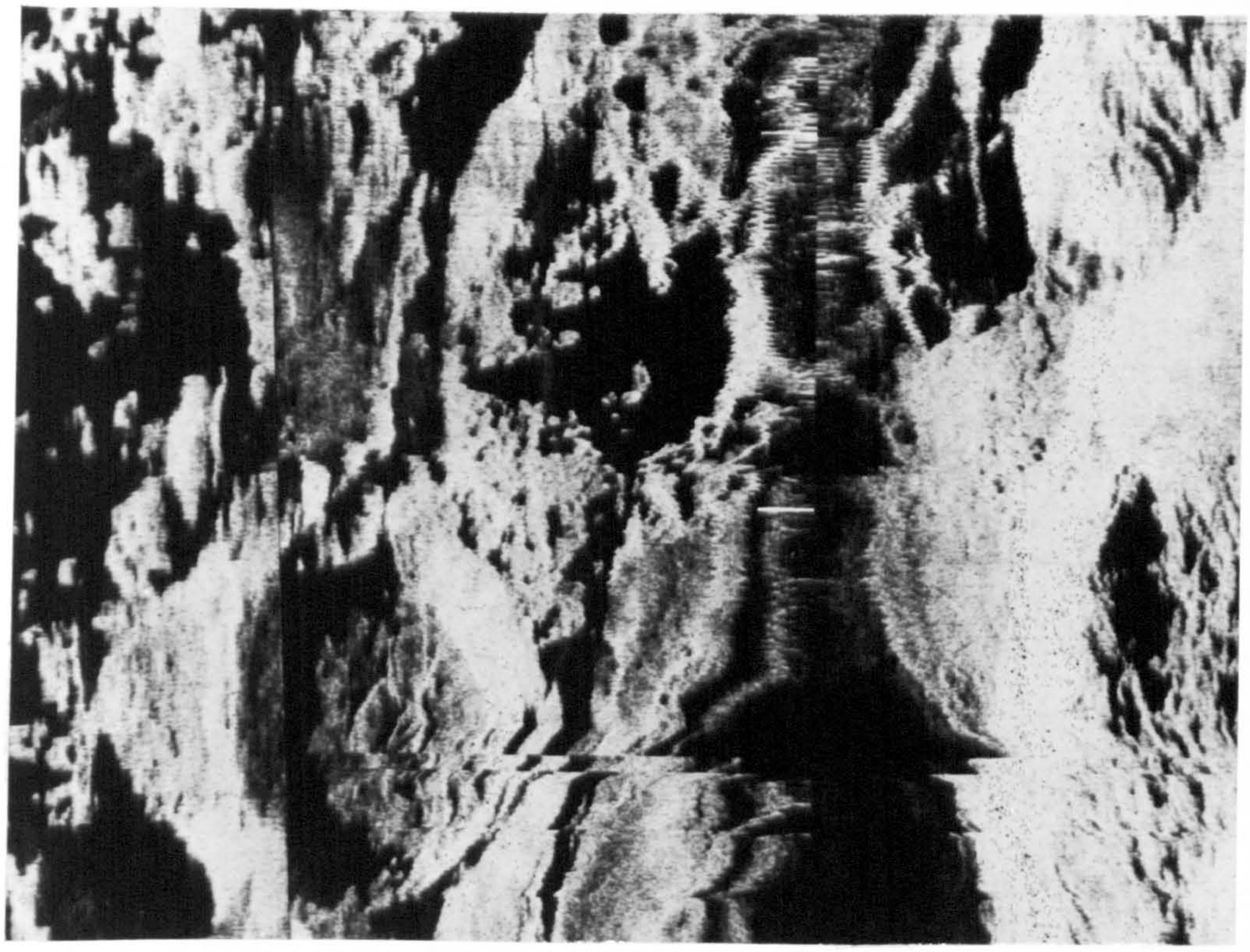

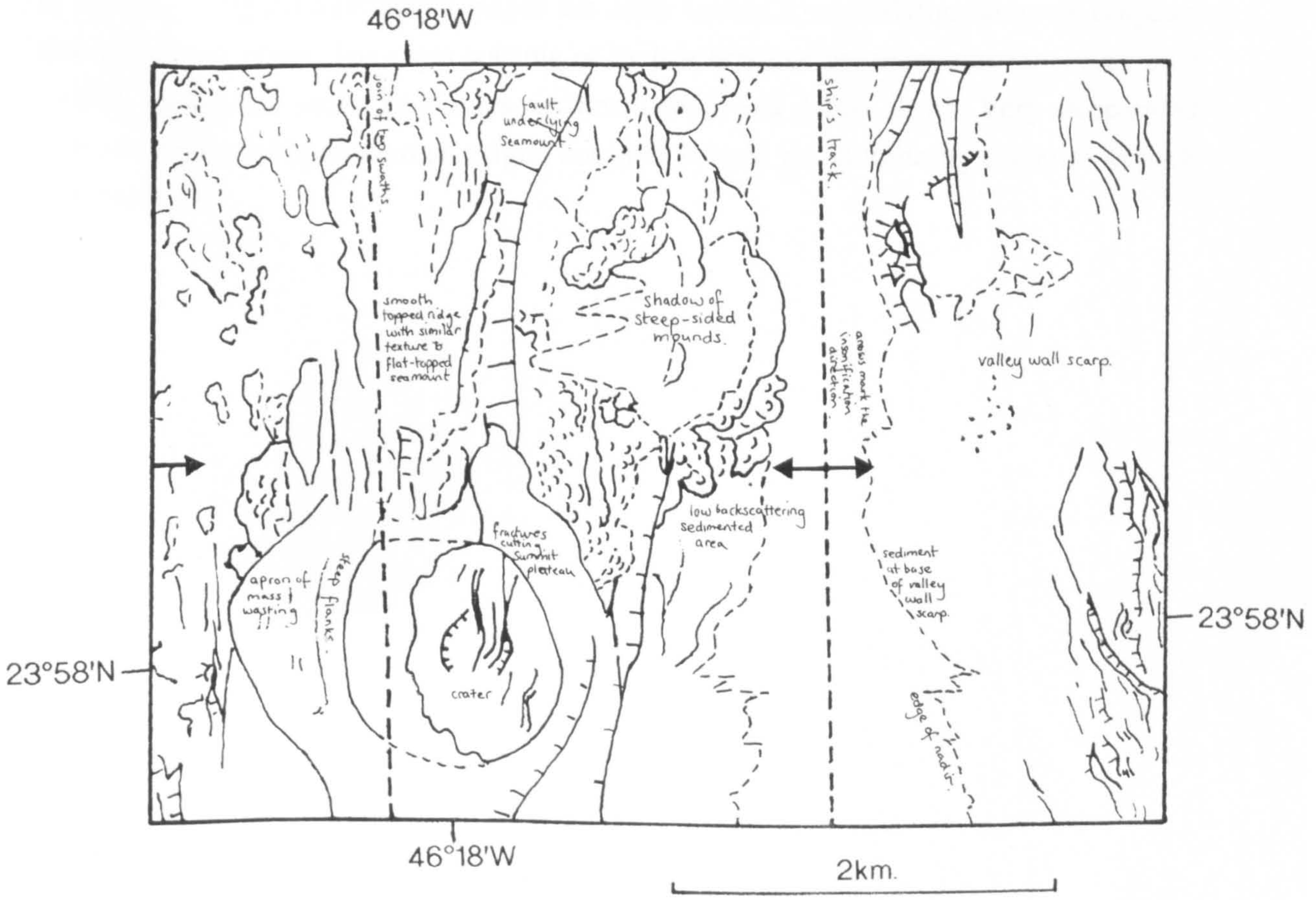

Figure 3.14 Steep-sided mounds to NE of flat-topped seamount cast long, pointed shadows, even when they are only 750m from the nadir. With slopes of about 60° and heights ranging from 160m to 220m they may be hydrothermal in origin. The flat-topped seamount is overlying a fault in the valley floor. It has a central crater which is disrupted by other fractures which cut the summit plateau. To the north of the seamount is a ridge which has a smooth, low backscattering texture similar to the seamount. This smoother ridge seems to be related to a more hummocky area to the north. The white ticks along the nadir are at half hour intervals and the insonification direction is shown by the arrows.

associated with such large edifices is sparse, as nearby dredge recoveries show no sign of hydrothermal precipitation. Hence, the origin of these features remains enigmatic.

Further evidence for hydrothermal activity in the MARNOK area is discussed in chapter 6.

3.8 Summary of Chapter 3

In this chapter I have established a basis for the geological interpretation of TOBI sidescan sonar, which will be utillised in subsequent chapters. I have identified a wide range of textural terrains of volcanic and tectonic origin which are later modified by sedimentation and mass-wasting. Deep-tow camera traverses, submersible dives, dredge localities and the 7.5kHz profiler provide the data with which the groundtruthing is achieved. Volcanic terrains include hummocky ridges and mounds (comprising pillow flows), flat-topped seamounts, cratered cones, areas of tumescence, smooth-textured sheet flows and low-relief pillow fields. Tectonic terrains include fissures and different scales of faulting. Aligned hummocky ridges are often related to underlying faults or eruption through a fault plane. The mass wasting of fault scarps can produce talus fans, erosional gullies, landslides, sediment slumps, sediment folds and debris flows. Very steep-sided mounds may be of hydrothermal origin, but there is little groundtruthing evidence to back this claim.

BLANK IN ORIGINAL

Chapter 4

Volcanology

Untamed, undomesticated, unregulated wilderness: Nature paints its scenes without regard for conventional order for straight lines or Euclidean shapes. Luckily so - the human mind seems to take as little pleasure in a straight line as in pure formlessness. The essence of the earth's beauty lies in disorder; a peculiarly patterned disorder.....

James Gleick from 'Nature's Chaos'.

4.1 Introduction.

Chapter 4 focuses on the volcanology of the area, starting with a comparison of the WASP traverses across the centres of the two segments. In section 4.2, the NVR life-cycles deduced from the traverses are related to the thermal and mechanical structure of the lithosphere, and the causes of variations in flow rate are assessed. This is followed by an analysis of some notable aspects of the surveys, namely the relationship of pillow flow front breccia to syn-magmatic tectonism (section 4.3) and the first comprehensive description of sheet flow morphologies from a slow spreading plate boundary (section 4.4). The mechanisms acting to produce sheet flow transformations in the deep-sea environment are discussed and compared with the findings of laboratory simulations (Gregg & Fink, 1995). In section 4.5 the focus switches to an analysis of the some of the more unusual volcanic morphologies on the sidescan data, including a hummocky steep-sided seamount chain named 'Thatcher's Nose' and some unique flat-topped seamount morphologies that have proved particularly useful in subsequent interpretations. Section 4.6 uses seamount statistical data to provide additional information to aid the interpretation of the different sidescan volcanic morphologies. The origins of hummocky ridges and flat-topped seamounts are discussed in the final two sections.

4.2 The life cycle of a NVR: evidence from the WASP traverses.

The WASP traverses were designed to compare the tectonic and volcanic condition of the centres of the two segments. The northern traverse (26W) over segment 2 crosses a well developed robust NVR, while in contrast, there is virtually no NVR development in the narrowgate of segment 1 (28W). The volcanic and tectonic style of the median valley floor, as revealed in the photoanalysis, also showed differences

between the two segments in the extent and morphology of lava flows, and the importance and style of tectonism. The construction and destruction of the NVR in these two contrasting settings can be documented using a combination of the volcanic and tectonic observations with detailed relative age estimates.

4.2.1 Location of the northern traverse

Figure 4.1a shows the location of station 26W which ran for about 5km across the entire NVR of segment 2 from 24°35.1'N 46°11.1'W to 24°34.6'N 46°08.4'W. The high resolution bathymetric profile is also shown in figure 4.1b. The traverse began in the western marginal basin (between the inner wall scarp and the NVR), rose up the western flank of the NVR and crossed almost perpendicular to strike, before finally descending down the eastern flank. The NVR consists of two peaks which rise over 500m above its flanking marginal basins. The higher western peak is separated by a central depression from the slightly lower eastern ridge.

The first frames were taken at 12:50 and the flash finally failed just after 18:00. During this time five hundred and fifty frames were exposed, though there was very limited operation of the flash system after the vehicle crashed into a small cliff at 16:50. The overlaps between adjacent frames revealed a westward drift in the path of the camera for the first 10 minutes, after which it looped round to traverse the same terrain in a progressively more easterly direction.

4.2.2 Location of the southern traverse

Station 28W traverses the inner valley of segment 1 about 1.5 km north of the bathymetric saddle of the narrowgate from 24°07.3'N 46°18.6'W to 24°06.3'N 46° 16.4'W (figure 4.2a). The high resolution profile (figure 4.2b) reveals considerably more detail of the volcanic and tectonic structure of this traverse than is apparent from the SeaBeam bathymetry (compare figure A2.3). Eight hundred frames were exposed during the 5km deployment.

At the western edge of the profile a horizontal terrace has been uplifted by inward dipping normal faults. A number of smaller terraces, also controlled by inward dipping faults, were traversed in the descent down to the NVZ. In contrast to segment 2, the NVZ of the narrowgate is in the bathymetric low of the valley cross-sectional profile. It is poorly developed in terms of axial topography, especially when it is compared with the robust NVR of the northern traverse. In the west of the NVZ, a very paltry NVR rises only 70m above the lowest point on the valley profile, while the constructional terrain to the east rises steadily at an angle of 10°-15° to achieve a height of 150m above the valley floor. However, some of this relief is probably gained through footwall uplift on the eastward dipping normal fault which truncates the NVZ

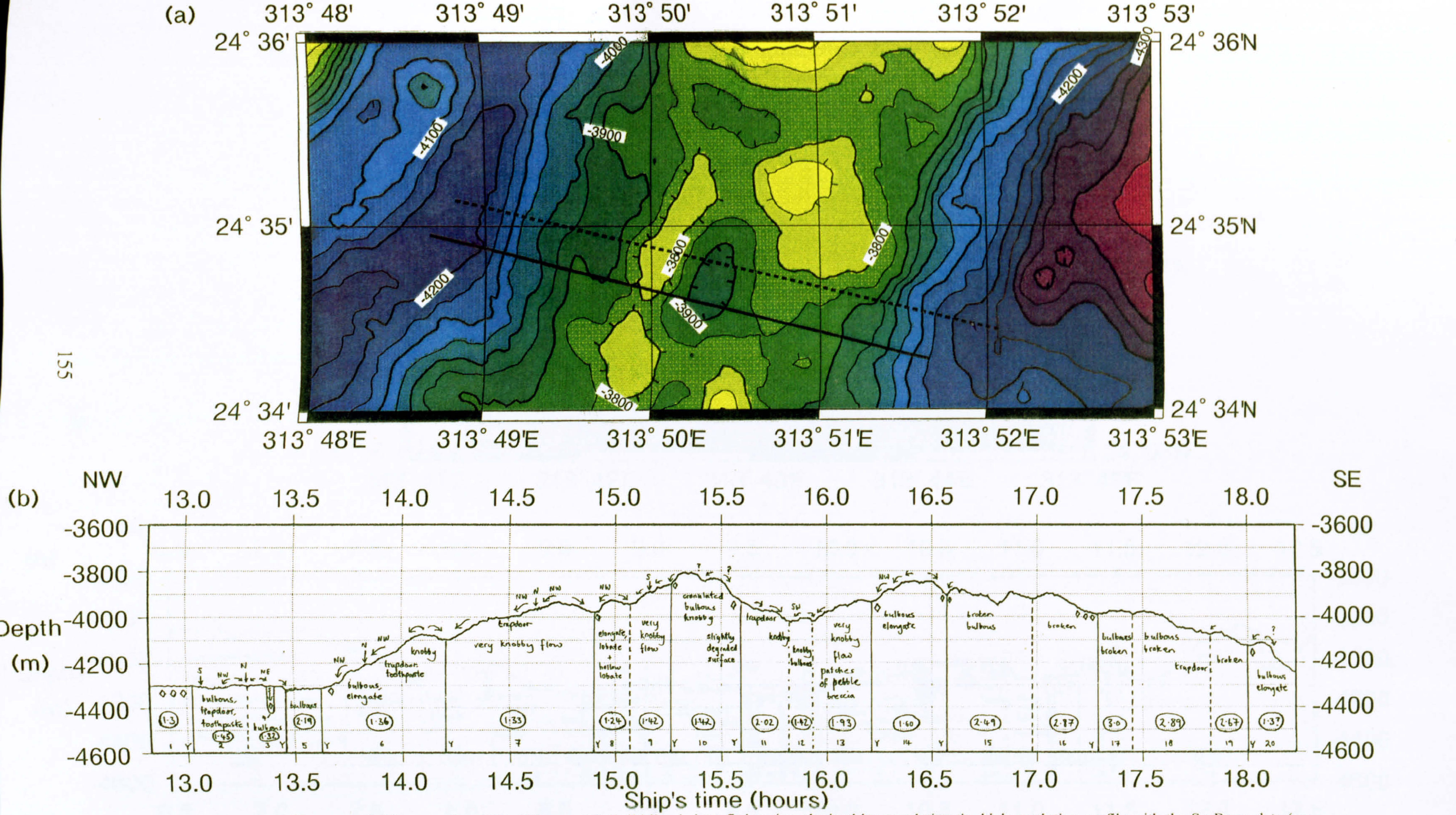

Figure 4.1 (a) Location of WASP traverse 26W across the NVR of Segment 2. Solid line is best fit location obtained by correlating the high resolution profile with the SeaBeam data (see Appendix 2.5; fig A2.2). The ship's track is shown as the dotted line. (b) High resolution profile obtained from WASP altimeter and instrument depth (scaled so there is approximately no horizontal or vertical exaggeration) showing interpretation of volcanic features based on the photoanalysis. Profiles are divided into numbered flow units with dominant lava morphologies labelled (diamonds indicate flow front and/or fault breccia). Flow directions are shown by arrows and the younger flows in contact relationships demarked by a 'Y'. Circled numbers are average relative age estimates for each flow based on sediment cover (see figure 2.1).

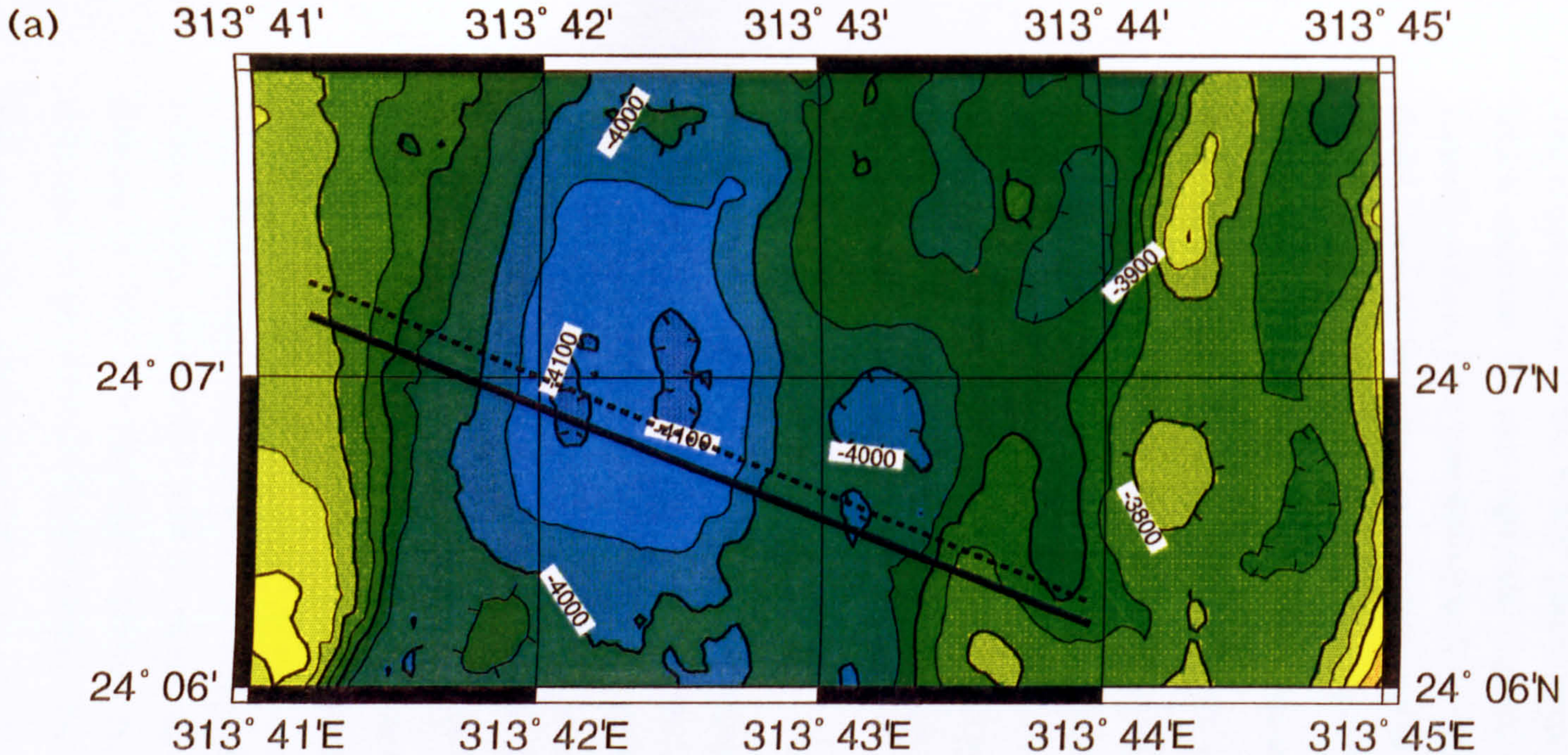

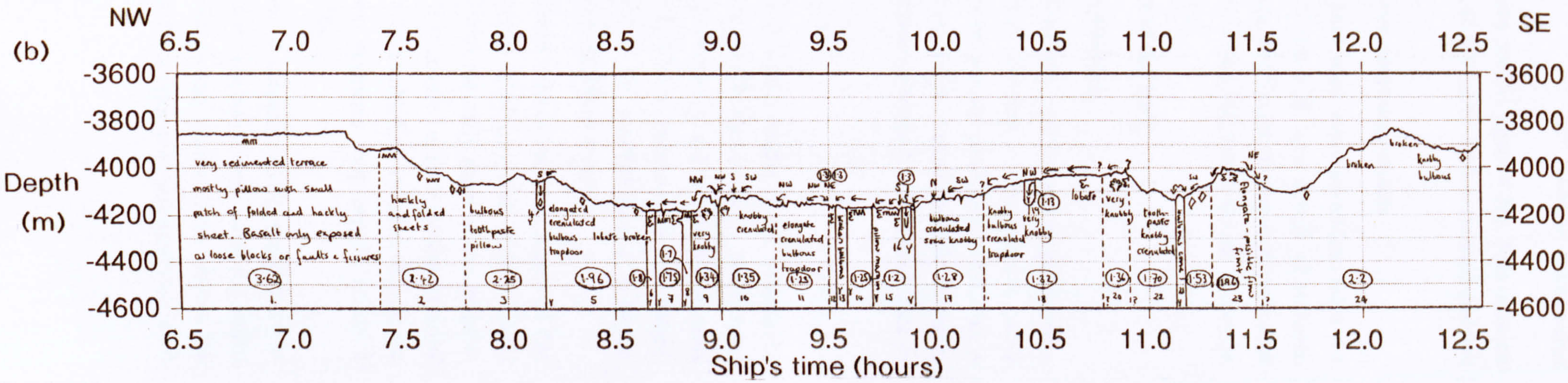

Figure 4.2 (a) Location of WASP traverse 28W across segment 1, just north of the narrowgate. The line of best fit (solid line) and the ship's track (dotted line) are virtually coincident, but this is a consequence of the poor resolution on the SeaBeam bathymetry (see Appendix 2.5; fig. A2.3). (b) High resolution profile as for figure 4.1. Relative age estimates for sheet flows are corrected for differences in morphology so they are comparable with the values for the sheet flows. Key for symbols is at end of Appendix 2.

at its eastern end (10.9 hours on the high resolution profile, figure 4.2b). This outward dipping fault forms the western wall to the first of two small fault controlled grabens situated to the east of the NVZ.

4.2.3 Contrasting features of photoanalysis over the two segments

The observations of the WASP phototraverses have been summarised into table 4.1 which contrasts the two segments. Figures 4.1b and 4.2b have details of volcanic features, such as flow morphologies, flow contacts, and the relative ages of individual flows. Tectonic features, the sediment profile, and broad age variations are shown on figures 4.3 and 4.4 (for 26W and 28W respectively)

4.2.4 Flow morphologies and the development of the NVZ

4.2.4.1 Approaches to interpretation of flow morphologies

The interpretation of flow morphologies has followed two complementary approaches. One emphasises the flow mechanics in relation to the stage of the eruptive phase (Ballard et al., 1979), while the other concentrates on intrinsic properties of the lava as the primary factor in determining the resulting flow morphology (Bonatti & Harrison, 1988). Both approaches can be related to the volcanic plumbing and thermal state of the segment.

4.2.4.2 Volcano building episodes

Studies both from ophiolites on land (Schmincke & Rautenschlein, 1987; Schmincke et al., 1983) and from the seafloor (Ballard et al., 1979; Stakes et al., 1984) have shown that volcano building episodes tend to commence in a brief but voluminous phase of eruption where sheet flows are produced. This is followed by a sustained, slower and steadier eruptive phase, which results in the establishment of a higher degree of channelisation and the formation of overlying pillow mounds.

The two segments in the MARNOK area are inferred to be in different phases of this eruptive cycle. The NVZ at the narrowgate is poorly developed, with areas of sheet flows and low relief pillow mounds, consistent with the early stage of the eruptive cycle. The robust, voluminous NVR of segment 2 is covered entirely by higher relief pillow flows, conforming with the model for a well established volcano. Hence, the contrast in flow morphologies between the two segments may merely reflect a difference in the extent of development of the NVZs.

Not only is the narrowgate NVZ in a 'early' phase of volcanic development, but it is unlikely to reach the mature stage in the near future; nor has it done so in the recent past. The considerable tectonic disruption of the young pillow flows within the narrowgate NVZ suggests that the NVZ is rapidly dismembered by tectonism before it

High resolution profile and interpretation from WASP phototraverse across NVR of segment 2

(Cross-section has approximately no vertical exaggeration)

Robust NVR, composed entirely of pillow flows has experienced relatively little tectonic dismemberment.

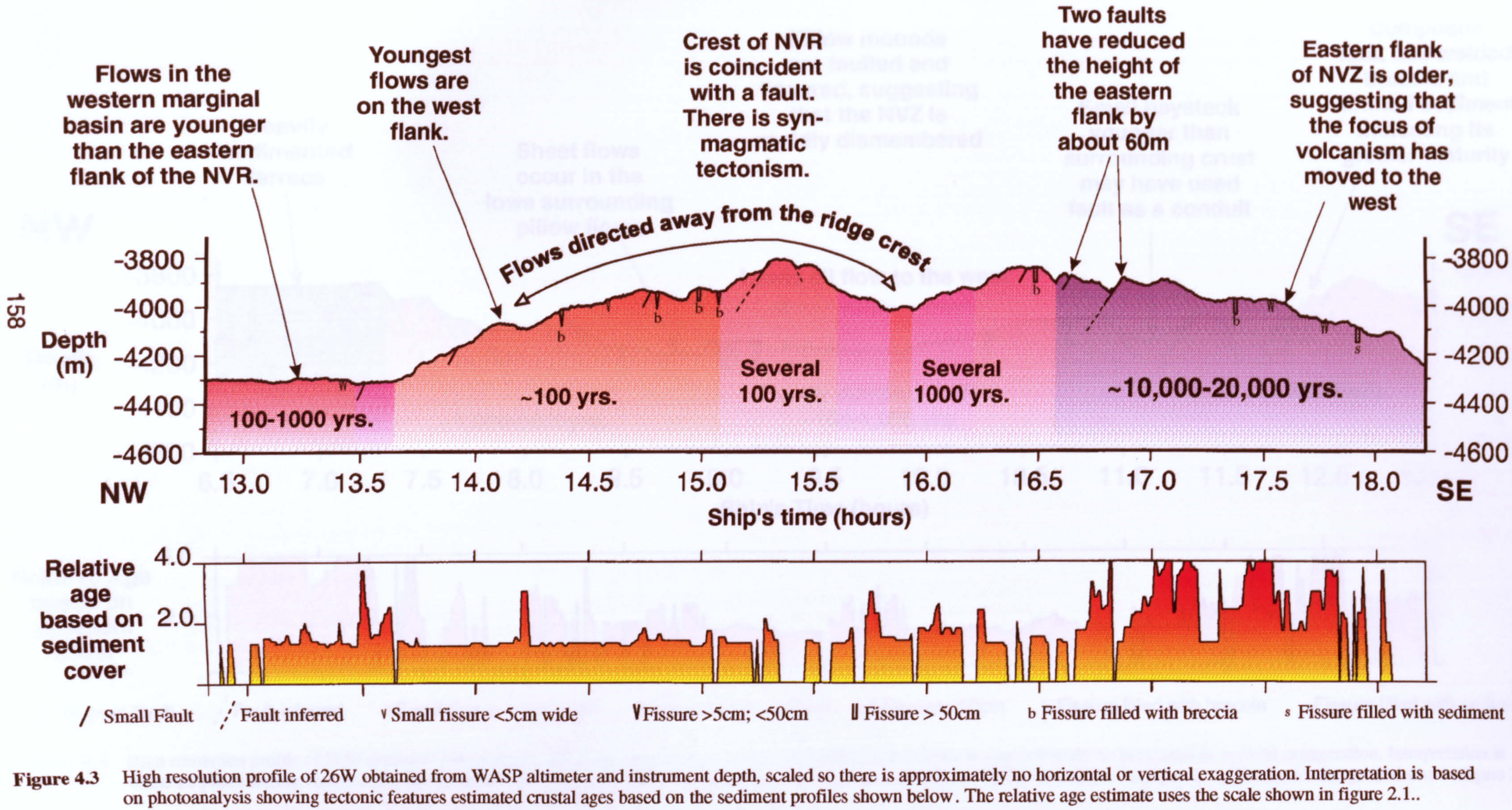

Figure 4.3 High resolution profile of 26W obtained from WASP altimeter and instrument depth, scaled so there is approximately no horizontal or vertical exaggeration. Interpretation is based on photoanalysis showing tectonic features estimated crustal ages based on the sediment profiles shown below. The relative age estimate uses the scale shown in figure 2.1..

High Resolution profile and interpretation from WASP phototraverse across the Narrowgate

(Cross-section has no vertical exaggeration)

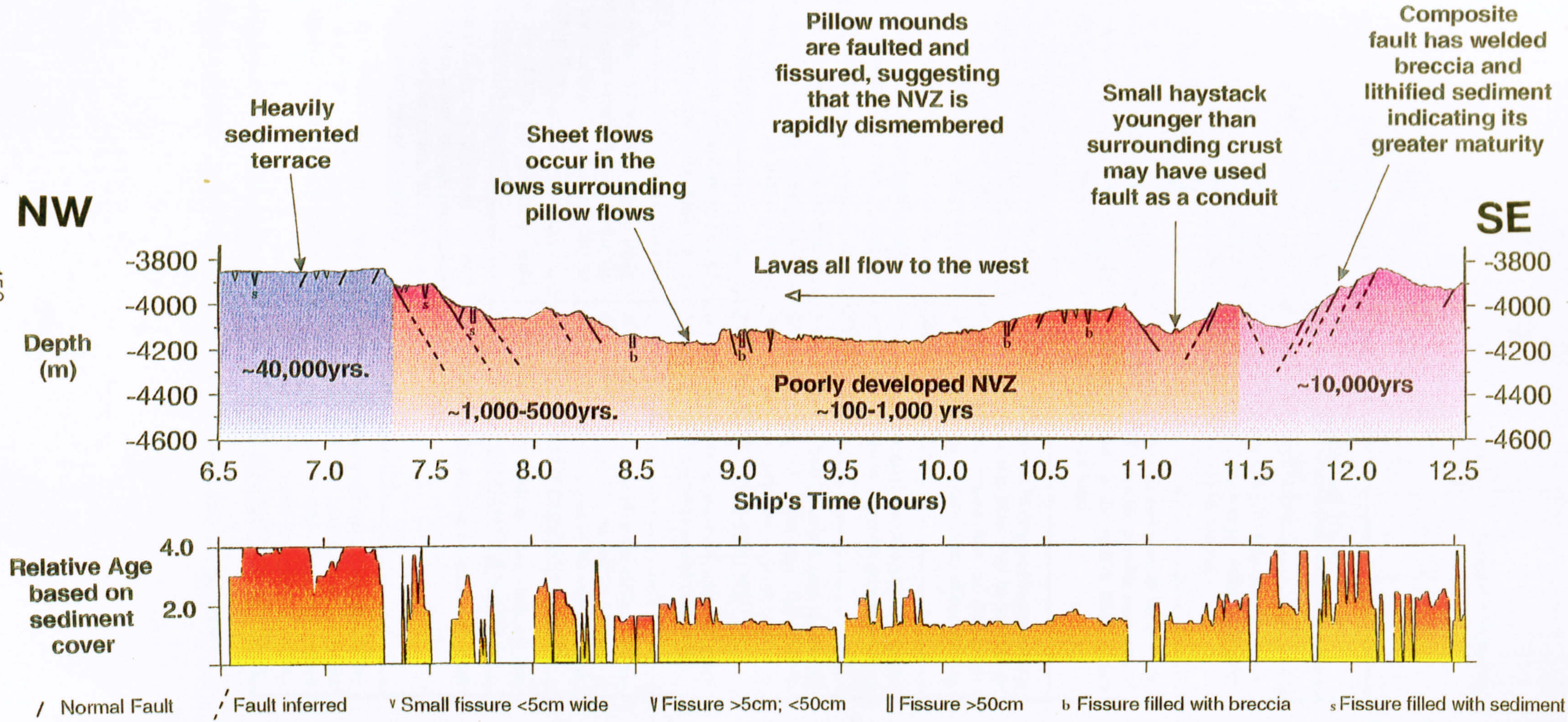

Figure 4.4 High resolution profile of 28W obtained from altimeter and instrument depth is scaled with ship's time so there is approximately no horizontal or vertical exaggeration. Interpretation is based on photoanalysis and shows tectonic features and estimated ages of the surface obtained from sediment profile shown below. Relative age estimate uses the scale shown in figure 2.1

Segment 1 (28W)	Segment 2 (26W)
Poorly developed NVZ < 2km in width.	Robust NVR is 4.5km wide.
Low relief pillow mounds and lava tubes are surrounded by sheet flows in horizontal lows. There is also a lobate sheet at the uplifted eastern faulted crest at the edge of the NVZ.	Valley floor comprises pillow flows only (mostly bulbous, phallic and knobby), which have piled up to form the two volcanic crests.
Lavas all flow westwards. This is because easterly dipping faults truncate both east and west edges of the NVZ forming a half-graben structure which maintains a westerly dipping slope.	Lavas are directed east and west, down from the crests of the NVR, with the possible exception of a couple of flows on the eastern flank, which may have been back-tilted.
Complex sequence of extrusion of NVZ flows. Youngest flows are concentrated at the centre of the NVZ, with a few inliers of older sheet and pillow flows. Local volcanic fronts tend to build eastwards.	Youngest volcanism is in centre of western flank, where a new volcanic crest may be starting to form. Volcanism focused first on the eastern crest and then the western crest, before moving to the western flank.
The western terrace is heavily sedimented and although it is virtually horizontal, it comprises pillows as well as sheets.	The western marginal basin comprises recent pillow flows which lie on moderately sedimented older flows.
The centre of the median valley is relatively symmetrical in terms of age relationships, but there is a strong age contrast with the heavily sedimented western terrace.	Eastern flank is heavily sedimented suggesting that the focus of volcanism has moved progressively westwards, producing an asymmetrical age variation across the NVR.
A syn-tectonic haystack erupted at the foot of a fault during the formation of the graben at the east of the NVZ.	A syn-magmatic fault cuts the western crest and may play a part in the development of the NVR.
Pillow flows in the NVZ are quite heavily faulted and fissured despite their relatively young age. There is no faulting or fissuring in the surrounding sheet flows.	Many fissures are located at the crests of pillow flows and are probably related to dyking at depth. With the exception of the eastern flank, the NVR is not greatly disrupted by tectonism.
Fissures in the NVZ are generally wider (maximum ~8m) than in segment 2	Maximum fissure width is ~1m. They are less closely spaced than in the NVZ of segment 1.
Inward dipping faults are dominant on both edges of the median valley, though two outward dipping faults to the east of the NVZ form two small grabens at eastern end of the traverse.	Faults all dip to the west, apart from a few small antithetic faults.
Large faults (50 - 300m throws) occur on both sides of the inner valley floor. The largest of these is a composite fault at eastern end of the traverse.	Larger faults seem to be mainly confined to the older eastern flank and have reduced the height of the eastern crest by 60m. Otherwise eastern and western crests would be identical heights. This faulting may be related to volcano collapse.

Table 4.1 Contrasting features of photoanalysis across the centres of the two segments.

is able to build up into an NVR. The faulting is restricted to the pillow flows, which suggests that within the narrowgate, subsidence of the pillow volcanoes is occurring in the very early stages of their development. If the early stage of the volcanic phase is followed by immediate tectonic dismemberment, then the volcanic edifice may never become established enough for sustained pillow eruption to take place. The low relief nature of the adjacent fault terraces and the presence of sheet flows off axis confirms that this has been the stable scenario for at least several 100,000 years and probably for 1Ma, as the fault terraces beyond the inner valley walls have a similar regular form.

The construction of mature volcanoes seems to have been a consistent feature of segment 2's volcanism of for several 10,000 years (figure 4.3), as there have been two, or perhaps three constructive episodes, which have moved from east to west across the valley floor. These construcitonal episodes are separated by minimal tectonic dismemberment. The older eastern crest of the NVR has been reduced in height by 60m by a fault (on flow 15, figure 4.1). This faulting is probably related to volcano collapse such as that documented in the FAMOUS area by Ballard and Van Andel (1977), although faults around the base of the volcanoes have previously been thought to have caused the subsidence. With an additional 60m relief the pillow volcano which forms the eastern half of the NVR would be the same height as the younger crest to the west.

The presence of marginal basins adjacent to the ridge suggests that the robust, volcano-building stage of segment 2 is not continuous, but probably episodic.

4.2.4.3 Physical conditions

Bonatti and Harrison (1988) suggest that the different lava morphologies are a response to variations in the stresses induced in a lava as it cools. The stresses induced in sheet flows are less than those produced in pillows. Factors tending towards lower stresses include high eruption temperature, low viscosity and high discharge rate.

Hence the lava flows in the narrowgate have faster flow rates, are probably hotter and have lower viscosity than the flows erupting on the robust NVR of segment 2.

4.2.5 Causes of changing eruptive style with development of volcanic edifice

Although the correlation between the development of volcanic edifices and flow type has been established, a question remains as to whether the switch from low relief sheets to high relief pillows is caused by the evolution of the surface topography as the extrusive mound increases in size, or by some other factor, such as a reduction in flow rate.

4.2.5.1 Relationship between flow morphology and gradient

Renard et al. (1985) have shown that pillow flows are consistently found on the steep slopes while sheets occur on flat terrains. The WASP traverse shows that a mobile sheet flow can erupt around steep pillow flow fronts and cool into a flat surface, thus smoothing out the relief of the NVZ. However, relatively flat surfaces do not always indicate the presence of sheet flows, as the horizontal western terrace of the narrowgate comprises low relief pillow fields as well as sheet flows. The western marginal basin of 26W also has a very shallow gradient and is floored by pillow flows.

Laboratory experiments using wax injected into a tank of cold water have shown that a rough and irregular surface creates an additional stress on the extruding material which will favour a pillow formation, but pre-existing gradients of up to 6° have little affect on the dominant flow morphology (Griffiths & Fink, 1992a). However, all things being equal, the dimensionless parameter of Fink & Griffiths (1990) suggests that a slope increase is more likely to promote sheet flows. Hence greater slopes cannot be the only factor governing the change in eruptive morphology during volcano building.

4.2.5.2 Physical properties of flows —the dominant control on lava morphology

This result agrees with Bonatti and Harrison (1988) who stress that it is the lava morphologies that create the different kinds of terrain and not the pre-existing relief which controls the type of flow that will form. Their calculations show that slope is a minor parameter. Instead, the physical properties of the flow, such as temperature and effusion rate are dominant in controlling morphology. It is parameters such as these which must cause the change in flow type with NVR development. The experiments of Griffiths and Fink (1992a) show that effusion rate is usually the main governing parameter.

4.2.5.3 Mechanisms for decreasing effusion rate with volcano growth

Models which emphasise the variation of pressure in the magma chamber predict an exponential decrease in the flow rate as the stored elastic strain energy is released during viscous flow along the eruptive conduit (Scandone, 1979; Wadge, 1981).

Shaw and Swanson (1969) developed an expression for mass discharge rates from a long narrow conduit. They showed that Q, the mass discharge per unit width, is given by:

$$Q = \frac{\rho^2 g S^3 h_z}{12 \mu L_z} \quad (1)$$

where ρ is the density, μ is the viscosity, S is the width of the conduit, h_z is the excess hydraulic head of pressure in the magma chamber, and L_z is the vertical length of the conduit between the magma chamber and the seafloor.

Hence, sheet flows, which have high values of Q, are favoured by:

a) large excess magmastatic pressure;

b) low viscosity magmas;

c) conduits with large widths and short lengths.

As a volcanic ridge is built up, the vertical length of the conduit from the magma chamber is likely to increase and as long as the eruption rate exceeds the replenishment rate of the magma chamber, h_z should decrease with elastic relaxation and as volatliles, which are a primary driving force of eruption are released. According to equation (1), these factors will reduce the flow rate and increase the likelihood that pillow flows will form.

Bonatti and Harrison (1988) suggest that a long, narrow conduit will also reduce the temperature and increase the crystallinity of the lava on eruption (because of greater conductive heat loss and enhanced probability of crystal nucleation and growth). These factors will compound the effects of conduit length on the flow rate and increase the stress on the lava even more. Systematic differences in the crystal/liquid ratio of sheet flows compared with pillow flows have been noted, supporting this hypothesis (Bonatti and Harrison, op. cit.).

Equation (1) shows that the flow rate is quite sensitive to the width of the conduit. There is a feedback mechanism between these two parameters. A faster effusion rate increases the proportion of heat delivered by advection to the walls of the conduit relative to that lost through conduction. A critical point may be reached if the initial width of the conduit is large enough and the length is short enough, where the walls of the conduit may start to progressively melt back (Bruce & Huppert, 1990). The widening of the conduit will in turn promote faster effusion rates in a positive feedback loop.

4.2.6 Implications of NVZ morphology to thermal and mechanical structure of the lithosphere

Voluminous sheet flows are common at fast spreading ridges (Ballard et al., 1981; Lichtman et al., 1984; Renard et al., 1985), where higher melt flux and elevated isotherms favour their eruption (Sleep, 1975; 1978).

The presence of sheet flows at the narrowgate presents us with a paradox. Unlike eruptions from fast spreading ridges, these sheet flows are very meagre and are associated with a very *poorly* developed NVZ. Yet although the surface morphology suggests that the centre of segment 1 has a relatively poor magma supply, the estimates of smoothed tectonic strain from Allerton et al. (1995) are low, implying that magmatism takes up a relatively large proportion of the extension.

These observations can be reconciled if most of the magmatism is intrusive, with only a small proportion reaching the surface to erupt as lava flows at the segment centre. This will result in a crustal structure which has a thick layer of gabbros and dykes, but a thin layer of lavas.

4.2.6.1 Magmastatic head and the building of volcanoes

The height to which volcanic edifice can grow is thought to be dependent on the hydraulic head of fluid magma (Eaton & Murata, 1960), so shallow magma chambers can only produce small edifices compared with deeper magma chambers. The narrowgate may have a relatively large intrusion:extrusion ratio because the magma chamber has reached its limiting magmastatic head. In contrast segment 2's magma chamber may be deeper, enabling the construction of a thick volcanic pile.

Thus, the difference in morphology of the two segments may primarily be a consequence of differing magmastatic heads of the magma bodies within the segments. The centre of segment 1 might have a shallow magma chamber with a low magmastatic head, which in itself will favour the formation of sheet flows because of the short conduit lengths (see section 4.2.5.3).

4.2.6.2 Relationship of the magmastatic head and the brittle/ductile transition

Some authors suggest that the level of magma ponding within the crust is controlled by the brittle-ductile transition (Rinehart et al., 1979; Smith & Cann, 1992). If this is so, then a low magmastatic head is in keeping with a thin brittle lid. The depth of the brittle/ductile transition is closely related to the elevation of isotherms, which in turn is related to magma flux. It follows that the narrowgate probably has a higher average melt flux compared with segment 2. This is the very result predicted from the smoothed strain measurements of Allerton et al. (1995), which suggest that segment 2 has a higher tectonic component of extension compared with segment 1.

4.2.6.3 Relationship of brittle-ductile transition to valley morphology

This line of reasoning becomes complete when the relationship of brittle-ductile transition to valley morphology is considered. Harper (1985) argues that narrow rift valleys should on average have shallower brittle/ductile transitions because the near-axis faults have not become locked. In contrast, wide valleys have deeper brittle-ductile transitions, as the near axis faults have become locked. The locking of faults is related to the development of rift valley asymmetry, which is also a feature of segment 2 (Allerton et al., 1995)

4.2.7 Factors controlling flow rate on the robust NVR

The following section attempts to determine which factors are the primary cause of variations in flow rate during the construction of the robust NVR of segment 2. The parameters investigated are time, location (with respect to the NVR) and gradient.

In section 4.2.5.3, I mentioned that an exponential decrease in the flow rate might be expected as an eruptive phase progresses and the elastic energy stored by deformation round the chamber is released (Scandone, 1979; Wadge, 1981). These early models are simplistic as they do not take into account either changes in the conduit dimensions and the physical properties of the lava or the accumulation of the erupted lava which alters the pressure over the conduit. More complex modelling by Stasiuk et al. (1993) shows how initially rapid decrease in effusion rate, followed by a period of steady, near constant flow rate, is consistent with lava pile-up over a vent.

Flow type	Description
1	Lobate sheet on flatter areas; elongate pillows where steeper.
2	Predominantly very knobby pillows.
3	Mixed morphologies: knobby, bulbous, toothpaste and trapdoor.
4	Knobby pillows rare; mostly bulbous, toothpaste and trapdoor.
5	Flow surface broken, degraded and covered with sediment so original pillow morphologies are not readily discernible.

Table 4.2 Flow types categorised on the basis of pillow morphologies.

The contacts of 20 'mappable' pillow flows were identified in the northern traverse. An eruptive sequence of flows on the NVR of segment 2 was established using the relative ages and contact relationships. Each flow was assigned a 'flow type' category based on the most common lava morphologies, as summarised in table 4.2 above. Flow types 1 to 4 are in order of decreasing average flow rate. In theory those flows

which occur later in the sequence should have a predominance of slower flow types. Flows of type 5 are not included in the following analysis, as the pillow morphologies have either been obscured by sediment cover or are degraded so that surface ornamentation has largely been destroyed.

Table 4.3 presents a summary of the flow characteristics and dimensions taken from the WASP traverse.

Flow number	Relative age	Flow type	Gradient (degrees)	Maximum height (m)	Minimum height (m)	Average height (m)	Surface length (m)	Distance from NVR axis (m)
2	1.45	4	9.39	4295	4310	4303	230	-2381
3	1.32	4	11.63	4295	4315	4305	143	-2199
5	2.19	4	3.92	4310	4320	4315	146	-2057
6	1.36	3	29.16	4075	4310	4193	457	-1725
7	1.33	2	20.55	3930	4100	4015	638	-1153
8	1.24	1	37.66	3925	3975	3950	104	-790
9	1.42	2	25.92	3860	3945	3903	204	-641
10	1.42	3	20.78	3810	3965	3888	272	-371
11	2.02	3	19.48	3965	4020	3993	159	-121
12	1.42	3	14.43	4005	4020	4013	87	0
13	1.93	2	26.05	3925	4020	3973	272	175
14	1.6	4	38.05	3845	4025	3935	314	455
15	2.49	5	24.69	3875	3950	3913	347	785
16	2.87	5	26.43	3895	3990	3943	259	1095
17	3	5	9.73	3975	3990	3983	146	1296
18	2.89	5	20.18	3975	4075	4025	324	1529
19	2.67	5	23.21	4075	4125	4100	172	1935

Table 4.3 Characteristics and dimensions of flows taken from 26W high resolution profile and phototraverse.

The flow dimensions are minimum values as they are limited by the 2-dimensional nature of the study. Most of the flows are partially buried by at least one adjacent

flow, the exceptions being flow numbers 3, 8, 10, 12 & 14 which downlap onto adjacent flows on both east and west sides. Figure 4.1 shows which of these contacts are inferred (dashed lines and dot-dash lines) and which are observed (solid lines). The NVR axis was taken to be the central point in the axial depression between the east and west peaks, which corresponds to flow 12. The distance from the NVR axis, was calculated by measuring the difference between the centre of flow 12 and the flow in question on the high resolution profile. This is a time measurement, which is converted to a distance measurement assuming that the vehicle was moving at uniform velocity.

The prediction that flow rates should diminish with time does not seem to hold for the flows of this traverse. In fact figure 4.5a shows a trend towards faster flow rates for the older flows. This shows that there are factors governing the flow rates and flow types other than a simplistic drop in magmastatic pressure caused by elastic relaxation. The information available from the phototraverse is limited to the latter stages of evolution of the NVR as the data analysis is restricted to flows from the surface. A cross-sectional view would be required to test the true extent of flow evolution during the construction of a NVR.

As the flow rate is inversely proportional to the conduit length there may be a relationship between the flow rate and the position of the flow on the NVR. For example, conduits will be longer for summit eruptions and also possibly for flank eruptions which may not be vertically above a magma chamber. Indeed, flows 10 and 14, which comprise the western and eastern summits of the NVR, have relatively slow flow rates and there is a decrease in flow rate with increasing distance from the axis along the western flank and into the western marginal basin.

However, in the end, a simple factor like gradient has perhaps the strongest correlation with flow type. Figure 4.5b shows that the steepest eruptions on the flanks of the NVR have the fastest flow rates, while those in the flat marginal basin are slower.

4.3 Pillow flows and faulting.

In chapter 3, I described the close relationship between some of the hummocky ridges and faults in the NVR. In this section I discuss the implications of this relationship to the volcanology of pillow flows. I propose that the development of a flow front breccia is aided by both constructional oversteepening and the presence of syn-magmatic faulting.

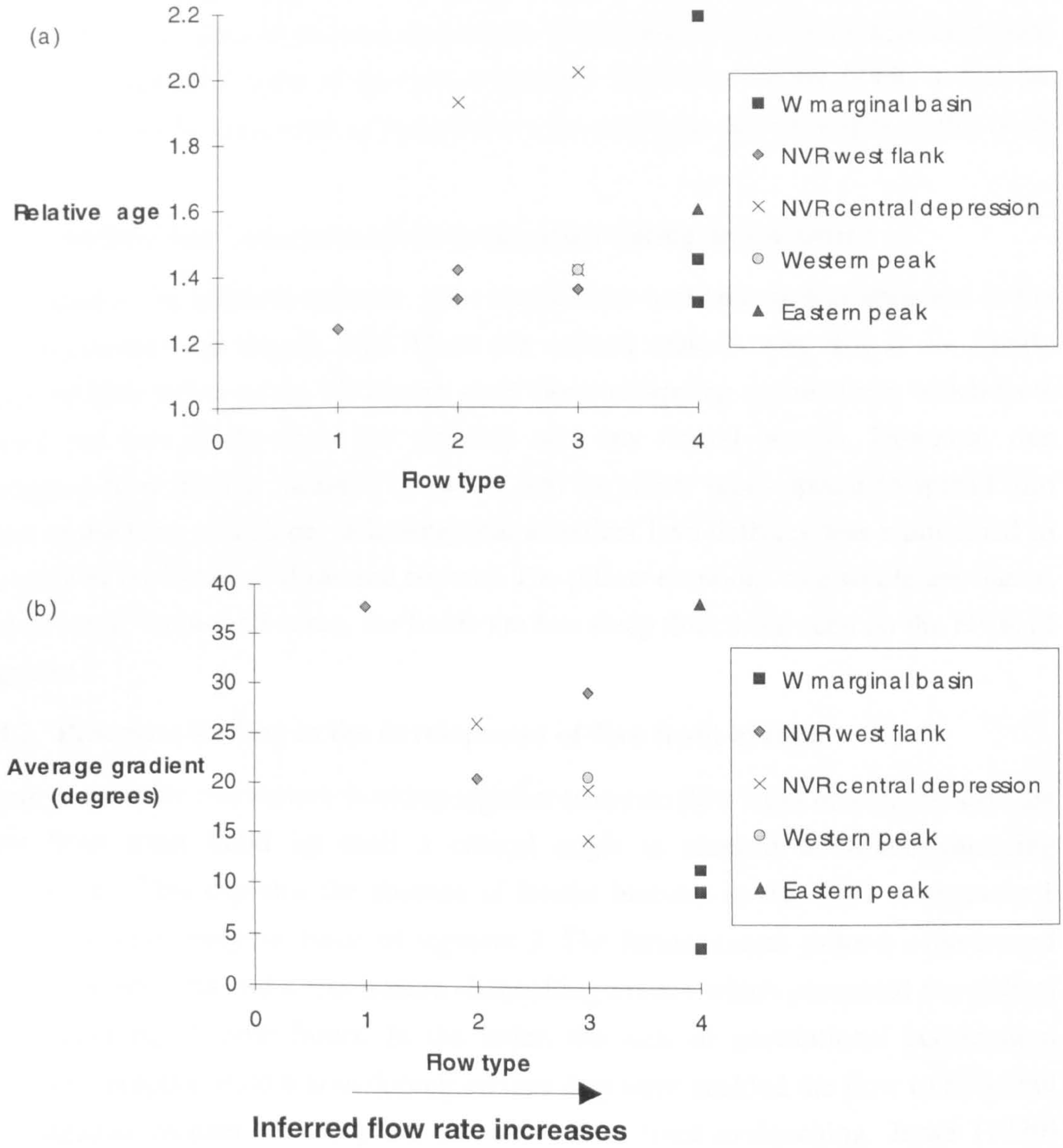

Figure 4.5 Graphs of flow type against (a) relative age and (b) average gradient of the flow surface, for different sites along the phototraverse of 26W.

4.3.1 Flow front breccia and syn-magmatic faulting on the NVR, segment 2

On the western crest of the NVR of segment 2, the faulting is syn-magmatic (figure 3.2, points E and F) and the pillow flows are relatively steep (figure 4.1). The pillow flows are at a similar angle on the flanks, but there are no faults directly observed. The pillow flow fronts on both crest and flanks have well developed talus ramps at their bases, resting at angles less than 30° and extending distances of 10m to 100m beyond the outcropping flow fronts. All the flow foot breccias comprise a surprisingly small proportion of elongated fragments and look virtually identical to talus ramps of NVZ faults.

In the western marginal basin of the northern traverse, there is one low relief flow that has no flow foot talus at its base despite the presence of a flow front with elongated pillows. The general shape of the flow is different from those on the NVR, in that the flow top is nearly horizontal compared with the moderate degree slopes of the NVR flows.

4.3.2 No flow foot breccias nor syn-magmatic faulting on segment 1

In contrast to the northern traverse, not a single flow-foot breccia was observed in the narrowgate traverse (figure 4.2). There are several reasons why this is so. Firstly pillowed flow fronts on the NVZ have sheet flows onlapping against them which have buried the foot of the flow and possibly also any frontal breccia. However, one elongated flow front is actually observed, and its pillow tubes appear to spread into lobes at the base of a slope, indicating that abundant lava delivery was maintained to the edge of the break of slope and beyond. The pillow eruptions as a whole are flatter, and in some, but not all cases, the fronts are less steep than those seen on the NVR of segment 2.

4.3.3 Processes leading to the development of flow front breccia

There seem to be two factors working together to create flow front breccia. Firstly, the flow front must build up until a critical angle is reached at which slumping commences. This explains the absence of frontal breccias in the NVZ of segment 1 and the western marginal basin of segment 2. The former seems to have experienced faster delivery rates and a less mature channelling system which prevented the critical oversteepening of flow fronts. In the latter, the lack of gravitational acceleration caused by eruption onto a non-sloping surface may have enabled the flow to build out in a steadier manner reducing the extent of flow front avalanching. Jones (1970) reports an example from Kalfstindur in SW Iceland, of a similar flow with no significant breccia at the base of an elongated front.

Secondly, certain aspects of the development of flow foot breccia are explained if variable amounts of syn-magmatic faulting as well as variable constructional oversteepening contribute to the accumulation of the flow front talus. This hypothesis accounts for the variability in the size of the frontal breccias between flows of similar dimensions and angles of slope. It also explains why the flow front breccias tend to lack large proportions of elongated fragments, but instead are very similar to fault-related talus ramps.

4.4 Sheet flow morphologies.

The sequence of flow transformations observed on the slow spreading, MARNOK narrowgate area is complex, and does not conform completely with the suggested flow

regimes of Griffiths and Fink (1992a) as described in section 2.3.5.3. Hence this data set should add to the understanding of submarine sheet flows and particularly the flow regimes under which they form.

The sheet flows of the narrowgate area are less laterally extensive than those reported from intermediate and fast spreading ridges. Morphological transitions occur within relatively short distances—within 4 adjacent frames there can be a range of several sheet flow morphologies.

4.4.1 Lobate to hackly flow transition

4.4.1.1 Effect of increasing viscosity

According to the scheme of Griffiths and Fink (1992a), hackly lavas occur at fast flow rates and should transform as flow rate diminishes into lobate flows. In the MARNOK sheet flows, the hackly, jumbled areas occur as patches within larger expanses of a westerly directed lobate flow and there are transformations from lobate to hackly as well as the predicted hackly to lobate.

Plate 4.6a shows a mosaic of a sheet flow which undergoes a number of textural transformations. The gentle hummocks of the lobate flow become more flattened until a planar, cracked sheet results. The planar fractured surface starts to wrinkle and fold and then rapidly becomes disrupted with blades and clasts of lava protruding at random angles in a chaotically broken manner (a classic hackly surface). The intermediate flow surface described here (flat, fractured surfaces with wrinkled margins) are suggestive of lavas with greater viscosities and/or thicker less pliable crusts than the ropy or lobate flow types. The cracks which dissect this intermediate surface are roughly orthogonal to the flow direction (plate 4.6a & 4.7a).

The extent of the intermediate 'folding' stage between a planar/lobate surface and jumbled/hackly texture is variable and seems to depend on the viscosity of the lava. The development of a flat, fractured surface is usually accompanied by a very rapid transition to a strongly granular hackly surface, and probably indicates higher viscosities. At lower viscosities the transitional folded and jumbled zone covers a much wider area (up to 10m wide) before the flow surface becomes fully jumbled. These lower viscosities are demonstrated by the presence of ropy lavas earlier in the sequence and thin-skinned folding of the surface within the transition zone itself.

This progression of lobate to jumbled flow morphologies is the opposite to that described by Ballard et al. (1979) from the Galapagos Rift and does not comply with the suggestion of Griffiths and Fink (1992a) that jumbled flows are equivalent to the lêvéed flows observed in the wax eruptions (i.e. only form at regimes of very high flow rate and relatively low viscosity). In this case, the transformation in flow

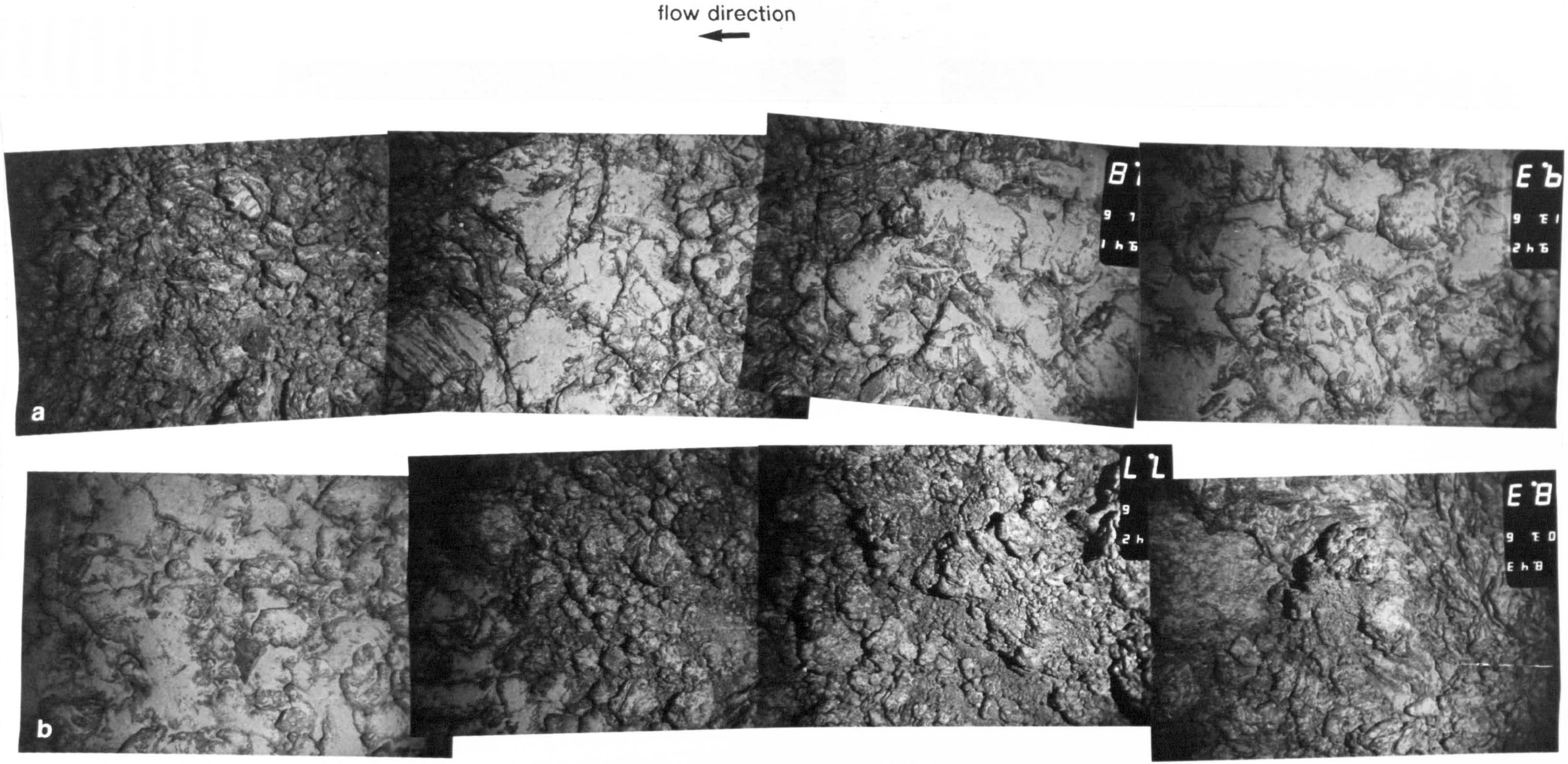

Plate 4.6 Mosaics of sheet flows with different flow morphologies. (a) Lobate flow becomes flatter and cracks develop in the planar surface which starts to wrinkle and fold before breaking into a jumbled mass. The transition between planar sheet and jumbled flow occurs relatively rapidly. Most of the jumbled flow surface is covered in granular and jagged gravel to pebble sized rubble but it does show relicts of folding with some clasts having pahoehoe-like surfaces or platy internal structures. (b) Jumbled, hackly lava flows round a spur of older seafloor. The flow surface is wrinkled and folded in front of the spur and becomes increasingly disrupted as it passes beyond the tip. A clot of hackly lava has twisted on to the surface of the older crust. Further on (to the left) the hackly margin downlaps onto a lobate sheet flow.

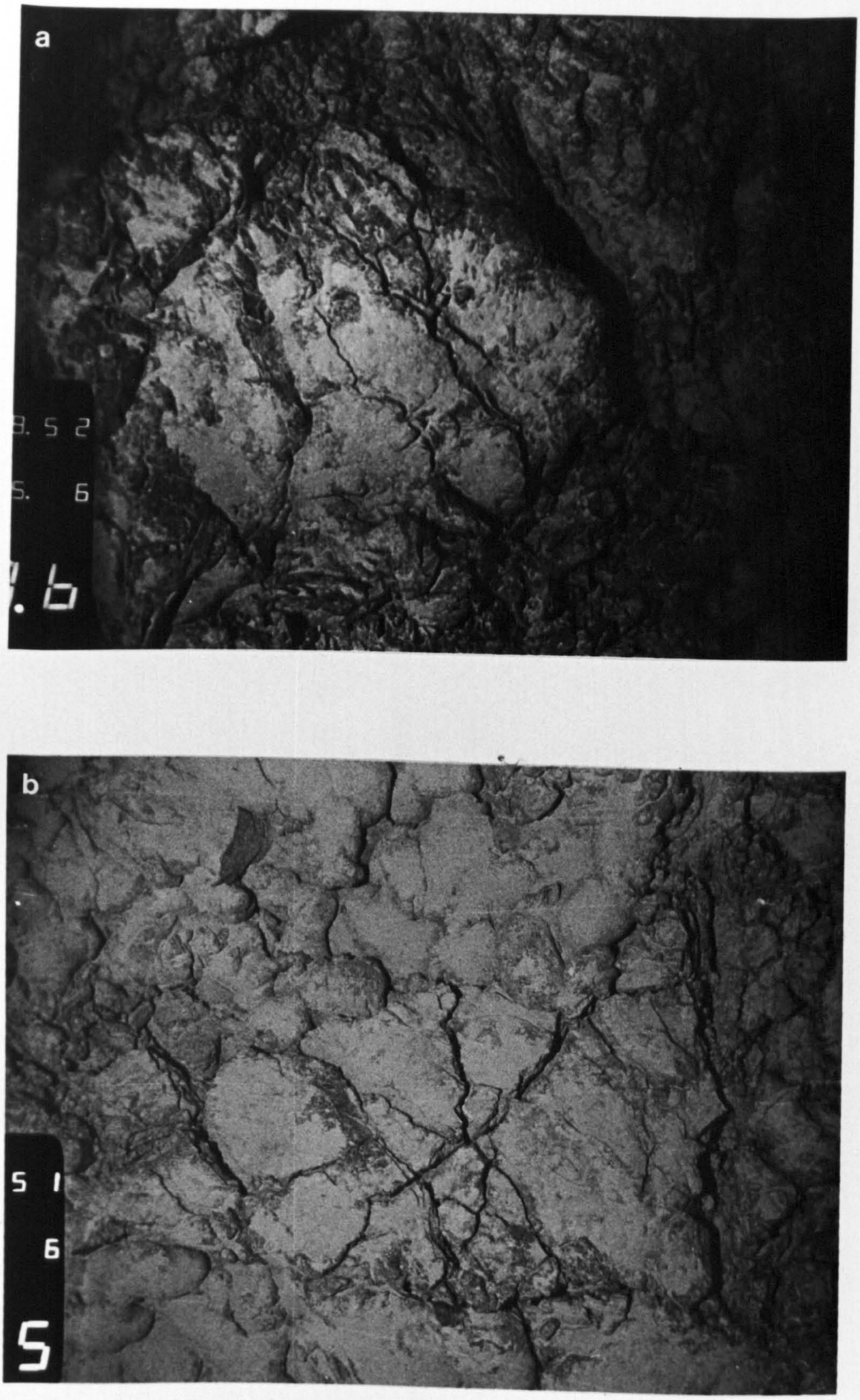

Plate 4.7 (a) Close view of a transitional area between flat fractured crust and hackly flow. The planar surface is crossed by cracks which are roughly orthogonal to the flow direction and it develops angular wrinkles at the margin where there is a sudden morphological change to a hackly flow type. This mode of surface deformation is thought to be indicative of a more viscous rheology. Note the contrast in apparent sediment cover between the planar surface and the hackly flow. (b) A small area of flat fractured crust lies on the surface of an older lobate flow. It is only a few centimetres thick and seems to emanate from the hackly flow front (just visible at the left of the frame). It is possibly a lobe which has erupted from the snout of the hackly flow analogous to the viscous pahoehoe which often oozes from the front of subaerial aa flows.

morphology is thought to be a result of the increasing viscosity found near the cooler front of a flow, akin to the pahoehoe-aa transition observed in subaerial lavas. This analogy is discussed further in sections 4.4.2 -4.4.4.

4.4.1.2 Interaction with the local topography

As well as occurring with increasing viscosity, the lobate to jumbled flow transition can also be induced by flow interaction with the local topography. When a lobate flow encounters a steep pillow front head on, the surface crust can sometimes rumple up at the contact to produce a jumbled form. To the sides of the obstruction, the lobate nature of the flow is maintained and beyond, the lava seems to wrap around and onlap the topography in the more gentle fashion.

Plate 4.6b shows the hackly lava flowing round a spur or raft of older seafloor. The flow surface is wrinkled and folded as it approaches this obstruction, but becomes increasingly disrupted as it shears round the tip causing a jagged clot of hackly basalt to twist upwards and run aground.

4.4.2 Comparison with subaerial sheet flows

4.4.2.1 The pahoehoe to aa transition

In many ways the jumbled/hackly surface resembles the clinkery brecciated texture of subaerial aa. The formation mechanisms for these deep water flows are uncertain, but there is some value in considering analogies with the subaerial pahoehoe-aa transition.

Subaerial pahoehoe flows either undergo transition to aa or remain as pahoehoe but become increasingly channellised and tube fed. This deep-sea study shows analogous situations where ropy pahoehoe and lobate morphologies sometimes transform to jumbled, hackly flow fronts and sometimes have pillowy margins.

Macdonald (1953), after an extensive study of subaerial lavas, observed that once a crust has an aa texture it remains as aa and never undergoes a transformation to pahoehoe. The typical sequence of Ballard et al. (1979) and some of the deep-sea transitions reported from this study where the surface texture changes along or across a flow from smooth to hackly and back again, are in conflict with the subaerial analogy.

4.4.2.2 Clast size: analogy with 'cauliflower' aa

Clast size is one aspect in which the hackly/jumbled lavas differ from mature subaerial aa. On many hackly/jumbled flows the surface breccia is homogeneous, but the clast size (granular to small pebbles) is considerably smaller than the blocks of mature subaerial aa flows. Other hackly flows have heterogeneous clast size distributions, ranging from sand-sized grains, through pebbles of a decimetre in

diameter, to clots several tens of centimetres wide. The larger clasts are similar in size to those typically present in the rubble of initial 'cauliflower' aa. Cauliflower aa has a surface breccia which is the thickness of 2 to 3 of the large fragments, on top of the massive lava (Kilburn, 1990). In comparison, the layer of rubble on the hackly/jumbled flows is thin, allowing the lava cooling surface to remain visible in places.

4.4.2.3 Flow snouts and frontal lobes

The snouts of subaerial aa flows often have dips of 40-50° (Kilburn & Guest, 1993). Plate 4.6b shows a hackly flow margin which has moved over the top of an older lobate sheet flow. Clearly the hackly flow front here has a much lower relief than subaerial aa snouts.

The fronts of subaerial aa flows advance by a mixture of continuous flow and rupture, so viscous protrusions and sheets (often pahoehoe) ooze out from the snout as rubble tumbles forward (Kilburn & Guest, 1993). In plate 4.7b, the small area of flat, fractured crust which lies on the older lobate flow and seems to emanate from the hackly flow front to the east (just visible at the left of the frame). It is possibly analogous to a frontal pahoehoe lobe of an aa flow. Plate 4.7a shows a close-up view of the flat, slightly wrinkled plate and associated hackly lava. The surface texture is similar to the viscous transitional texture described in section 4.4.1.1, confirming that it is related to the adjacent hackly flow.

4.4.2.4 Analogy with transitional pahoehoe flows

Peterson and Tilling (1980), in a detailed discussion of the pahoehoe - aa transition of Hawaiian lavas, identify two main transitional flow types.

Slab pahoehoe occurs where increased fracturing of the crust results in the collision, tilting and grinding together of floating plates. The underlying molten lava assumes a spiny, granulated character.

Spiny pahoehoe is very similar to untransitional pahoehoe on a broad scale as it has a gently undulating form with features such as festoons, ropy structures and bulbous toes. However, on a small scale the lava has a granular, spinose texture, with clots and lumps in areas of intense shear. Spiny pahoehoe seems to form where a lava of a high viscosity becomes exposed at the surface, and can occur in strongly sheared zones, in cracks between crustal slabs and sometimes as a transitional state across the entire surface of a flow.

These transitional flow types both have aspects which are similar to the jumbled and hackly flows observed on the seafloor. Lonsdale and Spiess (1980) suggest that the jumbled sheet flow is similar to slab pahoehoe in that it seems to form by disruption

of a previously sheety surface, sometimes leaving ropy textured clasts in the fragmented rubble.

However, the size and nature of the rubble on hackly surfaces are significantly different from that usually associated with slab pahoehoe. Whereas a typical slab pahoehoe comprises slabs several centimetres thick and as wide as 1m in maximum dimension, the clasts with obvious ropy textures in these jumbled flows have a much smaller aspect ratio (usually < 3) and comprise only a small percentage of the rubble. The blades of lava protruding chaotically from the jumbled flow surface are better described as broken folds than disrupted slabs.

The hackly flows are granular, clinkery and in many ways look similar to transitional spiny pahoehoe. The strong association of hackly flows with flat fractured surfaces similar to pavement lava, suggests that high viscosity is a feature of these flows, as is it with spiny pahoehoe. The role played by shearing to produce granular clots within hackly flows, is also closely analogous to the formation mechanism of the subaerial transitional flow type. The presence of stubby spines, a defining characteristic of spiny pahoehoe (Peterson & Tilling, 1980; Kilburn, 1990), is impossible to verify from photographic evidence, as spines are rarely longer than a few millimetres.

4.4.2.5 Comparison with aa flows in Iceland

Transitional flows on Krafla (Iceland) often comprise rafts and patches of planar sheeted surface surrounded by severely brecciated rubble (V. Hards, pers. comm.). A traverse across such a flow would be remarkably similar to areas of the narrowgate traverse, where hackly basalt and planar cracked slabs are closely associated. The degree of roughness of the surface is the main difference between the deep-sea and subaerial examples. The hackly flows of this study appear less blocky and less deeply cleaved than those in Iceland.

4.4.3 Mechanisms and factors controlling sheet flow morphology

When attempting to understand the mechanisms controlling the different sheet morphologies and the factors which govern their transformation, both the observations from the seafloor and the present understanding of subaerial lavas should be considered.

4.4.3.1 Crustal growth under stress

The subaerial pahoehoe - aa transition is thought to be governed by changes in the critical balance between physical flow parameters and lava rheology, and is explained in terms of crustal growth under stress (Kilburn, 1990; 1993). If the crust deforms faster than it can heal then autobrecciation creates an aa flow type. This will tend to occur downflow as both the viscosity and critical chilling time increase on lavas with

higher effusion rates and crusts with lower tensile strengths. The hackly texture is often preceded by a transformation from lobate to the supposedly more viscous fractured planar sheets, showing that the crust is indeed developing in response to changing rheology. However the mechanism may be slightly different as discussed below.

4.4.3.2 Compressive shearing

Jumbled flows are probably formed by crustal folding which becomes extreme until wholesale disruption of the surface results. There is strong evidence for this mechanism as jumbled flows frequently contain patches of lava-cooling surface with an ordered structure of folding. The fundamental mechanism for jumbled flow formation is probably almost identical to the widespread crustal failure and slow crustal healing which defines aa (Kilburn & Lopes, 1991; Kilburn, 1993) except that the crust is primarily under *compressive shearing* rather than *tension*. The corrugations of ropy pahoehoe seen in clasts on jumbled flows have been analysed in terms of surface folding of a viscous fluid (Fink & Fletcher, 1978), during *shortening* of the flow surface.

The compressive strength of lava is about ten times larger than the tensile strength (Jaeger & Cook, 1979), so the crustal forces required must either be considerably greater, or an element of shear must be included, to cause the brecciation. As jumbled and hackly flow types are almost always found interspersed, their formation mechanisms should also be strongly related. Crustal shearing may be an important linking factor aiding the initial disruption of the jumbled flow and also causing the granular clots of the hackly surface to develop.

The folded morphologies on jumbled clasts indicate that breakage on jumbled flows occurred *after* the crust had formed, while autobrecciation on a much finer scale must cause the clinkery surface of the hackly flow. In subaerial aa, high shear gradients cause surface lumps to twist upward and detach from the surface (Macdonald, 1953). The granular texture of many clasts in the hackly flows is similar to that formed by slow rupture on subaerial aa blocks (Kilburn & Guest, 1993). Finer sand and gravel sized particles are thought to form by cooling-contraction granulation (Kokelaar, 1986) and by attrition along fracture surfaces in a flow (Macdonald, 1972).

4.4.3.3 Topographic irregularities

Kilburn (1990) suggests that crustal autobrecciation may often be induced by acceleration over topographic irregularities, as this is the most likely source for increases in rate of shear over a large area of the flow. This mechanism has been observed to sometimes cause a transition to jumbled flow morphologies (as discussed

in section 4.4.1.2). Sometimes there is a clear external factor (presence of vent / topographic obstruction) which facilitates the transition from smooth crusted flow to disrupted crustal textures. Near a vent, the crust on a pahoehoe lava is thin and flexible, so it may be easily rolled, tumbled, torn and immersed by movements of a turbulent flow. In a similar way a lava which meets an obstruction will tend to dam up against it, bringing compressive and shearing forces to bear on the crust which will distort, fold and rupture it. Slow crustal healing relative to deformation rate must still be an important factor in generating these surfaces, otherwise the broken crust would tend to be covered by a smooth new crust.

4.4.3.4 Degassing

Sudden undercooling, which triggers accelerated crystal growth, can be a consequence of gas loss (Sparks & Pinkerton, 1978; Lipman et al., 1985), and the resulting increased viscosity will promote crustal autobrecciation. Degassing also causes development of high yield stress which would enable the formation of larger clots during shear brecciation. In addition, the porosity associated with high vesicularities greatly reduces the thermal inertia (the rate of response of the surface to heating or cooling) (Keszthelyi, 1994), and has been shown to promote rapid cooling in subaerial lava flows (Jones, 1993). Reduced thermal inertia in marine environments is likely to be a small effect compared with convective cooling, but nevertheless this connection between rapid degassing, rheology and the evolution of the lava surface may explain why Ballard et al. (1979) describe some hackly surfaces they tried to sample as a vesicular friable mass.

4.4.3.5 Rapid quenching prevents maturation of submarine flow morphologies

The heterogeneous clast size and the thinner layer of surface rubble seen on the deep-sea hackly and jumbled flows can be explained by the rapid quenching experienced by these flow surfaces. The underwater flows may have stopped moving relatively quickly after the downflow transition was completed, thus preventing high shear gradients and large stresses from acting for extensive periods of time. This hypothesis is supported by the short length of these hackly flows compared with many subaerial aas and can be related to the rapidly changing rheology of the lavas as they flow.

4.4.3.5.1 Effect of rapid quenching on clast size

The size of clasts formed by shearing of the lava surface is related to the slip line curvature, which itself is dependent on the changing rheology of the lava. (Kilburn & Guest, 1993). The change from even to cleaved crustal morphologies occurs as a lava moves downstream and acquires a more non-Newtonian behaviour. If the viscosity drops abruptly above a critical shear stress, then deformation will tend to concentrate

along cross-cutting slip lines isolating zones or lumps of the more slowly deforming lava. The size of the lumps depends on the curvature of the slip lines. Larger critical stresses favour larger mean clast sizes.

4.4.3.5.2 Effect of rapid quenching on clast heterogeneity

The number of clasts formed by shearing is governed by the viscosity. High viscosities slow the flow along the slip lines, and inhibit the upward twisting of the lumps that causes them to break off and form rubble. The heterogeneous clast size and the lack of surface rubble on hackly surfaces is consistent with deep-sea flows having a rheology which rapidly changes from Newtonian to non-Newtonian during a short period of active crustal deformation. Hence, at the time that the crust became frozen in its final form the surface texture of the flow preserves features suggestive of a highly variable rheology. In contrast subaerial aa flows, which continue deforming at high viscosities for a longer period of time, will show more uniform breccia mostly composed of larger lumps (figure 4.8).

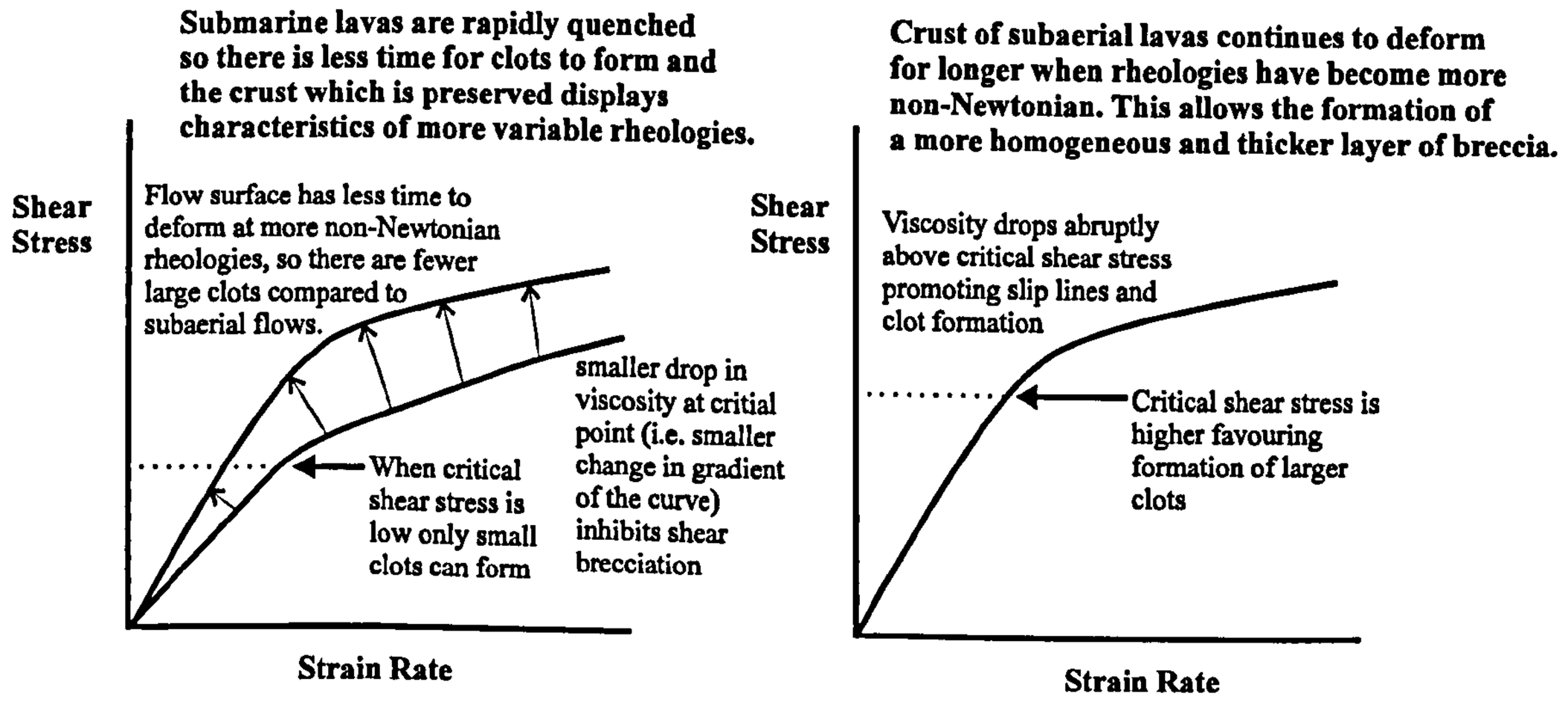

Figure 4.8 Sketch to illustrate the hypothetical differences in changing lava rheology that affect the formation the rubble layer of deep-sea, hackly flows compared with subaerial aa flows. (No scale implied.)

4.4.3.6 Changes in effusion conditions: explanation of hackly to lobate transition

The main problem with drawing on analogies with the pahoehoe - aa transition is the well documented observation of the hackly to lobate transition, when aa - pahoehoe transitions do not occur on land. A mechanism that can reconcile this issue is described below.

Firstly, Kilburn (1990) has observed that the state of the surface emerging from a bocca *can* actually vary from ropy pahoehoe to aa and back again. This happens where a smooth lava is erupted before a hackly patch and is carried downflow in front of the hackly surface so that there is an apparent transition, but in fact the smooth surface has never been previously disrupted. Kilburn (op.cit.) observes that when a lava is close to the transitional boundary, significant changes in crustal morphology may be triggered by very small, undetectable differences in effusion conditions.

He suggests that the pre-chilling history of a lava can be responsible for such syn-eruption transitions. Factors such as the position of a lava pocket in the parent flow and the flow duration are critical to the crystallisation kinetics as they control the degree of undercooling a lava experiences before it is chilled (Chalmers, 1964; Kirkpatrick, 1976; Dowty, 1980). This in turn is crucial in determining the small scale textural development of a lava, as the fast crystallisation rates, which occur for large degrees of undercooling, cause growth of stubby spines instead of the filaments associated with pahoehoe.

4.4.4 Causes of similarities and differences between subaerial and deep water basalt eruptions

As much of the discussion above draws on parallels between subaerial and deep-sea eruptions, it is important to consider the differences in ambient conditions between these two environments and their effect on factors such as rate of shear strain, lava rheology and kinetics which govern transitions like that from pahoehoe to aa (Peterson and Tilling, 1980; Kilburn, 1990; 1993).

4.4.4.1 Importance of quenching

A blacksmith quenching incandescent iron in a bucket of water demonstrates the most significant difference between these two environments: that things cool faster in water than they do in air. Griffiths and Fink (1992a) estimate that the time for a subaqueous lava surface to cool from an eruption temperature of 1423 K to the glass transition temperature is 0.07 seconds. The change from the near Newtonian behaviour (characteristic of aphyric basaltic magma prior to eruption) to a rigid crust will occur much faster in the subaqueous environment than in a subaerial one. Once chilling occurs the crust will quickly become strong and subsequent deformation will be restricted. In contrast, subaerial lava flows which cool more slowly will be mobile for longer while the rheology gradually becomes more non-Newtonian. Consequently, crustal autobrecciation is likely to operate over longer periods of time allowing more mature aa flows to develop.

4.4.4.2 Relative importance of radiation and conduction

Observations of subaerial lavas have shown that flow durations have magnitudes similar to the radiation timescale. This suggests that radiation-limited heat loss may govern flow lengthening on land (Crisp & Baloga, 1990).

For deep marine eruptions the rate of heat loss during the incandescent stage, where radiation is dominant, is different from that in air as the surface emissivity of the lava and surrounding superheated water is not the same as a lava/air interface. However, this is a largely negligible factor as convective heat transport is the dominant mechanism for heat loss in submarine eruptions, with radiation contributing only about 4% to the surface cooling (Griffiths & Fink, 1992a). The conductive thermal boundary layer of superheated water next to the surface of the lava rapidly (within 1 second) becomes unstable and is swept away by turbulent convection (Fink & Griffiths, 1990). During quenching, this convective transfer of heat away from the surface of the flow by water (with no boiling) is considerably more rapid than that by air.

The heat fluxes expected in submarine environments are more than an order of magnitude greater than those of subaerial eruptions (up to 5000kWm^{-2} compared with ~250kWm^{-2} -Griffiths & Fink, 1992b). As a consequence, single flows erupted under subaqueous conditions should have shorter durations and hence also shorter lengths. The sheet flows observed in this study are considerably less extensive than the several kilometres typical of subaerial aa flows (Kilburn, 1993). However, there are other factors apart from solidification time, such as effusion rate and availability of lava, that can affect flow length. Sheet flows on faster spreading ridges are more extensive than those observed in this study, implying that there are indeed other important parameters which govern flow length.

4.4.4.3 The Leidenfrost effect

The thin-skinned mode of surface deformation over wide areas of sheet flow implies that, to a certain extent, cooling and crustal thickening are not as instantaneous as might be expected. The persistence of incandescent material underwater for several seconds has been observed during pillow growth (Tepley & Moore, 1974). Griffiths and Fink (1992a) suggest that this visible radiation penetrates from the hot interior through a cooler glassy crust before it becomes opaque. Mills (1984) invoked the involvement of the Leidenfrost effect to explain the persistence of incandescent material underwater for several seconds.

The temperature contrast between erupted lava and seawater is great enough for non-nucleated film boiling to take place, which causes a gaseous film to coat the surface,

forming an insulating layer. Dissolution of superheated steam is known to substantially reduce the viscosity of a silicate melt (Sparks & Pinkerton, 1978) so giving the appearance of an elastic skin (Mills, op. cit.). The Leidenfrost effect will only act to insulate the flow while the surface is replenished by fresh lava, which will radiate sufficient heat to maintain the superheated water film. However, at water depths of 3.6 to 4.8km, the influence of the Leidenfrost effect on deep marine eruptions will tend to be reduced. The pressure at these depths should be greater than that for the critical point of seawater, where the gaseous phase is so compressed that the Van de Waals forces between molecules are still acting, so there is strictly no phase transition from liquid to gas. Instead, superheated water will form the boundary layer, but it will be minimally effective as an insulating layer because its thermal conductivity is considerably higher.

4.4.4.4 Effect of degassing

4.4.4.4.1 Hydrostatic pressure and inhibition of steam reactions

Another major difference between subaerial and deep-sea eruptions is the hydrostatic pressure which confines the deep-sea eruption. Bonatti and Harrison (1988) have calculated that this additional pressure is minimal compared with the stresses induced within the flow by cooling. However, the remarkable similarities between these deep water flows and subaerial forms can partly be explained by the effect of pressure on inhibiting explosive steam reactions (McBirney, 1963).

4.4.4.4.2 Difference in volatile contents

Volatile contents tend to be fairly low in MORB. Water ranges from 0.25-1.0 wt.% (Moore, 1965), which is consistent with saturation at 300-400 bars, but CO_2 is generally oversaturated (Dixon et al., 1988; Stolper & Holloway, 1988) implying that most MORBs rise too quickly from the magma chamber to maintain equilibrium. The few rare occurrences of popping rocks (which have undergone essentially no volatile loss prior to eruption) indicate that for the majority of MORBs, pre-eruptive volatile loss is a significant form of degassing (Gerlach, 1989; Sarda & Graham, 1990).

The magmas delivered to hot spot volcanoes which erupt subaerially, have higher CO_2 contents and discharge proportionally more CO_2 by magma chamber degassing (Gerlach, 1989). Hence, the volatile loss on eruption at a MOR is also likely to be lower than in Iceland and Hawaii, where fire fountaining and formation of large vesicles are associated with more extensive degassing under atmospheric pressure. The pressure increase caused by expansion of volatiles in the magma chamber is one factor which leads to faster flow rates during eruption. The endogenetic forces at the ridge may be at the lower end of those observed in subaerial eruptions because volatile

loss on eruption is less. In addition, magma supply rate, which also affects effusion rate, flow duration, and volumes, is greater for subaerial environments such as Iceland.

4.4.4.4.3 Effect of volatile solubility

The extent of volatile solubility is greater at the high hydrostatic pressures of the deep sea than at atmospheric pressure (Scarfe, 1973; Yoder & Tilley, 1962; Hamilton et al., 1964). However, the effect of volatile content on viscosity is quite small for magmas of basaltic composition (Williams & McBirney, 1979), so that an H_2O content of up to 4% does not significantly decrease the viscosity compared with a dry melt of the same temperature.

4.4.4.4.4 Degassing and pervasive crystallisation

Degassing on eruption does cause undercooling which induces pervasive crystallisation with a resultant stronger increase in viscosity and non-Newtonian behaviour. This has a far greater effect on subaerial magma rheology than atmospheric cooling, which penetrates into lavas only slowly because of their poor thermal conductivity (Sparks & Pinkerton, 1978). However, unless the degassing and pervasive crystallisation occurs in the magma before it comes into contact with the water, it is not likely to have an effect on the crustal morphology, as the quenching time is considerably less than the time required for homogeneous or even heterogeneous nucleation to take place (Griffiths & Fink, 1992a).

4.4.4.5 Other parameters

Other parameters which affect lava rheology are temperature, composition and extent of polymerisation (Dragoni, 1993). Although the temperature and compositional range tends to be greater in subaerial environments, values for the MOR should fall within the spectrum observed for subaerial eruptions. Polymerisation will tend to increase with pressure, but the nature and importance of its influence is not understood at present (Dragoni, 1993). The rate of shear strain is affected by aspects of the terrain such as ground slope as well as physical attributes of the flow. The range of ground slopes should be similar for the sea floor and subaerial environments. Bonatti and Harrison (1988) calculated that for small values of slope, the downslope stresses are virtually negligible compared with the stresses induced by cooling.

4.4.5 Measurement of deep-sea flow parameters

The differences discussed above between the deep-sea and subaerial environments are fairly speculative because, until very recently, an active deep-sea eruption has never been observed. Even on land, reliable quantitative data for flow parameters are lacking, rheological measurements are poorly constrained (Pinkerton, 1993) and there

is still some dispute about mechanisms and the relative importance of different parameters. Video and photographic data for the Coaxial event, an eruption on the Juan de Fuca Ridge in June 1993, have been analysed by Gregg and Fink (1994), and although no measurements actually exist, an attempt has been made to infer the flow parameters from this eruption. The results from this are consistent with my observation and subsequent discussion.

4.4.6 Summary and implications

After the consideration of the many factors that can theoretically affect lava morphologies, I conclude that quenching in the deep-sea environment is the main cause of morphological differences between subaerial and deep-sea flows. The shape and character of lava flows play a large part in controlling the shape and character of the volcanic edifices that they form. Hence I suggest that one of the main causes of differences between the volcanic morphologies described in this study and analogous volcanic features on land is the rapid quenching of basalt in the deep sea. I will return to this issue in chapter 7, where I present a comparison between crustal accretion in MARNOK and Iceland.

4.5 Variations in volcanic morphologies.

In chapter 3 I described the main categories of volcanic morphologies that make up the ridge crest. In this section I describe some of the more interesting and unique features which will prove useful in the later interpretation of flat-topped seamounts and hummocky ridges and their respective magmatic plumbing.

4.5.1 Thatcher's Nose

4.5.1.1 Sidescan morphology

A 4km long chain of 5 distinctive composite seamounts named Thatcher's Nose seems to be an extreme end-member form of a hummocky ridge (figure 4.9). Although each seamount is a discrete entity, they are clearly related by their similar morphologies, being conical composite domes formed by an agglomeration of small, rounded hummocks (<100m diameter). This is probably an example of a fissure eruption which has almost completely focused into regularly spaced centres. The seamounts are up to 1km across, about 100m-200m high, and are topped by summit cones with slopes of 25^{o} to 30^{o} which can provide up to another 100m of relief. The spire-shaped shadows which are cast by these summit cones (particularly the northernmost one) give 'Thatcher's Nose' its name.

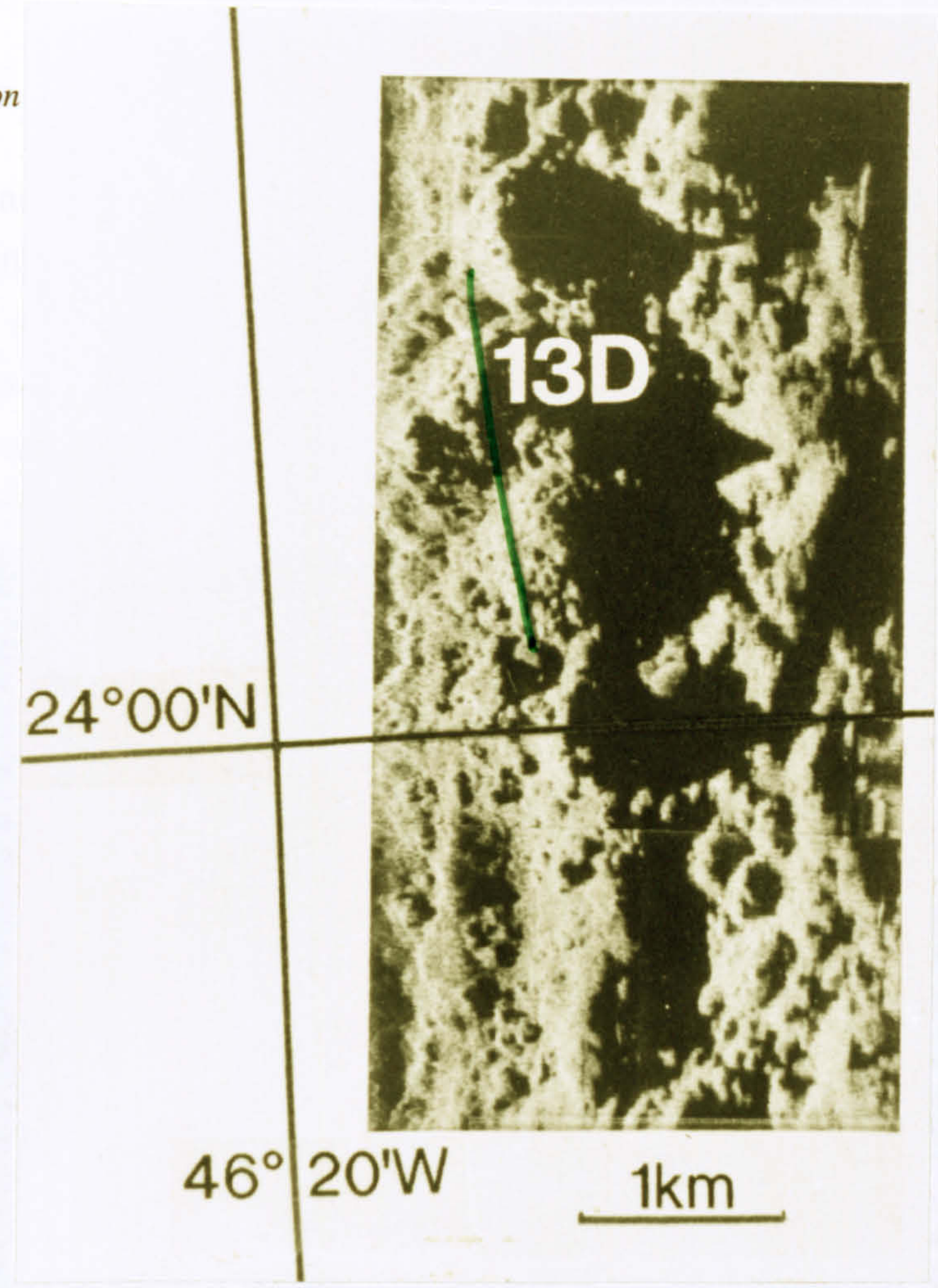

Figure 4.9 Linear alignment of composite hummocky volcanoes. Thatcher's Nose, the site of D13 is in the north of the frame. The 'Nose' refers to the sharp, spire-like shadow of the summit cone.

4.5.1.2 Highly phyric samples from 'Thatcher's Nose'

A dredge across Thatcher's Nose (D13) recovered samples which also proved to be unique within the sampling programme in terms of their composition and in particular their modal mineralogy, having approximately 3% olivine phenocrysts and 40% modal plagioclase megacrysts—about 20% more than from any of the other stations (figure 4.10; figure 4.11).

All the larger fragments are tabular in shape and up to 4cm thick with a thin (<5mm) rim of glass on the slightly convex upper surfaces. One sample comprises three of these tabular units stacked vertically. Each layer is 1.5cm thick with an upper 5mm of glass. The bottom 5-10mm of each layer, which is in contact with the glass of the layer below, is strongly oxidized giving the sample an orange banding.

4.5.1.3 Petrography of Thatcher's Nose

The megacrysts in these rocks have very rounded margins and sometimes embayed edges characteristic of resorption. A small number of megacrysts display considerable resorption and melt impregnation along the cleavage planes. The megacrysts have

little or no quench rim and quench microphenocrysts are also negligible in the surrounding glassy groundmass. The complete lack of quench growth implies that this rock was quenched while it was still above the liquidus temperature (i.e. the basalt magma itself was hotter than most lavas). It is unlikely that the absence of quench growth was primarily a result of kinetic factors, as the abundant megacrysts provide ample sites for heterogeneous nucleation.

Figure 4.10 Rock samples dredged from Thatcher's Nose are tabular slabs and cobbles all with about 40% modal plagioclase. Field of view is 35cm x 23cm.

This sample also contained about 3 modal percent of large (up to 7mm in diameter) pristine olivine phenocrysts. These also contain melt inclusions with similar characteristics to those found in the plagioclase megacrysts. The olivine is sometimes included within the plagioclase megacrysts, but it also occurs as individual, discrete phenocrysts in a way that is not commonly observed elsewhere.

4.5.1.4 Geochemistry of Thatcher's Nose

The whole-rock data are dominated by predictable signatures of plagioclase accumulation, but glass probe data show that the basaltic host is actually one of the most primitive lavas sampled within the MARNOK data set (MgO ~ 8.35%) Primitive lavas have higher temperatures than fractionated lavas, which accounts for the relatively high eruption temperature of the sample as indicated by the lack of quench growth described in section 4.5.1.3. The geochemistry of Thatcher's Nose will be discussed further in chapter 6, where it is related to the rest of the MARNOK area.

Figure 4.11 Photomicrograph of sample from Thatcher's Nose (13D-1-1b), which comprises 40% modal plagioclase megacrysts and about 3% olivine phenocrysts. The megacrysts have rounded and embayed margins and some show resorption along cleavage planes. The groundmass is glassy with no quench microphenocrysts. Field of view is 12mm x 7.2mm.

4.5.1.5 Eruption of highly phyric lava

The high modal percentage of phenocrysts causes a dramatic increase in the viscosity of the lava (Shaw, 1969; McBirney & Murase, 1984; Marsh, 1989; Dragoni & Tallarico, 1994) The modal mineralogy of Thatcher's Nose is particularly interesting because Marsh (op. cit.) predicts that magmas with any more than 25% crystallinity are unlikely to erupt because of their high viscosity (about 10 times more viscous than their liquidus composition). This prediction was confirmed by Bryan (1983) who showed that very few normal MORBs have greater than 25 vol.% phenocrysts. With 40% megacrysts, these rocks would fall well within the mush zone of Sinton and Detrick (1992), and in fact are not far from the rigidus (~50-60% crystals).

The ability of these magmas to erupt was probably enhanced by the primitive nature of the basalt host. A basalt which has itself crystallised 40% would have a relatively fractionated composition and would have cooled considerably from its liquidus temperature. However, in the case of Thatcher's Nose, the high crystal content is a

result of accumulation and the relatively high temperatures of the host magma will reduce the viscosity of the mixture enabling it to erupt.

4.5.1.6 Effect of high viscosity magma on volcanic morphology

It seems unlikely that a recovery of such unusual petrological specimens from a seamount with such a highly distinctive morphology is coincidental.

The high viscosity of the Thatcher's Nose lavas will have consequences for the flow attributes, affecting the rate and distance a flow is able to move. The high viscosity extrusive is not likely to spread easily and will tend pile up around the vent, forming the short flow units characteristic of the edifice.

The near-complete focusing which occurs at Thatcher's Nose compared with the partial focusing seen at other hummocky ridges may either be a consequence of the high viscosity lavas or the result of a small vertical extent of feeding dyke[1] (Bruce & Huppert, 1990). The spacing between the distinct mounds of Thatcher's Nose ranges from about 0.8km to 1.5km. The strong vent focusing along the line of the fissure suggests that the dyke may penetrate to depths approximately equivalent to the spacing of this focusing. However, the common height of the peaks is ~200m which, using magmastatic arguments, would give a depth to the top of the magma chamber of ~3km (from figure 8 of Smith & Cann, 1992)[2]. If the dyke had originated from only 1.5km depth then the seamounts of Thatcher's Nose would not have been able to grow to this height. Hence, it seems likely that the high viscosity of the lavas is main factor contributing to the unusual three-dimensional evolution of the fissure eruption.

Field studies have shown that high viscosity lavas tend to form larger pillows (Walker, 1992). This is inconsistent with the morphology of the samples, which suggests that the highly phyric lava erupted as a succession of thin sheet-like units. However, the modelling of Bonatti and Harrison (1988) suggested that the thickness of a lava flow should be independent of its viscosity. Hence, perhaps the sample morphology is not inconsistent with the hypothesis that Thatcher's Nose formed as a composite mound of short viscous flows.

---

[1]The interaction between vent focusing points along an eruptive fissure becomes negligibly small (i.e. there is complete focusing) if the vent separation exceeds the vertical extent of the dyke (Bruce and Huppert, 1990).

[2]Smith & Cann (1992) assume an exponential density increase with depth to calculate values of magma chamber depths which correspond to varying seamount heights. The exponential parameter λ, is estimated at 2.3×10^3 m^{-1}, based on the porosity distribution with depth in hole 504B (Becker, 1985). Using this porosity distribution, a graph of seamount height against depth to the top of the magma chamber was generated (figure 8 of Smith & Cann, op. cit.).

4.5.2 Flat-topped seamounts

The evidence from the previous chapter suggests that flat-topped seamounts comprise low relief pillow flows, with some sheet flows. This suggests that the main difference between the flat-topped seamounts and the hummocky terrain is the gross morphology of their constituent lava flows and the manner in which these flows build up to form the constructional features. The following section will look at varying aspects of the volcanic morphology of these seamounts that help us to understand their formation.

4.5.2.1 The nested seamounts —point source pulses

The three flat-topped 'nested' seamounts have erupted in a non-linear relationship with their centres at an angle of 100°, 800m apart (figure 4.12 i). Each seamount maintains its circular plan form despite the 10% overlap with the adjacent seamount. This morphology suggests that the focus of point source volcanism has moved in *discrete pulses* from north to south and then across to the east. In addition this morphology may indicate that the flat-topped seamounts are formed in relatively short periods of time, as the three component edifices are all similar ages and yet seem quite discrete and show a clear age progression.

An analogy to the nested seamounts is provided by the Lamont Seamounts within the Pacific. These are thought to be formed by highly focused buoyant magma which reaches the surface through pipe conduits (Barone & Ryan, 1990). The caldera of the mature, composite Mokuaweoweo (MOK) seamount in this chain comprises a number of coalesced craters which reflect the migration of the primary magmatic conduit beneath the summit region. The spacing between adjacent craters is about 1.5 - 3km, which is greater than that observed between the centres of the nested seamounts. However, given that the dimensions of the Lamont Seamounts are nearly an order of magnitude greater than those of the MARNOK seamounts, the spacing of the nested centres compared with the volume of magmatism is relatively large.

Barone and Ryan (1990) suggest that MOK formed as a result of the arrival of a close succession of short-lived magmatic plumes, each comprising a number of geochemically distinct diapirs (Fornari et al., 1988a & b). The pit craters which occur within the main craters are thought to indicate the positions of upper feeding pipes in the plumbing system (Fornari et al., 1984) and may be related to the arrival of successive diapirs. The morphology of the nested seamounts is consistent with formation from three distinct diapirs which are in close proximity in space and time.

Unlike the hummocky ridges and seamount chains such as Thatcher's Nose, the lack of linearity of the nested seamounts suggests that they are not related to a single fault or fissure. However, they are situated at the junction of the two segments where

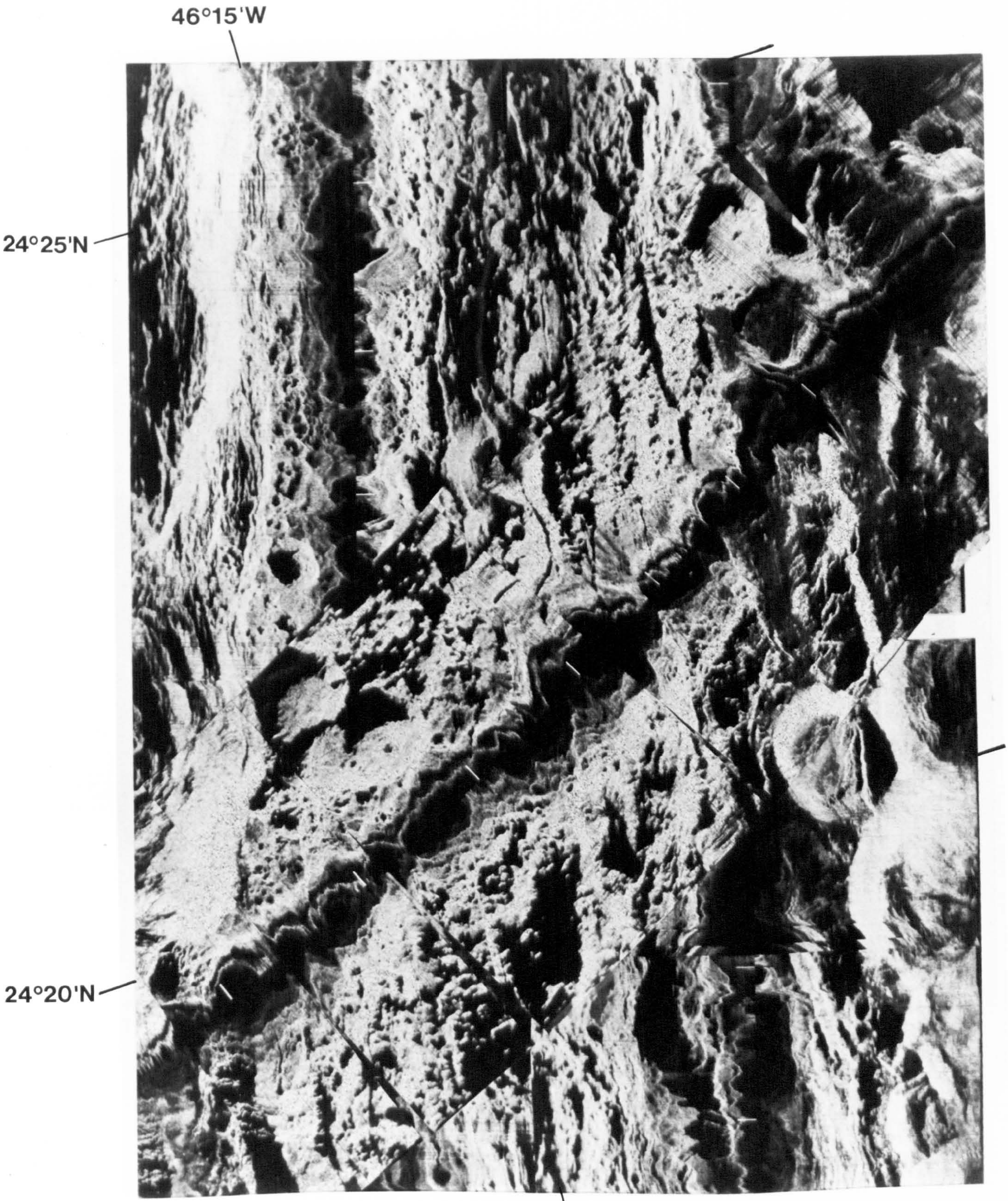

Figure 4.12a Sidescan mosaic of the area around the junction of segments 1 and 2.

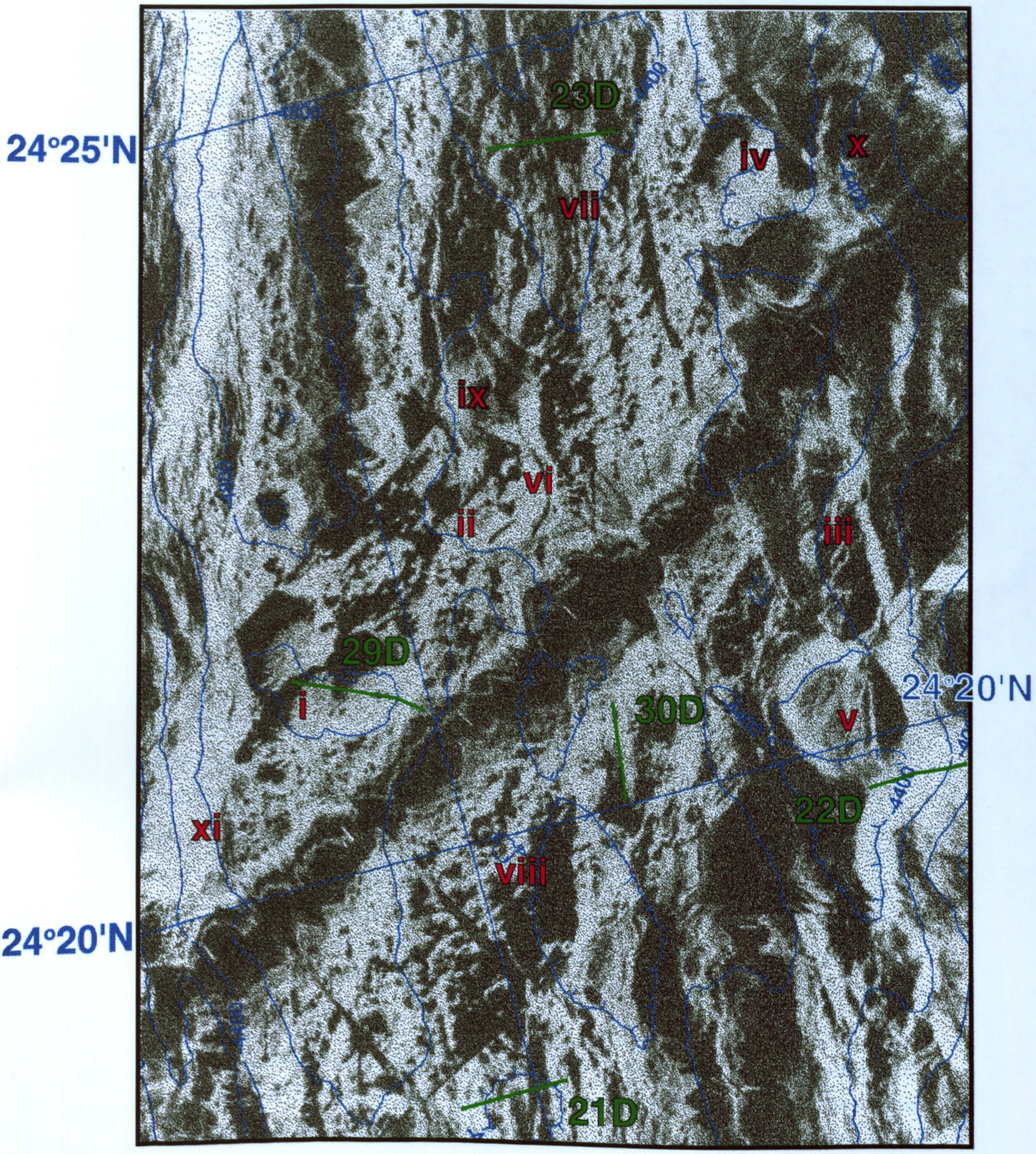

Figure 4.12b Positions of dredge sites 21D, 23D, 29D and 30D are marked. The following features are to be noted from figure 4.12a and are discussed in the text: (i) three nested flat-topped seamounts; (ii) oblique fractures cutting seamount have the same orientation as the oblique eastern wall fault; (iii) fault splays trending in same orientation as oblique fractures in the centre of the valley; (iv) flat-topped 'mantled' seamount surrounded by a rim of brightly backscattering hummocky terrain in highly sedimented, eastern marginal basin; (v) older flat-topped seamount with faulted eastern flank; (vi) cratered cone on summit of faulted seamount; (vii) axial fissure along crest of NVR of segment 2; (viii) N-S fault cutting hummocky terrain at end of segment 1 divides the main body of the NVR from the kinked tip; (ix) flat-topped seamount dissected by fault in centre of median valley; (x) sediment slumping on eastern wall; and (xi) landslide on western wall.

tectonic failure in two orientations is demonstrated by faults on both the valley walls. Oblique structures are also present in the NVZ (figure 4.12 ii & iii). It is possible that the unique structure of the nested seamounts is the result of the interaction of diapirs with two intersecting fracture systems, which provide some structural control on the path taken by the ascending magma. Vogt (1974b) has suggested that the position of some of the larger seamounts in the Pacific is controlled by the intersection of major crustal fractures. The same may apply here, on a smaller scale. This issue will be pursued further in section 4.8.

4.5.2.2 The mantled seamount —satellite volcanism

The initiation of satellite volcanism is thought to play an important part in the subsequent morphological development of a seamount (Fornari et al., 1984). Studies from the Pacific have often located areas of satellite volcanism around the base of seamounts (Batiza & Vanko, 1983; Searle, 1983), though usually the seamounts in question are larger than those of the MARNOK data set. The cones and lava fields surrounding the seamount provide an alternative extrusive site to the seamount summit which serve to drain off magmas and precipitate summit collapse. Eruptions with the lower magmastatic heads will preferentially erupt round the flanks, producing an effective bias to summit eruptions with greater endogenetic forces and rapid effusion rates (Fornari et al., 1984). The rapid effusion rates are more likely to produce a smooth-textured volcanic morphology. Barone and Ryan (1988) have reported a tendency of lava morphology to evolve from pillow to ropy pahoehoe and hyaloclastite as the summit plateau expands. Hence there is a link between the presence of satellite volcanism and the formation of a smooth-topped seamount.

As the sidescan data do not differentiate particularly well between the relative ages of the volcanism within the NVZ, it is usually not possible to discern whether the hummocky terrain surrounding the flat-topped seamounts is a possible candidate for satellite volcanism, or represents an entirely separate eruptive episode. There are two lines of evidence that do support the magmatic connectivity of flat-tops and the surrounding volcanic terrain.

The first, and best, is the positive identification of a flat-topped seamount surrounded by a mantle of hummocky terrain of similar age (figure 4.12 iv). This seamount, named the 'mantled seamount', is a prime candidate for satellite volcanism. In this case the hummocky mantle is recognisable because the seamount has erupted on the sedimented edge of the median valley, so the recent volcanism contrasts with the adjacent low backscatter.

On a first order estimate, the terrain immediately underlying the flat-topped seamounts tends to be of comparable age to the seamounts themselves. For instance, in the NTO

area, the older faulted seamount at the base of the eastern wall (figure 4.12 v) is situated on very poorly backscattering, highly sedimented crust, while the younger nested seamounts (figure 4.12 i) are underlain by undisrupted hummocky terrain. However, it must be noted that the amplitude of returns from the summit plateau of the older seamount are not as low as those from the immediately surrounding seafloor. This may be because the latter is more susceptible to sediment accumulation by downslope transport from the valley wall. Alternatively, the seamount is in fact slightly younger and there is no satellite volcanism of comparable age.

An alternative interpretation of the mantled seamount is that the hummocky rim represents a transitional stage between the hummocky mounds and the flat-topped seamounts. This is the only evidence within the MARNOK area that these two morphologies may be related, as is discussed further in section 4.6.6.

4.5.2.3 Large crestal seamount —fracture control

The largest flat-topped seamount in the MARNOK area is located astride the crest of the NVR in the north of segment 2 (figure 4.13 iii) and hence has been named the 'crestal seamount'. It is about 2.5km in diameter and occupies a central position over a syn-magmatic structure that extends for about 15km along the strike of the NVR (figure 4.13 iv - v - vi - vii).

It differs from the other flat-topped seamounts in its size and its location—most are situated on the edge of the median valley, at the ends of segments. The seamount is a relatively old feature with a poorly backscattering summit plateau and a fractured western flank. (This is an inward dipping fault plane, not a ring fracture, as the latter would have a more concentric form.) The texture of the summit plateau also differs from the other flat-tops of the MARNOK area. The summit plateau is ~1.5km in diameter; with an elevated western rim and a central summit depression, about 1km in diameter. To the east the smooth-textured summit grades into hummocky pillow mounds and there is no steep smooth-textured, curving flank on this side of the NVR. Thus, although this seamount has a very broad flat summit plateau, it is no higher than the surrounding hummocky terrain. It obviously represents a larger eruptive episode than the flat-topped seamounts at the ends of a segment, consistent with its location in the centre of the NVR. I suggest that the presence of the large syn-magmatic ridge is crucial to the origin of this seamount, as will be discussed further in section 4.8.11 and also in chapter 7.

This is not the only flat-topped seamounts to lie astride a fault, In fact, in the MARNOK area all the larger seamounts in the median valley floor overlie faults (e.g. figure 3.1—seamount v overlies fault xv). Many of the others lie adjacent to the

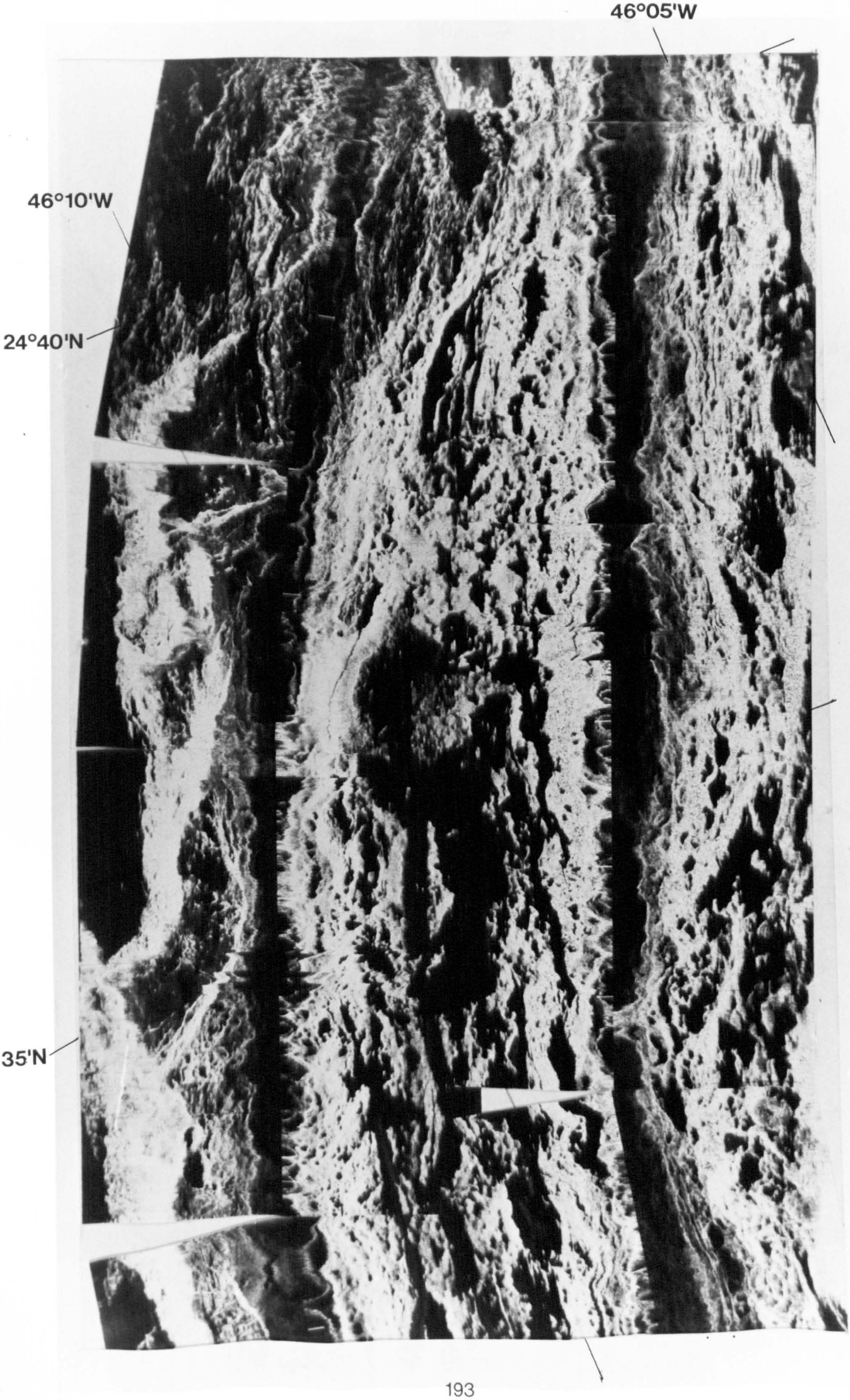

Figure 4.13a Sidescan mosaic of northern end of segment 2.

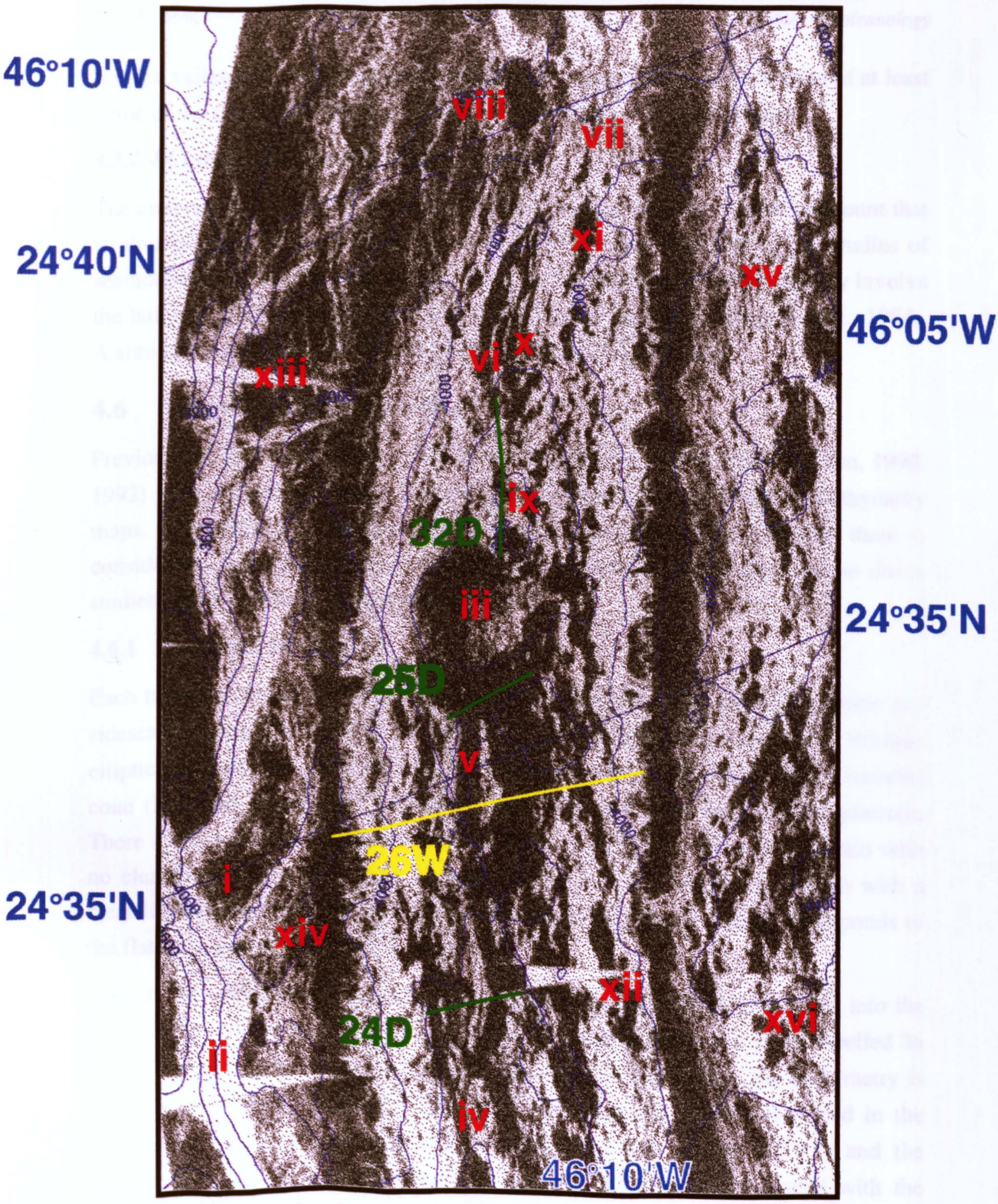

Figure 4.13b Positions of dredge sites 24D, 25D, 32D and WASP traverse 26W are marked. The following features are to be noted from figure 4.13a and are discussed in the text: (i) Lensoid sedimented horse block at base of the wall is formed as the fault tip curves to link with adjacent scarps; (ii) talus fan has prograded out to form a brightly backscattering convex toe at the base of the valley wall fault; (iii) large, flat-topped crestal seamount; (iv) southerly extent of syn-magmatic fault, which can be traced through (v), under the centre of the crestal flat-topped seamount to (vi) where it bends to the NE towards its northern termination at (vii); (viii) at the north of segment 2 there is no wall fault, but the crust is heavily fissured and sedimented; (ix) highly backscattering bathymetric summit of the NVR; (x) sharp faulted ridge, colinear with the summit ridge, emerges from beneath the hummocky terrain and is buried by further pillow flows at (xi); (xii) en-echelon set of faults formed on the eastern flank of the NVR as the valley opens out into the right lateral oblique zone; (xiii) heavily sedimented marginal basin; (xiv) marginal basin further south contains sedimented pillow flows; (xv) younger fissured crust located to the NE of the NVR, where the valley opens out into the oblique zone; and (xvi) untectonised crust in the eastern marginal basin, adjacent to the curving boundary fault.

median valley walls. Allerton et al. (1995) have suggested that the extrusion of at least some of the flat-topped seamounts is controlled by the valley wall faults.

4.5.2.4 Cratered cones —late stage volcanism

The cratered cone (figure 4.12 vi) has erupted onto an older flat-topped seamount that is already about 100m tall and is cross-cut by fractures (figure 4.12 ii). Studies of seamounts in the Pacific have suggested that the final phase of volcanism may involve the building of a rough conical mound over the summit plateau (Fornari et al., 1984). A similar process, but on a smaller scale, may have occurred here.

4.6 Seamount shape statistics.

Previous studies of seamounts on the MAR (Batiza et al., 1989; Smith & Cann, 1990; 1992) have focused on shape, size and distribution, based on SeaBeam bathymetry maps. The sidescan sonar gives additional textural information, although there is considerably less areal coverage available in the MARNOK area than in the above studies, so the statistical significance is limited.

4.6.1 Seamount categories

Each tabulated seamount was categorised in terms of the bathymetric description and sidescan texture. The bathymetric categories include elongated cone (EC - strongly elliptical plan shape), irregular cone (IC - sinuous and distorted plan shape), rounded cone (RC) and flat-top (FT - rounded cone with well developed summit plateau). There are three sonar categories: hummocky mounds (HM - hummocky terrain with no clear linearity on the sonar), hummocky ridges (HR - hummocky terrain with a clear linearity) and smooth tops (ST - smooth textured summit which corresponds to the flat-top category described in section 3.2.3).

Four of the edifices could not be given a sidescan category because they fall into the nadir region. On the tables and graphs below they are included as a group labelled 'In nadir', though their predicted sidescan morphology on the basis of the bathymetry is plotted as a symbol underneath. Thatcher's Nose (section 4.5.1) was placed in the hummocky ridges category while the nested seamounts (section 4.5.2.1) and the faulted seamount with the cratered cone (section 4.5.2.4) were included with the smooth tops.

4.6.2 Data tables

Table 4.4 contains data on seamounts situated within the inner median valley which have been calculated using method 1, adhering to the strict criteria of Batiza (1982), that more than 50m of relief is required on all sides (see section 2.2.4.2.1).

No	Latitude deg:min	Longitude deg:min	Basal diameter (m) long axis	Basal diameter (m) short axis	Summit diameter (m) long axis	Summit diameter (m) short axis	Aspect ratio AR	Azimuth of long axis (degrees E)	depth of base (m)	depth of summit (m)	depth of summit plateau	summit height (m) sh	cone height (m) ch	rb:average basal radius (m)	rs:average summit radius (m)	flatness f rs/rb	ξ sh/rb	ε	ϕ	Volume v (km3)	bathymetric description	sidescan description
1	23:54	313:36	750	425	250	150	1.8	14	4720	4660	4680	60	40	294	100	0.34	0.20	0.21	11.7	0.005	EC	HR
2	23:57	313:42	1750	1300	800	550	1.3	148	4600	4480	4500	120	100	763	338	0.44	0.16	0.24	13.2	0.100	FT	ST
3	23:58	313:40	2000	1450	200	150	1.4	36	4500	4420	4420	80	80	863	88	0.10	0.09	0.10	5.9	0.069	IC	HM
4	24:01	313:40	1350	800	500	250	1.7	23	4300	4240	4240	60	60	538	188	0.35	0.11	0.17	9.7	0.027	EC	Thatcher Nose
5	24:06	313:44	850	600	150	100	1.4	8	3820	3760	3760	60	60	363	63	0.17	0.17	0.20	11.3	0.010	RC	In nadir
6	24:10	313:41	1500	1050	325	250	1.4	24	3920	3840	3840	80	80	638	144	0.23	0.13	0.16	9.2	0.043	RC/EC	In nadir
7	24:11	313:43	1350	800	650	250	1.7	43	3960	3860	3880	100	80	538	225	0.42	0.19	0.26	14.4	0.039	IC	HR
8	24:13	313:45	1400	750	100	100	1.9	21	4180	4080	4080	100	100	538	50	0.09	0.19	0.21	11.6	0.033	EC	In nadir
9	24:14	313:42	1000	800	450	250	1.3	56	4100	4040	4060	60	40	450	175	0.39	0.13	0.15	8.3	0.013	IC	HM
10	24:18	313:43	900	900	500	500	1.0		4400	4320	4340	80	60	450	250	0.56	0.18	0.30	16.7	0.024	FT	In nadir
11	24:18	313:45	1250	1100	300	250	1.1		4420	4340	4340	80	80	588	138	0.23	0.14	0.18	10.1	0.037	RC/IC	HM
12	24:20	313:45	1000	800	250	150	1.3	24	4520	4460	4460	60	60	450	100	0.22	0.13	0.17	9.7	0.016	IC	HM
13	24:21	313:44	1450	750	950	250	1.9	113	4600	4520	4540	80	60	550	300	0.55	0.15	0.24	13.5	0.035	E	NESTED
14	24:22	313:45	1100	750	600	300	1.5	15	4500	4440	4460	60	40	463	225	0.49	0.13	0.17	9.6	0.015	RC	ST+CONE
15	24:23	313:46	1000	850	500	400	1.2		4500	4420	4440	80	60	463	225	0.49	0.17	0.25	14.2	0.023	RC	ST
16	24:27	313:49	800	750	200	125	1.1		4400	4300	4300	100	100	388	81	0.21	0.26	0.33	18.1	0.020	RC	HM
17	24:29	313:48	850	450	25	25	1.9	19	3700	3620	3620	80	80	325	13	0.04	0.25	0.26	14.4	0.009	EC	HR
18	24:29	313:46	850	650	125	125	1.3	18	4080	4000	4000	80	80	375	63	0.17	0.21	0.26	14.4	0.014	RC	HM
19	24:30	313:48	900	600	300	250	1.5	34	3640	3580	3600	60	40	375	138	0.37	0.16	0.17	9.6	0.009	EC	HR
20	24:30	313:49	1300	1150	300	300	1.1		3820	3740	3740	80	80	613	150	0.24	0.13	0.17	9.8	0.041	IC/RC	HM
21	24:31	313:49	650	450	100	50	1.4	112	3680	3600	3600	80	80	275	38	0.14	0.29	0.34	18.6	0.007	IC	HR
22	24:34	313:50	1150	600	100	50	1.9	28	3780	3700	3740	80	40	438	38	0.09	0.18	0.10	5.7	0.009	IC/EC	HR
23	24:34	313:49	1150	750	650	400	1.5	9	3840	3760	3780	80	60	475	263	0.55	0.17	0.28	15.8	0.026	EC	HR
24	24:35	313:51	875	775	400	200	1.1		3780	3720	3720	60	60	413	150	0.36	0.15	0.23	12.9	0.016	IC	HM
25	24:35	313:48	500	500	25	25	1.0		4080	4000	4020	80	60	250	13	0.05	0.32	0.25	14.2	0.004	RC	HM
26	24:36	313:51	500	500	100	100	1.0		3780	3720	3720	60	60	250	50	0.20	0.24	0.30	16.7	0.005	RC	HM

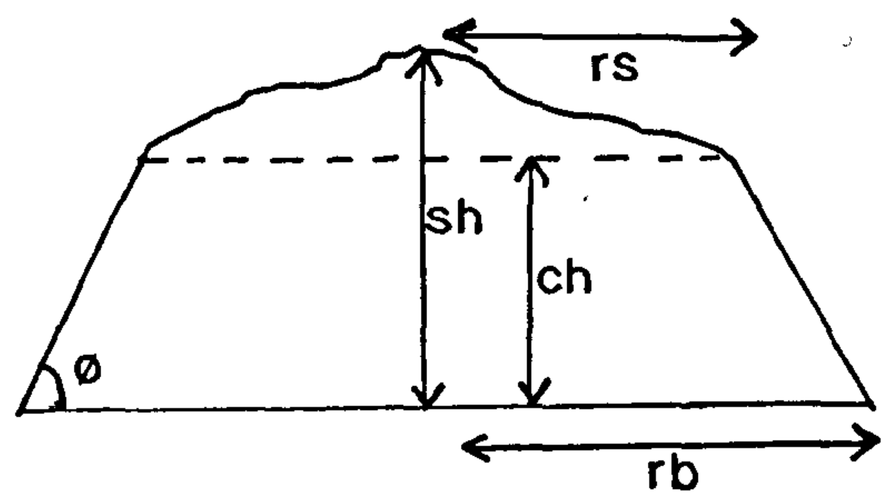

Table 4.4 Dimensions and parameters on seamounts situated within the inner median valley. which fit the criteria of having three or more closed contours with an aspect ratio of less than 2. The parameters which are not defined in the headings are ε (=ch/(rb-rs)); and ϕ, the angle of the right circular cone (=$\tan^{-1}\varepsilon$). The volume is calculated assuming a right-symmetrical truncated cone, v, (= $^{1}/_{3}\Pi(rb^{2}H\text{-}rs^{2}(H\text{-}ch))$ where H is the height of the untruncated cone (= rb x ε). The abbreviations for the bathymetric descriptions are EC - elongated cone (strongly eliptical plan shape), IC - irregular cone (sinuous and distorted plan shape), RC - rounded cone and FT - flat-top (with well developed summit plateau). The three sonar categories are HM - hummocky mounds, HR - hummocky ridges (hummocky terrain with a clear linearity) and ST - smooth tops (corresponds to the flat-top category described in section 4.1).

Table 4.5 contains data calculated using method 2, which uses concentric arcs in the contours to identify the steep flanks of flat-topped seamounts (see section 2.2.4.2.2). This table contains data on all the smooth-textured, flat-topped seamounts on the floor of the median valley (excluding one which is clearly considerably disrupted by a fault on the western wall of the nodal basin). In addition, table 4.5 contains information from the sidescan mosaics, such as descriptions of the flank and summit textures and the diameter of any summit depression or central collapse structure which is imaged by TOBI, but is beyond the resolution of the SeaBeam data. An estimate of the basal diameter and the diameter of the summit plateau are measured from the sidescan mosaics. These are compared with the values calculated from the bathymetry (see section 4.6.4.3).

4.6.3 Using method 2 to estimate parameters on the hummocky terrain

An attempt to apply method 2 to the hummocky terrain proved difficult because many hummocky mounds are situated on the crests and margins of hummocky ridges. As the relationship between these mounds and ridges is ambiguous from the sidescan, it is unclear whether they should be categorised together as a whole, single unit or as distinct and separate edifices. The contours defining the hummocky mounds tend to be more irregular and the flanks are not as steeply dipping and clearly concentric as those of the smooth-textured seamounts. Thus the limits of individual distinctive edifices are much less clearly defined and heights are impossible to estimate, owing to uncertainties as to whether an area of hummocky morphology consists of a single discrete edifice or a number of superimposed seamounts. The problems are compounded for hummocky ridges, where it is not only difficult to delimit the boundaries of separate distinctive edifices on the sidescan, but there is also no radial symmetry in the bathymetry to help to delineate the margins.

4.6.4 Comparison of seamount parameters for different methods

4.6.4.1 Seamounts falling outside the criteria for method 1

After examining the sidescan records it became clear that many of the distinct volcanic edifices imaged by TOBI were not included in the table of seamounts selected on the bathymetry criterion (method 1, table 4.4). The exclusion of these seamounts is largely owing to overlapping or adjacent volcanism, but in addition, some of the edifices were defined by one or two closed contours and hence just missed selection on the basis of the height criteria. As the 50m height cut-off was selected because of the limits of resolution, rather than for some generic reason, it should not be surprising that the trends previously recognised might extend to include

No	Position Latitude (deg:min)	Longitude deg:min)	Bathymetry (m) Basal depth	Summit depth	plateau depth	Basal radius Brb	Summit radius Brs	Summit height Sh	Cone height Ch	flatness f Brs/Brb	ξ Sh/Brb	ε	ϕ	Volume V (km3)	TOBI (m) Base radius Trb	summit radius Trs	diameter of summit depression	flatness f Trs/Trb	Texture of summit	Texture of flanks	S/m by definition ?
2	23:57	313:42	4700	4480	4500	975	350	220	200	0.36	0.23	0.32	18	0.299	900	588	375	0.65	Fine fault lineations cut the summit depression and the very smooth plateau. Poorly backscattering summit S/m is faulted on E side	On E side, fault runs underneath; On W, steep bright bs for 150m, beyond fan is less bright	y
10	24:18	313:43	4460	4320	4340	588	250	140	120	0.43	0.24	0.36	20	0.071					In nadir	In nadir	y
13a	24:21	313:44	4780	4580	4620	800	375	200	160	0.47	0.25	0.38	21	0.187	675	475	100	0.70	Nested s/m. Brightly backscattering	Very bright and smooth.	n
b	24:21	313:44	4660	4540	4580	700	275	120	80	0.39	0.17	0.19	11	0.067	563	413		0.73	(a) oldest, (c) youngest.	Hummocky ridge	y
c	24:21	313:44	4660	4520	4540	700	250	140	120	0.36	0.20	0.27	15	0.093	650	388	100	0.60	summit depression is clearest on (c); none on (b); faint on (a) All have irregular sinuous rim.	extends from s/m at 045	y
14a	24:22	313:45	4600	4440	4440	725	300	160	160	0.41	0.22	0.38	21	0.140	575	300		0.52	faulted	smooth high bs	y
14b	24:22	313:45	No bathymetric expression												263	138		0.52	cratered cone with deep shadow	slight low relief hummock	n
15	24:23	313:46	4600	4420	4420	600	225	180	180	0.38	0.30	0.48	26	0.103	625	300		0.48	poorly backscattering ridge //el texture; branching faults	Smooth high bs	y
27	24:36	313:50	3900	3640	3680	1150	550	260	220	0.48	0.23	0.37	20	0.533	1250	875	1000	0.70	highly backscattering rim on west poorly backscattering plateau with small gullies & some hummocks to E	smooth on W side fault to S, from NE: hummocky terrain	n
28	24:32	313:52	4260	4160	4200	300	200	100	60	0.67	0.33	0.60	31	0.014	400	250	100	0.63	smooth poorly backscattering abuts valley wall fault	smooth bright bs lava tube extending from rim?	n
29	24:24	313:48	4680	4560	4580	575	200	120	100	0.35	0.21	0.27	15	0.052	600	375	150	0.63	brightly backscattering; slightly irregular edges	v bright; smooth	n
30	24:20	313:47	4540	4320	4320	950	375	220	220	0.39	0.23	0.38	21	0.322	700	425		0.61	X-track:poorly backscattering; v diffuse hummocks	v smooth bright bs sharp downlap onto adjacent floor	n
	24:20	313:47													850	575	100	0.68	ridge //el: faults across E edge. More sedimented to East v smooth ; brighter than x-track	Bright smooth texture; perhaps some gullying	
31	23:53	313:39	5000	4840	4860	762.5	400	160	140	0.52	0.21	0.39	21	0.157	663	475	100	0.72	Moderately bs; slightly hummocky	Constructional: brightly bs, but no downlapping talus lava tube extends towards flanks	n
32	23:53	313:36	5100	4880	5000	800	213	220	100	0.27	0.28	0.17	10	0.095	575	250		0.43	V poorly bs; highly sed?	V bright, uniform downlapping onto surrounding volc terrain	n

Table 4.5 Dimensions and parameters for all the smooth-textured flat-topped seamounts on the floor of the median valley (excluding one which is clearly considerably disrupted by fault on the western wall of the nodal basin). The methodology for calculating the dimensions using radial concentric arcs in the contours is similar to that used by Smith & Cann (1992) and is described in the text and in figure 4.14. For each tabulated seamount there are descriptions taken from the sidescan of the flank and summit textures and the diameter of any summit depression or central collapse structure. An estimate of the basal diameter and the diameter of the summit plateau is also taken from the sidescan mosaics for comparison with the values calculated from the bathymetry. The flatness calculated from the sidescan dimensions is consistently greater than that taken from the bathymetry (see text for discussion) (bs = backscattering).

even smaller edifices. Method 2, with the aid of the sidescan for confirmation, provides a means of including these seamounts (numbers 27 - 32 in table 4.5).

Figure 4.14 demonstrates how method 2 uses semicircular concentric arcs in the bathymetry to define basal and summit radii for one of the above cases. Seamount number 30 is situated on the edge of the inner valley and its eastern flank is faulted so the adjacent slopes of the valley wall prevent the contours forming a complete closed circle around the volcano. Other seamounts recorded in table 4.5 which are not in table 4.4 include the large crestal seamount of segment 2 (number 27), the seamount with the mantled rim (number 29) and the seamount adjacent to the lava tube (number 31, figure 3.5).

4.6.4.2 Comparing bathymetric parameters from method 1 and method 2

The sidescan images indicate that the NVZ is constructed by the piling up of volcanic units. As a consequence, seamounts which are overlapped by later eruptions or abut existing volcanic terrain are not always defined by closed contours on the bathymetry maps. Smith and Cann (1990) recognised that their counts of seamounts from bathymetry criteria represent a minimum estimate of the actual population.

Hence, overlapping and adjacent volcanism results in method 1 giving anomalously small basal diameter measurements and shallow basal depth, although values for summit diameter are similar for the two methods (figure 4.15). Again method 2 seems to rectify this problem as demonstrated in figure 4.4. This shows seamounts 14 and 15 on the western edge of the NVR of segment 2. The parameters recorded using method 1 include only the closed contours of the summit plateaux, whereas the steeper western flanks form prominent semicircular bulges in the bathymetry which can be used in method 2 to give more realistic values for basal depth and diameter. Consequently all the parameters which are calculated using these measurements will also be different for the two methods. Examples include the cone angle (ϕ), height and volume measurements, which are smaller for method 1, while the flatness is greater.

It should be noted that although method 2 does provide more realistic data for the flat-topped seamounts, method 1 is still a fair means of comparing the smooth-top with the hummocky morphologies, as there is no reason why the smooth-tops should be overlapped by adjacent volcanism any more than the hummocky terrain. (In fact the smooth topped seamounts tend to be located at the ends of segments where they are *less likely* to be buried by adjacent eruptions).

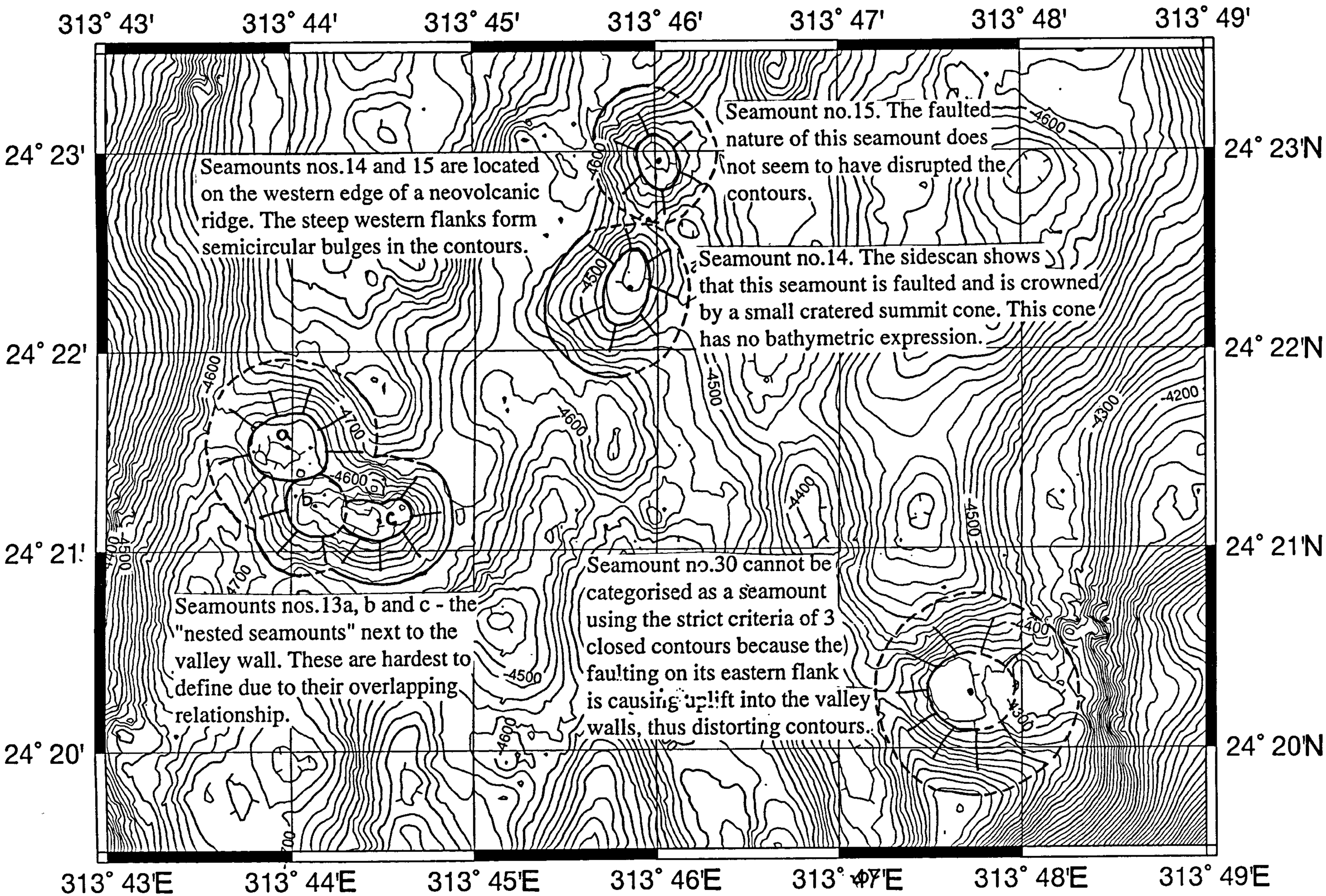

Figure 4.14 SeaBeam bathymetry coverage from the area around the 3rd order non-transform offset where many smooth textured flat-topped seamounts have been imaged on the sidescan sonar. The line interpretation uses a method similar to that of Smith & Cann (1992) and shows how seamount parameters can be estimated using concentric radial arcs in the contours to allow for adjacent volcanism and tectonism that disrupts the bathymetric expression of many seamounts. Seamounts identified on the sidescan can have dimensions measured using this method when they do not fall into bounds of the rigorous criteria used in method 1.

a)

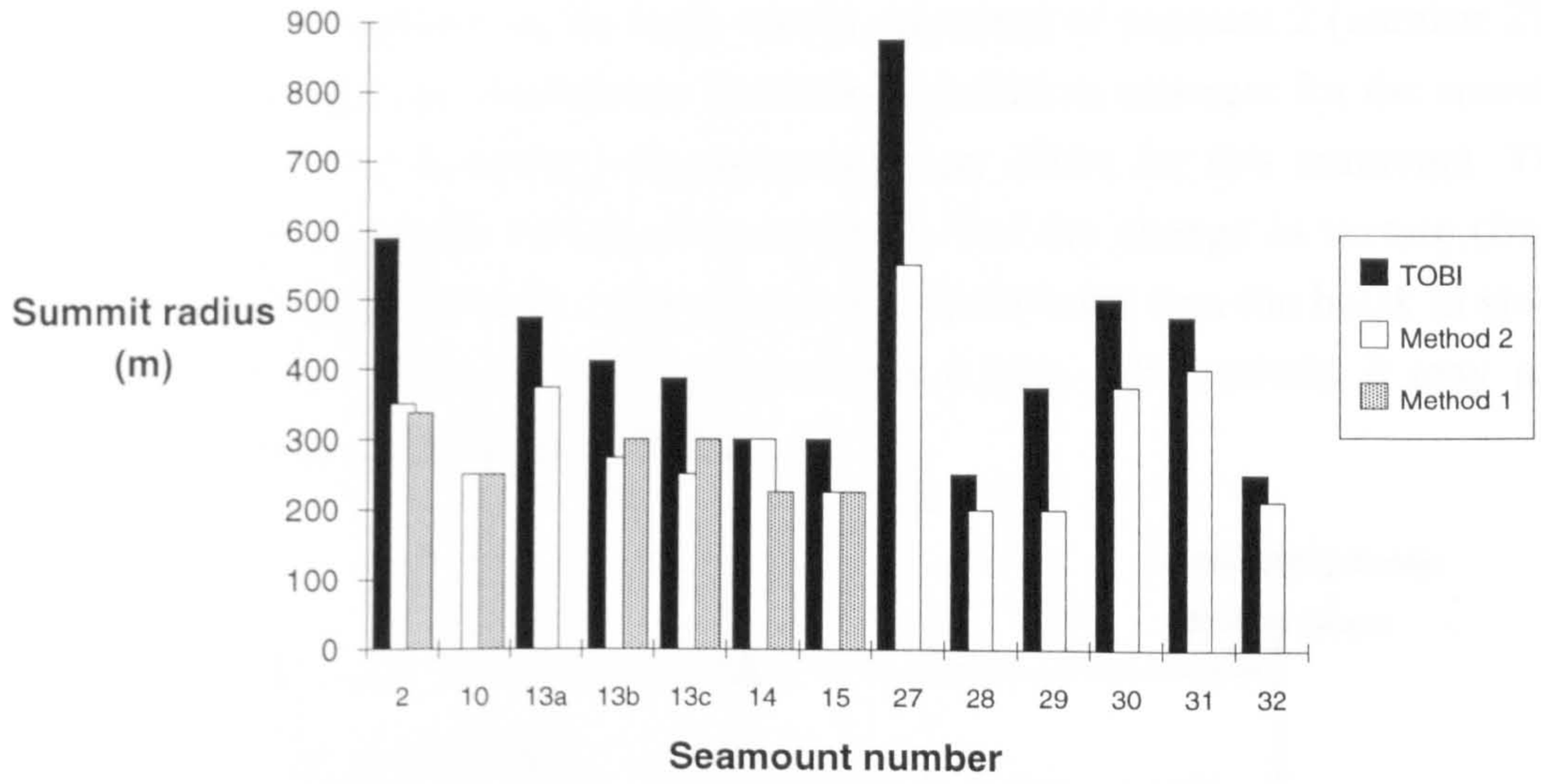

b)

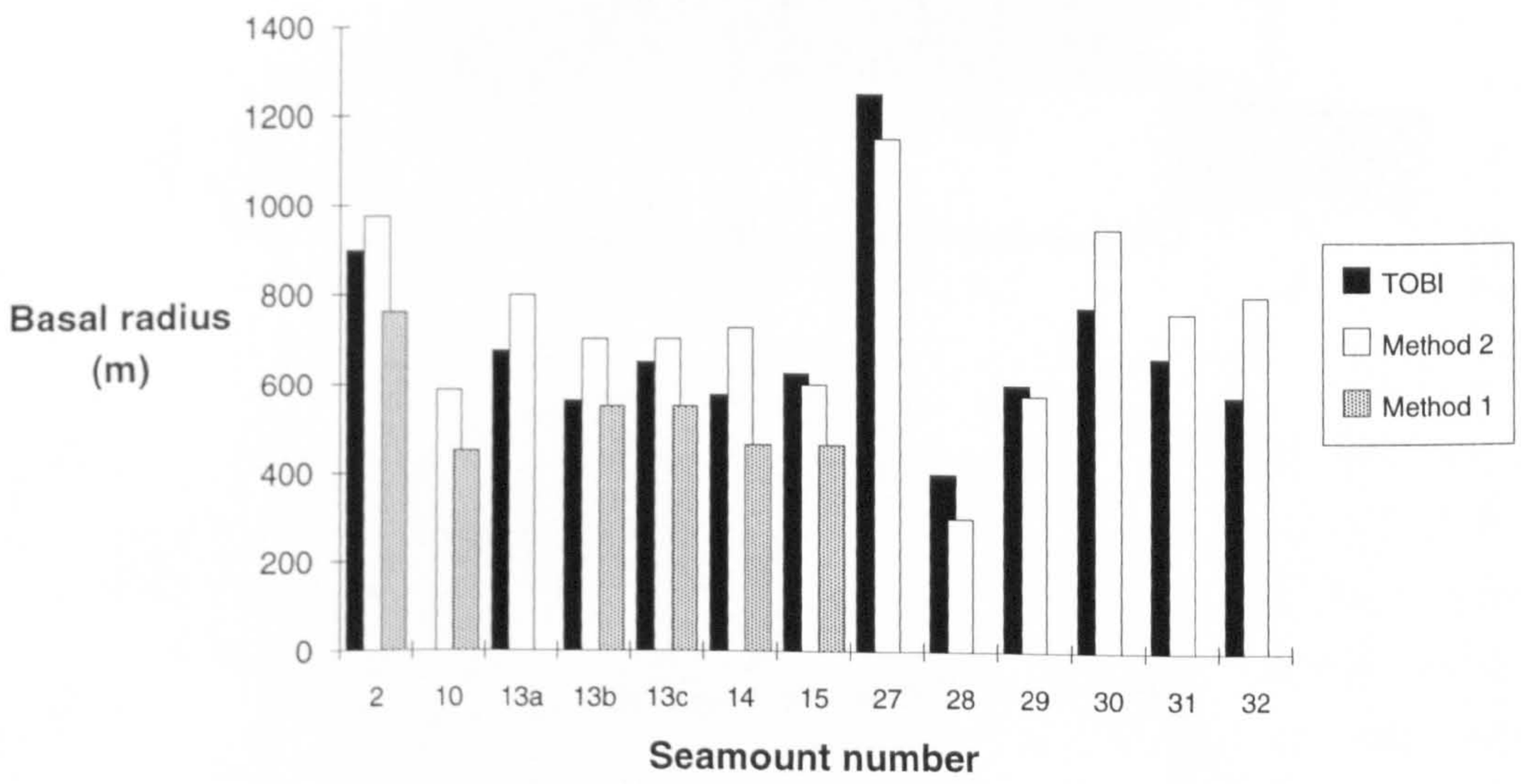

Figure 4.15 Histograms showing (a) summit radius and (b) basal radius for the 13 smooth-textured, flat-topped seamounts in table 4.5. The radii have been determined from the sidescan images and by two methods from the SeaBeam bathymetry. The TOBI images show consistently wider summit plateaux than indicated from the bathymetry.

4.6.4.3 Comparison of sidescan measurements with bathymetry

The radius of the summit plateau is consistently greater when measured from the sidescan (figure 4.15a). Layover would tend to distort the summit diameter in the across-swath direction, but there should be no effect in the along-swath direction. For most seamounts layover should cause an increase in summit diameter across swath, as the summits of the seamounts have higher relief than the area beneath the nadir.

However, even for the most dramatic changes in relief, layover only causes an increase in the radius by 100m (see upper profile of figure 2.6). This profile and layover estimate is made across the large crestal seamount of segment 2 (number 27). Figure 4.15 shows that the discrepancy between the sidescan estimate for the summit radius and the estimate from the bathymetry is nearer 300m for this seamount. The consistently larger estimates for the sidescan imply that the change in texture (from plateau to flanks) in the sidescan image occurs at a lower level than the break in slope determined from the SeaBeam bathymetry (figure 4.16a). Alternatively it may just result from the greater resolution of TOBI.

Figure 4.16 a) Sketch to illustrate how the summit and basal diameter measurements from the SeaBeam bathymetry and the TOBI sidescan can be systematically different. **b)** The mantled rim of pillow mounds causes the bathymetric break in slope at the base of the seamount to coincide with the textural transition.

In contrast, the basal diameters estimated using method 2 are mostly greater than those measured on the sidescan (figure 4.15b). This cannot be explained by layover artefacts in the sidescan, so again it must be a result of discrepancy between the textural break in slope and the bathymetric one (figure 4.16a). One seamount where the basal measurements virtually agree is the mantled seamount (number 29). Perhaps the mantling rim of pillow flows produces a bathymetric break in slope, higher up the flank as shown in figure 4.16b.

The correlation between the basal radius measurement for the sidescan and method 1 are no better, but also no worse, than those calculated for method 2. It must be noted that there are only five smooth-textured, flat-topped seamounts that have basal diameters estimated by all three techniques, so more data are needed to assess this result.

4.6.5 Do the sidescan terrains correspond to particular bathymetric shapes?

In the sidescan images there is a distinctive contrast between the three different textural categories for seamounts. In this section, I investigate whether particular seamount textures relate to specific seamount shapes. If there is an exclusive correspondence between shape parameters and seamount texture this tells us that the textural differences are not just a result of the flow character, but are inextricably linked to the shape of the edifice. Such a correspondence will also aid future studies on ridge volcanism, in areas where only bathymetry data are available.

Figure 4.17 shows a plot of two shape parameters, aspect ratio and flatness which discriminate between the different sidescan textures for the seamount data in the MARNOK area. The textural terrains show groupings with very little overlap, allowing field boundaries to be drawn on the graph. The smooth-topped volcanoes have low aspect ratios (<0.5) and a high degree of flatness (>0.4). The only smooth-top with a high aspect ratio is the set of three nested seamounts, which produce an elongated summit because of their overlapping relationship.

The hummocky terrain, on the whole, has lower degrees of flatness and there is a predictable division of the 2 subgroups (mounds and ridges) in terms of aspect ratio. The hummocky texture has the appearance of a ridge, rather than a mound, when the aspect ratio of a pillow volcano becomes greater than 1.4. One hummocky ridge, edifice number 23 (table 4.4), has a large value for flatness, which causes it to fall within the field of the smooth-textured seamounts. This high degree of flatness can be attributed to the interaction of two adjacent hummocky ridges of similar heights in slightly different orientations resulting in a broadening of the contours over the summit area.

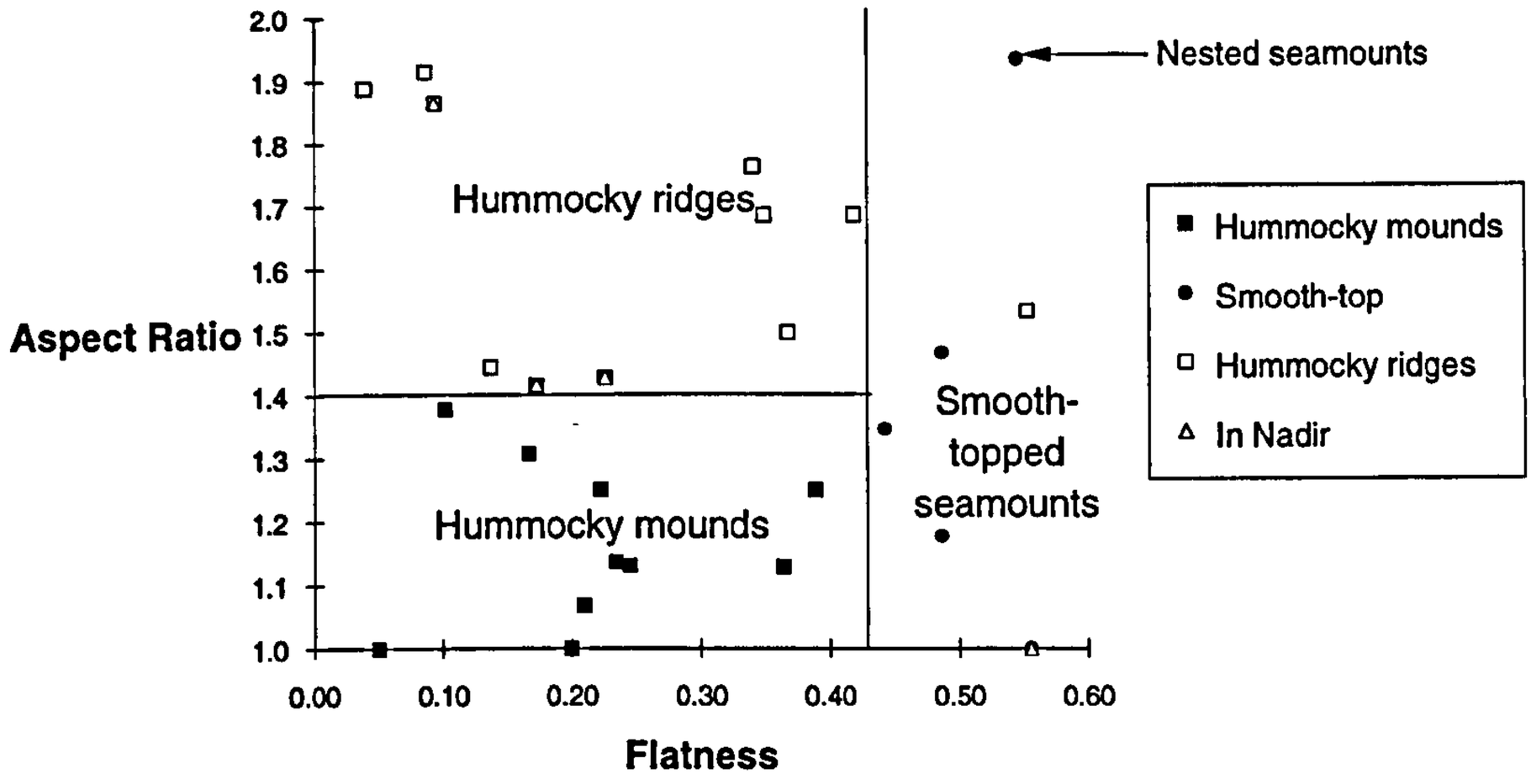

Figure 4.17 Aspect ratio against flatness, calculated using method 1, for seamounts with different sidescan textures.

4.6.6 Do flat-topped seamounts grow from hummocky mounds by lateral progradation?

One popular mechanism for the growth of summit plateaux invokes the relationship proposed by Eaton and Murata (1960), that volcano height is dependent on the hydraulic head of fluid magma. When the summit reaches its limiting magmastatic height the volcano can only grow by lateral progradation of lava flows (Vogt, 1974a). Hence, a progression from pointed cones to broad summit plateaux and steepened flanks is predicted and observed in the case of the Lamont Seamount chain in the Pacific (Barone & Ryan, 1990).

The mantled seamount is a clear piece of evidence that favours this hypothesis, as a flat-topped summit, surrounded by hummocky rim, is exactly the morphology expected from a hummocky mound which has started to grow a flat summit plateau on reaching a limiting height. The relative ages of the smooth summit flows and the hummocky mantled flows are vital to the interpretation of this feature. If the mantled flows are older than the summit flows then they are probably related to an earlier hummocky mound phase of growth. If they are contemporaneous with the summit flows then they are more likely to be satellite volcanism along ring fractures. Unfortunately, the age resolution from the sidescan is not good enough to resolve this issue; more detailed submersible or camera traverses, preferably including sampling, would be required.

The model described above predicts that the steepness of the flanks should positively correlate with the degree of flatness. In addition, smooth-topped volcanoes might be expected to have greater heights and volumes than hummocky seamounts.

Figure 4.18 shows that there is no such correlation for the seamounts tabulated using method 1. The smooth-topped seamounts fall into the middle of the range of flank gradients seen in the hummocky terrain.

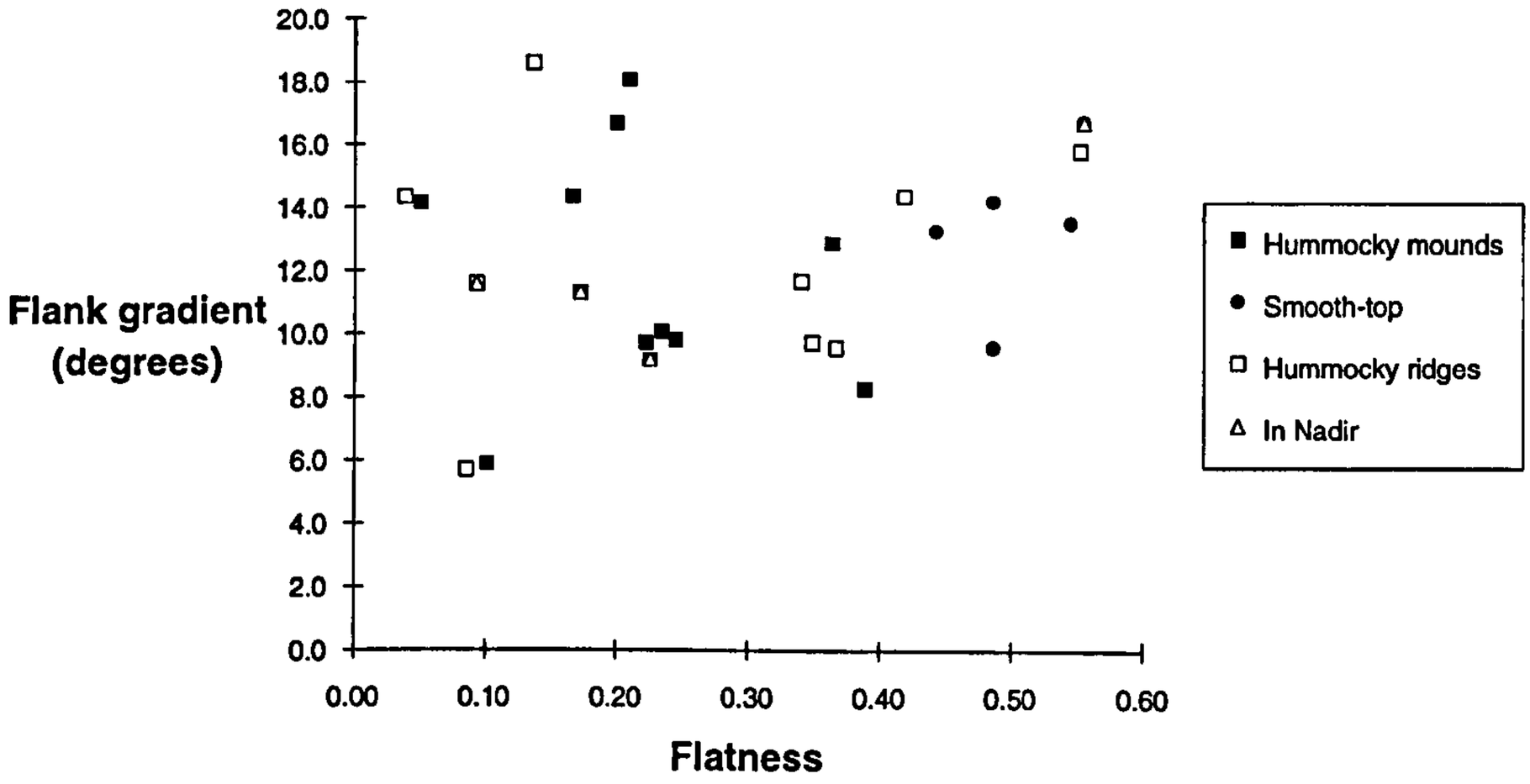

Figure 4.18 Graph of flank gradient against flatness shows no positive correlation for method 1.

However, in section 4.6.4.2 it was noted that method 1 did not give very realistic estimates of seamount height and flank gradient for the smooth flat-topped volcanoes. Method 2 produces more authentic parameter values, and in fact relies on the very existence of steep radial contours to define the flanks of the smooth-topped seamounts. Moreover, the problems which arose while trying to use method 2 for the hummocky mounds resulted from the fact that similar steep gradients were not found around hummocky mounds. Hence, a qualitative observation suggests that the flat-topped seamounts do have steeper flank gradients than the hummocky mounds.

Figure 4.19 shows the same parameters as figure 4.18, except the data from method 2 (which is for the smooth-topped seamounts only) are plotted. The smooth-topped seamount data for method 1 are also plotted for comparison. Whereas figure 4.18 showed no positive correlation for these two parameters, there is a trend in the method 2 data, which is statistically significant. This implies that there is indeed a relationship between the flattening of the summit plateau and the steepening of the flanks within the smooth-topped morphologies.

However, it should be noted that there is considerable weight added to this positive correlation by the one data point with a flank gradient of ~30°. This is from a very small seamount that is located right next to the median valley wall, and there is a strong possibility that the steep gradient is more a result of faulting than of

constructional steepening. With this point removed, the positive correlation is only significant at the 90% (rather than the 95%) confidence limit.

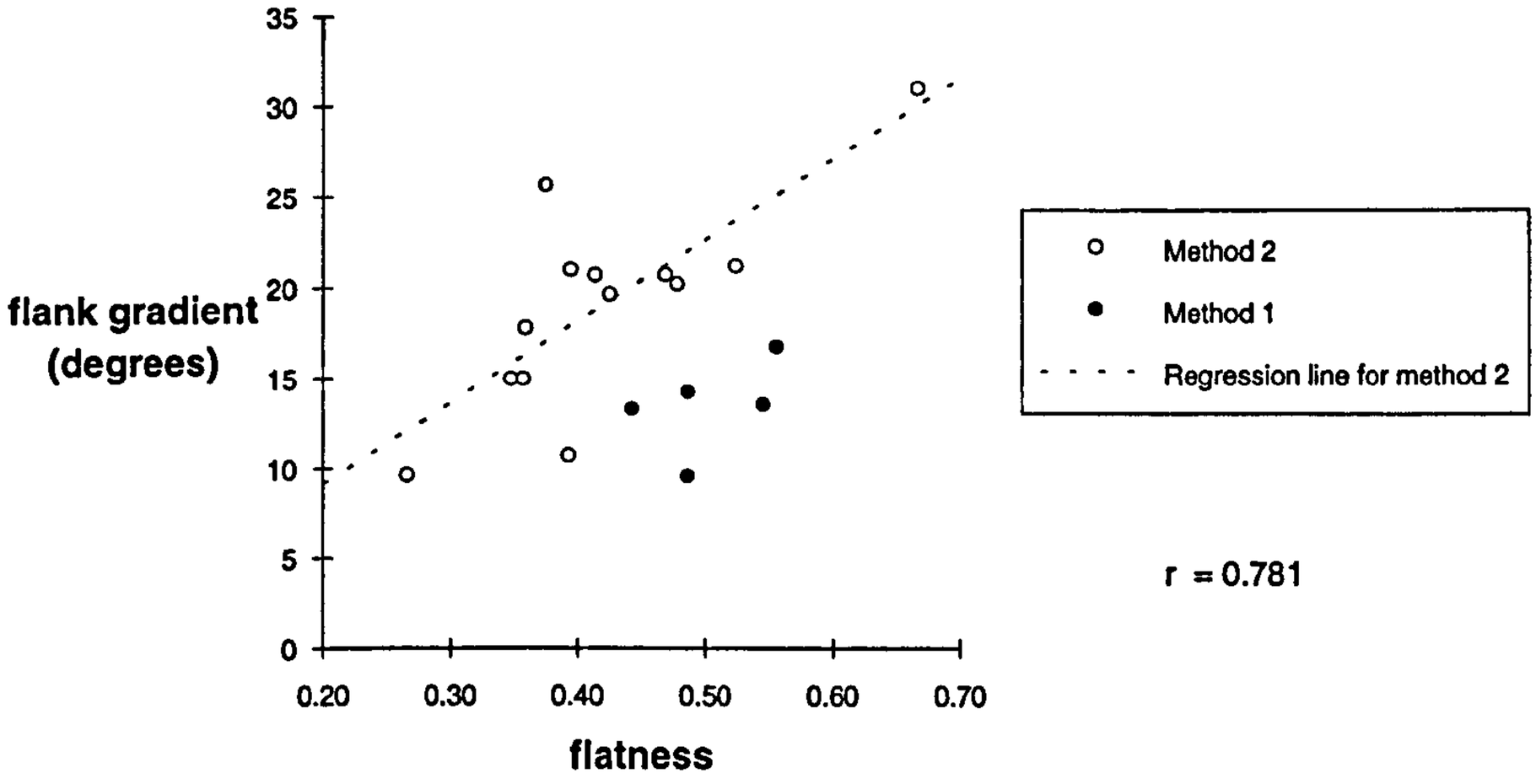

Figure 4.19 Graph of flank gradient against flatness for the smooth-topped seamounts, with data plotted from method 2 (table 4.5) and compared with parameters measured using method 1 (table 4.4). There is indeed a positive correlation of these parameters for the flat-topped seamounts measured using method 2 (compare with figure 4.18). A regression line is included for the method 2 data only. The t-statistic for the regression line is 4.15 which is significant at the 95% confidence level.

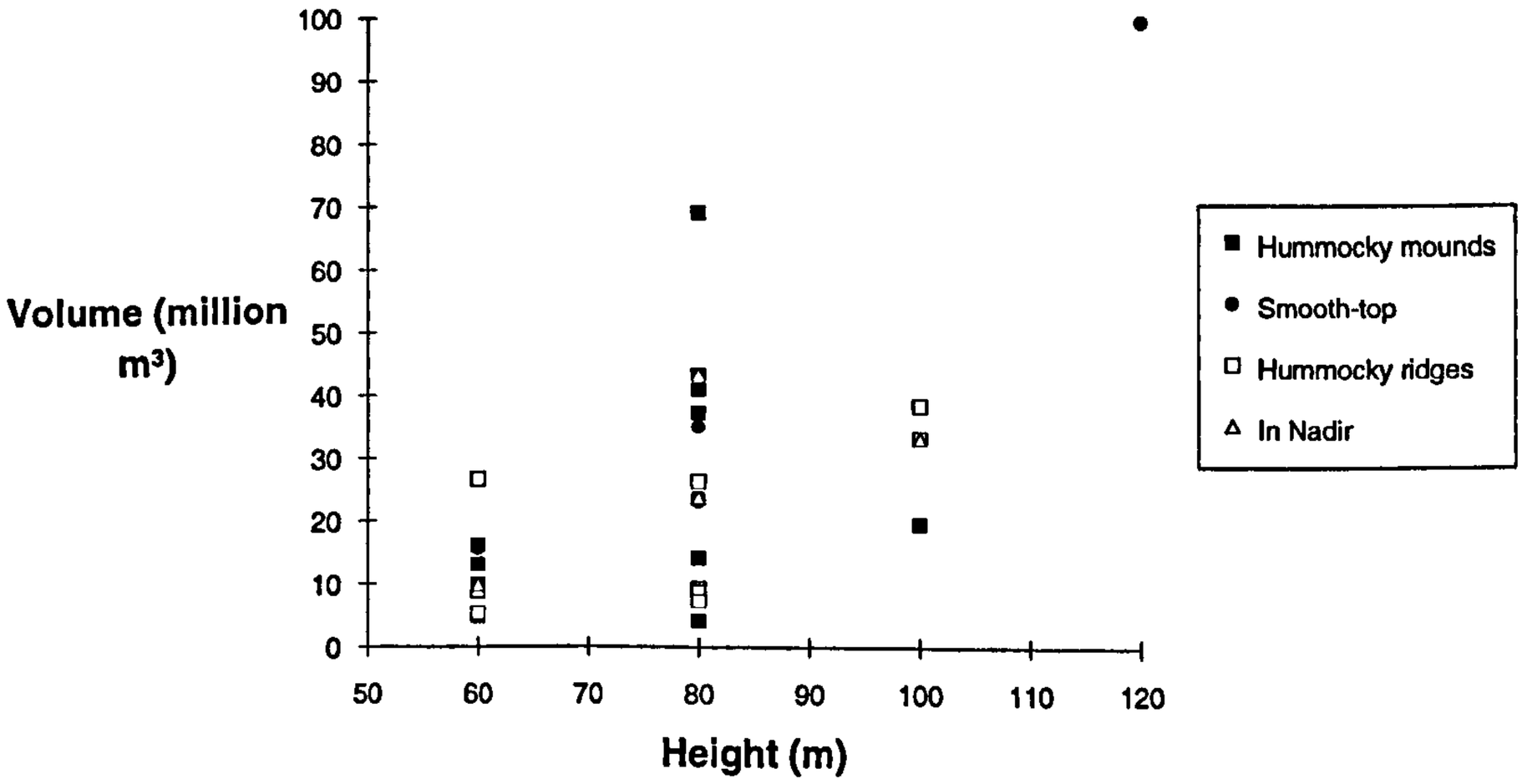

Figure 4.20 Graph of seamount volume against height calculated using method 1. Although the largest seamount defined using this method is a smooth-top, the smooth-tops in general are not particularly taller or more voluminous than the hummocky terrain.

The largest and most voluminous seamount defined using method 1 is a smooth-top in the transform domain (pictured in figure 3.1v). However, figure 4.20 shows that the heights and volumes of the other smooth-topped seamounts are no greater than those of the hummocky seamounts. The height data for method 1 are also plotted against

latitude in figure 4.21. This confirms that smooth-topped seamounts are no taller than adjacent hummocky mounds. I conclude that the seamount statistical data produce very little evidence that smooth-topped seamounts grow from hummocky mounds when they reach their limiting magmastatic head. Further evidence for and against this theory will be discussed later in this chapter.

4.6.7 Do larger seamounts occur at the ends of segments?

The level in the crust at which magma bodies accumulate is thought to be controlled either by the brittle-ductile transition or the level of neutral buoyancy. At normal slow spreading ridges, some authors favour the brittle-ductile transition (Rinehart et al., 1979; Kriens & Wernicke, 1987; Smith & Cann, 1992), and one of the consequences of this model is that larger seamount should occur at the segment ends. If the magmastatic head controls the height to which a volcano can grow (Eaton & Murata, 1960; Vogt, 1974a), the thickness of the brittle lid should potentially correlate with the height of seamounts above the local seafloor (Nisbet & Fowler, 1978; Smith & Cann, op. cit.). Within a ridge segment, the ends are thought to have a deeper brittle-ductile transition than the middle (Kong et al., 1992; Shaw & Lin, 1993) and so seamounts should grow to greater heights at the ends. Smith and Cann (1992) assume that the flat tops of the seamounts form because the limiting magmastatic head has been reached, forcing the seamount to build out laterally. Hence, it is the *flat-topped seamounts in particular* that should have greater heights at the segment ends and smaller heights in the segment centres.

A graph of seamount height against latitude for all morphologies, calculated using method 1 (figure 4.21) does show a slight decreasing trend in the maximum seamount height towards the centre of segment 1, though the relatively small number of data points could mean that this is just fortuitous. In contrast, there is a relatively uniform distribution along segment 2.

Graphs of depth of seamount base and summit against latitude (figure 4.22) show the dominance of the bathymetric swells of the segmentation. The smooth, flat-topped volcanoes sit perfectly on the trend defined by the hummocky morphologies, not appearing to have deeper bases or higher summits than hummocky terrain at the same latitude.

It has already been noted that method 1 does not produce very realistic estimates of seamount height for the flat-topped seamounts. As we are especially interested in these, the data for method 2 are plotted in figure 4.23.

In fact, the method 2 data (figure 4.23) prove to be of little use for looking at variations along-axis, as the smooth-topped seamounts are preferentially located at the

ends of the segment, with a particularly high concentration around the 3rd order non-transform offset. This has important implications, to be discussed later in this chapter.

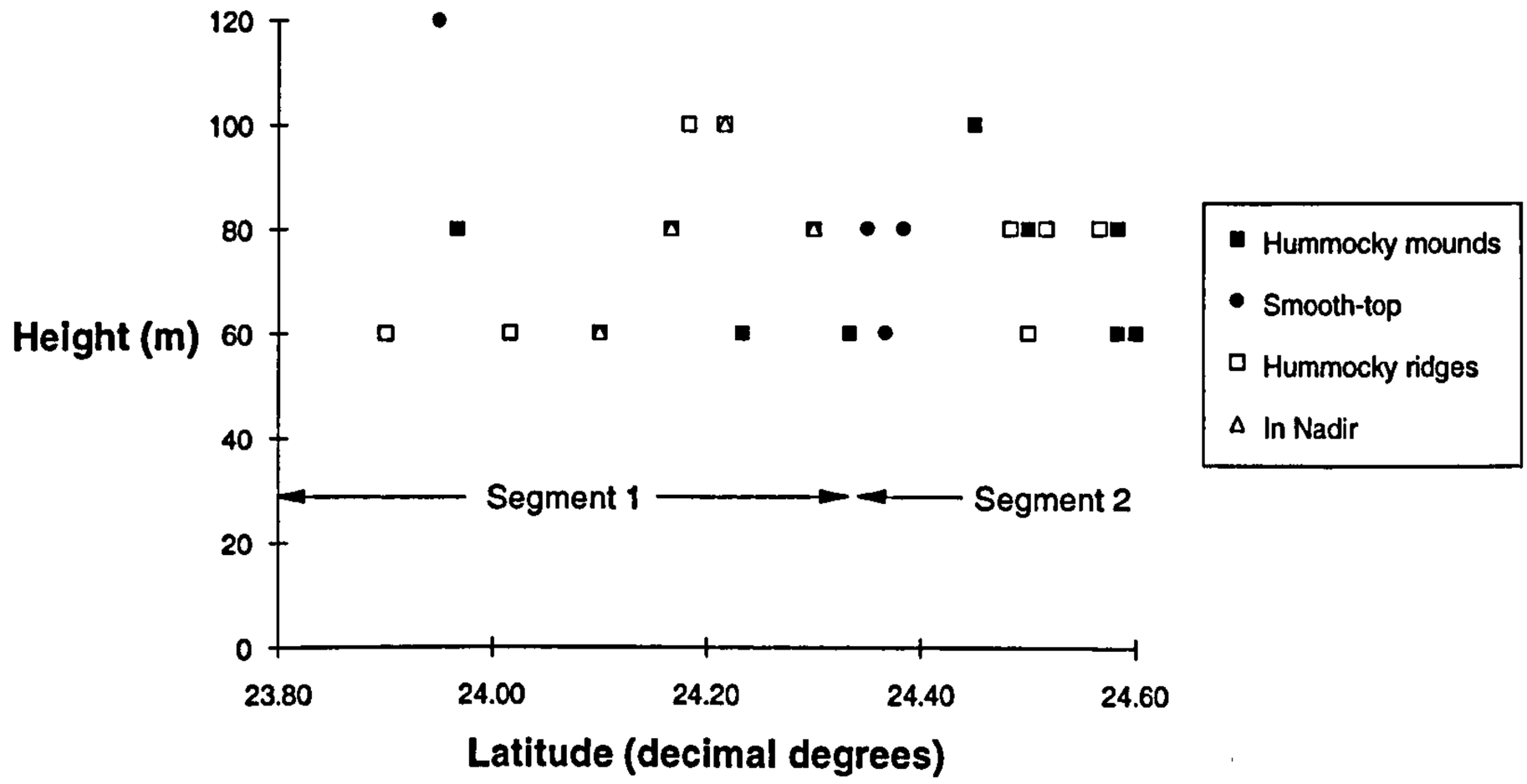

Figure 4.21 Graph of seamount height (calculated using method 1) against latitude. There is a slight decrease in the maximum seamount height towards the centre of the segment 1, but on the whole there is no strong correlation between tall seamounts and the segment ends. The smooth flat-topped volcanoes do, however, tend to concentrate at the NTO.

The crestal seamount at the northern end of segment 2 is the largest seamount in the MARNOK area, but the smallest smooth-top occurs just to the south of it. The locations of these two seamounts with respect to the ridge axis are quite different. The large one crowns the hummocky NVR, while the small one is immediately adjacent to the median valley wall. These are the only two smooth-topped seamounts that are not located either in the transform domain or near the NTO.

A key aspect, regarding the data in figure 4.23, is that there is considerable scatter in seamount height at a particular latitude. If the heights of the flat-tops are related to the depth of the magma chamber then this scatter implies that there must be highly localised spatial and/or temporal variations in the crustal density or any rheological boundary that causes magma to pond.

Using the method of Smith and Cann (1992)[3], which applies to magma ponding at the brittle/ductile transition, the range of seamount heights at the non-transform offset,

---

[3]Smith & Cann (1992) assume an exponential density increase with depth to calculate values of magma chamber depths which correspond to varying seamount heights. The exponential parameter λ, is estimated at 2.3×10^3 m^{-1}, based on the porosity distribution with depth in hole 504B (Becker, 1985). Using this porosity distribution a graph of seamount height against depth to the top of the magma chamber was generated (figure 8 of Smith & Cann, op. cit.).

(from 120m to 220m) correlates to variations in the magma chamber depth from 2200 to 2900m. The variations in segment 2 are greater still, as the tallest and shortest flat-topped seamounts (corresponding to magma chamber depths of 3600m - 2000m respectively) occur within 10km of each other. The average seamount height in the transform domain (200m), is greater than the average for the area around the NTO (160m) suggesting that the former may have magma ponding on average at greater depths.

a)

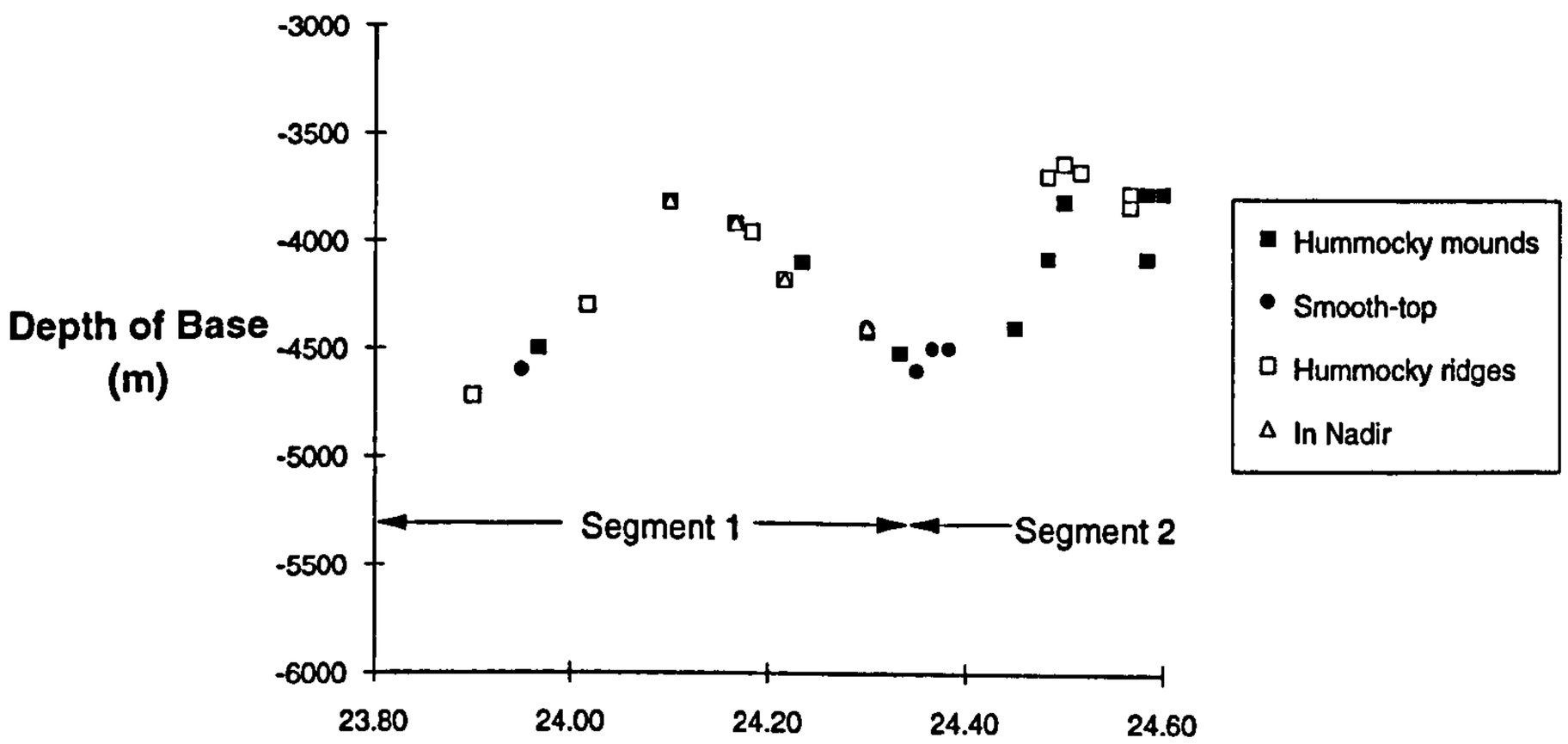

b)

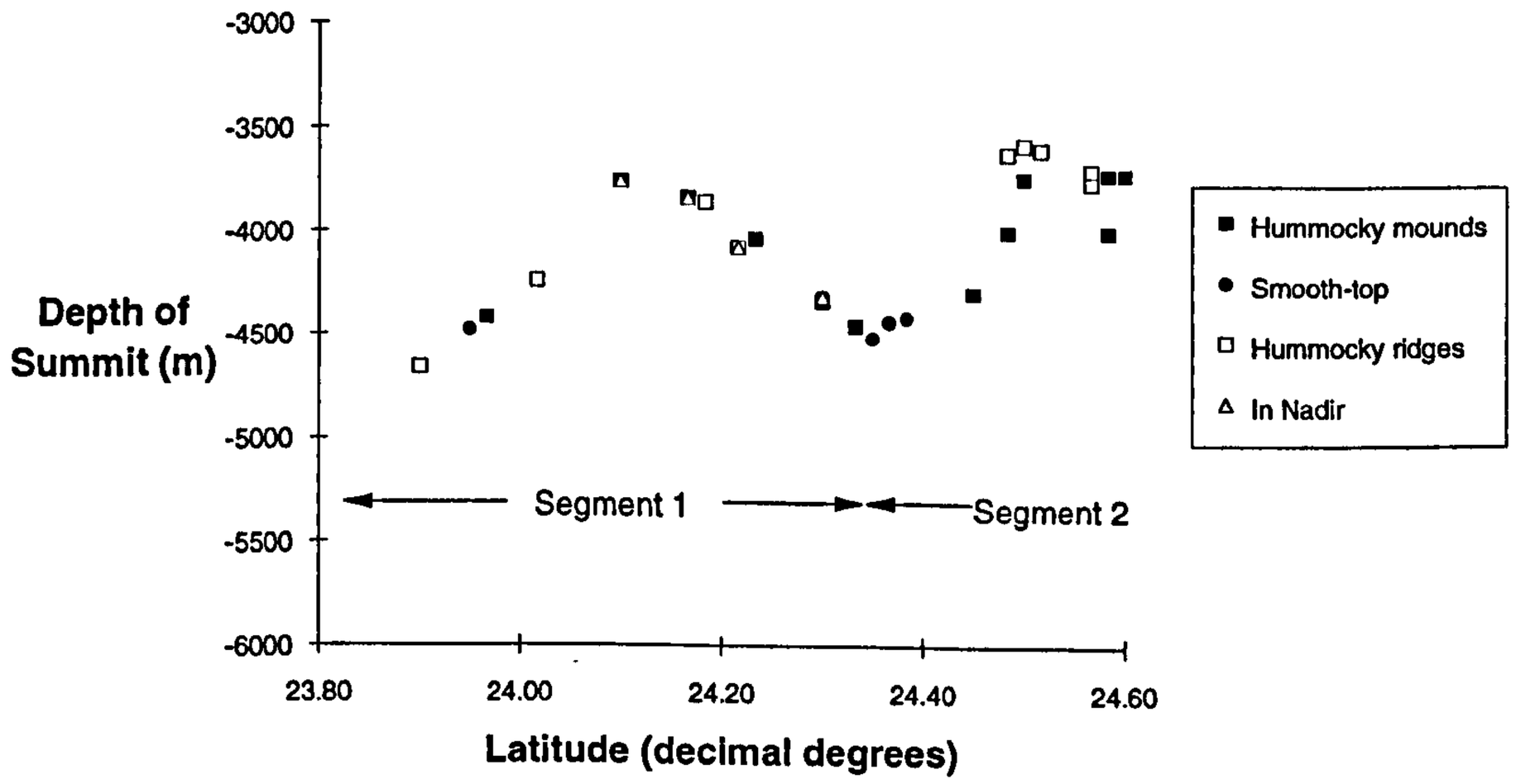

Figure 4.22 Graphs of a) depth of seamount base and b) depth of seamount summit against latitude show the bathymetric swells of the segmentation. The smooth, flat-topped volcanoes sit perfectly on the trend defined by the hummocky morphologies.

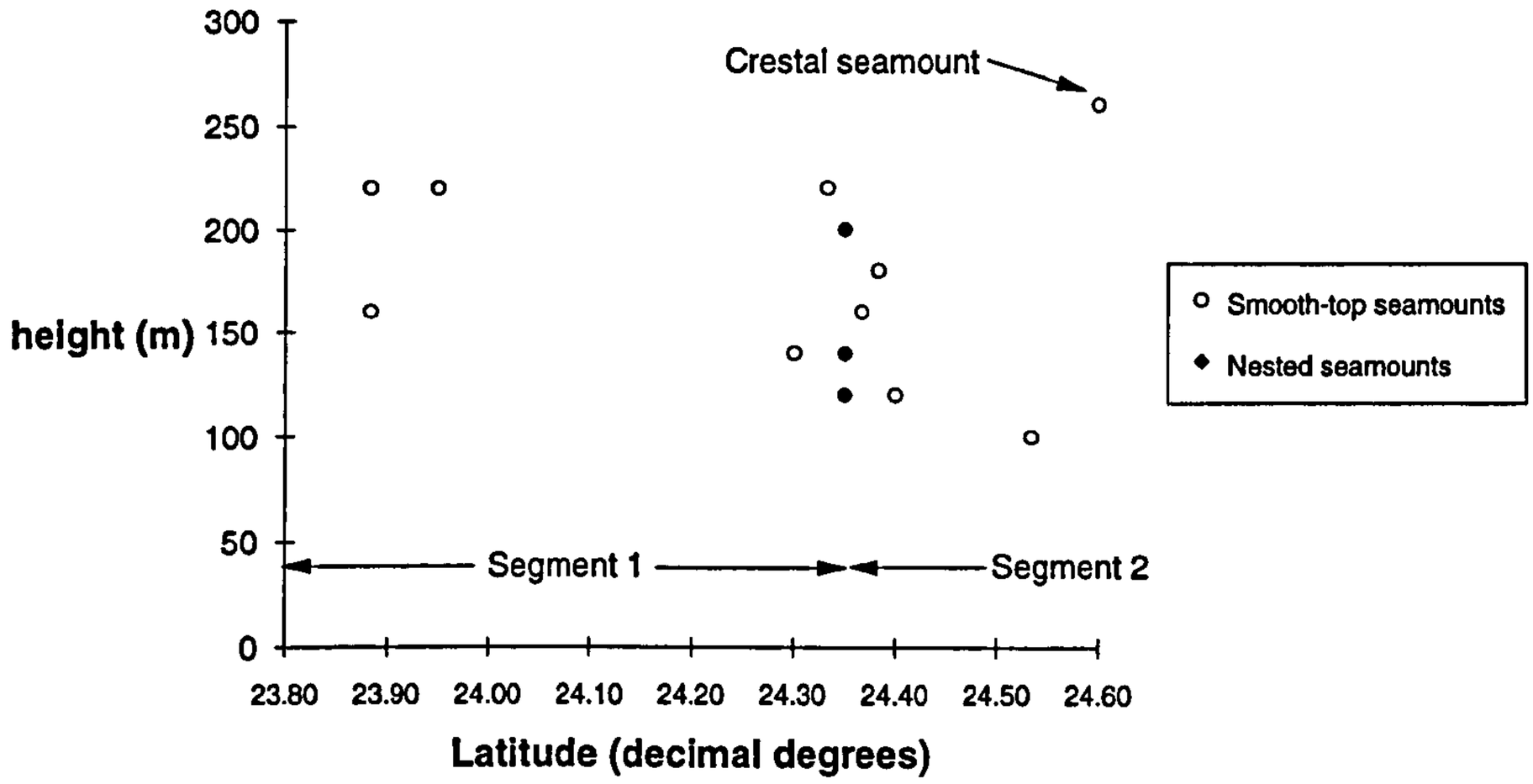

Figure 4.23 Variation in height of smooth, flat-topped seamounts (calculated using method 2) with latitude. These seamounts show a strong preference for the ends of segments.

These values for magma chamber depth are *less* than the depth of brittle/ductile transition at the MAR axial valley which is placed usually between ~4km and 8km from microearthquake studies (Lilwall et al., 1978; Toomey et al., 1985; Kong et al., 1992). However, estimates from ophiolites place the transition higher in the crust at about 2 km (Gass & Smewing, 1981; Harper, 1985).

So far there is little strong evidence from this study to support either ponding at the brittle/ductile transition or the growth of smooth topped seamounts as a result of limiting magmastatic head. These issues will be pursued further in the following sections.

4.7 Origin of hummocky terrain

4.7.1 Flows, cones and alignment mechanisms

Ballard and Moore (1977) suggested that pillow cones comprise a substantial proportion of the median valley floor. The TOBI sidescan confirms the profusion and near ubiquity of pillow flows, cones and haystacks. Mount Pluto in the FAMOUS area, is probably the first recorded hummocky ridge (Ballard & Van Andel, 1977). It was found to be a series of conical peaks, 20-30m high, aligned parallel to the trend of the median valley. As the summits of the peaks on Mount Pluto have remarkably concordant depths, it was suggested that they grew in response to a common hydraulic head of lava in a shallow magma chamber. Several suggestions have been made to explain the alignment of the hummocky cones.

4.7.1.1 Chains of tumuli over lava tube

The first is that they are essentially tumuli with chains of cones erupted along the upper surface of a lava tube (Ballard & Van Andel, 1977; Fornari, 1986). Chains of cones formed by this mechanism could have a highly sinuous form, or a straight one, depending on the path taken by the underlying lava tube.

4.7.1.2 Flow focusing along a fissure

These hummocky ridges are interpreted as fissure eruptions similar to those commonly observed in subaerial basaltic volcanism. In Iceland and Hawaii eruptions which start with extrusion along the entire length of the fissure commonly focus into a number of discrete points usually spaced equally along the fissure (Thorarinsson, 1969; Macdonald & Abbott, 1970; Björnsson et al, 1979; Delany & Pollard, 1982). In the extreme case, the flow of lava can become localised to a single vent (Richter et al, 1970; Thorarinsson et al, 1973). Smith and Cann (1993) comment that the ubiquitous nature of the hummocky ridges implies that for most eruptions the rate is not fast enough to sustain effusion along the entire fissure.

4.7.1.3 Damming against faults

Bryan et al. (1994) have highlighted that a linear geometry is not necessarily a reliable guide to underlying tectonic patterns and have shown that a set of five linear volcanic cones in the MARK area differ in morphology and apparent age. Two of the cones are thought to be tumuli while the others were formed in situ, but from different vents at different times. They propose a third explanation for the common linearity of these relatively unrelated features: that the flows are localised by damming against the steep valley walls.

4.7.1.4 Favoured mechanism

Most of the prominent hummocky ridges do not occur in bathymetric depressions, as would be expected if the 'damming' mechanism of Bryan et al. (1994) was widespread. Although the 'tumuli' hypothesis cannot be entirely ruled out, of these three mechanisms a structural control through faulting and fissuring is favoured for explaining most of the linearity observed in the hummocky terrain. This is partly because the groundtruthing brought to light the important role played by syn-magmatic faulting in creating a strong linearity within the volcanic terrain of the MARNOK area. In addition, the orientation of the hummocky ridges near the RTI can be correlated with fault scarps on the valley walls which again demonstrates a structural control.

4.7.2 Fractionation variation along fissure eruptions

Dredges 5D, 6D and 8D all sampled the same long, hummocky ridge near the RTI (see figure 5.1b). Basalts from these dredges were found to be related to the same parental magma, but to show a longitudinal variation in the degree of fractionation, with more evolved lavas at the tip nearest the RTI (figure 4.24).

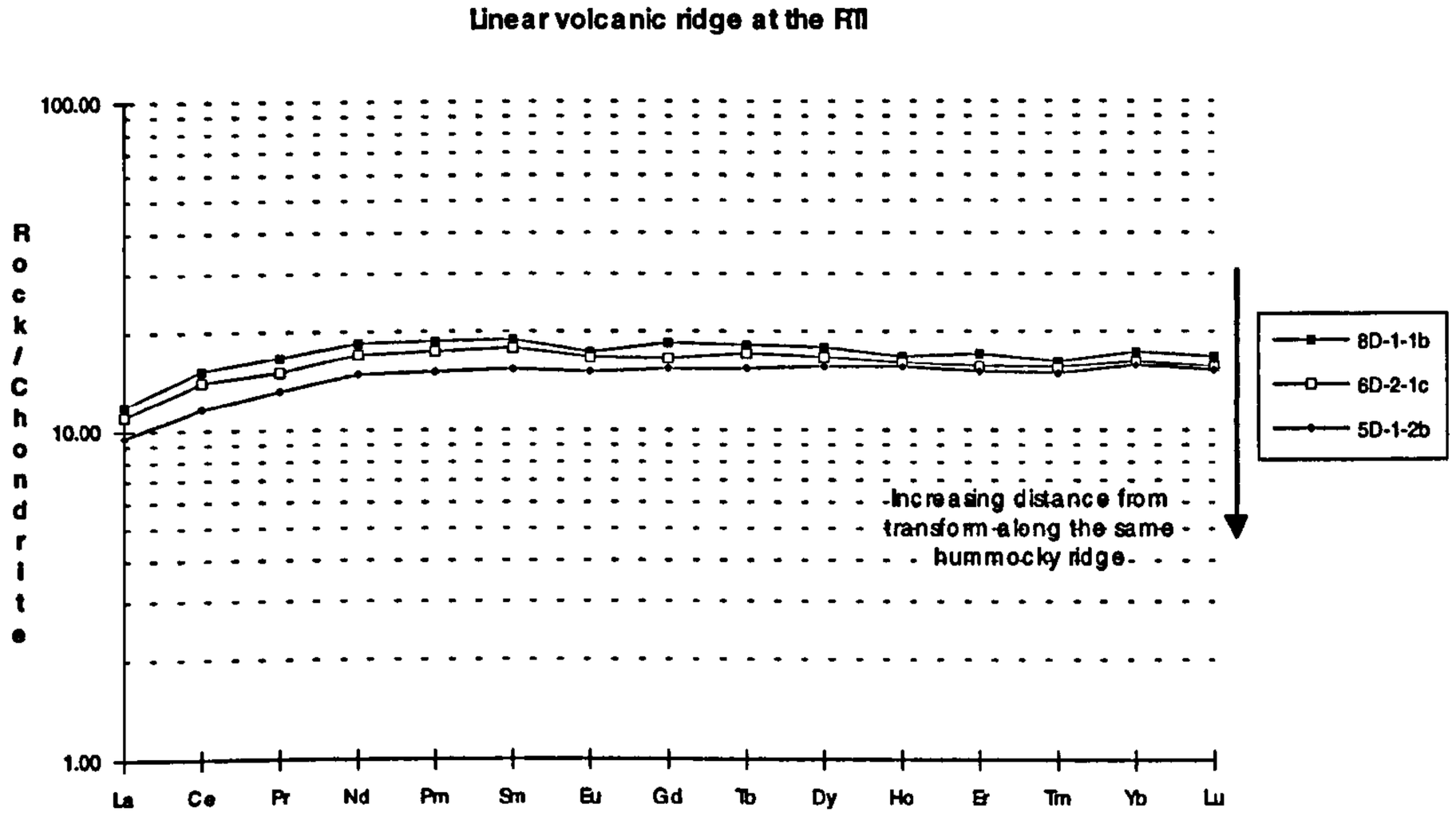

Figure 4.24 Chondrite-normalised rare earth plot shows subparallel patterns for samples from the same linear hummocky ridge approaching the RTI. The lavas are related to a common parent, but show greater degrees of fractionation towards the RTI. Normalising values are from Boynton (1984).

4.7.2.1 Lateral dyke injection

It is possible that the geochemical variations along the length of a hummocky ridge reflect movement of magma from a central magma reservoir via lateral dyke injection towards the ends of the segment. Similar variations are sometimes seen along Hawaiian rifts (R. Batiza, *pers. comm.*), although the primary mechanism is thought to be magma-mixing rather than crystallisation. In Iceland, the progression of seismic activity accompanying lateral dyke injection has been observed during a magmatic rifting episode (Björnsson et al., 1977), but a strong variation in the degree of fractionation such as that seen in the MARNOK area is not documented. An episode of lateral dyke injection has also recently been recorded at the Juan de Fuca Ridge (Embley & Chadwick, 1994) though once again there is no fractionation effect associated with this (Smith et al., 1994).

Progressive fractionation with increasing lateral transport *has* been reported in long dykes from Greenland (Upton & Thomas, 1980), although the length scale of the dyke is greater and the geochemical variations are smaller compared to the above examples from the MARNOK area. Rickwood (1990) also suggests that systematic variations in

the degree of fractionation can be used as a weak correlator of distance from the source (less evolved compositions occur closer to the source).

Lateral dyke injection is predicted from seismic studies of crustal thickness variations, particularly in layer 3, approaching the transform (Cormier et al., 1984; White et al., 1984), but other factors such as increased fracturing and hydrothermal alteration of the crust may also contribute to the variation in seismic structure towards the transform.

Although lateral dyke injection can not be ruled out, it seems unlikely that the chemical differentiation arose from dyking processes. The role of lateral dyke injection is discussed further in relation to the level of neutral buoyancy (LNB) and the brittle-ductile transition in section 4.7.3.

4.7.2.2 Density stratified magma chamber

Another process that may result in along-strike compositional variation is density stratification of the magma chamber. In the EPR segment at 9°30'N, the extent of fractionation (Batiza & Niu, 1992) correlates with the depth of the AMC, as observed by multi-channel seismics (Detrick et al., 1987). Batiza & Niu (op.cit.) propose that the along-axis fractionation systematics observed on the EPR are a result of a laterally zoned magma chamber, with dense Fe-rich melts at the deep distal ends of the axial magma chamber (AMC). A density stratified magma chamber is the favoured mechanism for causing the geochemical variations along the strike of a single fissure.

4.7.3 Ponding at LNB or brittle/ductile transition.

Lateral dyke propagation is facilitated by the accumulation and movement of magma along the LNB. At present there is no consensus as to whether magma ponds at the LNB, the brittle/ductile or somewhere in between. Batiza & Niu (1992) propose melt accumulation at the LNB on the EPR, while Ryan (1987) cites considerable evidence for the magma chamber occupying the LNB at Iceland. However, Smith and Cann (1992) calculate that the brittle-ductile transition occurs at a deeper level (~2-8km) than the LNB (about 450m) on the MAR. This suggests that lateral dyke propagation should be less important in areas of slow spreading ridge with normal crustal thickness (where the LNB is well above the brittle-ductile transition) than in Iceland and Hawaii where the LNB is below the brittle-ductile transition. However, even without ponding at the LNB, some degree of lateral dyke propagation on the MAR is to be expected, because feeder dykes will tend to spread laterally during ascent because of cross stream variation in elastic forces (Lister & Kerr, 1991).

Hummocky ridges usually have a 'pinch and swell' morphology which suggest that in most cases individual vents have not become completely isolated, although there is still an element of interaction between adjacent focusing points. Interaction between

vents becomes negligibly small if the vent separation exceeds the vertical extent of the dyke (Bruce & Huppert, 1990). The wavelength of the hummocks does not tend to exceed 500m, suggesting that the magma chamber is located at deeper levels than the LNB (at 450m)

4.7.4 Role of local and regional stress fields

The orientation of a dyke is controlled by the interaction of the local and regional stress regimes (Odé, 1957; Muller & Pollard, 1977; Nakamura, 1977), with magma propagating in a plane normal to the axis of minimum compressional stress (Anderson, 1936; 1938; Shaw, 1980). In Iceland the local stress field around large shallow crustal magma chambers can cause radial dykes and cone sheets to form, as well as causing deviations in the trend of associated fissure swarms (Thorarinsson & Sigvaldason, 1972; Gudmundsson, 1990; Gautneb & Gudmundsson, 1992). There were no radial or concentric hummocky ridges observed, but there is a strong relationship between the orientation of the hummocky ridges and the regional stress regime induced by the plate tectonic forces. This indicates that the stress regime resulting from the accumulation, inflation and deflation of magma bodies in the crust is negligible compared to the regional extension.

4.7.5 Injection through pre-existing faults

The observation that some lava flows seem to have erupted out of a fault plane can be explained by dykes following the path of least resistance through the crust. Examples of this happening have also been reported from Iceland (Gudmundsson, 1984). The criteria for dyke injection from a magma reservoir is:

$$p_l + p_e = \sigma_h + T \qquad (1)$$

where p_l and p_e are the lithostatic magma pressure and the excess magma pressure respectively, which combine to give the total magma pressure in the dyke, σ_h is the horizontal compressive stress perpendicular to the dyke and T is the tensile strength of the crust (Jaeger & Cook, 1979; Gudmundsson, *op. cit.*).

The magma will tend to follow a path where the term $\sigma_h + T$ is a minimum value (Delany et al., 1986; Rickwood, 1990; Gudmundsson, 1990). Pre-existing fractures will have a tensile strength of virtually zero as long as they have not been sealed by hydrothermal precipitation. A fault which propagates close to a magma body may be used as a conduit, allowing the magma to move towards the surface if the magmastatic pressure and buoyancy forces are sufficient. Eruptions with lower magmastatic pressure can utilise this mechanism, as less energy is required to rise up a pre-formed fracture than to generate the initial fracture in the crust.

4.8 Seamount formation

4.8.1 Distinct parental lavas

The three flat-topped seamounts that were sampled were found to have parental compositions which are distinct from nearby hummocky terrain. This is demonstrated for two of these seamounts in figure 4.25. The spidergram for the nested seamounts (29D) has an enriched trend, which crosses that of the hummocky ridge located 3km away (30D). There is a similar story in the transform domain, where the large flat-topped seamount (12D-1-1b—figure 4.1v) has a depleted trend compared with a hummocky ridge about 5km to the north. The differing parental magmas suggest that these volcanic constructions were fed by separate chambers in the crust. It should be noted that lavas from these seamounts are not all consistently enriched (or all depleted) compared with the hummocky terrain, but they are quite distinctly different, in that the variations between the seamounts and the hummocky ridges tend to be greater than the variations within the data set for the hummocky ridges alone.

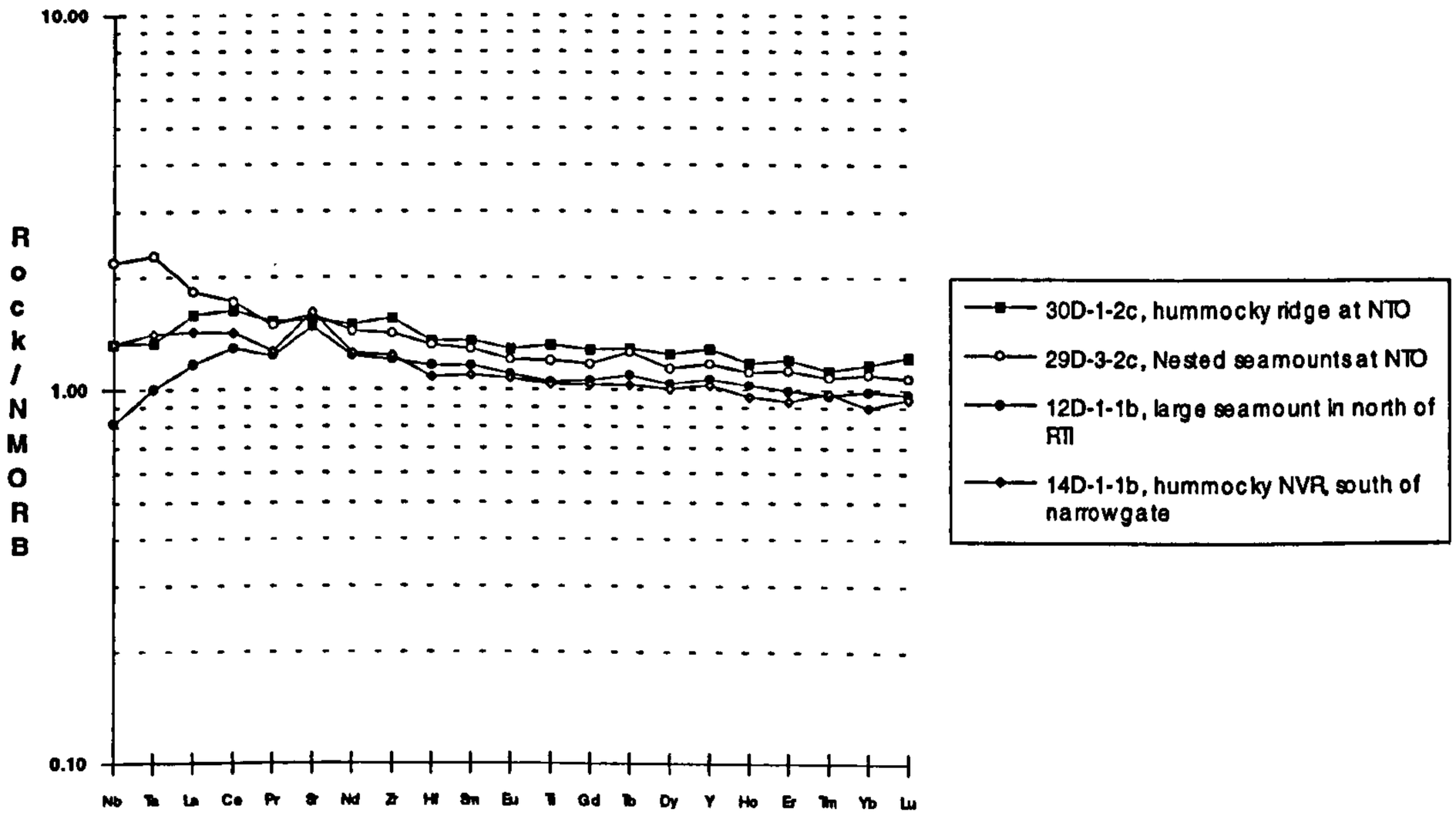

Figure 4.25 NMORB-normalised extended element diagram showing how patterns for flat-topped seamounts cross those of nearby hummocky terrain. Normalising values are from Sun & McDonough (1989).

The glass data show that the nested seamounts (29D) are consistently more primitive than the nearby hummocky terrain (30D). (MgO ~ 7.3wt% for 29D compared with MgO ~ 6.6wt% for 30D.) For the other two seamounts (4D & 12D), the range of glass data is not consistently more or less primitive than the recovery form the stations immediately north and south. Their degree of fractionation is roughly consistent with

a general trend with latitude that will be discussed further in chapter 6. If anything, 4D and 12D fall on the fractionated side of this trend.

4.8.2 Petrography of seamount samples

The petrography of the flat-topped seamounts is certainly not entirely distinct from that of the hummocky terrain, but there are certain features, particularly common to the seamount samples, that are worthy of note.

Firstly, many of the phenocrysts seem to be intermediate between a quench and intratelluric texture, in that they show the morphology of quench crystals (accicular, plagioclase, variable shaped olivines—some skeletal), but are rather large for typical quench growth. In fact, despite their textural similarily to quench morphologies, they cannot be typical quench growth as they are relatively large and yet are surrounded by glass, sometimes including the tiny microlites of "true quench". These microphenocrysts frequently occur in glomerophyric clusters, some of which have quite complex radiating forms. Plagioclase and olivine are commonly intergrown within these clots, implying that these phases fractionated simultaneously. Zoned phenocrysts are almost entirely absent from these lavas. Large plagioclase megacrysts (± glass inclusions) are present in small quantities, but do not have strong resorption features.

The above petrological features suggest that the seamount lavas spent relatively little time in crustal magma chambers and underwent very little interaction with other melts within the crust (as demonstrated by the lack of zoned phenocrysts and other disequilibrium textures). The few refractory plagioclase megacrysts that did become entrained in these lavas may have had relatively little time to react with the host lava. The large "quench like" phenocrysts and clusters are particularly interesting as they suggest that the lavas underwent a period of rapid decompression, but that there was a relatively long time period between the associated crystal nucleation and final eruption at the surface. This suggests that they either passed through relatively long conduits, or there was a pause between an initial stage of rapid decompression and their final eruption at the surface.

4.8.3 Summary of observations relevant to the seamount formation mechanisms

This section presents a summary of the observations, made in this and earlier chapters, which are relevant to the origin and evolution of flat-topped seamounts. These observations are drawn upon in the discussion that follows.

1. Distinct geochemistry (section 4.8.1).
2. Petrography indicates little crustal ponding or interaction with other melts, but a relative long period of time spent in eruptive conduit.

3. Distinct bathymetric shape—low aspect ratio and flat-top (section 4.6.5).
4. Vent fed, small pit craters are common, but large calderas are not (section 3.2.3).
5. Preferential location at the ends of segments (section 4.6.7).
6. Often located over faults and next to the median valley walls (section 4.5.2.3).
7. They are no taller than adjacent hummocky mounds (section 4.6.7).
8. They comprise a mixture of low relief pillow fields and sheet flows, suggesting average effusion rate is greater than for hummocky mounds (section 3.2.3).
9. Seamounts may grow by lateral progradation of summit (positive correlation between flank gradient and flatness), although there is no evidence that they form from hummocky mounds (section 4.6.6).
10. Seamounts in the MARNOK area have a wide age range. There is no single focused period where seamount construction was common (section 3.4.3).
11. Seamounts form by relatively short lived, point source pulses of magmatism (section 4.5.2.1).
12. There may be satellite volcanism, especially on the mantled seamount (section 4.5.2.2). Alternatively this may be a transitional morphology between the hummocky mounds and the flat-topped seamounts.
13. Possible relation to lava tube (section 3.2.5).

4.8.4 Unique characteristics of flat-topped seamounts

The combination of circular form with flat-top and steep sides makes the flat-topped seamounts a distinctive category. When considering the formation of these seamounts there are a number of questions relevant to seamount growth mechanisms, such as:

- Why do only point source volcanoes seem to develop flat summit plateaus, while elongated fissure eruptions do not?
- Why should these seamounts be preferentially located at the ends of segments?
- Why might their effusion rates be faster than hummocky ridges?
- Why should many of the seamounts be underlain by faults, either faults on the median valley floor or adjacent to the median valley walls?

The only feature which could possibly be classified as a smooth-topped ridge occurs just to the north of the flat-topped seamount shown in figure 3.14. It does not have the steep sides of the circular seamounts, and is possibly related to the broad hummocky plateau region to the north.

There is clearly some process connecting radial symmetry with the formation of smooth-textured, steep-sided summit plateaux, although the presence of hummocky mounds indicates that radial symmetry does not always result in the formation of a flat-top. Various hypotheses regarding seamount formation will be evaluated in the discussion below.

4.8.5 Megatumuli

In the MARK area, Serocki Volcano and the nearby lower lava delta have flat-topped cratered morphologies, which are very similar to the flat-topped seamounts (Humphris et al., 1990). Serocki is surrounded on two sides by bathymetric highs. One of these adjacent highs was the source of a voluminous flow which ponded in the small valley and later inflated to form the feature now known as Serocki Volcano. Hence, this smooth-topped 'volcano' is actually a megatumulus. The textural similarity of this feature to the flat-topped seamounts implies that the lava inflation is worth considering as a possible formation mechanism.

The large flat-topped seamount on the crest of NVR of segment 2 cannot be a megatumulus as it is bathymetrically higher than any hummocky terrain of comparable age. However, the texture and position of this crestal seamount differs from many of the other flat-tops in the study area which seem to preferentially occur at the edge of the median valley in the lows next to the valley wall faults or at the segment ends.

In subaerial eruptions, megatumuli are fed by pahoehoe flows or lava tubes. Most of the seamounts show no sign of a feeding tube. The flat-topped seamount in figure 3.17 is an exception as it may have been fed by the lava tube which appears to have emanated from the hummocky cones to the east (as described in section 3.2.5). If so, then this flat top seamount may well be a megatumulus with similar dimensions to those in the MARK area (Humphris et al., 1990) and those reported from on land in Etna (Guest et al., 1984) and Hawaii (Holcomb et al., 1974).

Given that there is only higher ground to the NE of the seamount, it seems unlikely that there would have been a valley for the flow to originally pond in. However, the presence of an initial topographic depression is not a necessity for the formation of megatumuli because those observed on Etna preferentially form on the edge of steep slopes which provide a high fluid pressure near the end of the flow, allowing the tumuli to develop to a large size. In Hawaii, small lava shields sometimes form directly above an eruptive centre, whereas others grow over a fissure system which is fed from a main centre some distance away (Holcomb et al., 1974), so some of the flat-tops may be megatumuli and some may be directly pipe fed. It will be impossible to resolve this issue completely without higher resolution studies and more detailed geochemical sampling.

One of the main problems of this theory is that it goes little way to resolving the issues cited in 4.8.3. There is no reason why a megatumulus should have a distinctive parental magma. Indeed the geochemical similarity of Serocki volcano to the nearby cones is one of the main lines of evidence that Serocki is a megatumulus. There is also no reason why megatumuli should preferentially occur at the ends of segments, given that the lava ponding is a local effect. In addition, a possible feeding tube is identified in only one case, so I conclude that most of the flat-topped seamounts are not megatumuli, although there may be the odd exception.

4.8.6 Summit depressions, satellite volcanism and plateau formation

The link between satellite volcanism, caldera formation and the growth of a smooth-textured summit plateau has already been described and discussed in section 4.5.2.2. It was concluded that the mantled seamount provides the best evidence for satellite volcanism around flat-tops, although similar hummocky rims were not clearly identified elsewhere. The mantled seamount has only a small central pit crater, so if satellite volcanism has been established it has not resulted in caldera formation on a scale described in the Pacific (Batiza & Vanko, 1983; Fornari et al., 1984; 1987a).

The creation of a summit depression on a seamount will tend to structurally constrain the style of eruptive volcanism so that it occurs principally along ring fractures. This localises eruptions around the margins of a vent, causing the progradation of summit area and establishment of a plateau (Simkin, 1972). The connection between crater development and formation of a summit plateau is supported by the observation that smooth-topped seamounts invariably have central depressions, while the hummocky mounds sometimes have summit cones, but none have developed central pit craters. There does seem to be a loosely constrained relationship between the size of the central pit crater and the diameter of the summit plateau, but there are no ring fractures observed at the edges of the plateaus (with the possible exception of the rim of the crestal seamount as discussed below).

It is obvious that caldera collapse is not a prerequisite for the formation of summit plateaux. If it were the primary mechanism leading to the development of summit plateaus on the MAR, I would expect satellite volcanism and large calderas to be more common features than they are in this data set. The relationship between the formation of pit craters and summit plateaus is not likely to be causal, but together they are features of a particular style of volcanism, which involves a pulse of volcanic activity, probably with relatively fast effusion rates, followed by magma withdrawal into pipe-like conduits.

The large crestal seamount has a curving fault defining the rim of its summit plateau, and a broad central depression. These features are consistent with a chamber-induced

stress field, and may be related to the presence of an individual high level magma chamber, as has been suggested for similar features in the Pacific (Batiza & Vanko, 1983; Batiza et al., 1984) and on land (Stearns & Macdonald, 1942; Jaggar, 1947; Ryan et al., 1981).

4.8.7 Excess magma production - dynamic pulse

In the Pacific, high concentrations of seamounts are also associated with ridge segments that have elevated crests (Fornari et al., 1987b), although in a recent study only a very weak correlation was seen between seamount volume and ridge cross-sectional area and depth (Scheirer & Macdonald, 1995).

The TOBI data recently collected over the segments south of the Atlantis Transform have shown that, although most segments only have flat-topped seamounts at their end, two segments have numerous large, flat-topped volcanoes at their centres, as well as their ends (Briais et al., 1994). Both of these segments are characterised by particularly large mantle Bouger anomalies and shallow axial valley mid-points compared with other segments in the area. They are interpreted by Sempéré et al. (1993) as being dominantly 'magmatic'. The flat-topped seamounts within a segment were thought to be relatively uniform in age, whereas the hummocky terrain showed a continuum of tectonic dismemberment.

This uniformity in seamount age has led Briais et al. (1994) to suggest that the flat-topped seamounts are formed during bursts of high magmatic activity. Part of the magma pulse goes to replenish the magma chamber and the rest is dynamically emplaced to form the flat-topped seamounts. In the centres of segments, these dynamically emplaced seamounts later become buried by hummocky construction which occurs as the result of passive emplacement from a cooling and fractionating magma chamber, controlled by tectonic extension of the axial valley. The flat-topped seamounts at the end of the segment are preferentially preserved at the surface because the ongoing fissure eruptions are less voluminous at the ends, so they are less likely to be buried.

Briais et al. (1994) suggest that this model can be tested in two ways. Firstly, the ages of flat-topped seamounts within a single segment are likely to be homogeneous, falling into groups corresponding to one or two magmatic phases. Secondly, the composition of basalts from the flat-tops is likely to be more primitive than that from the hummocky terrain which has been able to fractionate in a magma chamber.

At the NTO in the MARNOK area, the nested seamounts and the mantled seamount have very similar textures and appear to be similar ages. However, apart from these two there is no uniformity in the apparent ages of seamount across the study area, and

no half-buried seamounts were seen in the segment centres despite the relatively young apparent ages of some of the seamounts at the ends. The geochemical results, discussed in section 4.8.1, show that although the flat-topped seamounts have parental magmas which are distinct from the adjacent hummocky terrain they are not consistently more primitive.

Hence, I discount the theory that the flat-topped seamounts are merely buried more quickly in the centre of the segment. If seamounts are formed by dynamic magmatic pulses, these pulses must be preferentially located at the ends of the segments and be relatively randomly distributed in time.

4.8.8 Lithospheric "snowploughing"

Both widespread and detailed studies of the flanks of the EPR have found that seamounts tend to cluster, often forming chains subparallel to relative and absolute plate motions, near transforms, their fracture zone extensions and some large overlapping spreading centres (Batiza, 1982; Batiza & Vanko, 1983; Fornari et al., 1987a). However, most of the Pacific chains do not occur directly along the fracture zones, but several tens of kilometres away. This suggests that they do not form purely as a result of the weakness of the lithosphere near a discontinuity (Scheirer & Macdonald, 1995).

Pockalny et al. (1991) proposed that these seamounts might be formed by the migration of the EPR ridge-transform system in an absolute reference frame. Their hypothesis suggested that secondary upwelling in the mantle is induced by the migration of older thicker lithosphere, snowploughing the shallow asthenosphere in front of it.

A similar theory might explain the clustering of seamounts at the ends of segments in the MARNOK area. However, the absolute plate motion of the African Plate is virtually zero, while the NorthAmerican Plate is moving westward approximately parallel to the fracture zones (Minster & Jordan, 1978), so the 'snowploughing' theory cannot be responsible for the flat-top seamount distribution in the MARNOK area.

4.8.9 Limiting magmastatic head

In section 4.6.6, I described the hypothesis that a flat top is indicative of a volcano reaching its limiting magmastatic head. The source depths that were calculated from the seamount heights, using the method of Smith and Cann (1992), produce reasonable values for depth of magma ponding, falling within seismic layer 3 at 2km to 3.6km depth. Apart from this, the statistical evidence supporting the hypothesis that hummocky mounds evolve to flat-topped seamounts is relatively poor, though the mantled seamount is a possible example of a transitional form.

There are two issues at stake here: firstly whether a summit plateau is indicative of a limiting magmastatic head, and secondly, if it is, what this reveals about the location magma ponding in the crust.

The analysis in section 4.6.6 showed that there is little evidence that the flat-topped seamounts are any larger than the hummocky mounds. If the flat-topped seamounts have reached their magmastatic limiting height, while the hummocky terrain has not, this implies that the flat-topped seamounts must be erupted from *shallower* magma chambers. If the source of flat-topped seamounts is different from the hummocky mounds, then the evolution from hummocky to flat-top is still a credible mechanism, without the need for flat-tops to be more voluminous or taller than the average hummocky mound. Given that the mantled seamount is reasonable evidence of a transitional morphology this hypothesis cannot be discounted. Hence, I will go on to discuss its consequences for crustal plumbing.

Following the reasoning above, if the flat-tops originate from *shallower* magma chambers, their preferential location near the ends of the segments implies a trend which is *opposite* to that predicted for magma ponding at the brittle-ductile transition. For simple vertical conduit models, seamounts at the segment centre should be more likely to reach their magmastatic head than those at the end, where the brittle-ductile transition is deeper (compare cases A and B in figure 4.26). In addition to the greater ponding depth, the magmastatic head at the end of a segment is likely to be greater because the brittle lid might contain a greater thickness of lithospheric mantle which will increase its average density (case C, figure 4.26).

The only way these data can be reconciled with magma chambers at the brittle-ductile transition is by invoking non-vertical conduits. If there is a very strong component of lateral injection involved in the extrusion of the seamounts (case D, figure 4.26), the depth to the magma source is actually less than that for vertical conduit. In this manner seamounts at the ends of segments are more likely to reach their magmastatic head.

However, the degree of lateral transport required for this to have an effect is probably unreasonable, especially given the discussion on lateral dyke injection in section 4.7. This model is also critically dependent on the shape of the brittle-ductile transition along-axis. The alternative is that some factor other than the time-averaged brittle lid thickness is controlling the levels at which magma ponds within the crust.

4.8.10 Conduit geometry and flow rate

Fissure eruptions in Iceland and Hawaii are commonly observed to begin very rapidly with magma erupted along the entire length of the fissure. As the eruption focuses into

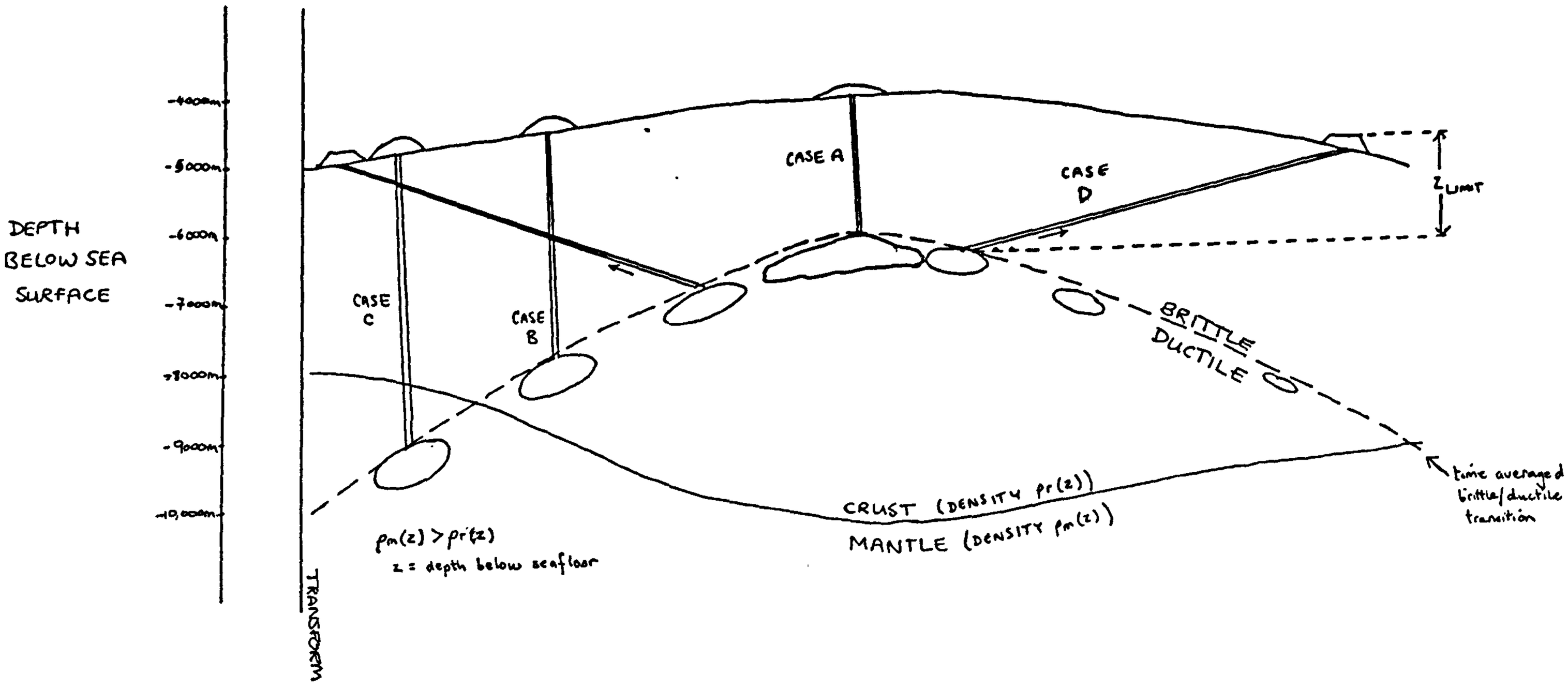

Figure 4.26 Sketch to illustrate how the depth to the magma chamber can vary along a segment. The limiting magmastatic head and hence, the maximum height of a seamount, depends on the vertical distance between the seamount and the magma source. Case A: vertical extrusion near middle of segment. Case B: vertical extrusion near the end of a segment. Case C: average density of rock above magma pond is greater as the brittle-ductile transition occurs within the mantle. Case D: lateral extrusion towards end of segment from source nearer the middle will reduce the vertical distance to the magma chamber, and hence increase the probability that a seamount will reach its magmastatic limit. However, the degree of lateral propagation required for this to have a significant effect may well be unreasonable.

discrete point sources the effusion rate slows, but can be sustained for a considerable period of time (Macdonald & Abbott, 1970; Richter et al., 1970; Thorarinsson et al., 1973). I suggest that hummocky mounds originate from slow point source eruptions, while flat-topped seamounts start as short fissure eruptions which focus into vents at an early stage in the eruption, when the effusion rate is still relatively fast. Indeed, mapping of volcanic constructions in the Troodos ophiolite has revealed sheet volcanoes and pillow volcanoes, with flow rate being defined as the main reason for the differences in these morphologies (Schmincke & Bednarz, 1990).

The question remains as to why none of the elongated hummocky ridges have formed flat tops analogous to the circular seamounts. The conduit morphology itself may explain why sheet flows from a the vent may build up to form discrete edifices while sheet flows from a fissure eruptions do not form mounds. Because the circumference of a pipe/vent would be shorter than the length of the fissure (the eruption would not focus if this were not the case), the site of extrusion is more focused and hence the magma is more likely to pile up round a pipe/vent than along a fissure.

The thermal models of Bruce and Huppert (1989; 1990) can be used to predict that the evolution of vents from fissure eruptions is more likely to happen at the ends of a segment. The three factors that enhance blocking in a 2D model are cooler ambient crust, narrower dykes and greater distance between magma chamber and surface. These factors should also promote fissure focusing in the 3D scenario. The segment ends certainly have cooler ambient crust and will also have greater conduit lengths if ponding is at the brittle ductile transition or lateral transport is important.

Hence, cooler crust at the segment ends enhances the probability of fissures rapidly evolving to pipe vents. Once a vent is established, it is more likely to form a tall edifice which will reach its magmastatic head because of its geometry. This mechanism reconciles two aspects of the data: why flat-topped seamounts preferentially form at the ends of segments, and why there are no constructive ridges with summit plateaus. However, a differing source for the seamounts and the hummocky ridges is still required to reconcile their similar heights and their distinct geochemical parents.

4.8.11 Single plume model, with fracture control

The single plume model was introduced in the comparison between the nested seamounts and MOK (section 4.5.2.1). Unlike the Lamont Seamounts, the smooth, flat-topped seamounts on the MAR do not form trails generated by mini-hotspots, but they may reflect a similar mechanism of melt diapir interaction with the young oceanic crust.

There are certainly aspects of seamount formation in the Pacific that seem to be common to Atlantic seamounts. Both areas have seamounts preferentially located next to ridge discontinuities and show distinctive chemistry (Batiza & Vanko, 1984). In the Pacific, basalts from seamounts tend to have more primitive compositions, and are formed from lower average degrees of partial melting than non-seamount basalts. The nested seamounts show the same trends in the geochemical data, but the other seamounts are not consistent with these geochemical systematics.

Batiza and Vanko (1984) propose that this combination of factors is a consequence of the seamount parental magmas not being cycled through an axial magma chamber. The seamounts form preferentially near fracture zones because the thermal and mechanical regime favours the ineffective mixing of lower average extents of partial melt and less total melt production. In addition, the fractures within the young crust provide a line of weakness which is preferentially exploited by a rising diapir of magma. This then erupts at the surface as a flat-topped seamount. In the NTO, the interaction of three small, closely-spaced diapirs, with two intersecting fracture systems, led to the formation of the nested seamounts.

The crestal seamount is an interesting case, as it sits right in the centre of the partly faulted and partly constructional ridge crest that dominates the NVR for 15km. The seamount itself is not faulted, although it seems to be intimately associated with the underlying faulted ridge crest in terms of its central position and the way the flanks and the plateau blend in with the structure. Hence the seamount formed after the faulting episode took place along the ridge, but was still somehow controlled by or related to the structure, so the magmatism was focused into the centre of it.

The distinctive chemistry of the MARNOK seamounts can be explained by the passage of melt diapirs through the crust with relatively little homogenisation in a magma chamber. This mechanism is also consistent with the circular, vent-fed form of the seamounts, with the location of seamounts above fractures, and their preferential distribution at the ends of the segments. In all, this mechanism reconciles most of the observations, though it does not explain why diapirs should produce seamounts with flat-tops.

In chapter 7, I present a comprehensive model, which adapts the single plume model in a way that reconciles all the observations and is consistent with observations of rifting episodes within Iceland.

4.9 Summary of Chapter 4.

- The narrowgate NVZ comprises relatively short-lived eruptive episodes with high effusion rates, which subsequently are rapidly dismembered by tectonism, preventing the formation of a mature volcano. The narrowgate morphology—narrow symmetrical rift valley; poorly-developed, narrow NVR; low tectonic strain—is consistent with the presence of a shallow magma chamber located at the brittle/ductile transition and a relatively high and strongly focused magmatic supply.

- The robust NVR of segment 2 was constructed during two or three prolonged episodes from pillow lavas, indicating low effusion rates. The gradient is the primary control on the flow rates of these lavas. During this time the NVR experienced little tectonic dismemberment, although a prominent syn-magmatic fault dominates the western crest and may control the construction of the NVR. A 60m reduction in height of the eastern crest, virtually all accommodated on one fault, is thought to be related to 'volcano collapse' though it should be noted that the structure controlling this subsidence is on the flank not the base of the NVR. The segment 2 morphology—wider, asymmetric rift valley; robust NVR; relatively high tectonic strain—is consistent with a deeper magma chamber at a deeper brittle/ductile transition and a lower (and less focused) magma supply, which is perhaps more strongly episodic.

- The hackly/jumbled sheet flow type is analogous to transitional pahoehoe. It is indicative of high viscosities as well as the high flow rates predicted by Griffiths and Fink (1992a). After the consideration of many factors, I conclude that rapid quenching under high hydrostatic pressure has been shown to account for the differing characteristics of hackly deep-sea flows and mature subaerial aa. I suggest that rapid quenching my also be a primary factor in producing the differences between deep-sea and subaerial volcanic morphologies.

- A combination of constructional oversteepening and syn-tectonic magmatism contribute to the formation of pillow flow front breccia. Syn-tectonic magmatism is more common in segment 2 than it is in segment 1. In segment 2 lavas sometimes seem to use fault planes as conduits.

- Thatcher's Nose is a chain of composite hummocky seamounts with steep summit cones. It is formed from a relatively primitive magma which has entrained 40% modal plagioclase megacrysts. The high viscosity of this highly phyric lava is responsible for the distinctive shape of the edifice.

- Hummocky ridges are structurally controlled eruptions which have undergone a small degree of flow focusing. Lavas sampled along a single hummocky ridge are all related to a common parent, but can show a variation in the degree of fractionation along their length, which may result from the tapping of a density stratified magma chamber, ponded at the brittle-ductile transition. The degree of lateral dyke propagation is likely to be less on the MAR than in areas with thick crust, such as Iceland and Hawaii, where magma ponds at the LNB. A small degree of lateral dyke propagation will occur, but is not likely to be responsible for the variations in degree of fractionation.

- The flat-topped seamounts are preferentially located at the ends of segments, although they are no taller than adjacent hummocky mounds. They are often located over faults and next to the median valley walls. Their parental magmas are distinct from nearby hummocky terrain. The petrography indicates little crustal ponding or interaction with other melts, but a relatively long period of time spent in eruptive conduit. These features are best reconciled by the interaction of melt diapirs with crustal fractures, allowing magma to pass through the crust with relatively little homogenisation in a magma chamber. The flat-tops probably result from relatively high effusion rates from pipe-shaped conduits rather than from edifices reaching their limiting magmastatic heights.

BLANK IN ORIGINAL

Chapter 5

The transform and the RTI

Sit down before fact as a little child,
be prepared to give up every preconceived notion,
follow humbly wherever and to whatever abyss nature leads,
or you shall learn nothing.

Thomas Huxley

5.1 Introduction.

The morphological effect of the transform extends right up to 24°04'N, 26km from the Principal Transform Displacement Zone, (PTDZ). This is a typical of previous estimates made of the transform domain (Fox & Gallo, 1986) and ties in with estimates of the length scale of the TFE discussed in chapter 1. The clearest manifestation of the change in the stress regime is seen in the median valley walls, as will be discussed in greater detail in section 5.3, but I start in section 5.2 with a description of the tectonic, volcanic, geochemical and petrological variations seen along axis. This is followed in section 5.4 and 5.5 by descriptions and interpretations of features in the nodal basin and the transform, respectively. Section 5.6 is a discussion which includes topics such as the interaction of extensional and strike-slip tectonics in the RTI, the role of asymmetric spreading and the possible causes of serpentinite diapirism in the transform.

5.2 The median valley floor in the transform domain.

The following section will focus on the changing character of the volcanic and tectonic terrains seen along the valley floor. This includes variations in the volcanic morphologies, the faulting that cuts the NVZ and the boundary between the neovolcanic and tectonic fissured terrains. Many of the described features can be seen on figure 5.1a (refer to figure 5.1b for labels). Figure 5.1b also shows the locations for the dredge sites in this area which will be referred to in section 5.2.3.2. The account will start at the northern extent of the transform domain and continue southwards towards the transform valley.

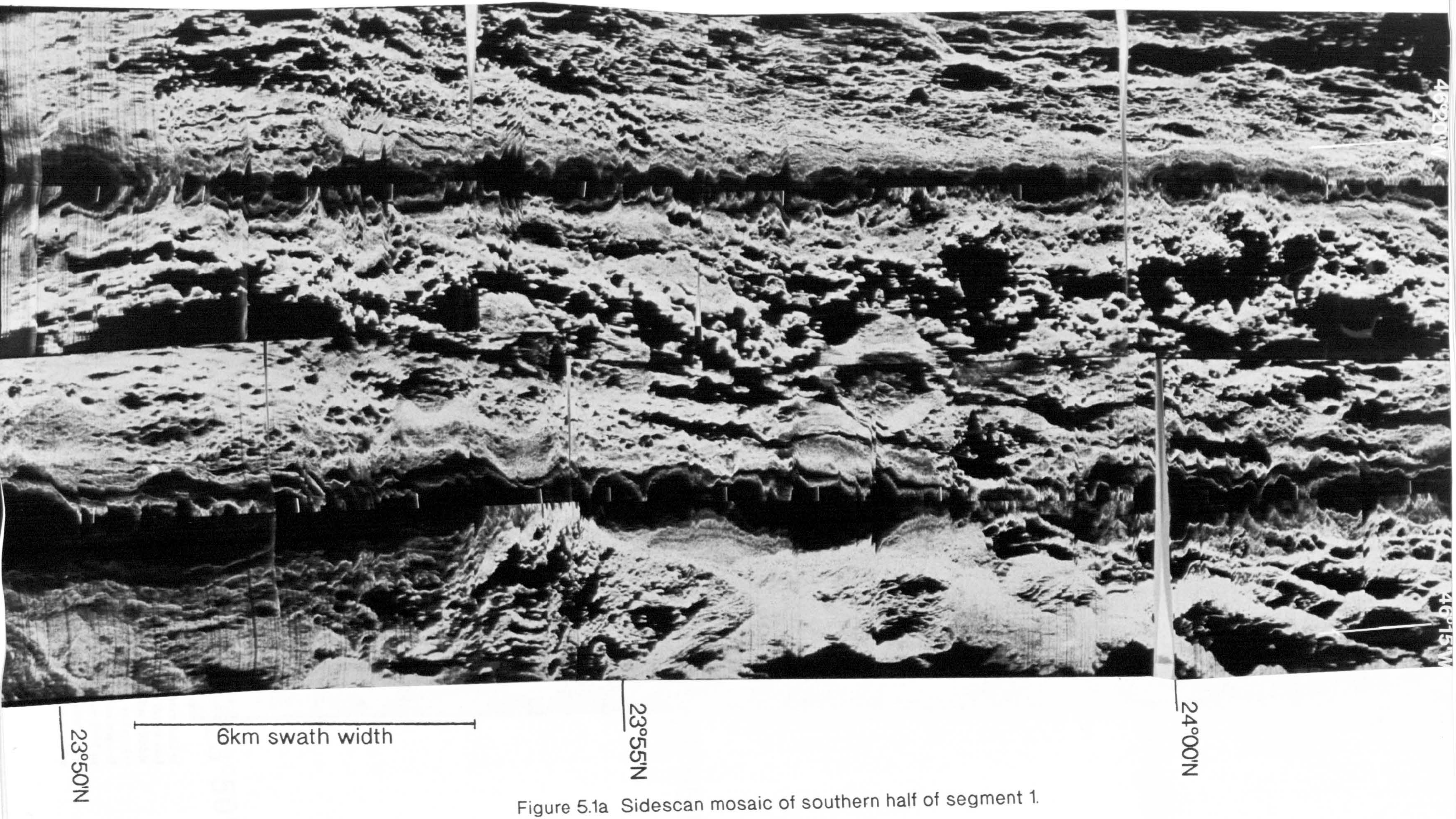

Figure 5.1a Sidescan mosaic of southern half of segment 1.

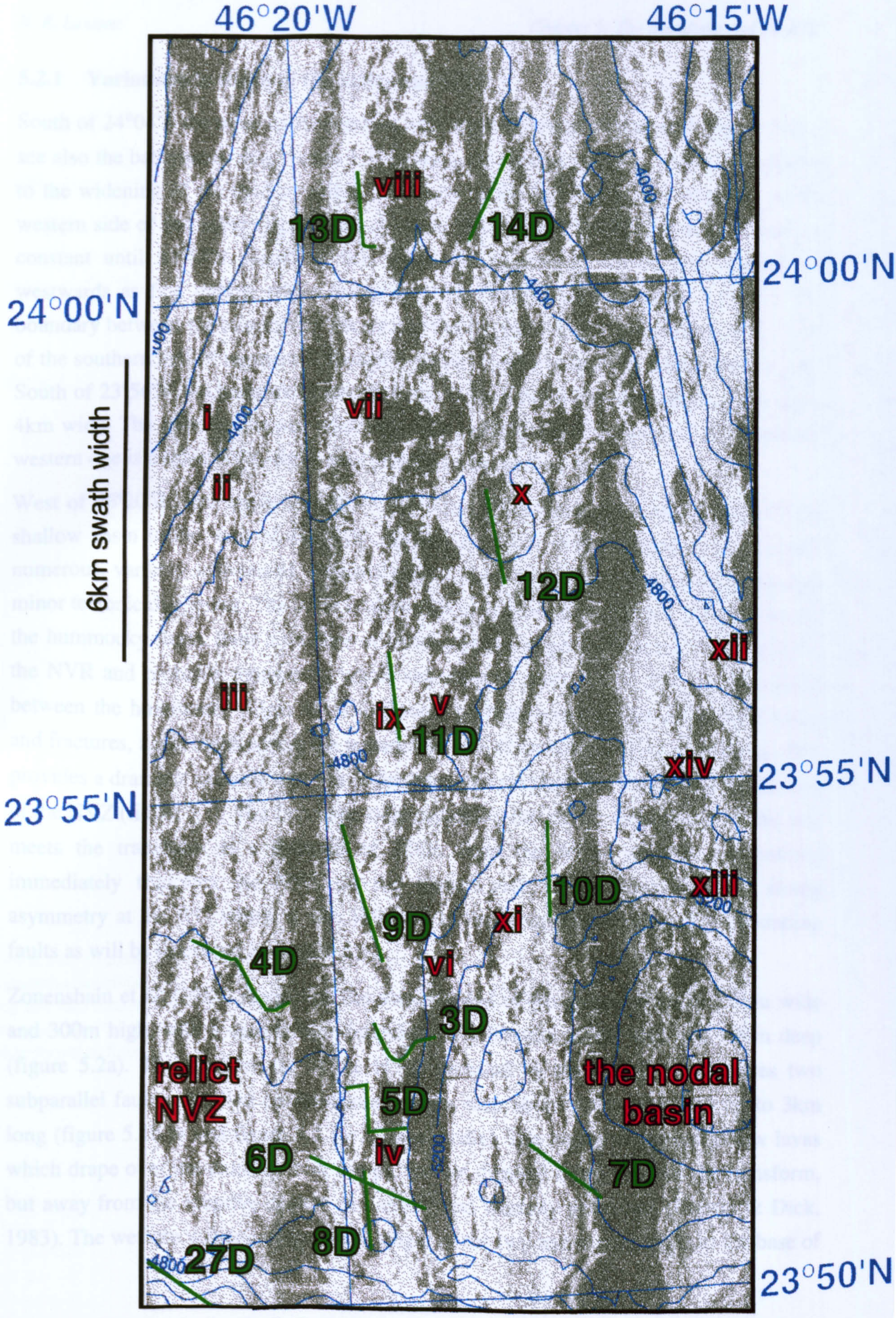

Figure 5.1b Positions of dredge sites 3D, 4D, 5D, 6D, 7D, 8D, 9D, 10D, 11D, 12D, 13D, 14D and 27D in the southern half of segment 1. Labels refer to discussion in the text: (i) median valley widens as western valley wall faults decrease in throw and deviate to the west; (ii) expanse of fissured terrain on western side of valley increases as valley widens; (iii) fine blibble ridges onlap fissured terrain where NVZ widens; (iv) sharply defined hummocky ridge trends into the transform valley; (v) oblique hummocky ridge; (vi) NVZ curves out to the west and then strikes N-S towards the transform, following the edge of the nodal basin; (vii) hummocky mound; (viii) Thatcher's Nose; (ix) high backscattering, smooth-textured pillow field or sheet flows; (x) flat-topped seamount; (xi) tectonised, smooth-textured seamount on walls of nodal basin; (xii) eastern wall abruptly deviates to strike of 120 degrees; (xiii) northern wall of nodal basin trends at 100 degrees; (xiv) terrace of older crust is stranded near the valley floor between eastern wall fault and northern wall of the nodal basin.

5.2.1 Variations in width of the valley and NVZ

South of 24°04'N the trend of the western wall starts to deviate to the west (figure 5.1b i; see also the bathymetry map: figure 1.3) causing the median valley to widen. In response to the widening of the median valley, the width of the fissured terrain increases on the western side of the valley (figure 5.1b ii), while the width of the NVZ remains relatively constant until 23°57'N. South of this point, the hummocky terrain also widens out westwards as fine blibble ridges onlap onto the fissured terrain (figure 5.1b iii). The boundary between the hummocky terrain and the fissured terrain is not sharp along most of the southern half of segment 1, though in places a clear onlapping relationship is seen. South of 23°56'N, the hummocky terrain forks to form two composite ridges, each about 4km wide. The easternmost one adjacent to the nodal basin is the present NVZ and the western one is a relict NVZ which runs parallel to the present one.

West of 46°20'W, and south of 23°55'N the relict NVZ forms the eastern extent of the shallow basin to the west of the NVR. Karson and Dick (1983) report that it contains numerous, variably sedimented, coherent pillow flows which have been affected by only minor tectonic disruption. The basin is about 12km wide at the transform (figure 1.3) and the hummocky flows form a number of constructional ridges, which are sub-parallel to the NVR and probably represent a whole sequence of relict NVZs. The depressions in between the hummocky ridges are also floored by hummocky terrain rather than faults and fractures, again emphasising the remarkable lack of tectonic activity in this area. This provides a dramatic contrast with the sedimented and rubble-filled nodal basin to the east of the NVZ (figure 5.1). The first large ridge parallel scarp on the western side of the axis meets the transform at a distance of 12km from the NVZ, whereas the faulting immediately truncates the NVZ on the eastern side. This demonstrates a strong asymmetry at the RTI which is also reflected in the comparative sizes of the bounding faults as will be discussed in section 5.3.

Zonenshain et al. (1989) report that the southern end of the present NVZ is 2.5km wide and 300m high, with a central fault-bounded axial fracture 500m wide and 100m deep (figure 5.2a). The southern tip of the NVZ, revealed by the sidescan, comprises two subparallel fault-controlled constructional ridges each about 400m wide and up to 3km long (figure 5.1b iv and figure 5.3 for a larger scale). The highly elongated pillow lavas which drape over pre-existing fault scarps, are not directed down towards the transform, but away from the eruptive centres in easterly and westerly directions (Karson & Dick, 1983). The western volcanic ridge is the longer of the two and extends right to the base of

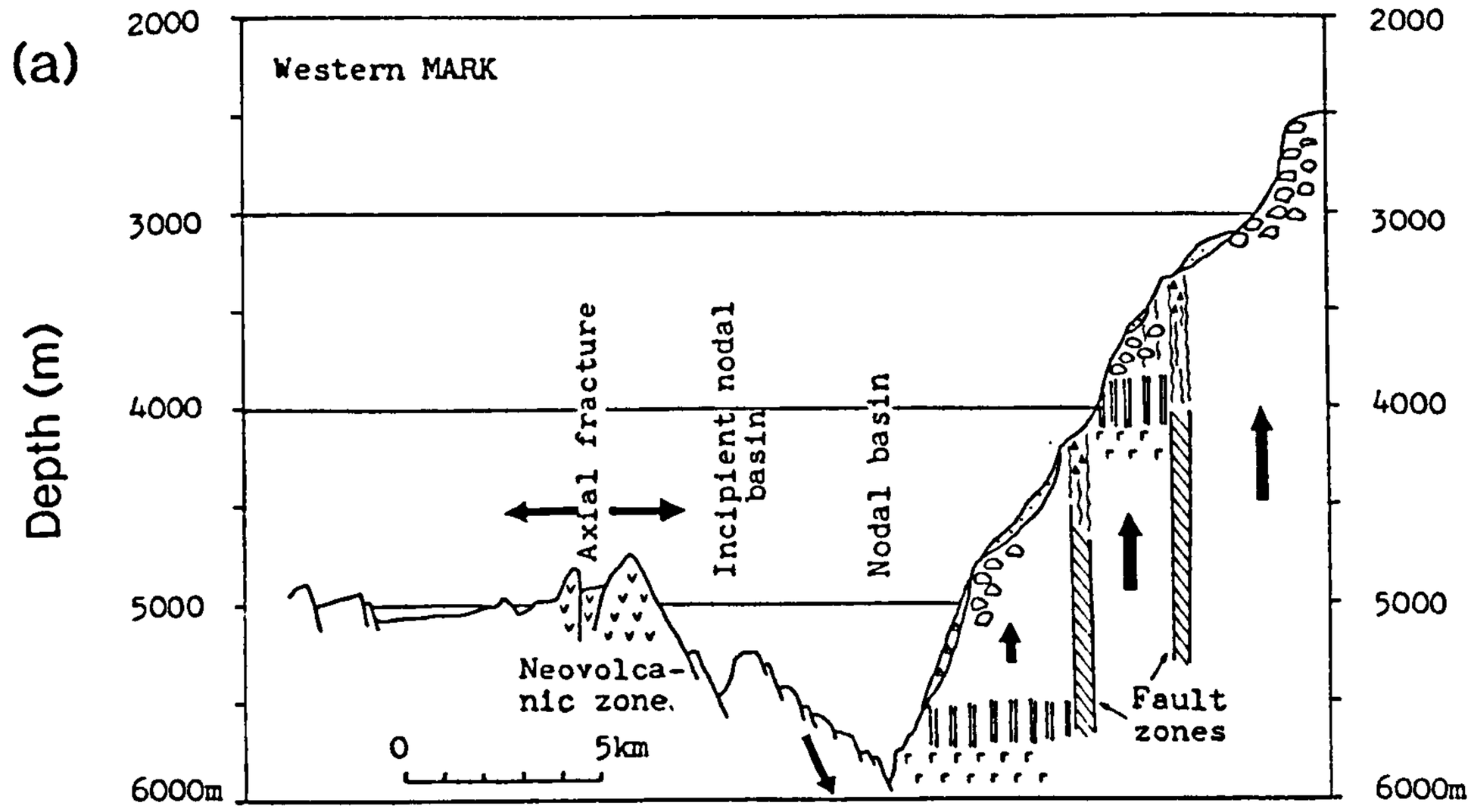

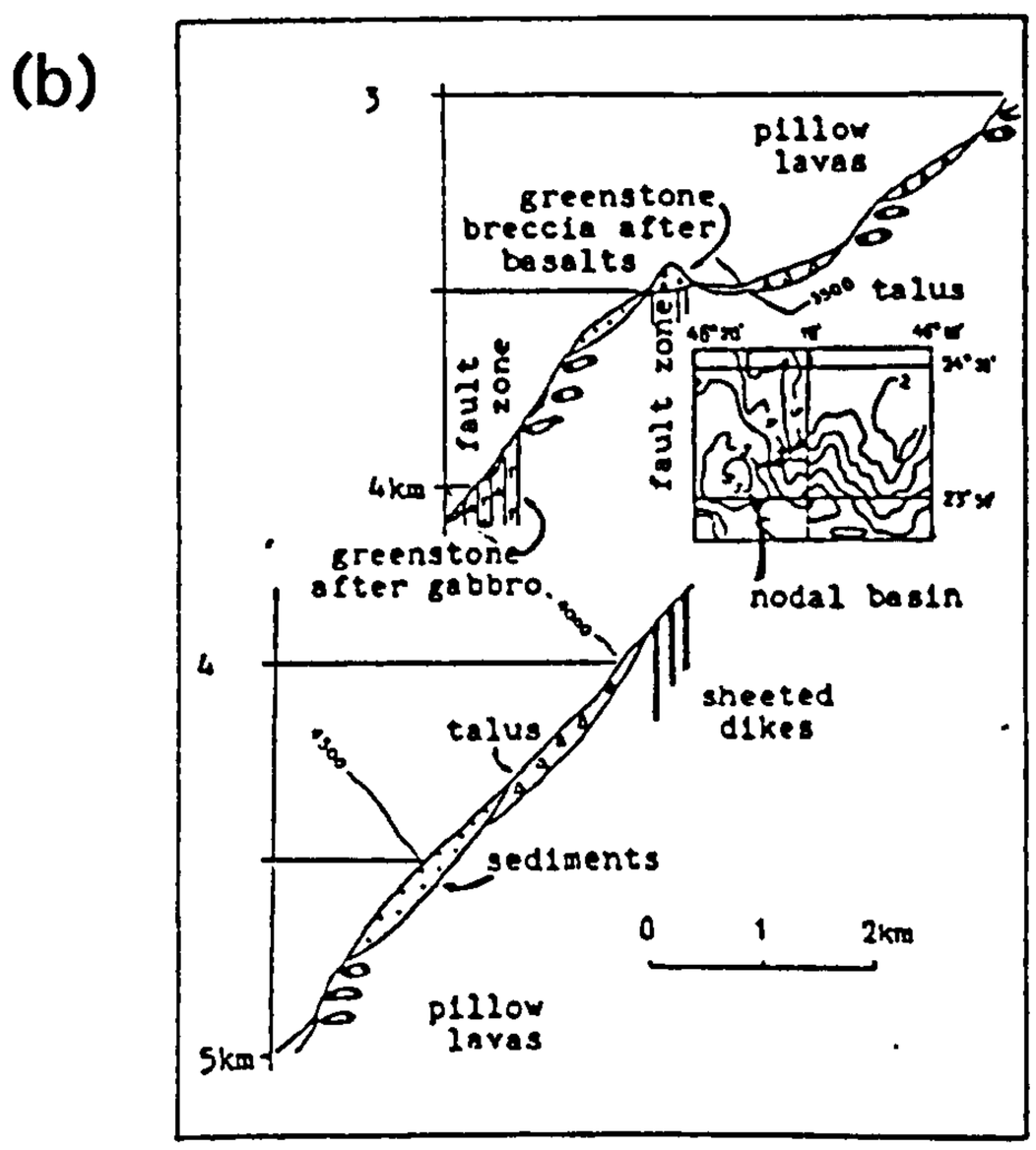

Figure 5.2 (a) Transect 5 of Zonenshain et al. (1989) across the nodal basin and inside corner high. An interpretative morphological and geological cross-section based on high resolution bathymetry, piston coring and two submersible dives. **(b)** The MIR-1 and MIR-2 submersible dive profiles up the inside corner high also taken from Zonenshain et al. (1989). Location of the cross-section and submersible dives is shown in figure 5.10.

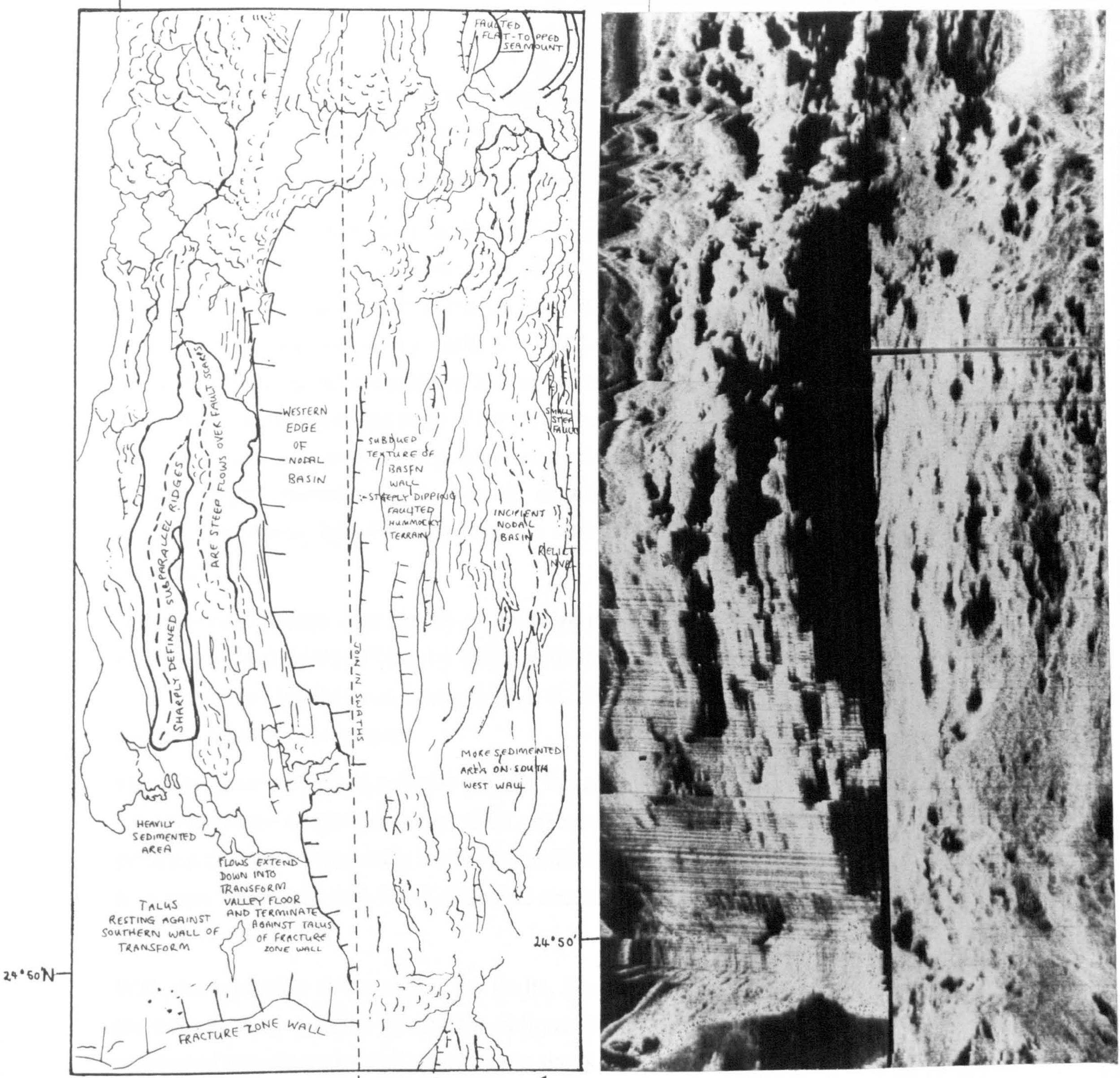

Figure 5.3 Ridge-parallel mosaic of western wall of the nodal basin and the adjacent NVZ. The far range of the western swath is in shadow corresponding with the edge of the nodal basin. The western wall of the nodal basin is imaged by the eastern swath and has a subdued texture compared to NVZ. The amplitude decreases to the east as the depth increases. This may be a result of increasing sediment cover, but is partly an artefact of the changing incidence angle of the beam over the steeply dipping slope. The 'incipient basin' identified by Zonenshain et al. (1989) is imaged just to west of the nadir of the eastern swath. In the NVZ the sharp textures and high aspect ratio of the two parallel hummocky ridges suggest a strong tectonic control to the constructional volcanism. The hummocky ridges extend into the transform valley floor and terminate abruptly against the talus and debris slides of the brightly backscattering southern wall.

the fracture zone valley floor where it terminates abruptly against the talus and the debris slides of the older fracture zone wall (near 8D, see also figure 5.3).

5.2.2 Orientation of structures and constructional ridges

A change in the orientation of the hummocky terrain accompanies the change in width of the NVZ at 23°57'N. To the north-west of the nodal basin, a prominent oblique-trending hummocky ridge (figure 5.1b v) has its long axis aligned at 040°, at a similar orientation to faults on the adjacent valley walls. The NVZ as a whole curves out to the west and then round to follow an approximately N-S strike towards the transform in a manner which parallels the contours of the edge of the nodal basin (figure 5.1b vi). At the southern tip of segment 1, the two narrow, sharp, hummocky ridges (figure 5.1b iv), generally trend N-S, but the longer western ridge is actually slightly kinked, striking 010° in the north but bending eastwards into the transform to strike at 8° W of N for the southern-most kilometre.

The dominant feature near the tip of the ridge on the transform-parallel TOBI swath is a rectangular fault block, 750m by 500m with the long-axis trending at 320°, tilted away from the axis (labelled on figure 2.10a). A faulted ridge about 200m wide forms the southern edge of the structure.

The only constructional transform-parallel feature in the NVZ is the feature interpreted as a large lava tube which has issued from a nearby cone field and resulted in an area of lava inflation (figure 3.5; this falls within the nadir of the ridge-parallel swath in figure 5.1). It is at least 700m long and 150m wide and occurs near the north-west corner of the RTI at 23°53.4'N, 46°20.5'W.

With the exception of the above, the faults, fissure and constructional ridges in the NVZ are entirely ridge-parallel or slightly oblique. Karson and Dick (1983) reported a small number of transform parallel structures in the NVZ of the RTI, but they can not be traced on the sidescan images, even on the transform parallel swath, and hence must be very minor and discontinuous.

5.2.3 Volcanic diversity in the RTI

5.2.3.1 Diversity in volcanic morphology

The morphological diversity of the NVZ dramatically increases in the transform domain. In addition to the hummocky ridges there are hummocky mounds (figure 5.1b vii), chains of hummocky seamounts with summit cones (Thatcher's Nose; figure 5.1b viii), and smooth-textured areas (figure 5.1b ix), which may be sheet flows but are more likely to

be pillow fields as discussed in section 3.2.6.3. There are two flat-topped seamounts imaged within the NVZ (figure 5.1b x and the other on the transform-parallel swath—figure 3.5), but the bathymetry suggests that there are probably a further two which fall in the nadir of the swath. Beyond the NVZ there are two more flat-topped seamounts—one on the walls of the nodal basin (figure 5.1b xi) and the other in the western (non-transform) basin. The former is heavily tectonised, while the later seems to be older but is relatively untectonised.

5.2.3.2 Diversity in geochemistry

5.2.3.2.1. Petrological segmentation

The diversity in volcanic morphologies in the TD is matched by a corresponding diversity in parental magmas, as illustrated by the crossing trace element patterns in figure 5.4. The spidergram for Thatcher's Nose (13D-1-1b; figure 5.1b viii), has particularly low concentrations of incompatible elements, a prominent peak at Sr, and a smaller peak at Eu —all features relating to the high concentration of plagioclase megacrysts in this sample. However Thatcher's Nose also has a distinct enrichment in highly incompatible elements (as demonstrated by the upward trend towards the left hand side of the spidergram), which cannot be an effect of even 40% plagioclase accumulation (see section 2.9.5). Hence the parental magma of Thatcher's Nose is considerably different from that of the hummocky ridge only 2km to the east (14D-1-1b; see figure 5.1). A sample from the large seamount (12D-1-1b; figure 5.1b x), which is 5km south of 14D and Thatcher's Nose, in contrast has a relatively depleted pattern, implying a parental magma which is distinct from both the hummocky ridge to the north and the smooth-textured pillow field, 2.5km to the south (11D-1-1b; figure 5.1b ix). This implies that the petrological segmentation, which is defined by the spatial distribution of NVZ lavas with common parents, is less than the dredge spacing over this part of the survey area.

There is, however, a remarkable similarity in the trace element patterns for the large seamount (12D) and the hummocky ridge (9D) on the western edge of the NVZ, 6km to the south of it (figure 5.5). Although it is possibly a coincidence that the parental magmas of these two features have the same composition, the coherence of these two samples in terms of major elements and compatible traces, as well as the incompatible trace elements, suggests that they are very closely related. They are also of similar age and have similar petrographic features, although 9D has more plagioclase and shows more evidence of disequilibrium textures. This implies that the same magma batch that formed the flat-topped seamount also erupted as a hummocky ridge over 6km to the south,

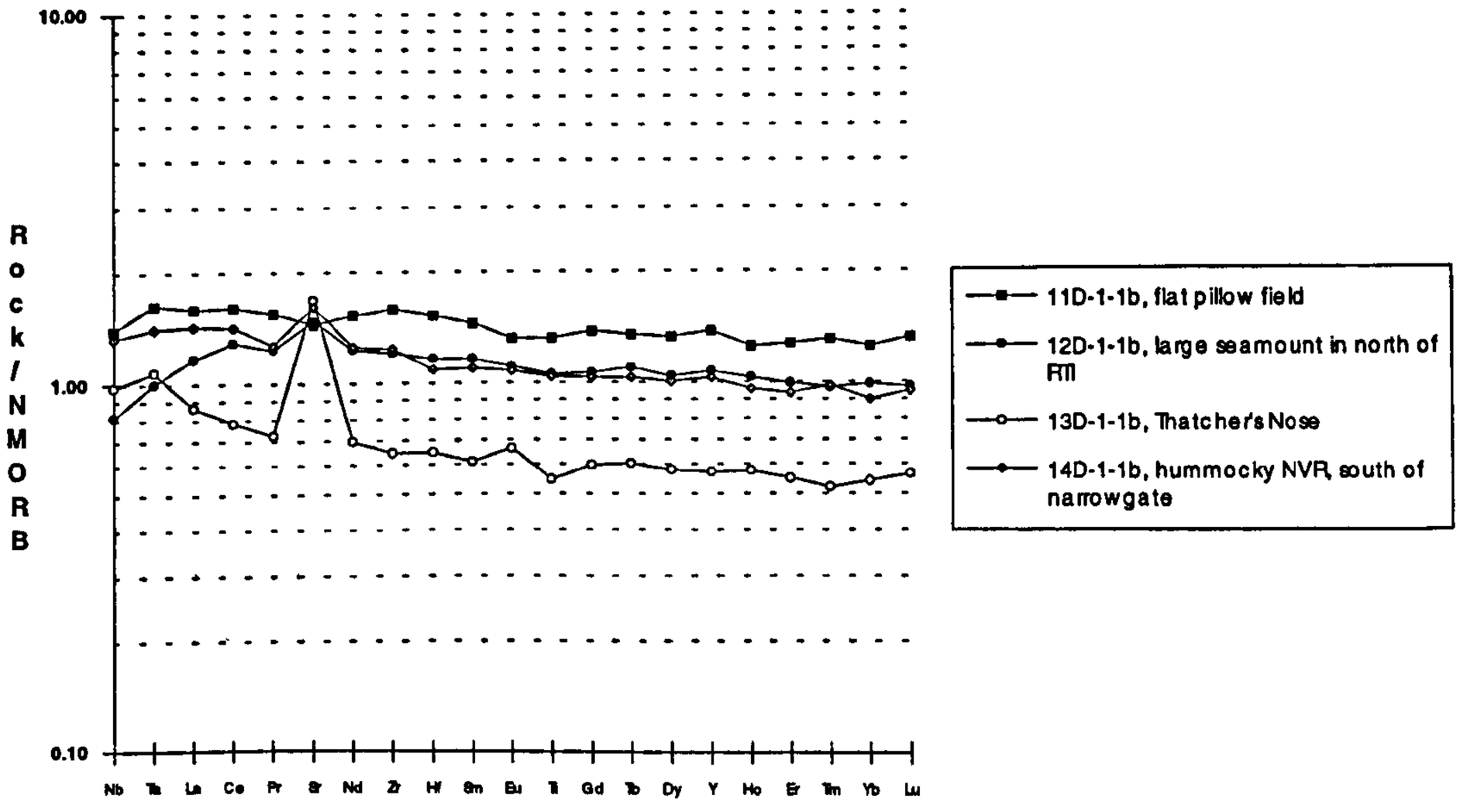

Figure 5.4 MORB-normalised, extended element spidergram for different volcanic morphologies in the northern half of the TD.

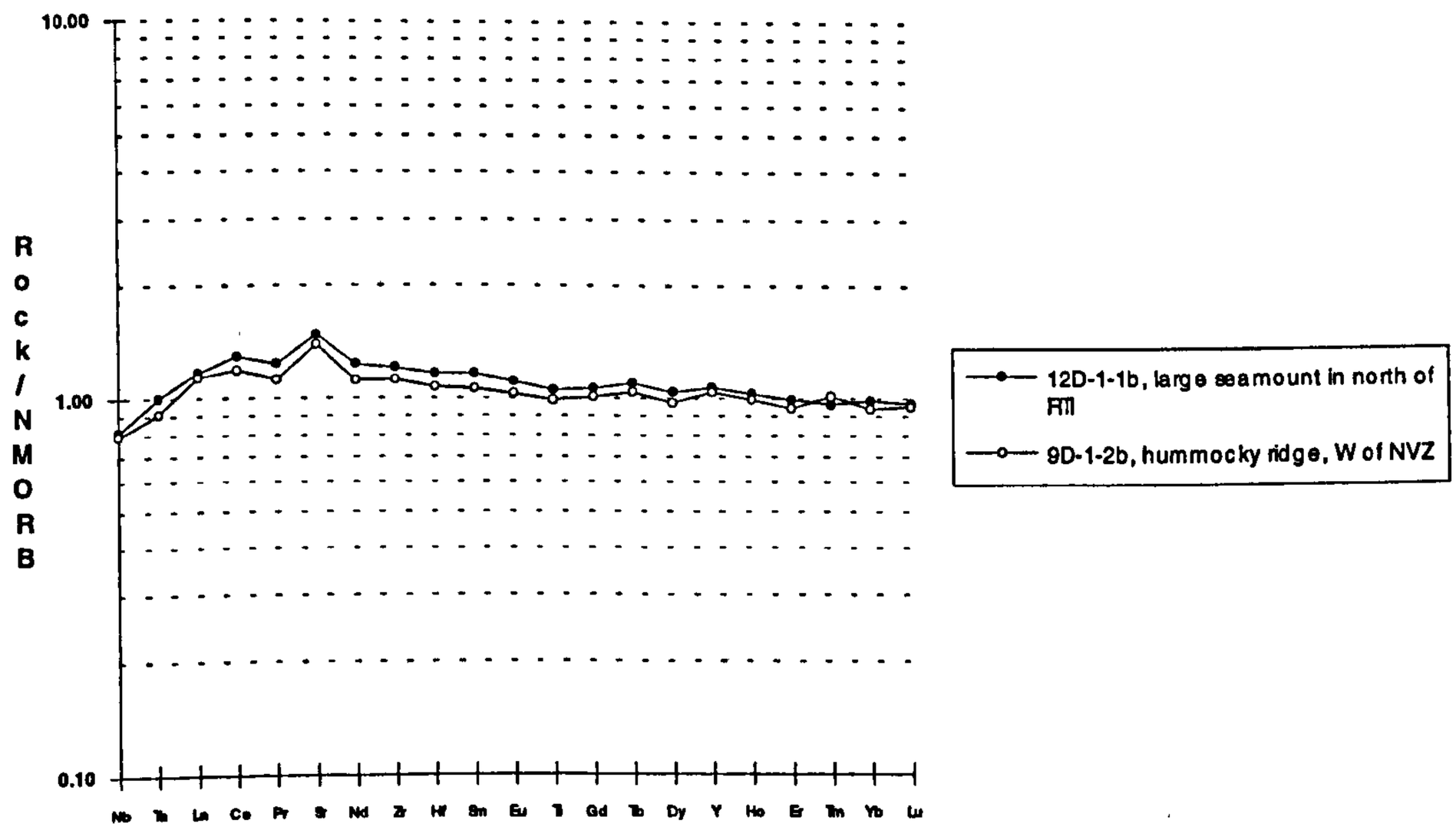

Figure 5.5 MORB-normalised, extended element spidergram showing virtually identical trace element patterns for the large flat-topped seamount in the north of the TD and an area of hummocky ridge 6km to the south of it.

although the smooth textured pillow field (11D), which is considerably closer to the seamount has quite a different parental composition.

This implies that the small scale of petrological segmentation described above may be related to temporal variations in the composition of the magma chamber, as much as, if not more than, spatial variations. This also has implications for my final discussion on magmatic plumbing in chapter 7.

At the southern end of the TD, adjacent to the nodal basin, the dredge spacing is closest, so the scale of petrological segmentation should be easier to define. In section 4.7.1 I reported variation in fractionation along the length of a hummocky ridge. The ridge in question is the prominent, narrow ridge at the very tip of the NVZ (figure 5.1 iv). The lavas sampled along it have virtually parallel REE patterns (figure 4.24), implying that they come from the same parental magma. Figure 5.6 shows the MORB-normalised spidergrams for 5D (the least fractionated sample at the northern end of this hummocky ridge) and 3D (a slightly tectonised hummocky area, about 1km to the north of 5D—see figure 5.1). The trace element patterns are identical for the highly incompatible trace elements on the mid- to left hand side of the graph, but are subtly different for the HREE and Y. However, this difference is verging on the analytical error (see appendix 3), so I suggest that these samples are from essentially the same parental batch, which may have been slightly modified between the two eruptions.

The flat-topped seamount (4D), located about 2km to the NW of 5D (see figure 5.1) also has a very similar trace element profile to the hummocky ridges at the tip of the NVZ, but this time the divergence is beyond analytical error for some elements (figure 5.7). The crossing spidergram suggests that these samples are likely to be from distinct parental batches which nevertheless are relatively similar in composition. Finally, in figure 5.8, sample 5D-1-2b is compared with sample 7D-1-3b from the western wall of the nodal basin (see figure 5.1). Although these samples are a similar distance from the transform, they are probably separated in age by several hundred thousand years. Their crossing trace element profiles suggest that this time gap was long enough for the parental magma composition underlying the ridge crest to change considerably.

In summary, the parental magma composition seems to change at least every 3-6km along axis, and there are also variations spaced at 2km or more across axis. Therefore fresh inputs of magma changing the parental compositions erupting at the ridge crest are likely to take place at least every several 100,000 years. The superposition of temporal and spatial variations in the magma chamber composition is likely to lead to complex patterns

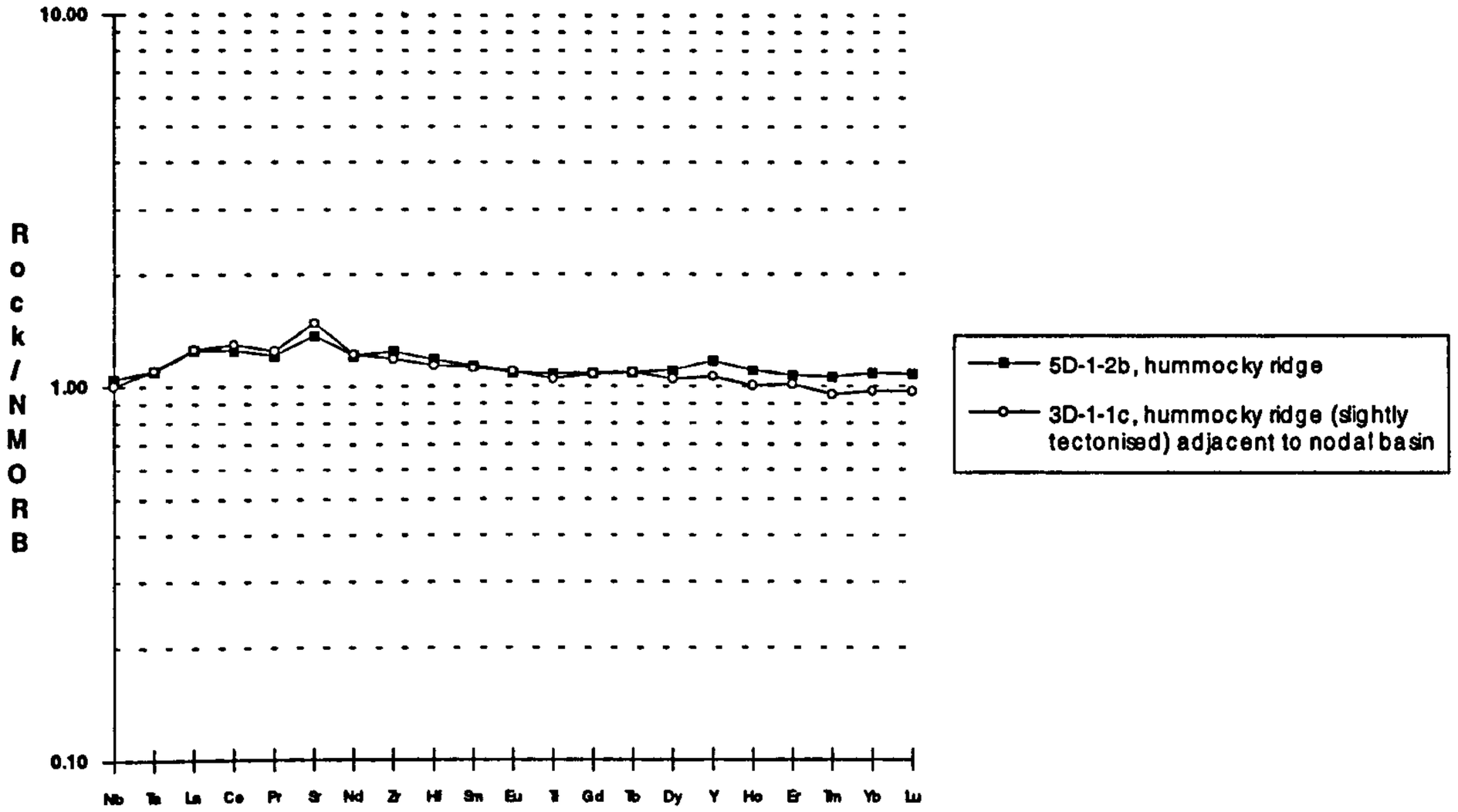

Figure 5.6 MORB-normalised, extended element spidergram showing trace element patterns for two adjacent hummocky ridges at the tip of the NVZ. These are identical for the highly incompatible trace elements, but show a subtle difference, verging on the analytical error, for the HREE and Y.

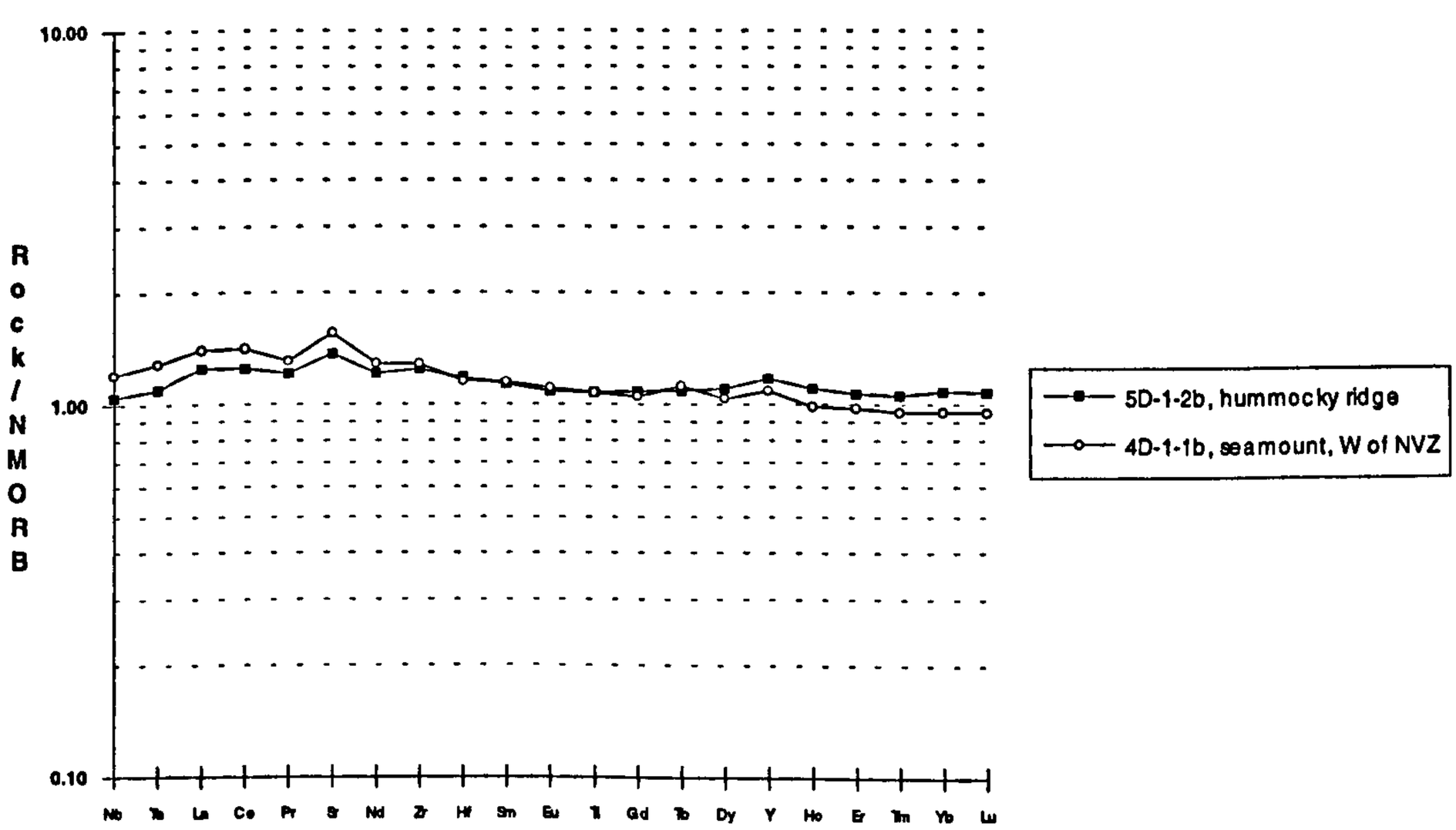

Figure 5.7 MORB-normalised, extended element spidergram showing trace element patterns for the hummocky ridges at the tip of the NVZ (5D) and the flat-topped seamount to the NW of it (4D). These traces are similar, but beyond analytical error for some elements. The divergence on the left hand side of the spidergram, as well as the right hand side suggests that these samples are likely to be from different parental batches.

of petrological segmentation along the ridge axis. Hence, in order to fully resolve the petrological segmentation at the RTI, sampling would be required on a finer scale than that available from the CD57 survey. The scale of petrological segmentation in the RTI will be compared with that seen over the rest of the MARNOK ridge crest in chapter 6. This is followed by a discussion relating petrological segmentation to magma supply.

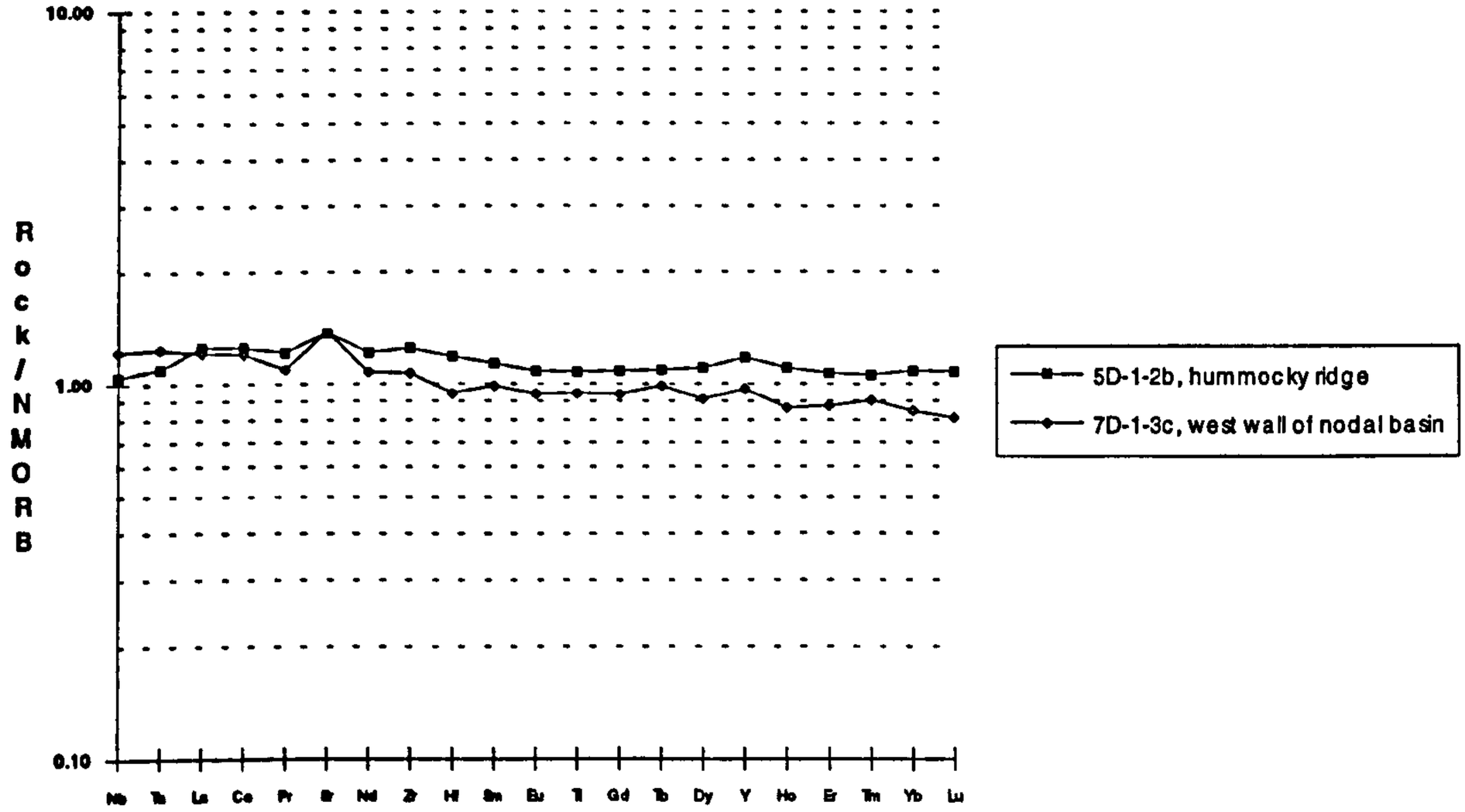

Figure 5.8 MORB-normalised, extended element spidergram to compare trace element patterns for a "zero age" sample from the hummocky ridges at the tip of the NVZ (5D) and the strongly tectonised western wall of the nodal basin (7D).

5.2.3.2.2. Variation in fractionation along axis

The lavas across the transform domain show a well defined increase in the extent of fractionation towards the transform (MgO~8.35 wt.% at Thatcher's Nose and ~6.55 wt.% in 8D, at the southernmost tip of the NVR). The data will be presented in context with the data for the rest of segments 1 and 2 in chapter 6, where the implications of this trend will be discussed.

5.2.3.3 Diversity in petrography

The variation in extent of fractionation is reflected by the phenocryst assemblages and relative modal abundances. All the samples contain plagioclase and olivine microphenocrysts, except Thatcher's Nose which contains no quench growth. Clinopyroxene is on the liquidus of only the most fractionated samples form the southern

tip of the NVZ (5D, 6D and 8D). Plagioclase phenocrysts (zoned and unzoned) are common, but olivine is rare as an intratelluric phase.

High modal abundance of the plagioclase megacryst in Thatcher's Nose has previously been referred to in chapter 4. However, Thatcher's Nose is not the only example of relatively large degrees of crystal accumulation. High modal abundances of plagioclase are very common at the southern end of the RTI, up to 10km from the transform. Some samples from 6D, on the southern tip of the ridge, contain up to 30% modal plagioclase megacrysts, while 3D, 8D, and 9D (all adjacent to the nodal basin) recovered samples with up to 20%. As previously mentioned in section 4.8.2, the flat topped seamounts are relatively free of zoned intratelluric plagioclase and plagioclase megacrysts.

The implications of these variations will be discussed in section 5.6.6, will be related to the rest of the MARNOK area in chapter 6 and are relevent to a general model of magmatic plumbing discussed in chapter 7.

5.2.4 Age variations

Petrographic and hand-specimen age estimates suggest that Thatcher's Nose, and the nearby 14D site, in the north of the TD are the youngest basalts recovered in this area. Considerable amounts of pelagic ooze were recovered from the seamount 12D, which also contained some of the oldest basalts in the area. There were also relatively old rocks obtained from the very southern tip of the NVR.

The dredges from the nodal basin sampled only sediment from the northern edge (10D), but 7D, which was located over the incipient nodal basin/relict NVR (see section 5.4.1.4), recovered remarkably fresh pillows (comparable with many of the samples from the NVZ). As expected, the samples from the southern transform wall were considerably older than those from the NVZ.

The oldest, most altered sample recovered from the NVZ was from the smooth-textured pillow field dredged during 11D. This suggests that the flat-lying pillow field is older than most of the surrounding volcanic constructions. Indeed, it seems from the sidescan data that hummocky ridges have built on top of this low relief area. This observation agrees with the theory discussed in chapter 4, that the early phases of volcano growth involve low relief lava flows.

5.2.5 Hydrothermal activity

Despite the presence of the steep-sided mounds, similar to the supposed 'hydrothermal supermounds' reported by Murton and German (1992) (section 3.7.1), there is no

evidence for extensive hydrothermal activity in the dredge recoveries, except from the southern transform wall where a hydrothermal quartz-chlorite-epidote-pyrite vein was recovered.

5.3 Valley wall faulting in the RTI.

5.3.1 The eastern wall duplex

At 24°04'N the character of the eastern valley wall changes from a continuous valley parallel fault in the north to a complex arrangement of faults, resembling a duplex; thus marking the onset of the transform domain.

The duplex comprises an intricate arrangement of splays and numerous short horse terraces, which have formed as oblique faults have developed and propagated through each other (figure 5.9). The faults fall into two broad categories, those trending NNE (which are the dominant trend) and those trending NNW. There is gradual evolution southward in the orientation of and relative size of the faults. Where the transition in faulting style first occurs a ridge-subparallel orientation remains prominent, but becomes increasingly oblique forming an en-echelon set at 015°-020°. This is cut by small splays with a NW-SE trend and some with almost transform-parallel orientations of 100°-110°.

South of about 24°01'N, the en-echelon set becomes more oblique (strikes of 025°-040°) and the symmetrical conjugate trend (~140°-165°) grows in importance. There are no fault orientations subparallel to the transform imaged here. The number of faults seems to reduce, but those that remain are more extensive and on the whole have larger throws. The longest of the inward facing en-echelon normal faults can be traced across the valley wall for 5.5 km on the sidescan, but on the bathymetry their trends can not be followed much beyond the crest of the wall fault. At 23°57'N the eastern wall abruptly deviates to a strike of 120° (figure 5.1b xii), while the northern wall of the nodal basin at ~23°54'N trends at 100° (figure 5.1b xiii). A terrace of older crust (figure 5.1b xiv) remains stranded in between them, being neither uplifted into the valley wall nor down faulted into the nodal basin.

A major structural trend striking obliquely at ~040° and dipping down to the SE is clearly seen in the bathymetry across the RTI region (see figure 1.3 just to the south of the "Narrowgate" label). This trend is strongest to the north of the RTI where it strikes across the flanks for 15-20km, adjacent to the strike-slip duplex described above. The strike is approximately parallel to one of the sets of faults in the duplex described above. It is also subparallel to the edge of the median valley on the non-transform (western side), and to a

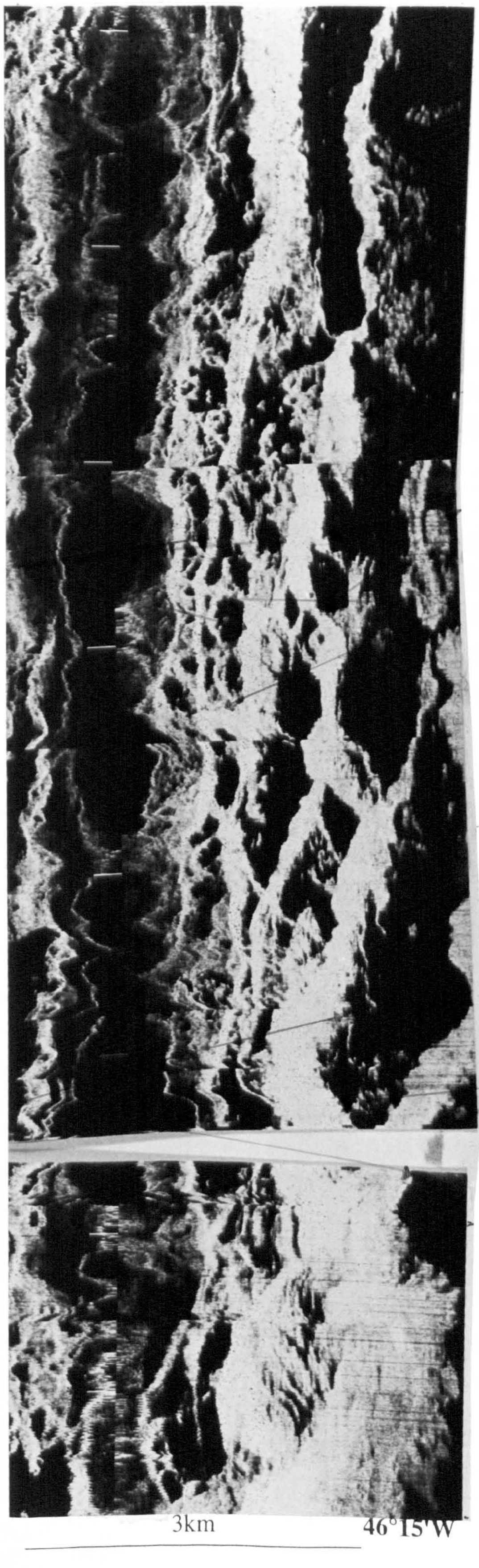

Figure 5.9
The eastern wall duplex in the transform domain

lesser extent the NW corner of the nodal basin. In addition the oblique hummocky ridges of the NVZ also follow this trend. The significance of this major oblique trend which characterises so many features to the north of the transform will be discussed further in section 5.6.1.

5.3.2 Development of asymmetry

The widening of the median valley south of 24°04'N is accompanied by a decrease in throw of the western wall and a corresponding increase in elevation of the eastern wall. Thus the median valley becomes increasingly asymmetric. At the transform, the eastern wall of the inside corner has over 3km of relief compared with a couple of hundred metres for the fault 12km from the axis on the western side of the valley.

5.4 The nodal basin.

The high resolution bathymetry and submersible dives of Zonenshain et al. (1989) (transect 5—figure 5.2b) have been useful in determining the character of the of the nodal basin. This especially applies to the north eastern wall of the nodal basin, about 6km from the transform valley, which is the location of the two submersible dives (see blue lines on figure 5.10). The deeper submersible dive traverses a region where the TOBI profiler's loss of lock on the seafloor has caused a 'black hole' over the nadir of the sidescan image on the transform-parallel swath. This has grossly distorted and reduced the coverage of the swath, but terrains can be roughly traced across the deficient area to allow some correlation with the dive section.

5.4.1 Ridge-parallel structures

5.4.1.1 The eastern wall

The submersible dives of Zonenshain provide considerable information on the tectonics and mass wasting of the eastern wall that is not immediately obvious from the sidescan sonar. This is partly because of the absence of data from the nadir "hole", but also because many of the standard textural terrains seem to have been modified by the extreme tectonism and mass wasting associated with this area. For this reason the sidescan interpretation from the eastern wall requires some interpolation from the results of the submersible dives. This intermingling of the two data sets is not intended to be a groundtruthing exercise as there is little one-to-one correspondence between features identified on the dives and features recognised on the sidescan.

A brightly backscattering, smooth textured terrain (figure 5.10i) extends along the lower eastern wall of the basin up to about 4700m where it contacts abruptly with a very heavily

313° 41' 313° 42' 313° 43' 313° 44' 313° 45' 313° 46' 313° 47' 313° 48' 313° 49' 313° 50'

23° 54'
23° 53'
23° 52'
23° 51'
23° 50'
23° 49'

tectonised flat-topped seamount

large nadir 'hole' where profiler lost lock the bottom

hummocky volcanic terrain

sedimented bottom of nodal basin - note how sediment cover is not as thick as on the uplifted block of the eastern wall

sediment flux into nodal basin from transform valley

southern faulted wall of transform

PILLOW SCARP

Block A

Block B

Block C

UPLIFTED BLOCK OF OLDER CRUST

contact between crust of blocks

UPPER SUBMERSIBLE DIVE

LOWER SUBMERSIBLE DIVE

FAULT ZONE

PILLOWS

SEDIMENT

TALUS

FAULT ZONE

PILLOWS

TALUS

FAULT ZONE

PILLOWS

fault bounded ridges curve east into transform

Highly sedimented transform valley floor

i ii iii iv v vi vii viii ix x xi xii xiii xiv xv xvi xvii

313° 41' 313° 42' 313° 43' 313° 44' 313° 45' 313° 46' 313° 47' 313° 48' 313° 49' 313° 50'E

Figure 5.10. Transform-parallel swath over the nodal basin and inside corner. In the NW, the hummocky texture extends from the NVZ, down to almost the bottom of the basin. The eastern wall has a smoother texture as a result of mass wasting and sedimentation. Major fault zones correspond to a sharp change in the amplitude. Transform-parallel texture is best developed along the southern wall, where sediment slumping and debris flows are prevalent due to material being transported down from the transform valley. The faulted ridges of the inside corner high have erosional gullies at the crest

Figure 5.40. Transform-parallel swath over the axial basin and inside corner. In the NW, the hummocky texture extends from the INTZ, down to almost the bottom of the basin. The eastern wall has a smoother texture as a result of mass wasting and sedimentation. Major fault zones correspond to a sharp change in the amplitude. Transform-parallel texture is best developed along the southern wall, where sediment slumping and debris flows are prevalent due to material being transported down from the transform valley. The faulted ridges of the inside corner high have erosional gullies at the crest

sedimented block of crust (figure 5.10ii). The dramatic linear contact on the sidescan suggests that this is a relatively major structural boundary between a younger (and lower) rock scarp and an older uplifted block which is now tectonically inactive. The structural contact also corresponds to a slight break in slope, which can be traced across the 'black hole' of the nadir region (from ii to iii in figure 5.10). The contact is drawn in a manner which coincides with the sediment/pillow scarp contact at 4700m depth, identified on the lower submersible dive of Zonenshain et al. (1989). The strike of this fault zone varies from N-S to 030°, but averages at ~020°—an orientation similar to that of the dominant en-echelon set in the eastern wall duplex of the median valley. Zonenshain et al. (op. cit.) report that the upper crustal block not only has a shallower angle of slope, but the sediment cover is several meters thicker. This accounts for the abrupt decrease in backscatter. The strong backscatter from the lower pillow basalt fault scarp (figure 5.10i) must be a result of its steep angle, as the account from the submersible describes it as being strongly sedimented.

At about 4300m depth, Zonenshain et al. (1989) report a contact between the sediment and a talus ramp (figure 5.2), but there is no noticeable corresponding change in sidescan texture (figure 5.10 iv). This is probably because the talus is inactive and covered in sediment itself, so both areas produce a smooth, poorly backscattering texture.

The dives also identified a major fault zone, between 3400m and 4100m depth, which divides the lower nodal basin basaltic floor from the uplifted blocks of the inside corner high. This major fault zone actually comprises two smaller vertical fault zones, the lower at 4100m to 3900m depth and the upper at 3400m to 3500m depth, with a 2.5km separation. Zonenshain et al. (1989) report no recent talus accumulations on the uplifted blocks, suggesting that tectonic activity ceased some time ago.

Outcrops of lower crustal lithologies were reported from the fault zone at 4000m. This suggests that this fault zone has accommodated a relatively large amount of displacement, even given an anomalously thin volcanic layer (Zonenshain et al., 1989). Despite the expected size of this structure, it is remarkably poorly defined on the sidescan, especially compared with the sharp backscatter contrast of the major boundary deeper on the eastern wall (from which only upper crustal lithologies were reported). A barely noticeable, small area of low backscattering, mottled, blocky texture (figure 5.10 v) may correspond to the outcrops of greenstone after upper gabbro and sheeted dyke. This highlights that major fault zones can be very subtle features on the sidescan, unless they also correspond to major changes in sediment cover.

5.4.1.2 The curving ridges of the inside corner high

The crest of the eastern wall forms the first of two ridges which curve down to the east (towards the ridge offset) into the transform valley from the inside corner high. (far east of figure 5.10). On the eastern wall, near the transform, there are recent rock debris slides, forming curvilinear trails of loose fragments hundreds of metres long (figure 5.10 vi). The active mass wasting is a sign that the area adjacent to the transform is still exposed to tectonic disturbance and contrasts with the sedimented gullies further north (figure 5.10 vii). (However, some of this variation may be a result of the join in the swaths and the corresponding different look-angles.)

Although the very crest of the inside corner high was not covered by the sidescan swath, there is no evidence on the current data set for recent volcanism, such as that reported from inside corner highs at faster spreading rates (Barth et al., 1994). The eastern facing backs of the two fault blocks are moderately backscattering on the upper slopes, but become increasingly covered in sediment which ponds into the valley between the ridges. They have a rather ambiguous texture—there are small patches of hummocky shadows, but most is diffuse, relatively smooth, and certainly different from the sedimented pillow mounds on the back of fault blocks on the western terraces (figure 3.11).

The curvature of the inside corner ridges is in the opposite direction to that expected from drag along the transform, and will be discussed further in section 5.6.3.4.

5.4.1.3 Tectonism on the western wall of the nodal basin

There is a noticeable difference in texture between the hummocky NVZ and the western wall of the nodal basin. The texture of the latter comprises subdued hummocks with narrow discontinuous shadows (figure 5.3) which become increasingly stretched and lineated with depth as the pillow flows are broken down into a ridge-parallel tectonic fabric. High resolution bathymetry reveals a staircase of normal faults inclined outward from the NVR (Zonenshain et al., 1989). This and increasing sediment cover accounts for the difference between the tectonised fabric of the nodal basin wall and the fissured terrain which commonly occupies the edge of the median valley floor. There is some increase in sediment cover (reflected by a decrease in the backscatter amplitude) towards the bottom of the basin, but this is much thinner than expected (Fujimoto et al., 1994). Data from the piston coring of Zonenshain et al. (op. cit.) show that this sediment includes red clays as well as the pale hemipelagic ooze.

5.4.1.4 Incipient nodal basin and relict volcanic ridge

At 5200m depth, half way down the western wall of the nodal basin, a 300m high ridge and the intervening basin were interpreted by Zonenshain et al. (1989) as an extinct axial volcanic ridge and an incipient nodal basin (figure 5.2). These two features may coexist side by side, but either one of them alone can also account for the ridge and basin topography. An 'incipient nodal basin' should have recently become a focus for inward dipping normal faulting, the ridge being the uplifted footwall of this fault. If this is so, then a distinct fault line cutting along-strike might be expected. Alternatively the depression in the western wall may be a constructional low related to the adjacent relict volcanic ridge, in which case, no inward dipping fault scarp would be present.

The main evidence supporting the "relict NVR" theory comes from the dredge site 7D which recovered pillows that were comparable in their freshness to NVZ rocks. However, the texture of the ridge is no more constructional in character than the rest of the western wall of the basin (figure 5.3). If the ridge is essentially a constructional high, then the positive relief of the NVR must have been maintained despite tectonic dismemberment by the outward dipping normal faults. This faulting must also have occurred uniformly across the NVR, rather than focusing at the edges of the constructional ridge. Unfortunately the inward dipping slope is in shadow on the ridge-parallel swath, so it is not possible to determine unequivocally whether it is tectonic or constructional in character.

There is certainly no well developed fault zone present, but the shape of the shadow cast by the ridge suggests that some element of inward dipping faulting seems likely. Hence, Zonenshain et al.'s (1989) interpretation of an incipient nodal basin is tentatively supported.

5.4.2 Oblique and transform parallel structures.

5.4.2.1 The eastern wall

The major fault zone on the eastern wall of the nodal basin that is delineated by the strong backscatter contrast (figure 5.10 ii) seems to be cross cut by more recent transform parallel structures. Strike-slip motion along these *may* have rotated crustal blocks, thus varying the orientation of the sharp backscatter contrast in at least three sections from north to south across the eastern wall of the nodal basin (block A, B and C marked on figure 5.10). At 23°52'N 46°14'W, a 1km section of the major boundary strikes at 140° (block B). This corresponds to an anticlockwise rotation of up to 60° relative to the same feature further north. It also parallels the lesser en-echelon fault set on the valley wall

duplex. Additional strike-slip motion has rotated the same major boundary to a transform parallel orientation (between 090° and 120°) in the south eastern corner of the basin (block C). Athough I suggest that these blocks may have rotated, with the present information available, there is no method of confirming a previous 'unrotated' state.

Some oblique and possibly transform-parallel structures also occur in the north east of the basin. At a slope break near 3500m, metasomatised upper crust marks the location of the upper fault zone (Zonenshain et al., 1989). This takes the form of another sharp boundary (figure 5.10 viii) between pillow outcrop (figure 5.10 ix) and sedimented talus (figure 5.10 x) that can be traced for about 1km in a NW-SE orientation. It seems to be cut by a transform parallel structure, but this may be just the gullying at the crest of the eastern wall.

5.4.2.2 The PTDZ

The transform-parallel lineation becomes better developed towards the southern edge of the nodal basin until, at 23°50'N, there is a distinct terrain boundary, which probably corresponds to a major fault zone (figure 5.10xi). This feature forms a well defined trace, trending at 100°, along the break in slope on the southern wall of the nodal basin at 5000-5300m depth. The terrain boundary separates the younger crust to the north from the older steeply dipping terrain to the south and is almost certainly the trace of the current strike-slip motion, known as the Principal Transform Displacement Zone (PTDZ). The PTDZ continues westwards, although its trace is relatively unclear, from the southern wall of the nodal basin along the southern transform wall where it intersects with the NVZ. The corresponding area on the ridge-parallel swath (figure 5.3—lower right hand side) shows no sign of this major terrain boundary. Instead it has a smooth, featureless texture implying that the structural fabric is predominantly transform-parallel and that the southern wall of the nodal basin is more sedimented than the western wall.

Between 46°17'W and 46°18'W there is a slight compressional kink in the trend of the PTDZ from the 100° transform-parallel orientation to ~80° (figure 5.10 xii). A compressional bend in major strike-slip fault is usually accompanied by a contractional duplex, forming a positive flower structure (Woodcock & Fischer, 1986). Such a structure is not immediately apparent from the sidescan image, but small discontinuous scarps, trending between 105° and 120° to the west of the main fault trace, may be related to duplex formation (figure 5.10 xiii).

5.4.3 Sediment flux from the transform

About half way along the southern nodal basin wall the PTDZ becomes buried by low backscattering, smooth textured sediment (and/or debris) slumps (figure 5.10xiv). These have brighter, lobate fronts which appear to downlap, one on top of another, and are curved in a direction that implies an influx down hill, towards the north and north west. Further to the south east, the lobate margins become less curved and more elongated with a transform-parallel strike (figure 5.10xv). Their continuity and sharpness are reminiscent of fault controlled features and yet the amplitude and slightly arcuate downlapping contacts resemble the adjacent slump deposits (figure 5.10xiv). Fault splays from the PTDZ may have controlled the flow of debris and sediment to produce these features. The dominance of mass wasting features along the south eastern edge of the nodal basin almost certainly results from the transportation of material into the basin from the transform valley.

The dramatic variation in sediment thickness between the slump deposits (figure 5.10xiv) and the partially tectonised volcanic terrain (figure 5.10xvi) to the west is highlighted by a distinct contact of contrasting backscatter. The slumps also downlap onto a smooth, moderately backscattering area (figure 5.10xvii), situated below and to the north of the tectonised volcanic terrain. The smooth area extends in an approximately transform-parallel strip from the western wall across the centre of the basin. This probably corresponds to the accumulations of talus which have been observed merging towards the bottom of the basin (Karson & Dick, 1983). Alternatively it may just reflect increasing sediment cover of lower relief (perhaps highly dismembered) volcanic terrain.

5.5 The transform.

5.5.1 Decreasing fault activity along the northern transform walls

Active and reactivated faults in the transform can be identified by the high backscatter return from freshly deposited debris. After the initially rapid uplift near the inside corner high, tectonic actively on the northern wall of the transform seems to decrease with age. On the sidescan images, areas wall similar gradients and at similar depths have quite different characters depending on their distance from the RTI. Figure 2.7a shows a section of the northern transform wall at a distance of about 30km from the ridge axis. A large proportion of it has the strongly backscattering and relatively smooth texture, typical of active talus deposits. The commonly-occurring, transform-parallel texture may be generated by the composite step faults identified by Karson and Dick (1983).

Over a distance of about 5km, the nature of the transform wall scarp undergoes a transformation to much lower amplitudes. To the east of the 46°W longitude line (35km from the axis), most of the northern wall is poorly backscattering with isolated, irregular, bright patches (figure 5.11). Assuming an analogy with the eastern wall of the nodal basin, the bright patches are steep fault scarps or fault zones and sparsely sedimented outcrop. The sudden decrease in amplitude of the backscatter, especially at a high angle of incidence, suggests that the tectonic activity reduces abruptly and the talus rapidly becomes covered in a thick layer of sediment. A similar dramatic acoustic contrast occurs between the inner valley of the ridge axis and the fault terraces beyond. It is possible that the sudden increase in sediment cover is over-emphasised as a result of a non-linear response of the backscatter amplitude to the attenuating properties of sediment cover, as suggested by the groundtruthing..

The camera traverses of Karson and Dick (1983) confirm these observations. The younger transform walls show steep, fresh-looking outcrops which are being actively degraded to feed extensive talus ramps and debris slides. The older walls differ from the younger ones with their thicker sediment cover, less active and apparently less extensive debris slides and localised ferromanganese deposits.

5.5.2 Reactivation of the southern transform walls at the RTI

The southern transform wall belongs to the old plate and so as expected has low backscatter over all but the steepest scarps (figure 5.11 and figure 5.12). Figure 5.12 shows the section of the southern walls immediately to the east of the RTI. Only the steepest rocky buttresses remain relatively free of a thick sediment drape.

This contrasts strongly with the southern transform wall opposite the ridge axis, where fault reactivation is accompanied by a narrowing of the transform valley, an increase in the gradient of the southern transform scarp and the development of reactivated debris slides (figure 2.7b). (See TOBI figure location diagrams at the start of this thesis to compare the relative positions of figure 2.7b, 5.11 and 5.12. Consolidated and unconsolidated debris deposits mingle together. The former contain lumps of consolidated talus from older deposits and large blocks of deeper crustal lithologies (Karson & Dick, 1983). Detached blocks of consolidated material are especially common within gullies on the southern transform walls.

314° 00' 314° 01' 314° 02' 314° 03' 314° 04' 314° 05' 314° 06' 314° 07'

23° 48'

23° 47'

23° 46'

23° 45'

outcrops (probably fault scarps)

Sedimented gullies in the northern wall.

NARROW MEDIAN RIDGE

outcrops of fault scarps

vi

iv

i

v

iii

-4100 -4200 -4300 -4400 -4500 -4600 -4700

314° 00' 314° 01' 314° 02' 314° 03' 314° 04' 314° 05' 314° 06' 314° 07'E

23° 48' 23° 47' 23° 46' 23° 45'N

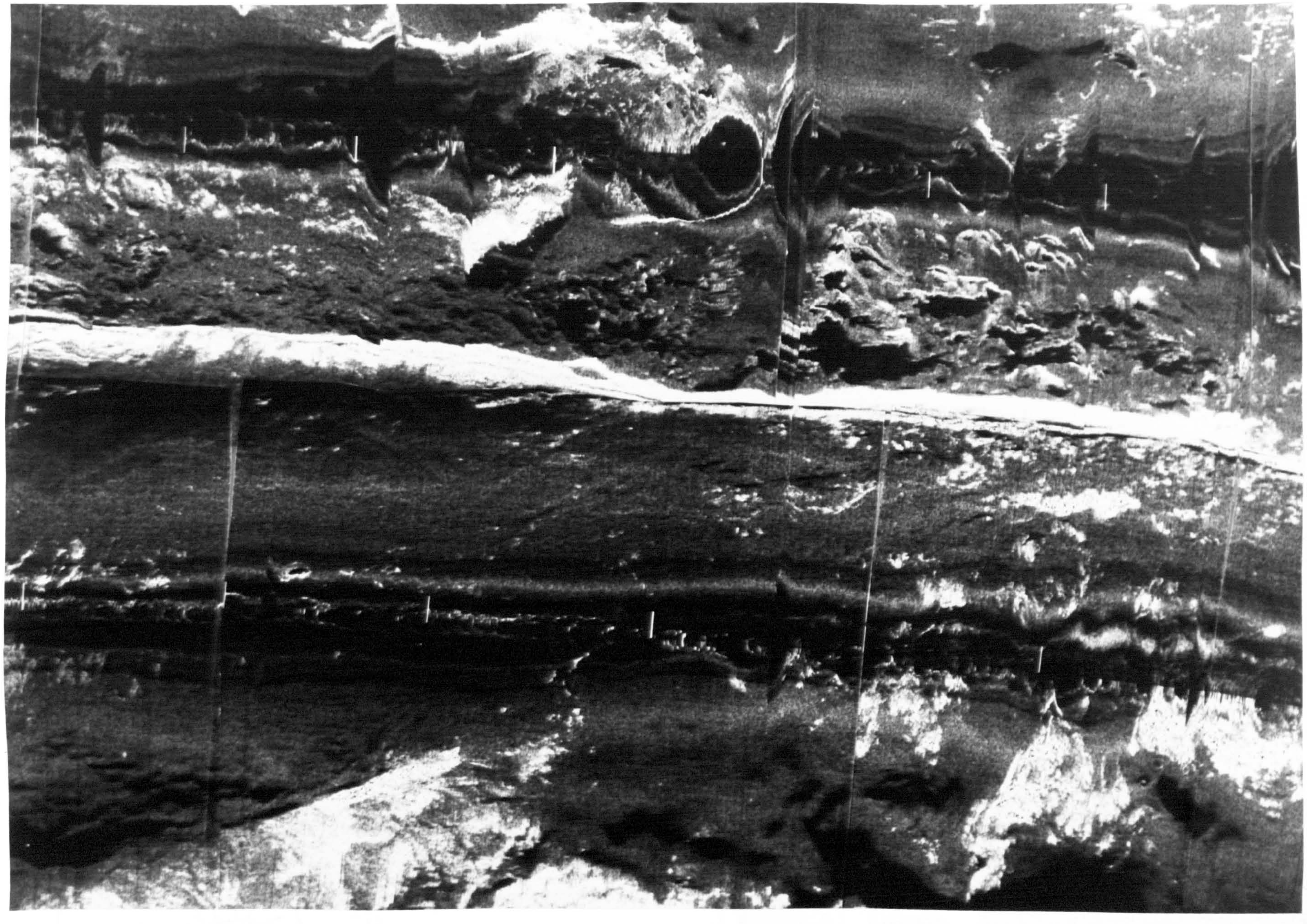

Figure 5.11 The transform valley and median ridge at the eastern extent of the MARNOK area.

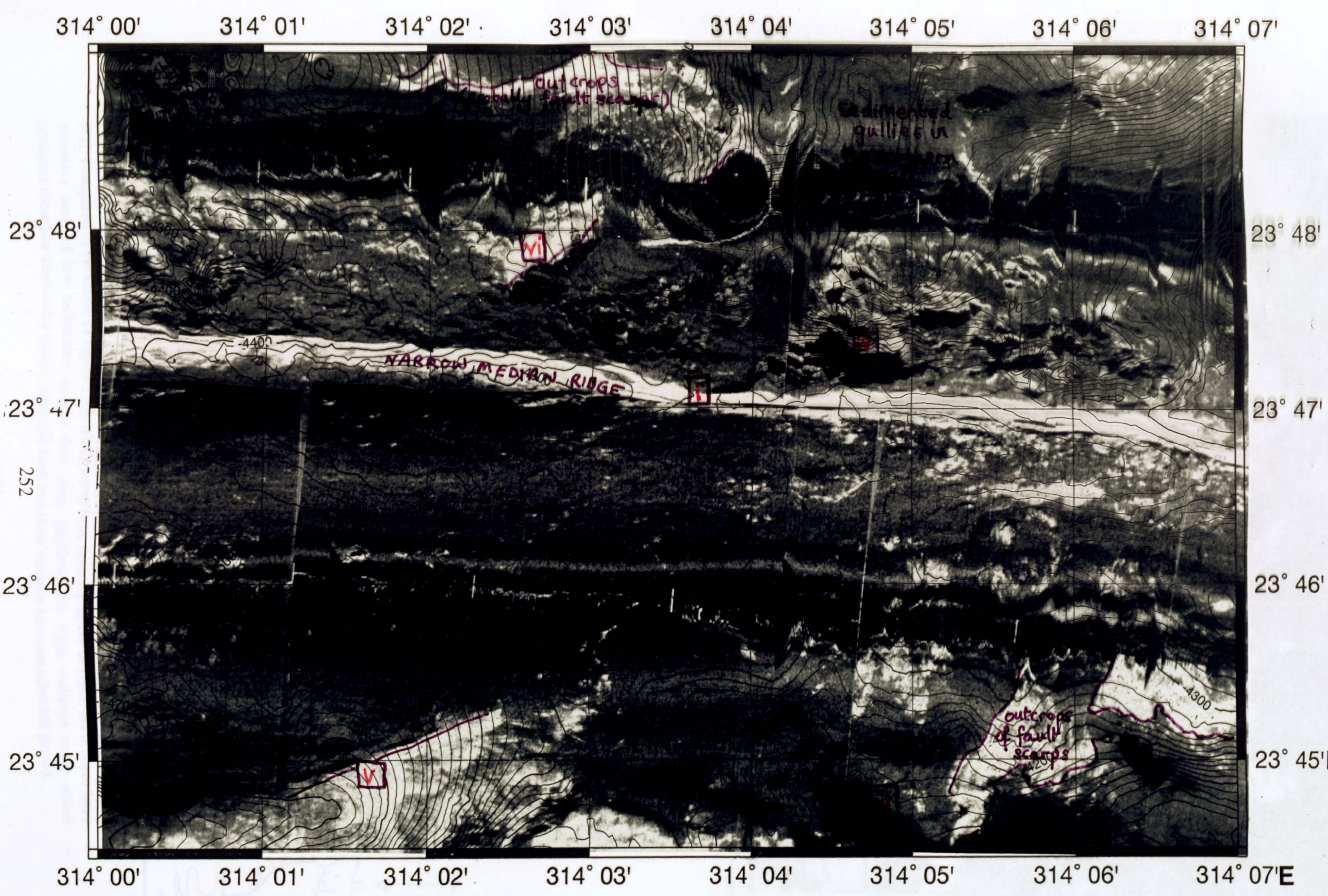

Figure 5.11 The transform valley and median ridge at the eastern extent of the MARNOK area.

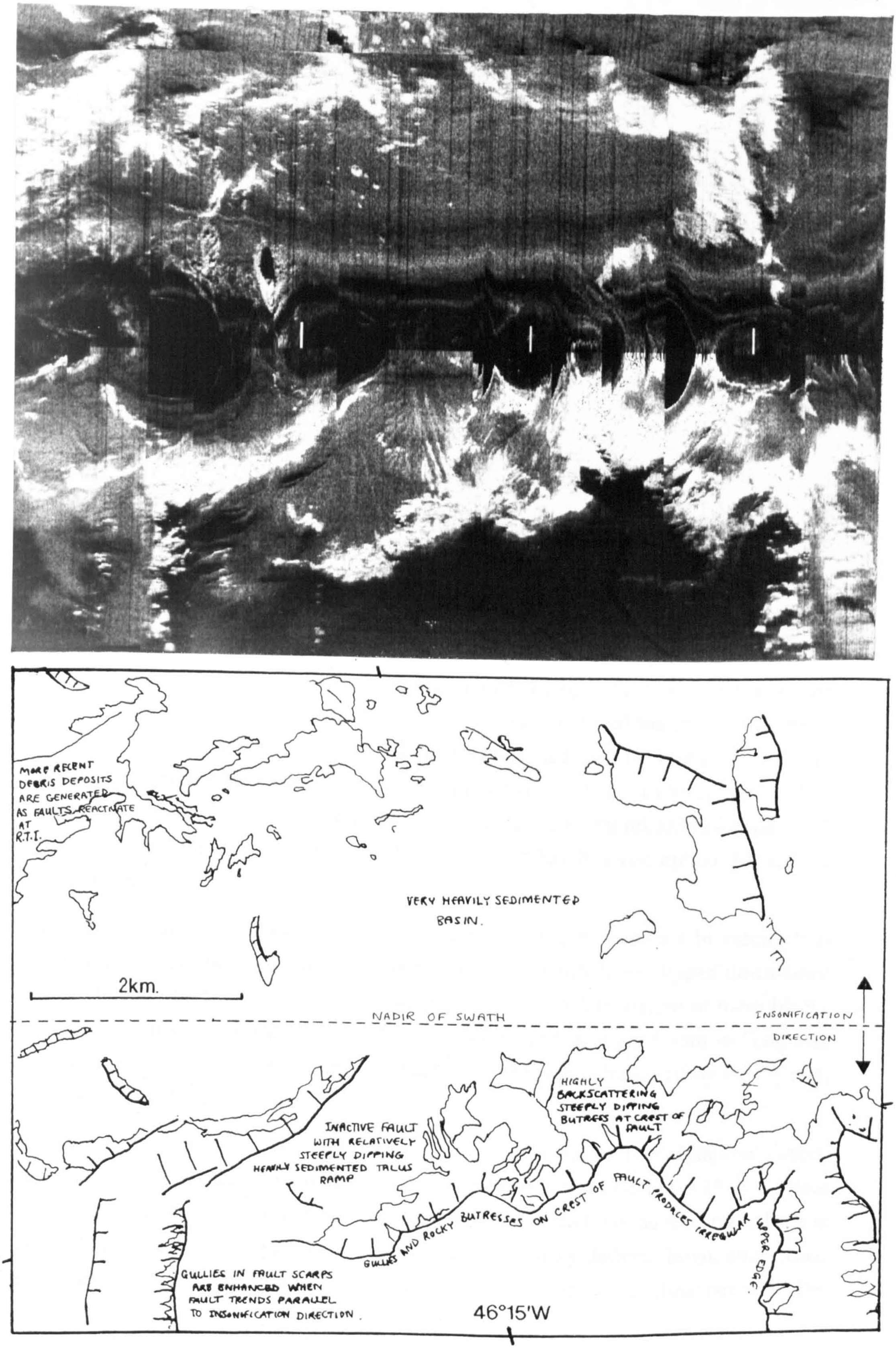

Figure 5.12 Transform-parallel swath of the southern wall of the transform valley to the east of the RTI. Compared to the scarps of figure 2.7b, which have been recently active or reactivated, these have extensive areas of low backscatter despite their steep gradient. The thick sediment cover which produces these low amplitudes occurs when the fault has been inactive for a considerable period.

5.5.3 The median ridge

Immediately south east of the nodal basin, the transform's median ridge reaches a maximum width of about 5km. It comprises a transform-elongated fault block modified by mass wasting and serpentinite diapirism. The diffuse undulations of the steep northern slope (figure 5.13 i) are very similar to areas on the median valley wall that are thought to be landslide deposits. These landslides are thought to have a high proportion of serpentinite and may be related to diapirism (Cann et al., 1992a&b). The recent dive to median ridge recovered deep crust and mantle rock, thought to be from diapiric intrusions (Fujimoto et al., 1994).

A transform-parallel axial rift 1km long and greater than 50m wide (figure 5.13 ii) cuts sharply along the western crest of the median ridge. This large, fissure-like feature points to an element of extension across the median ridge, but it may also be related to subsidence of the northern slope; the rift being the precursor to a slide scar. Other discontinuous transform parallel features near the crest may also be slide scars (figure 5.13 iii) or alternatively they may be faults which have been partially buried by sediment and debris. Evidence for the diapiric nature of parts of the median ridge can be seen at the summit, which is relatively smooth and gently rounded (figure 5.13 iv). Such a texture would be expected from the gentle extrusion of soft serpentinized material. The smooth rounded summit to the west contrasts with the sharp faulted crest to the east (figure 5.13 v). This suggests that the eastern extent of the median ridge comprises harder rock with a higher shear strength, that has undergone considerable transform-related deformation. A highly sheared fault block composed of basalt and metabasalt is one option that fits the above criteria.

Some of the landslips below the sharp faulted crest are quite coherent in nature. It is possible to resolve blocks of material (figure 5.13 vi) which have slipped down-slope leaving brightly backscattering scars above (figure 5.13 vii). The largest of these blocks (figure 5.13 viii) has dimensions of 1500m by 800m, and is aligned with its long-axis transform-parallel. The semiconsolidated nature of the block is indicated by the distinct, steep margin of the lobate front.

In contrast, the dome-like deposits further west, beneath the rounded (diapiric?) crest, have a smoother surface texture and a gentler, diffuse margin (figure 5.13 ix). These landslide deposits have disseminated and the debris has spread out, so the original shape of the block has been completely lost. They leave no sharply defined, bright slide scars, suggesting that the slope as a whole is softer and has a much lower shear strength. The

313° 49' 313° 50' 313° 51' 313° 52' 313° 53' 313° 54' 313° 55'

23° 49'

23° 48'

23° 47'

23° 46'

-4600 -4700 -4600 -4500 -4400 -4300 -4200 -4100 -4000 -4100 -4200 -4300 -4200 -4100 -4000 -3900 -3800 -3700 -4000 -4100 -4200 -4300 -4400 -4100 -4200 -4300 -4400 -4500 -4400 -4300 -4200 -4100 -4000 -4100 -4200 -4300 -4400 -4500 -4600

i ii iii iv v vi vii viii ix x

313° 49' 313° 50' 313° 51' 313° 52' 313° 53' 313° 54' 313° 55'E

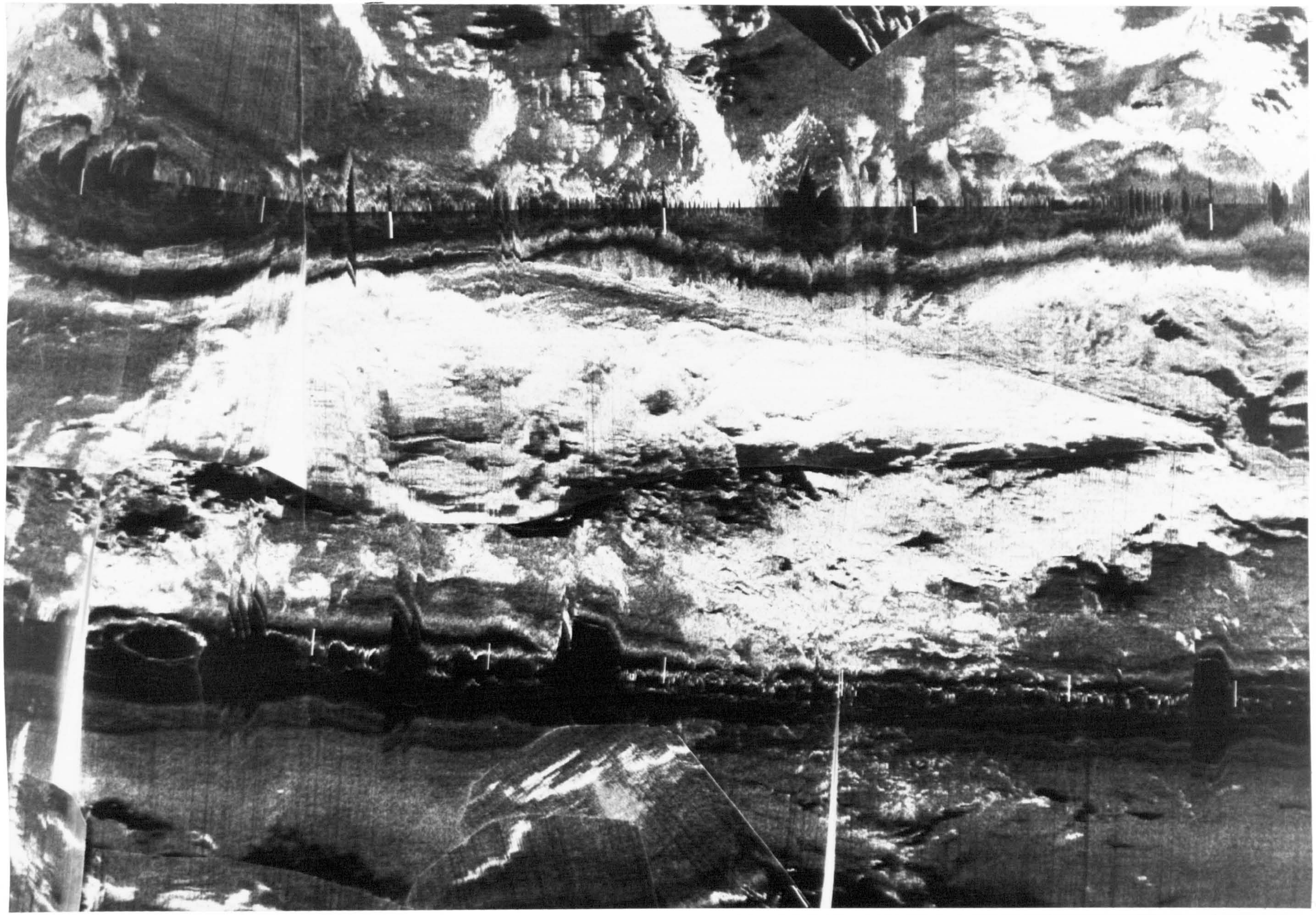

Figure 5.13a Transform-parallel swath over the transform median ridge. Diapiric serpentinite seems to form a strong to moderately backscattering texture of diffuse low amplitude domes. A transform-parallel axial rift is imaged to the west of the crest, where the amplitude of the backscatter is lower. There are slump deposits with lobate margins on the northern flank of the ridge some of which have arcuate failure surfaces above.

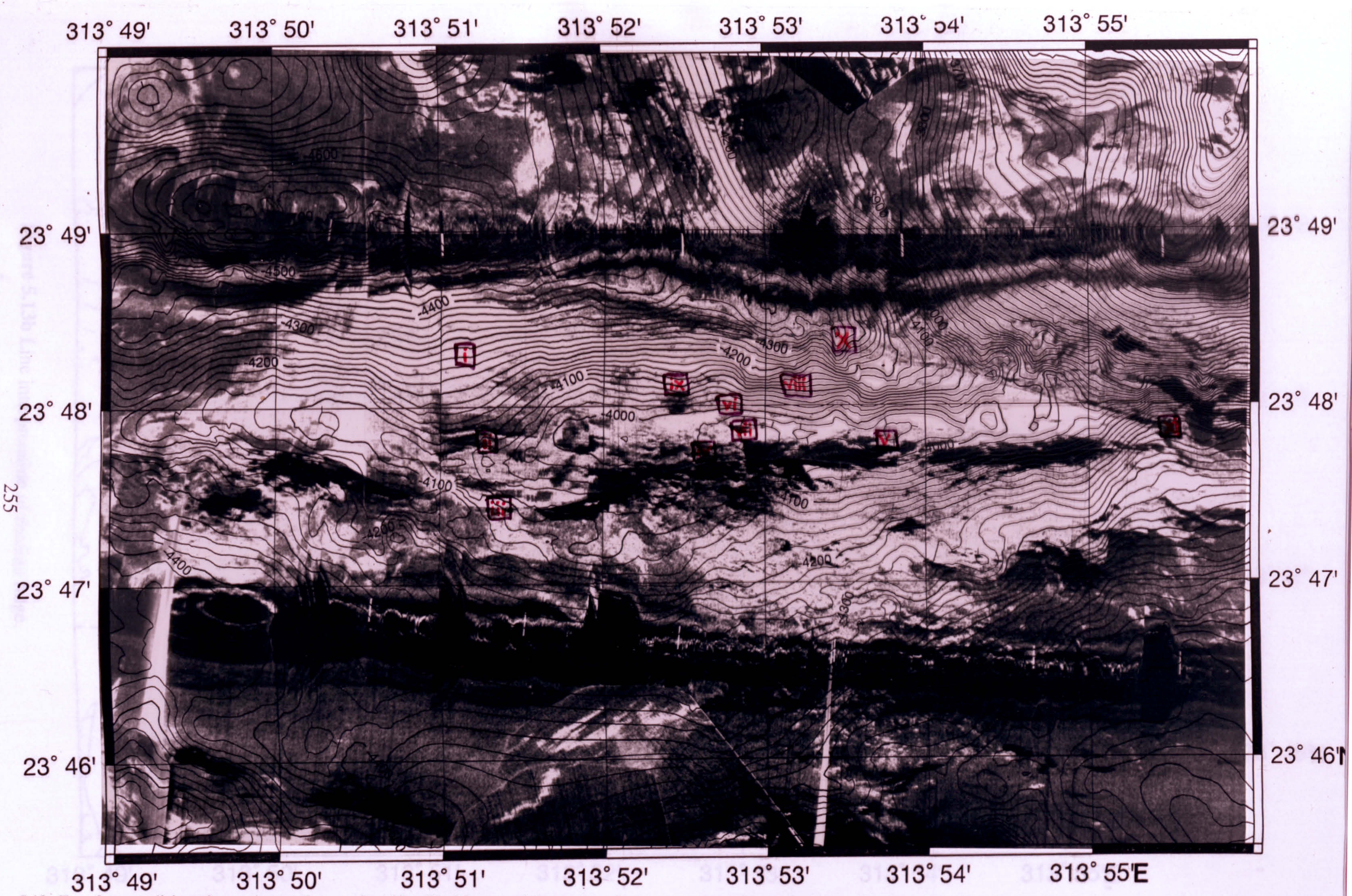

Figure 5.13a Transform-parallel swath over the transform median ridge. Diapiric serpentinite seems to form a strong to moderately backscattering texture of diffuse low amplitude domes. A transform-parallel axial rift is imaged to the west of the crest, where the amplitude of the backscatter is lower. There are slump deposits with lobate margins on the northern flank of the ridge some of which have arcuate failure surfaces above.

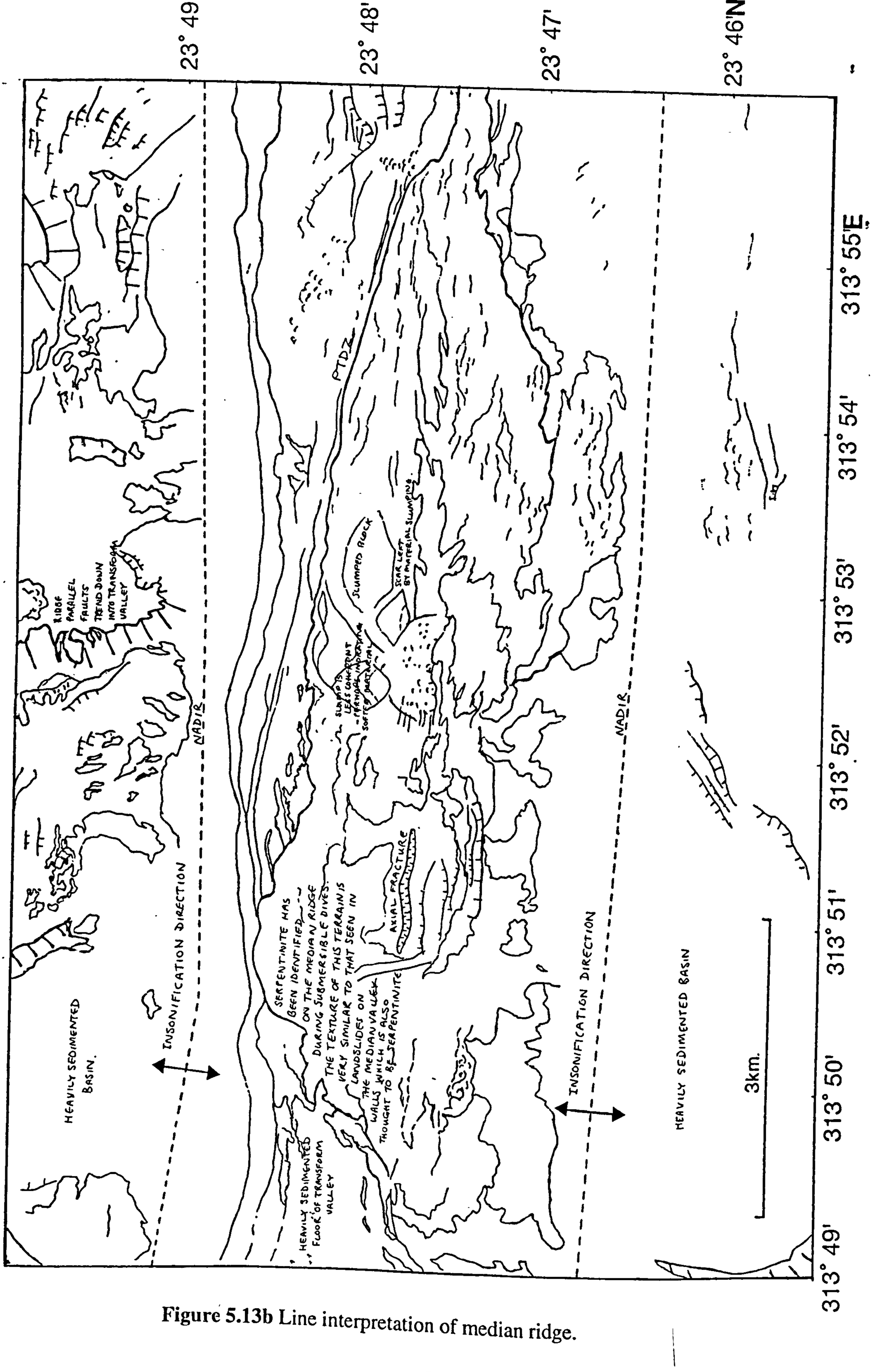

Figure 5.13b Line interpretation of median ridge.

deposits downlap onto each other, suggesting that active slope failure is relatively common. I propose that the changing character of the broad median ridge and the landslide deposites on its flanks are a result of an increasingly higher proportion of soft serpentinite towards the west.

Figure 5.11 shows the easternmost extent of the transform, imaged by TOBI (from 45°52'W to 46°00W). The median ridge here is narrow (<500m wide) and dips sharply to the north. The kink in the median ridge at 23°45'N 45°56'W (figure 5.11i) is thought to be real and not a navigation induced artefact. It implies that there may have been a minor element of transtension across the transform. This agrees with microearthquake studies further east which have revealed transtensional deformation between 45°00'W and 45°30'W (Wilcock et al., 1990).

5.5.4 The PTDZ and other transform related structures

The basins between the median ridge and the transform valley walls are deeply sedimented. There is structure within this sedimented surface, which in some cases may be the result of sediment slump folds (figure 5.11 ii) and in other cases may reflect a draping of topography (figure 5.11 iii).

From the southern wall of the nodal basin, the PTDZ trends at an average of about 100° along the northern edge of the median ridge (figure 5.13 x), occupying a zone, probably no more than 50m wide. In contrast, no clear fault lineament can be identified on the southern edge of the median ridge, only variably onlapping sediments. This means that the median ridge is essentially part of the southern older plate.

To identify areas of transtension and transpression, the trace of the PTDZ can be compared with the small circle of perfect strike slip motion defined by the current plate motions and the regional asimuth of the transform (DeMets et al., 1990; Pockalny et al., 1988; Roest et al., 1984). To the south east of the nodal basin, between 46°12'W and 46°05'W, the PTDZ trends at 105°, corresponding to an element of transtension. Further east, between 46°05'W and 46°01'W, there is probably a small element of transpression. The PTDZ is virtually parallel to the direction of plate motion in the area shown in figure 5.11, where the median ridge is narrow.

Occasionally fault scarps other than that of the median ridge protrude out of the deeply sedimented transform valley. The smaller structures tend to be orientated parallel and subparallel to the PTDZ (figure 5.11iv) and may be related to transtensional shears. Some of the larger scarps have a stronger sense of obliquity at 060°-080° (figure 5.13xi; figure

5.11v and vi), consistent with the rotation of originally ridge-parallel fault blocks in a dextral strike-slip environment.

5.6 Discussion.

5.6.1 The stress regime in the median valley approaching the RTI

5.6.1.1 Expected and observed stress regime

The simple shear of dextral strike-slip, coupled with the extension of the axis, would rotate the axis of minimum compressive stress round towards a NE-SW orientation (Fox & Gallo, 1984). This would tend to produce fissures and faults aligned NW-SE. Features immediately adjacent to the transform, such as the very tip of the NVR and the curved ridge tips of the inside corner high, fit this model, but the oblique-trending features to the NW of the nodal basin are in an orientation which is opposite to that expected from the rotation of the stress regime.

5.6.1.2 Proposed model: flexural downbend of lithosphere into nodal basin

The strong degree of coherence between the edge of the nodal basin and the orientation of the hummocky ridges suggests that similar stresses may be responsible for the formation of these features. The formation of the nodal basin is thought to be induced by a lithospheric response to both extreme thinning caused by the highly asymmetric extension (Karson, 1990; Tucholke & Lin, 1994) and a loss in dynamic support of the upwelling mantle induced by horizontal flow and viscous edge effects (Sleep & Biehler, 1970; Parmentier & Forsyth; 1985; Collette, 1986; Bercovici et al., 1992). Consequently the orientation of the hummocky ridges near the RTI may have a lithospheric control. The forces producing the depression of the nodal basin also may produce a flexural downbend of the lithosphere to the north and west of the basin where there is no major structure for this subsidence to be partitioned into (figure 5.14). The hinge of this flexure will tend to experience tension, thus giving the fissure-controlled hummocky ridges an orientation that differs from that expected from the regional stress field defined by the general plate motion.

5.6.1.3 Mantle flow models

It is also worth noting that the 3-dimensional mantle flow models of Rabinowicz et al. (1993) predict shear stresses on the base of the plate induced by mantle flow, which would also produce the observed trends in the oblique hummocky ridges. Hence an alternative hypothesis is that the orientation of the fracturing is controlled through lithospheric coupling to the mantle flow at the RTI.

5.6.1.4 Implications of flexural model: comparison with Reykjanes Ridge

The flexural model implies that the lithosphere at the RTI ridge axis is thick enough to act as a coherent plate and/or there is a strong coupling between the brittle plate and the ductile flow of the mantle beneath. This hypothesis is contrary to the theory that the newly formed crust at the axis is too weak to act as a coherent plate. It is also at variance with studies over the Reykjanes Ridge where the structural control of the plate tectonic generated regional stress field (faults normal to the spreading direction) can be separated from the stresses induced though a passive response to the thermal evolution of the lithosphere (faults parallel to the valley walls). At the edge of the Reykjanes Ridge axial zone there is a sharp change in the mean strike and the mean throw of faults as the valley-parallel faults start to overprint the spreading orthogonal faults of the axial zone (Murton & Parson, 1993; McAllister & Cann, 1995 *(in press)*). Hence lithospheric forces cause tectonism only at the edge of the axial zone on the Reykjanes Ridge, whereas the oblique hummocky ridges of the MARNOK RTI occur in the centre of the NVZ.

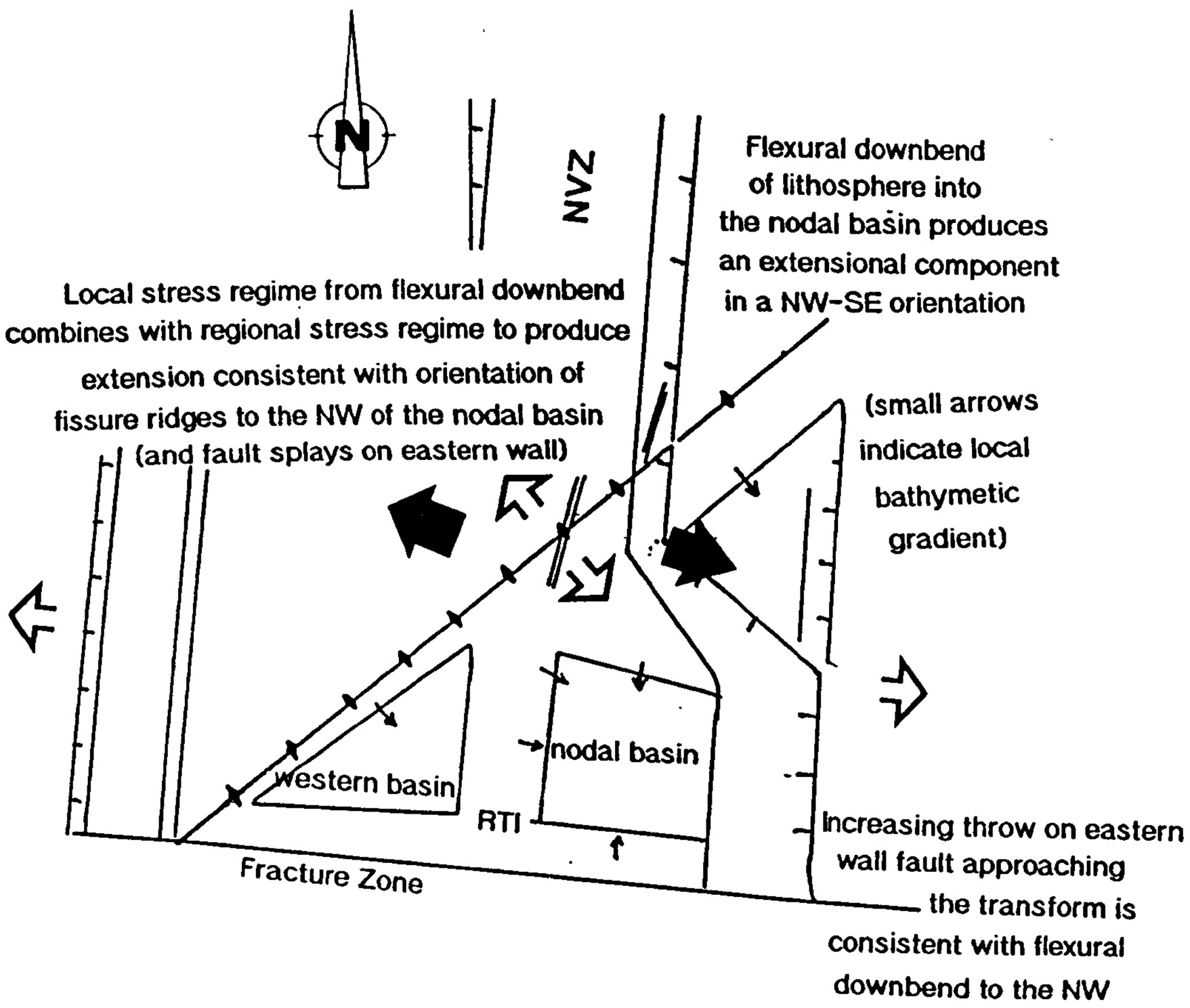

Figure 5.14 Schematic diagram to show how the combination of a flexural downbend in the lithosphere and the regional extensional stress can produce a stress field compatible with the orientation of oblique the hummocky ridges to the NW of the nodal basin. The flexural downbend is associated with the formation of the nodal basin and the increasing throw on the eastern valley wall towards the transform.

5.6.1.5 Causes of differences in plate strength between MARNOK and the Reykjanes Ridge

The action of lithospheric forces in the axial zone may be expected to vary between the Reykjanes Ridge and the MARNOK area because of a number of factors. The plume influence on the Reykjanes Ridge causes a reduction in the stresses induced by thermal cooling of the lithosphere, as is seen in the transition from median valley to well developed axial high. In contrast, the RTI area of a major transform offset should be vulnerable to enhanced stresses from lithospheric cooling because of the adjacent cold plate and the reduced upwelling. The enhanced hydrothermal cooling induced by the fracture zone will also tend to lead to a thicker lithosphere at the RTI.

Chen and Morgan (1990a) suggest that the dominant factor in the generation of ridge axis topography is the coupling between the brittle plate and the ductile flow of the mantle beneath. This coupling is strongly temperature dependant and so is particularly weak on the Reykjanes Ridge, resulting in the absence of the axial valley. Chen and Morgan (1990b) have assessed the factors which increase this coupling. They suggest that the reduction in magmatic input at the end of the segment and the 'cold edge', are of secondary importance, while the thermal structure of the lithosphere is very sensitive to hydrothermal circulation. Hence, coupling between brittle plate and ductile flow is likely to be particularly strong near the axis in the RTI, and hence the formation of the nodal basin should have quite a strong effect on the stresses acting on the adjacent NVZ.

5.6.2Structural analysis of the eastern wall duplex

Figure 5.15a shows the expected orientation of fractures in a system which couples dextral strike slip with extension. The orientation of the two conjugate fault splays in the north of the eastern wall duplex is consistent with the orientation of Riedel shears in the dextral transtensional environment. The dominant en-echelon set of faults parallels the R' shear, whereas the NW-SE trend parallels the R shear (compare figure 5.15a, Riedel shears with figure 5.9). A small degree of shear seems to offset the dominant en-echelon set of faults where they are intersected by the splays with the NW-SE trend; the offset being consistent with the expected shear sense (figure 5.15).

However the observed fault pattern is not entirely consistent with a dextral transtensional environment. Firstly, the motion along Riedel shears should be dominantly strike slip, whereas the wall faults are essentially normal faults. Secondly the dominant en-echelon normal fault trend strikes to the east of north, whereas the expected normal fault orientation strikes to the west of north (compare figure 5.15a, normal fault with figure

5.9). In fact, the dominance of the 015°-020° normal fault trend is more consistent with a sinistral strike slip environment (figure 5.15b). This discrepancy can be explained if the flexural downbend of the lithosphere into the nodal basin is taken into account.

In section 5.2.2 I mentioned that the fault splays in the eastern wall parallel the oblique hummocky ridges to the NW of the nodal basin. As the oblique orientations of the hummocky ridges are hypothesised (in section 5.6.1) to be a result of the flexural downbend of the lithosphere into the nodal basin, it seems reasonable to assume that normal faults with the same orientations on the valley walls are controlled by the same mechanism (figure 4.14).

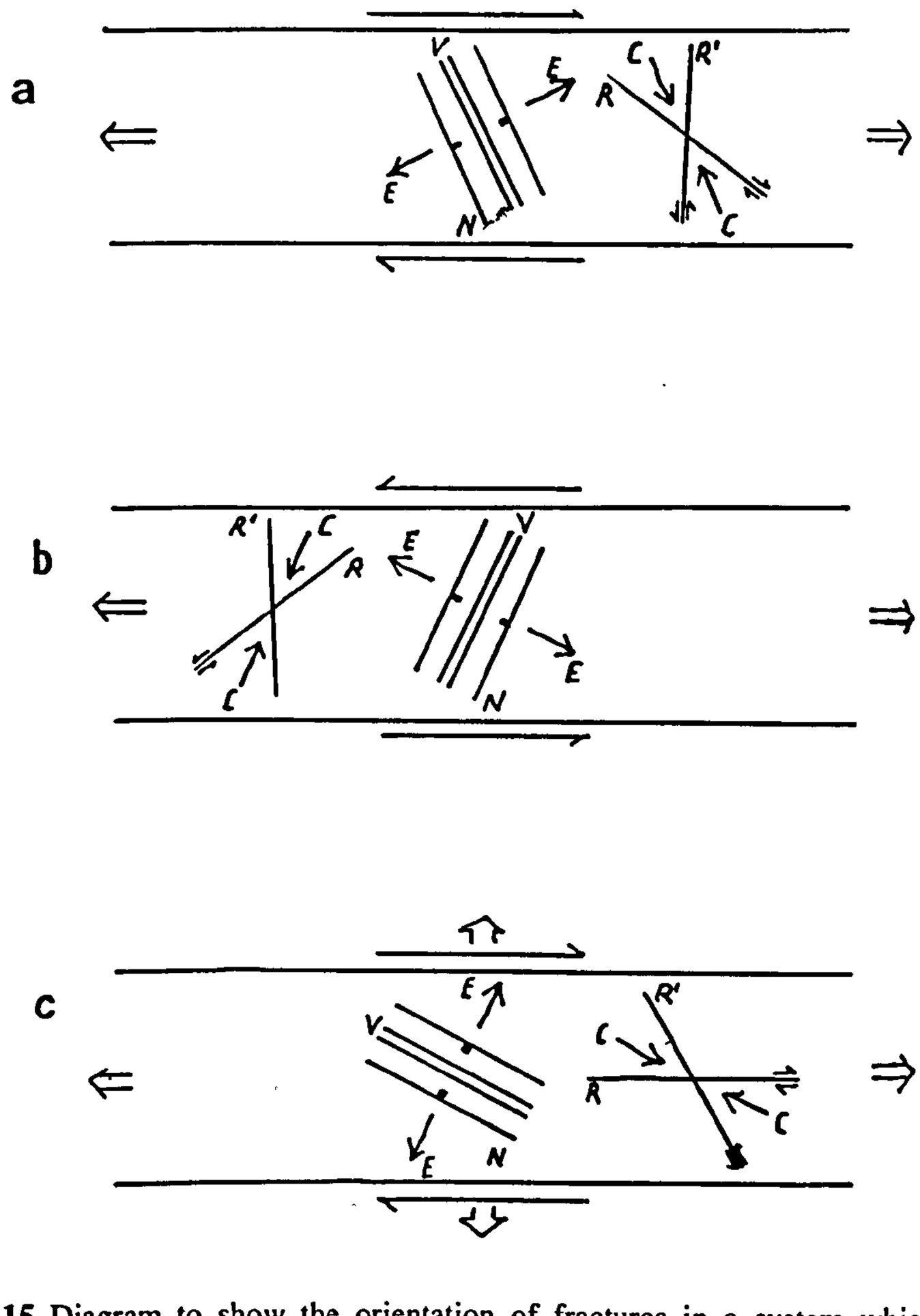

Figure 5.15 Diagram to show the orientation of fractures in a system which couples strike slip with extension. E is the extension axis; N, the normal faults; R, R', the Riedel shears or wrench faults; V, the dykes or extension fractures: a) extension coupled with dextral shear; b) extension coupled with sinistral shear; c) dextral shear with a component of orthogonal extension. Adapted from Sanderson & Marchini (1984).

5.6.3 Tectonics of the nodal basin

The nodal basin seems to be controlled by the interaction of a series of ridge-parallel, transform parallel and oblique NW-SE trending faults.

5.6.3.1 The northern wall

The strike of the northern wall of the nodal basin is consistent with the interaction of the dextral strike slip regime with the strong extentional subsidence to the south as illustrated in figure 4.15c.

5.6.3.2 Large-throw faulting on the eastern wall

The drastic change in character from the western wall of the nodal basin to the eastern wall demonstrates the strong partitioning of strain into the bottom of the basin. The newly formed crust is faulted on a series of normal step faults on the western wall. Although these somewhat dismember the crust, the original volcanic forms are still recognisable. However on the eastern wall, large-throw faults form steep scarps and all volcanic character is lost. The occurrence of dykes and gabbro half way up the eastern wall (Zonenshain et al., 1989) suggests that not only are the throws of these scarps large, but the crust is probably also anomalously thin.

A minimum of three major fault zones were identified on the eastern wall—two by Zonenshain et al., (1989) at ~4000m and 3500m and one by TOBI at ~4900m. The sharp variation in backscatter across the lower of these fault zones suggests that it is presently active while the two above have become inactive and are no longer generating any fresh talus. Hence the upper two thirds of the inside corner high are being passively uplifted by faulting on the lower third.

5.6.3.3 Effect of transform parallel structures on spreading rate

The transform parallel structures on the eastern wall of the nodal basin suggest that strike-slip deformation is distributed over a wider zone in the nodal basin than in the transform valley, although the main focus of this deformation is still concentrated on the PTDZ on the southern wall. Searle (1995) points out that if shear is distributed into a broader zone at the RTI, then extension on the southern spreading segment must decrease gradually southwards, as it is transformed into shear. This is consistent with the reduction in the half spreading rate by 5mm yr^{-1}, to the east in the RTI area (see section 1.4.1).

5.6.3.4 Fault block rotations?

Clockwise fault block rotations have been recorded at a fossil RTI in the Troodos ophiolite (MacLeod et al., 1990). In the MARNOK nodal basin, the only evidence for possible fault block rotation occurs on the southern half of the eastern wall, where the lower fault zone is truncated into three sections, seemingly by transform sub-parallel structures (as described in section 5.4.2.1 and marked 'block A, B and C" on figure 5.10). However, the boundary of this fault zone is rotated anticlockwise into the transform, rather than clockwise, and so fault block rotation is incompatible with the stress regime.

An alternative mechanism for explaining these features draws on the rotation of the minimum compressive stress vector due to the coupling of extensional and strike-slip regimes. This will tend to generate normal faults in a NW-SE orientation, adjacent to the transform. It is also the mechanism usually attributed to causing the curvature of the inside corner high ridges towards the ridge offset, as recognised in many transforms (Searle, 1986).

The hummocky ridges at the very tip of the NVZ show a similar, but less accentuated curvature. This suggests that the curvature of the inside corner high ridges at MARNOK may largely be a consequence of the faulting process in the south-eastern corner of the nodal basin.

5.6.3.5 Significance of the incipient basin

The presence of an incipient nodal basin on the western wall of the nodal basin is in keeping with the model of Pockalny et al. (1988) which emphasises the interplay between temporal variations in crustal production rates and extensional tectonism. They explain the presence of regularly spaced, apparently 'relict' nodal basins along the transform by a magmatic cyclicity. The formation of the nodal basin takes place while the magmatism is waning. It is because of this magmatic cyclicity that there is an accompanying tectonic cyclicity with tectonic strain localising on a newly formed inside corner fault each cycle. The upper two thirds of the inside corner high may be inactive because tectonic activity has started to step inwards to the incipient nodal basin.

5.6.4 Half-graben structure.

The following features are consistent with strongly asymmetric valley wall faulting across the RTI:

1. The 3km high eastern wall of the inside corner which contrasts dramatically with the virtual absence of wall faulting on the western side of the ridge crest.

2. The widening of the valley on the non-transform side leading to preservation of relict NVRs, virtually intact, in the western basin, compared with the rapid tectonic dismemberment on the eastern side.

This is in keeping with recent models (Karson, 1990; Tucholke & Lin, 1994) which emphasise rift valley asymmetry near axial discontinuities. They propose that the inside corner comprises an exposed detachment surface, largely of lower crust and mantle rocks. This is not consistent with Zonenshain et al.'s (1989) observation that the eastern wall of the nodal basin is dominantly upper crustal material with lower crustal rocks exposed only in a couple of fault zones. However, as noted in section 5.4.1.2, the sidescan texture on the back of the curved terraces of the inside corner high seems different from that of the western terraces. The sidescan cannot be used to positively confirm that this comprises lower crustal and mantle lithologies, but it certainly does not discount the theory.

5.6.5 Serpentinite diapirism on the median ridge

The transform median ridge is thought to comprise fault-bounded blocks of dismembered crust and upper mantle uplifted by serpentinisation of ultramafic rocks and/or compressive stresses associated with transform tectonism (Pockalny et al., 1988).

The interpretation of the median ridge in section 5.5.3 essentially agrees with the above model, except that I propose that the proportion of soft serpentinite increases towards the RTI. This is accompanied by increasing larger degrees of slope failure and a change in the style of slip scars and landslide deposits on the steep flanks. The increasing proportion of low shear strength serpentinite to the west thus results in a widening of the median ridge and a reduction in gradient across its flanks.

In section 5.6.5 I interpret the rift along the western crest of the median ridge (figure 5.13 ii) as an extensional feature either related to a general tectonic extension across the median ridge or as the precursor to a massive slope failure on the northern flank. The comparison of the PTDZ orientation with the small circle of perfect strike slip motion (section 5.5.4) showed that stress regime across the median ridge changes from slightly transpressional (in the east) to slightly transtensional (in the west) near the point where the median ridge widens at about 46°05'W (figure 5.13 xi). Hence, the rift in the western crest, mentioned above, *is* in a transtensional area of the median ridge, but if it was formed purely as a result of transtensional stresses I would expect it to have a slightly oblique trend. Thus, I favour the interpretation that this feature is related to subsidence

and possible slope failure in this area. However, it may be related to the transtensional regime indirectly, as discussed below.

I propose that the median ridge comprises one or more crustal blocks which have become caught up in the transform, where they undergo intense shearing. In the MARNOK area, the PTDZ is to the north of the median ridge so the block has been transported westwards, towards the RTI, where the PTDZ starts to trend slightly northwards towards the nodal basin. At this point it comes under the influence of a component of extension. This is likely to result in a degree of dilational shearing, allowing penetration of water to deep level of the crust and upper mantle. The hydration of the crust and mantle at depth induces the serpentinisation reaction, which only takes place above 600°C —approximately at the level of the crust-mantle boundary (Bonatti, 1976). The buoyancy of the serpentinite causes it to protrude in diapiric masses (perhaps aided by the transtensional shearing) and these coat the median ridge near the RTI. The hydration of the mantle may also be aided by the close proximity of the large-throw fault of the inside corner, which may also allow water penetration to deep levels.

Although it is impossible to say for sure whether the median ridge comprises a crustal block and serpentinite or just sheared serpentinite on its own, I prefer the former as it accounts for the progressive change in the character along the median ridge.

The massive influx of debris and sediment, into the SE corner of the nodal basin, issues from the widened western end of the median ridge and may have been aided by gravity sliding, related to the very low shear strength of serpentinite.

In the eastern extent of the data set, where PTDZ is approximately parallel to the direction of plate motion, the median ridge is very steep and narrow, (figure 5.11i), and shows no sign of the serpentinite textures and landslides which characterise the area near the RTI. The kink in the median ridge in the east should produce a small localised area of transtension, but this should be relatively minor. The only accompanying evidence for transtension is the presence of some small shear features to the east (figure 5.11 iv).

This hypothesis predicts that median ridges which are located in transtensional environments or near RTIs are more likely to show evidence for serpentinite diapirism. I also suggest that one of the results of serpentinite diapirism is a progression to a wider and flatter morphology. At the western end of the Vema Fracture Zone, a similar smooth sonar texture is seen which has also been interpreted as serpentinite (Kastens et al., 1986). The Vema median ridge is similar to the MARNOK median ridge in that the degree of serpentinite protrusion seems to increase towards the RTI. However, at Vema, the median

ridge has been uplifted as a result of serpentinite diapirism, whereas I suggest that in MARNOK enhanced slope failure is the primary consquence of the serpentinite protrusion. These opposing results might be explained by compositional and rheological differences in the type of serpentinite protruded.

5.6.6 Magmatic aspects of the transform domain.

The irregular and sometimes gradational nature of the boundary between the hummocky terrain and the fissured terrain suggests that volcanism has not strongly focused on a particular weak point in the crust (figure 5.16). This implies that volcanic episodes did not follow each other closely enough to maintain a warm weak focus for crustal failure. In addition, it seems likely that the distribution of volcanic edifices on the surface somehow reflects the organisation of magmatic centres in the crust. The heterogeneous character of the NVZ implies that volcanism is taking place in small discrete episodes, which are probably from individual magma bodies separated in space and time. The geochemistry confirms that these distinctive edifices are derived from separate parental magmas.

Sinton and Detrick's (1992) composite magma chamber model proposes that at slow spreading rates the AMC predominantly comprises a zone of crystal mush, because the melt supply rate is not great enough to generate a magma lens. This model is consistent with the predominance of plagioclase accumulation within the MARNOK area. Plagioclase tends to be less dense than basalt magma and so is likely to rise up towards the top of such a chamber. In particular, the high abundance of plagioclase megacrysts and phenocrysts in the transform domain suggests that the crystal mush zone has a relatively high crystal/magma ratio, consistent with the low magma supply proposed above.

The presence of a lava inflation feature (the tube and tumuli of figure 3.5) is perhaps a little surprising as they are usually associated with areas of robust and voluminous volcanism. Their occurrence at the RTI, where volcanism is relatively sparse, suggests that they may be more common than previously thought, and possibly go largely unrecognised in many areas because they blend in with the ubiquitous pillow mounds.

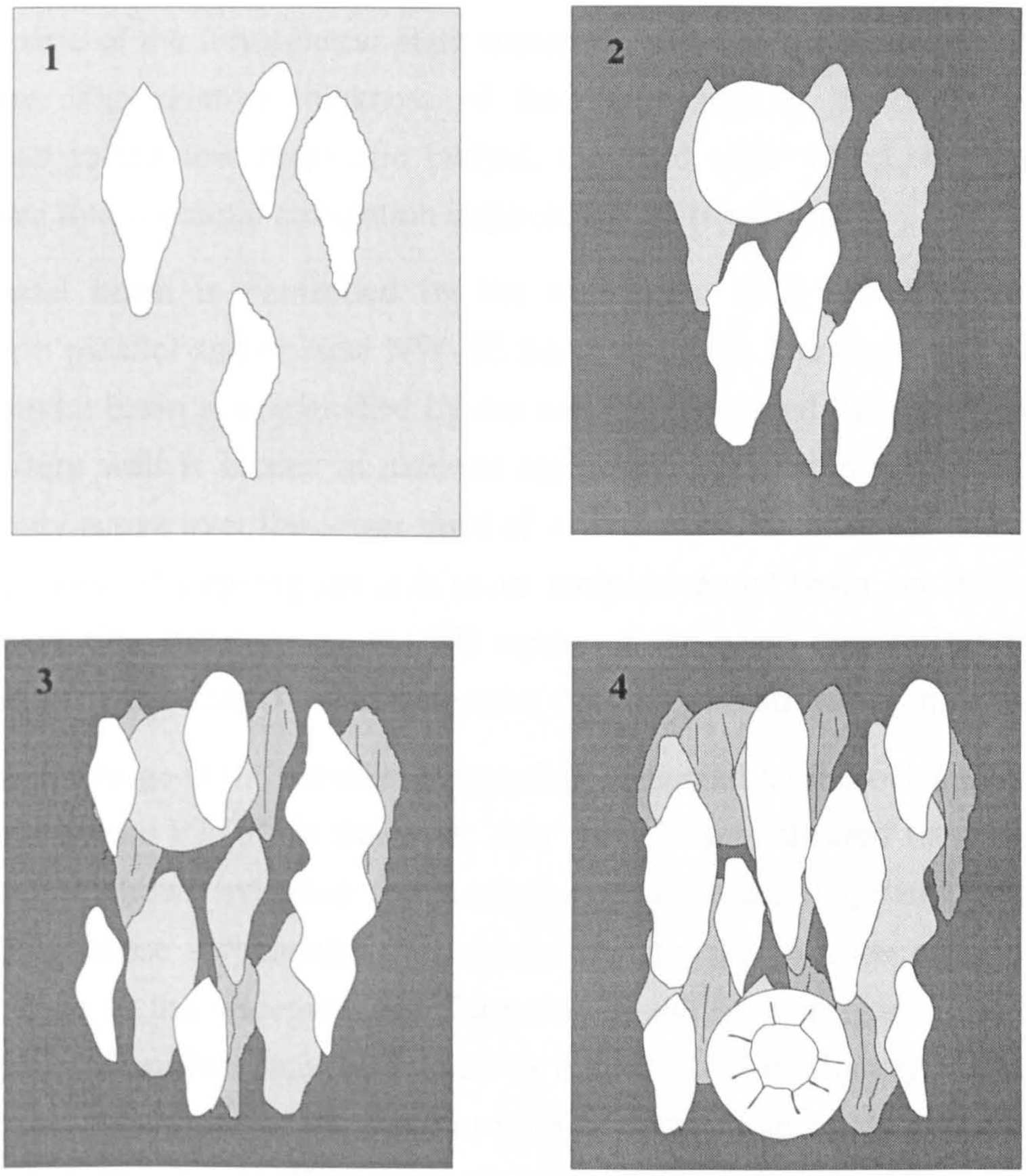

Figure 5.16 Cartoon to illustrate the building of an NVR, when the volcanism is not strongly focused in space and time. This results in an NVR which does not always have a clearly defined, continuous boundary with the fissured crust. There are also small irregular patches within the 'hummocky' terrain that seem more tectonised than other areas. Compare this model with the character of the NVZ in the TD.

5.7 Summary of chapter 5.

- The transform domain extends 26km from the Principal Transform Displacement Zone. Its northern extent is is identified by a change in the stress regime, as manifest on the median valley walls. The orientation of fissure ridges and faults to the north and north west is consistent with the coupling of the regional stress field with a local NW-SE stress field. I propose that this local stress field is caused by flexural downbending of the lithosphere in response to the formation of the nodal basin and the increasing throw on the eastern wall fault towards the transform.

- The flexure of the lithospheric plate across the axis has implications for its thermal structure. The relative thickness of the lithosphere at the MARNOK RTI is attributed to the low magmatic budget, the 'cold edge' effect, but mostly to the increased hydrothermal circulation imposed by the transform.

- The nodal basin is controlled by the interaction of a series of ridge-parallel, transform parallel and oblique NW-SE trending faults. The north and western walls of the nodal basin are controlled by the subsidence caused by loss of viscous head. The eastern wall is related to extreme asymmetric extension across the ridge axis, but is only active over the lower third of its exposure. Extensional tectonics may be in the process of stepping inwards to an 'incipient nodal basin' on the western wall. The orientation structures in the SE corner of the basin may reflect the changing orientation of the stress field as extension couples with strike-slip motion.

- The median ridge in the transform comprises a sheared fault block and is bounded to the north by the PTDZ. In the west, near the RTI this sheared fault block widens, flattens and shows evidence for increasing serpentinite diapirism. The low shear strength of these serpentinite protrusions are thought to initiate the slope failure which leads to the widening and flattening of the median ridge. The initiation of serpentinite diapirism may be related to this area being slightly transtensional, or may be a consequence of the close proximity of the large inside corner wall fault as both these features may allow seawater penetration to great depths.

- There is a correlation between distinct volcanic morphologies and distinct parental magmas in the TD. In the north of the TD the petrological segmentation is on a smaller scale than the dredge spacing, whereas near the tip of the ridge crest it can be estimated at ranging from 3-6km along axis, and correlating with distinct volcanic constructions, as identified on the sidescan. The heterogeneous character of the NVZ implies that volcanism is taking place in relatively unfocused, small discrete episodes, which are probably from individual magma bodies separated in space and time. The high abundance of plagioclase megacrysts and phenocrysts suggests that the magma chambers have a relatively high crystal/magma ratio, consistent with low magma supply.

BLANK IN ORIGINAL

Chapter 6

Segmentation

Man's hand assaults the flinty rock and lays bare the roots of the mountains.
He tunnels through the rock, his eyes see all its treasures,
He searches the sources of the rivers and brings hidden things to light.
But where can wisdom be found? Where does understanding dwell?
Man does not comprehend its worth.
The deep says 'It is not in me'. The sea says 'It is not with me'.
It cannot be bought with the finest gold, nor can its price be weighed in silver.

Job 28 vs 9-15.

6.1 Introduction.

This chapter looks at aspects of second order segmentation. It starts with the presentation of a geological map of the MARNOK area and a description of the volcanic, tectonic hydrothermal and relative age variations seen along the ridge axis. The contrast between the east and west valley walls and brief descriptions of the ridge flanks are also included.

The remainder of this chapter will bring together data from the whole of segments 1 and 2 (i.e. including the TD), so that the relative importance of second order and first order segmentation can be assessed.

Geochemical systematics with segmentation are presented. This includes along-axis variations in extent of fractionation, melting, mantle source, and petrological (fourth order) segmentation. The deep-tow magnetic inversions performed by Hussenoeder et al. *(in prep.)* are discussed to assess the primary cause of the variations in magnetization in the MARNOK area.

These observations are then discussed in terms of mid-ocean ridge dynamics, concentrating on the episodicity and focusing of magma supply, its relationship to hydrothermal activity and the depth of the brittle-ductile transition, and the magmatic crustal residence time. Finally a model of segment accretion is developed.

6.2 Geological map.

A geological map of the MARNOK area (figure 6.1) provides a summary of the interpretations of the sidescan sonar. It includes some information already discussed in previous chapters, such as: the preferential location of flat-topped seamounts at the NTO and in the RTI; the widening of the median valley from the narrowgate to the

transform; the diverse volcanic character and tectonic asymmetry of the RTI; and, in the transform, the change in orientation of the PTDZ at about 46°05'W and the curving ridges of the inside corner high.

In addition, the map summarises the geology of the rest of segment 1, the NTO and all of segment 2. The northern half of segment 1 has a uniform hummocky NVZ which tapers into the NTO (24°22' N), as would be expected, but also narrows at the bathymetric saddle in the segment centre (24°06' N). It was at this narrowgate saddle point that the WASP traverses revealed a very paltry, low relief NVR (section 4.2). The wall faults flanking this uniform NVZ have relatively small throws and are symmetric about the axis.

In segment 2, the wall faulting is more asymmetric and the robust NVR comprises hummocky ridges which are often associated with pronounced syn-magmatic faults along the crest. The NVR of segment 2 also tapers towards the NTO, but generally remains a relatively consistent width throughout its length. It terminates in the north rather abruptly against an oblique trending slope of older crust.

In general, the increase in volcanic complexity is accompanied by an increase in tectonic complexity in terms of the faulting patterns observed in the valley walls. The following two sections present the data on the northern half of segment 1 and all of segment 2 in a more detailed form. A discussion on the morphometric contrasts between the segments follows later in this chapter.

6.3 Variations in median valley floor along-axis.

The following section will focus on the changing character of the volcanic and tectonic terrains seen along the valley floor. This includes observations on the volcanic morphologies in the NVZ, the faulting that cuts the NVZ, the character and age contrast of the neovolcanic-fissured contact, the textures of the marginal basins, age variations along and across-axis and evidence of hydrothermal activity.

Section 6.4 will focus on the median valley walls, so they will only be mentioned in passing in this section. For the purposes of this description, the MARNOK area north of the TD has been divided into 3 regions: segment 2 (the northern half of which is shown in figure 4.13); the NTO and the area near the junction of the two segments (figure 4.12); and the north half of segment 1 (figure 6.3). The account will start in the north and continue southwards towards the narrowgate.

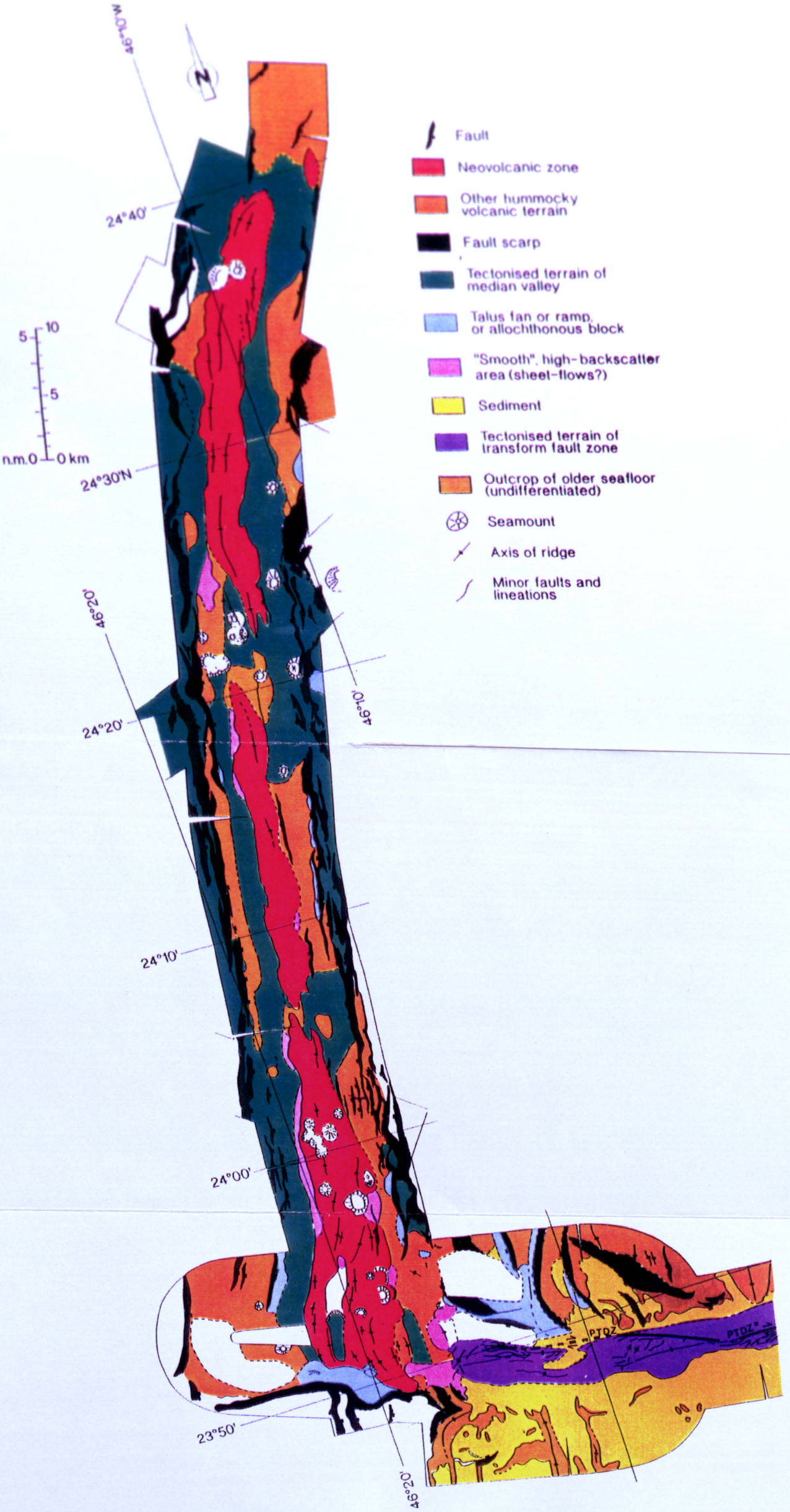

Figure 6.1 Geological map of the MARNOK area.

6.3.1 Segment 2

6.3.1.1 The NVR and syn-magmatic faulting

The robust NVR of segment 2 is 37km long and is composed almost entirely of hummocky terrain in a broad composite pile. There is a strong degree of elongation near the crest while the flanks are more homogeneous, suggesting that larger structures (probably faults) dominate at the crest, while there is less evidence of prominent fault (or fissure) control on the flanks. However, this across-axis variation, to a certain extent, may be an artefact of the shallower grazing angles at the summit of the NVR.

The northern half of the NVR is dominated by the crestal seamount (figure 4.13iii). As described in section 4.5.2.3, the seamount occupies a central position over a syn-magmatic structure (figure 4.13iv-v-vi-vii). Towards its northern end, the sharp crested fault curves to the north east to follow the trend of the median valley for about 3km (figure 4.13vi-vii). The curving tip of this ridge is consistent with an element of sinistral shear, from the easterly-stepping ridge axis, rotating the axis of principle compressive stress. North of figure 4.13vi, the fault bends back again and continues for another kilometre into the strongly tectonised and sedimented edge of the median valley (figure 4.13 viii). A feature colinear to it extends for a further 5km with varying throw into the oblique-trending flanks to the north of segment 2. Note that there is no valley wall fault here.

The highest point of the NVR is a 3km long, broad, hummocky area (figure 4.13ix) to the NE of the crestal seamount. Two sharp-edged, faulted ridges emerge to the north from beneath this hummocky summit (figure 4.13vi and 4.13x). The eastern faulted ridge (figure 4.13x) can be traced for only a kilometre before it disappears again beneath another area of strongly backscattering, hummocky terrain (at figure 4.13xi). Hence, this eastern ridge is colinear with two relatively recent volcanic episodes (the hummocky summit—figure 4.13 ix and the hummocky tip of the NVR—figure 4.13 x), while the western ridge is colinear with the older crestal seamount.

These observations confirm that there is a close relationship between faulting and volcanic construction. The NVR seems to be built up by eruptions associated with closely spaced, subparallel faults. Both WASP and TOBI images show that some of the faults seem to have acted as conduits for magma (see section 3.2.2.2). The construction of the robust NVR may be controlled by these faults helping to focus the magma in its passage through the crust. Fissure eruptions probably also play an important role, though they are less easily identified on the sidescan images. These

large faults also indicate that the lithosphere across the median valley of this segment is relatively thick, as will be discussed later in this chapter.

The southern end of the NVR has a similar character to the northern end, except it lacks any crestal seamounts and is slightly less voluminous.

6.3.1.2 Faulting on the NVR

While the above section focused on syn-magmatic faults, this section describes faulting which has no associated magmatism. Faults cutting the hummocky crest and flanks of the NVR range in length from a couple of hundred metres to 5km. In some places they show a remarkable congruence with the valley wall faults, while in others there seems to be very little relationship between the wall faulting and the tectonism on axis. For instance, the small kink in the wall faults at 24°26'N is paralleled by a change in strike of the faulted hummocky ridge near the crest of the NVR. In contrast, the faults cutting the NVZ near the centre of the segment (between 24°29'N and 24° 35'N) are roughly parallel to the trend of the NVR and the median valley as a whole, while the median valley wall faults show considerable complexity with intersecting fault trends and large lateral offsets.

To the north of the segment where the valley opens out into the right lateral oblique-trending zone, the faults cutting the eastern flank of the NVR form a right lateral en-echelon set (figure 4.13xii), consistent with the expected stress regime. Each fault in this set is about 3km long, the offset between them is a couple of hundred metres and the overlap varies but is relatively minor. The fault tips splay and curve across the bridge, suggesting that, with time, fault horses will develop.

6.3.1.3 Age variations

The broad, hummocky summit of the NVR (figure 4.13ix) is the youngest part of the ridge crest, as its strongly backscattering, uniform hummocky texture contrasts with the moderately sedimented and tectonised crust seen elsewhere. This recent eruption impinges onto the north eastern flank of the older crestal seamount.

The eastern flank of the NVR is more extensively faulted than the western flank, suggesting that it is older. The observations from the WASP traverse to the south of the crestal seamount (figures 4.1 and 4.3) confirm that the eastern flank is considerably older than the west, and suggest that the western, faulted ridge crest is only several hundred years old. If this is so then the summit eruption to the NE of the crestal seamount (figure 4.13ix) is probably very recent (within the last 100 years).

Dredges 23D and 32D each recovered one unit with sediment embedded in cracks in the basalt. The presence of sediment in 32D was quite surprising as this dredge traversed the supposedly recently erupted crest (figure 4.13ix). It is possible that these

older rocks were sampled from the older terrain at the north and south of the dredge path. The remainder of the units of 32D were moderately fresh, but there were certainly no very fresh glassy samples from a very recent eruption. Hemipelagics were most prominent in 24D, where they coated a number of units. However, unlike the RTI area there were no large recoveries of sediment in the pipe dredge. Petrologically, there were no systematic variations in extent of alteration/age along-axis.

6.3.1.4 The marginal basins

The marginal basin on the NW side of the NVR of segment 2 is very poorly backscattering indicating that sediment cover is more than a metre thick (figure 4.13 xiii). There is a more lineated, fissured character near the northern tip of the NVR (figure 4.13 viii) whereas, further south, the western marginal basin has a diffuse hummocky texture (figure 4.13 xiv) suggesting that it is both less strongly tectonised and has slightly less sediment cover. In contrast, the marginal basin to the East of the NVR contains relatively highly backscattering terrain. It is faulted and fissured to the north (figure 4.13xv), where the valley trends obliquely, but further south it seems no more disrupted than the NVR itself (figure 4.13xvi). This well preserved area of the marginal basin occurs north of 24°30'N, adjacent to the very steeply-dipping, curving boundary fault (see figures 1.3 and 1.4).

To the south of the area shown in figure 4.13, both eastern and western marginal basins comprise poorly backscattering, diffusely hummocky terrain, although the marginal basin is wider on the eastern side and contains more debris from sediment slumps and landslides, while on the western side fissuring is more apparent. The contact of the NVR with the older crust in the marginal basins seems relatively sharp, (especially in the west), but for most of segment 2 the actual contact is not observed as it falls within the nadir.

The well-defined age contrast between the NVR and most of the marginal basin suggests that the NVR was built after a relatively long period of magmatic quiescence. Allerton et al. (1995) suggest that the particularly strong contrast between the neovolcanic terrain and the old sedimented and tectonised crust at the northern end of segment 2 may indicate that the tip of the NVR is propagating northwards. The presence of relatively young material in the area to the NE of the NVR reflects the oblique trend of the median valley at this point. The area adjacent to the curving boundary fault may have remained untectonised because of the strong strain partitioning which seems to occur on this corner where the trend of the valley changes from normal spreading to oblique.

6.3.1.5 Hydrothermal activity

Several of the dredges from segment 2 recovered basalts coated with intense 'sooty' hydrothermal deposits (e.g. figure 6.2). These deposits were restricted to the older samples from segment 2, from dredges D23, D24, D30, D32. Some of these dredge sites also recovered younger units that did not have the hydrothermal coating. The two other dredges from this segment were D25, where the recovery was very poor, and D31, which sampled only fresher material. The absence of hydrothermal deposits on samples from D31 can be explained if there has been a reduction or cessation of the hydrothermal venting before eruption of these younger basalts. Alternatively, the time elapsed since the eruption may be insufficient to allow for a noticeable precipitation of hydrothermal material.

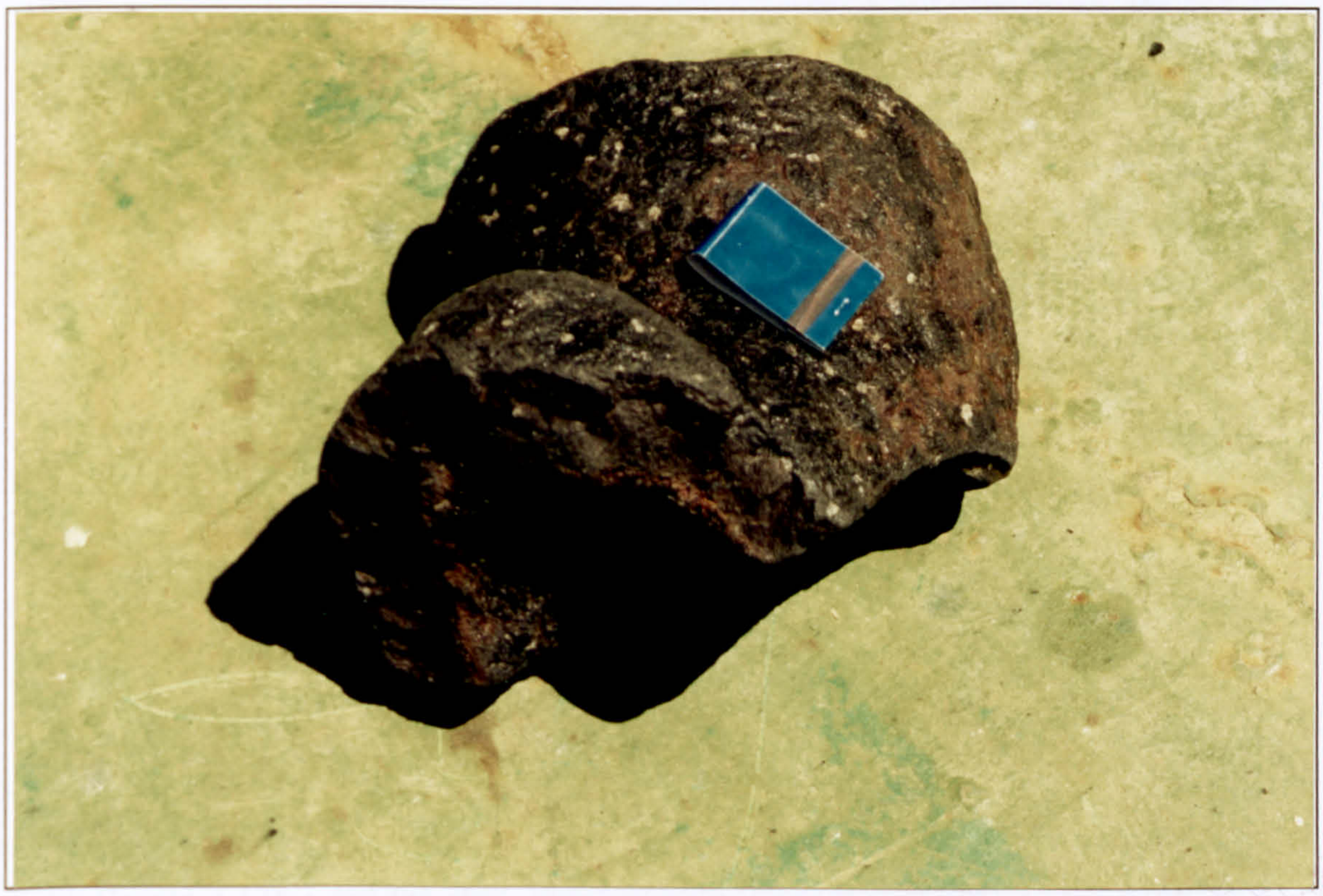

Figure 6.2 Plagioclase phyric pillow with very thin palagonitised glassy rim and patches of black sooty coating thought to be Fe-Mn hydrothermal precipitate. The blue match packet for scale is 8cm long.

6.3.2 The NTO

6.3.2.1 The intersection of the NVRs

It is unclear from the bathymetry whether there is a slight overlap in the NVRs of the two segments, such as is seen at faster spreading rates, but the sidescan image clarifies that this is not the case.

The hummocky NVR of segment 2 trends at 186° towards the NTO and seems to be cut by a progressively greater number of tectonic features which are not syn-

magmatic, including a large axial fissure (figure 4.12vii), which can be traced for over 1km along the crest at about 24°24'N.

The hummocky NVR of segment 1 trends at an angle of about 190° towards the NTO until at 24°20'N it kinks to the east by almost 10°. The kinked tip is separated from the main body of the NVR by a ~N-S trending fault (figure 4.12viii), which will be described further in section 6.3.2.3. The tip of the NVR trends for 3km at about 198° and terminates just to the south of the cratered cone at 24°22'N (figure 4.12vi). This seamount and the flat-top immediately to the north of it (figure 4.12ix) are both dissected by faults, so although they are continuous along-strike with the hummocky tip of segment 1, they are not presently active.

These two faulted seamounts are located ~1km to the west of the tip of segment 2. The dive by Zonenshain et al. (1989) showed that the flows which make up the hummocky tip of segment 2 are fractured and covered by up to 0.5m of sediment (figure 2.8), suggesting that volcanism ceased about 10,000 years ago. Hence, although the neovolcanic textures are relatively continuous across the NTO, active volcanism does not overlap between the two segments, and the whole area is relatively tectonised.

6.3.2.2 The flat-topped seamounts

The most striking feature of the area around the 24°22'N NTO is the large number of distinctive seamounts (figure 4.12i,iv,v,vi,ix), showing quite a wide range in textural ages. All of these seamounts are flat-tops, one with a 'late stage' cratered cone. The nested seamounts (figure 4.12i), the mantled seamount (figure 4.12iv) and the large, fractured seamount (figure 4.12v) are all situated at the edges of the median valley adjacent to the wall faults. As the nested and mantled seamounts have relatively young morphologies, they were probably erupted in this site, and were not transported, post-eruption, to the edges of the median valley. In contrast, the seamount with the cratered cone (figure 4.12vi) and the fault-dissected seamount immediately to the north of it (figure 4.12ix) are older, but occupy a relatively central position in the median valley.

This rather unusual age distribution highlights that the flat-topped seamounts are commonly erupted right at the edge of the median valley, adjacent to the wall faults—a location that the hummocky pillow mounds are never seen to occupy. However, they are not restricted to this off-axis locality, and can occur amidst the hummocky terrain in the NVZ.

6.3.2.3 Faulting

The N-S trending fault (figure 4.12viii) separating the kinked tip of segment 1 from the main body of the NVR can be traced for 3km along-strike but has a relatively

small throw. It forms one of a series of small throw faults, which cut across the NVZ near the NTO, oriented between 005° and 015°, subparallel to the main valley wall faults. These faults sidestep in a roughly right lateral en-echelon fashion, consistent with the slight offset in the NVRs of the two segments.

There is also a minor set of structures that strike at 057° in the same orientation as the oblique eastern wall fault trend (figure 4.12ii). This oblique trend can be seen developing more strongly at the eastern edge of the median valley floor in the form of small fault splays (figure 4.12iii) which have propagated from the larger N-S trending scarps. Allerton et al. (1995) suggest that the major oblique valley wall fault (figure 1.4), which has a similar orientation to these minor faults, formed as the curving, propagating tip of the valley-parallel wall fault, in a manner which is observed here. The oblique faults are probably transfer faults.

6.3.2.4 The marginal basin

There is a decrease in the backscatter, reflecting an increase in sediment cover towards the edge of the valley. The sediment cover is considerably thicker in the eastern marginal basin, probably as a result of sediment slumps down the valley walls (as will be discussed further in section 6.4). There is surprisingly little evidence of intense fissuring between the faulted hummocky terrain and the valley walls, even in the less sedimented western marginal basin. The first intensely tectonised crust virtually coincides with the base of the valley wall fault.

6.3.3 Northern half of segment 1

6.3.3.1 The NVZ

The median valley of the northern half of segment 1 is marked by its uniformity. The NVZ comprises a very regular, low relief, hummocky NVR. Elongated hummocky ridges dominate and hummocky mounds are rare, while other distinctive seamount morphologies are entirely absent from the sidescan images. However, the bathymetry indicates that there may be two seamounts adjacent to the western wall at 24°18'N and 24°11'N which have fallen in the nadir of the sidescan swaths. From the shape defined by the contours it seems likely that the seamount at 24°18'N (relatively close the NTO) is a flat-top, while that at 24°11'N is a hummocky mound.

In contrast to the NVR of segment 2, the hummocky ridges here are much shorter and at no point along the crest does one single structure seem to be dominant. The width of the NVR is relatively constant along-axis but narrows towards the bathymetric saddle (figure 6.3ii). Hence, in contrast to standard views of segmentation, the bathymetric centre of the segment is actually where the NVZ is least extensive. The

46°20'W

24°15'N

24°10'N

24°05'N

Figure 6.3a Sidescan mosaic of northern half of segment 1.

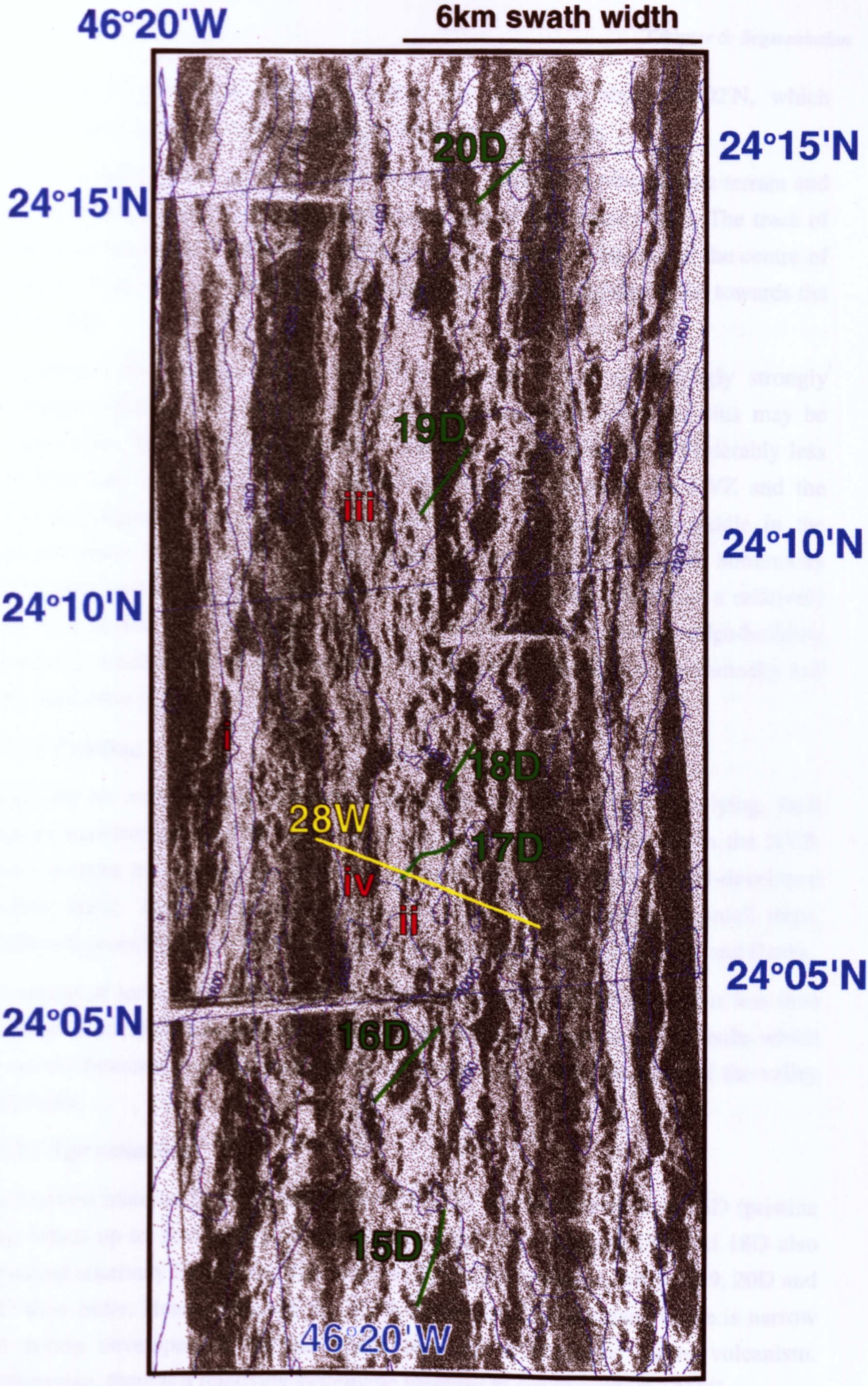

Figure 6.3b Positions of dredge sites 15D, 16D, 17D, 18D, 19D, 20D and WASP traverse 28W are marked. The following features are to be noted from figure 6.3a and are discussed in the text: (i) bridge between en-echelon faults; (ii) NVZ narrows at the narrowgate bathymetric saddle; (iii) sharp contact between the hummocky terrain of the NVR and the fissured terrain; and (iv) sedimented fault terrace near the narrowgate has a relatively strong age contrast with the adjacent NVZ.

uniformity of the NVR continues across the saddle to about 24°02'N, which approximately coincides with the edge of the transform domain.

There is a well-defined sharp contact between the hummocky neovolcanic terrain and older fissured and faulted terrain either side of the NVR (figure 6.3iii). The trace of this contact shows that the NVZ is actually offset slightly to the east of the centre of the valley floor, as is suggested by the bathymetry which is slightly higher towards the eastern wall.

Compared with segment 2 and the NTO, segment 1 has a seemingly strongly tectonised region between the NVZ and the median valley walls, but this may be accounted for by the smaller degrees of sediment cover, which is considerably less than that seen in segment 2. The largest age contrast between the NVZ and the tectonised edges of the median valley occurs near the narrowgate saddle in the segment centre (figure 6.3iv). The sharpness of the contact between the hummocky and fissured terrain implies that volcanism is highly focused and/or has a relatively long time period of episodicity. However, the time period between ridge-building episodes is smaller than in segment 2 as the age contrast between the hummocky and tectonised crust is less.

6.3.3.2 Faulting

There are no marginal basins in the narrowgate segment, as low, flat-lying, fault terraces intersect the median valley floor almost immediately adjacent to the NVZ. These terraces are moderately sediment-covered and usually have a well-developed tectonic fabric. They uplift the edges of the valley floor in a series of small steps, which will probably go on to become the larger terraces in the valley walls and flanks.

The extent of tectonism of the NVR is relatively constant along-axis and is less than that seen at the NTO and over some parts of the NVR of segment 2. The faults which do cut the hummocky NVR are ridge-parallel, consistent with the trend of the valley wall faults.

6.3.3.3 Age variations

The freshest material in the entire MARNOK area was recovered from 16D (pristine glass crusts up to 3cm thick), closely followed by 15D. Dredges 17D and 18D also contained relatively fresh glass with only partial palagonitisation, while D19, 20D and 21D were older. Hence, although the NVR at the centre of the narrowgate is narrow and poorly developed, it has also been the site of the most recent volcanism. Furthermore, there is a relatively systematic increase in age towards the NTO.

6.3.3.4 Hydrothermal activity

There is considerably less evidence for hydrothermal activity in segment 1 than in segment 2. The dredge material near the centre of the segment has virtually no Fe-Mn coat, with only a thin, mottled hydrogenous coating on the older units. At the northern end of the segment, dredges 19, 20 and 21 recovered some samples with a thin black coating, which was nevertheless greater than that expected for hydrogenous precipitation in the valley floor. There is a gradual decrease in intensity of the hydrothermal coating to the south, which may be a result of the varying influence of a hydrothermal plume centred somewhere in segment 2. Alternatively, it may reflect a difference in the ocean floor currents between the two segments, which will in turn affect the distribution of material from hydrothermal plumes.

6.4 Variations in the median valley walls and flanks along-axis.

The asymmetry of valley wall faulting has been recognised for many years from bathymetry maps and submersible dives (Karson & Dick, 1983; 1984; Collette, 1986; Severinghaus & Macdonald, 1988; Tucholke & Schouten, 1988). Zonenshain et al. (1989) recognised two types of valley wall slope with contrasting characteristics from submersible dives in the TAG and MARNOK areas. The 'normal' slopes are block-faulted and have relatively small elevations above the valley floor. In contrast the 'abnormal' slopes have relief of 1-3km, reveal an almost undisturbed section from upper to lower crust and are covered in features related to large scale mass wasting.

Recently there has been an increasing emphasis on detachment faulting and the role of half-graben development as an important aspect of ridge tectonics at slow spreading rates (e.g. Mutter & Karson, 1992; Tucholke & Lin, 1994; Escartín & Lin, 1995). The following section deals with the varying character and orientation of the wall faulting seen along-axis, focusing on the additional information about the development and character of inner wall faults which is revealed from the sidescan sonar imagery. This includes aspects such as small-scale structure and assessment of fault maturity from extent of sedimentation and mass wasting processes.

6.4.1 Segment 2

The varying fault orientations associated with the oblique ridge trend to the north of segment 2 have already been described in chapter 1. The sidescan confirms that where the bathymetry is the steepest (>35°) there are brightly backscattering wall scarps. The textures are similar to the 'mature' stage of Allerton et al. (1995) with well-developed talus ramps and a slightly gullied, crest-free face. The lower fault terraces and horses on the northern half of the segment are highly sedimented, while to the south near the NTO, fissured terrain becomes more dominant on terrace surfaces, reflecting the

gradation also seen in the marginal basin. This may imply that where two orientations of faulting are present (as in the northern half of the segment), there is more strain partitioning into the faults and less fissuring of the older crust as a whole. Alternatively the fissures in the north of segment 2 are buried under the sediment cover.

As mentioned in section 6.3.1, there is no brightly backscattering valley wall fault across the north of the segment, but the NVZ abuts straight onto darkly backscattering flanks.

The oblique swath over the eastern flank of segment 2 shows a wide, heavily sedimented terrace, truncated to the east by a steep, curving fault wall, which is easily recognisable on the bathymetry. The horizontal terrace contains patches of relict hummocky terrain near the crest of the valley wall scarp. Further off-axis the texture becomes increasingly smoother, probably as a result of increasing sediment cover. There is little evidence of tectonic dismemberment within the horizontal expanse of the terrace, suggesting that off-axis, as well as on-axis, most of the extension is partitioned into the curved boundary faults.

6.4.2 Junction of segment 1 and segment 2

6.4.2.1 Eastern wall

The throw on the eastern wall fault increases towards the discontinuity, and with this increase in throw comes additional textural variation, which is particularly well displayed on the central oblique swath (figure 3.8). Here, the sidescan image has highly variable amplitudes over the fault scarp, which can be quite deceptive when viewed without the bathymetry. This large-throw, eastern wall fault is dominated by features relating to mass wasting and thick sediment cover (the "drape" stage of Allerton et al., 1995). In contrast to the other valley wall scarps (with the exception of the inside corner) much of the mass wasting is of material that is associated with a highly mature fault plane (i.e. slumping of the draped sediment and the slope failure of debris fans.) These features confirm the greater age of this large throw fault.

A flat-topped seamount (figure 3.8 viii), 1.5km in diameter, is preserved intact at the very edge of the uplifted block, so that its steep sides contribute an extra 160m to the height of the fault scarp. Ballard and Van Andel (1977) propose that rifting preferentially occurs around the edges of volcanoes allowing them to be uplifted into the flanks as intact units. This certainly seems to be the case for this seamount but others, both in the flanks (figure 3.10iii) and on the median valley floor (e.g. figure 4.12v and ix and figure 5.1xi), have been dissected by faults.

Scree chutes and trails of loose fragments extend down from the crest of the seamount for about 400m (figure 3.8 ix), where it contacts with an area of thick sediment cover. Active mass wasting of the steep-sided seamount has continued for longer than the rest of the fault crest which has a well developed sediment cover. In addition to the heavy sediment cover, this eastern wall is characterised by landslides and sediment slumps.

About half way down the eastern wall, there is a concave slide scar (figure 3.8x), with an unconsolidated mass flow deposit below, extending about 1km down-slope (figure 3.8xi). A sediment slump (figure 3.8 iv; figure 4.12 x) has already been described in detail in section 3.5.4. The volume of the sediment slump, which can be estimated assuming there was originally along-strike continuity of the contours, is found to be about 0.5 - 0.75 km^3. This is a small feature compared with the 19km^3 for the debris wedge at 26°25'N (Tucholke, 1992). In section 3.5.4, I commented that the slide scar of this slump was difficult to identify. However, a well formed slide scar might not be expected for such a relatively small deposit, which comprises mostly sediment, especially given that debris volume expansion of about 20% may have occurred (Tucholke, op.cit.).

The sediment slump seems to downlap onto a much brighter area of wall scarp to the north (figure 3.13viii), which is probably a landslide similar to those recognised by Cann et al. (1992a & b).

6.4.2.2 Western wall

In addition to the landslide on the eastern wall (figure 3.13viii), there is another landslide on the western wall (figure 3.11, and figure 4.12 xi). Landslides and other features that have developed from slope instability seem to be common at the NTO compared with other parts of the median valley. This can be explained by the increase in throw and age of the fault scarps, but may also be related to the additional break-up and weakening of the crust caused by the intersection of faults with different orientations at the NTO.

6.4.3 The northern half of segment 1

The faults bounding the uniform hummocky ridge in the northern half of segment 1b are strongly linear and relatively continuous, with an abundance of small splays and narrow terraces of fissured terrain. The talus fans are poorly developed forming a sharp linear contact with the valley floor. They correspond to the immature stage of fault scarp evolution.

Figure 3.11 shows the western terraces which were crossed by the central oblique swath. As is expected from the bathymetry, the western side of the rift valley

comprises a number of small throw faults, each of which uplifts in turn a strip of fault terrace. These terraces comprise highly sedimented volcanic terrain and the scarps show an evolution in texture consistent with their progressive ageing off-axis. They contrast markedly to the large throw eastern wall of figure 3.8, and the wide, rounded terrace blocks to the east of segment 2.

The southern oblique swath also crosses the western flanks of segment 1, but further south. The textures are similar to those described above, except the throws on the scarps are smaller and the spacing between terraces is wider, mimicking the trends seen on axis in the TD.

The closely spaced, ridge-parallel terraces extend for about 15km off-axis, where they are interrupted by an outward (westerly) dipping slope, which forms the edge of an off-axis basin (figure 3.10). This westerly dipping slope has a sedimented volcanic texture (figure 3.10v) and even a flat-topped seamount is preserved virtually intact near the foot of the slope (figure 3.10ii). In contrast, the basin is clearly fault bounded to the north and south, and probably also to the west, (although the nature of the western wall is ambiguous, because of the poor image quality obtained while the vehicle was turning). On the NW wall of the basin, there is a rather anomalous segment of an E-W trending fault block (figure 3.10vi). This may reflect fault block rotation resulting from the unusual tectonics in this basin.

6.4.4 Summary

The orientations of the wall faults of segment 2 reflect the onset of the right lateral, oblique trend to the ridge. Although the ridge offset to the south of segment 1 is obviously much greater, the strike slip motion must be strongly partitioned into the PTDZ as the overall trends of the fault scarps remain relatively ridge-parallel along the length of segment 1. There are, however, some localised manifestations of the changing stress regime, as discussed in chapter 5.

The wall faults of segment 1 differ from those of segment 2, not only by their orientation, but also by their degree of maturity. The narrowgate wall scarps have a relatively short life span and thus form a series of closely spaced terraces with immature characteristics on the inner walls. As the valley becomes more asymmetric, those wall faults with greater relief show characteristics of enhanced maturity, reflecting their greater age. Hence the valley walls of segment 2 are more mature than segment 1, and the eastern walls at the NTO (and the RTI) are highly mature.

These observations are consistent with the theory of Harper (1985) that greater valley widths arise from the locking of valley wall faults (i.e. the locking of faults is associated with a greater lifetime for the inner walls). This is seen in the contrast

between segments 1 and 2 and also between the narrowgate and the RTI of segment 1. Another consequence of fault locking is the development of asymmetry, which is also well illustrated in the MARNOK area.

In section 5.6.4 I discussed the rift valley asymmetry at the RTI. This is matched, to a lesser degree, by asymmetry at the NTO. To date the evidence from the MARNOK NTO is not consistent with a large detachment fault as the faulted terraces of the eastern wall seem to comprise sedimented volcanics rather than exposing large areas of lower crustal and upper mantle lithologies.

The presence of the off-axis basin on the western flank of the narrowgate segment is evidence that the dynamics of crustal rifting on this segment change at a distance equivalent to 1.2 Ma off-axis(as calculated from the magnetic anomalies).

6.5 Petrography.

6.5.1 Fractionating assemblages

All samples show evidence for crystallisation of plagioclase and olivine, commonly with higher modal abundances of plagioclase than olivine. Both olivine and plagioclase are common as microphenocrysts. Olivine is rare as a phenocryst phase, while plagioclase phenocrysts and xenocrystic megacrysts are common. Olivine and plagioclase both occur in glomerophyric clusters of quench and intratelluric origin, while clinopyroxene sometimes joins them in quench clusters, but is not seen in the intratelluric ones.

Some of the samples recovered from the hummocky summit of the NVR in segment 2 (32D) are unique in the MARNOK area, in that they have relatively abundant olivine microphenocrysts, while plagioclase is virtually absent. A completely aphyric lava, devoid of all phenocrysts and microphenocrysts was also unique to this site. Only samples from the segment ends have clinopyroxene in reasonable abundance, and then it is usually restricted to the quench phase of growth. Iron oxide opaques are also solely evident in samples from the ends of segments, where they can form up to 10% of a non-glassy groundmass.

The inter-crystal relationships show that olivine and plagioclase are crystallising simultaneously, but occasionally olivine is enclosed by plagioclase, indicating that the likely order of crystallisation throughout the MARNOK area is: ol $\rightarrow$ ol + plag $\rightarrow$ ol + plag + cpx. This suggests that these rocks had the low-alumina parents typical of N-MORB and fractionated under dry conditions (Miyashiro et al., 1969; Michael & Chase, 1987).

6.5.2 Olivine phenocrysts and microphenocrysts

Olivine microphenocrysts range in size from 0.1mm to 0.8mm and can be euhedral, subhedral, anhedral and skeletal. Skeletal textures of quench olivine are particularly prevalent in a number of samples (e.g. 3D-1-1c, 4D-1-1b, 6D-1-1b, 19D-2-1b and 30D-1-2c). The morphology of these quench crystals suggest cooling rates of about 7-15°C hr^{-1} and supercooling of 20-30°C (Donaldson, 1976). All the above samples are from segment 1.

Skeletal forms are rare in segment 2, but some of the samples from dredge 32D at the bathymetric summit of segment 2 (32D-2-1c and 32D-3-1b) contain some microphenocrysts with a highly embayed form, indicative of even greater cooling rates and degrees of supercooling (~ 40°C hr^{-1} and 50°C respectively). These samples have some of the highest proportions of olivine microphenocrysts from the study are and contain plagioclase microlites only as a devitrification texture. Hence they are likely to be some of the most primitive samples in the area. They are also relatively old, with no fresh glass preserved and hence I suggest that they may be from the older crestal seamount rather than the young hummocky terrain which forms the bathymetric summit.

The olivine phenocrysts and microphenocrysts show a limited compositional range (Fo_{88} to Fo_{81}) and most crystals are relatively homogeneous. Olivines within a single sample have limited compositional variation, and the Fo content positively correlates with the MgO of the host glass, suggesting that they are in equilibrium with the melt. The Fo content of the olivine shows a relatively well-defined correlation with the second order segmentation (figure 6.4), being high in the centre of the segments and low at the ends. This is consistent with the variations in fractionation revealed by the basalt geochemistry (as will be described in section 6.6).

6.5.3 Plagioclase phenocrysts and microphenocrysts

Acicular quench plagioclase varies in length from 0.2mm to 3mm and ranges in composition from An_{58} to An_{80} (figure 6.5). The along-axis systematics are not as well defined as for olivine, and the compositional variation within a single sample is also relatively large. The compositional variation is virtually doubled if the phenocryst and megacrysts are taken into account.

The phenocrysts are usually euhedral laths, 0.5-3mm in length, but some phenocrysts have a very rounded form resulting from considerable resorption. Some of the larger resorbed phenocrysts may have been confused with megacrysts. The phenocrysts can be zoned (both reverse and normal) or unzoned, and rare melt inclusions may be present. The phenocrysts in samples at the ends of the segments show particularly

strong zoning, suggesting that the magma chambers from which they originate have considerable compositional variation. In contrast, zoning is present, but much weaker in the segment centres, reflecting more steady state magma compositions. Features of resorption and disequilibrium are seen throughout the area, but again are particularly prevalent at the segment ends.

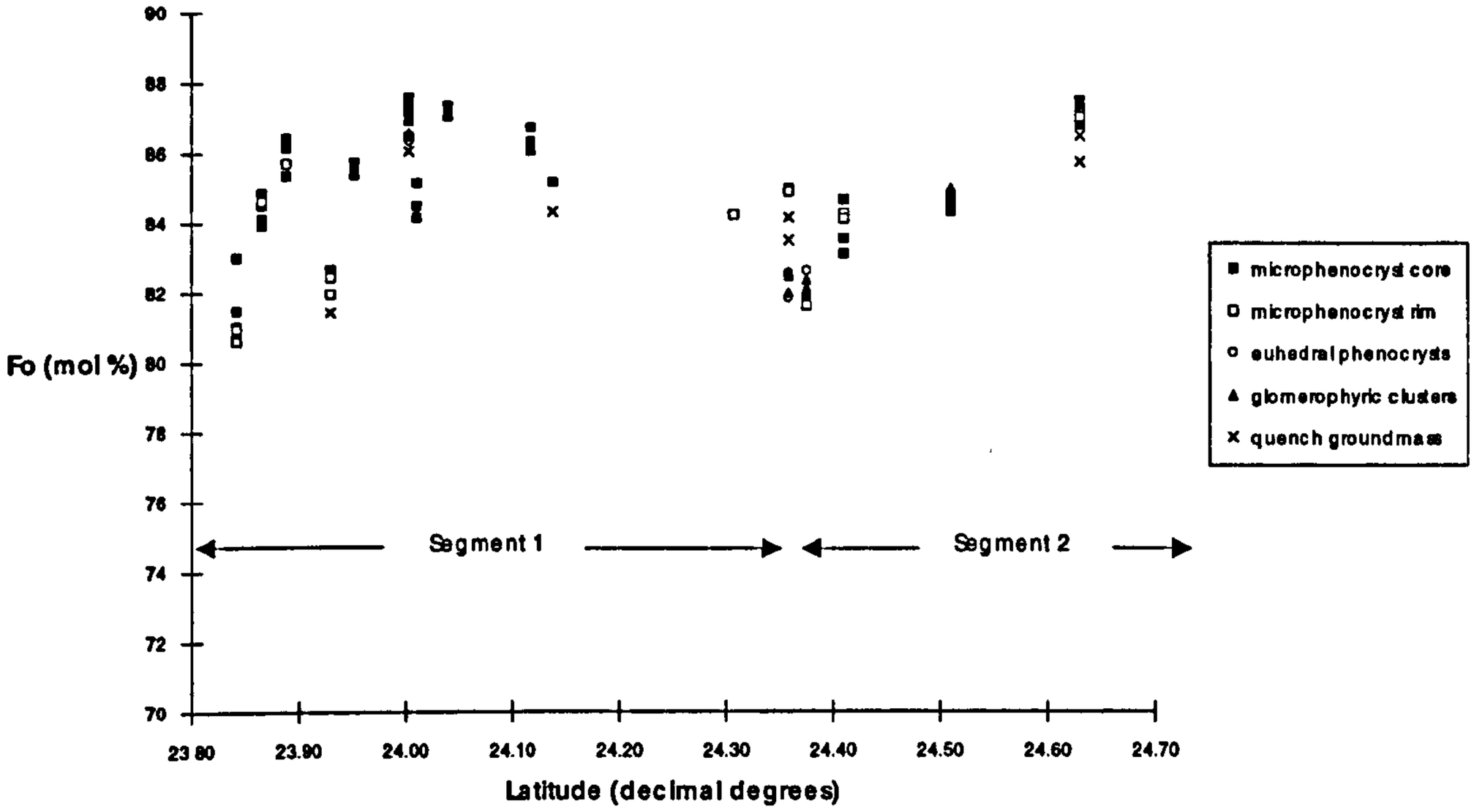

Figure 6.4 Variation in olivine compositions with latitude. Higher Fo values correspond to highs in the along-axis bathymetry.

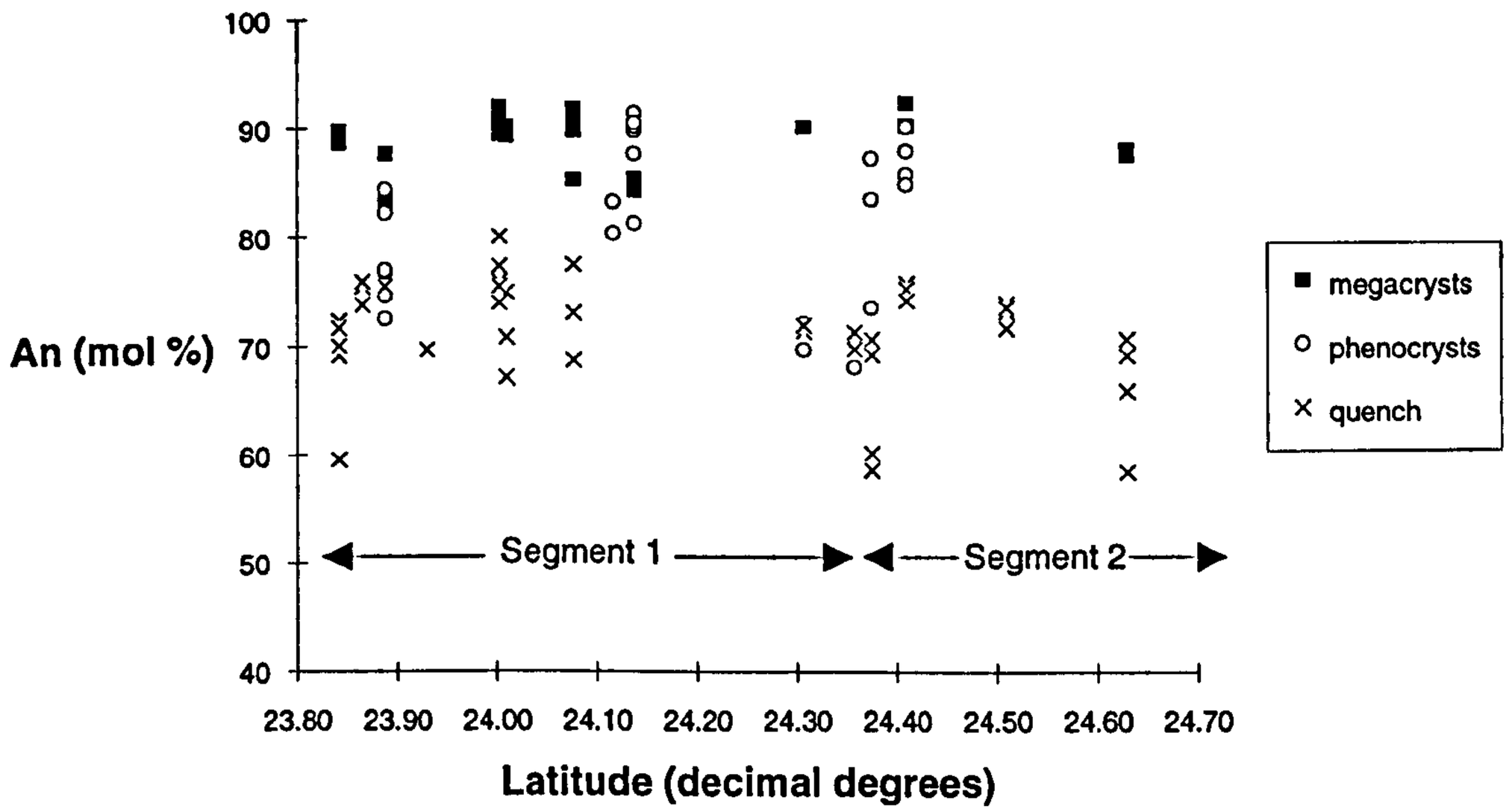

Figure 6.5 Variation in plagioclase compositions with latitude. There is a wide range in An values within a single sample. The along-axis systematics for quench compositions are not as well defined as for olivine. The megacrysts have consistently higher An and show no systematic variation along axis.

6.5.4 Plagioclase megacrysts

The plagioclase megacrysts show many of the characteristics previously described by Donaldson and Brown (1977) and Bryan et al. (1981). They range up to 15mm in length, commonly have a rounded, subhedral (resorped) form and abundant melt inclusions. The cores of many of the megacrysts are relatively unzoned compared with some of the phenocrysts. They often have a narrow quench rim but mantles between the core and the rim are rare, suggesting that these megacrysts have undergone relatively little growth within the magma chamber from which the phenocrysts originate. They have refractory compositions ranging from An_{83} to An_{92}, which show no systematic variation along-axis, or with the MgO content of the host lava. The latter factor suggests that they are not in equilibrium with their basalt host and hence are xenocrystic in origin. Although they occur throughout the MARNOK area there is a greater accumulation of these megacrysts in the transform domain (as discussed in chapter 5).

6.5.5 Xenocrystic clot

One additional interesting petrographic feature is crystalline clot in sample 21D-2-1b from the northern end of segment 1. The clot is about 15mm in diameter and comprises an agglomeration of plagioclase phenocrysts, which are clearly in active disequilibrium with the host glass. The plagioclase crystals forming the clot are mostly subhedral, 1-2mm in length, have rare melt inclusions that tend to be large and blebby and some, but not all, are strongly zoned. This crystal clot seems to have been in the process of breaking up as its boundaries are highly irregular and there are a large number of separate xenocrysts with similar reaction textures in close proximity to the xenolith. Elsewhere in the sample the distinctive texture is still seen but is rarer and the reaction rim is much less pronounced. The resorbed plagioclase phenocrysts mentioned in section 6.5.3 may have originated from the incorporation and dismemberment of similar clots into a magma.

The crystals within the clot are fairly tightly packed, but there are small interstitial spaces which are now occupied by melt. The crystallinity of the xenolith must be at least 90% which would place it in the transitional zone of Sinton and Detrick (1992), being nearly completely solidified crust.

6.5.6 Summary

The petrographic evidence described above highlights the complex history of fractionation, magma-mixing and resorption which occurs within the intratelluric environment of the Mid-Atlantic Ridge. The ends of the segments are characterised by

magma chambers which have evolved over a greater compositional range and erupt assemblages that are systematically more fractionated than the segment centres. The ends of the segment also have textures indicative of higher degrees of disequilibrium between components of magma mixing and show more evidence of accumulation from a crystal mush (and from the transitional walls in the case of the crystalline clot in the NTO).

The compositional and morphological diversity of plagioclase compared with olivine can be attributed to their differing densities with respect to basalt magma. Whereas olivine is denser than the basalt magma and tends to be removed from the system by crystal settling, plagioclase is buoyant and so is likely to remain in the chamber for longer, eventually rising up towards the roof where it may easily become recycled, or incorporated in magmas during eruption.

6.6 Geochemistry.

6.6.1 Fractionation

6.6.1.1 Glass data

Over 500 electron probe analyses from glass separates and the rims of whole-rock specimens ('sections') were obtained by Paul Browning of Bristol University. Glass analyses were obtained from most of the dredge localities by careful hand picking of the more altered and devitrified samples. The glass compositions are typical for MORB: MgO varies from 8.6 to 6.2wt.%, FeO from 8.3 to 10.9wt.%, TiO_2 from 1.3 to 2.2wt.%; Na_2O from 2.7 to 3.4wt.% and Ca from 10.7 to 12.2wt.% (figure 6.6). Five FTIR determinations on samples bracketing the full range in MgO indicate that H_2O contents vary from 0.17 to 0.38 wt. % (Pearce et al., 1993). The whole-rock variation diagrams show similar trends, but with a greater degree of scatter, owing to the effects of crystal accumulation.

Least-squares analysis of the glass data (P. Browning, pers. comm.) indicates that the range in glass chemistry for the more compatible elements can be explained by about 25% crystallisation of olivine and plagioclase in the proportion of about 1:2 (with no need to invoke clinopyroxene). For incompatible elements such as TiO_2 and H_2O, higher estimates of 50% crystallisation for the equivalent samples underline the role of open-system fractionation. These calculations can be confirmed by use of the lever rule on a suitable variation diagram such as is shown in figure 6.7. In figure 6.7 the spread of data indicates 48% fractionation of a 44:56 mixture of olivine:plagioclase.

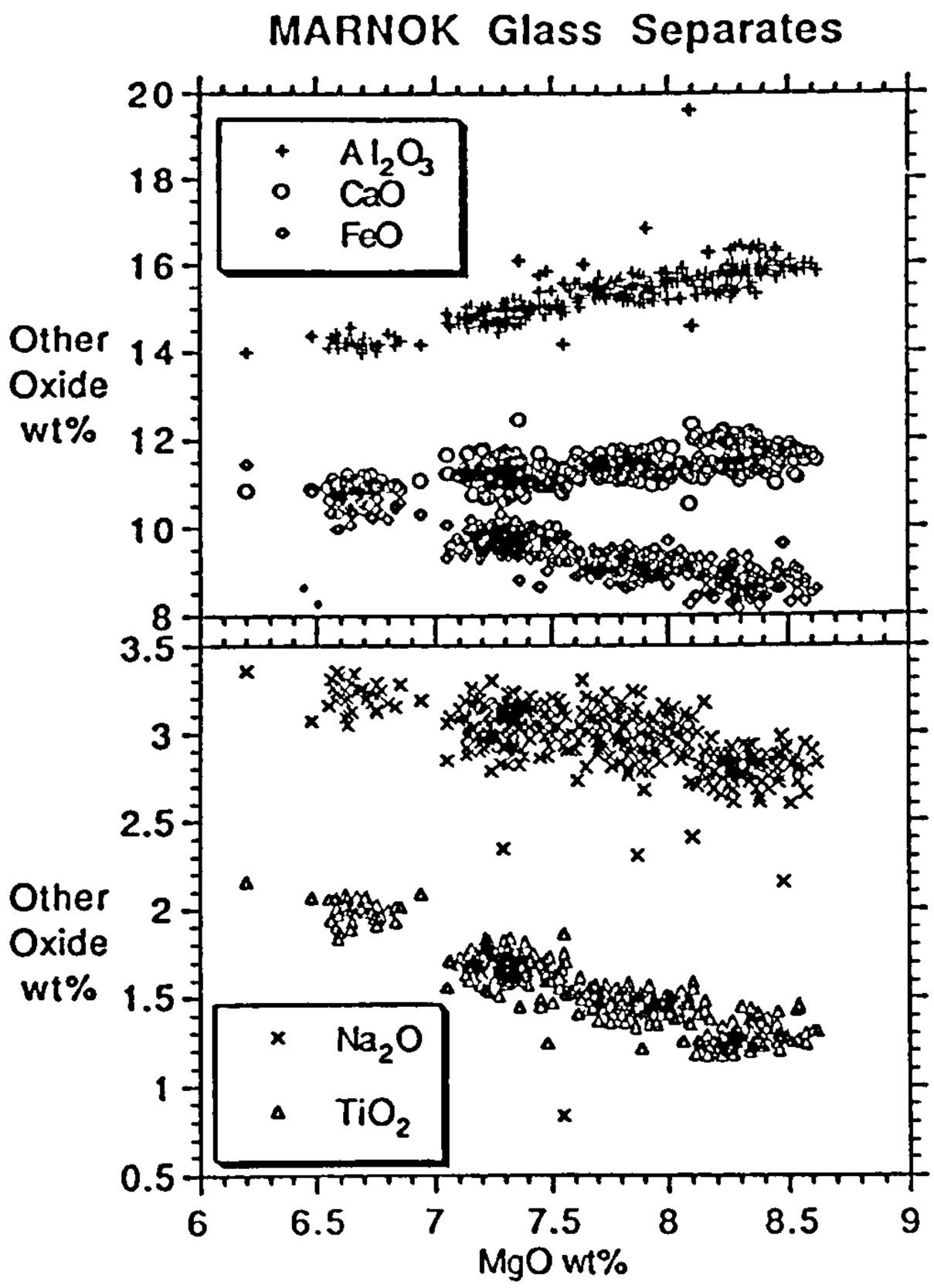

Figure 6.6 Variation diagram for MARNOK glasses (provided by P. Browning)

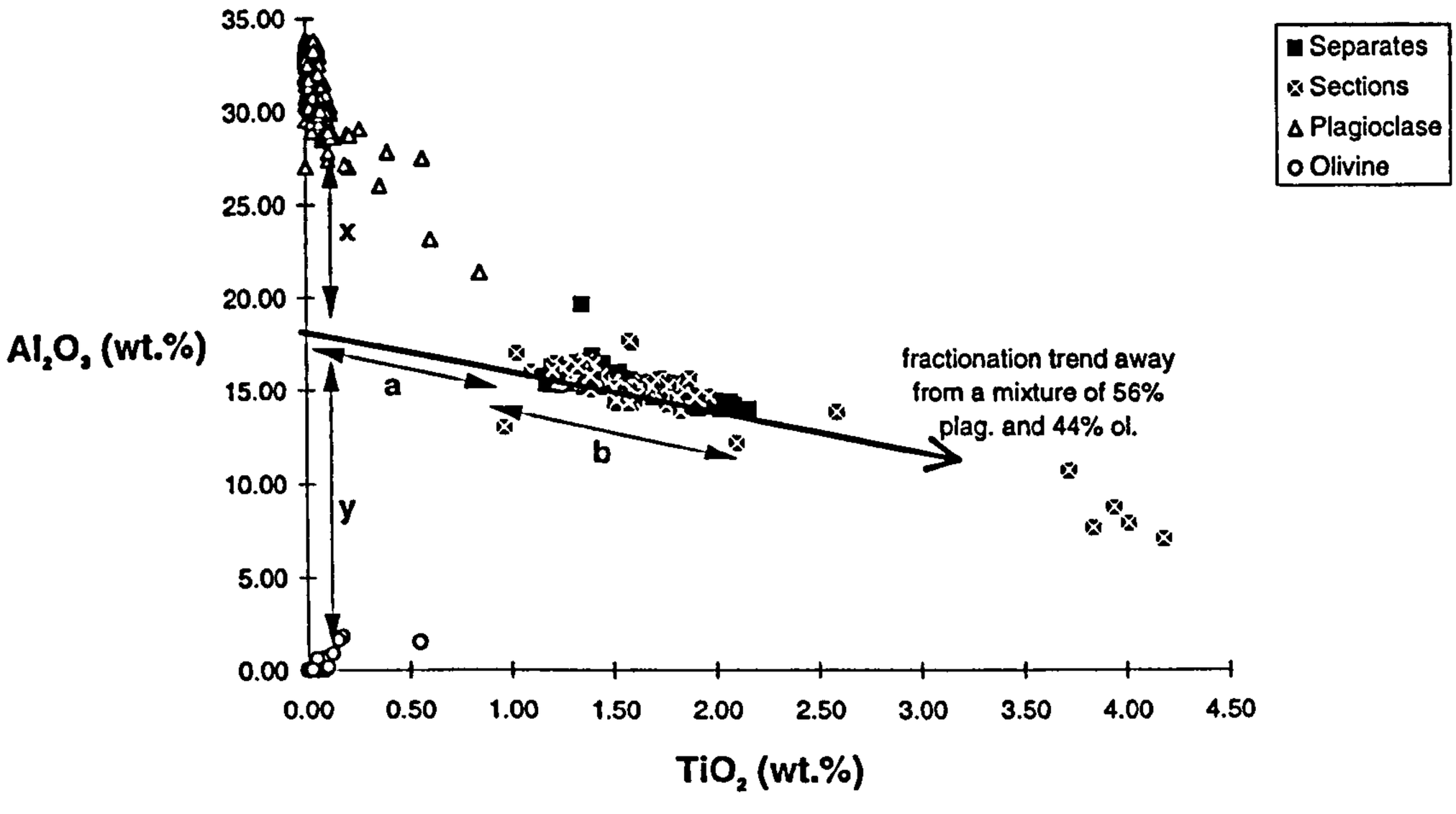

Figure 6.7 Variation diagram showing strong trend in glass data away from a mixture of plagioclase and olivine. The majority of the spread in glass compositions corresponds to 48% crystallisation (= b/(a+b)x100; calculated from the lever rule). The relative proportions of the fractionating phases can also be calculated using the lever rule: % plag = y/(x+y)x100 = 56% and % olivine = x/(x+y)x100 = 44%.

Dungan and Rhodes (1978) suggest that clinopyroxene is prevented from reaching the cotectic by repeated cycles of magma chamber replenishment and crystallisation in an open system chamber. However, it should be noted that the experimental work of Tormey et al. (1987) on Kane-area basalts indicates that crystallisation of olivine, plagioclase and clinopyroxene may have taken place at elevated pressures, while olivine and plagioclase dominate low-pressure crystallisation. In our dredged samples, the effects of any high pressure fractionation must have been almost completely masked by the shallow processes, as the glass data form a good trend along the 1 atmosphere cotectic.

Melt inclusions

The melt inclusions in the calcic plagioclase megacrysts have experienced post-entrapment loss of a plagioclase component (Paul Browning, pers. comm.), as the kinetics of the nucleation process favour precipitation onto the surrounding megacrysts. This is illustrated if the glass-inclusion data are added to the plot of TiO_2 against Al_2O_3 (figure 6.8). The glass-inclusion data plot directly away from plagioclase, as plagioclase precipitation from the inclusions has depleted the inclusions in plagioclase components such as Al_2O_3, and enriched them in incompatible components such as TiO_2. When the compositions are extrapolated along plagioclase control lines to intersect the glass trend, they give a composition more primitive than any of the erupted glasses. We can thus infer that the plagioclase megacrysts formed early in the fractionation history of the magmas.

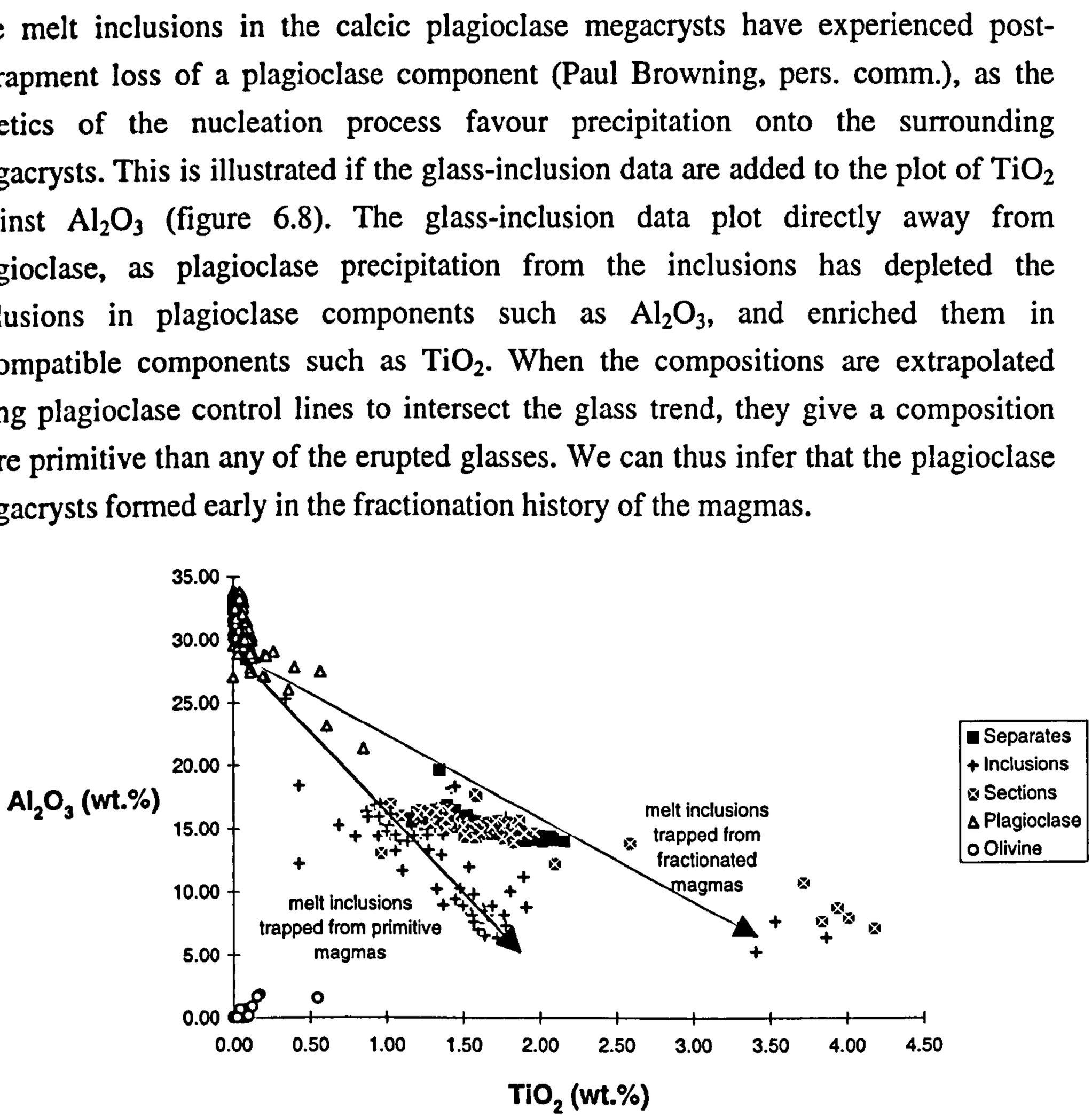

Figure 6.8 Variation diagram showing strong trend in glass inclusion data away from plagioclase, caused by post-entrapment precipitation on to the megacryst host. Most of the inclusions were trapped from primitive magmas, early in the fractionation history of the samples. A small number were trapped from fractionated liquids.

In terms of MgO, the melt inclusions overlap the compositional range of the separated glasses, but also extend to compositions approaching 18 wt. % MgO. When this figure is corrected for the post-entrapment fractionation of plagioclase, the MgO content of the glass inclusions prior to entrapment is about 11.5 wt. % (Paul Browning, pers. comm.), which is close to many estimates of primary MORB magmas.

6.6.1.2 Correlation of fractionation with ridge segmentation

Figure 6.9 shows a striking relationship between the MgO content of the dredged glasses and their position with respect to the second order segmentation. This corresponds to a variation in fractionation (primitive lavas at the segment centre and fractionated lavas at the ends), which has already been anticipated from the mineral chemistry. MgO values reach a maximum value of about 8.5 wt.% just to the south of the narrowgate saddle point, at Thatcher's Nose (13D) and the hummocky terrain immediately to the east of it (14D). There is a steady decline in MgO to values of around 6 wt. % at the transform intersection and 6.5 wt. % at the NTO. The steeper drop in MgO towards the transform compared with the NTO, may be a manifestation of the TFE.

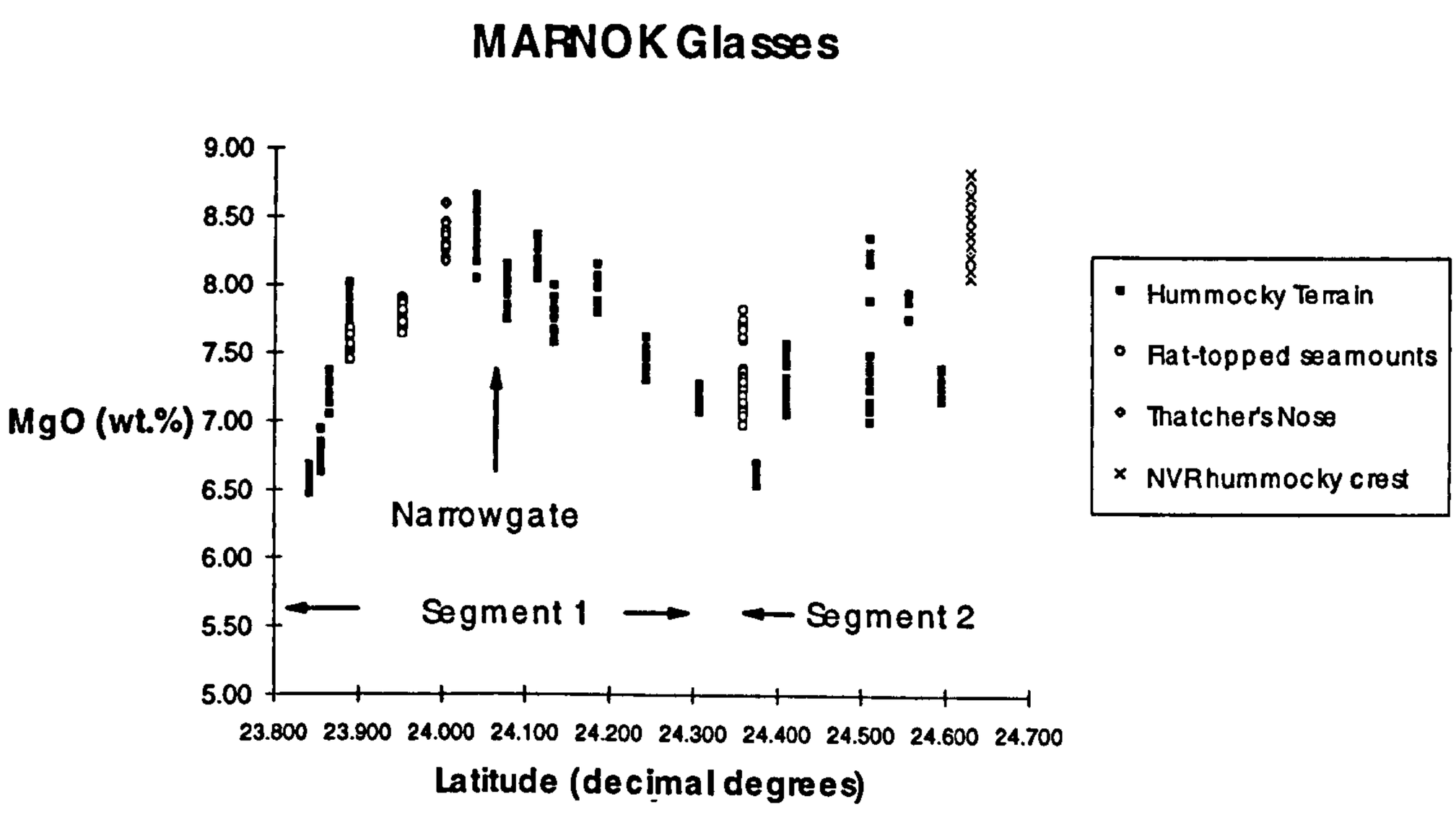

Figure 6.9 MgO of probed glasses plotted against latitude showing the least fractionated glasses occur in the segment centres.

Complete site coverage for the second segment was not achieved but a trend of increasing MgO content towards the centre of this segment is still apparent. However, it should be noted that there is certainly considerably more scatter in the along-axis trend than over segment 1. The highest MgO lava was dredged from the bathymetric

summit of the NVR in segment 2, which is actually located towards the northern end of the segment. Hence the MgO correlates with axial height along a segment.

6.6.2 Mantle source variations

Long-lived mantle source variations are best investigated using radiogenic isotopes. A representative suite of whole-rock basalts, glasses and separated plagioclase phenocrysts were analysed for Sr, Nd and Pb isotope ratios by Pamela Kempton at NIGL, Keyworth. The description of the isotope systematics given below is a summary of her results and interpretations and is included here because of its considerable relevance to the interpretation of the rest of the MARNOK data set. In addition the section on isotopic disequilibrium and the origin of the plagioclase megacrysts is largely taken from the cruise report (Pearce et al., 1993) and is the result of the combined studies of the CD57 petrologists including myself. The analytical procedures, reference standards and isotopic corrections are detailed in appendix 3. All the samples were leached for 30 minutes in 6M HCl to minimise the effects of seawater alteration. In addition to the leached samples, some unleached basalts and leachates were also analysed to help assess the affect of alteration.

6.6.2.1 Effect of alteration

Despite their fresh appearance, most samples show some effects of seawater alteration. Sr isotope ratios are reduced, with leached residues having lower values than both unleached whole-rocks and leachates. The older samples dredged from the median valley wall (22D) have the highest $^{87}Sr/^{86}Sr$ ratios of the MARNOK leached samples, suggesting that, even when leached, they retain a small signature of interaction with seawater not seen in the other samples. Alternatively they may have had a slightly more radiogenic source. Since the Nd and Pb isotope compositions of both leached and unleached samples are similar to those of other basalts from the area, I prefer the former interpretation. As expected, leaching has not affected Nd isotope ratios, but Pb isotopes do show a variable effect resulting from seawater alteration. $^{206}/_{204}$ Pb is reduced, typically by about 0.5, in the leachates compared with the whole-rock although there are a number of occasions where it is also significantly increased. $^{207}/_{204}$ Pb tends to increase by about 0.1, while $^{208}/_{204}$ Pb both increases and decreases on a roughly equal basis.

6.6.2.2 Isotope systematics with segmentation

Sr, Nd and Pb isotope plots for leached residues are shown as a function of latitude in figure 6.10. MARNOK basalts show a relatively restricted range in isotopic values ($^{143}Nd/^{144}Nd$ = 0.513118 - 0.513182, $^{87}Sr/^{86}Sr$ = 0.70242 - 0.70255, $^{206}Pb/^{204}Pb$ = 18.227 - 18.518) and lie within the fields of other North Atlantic MORB. The

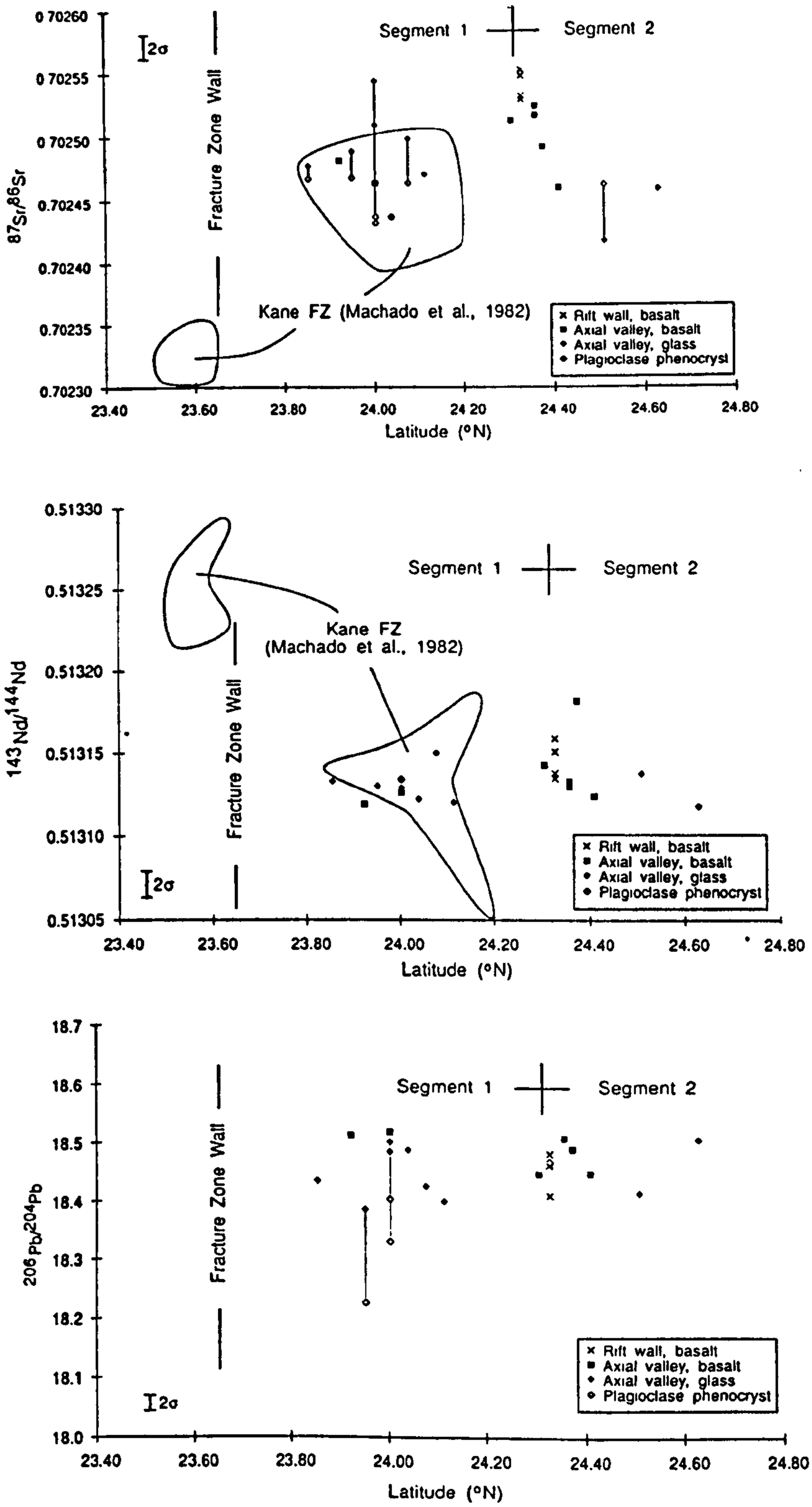

Figure 6.10 Isotope variations with latitude for (a) 87Sr/86Sr, (b) 143Nd/144Nd, (c) 206Pb/204Pb. The isotopic variation within the MARNOK area is not that much greater than the analytical error. There is no systematic variation within or between segments, but the data do confirm the isotopic anomaly across the fracture zone, as reported by Machado et al. (1982).

MARNOK data from the CD57 cruise fall in the range of Sr and Nd data published by Machado et al. (1982) from the MARNOK area, but are distinct from basalts dredged from the eastern end of the fracture zone (figure 6.10) which have higher Nd and lower Sr isotope ratios.

Although the total range of values is not large, there is a small isotopic variation outside the range of reproducibility for Sr, Pb and (possibly) Nd. The range of ratios is no greater between segments than within a segment, suggesting that the magmas from the two segments are derived from mantle of comparable isotopic range, but that the source area is slightly heterogeneous on the scale of tens of kilometres. The isotopic variations of the leached basalts and glasses do not seem to correlate with any other geochemical aspect of the data, such as the variable enrichments in highly incompatible elements. Thus the long term mantle source for the MARNOK area can be assumed to be relatively homogeneous.

6.6.2.3 Isotopic disequilibrium and the origin of the plagioclase megacrysts.

There is isotopic disequilibrium between glass and associated plagioclase phenocrysts in several samples, but particularly in the plagioclase-rich material recovered from Thatcher's nose (13D-1-1). In all but one case (31D-1-1), plagioclase has lower $^{87}Sr/^{86}Sr$ and $^{206}Pb/^{204}Pb$ ratios than the associated glass.

As mentioned in section 6.5.4, the megacrysts are also in disequilibrium with their basalt host in terms of their anorthite content (An_{92}). In addition, they trap melt inclusions which have been determined as containing MgO=11.5 wt. % (P. Browning, pers. comm.). Studies of similar megacrysts from other Atlantic MORB (e.g. Donaldson & Brown, 1977; Dungan & Rhodes, 1978; Kuo & Kirkpatrick, 1982) have raised questions as to why the megacryst cores are so calcic and why the trapped melt is so magnesian yet trapped by plagioclase rather than olivine. Our findings raise the additional question of why the megacrysts and their host glass are not in isotopic equilibrium.

The calcic nature of the plagioclase is significant because this composition is too refractory to have crystallised from the magma parental to the MARNOK basalts. Compositions of An_{92} can only have been in equilibrium with magmas that have much higher Ca/Na ratios than MORB or had H_2O contents in excess of 5 wt.% to cause sufficient depression and steepening of the liquidus. The former explanation requires crystallisation from magma derived from depleted (high Ca/Na ratio) mantle; the latter requires addition of water well beyond that normally found in MORB mantle or magma. The water contents of MARNOK glasses are normal for MORB and the low Pb and Sr isotopic ratios in the megacrysts suggest that seawater addition has been negligible. I therefore favour crystallisation of melts derived from depleted mantle as

the cause of the calcic nature of the megacrysts. This conclusion corresponds to that reached by Donaldson and Brown (1977), Dungan and Rhodes (1978) and others, where it is further supported by analysis of inclusions in olivine. It provides further evidence for the presence of refractory melts at mid-ocean ridges and hence for multistage (or dynamic) melting models (e.g. Duncan & Green, 1980; Elliot et al., 1991).

Given this interpretation, the low Pb and Sr isotope ratios in the megacrysts still require explanation. There are two principal possibilities: the mantle melt may have less radiogenic Sr and Pb isotope ratios as well as high Ca/Na ratios; or the higher Sr and Pb isotope ratios in the glasses may reflect assimilation of hydrothermally-altered rocks from the walls of the magma chamber, the megacrysts having grown in deeper levels unaffected by assimilation. Future stable isotope analyses may resolve this issue.

Although there is little dispute that the megacrysts and their inclusions provide evidence for magma mixing, the site of growth of the megacryst cores and incorporation of the melt inclusions has already prompted some debate (e.g. Stakes et al., 1984). I support models in which melts with high Ca/Na ratios separate at high levels in the melting column and crystallise calcic plagioclase (together with olivine and spinel) in magma reservoirs beneath or at the base of the main region of magma accumulation. In the composite magma chamber model of Sinton and Detrick (1992), initial growth of the megacrysts may take place in the lower mush zone or the transition zone through which primitive melts percolate.

After a period of growth sufficiently long to allow the formation of the plagioclase megacryst cores, the crystals may eventually be carried up, perhaps with an influx of primitive magma, into the upper crust where they become mixed with more fractionated melt compositions in the main magma reservoir. During this mixing process, the megacrysts became partially resorbed and trap samples of the ambient liquid compositions, available in the chamber, as inclusions. Because of their low density, the plagioclase crystals will tend to separate from denser fractionation products and rise to the top of the chamber, to be erupted as the crystal-rich pillow lavas.

Highly phyric lavas, such as those which characterise the prominent seamounts of Thatcher's Nose, were probably formed by the mobilisation of megacrysts from the mush zone by new injections of primitive magma rising from the mantle. Indeed, without a primitive matrix to lower the overall viscosity, the high crystallinity of the sample would have probably rendered it too viscous to erupt, as tholeiitic magmas are

thought to be essentially uneruptable when their crystallinities exceed 25% (Marsh, 1989).

6.6.3 Melting variations

Fractionation-corrected Na_2O ("Na_8") which is commonly used as a measure of bulk mantle melting (Klein & Langmuir, 1987; Plank & Langmuir, 1992; Niu & Batiza, 1991), has a relatively uniform value of about 2.8 across the entire MARNOK area (figure 6.11). There may well be small average variations between the samples but these are within analytical error. The spread in values at one locality is greater than the maximum difference between averages of different localities. Hence there is no observed systematic variation in the degree of melting along a segment. This is an important result as it favours melt migration models over mantle flow models as a cause of the crustal thickness variations along-axis.

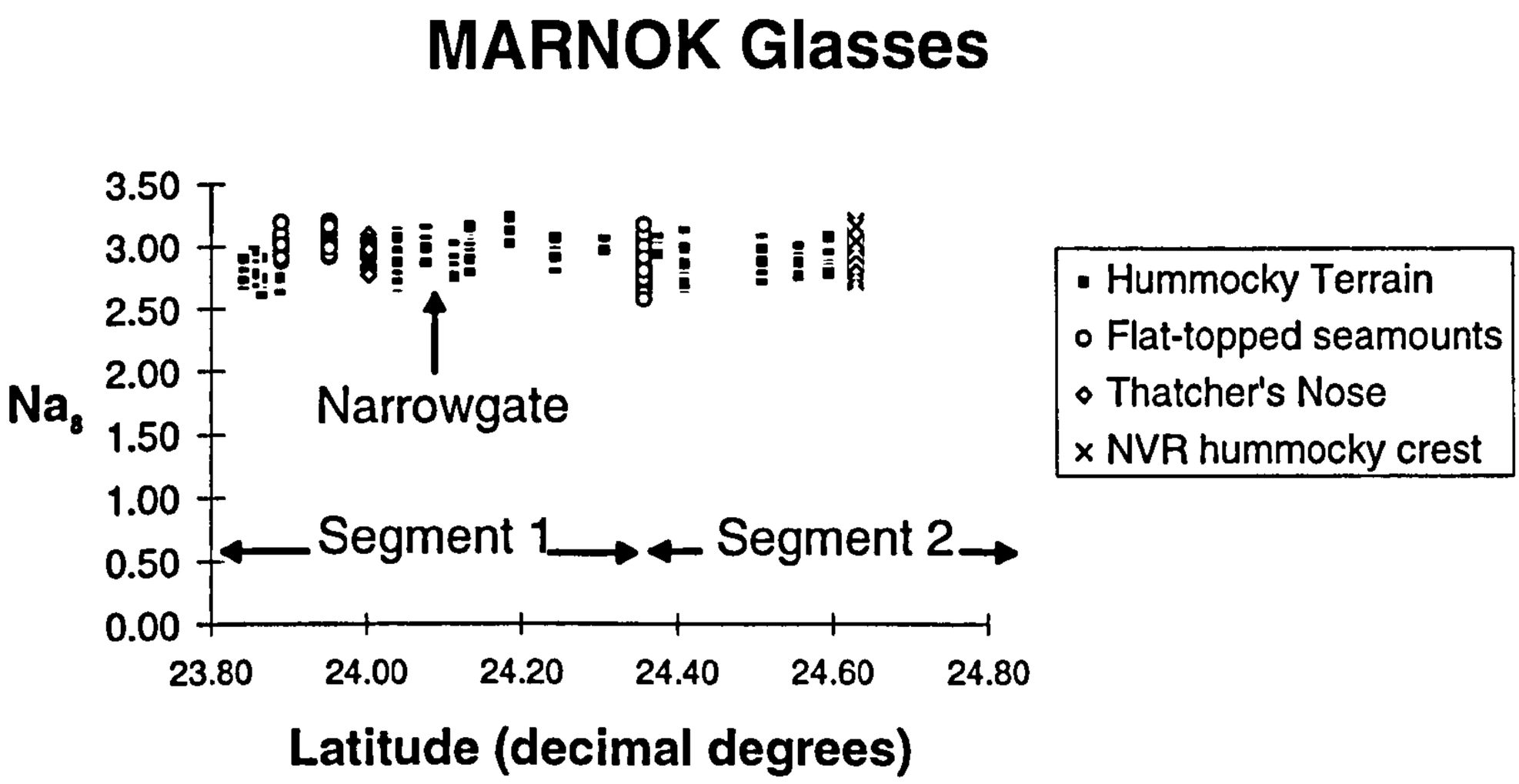

Figure 6.11 Na_8, (calculated using the equation of Plank & Langmuir (1992)), shows little variation when plotted against latitude. This implies that the bulk degree of melting along the length of the segments is relatively uniform.

Figure 6.12 shows Ce_8 against Na_8 for the MARNOK data. The rationale behind the interpretation of this plot is based on work by Plank and Langmuir (1992), as was described in section 2.9.6.3. As there are no ion probe data for the MARNOK glasses, it was necessary to use the whole-rock ICP-MS data to obtain the values for Ce_8. Most of the samples shown in the plot have both probe and ICP data obtained from the same rock chip. However, for a small number, probe data were not available for the particular sample analysed for ICP-MS. In these cases, the probe analysis for a rock

from the same unit, with similar petrographic features and whole-rock chemistry, was used instead. The selection of an appropriate probe analysis can produce a small variation in the location of the sample in the graph. This is illustrated by the difference between the two points plotted for the nested seamount. Although Ce_8 is fractionation corrected, the use of whole-rock data rather than probe data will mean there is a degree of scatter within the calculated Ce_8 values which is introduced by effects of crystal accumulation. This will result in anomalously low values for Thatcher's Nose (13D), 23D, and 31D, which have large degrees of crystal accumulation. This is evident from the location of these two samples in figure 6.12, which both have lower Ce_8 values than the rest of the MARNOK data.

An estimate of 13% batch melting is obtained by comparing the MARNOK data with that of the melting baseline. The scatter of data above the melting baseline indicates that small amounts of mixing with a small melt-fraction component can explain the variations in the highly incompatible element data.

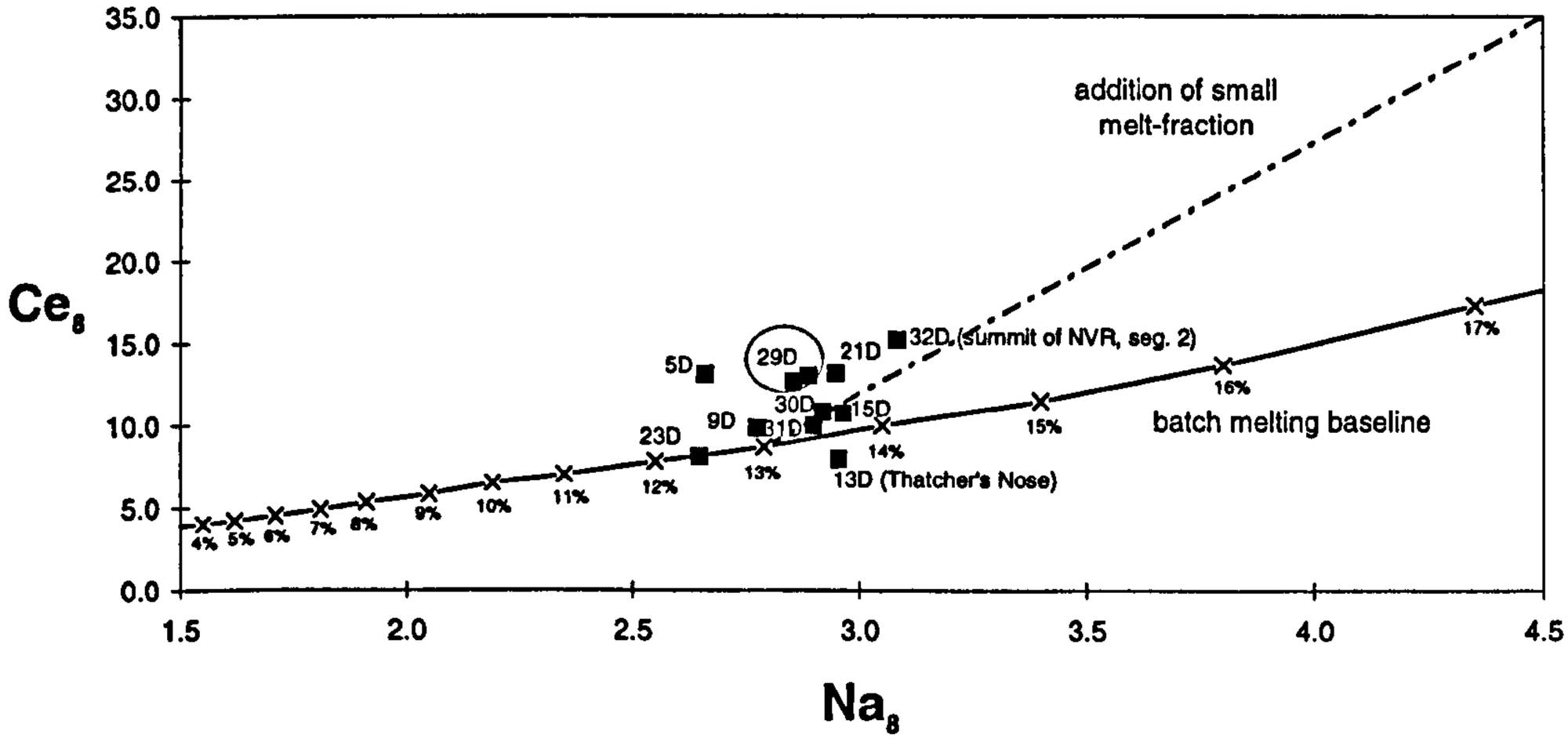

Figure 6.12 Ce_8 against Na_8 plot, such as used by Plank & Langmuir (1992) to quantify mantle melting. The MARNOK Na_8 data are calculated from the probe glasses, while Ce_8 uses the appropriate MgO data from the probe to fractionation correct the whole-rock analysis for Ce. This does not correct for the effects of plagioclase accumulation, so samples with significant phenocryst/megacryst contents will have anomalously low Ce_8 values.

Trace element ratios, such as Nb/Zr, should show virtually no variation with fractional crystallisation (section 2.9.2.2). The ratio is also not affected by plagioclase accumulation (section 2.9.5.2). There is quite a substantial difference in the degree of incompatibility between Nb and Zr. Hence the Nb/Zr ratio should be particularly useful in distinguishing the addition of small melt-fractions. In addition, both of these elements are immobile and so will not be affected by alteration. Figure 6.13 shows the whole-rock variation in NbZr, which is effectively a measure of the addition of small-

degree melts, against Zr, which primarily varies with fractionation. The MARNOK data are subdivided into categories corresponding to the position within the segment. The samples showing the greatest effects of small melt component addition all occur either at the NTO or in the TD. Thatcher's Nose (labelled TN) and the nested seamounts (NS) stand out from the rest of the data, being particularly affected by the small melt-fractions. The samples from the TD are not all enriched by these small melt-fractions as the Nb/Zr values for some are comparable with the values from the north of segment 1. The emphasis is on the variability in the TD rather than a systematic enrichment.

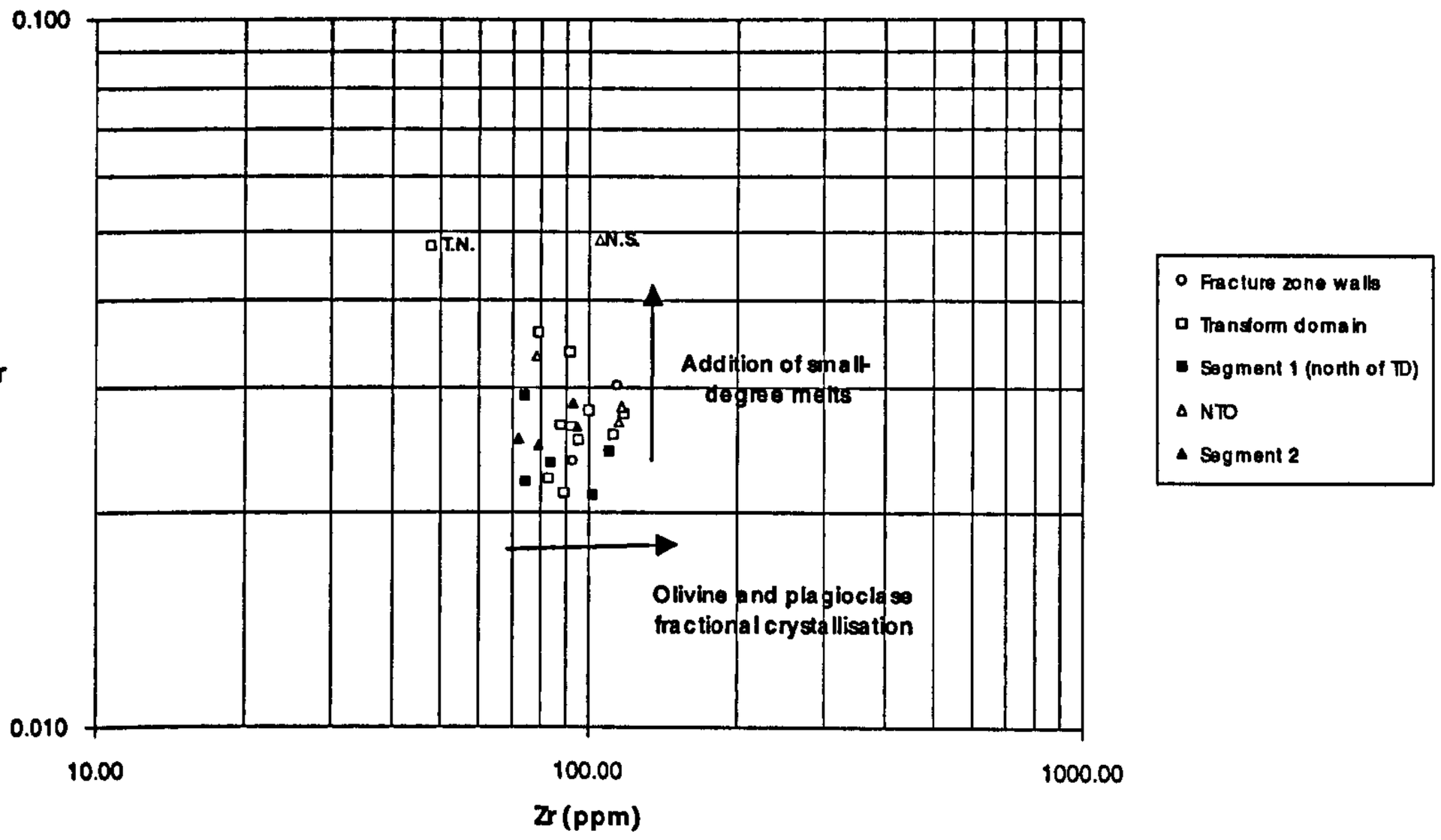

Figure 6.13 Graph of Nb/Zr against Zr, used to show the variable addition of small melt-fractions within the MARNOK basalts. Thatcher's Nose (labelled TN) and the nested seamounts (NS) have particularly strong enrichment from small melt-fractions.

6.6.4 Petrological segmentation

In Chapter 5, I showed that the petrological segmentation in the transform domain is about 3-6km. I will now compare this estimate with variations in parental magmas seen across the rest of the MARNOK area.

Figure 6.14 shows the extended element spidergram for samples from segment 2. The patterns for 23D-2-2b and 24D-1-1b are virtually identical and the handspecimen and petrographic age estimates suggest both are relatively young, but 23D-2-2b is the younger of the two (~100 year, compared with several hundred years old). Samples 31D-1-2b and 32D-1-2c also have similar extended element patterns. 31D-1-2b is of comparable age to 24D-1-1b, but 32D-1-2b is older (age is difficult to estimate because of hydrothermal coating) There is significant divergence between these two

pairs of patterns implying that there are two parental magmas sampled. However, the sample pairs with similar parents are not located adjacent to each other along the ridge crest. 32D is furthest north, with 24D, 31D, and 23D at increasing distances to the south. If the ages and petrology of the samples were identical then these relationships could be explained by the composition of the magma chamber changing over time. Although 23D-2-2b and 24D-1-1b are reasonably similar in many respects, they are unlikely to be from the same magma chamber, as 31D-1-2b (which has a different parental magma) is located directly between the two and is of comparable age.

Hence I conclude that although there are two distinct parental magmas sampled from segment 2, this does not necessarily mean there are two petrological segments, as the sample locations, petrological character and age data point against this. Instead, the similar parental magmas at different parts of the ridge crest may imply a uniformity at a deeper scale. Uniform melt batches may feed relatively large lengths of ridge crest, which then evolve as separate systems within the crust. Some of these separate systems may become modified by later melt batches while others have not. Therefore if the petrological segmentation is a measure of the connectivity of the crustal plumbing system along-axis, I tentatively suggest that it may be less than the dredge spacing in segment 2 (i.e. <6-11km). However, more detailed sampling is required to provide a better constraint for this result.

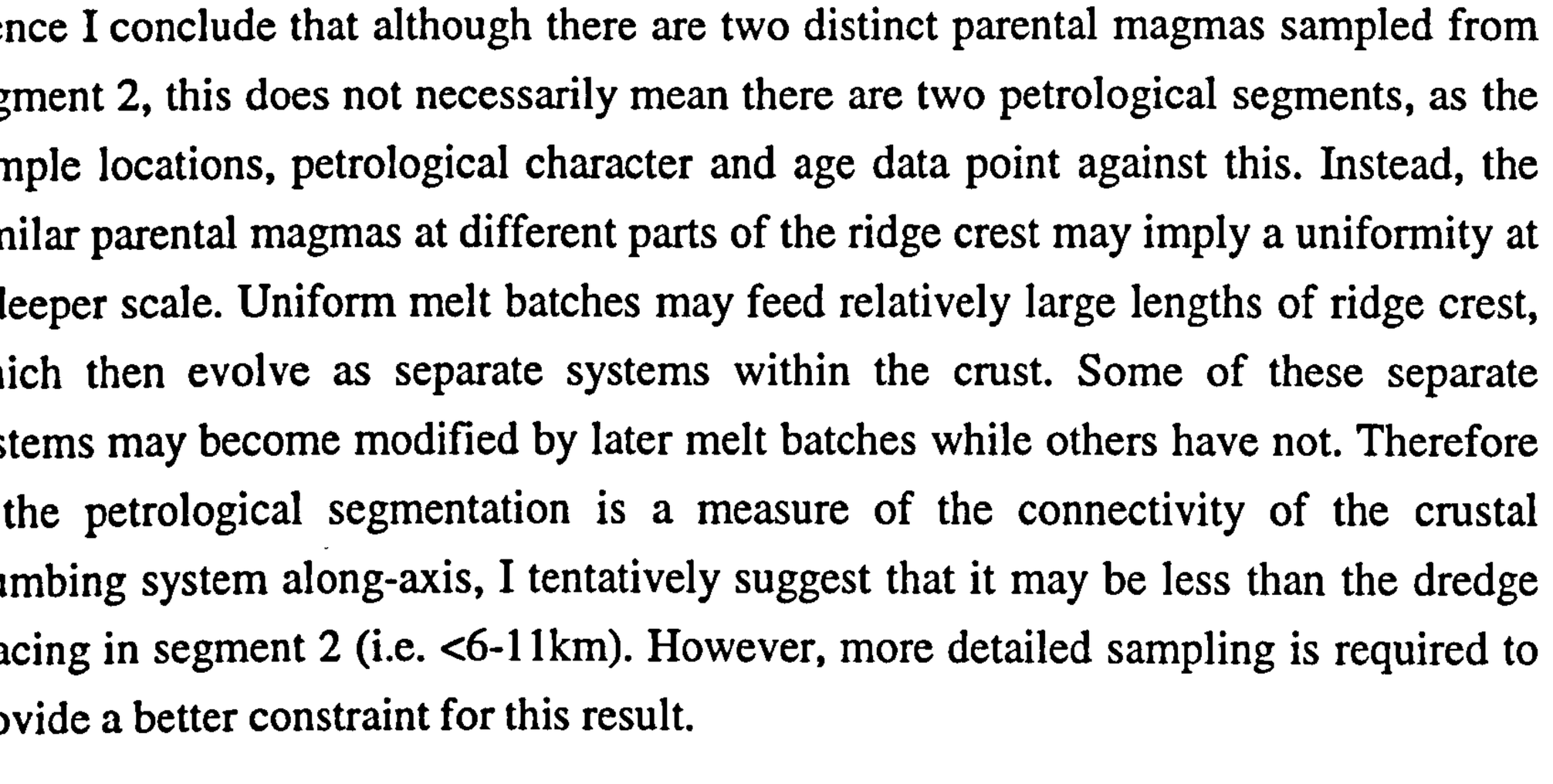

Figure 6.14 MORB-normalised extended element plot of samples from segment 2. There seem to be two parental magmas, which are relatively similar.

Figure 6.15 shows spidergrams for samples from the NTO area. The enriched trace element pattern for the nested seamounts (29D) is immediately obvious. The significance of it crossing the other samples from the area has already been discussed

in section 4.8.1. 21D-1-1b and 30D-1-2c are both from the northern tip of the hummocky NVR and they show very similar profiles suggesting that they are probably parts of the same petrological segment. Sample 22D-2-2c is from the valley walls, and hence there is a considerable age gap between this and the NVZ samples. Given this, its trace element pattern is remarkably subparallel to that of the samples from the hummocky ridge crest, although there is a slight enrichment of highly incompatible elements. The data from the NTO confirm the result from the TD that contrasting parental magmas and contrasting volcanic morphologies are related. In fact, the more unusual the volcanic morphology, the more likely it is to have a highly distinctive trace element pattern.

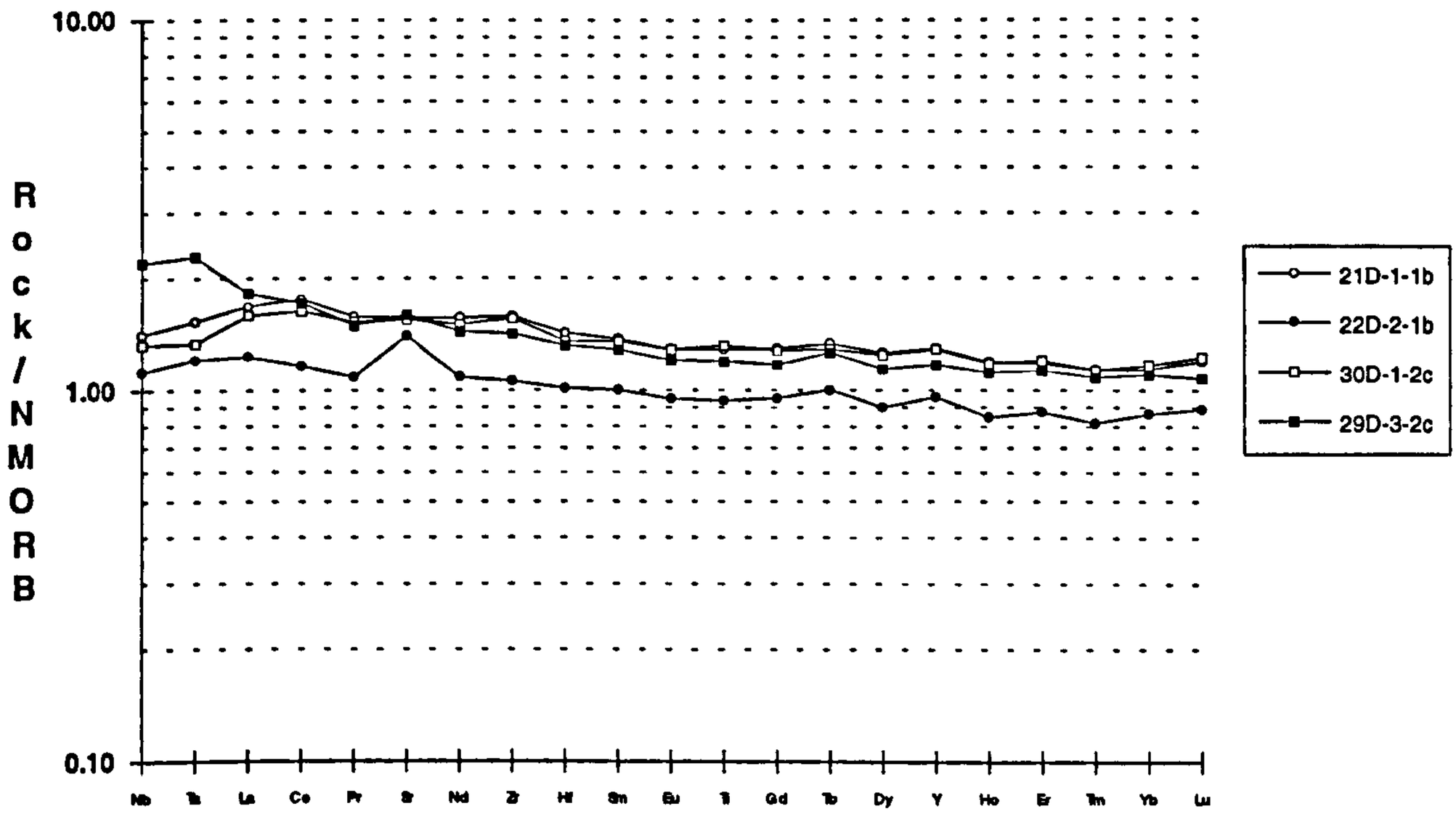

Figure 6.15 MORB-normalised extended element plot of samples from the NTO. 21D-1-1b and 30D-1-2c are both from the northern tip of the hummocky NVR of segment 1. 22D-2-2c is from the valley walls. The nested seamount (29D-3-2c) is has a strongly contrasting parental magma to the other samples from this area.

Figure 6.16 shows the extended element spidergrams for samples from the uniform hummocky ridge along the northern half of segment 1. These show a wide spread in absolute values of the trace elements, reflecting the large range in fractionation discussed in section 6.6.1. Despite this wide spread in fractionation, the shapes of the patterns are remarkably coherent. Between La and Lu the only variable enrichment occurs at Sr, which reflects variable plagioclase accumulation. Between La and Nb, three of the samples, 15D-1-2b, 16D-1-1b and 20D-1-1b remain subparallel, while 17D-1-2a and 19D-1-2a show respectively a slight enrichment and a slight depletion in Nb and Ta.

The length scale of petrological segmentation, estimated from the spacing of dredge samples with similar parents, ranges from 6-11km. This is greater than the length scale of petrological segmentation in the TD. The chemical contrasts between adjacent parental magmas in segment 1 is also relatively small compared with some of the contrasts in the TD and the NTO. Again this difference is also reflected in the morphological diversity of the regions, the RTI and NTO areas having a number of discrete edifices, while the NVR north of the narrowgate is very uniform.

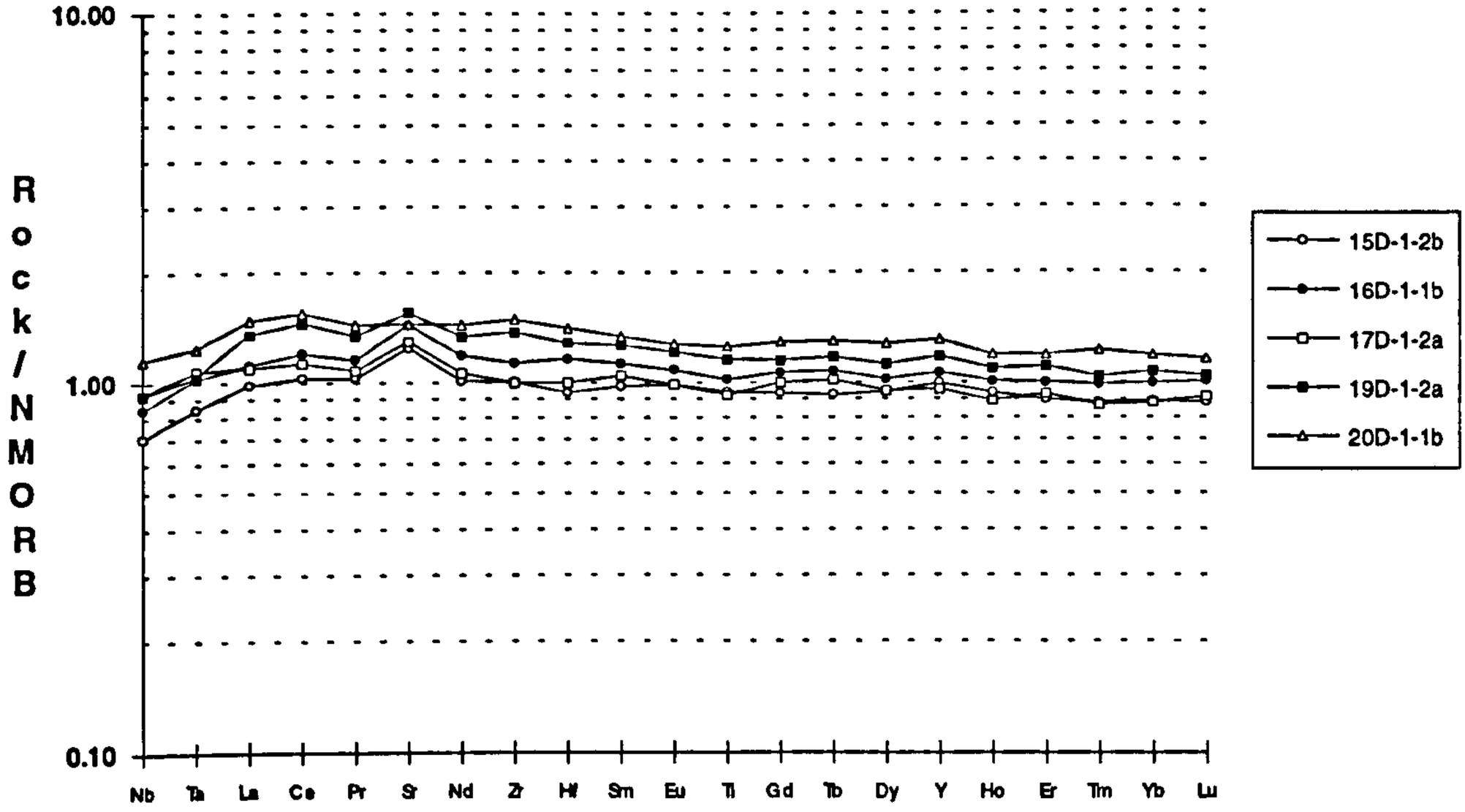

Figure 6.16 MORB-normalised extended element plot of samples from the uniform hummocky NVR across the northern half of segment 1. These samples are generally very uniform, but there is a slight divergence for 17D-1-2a and 19D-1-2a for the most incompatible elements at the left hand side of the plot.

6.7 Deep-tow magnetics.

Figure 6.17 shows the position of the four deep-tow magnetic profiles which have been studied by Hussenoeder et al. (*in prep.*). The northernmost profile crosses segment 2, the second is at the junction of the two segments, the third crosses the NVR 7km south of the narrowgate, and the southernmost one traverses the nodal deep and then extends onto the inside corner high. The results of magnetic inversion solutions of the four deep-tow profiles compared with the sea surface solutions are reproduced in figure 6.18 from Hussenoeder et al. (*in prep.*).

6.7.1 The northern traverse: across segment 2

The correlation of the central axial magnetic high (CAMH) with the position of the most recent volcanism, identified by the deep-tow camera traverses, is extremely

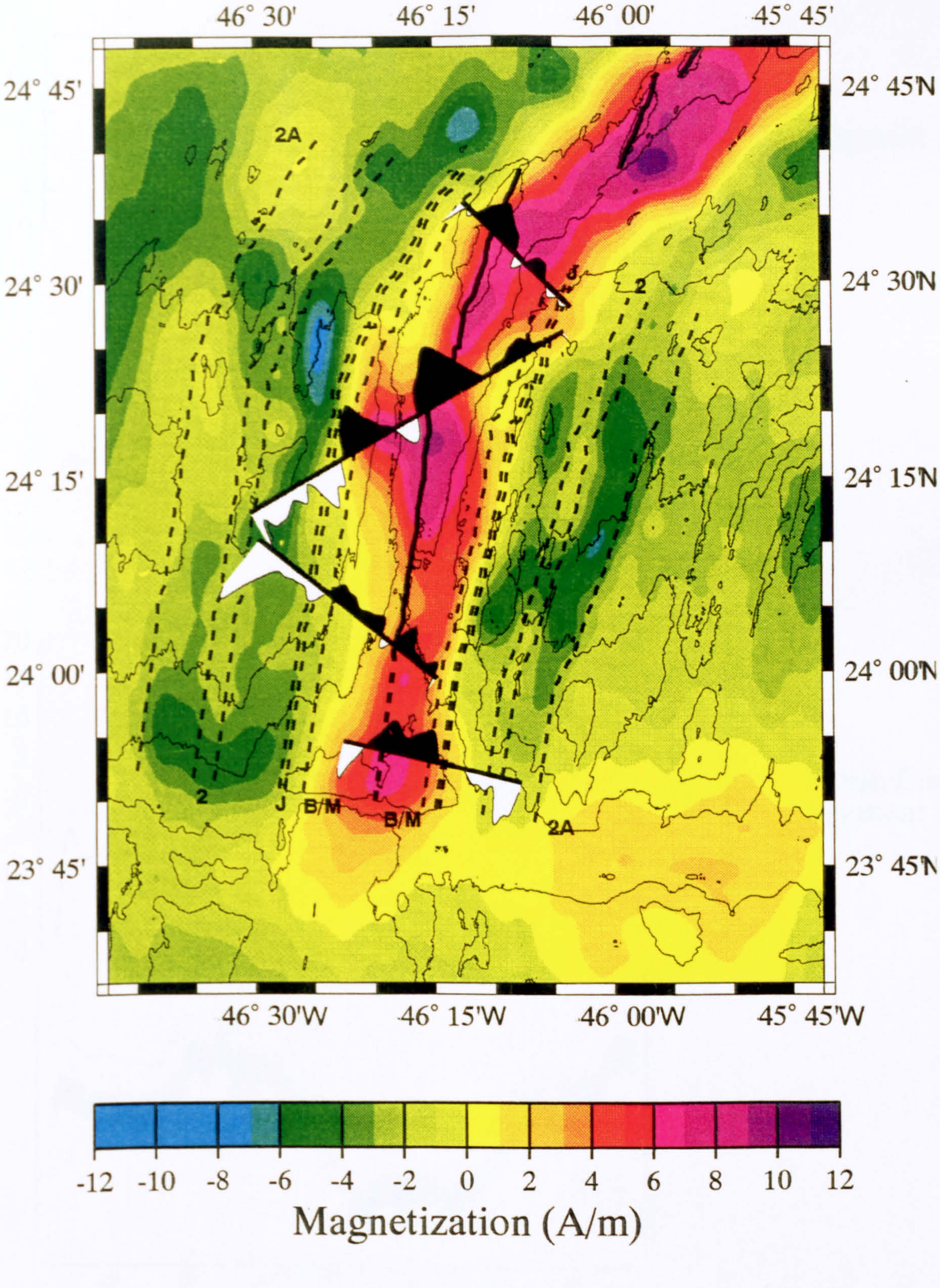

Figure 6.17 Magnetisation over the MARNOK area with the four deep-tow profiles superimposed. The northern profile crosses segment 2; the second is at the junction of the two segments and the third crosses the NVR 7km south of the narrowgate. The southernmost profile crosses the nodal deep and extends onto the inside corner high. Anomaly picks are marked with dashed lines (B/M is Bruhnes/Matuyama reversal at 0.72Ma, J is Jaramillo event at 0.90Ma; anomaly numbers 2 and 2A are also marked and correspond to periods of normal polarity at 1.66-1.87Ma and 2.47-3.40Ma respectively). They show how the half spreading rate to the east increases from 8mmyr^{-1} near the transform to 13mmyr^{-1} at segment 2. To the west, the half spreading rate is uniform along the length of the axis at 13mmyr^{-1}. Figure is taken from Hussenoeder et al. *(in prep.)*.

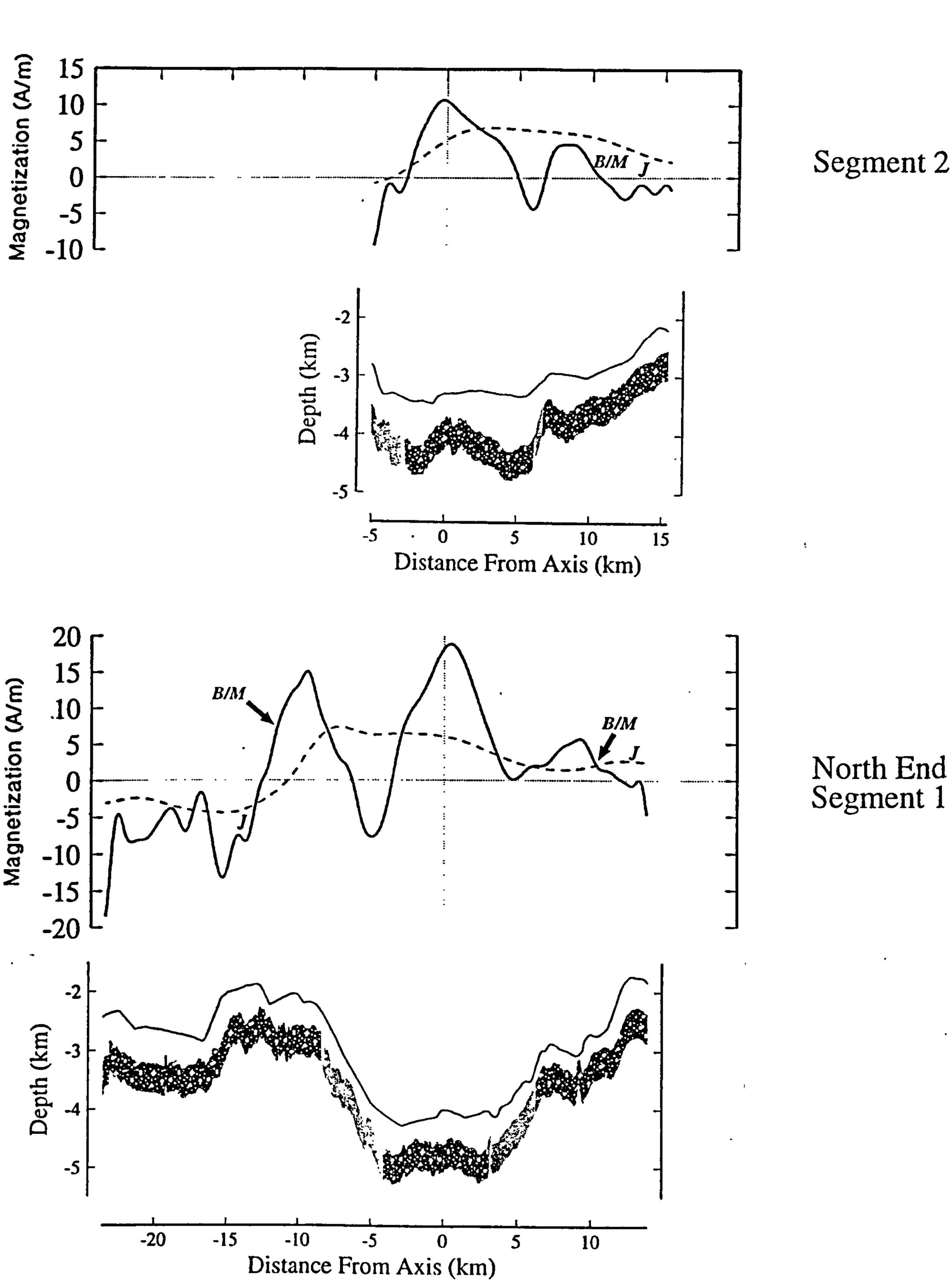

Figure 6.18 Magnetic inversion solutions from four TOBI deep-tow passes over the axis, adapted from Hussenoeder et al. *(in prep.)*. The magnetization from the sea surface survey is shown by the dashed line, and the Bruhnes/ Matuyama boundary and the Jaramillo event are marked B/M and J respectively. The bathymetry is shown below, with the areas of source destruction marked by the paler shading. Profiles are across (a) segment 2 and (b) the third order non-transform offset as shown in figure 6.17.

(c)

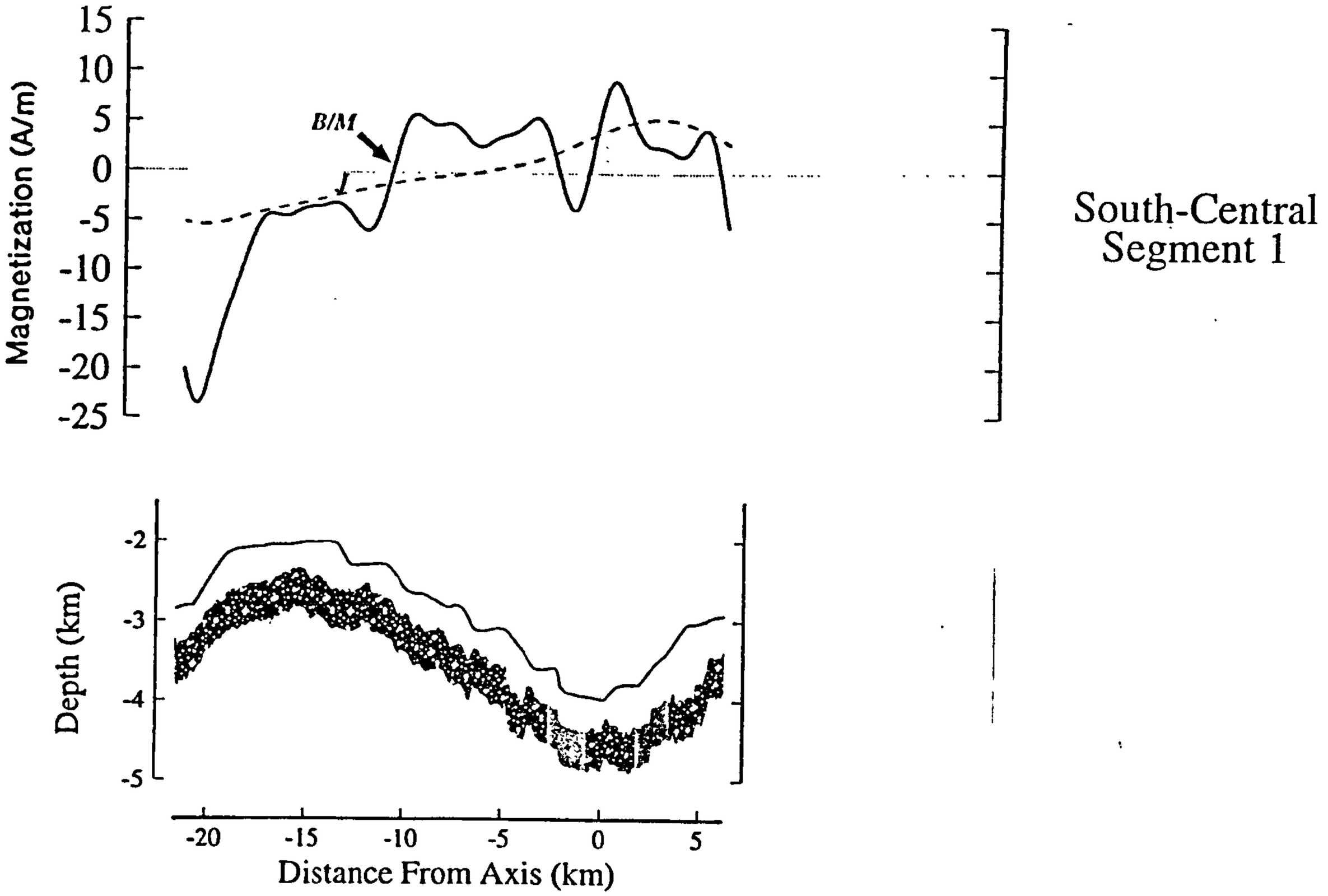

(d)

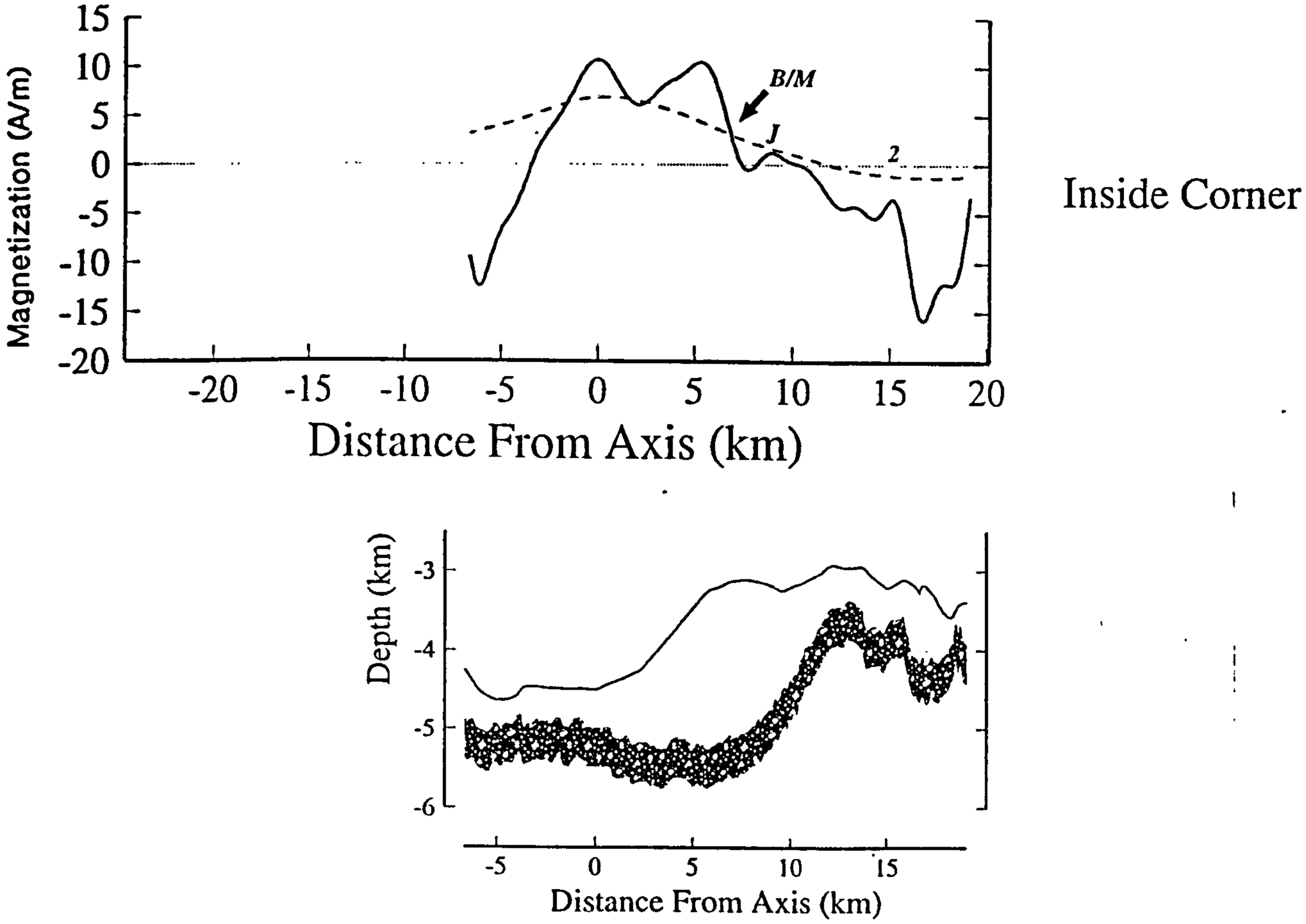

Figure 6.18 (continued) Magnetic inversion solutions from four TOBI deep-tow passes over the axis, adapted from Hussenoeder et al. *(in prep.)*. Profiles are across (c) the narrowgate of segment 1 and (d) the RTI and the inside corner high, as shown in figure 6.17.

good. Over the northern transect the magnetization peaks at 10 A/m just to the west of the main peak of the NVR (figure 6.18a) exactly where the WASP profiles verified that the most recent flows occurred (compare with figure 4.1b where flow 8 has youngest relative age of 1.24).

Hussenoeder et al. (*in prep.*) produced a remarkable fit to the high resolution inversion using a forward model that assumed a magnetization decay with an exponential time constant of 0.3Ma and introducing zones of magnetization destruction where the valley walls are the steepest.

The magnetization peak over the axis is broad, corresponding to the hummocky texture of the sidescan which has a width of about 5km across the well developed NVR. The peak is not symmetrical about the central anomaly as values on the west are elevated with respect to those in the east. The magnetization also drops off more dramatically to the west to reach zero over the valley wall scarps. This is successfully modelled by Hussenoeder et al. (*in prep.*) by introducing slightly asymmetric zones of magnetization destruction over the valley walls. The WASP traverse clearly showed that the flows on the eastern flank are older and more tectonised, which is consistent with the slightly lower levels of magnetization in Hussenoeder et al.'s solutions (*in prep.*).

To the east of the eastern inner valley wall scarp the magnetization increases again to peak at about 5A/m. On the sidescan images, the terrace on the back of the wall scarp has a very poorly backscattering but hummocky texture. The preservation of magnetization of this terrace implies that it has been lifted up into the valley walls as a reasonably coherent block, allowing the magnetic source layer to remain relatively undisturbed.

The exponential time constant fitted by Hussenoeder et al. (*in prep.*), in their forward model of the magnetization, is more rapid than the time constant of 0.6Ma inferred from the FAMOUS data (Macdonald, 1977). Even using the faster magnetic decay rate there is about an order of magnitude difference between the estimated age variations across the valley floor calculated from the magnetics and that estimated from the WASP phototraverse. This is probably explained by the surface veneer of recent volcanism, as explained in section 2.6.3.

6.7.2 Traverse across the junction of segments 1 and 2

The inversion solution across the junction of the two segments has a sharper and higher CAMH (figure 6.18b) indicating focused accretion within the 2-3 km wide hummocky area identified on the sidescan, and rapid destruction of the magnetised layer off-axis. Compared with the northern profile, the texture of the sidescan suggests

that the NVR which has produced these high values for magnetization is actually quite tectonised. The sidescan and the bathymetry show that the median valley comprises two tapering ridges one from each the two segments. The CAMH occurs just to the west of the crest of the eastern ridge, which is the higher of the two, but seems the more tectonically disrupted on the sidescan images. Although there was no WASP camera run over this area, the older tectonised character of the crust at this locality was confirmed by the submersible dive of Zonenshain et al. (1989) (figure 2.8), which occurs just to the north of the TOBI profile. The high value of the magnetization but the tectonised nature of the ridge, suggests that some factor other than age is dominating the magnetic variations within the rift valley.

In the forward model of Hussenoeder et al. (*in prep.*), large zones of source destruction are imposed, in keeping with the larger throws on the valley wall faults at the non-transform offset. The magnetization increases up the western wall and reaches a second peak, almost as strong as the CAMH, on the edge of the uplifted terrace. This implies that the western terrace has been uplifted as a coherent unit into the flanks with very little destruction of the magnetic source layer, except over the wall fault. However, Hussenoeder et al. (*in prep.*) suggest that the size of the peak implies that any negatively magnetised crust may have been obscured at this point, causing a jumbling of the Jaramillo event and the later Brunhes. A second major trough in the magnetization intensity occurs just to the west of the Jaramillo event, near the foot of the scarp which forms the edge of the large off-axis basin (section 6.4.3 and figure 3.10). The magnetization is relatively weak across the basin, implying a thinner source layer or reduced intensities as a result of crustal ageing or possibly some other effect.

Over the eastern wall fault the trough in the magnetization occurs about 500m up the valley wall, over the poorly backscattering disrupted area that may be the debris deposit from a landslide (see section 6.4.2.1 and figures 3.8 & 3.13). The absence of coherent magnetization in the landslide may add to the magnetic source destruction caused by the fault. Unlike the western terrace, a large secondary peak does not occur over the eastern terrace. The asymmetry in the magnetization of this profile may be related to the asymmetry of the median valley which is reported by Allerton et al. (1995). On the western side of the valley the crust is uplifted by cyclic faulting which results in the formation of discrete terraces, preserving relatively high magnetization beyond the inner valley walls. In contrast, on the eastern side the detachment faulting causes greater disruption of the magnetic source layer, resulting in lower average values of magnetization.

6.7.3 Traverse just south of the narrowgate

The southernmost oblique traverse of TOBI just south of the narrowgate also has a sharp magnetization spike (figure 6.18c), but the amplitude is lower than that seen over the non-transform offset. The freshest, highly glassy lavas obtained during the survey were dredged from this area, which again emphasises that the size of the CAMH does not seem to correlate with the age of the surface volcanism. The WASP traverse over the narrowgate showed a high contrast in the crustal character across the valley floor, with a narrow focused region of recent eruptions bounded by small horsts and grabens to the east and an older, highly sedimented terrace to the west. The forward modelling of Hussenoeder et al. (*in prep.*) found that the best-fit solution required a relatively narrow region of source destruction over the small-throw valley wall faults. Hussenoeder et al. (*in prep.*) also extended this zone of source destruction for some distance across the median valley floor, slightly further across the valley from the western edge than the eastern edge. This source destruction correlates with the highly sedimented terrace observed on WASP and implies that the faulting which led to the formation of this terrace also destroyed the magnetic source layer. Hussenoeder et al. (*in prep.*) point out that the proximity of the western zone of source destruction has shifted the CAMH slightly to the east, so it does not accurately mark the location of the most recent eruptions.

Similar age contrasts to those described here over the MARNOK narrowgate were observed in the FAMOUS narrowgate area. At FAMOUS, a very recent eruption with an unusually high directly measured magnetization (84 A/m) was recovered in the centre of the narrowgate, which otherwise had a relatively old value of $4x10^4$ years for the average crust (Van Wagoner & Johnson, 1983). It may be significant that both narrowgate areas have experienced very recent and focused accretion into relatively old surrounding crust.

6.7.4 The southern traverse across the RTI

In figure 6.18d the CAMH falls over the hummocky ridge of the NVZ as defined on the sidescan sonar, but a second peak which has approximately the same amplitude occurs half way down the western wall of the nodal basin, corresponding to the relict NVZ identified in the high resolution bathymetry by Zonenshain et al. (1989) and hummocky terrain on the transform-parallel swath (figure 3.18). The magnetization is low over the eastern wall of the nodal basin, implying once more that source destruction is initiated by faulting.

6.7.5 Sources of magnetic variations

On the whole, the correlation of the central axial magnetic high (CAMH) with the position of the most recent volcanism, identified by the deep-tow camera traverses, is extremely good. In addition, the forward models of Hussenoeder et al. (*in prep.*) produced good fits, assuming exponential decay of a magnetic source layer and its destruction in the valley wall faults. Hence crustal ageing and faulting account for most of the variation across-axis. Hussenoeder et al. (1995) suggest that the high magnetization outside the inner valley walls may indicate a cyclic faulting process whereby large unaltered blocks of crust are lifted out of the rift valley by adjacent zones of faulting. When the relatively high magnetization does not occur outside the valley walls it may indicate that more prolonged detachment faulting has been active.

In some cases (e.g. near the NTO) the CAMH does not fall over the area that seems least tectonised. In addition, the along-axis variation in apparent age of the surficial rocks (inferred from the sidescan) does not correlate with the magnetization highs, which are greater at the ends of the segment. Although it is accepted that the surficial volcanism does not necessarily represent the state of the magnetised layer as a whole, this complete lack of correlation implies that there is some factor other than the age of the most recent eruption that is controlling the along-axis variations in magnetization.

This 'other factor' is probably the trend in the degree of fractionation along-axis as described in section 6.6.1. Primitive lavas with relatively low Fe and Ti occur in the centre of the segment. There is a greater range in the degree of fractionation at the ends of the segment with some of the lavas having relatively high values of Fe and Ti (figure 6.19). This increase in the degree of fractionation at the segment ends was accompanied by the petrographic identification of Fe-Ti oxides in groundmass of samples.

Hence, it is suggested that the variation in degree of fractionation of the lavas and the corresponding increase in the concentration of magnetic minerals towards the end of segment are the main factors controlling the magnetization trends along-axis. In the south Atlantic, similar magnetization highs, which are suggested to be the result of geochemical variations, are located at the intersection of the MAR with both large and small offsets (Carbotte et al., 1991; Grindlay et al., 1992). My results confirm the predictions of these south Atlantic studies.

However, it must be noted that the magnetization at the 3rd order non-transform offset is higher than that near the transform, whereas the degree of fractionation is comparable. This may be the result of a thinner crust or enhanced hydrothermal circulation near the fracture zone.

a)

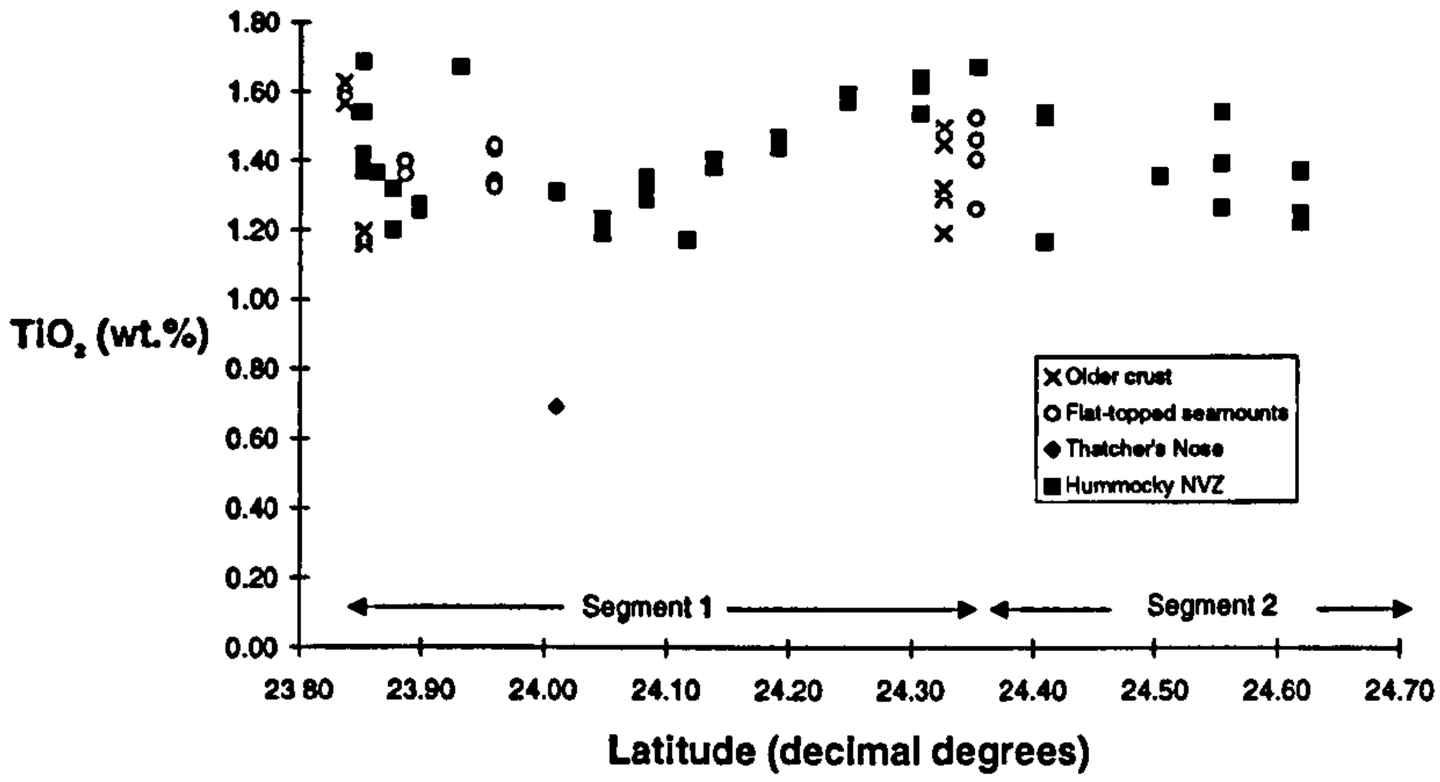

b)

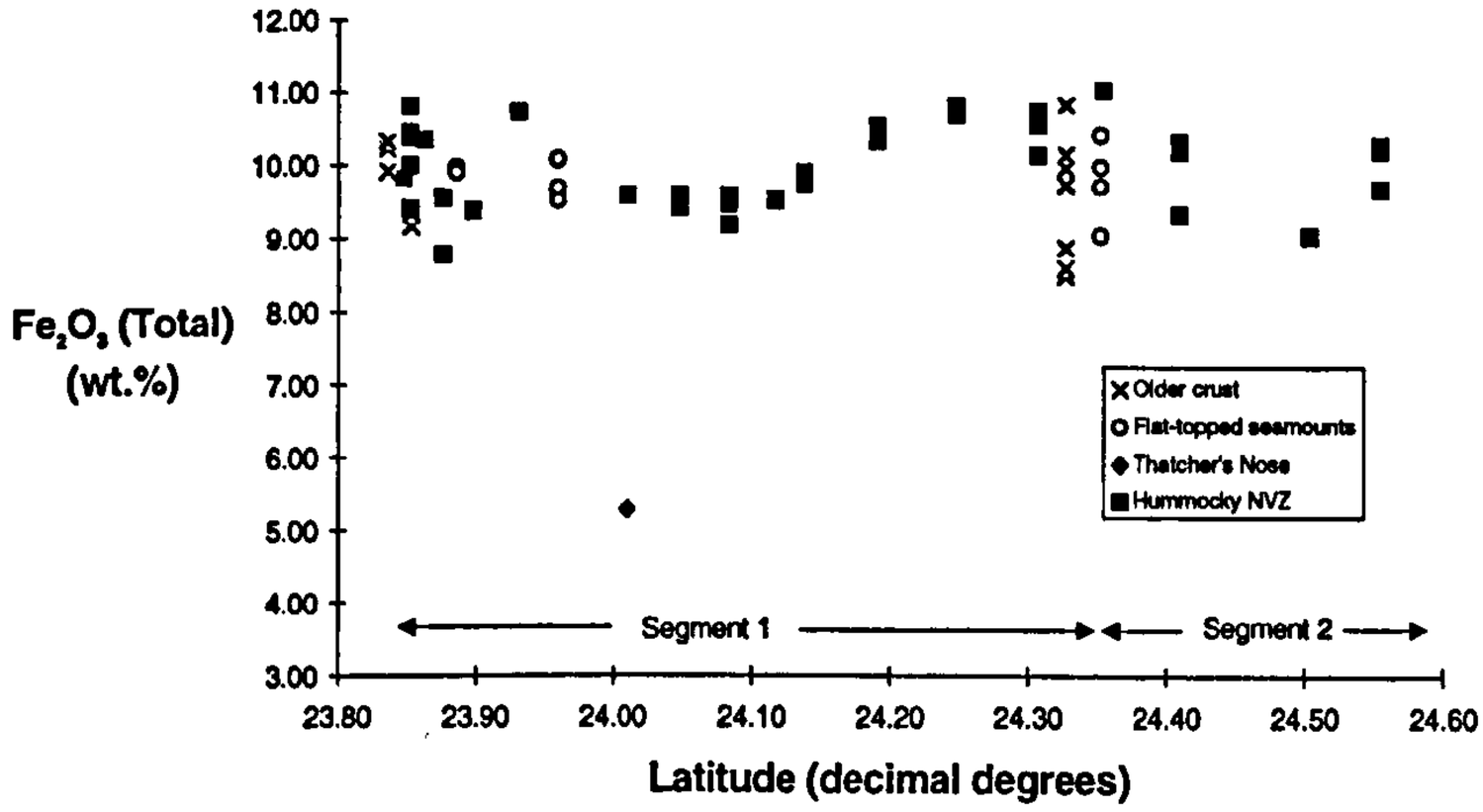

Figure 6.19 Variations in whole-rock composition (a) TiO_2 and (b) Fe_2O_3 (total) with latitude. (Fe_2O_3 (total) is total iron oxide with FeO adjusted to the higher oxidation state. Note how rocks with more fractionated compositions occur at the ends of the segment .

6.8 The transform effect related to second order segmentation

Many of the physical attributes of ridge transform intersections are observed in the southern half of segment 1. The effect of the changing stress regime and the mechanisms which lead to nodal basin formation explain several features observed in the transform domain, as described in chapter 5. However, the geochemical systematics presented in section 6.6 are inconsistent with the decrease in batch melting thought to accompany the TFE (Langmuir & Bender, 1984) and the second order segmentation is the primary control on the extent of fractionation. There are some indications of reduced magma supply, namely the relatively small scale petrological segmentation, the slightly steeper decline in MgO towards the transform, the importance of plagioclase accumulation signifying a large ratio of crystal mush to magma in the subcrustal magma chamber, and the volcanic diversity of the NVZ in the sidescan images. However many of these features of reduced supply rate are also

seen in the NTO. The presence of the transform merely seems to have the effect of reducing the magma supply over a longer section of the ridge axis.

The relative lack of a magmatic transform effect leads me to the conclusion that transform segmentation is primarily of a tectonic origin.

6.9 Interpretation of rift valley evolution.

The gross morphology of a ridge segment and the chemical evolution of the magma during the crustal accretion process will depend on the complex interplay between:

a) magmatic factors: magma supply; melt migration, mixing and fractionation within and below the crust; eruption and intrusion episodicity;

b) tectonic factors: strain partitioning; the periodicity and style of faulting (symmetric or asymmetric);

c) hydrothermal circulation and particularly the part it plays in increasing the brittle ductile transition under the ridge crest.

The following discussion leads to a model where I relate the geochemical/petrological systematics and segment morphology to the episodicity and size of magmatic injection events from the crust.

6.9.1 Episodicity and focusing of volcanism

The relative age contrast between the NVZ and the older tectonised crust of the valley floor can be used as a measure of the time period between major volcanic episodes, while the sharpness of the contact is controlled by the degree of focusing and the relative extent of volcanic and tectonic episodes.

Small regular eruptions which are strongly focused on a zone of weakness in the valley floor, would produce a gradational age variation between hummocky neovolcanic and fissured older crust. If small regular eruptions are not focused at a particular point on the rift valley floor, a pattern of varying age contrasts would develop with no continuous, clearly defined boundary between hummocky and fissured terrain. Instead the valley floor would be characterised by fissured and faulted patches in areas separating hummocky ridges, as illustrated in the interpretation of the NVZ in the TD (figure 5.16). A sharply defined, continuous terrain boundary indicates that eruptions are relatively voluminous and are also separated by substantial periods of volcanic quiescence, so that recent flows downlap onto older strongly fissured crust.

The combined WASP and TOBI interpretations of segment 2 imply that a major "ridge-building" volcanic episode took place after a time period sufficient to allow heavy sedimentation of the valley floor (indicated by the low backscatter in the marginal basin). The robust NVR was constructed by voluminous eruptions which occurred relatively steadily over a period of at least several tens of thousands of years in a number of volcanic phases, which have moved progressively westward. These volcanic phases were separated by short periods of quiescence, during which faulting across the flanks of the volcanoes caused small amounts of subsidence associated with volcano collapse. However, the NVR as a whole experienced relatively little tectonic dismemberment, probably because the extensional stresses in the crust had been relieved by the robust magmatism. The maturity of the median valley wall faults suggests that the median valley as a whole is relatively long lived. The widely spaced terraces on the flanks confirms that the successive wall faults initiate about every 0.4Ma compared to segment 1 where the closely spaced terraces form every 100,000yrs - 150,000yrs infrequently compared with segment 1, uplifting relatively wide blocks of median valley floor into flanks.

The NVR in the northern half of segment 1 is not only less voluminous but the episodicity of ridge-building phases is much shorter (not much longer then 1000 years in the segment centre), as indicated by the relatively small age contrast between the marginal basins and the NVZ throughout this half of the segment. The very sharp and continuous contact between the hummocky NVR and the older valley floor suggests that eruptive events were focused both in space and time. The NVZ is rapidly dismembered during periods of magmatic quiescence (of at least several thousand years in the segment centre). The highly tectonised crust is then uplifted in a succession of narrow terraces into the flanks. In the centre of the segment, the large age contrast between the western terrace and the NVZ may partly be a result of a jump in the focus of volcanic activity from the small bathymetric ridge near the eastern wall (beyond the end of the phototraverse) to the present position of the NVZ. However, the narrowing of the NVR in the centre of the segment suggests an increased proportion of intrusive to extrusive components to the building of the crust. This has been related to the magmastatic head and the brittle-ductile transition in chapter 4. The closely spaced terracing of the median valley walls and the immature character of the inner walls points to a shorter life span of the inner wall faults (with a new fault developing every 100 000 years -150 000 years) concurrent with the short life span of the NVZ.

As previously discussed in chapter 5, the transform domain is characterised by small episodes of relatively unfocused volcanism in a strongly asymmetric median valley.

The epidsodicity of these discrete constructional events is probably greater than the widely spaced NVR-building episodes of segment 2, but less than that in the north of segment 1.

In their model of composite mid-ocean ridge magma chambers, Sinton and Detrick (1992) predict that at slow spreading ridges where eruptable magma is only intermittently available, eruptions are likely to be closely coupled to new injections of magma from the mantle. If this is the case, then the eruption periodicity can be used to gain a first order assessment of the injection periodicity. Thus segment 1 may have been experiencing small but regular injection events which are highly focused across-axis at the narrowgate and the north, but less so in the RTI. The injection events are probably less frequent in the TD and the melt batches may also be smaller. The arrival of melt at segment 2 seems to be highly variable, with a period of magmatic starvation followed by several closely spaced, relatively voluminous injections, associated with the construction of the robust NVR.

6.9.2 Hydrothermal activity.

There is evidence of hydrothermal venting in segment 2, which may be related to the robust episode of magmatism which formed the NVR. Well established hydrothermal circulation will also help to increase the brittle lid thickness in this segment in concordance with the hypothesis that segment 2 has a thick brittle lid (discussed in section 4.2.6) In contrast there is little evidence for hydrothermal venting in segment 1, possibly because the magmatic injection events are never large enough to initiate and sustain it.

6.9.3 Fractionation and crustal residence time.

A principal result of this project is the recognition of the increased basic composition of the rocks toward the centres of the segments. Similar along-axis fractionation systematics at propagating ridges (Christie & Sinton, 1981; Sinton et al. 1983), are thought to ultimately reflect the residence time of magmas within the crust, buffered by the supply rate of primitive magma from the mantle. This correlation of basalt composition with the crustal structure, inferred from the bathymetry, suggests that a balance between magma supply, crystallisation rate and eruption rate is operating on the scale of a single ridge segment at slow spreading rates.

The magma supply is greatest in the centre of the segment and decreases towards the ends, consistent with the decrease in crustal thickness along-axis. More frequent input of primitive magma in the centre of the segment will lead to more primitive average compositions. In addition, a higher supply rate at the segment centre will tend to maintain the magmastatic pressure under the ridge, promote regular eruptions and

prevent the composition in the chamber from becoming too evolved. Conversely, at the cooler ends of the ridge segment, crystallisation dominates, leading to the eruption of more fractionated magma compositions.

The particularly coherent along-axis variation in fractionation seen in segment 1 compared with the noisier trend in segment 2 can be attributed to the episodicity of injection events. In the north of segment 1, where there are very regular injection events, a constant balance between supply and eruption is maintained through time. Hence the crustal residence time at a particular location will remain relatively constant. In segment 2, where the injection events are irregular, the crustal residence time will also be more variable, leading to more variable degrees of fractionation at a particular location.

The discussion, so far, assumes that the primary magma arrives at the base of the crust in episodic pulses, rather than as a continuous steady flux. This view is supported by fluid dynamical models, which predict magma ascent during porous flow of compacting mantle to be in the form of solitary waves (Whitehead, 1986; Scott & Stevenson, 1986). However, evidence from Hawaiian shield volcanoes suggests that supply to their shallow reservoirs is continuous on a scale of hours to minutes (Decker, 1987). At slow spreading ridges, where the overall magma supply is much lower, continuous constant melt flux is less likely.

6.9.4 Relationship between faulting and crustal residence time

The TOBI and WASP observations have emphasised the close relationship between volcanism and tectonism that occurs at slow spreading ridges. The coupling of magmatic and tectonic activity is likely to be an important factor at low magma supply ridges, where tectonism is relatively more important and it is harder to build up the magmastatic pressures to initiate magma-driven fracture.

Syn-magmatic faulting was particularly noted in segment 2, where it is a feature of NVR construction. Hence, certainly in segment 2, faults which are not caused by the magma overpressure may have an effect on the crustal residence time. At the narrowgate segment, fissures are probably the primary structural control on magmatism.

At the centre of the narrowgate segment the continuous dismemberment of the NVZ may provide a scenario whereby the magma batches are immediately tapped on arrival in the crust. At the ends of the segment there may be more partitioning of the strain into the valley wall faults and the brittle-ductile transition is likely to be deeper, so fissuring is less likely to tap magma batches. In segment 2 the construction of the

thick volcanic pile has inhibited the immediate eruption of magma at the centre of the segment, allowing a broader range in the MgO contents than segment 1.

6.9.5 Relation of magmatic systematics to a composite magma chamber

In their composite magma chamber model, Sinton and Detrick (1992) suggest that fractionation at slow spreading ridges takes place almost entirely during the migration of melts through a crystal mush zone. This mush zone is thickest in the centre of the segment where the magma supply is greatest and the crust is also thickest. If fractionation occurs by vertical percolation through the mush zone, then the magma at the centre of the segment has further to travel through the mush and might be expected to interact more than at the ends. Hence, to reconcile the model with the observations from the MARNOK area, a mechanism must be found that will decrease the interaction of magma with mush at the centre of the segment relative to that at the ends. The additional buoyancy caused by the greater melt-fraction at the segment centre may produce an increase in the percolation rate and hence reduce fractionation at the centre. Alternatively, lateral transport of the melt through the mush zone along the direction of strike would cause those magmas erupting at the ends of the segment to have been exposed to the mush for longer than those erupting at the centre.

Sinton and Detrick's (1992) hypothesis that eruptions may be closely tied to replenishment from the mantle at slow spreading rates, also helps to reconcile this issue. At the ends of the segment, the replenishment rate is low and eruptions are less frequent. Consequently, magma within the mush has longer to fractionate before the arrival of a fresh injection of primitive lava. Mixing between the mush and the primitive lava occurs prior to eruption, producing the characteristic phenocryst-rich mixed magmas. This is confirmed by the petrological evidence that samples from the ends of segments have experienced magma mixing between fractionated and primitive components, with strong zoning of phenocrysts and other features resulting from high degrees of disequilibrium. The relative proportions of mush to primitive lava are greater at the ends of the segment, explaining the higher modal abundances of accumulated plagioclase in the RTI and the NTO.

Further fractionation in a composite chamber takes place in lenses of melt which accumulate in the crust above the mush zone (Sinton & Detrick, 1992). These melt lenses are thought to be a steady state feature of fast spreading ridges, but in slow spreading ridges the magma supply is thought to be too low for melt to accumulate in a convecting body above the mush zone. The several closely spaced, relatively voluminous injections, associated with the construction of the robust NVR in segment 2 may have been sufficient for magma to segregate into a melt lens for a period of

time. This may be another factor contributing to the more variable fractionation profile observed along segment 2.

6.9.6 Magma supply and petrological segmentation

The multiple parental magma batches with distinct melting histories which are observed in this study preclude extensive mixing and along-axis transport in the crust. Where the supply is small, rising melt is less likely to intercept and mix with an accumulation of ponded magma within the crust. In such a case the geochemical signature relating to the individual melting history of the magma batch is preserved through its passage through the crust. This process may account for some of the more diverse trace element patterns from edifices in the NTO and the TD (e.g. the nested seamounts and Thatcher's Nose). The length-scale of petrological segmentation is related to both along-axis mixing within a magma chamber, the length-scale of batch injection events, and temporal variations in these two factors.

In the MARNOK area, the length scale of petrological segmentation ranges from 3-6km in the RTI up to 11km in the north of segment 1. This is smaller than the typical 15km->40km length of petrological segments reported from the EPR at 12°N (Reynolds et al., 1992), consistent with the lower melt flux, and smaller, more discontinuous magma chambers in the MAR.

6.9.7 The brittle/ductile transition related to ridge crest faulting

In chapter 4 it was proposed that one of the primary differences between segment 1 and segment 2 is the depth to the brittle ductile transition. In segment 1 the relatively frequent injection events will maintain elevated isotherms. This is coupled with and rapid tectonism which causes thinning of the brittle layer and lack of a well developed hydrothermal system.

In segment 2, the isotherms will have been temporarily elevated on the initiation of the magmatic pulse. However the large magma batch is accompanied by the establishment of a hydrothermal system which will rapidly penetrate to deep levels to increase the brittle lid thickness. In addition, extensional tectonism tends to be partitioned into the valley wall faults rather than causing extensive fissuring and dismemberment of the crust in the centre of the median valley.

There are two additional observations that are consistent with the hypothesis that the centre of segment 1 has a thinner brittle lid compared with the centre of segment 2. Firstly the development of faulting is thought to be related to the thickness of the lithosphere at a MOR. The faults along the centre of the robust NVR of segment 2 are larger and more continuous than those which cut the NVZ of segment 1. In contrast a thin/weak brittle layer at the ridge crest will result in tensile failure so that fissures

predominate rather than faults. This accounts for the fissure controlled volcanism in the narrowgate segment compared with the fault controlled volcanism in segment 2.

Secondly, a robust NVR must itself be supported by thick lithosphere. Carbotte and MacDonald (1994) use this argument to explain the differences in topographic high between fast and intermediate spreading ridges. The rapid dismemberment of the NVZ of segment 1 implies that the lithosphere is very thin and weak so that it can only support a small constructional edifice.

6.9.8 The model

To some extent the difference in morphology of the rift valley between segment 1 and segment 2 is a consequence of the width of the inner valley floor. Segment 1 has a narrow valley so the volcanism can fill the entire inner valley floor. Conversely segment 2 has a wide valley floor so the constructional activity builds a ridge which stands apart from the median valley walls.

However, the observations made during this study and the above discussion indicate that the morphological differences between these segments are primarily related to the underlying magmatic supply and the subsequent effects on the brittle-ductile transition, and the residence time of magma within the crust.

These differences in magmatic supply are consistent with the observations of Sempéré et al. (1993) that the narrowgate-type segments show strongly focused mantle Bouguer anomalies, while the group 2 segments have no strong, well defined central anomaly. The highly focused and regular sub-crustal melt flow, both along and across axis in the narrowgate segment would produce the inferred crustal thickness variations along-axis. In turn, the more episodic and less focused supply of segment 2 would result in the poorly defined anomaly of the group 2 segments.

A model for crustal accretion in the MARNOK area, combining the features discussed above, is presented in figure 6.20. This model tends towards a magmatic control of second order segmentation, in terms of magnitude and episodicity of magma supply. Focused melt migration as opposed to focused mantle upwelling is the preferred cause of crustal thickness variations along-axis, as is indicated by the constant batch melting described in section 6.6.3. This also seems consistent with the petrological effects of the second order segmentation outweighing those of the transform segmentation.

Although my model presents magma supply as the driving force behind second order segmentation, Allerton et al. (1995) propose that it is the episodicity of the valley wall faulting that drives the tectonic thinning of the lithosphere and in turn produces the pulses in upwelling aesthenosphere that drive local adiabatic melting and melt focusing. This tectonically controlled model is also consistent with the observations,

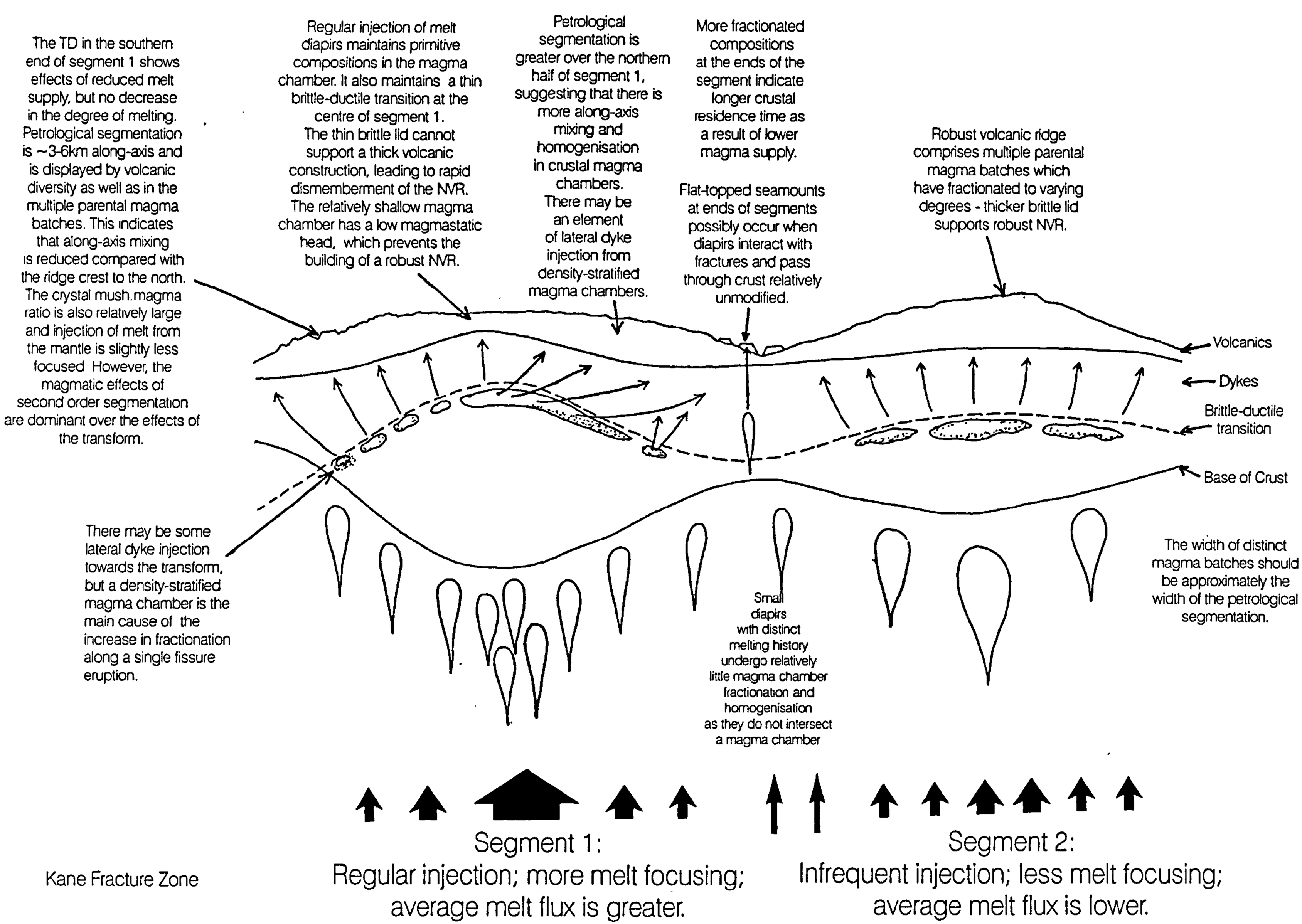

Figure 6.20 Model of crustal accretion in the MARNOK Area

though further modelling is necessary to deduce whether such shallow processes could produce the variations in melting required.

6.10 Summary of chapter 6

- I present a systematic description of variations in volcanic, tectonic and hydrothermal features, as well as temporal variations of the median valley floor along-axis. This is followed by an assessment of along-axis variations in the valley walls and flanks. The two second order segments in the MARNOK area contrast with each other in many respects.
- Segment 1, adjacent to the transform, is a narrowgate-type segment, with a symmetrical median valley at the centre, which becomes increasingly asymmetric towards the ends. The northern half of segment 1 has a very uniform low relief NVR (~100m high), which is flanked by a narrow zone of unsedimented, fissured terrain and continuous ridge-parallel narrow fault terraces. The bathymetric saddle is characterised by short-lived eruptive episodes with high effusion rates, which are subsequently rapidly dismembered by tectonism, preventing the formation of a mature volcano. This segment shows little evidence of hydrothermal activity.
- With the exception of the RTI area, the inner valley of segment 2 is slightly wider than that of segment 1. It has a robust NVR, 400-600m high, which is characterised by syn-tectonic magmatism. The older crust in the marginal basins reflects a large time gap between ridge-constructing episodes. The northern half of the segment lies within a NE trending oblique portion of the MAR. The valley floor located within this oblique zone and in the marginal basin to the NE of the NVR comprises relatively young, but slightly tectonised crust, reflecting the changing orientation of the NVZ to the NE of segment 2. Rocks recovered from this segment have hydrothermal precipitates.
- The second order segmentation dominates the magmatic systematics. I report a variation in the degree of fractionation along-axis in segment 1, with primitive lavas at the centre of the segment and more fractionated compositions at the ends. A trend of increasing MgO content towards the axial-high of segment 2 is also apparent, but has more scatter than that of segment 1. The ends of the segments also have a greater variation in parental compositions.
- Variations in magnetization along-axis are controlled by variations in the geochemistry of the lavas. The higher proportion of magnetic minerals associated with the fractionated lavas produce highs in the crustal magnetization at the end of the segment.

- There is no variation in the bulk degree of melting along-axis, favouring melt migration rather than mantle upwelling as the primary control on the variation in crustal supply along-axis in the MARNOK area.
- There is no decrease in bulk melting towards the transform. Instead, the magmatic transform effect manifests itself by a reduction in the magma supply over the TD. The relative lack of a magmatic transform effect leads to the conclusion that transform segmentation is primarily of a tectonic origin.
- The differential enrichments in highly incompatible trace elements cannot be explained by variations in fractional crystallisation, nor by differences in bulk degree of melting if all melt-fractions are pooled. They can be derived from mantle sources with varying degrees of short-lived enrichment. This is equivalent to the selective tapping of small melt-fractions from the base of a melting column during the melting of an adiabatically upwelling source.
- The scale of petrological segmentation ranges from 3-6km in the RTI up to 11km in the north of segment 1. It tends to correlate with distinct volcanic constructions on the sidescan, especially in the TD. Petrological segmentation has a length scale which is smaller than that reported from the EPR (Reynolds et al., 1992), consistent with the lower melt-flux in the MAR. This result precludes extensive mixing and along-axis transport in the crust. The variations in parental lavas along the ridge crest will be the result of temporal as well as spatial changes in the magma chamber.
- Having considered the magmatic, tectonic and hydrothermal variations along-axis, I propose a model that relates the morphological and petrogenetic variations in second order segmentation to aspects of the melt supply. These variations can occur both within a single segment or can explain the contrasting segment types identified by Sempéré et al. (1993). Regular, focused injections of magma associated with a relatively large overall melt-flux maintain a shallow brittle-ductile transition in the centre of the segment. This results in symmetrical valley wall faulting according to the hypothesis of Harper (1985). These magmatic conditions will also promote the development of a relatively continuous, well-mixed magma chamber with low crustal residence times in the segment centre, and thus account for the primitive compositions erupted at the axial-highs. With decreasing magmatic input, the brittle-ductile transition is lowered, the valley wall faulting becomes asymmetric, the median valley widens, the residence time of magma within the crust increases and more fractionated compositions erupt.

BLANK IN ORIGINAL

Chapter 7

Global comparisons

Where can I flee from your presence?
If I go up to the heavens, you are there;
if I make my bed in the depths, you are there.
If I rise on the wings of the dawn,
if I settle on the far side of the sea,
even there your hand will guide me,
your right hand will hold me fast.
Psalm 139 vs 7-10.

7.1 Introduction

In this penultimate chapter I will relate my findings on the MARNOK area to two other parts of the ridge system, in an attempt to place them in a more global context. In section 7.2, I focus on Iceland, where crustal accretion is observed in a subaerial, high melt-flux environment. With the additional information this provides I go on to develop a model of magmatic plumbing at accretionary plate boundaries. In section 7.3, I go on to assess this model by reviewing some evidence from the Reykjanes Ridge and the EPR. In section 7.4, I return to the topic of segmentation and particularly second order segmentation. One of the obvious areas to compare with MARNOK is MARK on the eastern end of the Kane transform. Although MARK has been the location of many studies, the segment immediately to the south of the transform is anomalous, because of an incipient eastward ridge jump, revealed by a 10mgal gravity low centred on the eastern rift mountains (Morris & Detrick, 1991). This results in highly complex relationships between the gravity (and inferred crustal structure) and basalt petrogenesis (Reynolds & Langmuir, *in press*). Because of these complexities at MARK, I choose the 26°S ridge segment for a comparison with MARNOK instead. The 26°S ridge segment has recently been the subject of a comprehensive geochemical sampling program (Niu & Batiza, 1994), a gravity survey (Blackman & Forsyth, 1991) and joint bathymetric and magnetic surveys (Carbotte et al., 1991; Grindlay et al., 1992).

7.2 Comparison with crustal accretion in Iceland

One of the problems of studying crustal accretion at mid-ocean ridges is that most of the 'action' takes place under several kilometres of water. The direct observation of magmatic eruptions is virtually unheard of. However, in Iceland, where hot-spot

influence causes the MAR to become emergent, magmatic rifting events have been well-documented (Björnsson, 1985; Björnsson et al., 1977; 1979; Sigurdsson, 1987; Sigurdsson & Sparks, 1978) and previous rifting episodes have been reconstructed with a combination of detailed field work, petrological studies and geochemical analysis (Jakobsson et al. 1978; Walker, 1992a).

Parallels have been drawn between the morphological character of the Reykjanes Ridge and rifting zones in Iceland (Murton & Parson, 1993). They suggest that linear seamounts correspond to fissure volcanoes, conical seamounts to scoria cones and flat-topped seamounts to small shield volcanoes. The same crustal building blocks occur in the MARNOK area and can similarly be related to Icelandic Volcanism.

7.2.1 Relationship of lava shields to flat-topped seamounts

7.2.1.1 General morphology

The MARNOK seamounts and their summit craters are comparable in size to the smaller monogenetic lava shields on the Reykjanes Peninsula (Jakobsson et al., 1978), and elsewhere in Iceland (Walker, 1971). Shields formed under subglacial conditions have remarkably similar morphologies to these deep sea volcanoes, having flat tops and steep flanks (Searle, 1983), though they often comprise thick layers of hyaloclastites (Mathews, 1947), which should not form under the high pressures of the deep-sea environment. The flat-topped seamounts and the subglacial shields are generally less laterally extensive than the shields formed subaerially. The gentle slopes of subaerial shields are generally attributed to the low viscosity of the basaltic lava. The shield volcanoes on Iceland are composed of many thin, irregular compound flow units (0.5m-1m thick) and are mostly pahoehoe, though aa flows sometimes occur (Walker, op. cit.).

Although the morphology of the smooth, flat-topped seamounts imaged by TOBI strongly suggests that they formed within a single eruptive episode from a single vent, it is impossible to validate such a hypothesis without detailed sampling and study. The presence of low relief flows comprising a mixture of pahoehoe and pillows has been confirmed by the groundtruthing. Although flow contacts are not clearly defined on the sidescan images, it seems likely that growth of the seamount is exogenous with the successive stacking of low relief flows or lava tubes. The slightly sinuous irregular margins observed on the young flat-topped seamounts is consistent with this.

The flat-topped morphology of the subglacial table mountains in Iceland is not restricted to the lava shields and is thought to result from the constraining effect of the ice sheet. In the deep-sea environment there is no ice sheet present to physically constrain the eruptions, but their similar morpholgies probably result from the

common presence of water. I suggest that the rapid quenching induced by eruption into water may restrict the distance compound lava sheets can flow, resulting in a steep rampart around the flanks of the edifice as successive flows stack up round the vent. In chapter 4, I discussed how rapid quenching is the primary cause of differences in sheet flow morphology between subaerial and deep sea environments. Given that the morphologies of volcanic edifices are ultimately a reflection of their constituent flows it seems reasonable to suggest that quenching is also a primary cause of the differences in volcanic morphology between the MAR and subaerial Iceland.

7.2.1.2 Petrological characteristics

In section 4.8.2 I described the petrological characteristics of the flat-topped seamounts, drawing particular attention to the anomalously large "quench-like" morphologies and complex radiating clusters. In addition I suggested that the olivine phyric samples with the embayed and skeletal crystal textures indicative of large degrees of supercooling may have originated from the flat-topped crestal seamount near the bathymetric summit of segment 2. I pointed out that these are not in fact true quench crystals as they are relatively large and yet are located in a glassy groundmass. I suggested that these morphologies signify rapid decompression, but with a relatively large time period between crystal nucleation and final eruption at the surface. Such a texture would be formed if a sample erupted through a very long conduit or rose part of the way to the surface, and then stopped for a while before it finally erupted.

Walker (1992a) also describes radiating clusters of feldspar microphenocrysts that seem to mimic quench textures, yet coexist with true quench growth. She found that 90% of the samples with this texture were located at lava shields. Her lava shields samples were also devoid of plagioclase megacrysts, but she describes the common occurrence of olivine and the occasional plagioclase phenocrysts with oscillatory zoning, which she suggests have been produced by turbulent flow in a conduit. Jakobsson found similar petrological features in the shields of the Reykjanes Peninsula. The anomalous "quench" growth in Icelandic lava shields can be attributed to the large vertical extent of their eruptive conduits. The remarkable similarity between the petrology of Icelandic shields and the MARNOK flat-topped seamounts is strong evidence to suggest that the two have closely similar origins.

7.2.1.3 Geochemical characteristics

In chapter 4 I showed that the flat-topped seamounts had distinctive parental magmas when compared with nearby hummocky terrain and that the diversity of parental magmas was greater for the flat-topped seamounts than for the hummocky ridges. I suggested that they represented diapirs which had passed through the crust with relatively little interaction with other melt batches, thus allowing their distinctive

melting signatures to be preserved. Walker (1992a) also showed that each lava shield within her study area was distinct in terms of elemental abundances at a given degree of differentiation. She also reports that shields are generally less fractionated. I found no systematic difference in the degree of fractionation of flat-tops, though it should be noted that the nested seamount in the NTO is noticeably more MgO-rich than the nearby hummocky terrain (figure 6.9).

7.2.1.4 Source regions and effusion rates

Lava shields in Iceland are thought to originate from a deeper source than the fissure eruptions (Walker, 1971; Saemundsson, 1979), probably at the crust-mantle boundary (Walker, 1992a). Seismic tomography has revealed high density volumes under some of the Icelandic lava shields that may be in the form of conduits extending to depths of up to 5km (Foulger & Toomey, 1989). This agrees with the inference that the flat-topped seamounts are vent-fed and that their circular form is primarily the result of lavas effusing outwards from this pipe.

In my analysis of seamount statistics in the MARNOK area I discounted the hypothesis that a limiting magmastatic head is responsible for the formation of the flat-top on some MAR seamounts, in favour of the suggestion that they are a result of relatively rapid effusion rates from a vent. However, in Iceland, shield volcanoes commonly have lower eruption rates than fissures, which is the opposite of that proposed above for the MAR. This discrepancy may be a result of the considerably thicker crust and longer conduits for shields in Iceland. Shields with flatter shapes, similar to the flat-tops of the MAR, comprise lavas with faster effusion rates (Rutten, 1964; Walker, 1971) and it has been argued that this is a consequence of their having shallower sources. Hence, in Iceland, as well as the MAR (and Troodos—Schmincke & Bednarz, 1990), it is the effusion rate which primarily controls the shape of a vent-fed seamount. If flat-topped seamounts on MORs also originate from the crust-mantle boundary they will have shallower sources than most Icelandic shields and hence, all other things being equal, they should have faster effusion rates and flatter forms than the subaerial Icelandic shields.

If the flat-topped seamounts, like shields, come from relatively deep sources compared with the crustal magma chamber, the conduit length arguments put forward in section 4.2.5.3 predict that the eruptions from the crustal magma chamber should have the faster effusion rates, rather than the deeper source seamounts. An explanation for this disparity may lie in the magma chamber processes, especially degassing of CO_2 which is thought to be a primary factor in enhancing and maintaining magmastatic pressure throughout an eruption. The gas bubbles, which are more compressible than the magma, maintain the pressure during an eruption by allowing

gas to exsolve from the melt. On one hand, a crustal magma chamber may contain more gas bubbles than a pocket at deeper levels because there is a greater proportion of connected fractionating magma (Smith & Cann, 1992). On the other hand, Bottinga and Javoy (1990) point out that by the time MORB reaches a crustal magma chamber, it will have already undergone considerable volatile loss, and as bubble nucleation is inhibited at low pressure, there is likely to be little additional exsolution of gas on eruption from a low pressure magma chamber. If the effects of previous volatile loss and suppressed bubble nucleation at low pressure outweigh the effects of a larger magma body, then the higher pressure "shield-like" eruptions will have greater effusion rates.

7.2.2 Rifting episodes

In this section I will review how the dynamics of shield and fissure eruptions are related in Iceland and will compare this with evidence for similar processes in the MARNOK area.

Studies of the crustal accretion during the Krafla rifting episode showed that magma injection along the length of a fissure swarm was fed from a central crustal magma chamber, whilst a small shield volcano at the tip of the swarm simultaneously erupted a chemically distinct primitive lava (Björnsson, 1985). There was a discrepancy between the volume of intruded magma expelled from the central magma chamber and the volume increase deduced from widening of the fissure swarm. Björnsson, (op. cit.) estimated that the dyke intrusion from the central magma chamber is confined to the upper 2km of the crust, being fed horizontally by lateral movements of magma along a propagating fissure.

However, GPS surveying results, which can be used to determine crustal deformation in Iceland from the rifting episode, have shown that crustal rifting ruptures the entire elastic layer[1], with the lower part of the dyke complex being fed from below (Hofton, 1995), in accordance with the model of Björnsson (1985). This facilitates the withdrawal of magma from the partially molten layer at the base of the crust (which is ~8km-16km thick). The melt drawn up from the partially molten layer replenishes the magma chamber in the centre of the fissure swarm and produces eruptions of chemically distinct primitive lavas at the tip of the fissure swarm in the form of a shield volcano (Björnsson, op. cit.). The dyke-forming mechanism at larger distances from the central magma chamber is thought to follow the classical model of magma

---

[1]Hofton (1995—PhD) uses an elastic-viscoelastic model and an elastic layer thickness of 10km to model this.

ascending vertically in fissures, rather than the lateral propagation documented in the centre of the swarm (figure 7.1).

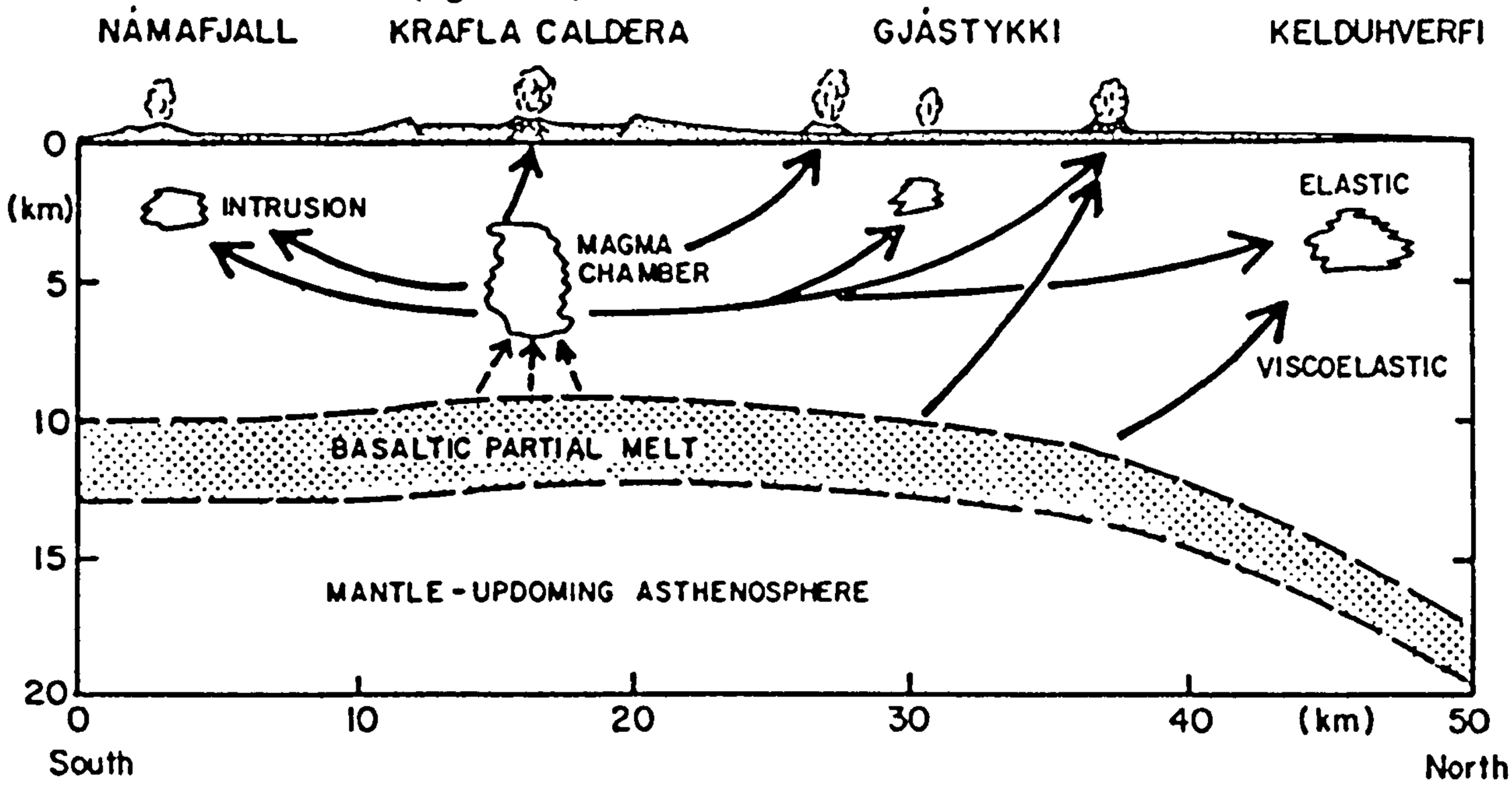

Figure 7.1 A simplified model of the Krafla volcanic system, cross-section from north to south along the length of the fissure swarm, with arrows indicating magma movement. (Taken from Björnsson, 1985.)

A similar process may be operating in the north of MARNOK segment 1. Firstly, the relationship between the volcanic morphologies is similar. For instance, the nested seamounts are in line with the northern tip of the hummocky ridge, are relatively primitive compared with nearby hummocky terrain, and have a parental magma which has not homogenised with the lavas of the hummocky NVZ. Hence, the formation mechanism of the nested seamounts may be similar to the shield at the tip of the Krafla swarm. I suggest that the eruption of the seamounts can be triggered by an eruptive episode elsewhere in the segment (usually near the centre), which propagates stress through the deep levels of the crust, initiating the rise of a diapiric plume, probably from the base of the crust. At higher levels in the crust, this diapiric plume may utilise previous fractures, which may also be disturbed by the nearby upper-crustal rifting event. This helps to explain the location of flat-topped seamounts towards the ends of the segment and their frequently-observed relationship with underlying fractures.

7.2.3 The implications of plagioclase megacrysts for magmatic plumbing

The existence of deep melts which are distinct from the crustal magma chamber has already been proposed in chapter 6 to explain the existence of the plagioclase megacrysts. These were hypothesised to have crystallised from melts derived from depleted mantle near the base of the crust (section 6.6.2.3) and probably comprise the lower parts of the mush zone in the composite chamber proposed by Sinton and

Detrick (1992). However I found that plagioclase megacrysts were rare in the dredges from flat-topped seamounts and the few that are present show only minor amounts of disequilibrium with the host magma. They are completely absent from the shield samples of Walker (1992a). This suggests that, although the plagioclase megacrysts and the flat-topped seamounts both represent parts of crustal plumbing system that are distinct from the main crustal magma chamber, there is relatively little interaction between the two.

The highly refractory "instantaneous" melts which form the plagioclase megacrysts will have a particularly large density contrast with their depleted residue (Niu & Batiza, 1991) and so are likely to segregate very quickly. They will have relatively little interaction with the slower moving diapirs (or solitons) of accumulated melt rising from lower in the melt column until they collectively pond in a crustal magma chamber.

7.2.4 Magmatic plumbing system

From my observations in the MARNOK area and with the additional implications of the comparison with Iceland, I propose that accumulated diapirs reaching the base of the crust take one of three possible paths as described below.

1 A melt arrives at the base of the crust and begins a slow percolation through the crystal mush in the lower crust until it ponds at the brittle-ductile transition and mixes with any other magma also ponded at the top of the composite magma chamber. As the magma percolates through the crystal mush it fractionates (Sinton & Detrick, 1992), and may accumulate small quantities of plagioclase megacrysts. This is probably the fate of most diapirs, especially those in the centre of the segment (figure 7.2).

2 The arrival of a diapir at the base of the crust corresponds with a rifting episode. By analogy to Iceland (as described in section 7.2.2), the magma is drawn up through the crystal mush relatively rapidly. Because of its more forceful passage through the crystal mush it undergoes relatively little fractionation, but is able to accumulate more of the megacrysts. Thus it replenishes the magma chamber, and also introduces megacrysts which are in disequilibrium and undergo subsequent resorption. In some cases, especially where the magma chamber is very poorly developed, the rising primitive melt will temporarily mix with the magma within the chamber, but as the rifting episode continues, it may itself be erupted as a crystal-rich lava with a relatively MgO-rich basaltic host. Thatcher's Nose is an example of the kind of edifice which may form as the result of such a scenario (figure 7.3).

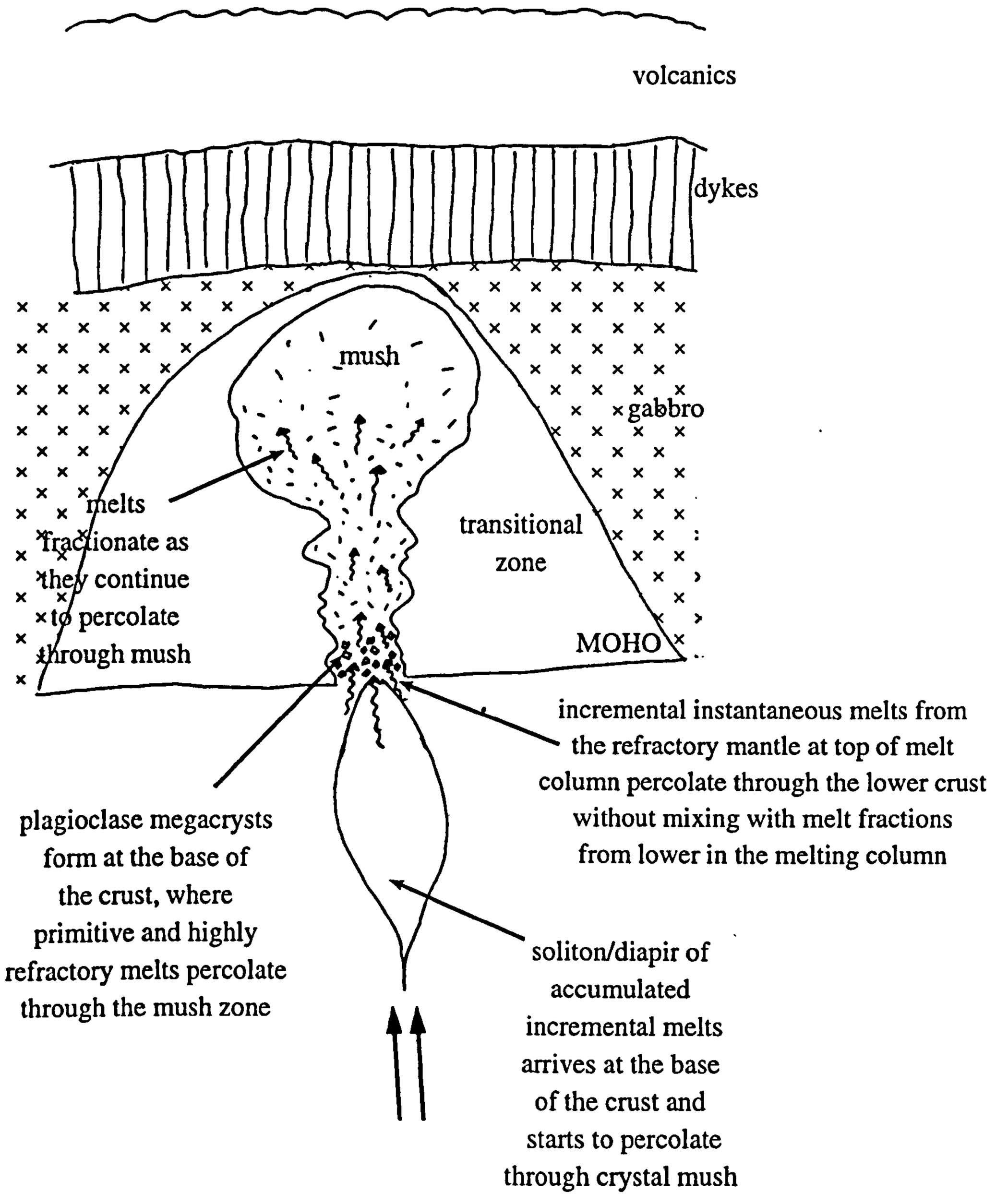

Figure 7.2 Soliton or diapir of accumulated incremental melts arriving at the base of the crust percolate up through the crystal mush, becoming increasingly fractionated until it reaches the upper levels of the crustal magma chamber. Incremental instantaneous melts from the refractory mantle at the top of the melting column enter the base of the crust, without accumulating with melt fractions from deeper parts of the melt column. There they fractionate the refractory megacrysts.

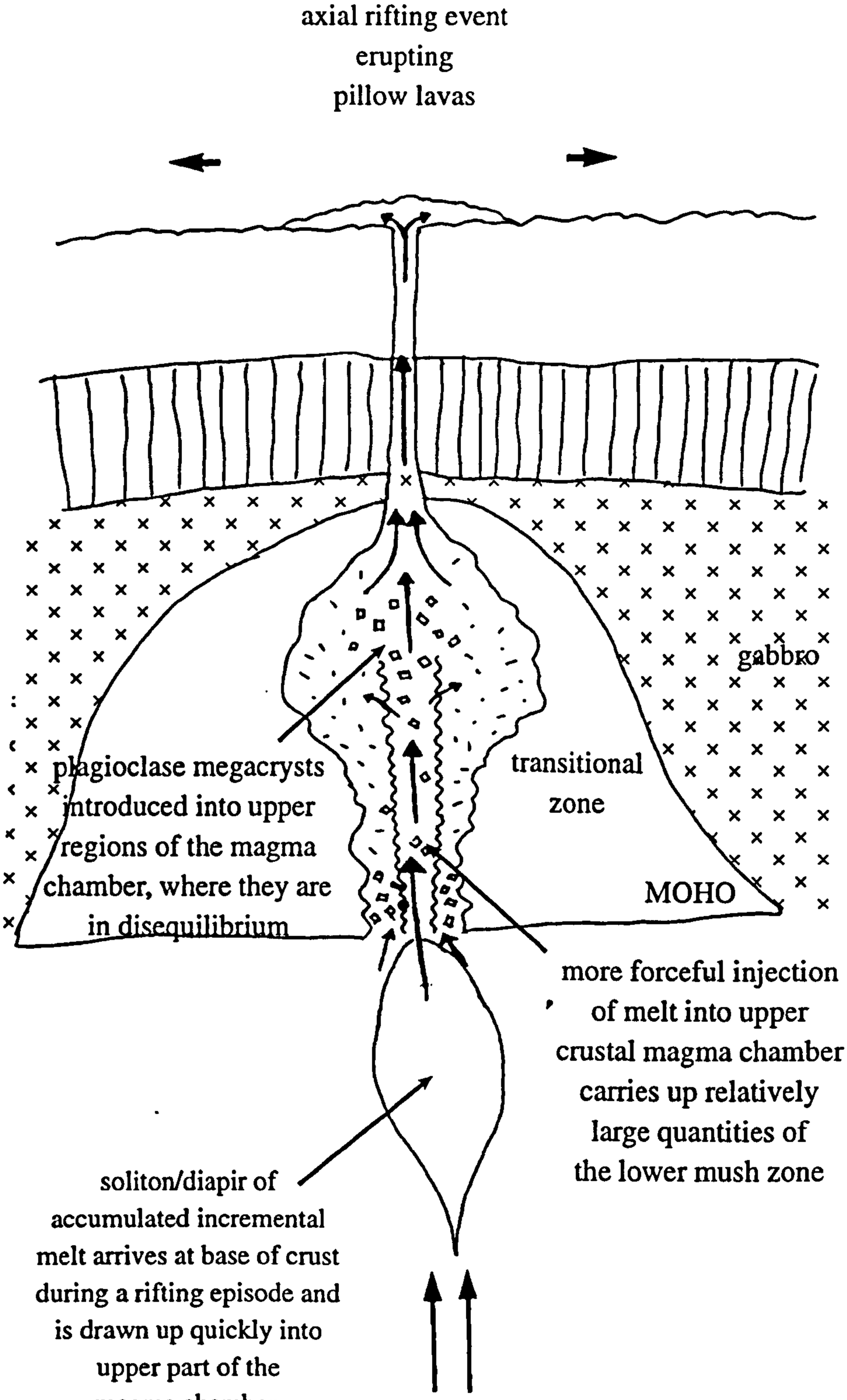

Figure 7.3 If a soliton or diapir of accumulated incremental melt arrives at the base of the crust during a rifting episode, it is drawn up rapidly in the upper parts of the magma chamber, carrying with it accumulated plagioclase megacrysts from the base of the crust. Thus the plagioclase megacrysts are injected into an environment in which they are in disequilibrium, and are likely to be erupted at the surface.

3 Arrival of a diapir at the base of the crust corresponds with a rifting episode, but does not encounter a crustal magma chamber. The interplay of the extensional forces causing the tectonic disturbance in the upper crust, with the buoyancy of the melt diapir, aids the initiation of buoyancy-driven magma fracture (Spence & Turcotte, 1990) in the lower crust. The dyke that results rapidly collapses into a pipe-like conduit because of its large vertical extent and the relatively cool temperature of the magmatically-starved surrounding crust (Bruce & Huppert, 1989; 1990). As there is no magma chamber, it is not drawn up rapidly through a crystal mush (as in case 2), but instead fractures its way through the lower crust and so accumulates virtually no plagioclase megacrysts. It erupts at the surface as a flat-topped seamount (figure 7.4).

If a diapir feeds a relatively large portion of ridge, different parts of it may pass through the crustal plumbing system in different ways. This may account for the virtually identical parental magmas for 12D and 9D (see section 5.2.3.2; figure 5.5), but their differing petrological characteristics.

7.2.5 Implications of the proposed magmatic plumbing system

The proposed magmatic plumbing system has a number of implications. Firstly, different volcanic morphologies should dominate under different conditions of magma flux. A ridge segment which is magmatically robust should be dominated by hummocky fissured terrain, with possibly a small number of seamounts at the ends of the segments where the magma flux is lower. A segment which has a relatively large proportion of flat-topped seamounts should have intermittent magmatism, so that the crustal magma chamber becomes solidified, causing the eruption of seamounts when a new rifting episode is initiated. Segments with a very low magmatic budget should be highly faulted and contain the occasional seamount or hummocky ridge.

7.3 Magmatic plumbing systems elsewhere in the ridge system

7.3.1 The Reykjanes Ridge

Parson et al. (1993) suggest a cyclic pattern of volcanic construction and tectonic dismemberment to account for the observed morphology of the AVRs on the Reykjanes Ridge. The cycle comprises initial fissure eruptions which build up a hummocky NVR, followed by localised point-source eruptions and subsequent tectonic dismemberment. It seems plausible that this cycle reflects waning magmatism which would be consistent with my above proposal.

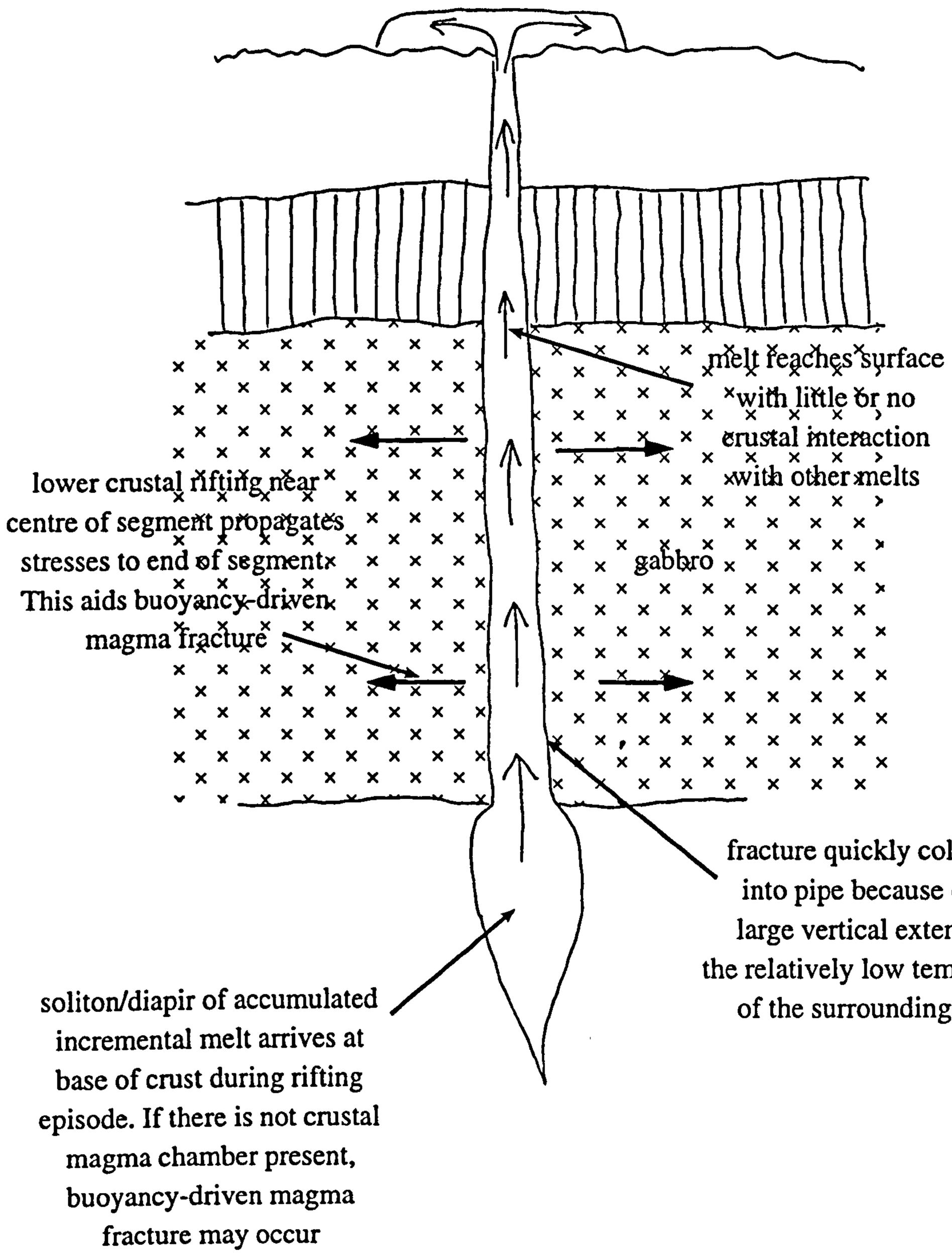

Figure 7.4 A soliton or diapir of accumulated incremental melt arrives at the base of the crust during a rifting episode, but does not encounter a crustal magma chamber. The interplay of the extensional forces causing the tectonic disturbance in the upper crust, with the buoyancy of the melt diapir, aids the initiation of buoyancy-driven magma fracture in the lower crust. The dyke that results rapidly collapses into a pipe-like conduit, which affords little or no crustal interaction with other melts before it erupts at the surface as a flat-topped seamount.

An anomalously large proportion of seamounts are located at 60°N on the Reykjanes Ridge, near the transition in ridge morphology from axial-high to axial graben (Appelgate & Shor, 1994; Magde & Smith, 1995). This particular AVR comprises a remarkable 83% smooth flat-tops, compared with an area to the south, which has 78% hummocky seamounts (Magde & Smith, op. cit.) It is suggested that the proliferation of smooth-topped seamount on the 60°N AVR is associated with a pulse of hot spot material. This is supported by the identification of a southward converging V-shaped basement ridge (Vogt, 1971; Vogt & Avery; 1976) which presently intersects the ridge axis at ~60°N.

In the model proposed in sections 7.2.4 and 7.2.5 a large pulse of magma suddenly arriving at a relatively magmatically starved AVR would result in an abundance of flat-top seamounts. Unfortunately, neither Appelgate and Shor (1994) nor Magde and Smith (1995) give any indication of whether this AVR had a high or low melt-flux prior to this large pulse of volcanic activity. However, Appelgate and Shor (1994) point out that there is no systematic variation in seamount morphology to the north of 60°N. Given that the hot-spot pulse should have recently affected the AVRs immediately to the north, I would expect there to be evidence of large seamount abundances in these AVRs. As there is no such evidence, I propose that the morphological response of the AVR to the hot-spot pulse is dependent on the extent of magmatic 'robustness' prior to the arrival of the pulse.

7.3.2 The EPR

Although this discussion is primarily concentrated on slow spreading rate, out of interest I will mention a case on the EPR, where the relationship between hummocky fissure eruptions and flat-topped seamounts is similar to that seen in the MARNOK area. From the overlapping spreading centres near 12°53'N, Hekinian et al. (1985) report a small flat-topped volcano, 80m in height and 1km in diameter located immediately to the south of the currently active western spreading centre. The samples they collected from the hummocky ridge were all depleted tholeiites, while the specimen from the seamount was enriched in K_2O, Na_2O and TiO_2. This scenario is directly analogous to the nested seamounts on the northern tip of segment 1 in the MARNOK area, although the EPR at this locality is likely to be propagating southwards. The location of the seamount at the propagating tip is consistent with the hypothesis presented in 7.2.4 and 7.2.5, as there is unlikely to be an established magma chamber at this point, but the crust will be under considerable stress.

There are many aspects of seamount volcanism in the Pacific that are consistent with observations in the Atlantic, although the abundances are larger and the characteristic heights are smaller in the Atlantic (Smith & Cann, 1990). Small, near-axis Pacific

seamounts have a non-uniform distribution, concentrating near discontinuities (Fornari et al., 1987b; Scheirer & Macdonald, 1995), they are chemically distinct from axial lavas and are thought to form from melts which bypass the principle zone of melting and undergo less cooling at crustal levels (Batiza & Vanko, 1984; Wilson, 1992).

There are probably important differences between seamount volcanism at fast and slow spreading ridges which are related to the availability of melt and the penetrability and thermal structure of the lithosphere. My model is consistent with the smaller abundances of seamounts in the Pacific, as magma chambers are more voluminous and continuous at fast spreading rates. The larger heights in the Pacific may also be related to the availability of magma, and to the thickness of the lithosphere on which the larger, off-axis seamounts form. (Smith and Cann, [1990] point out that the young thin lithosphere in the MAR median valley floor will not be able to support large structures.)

7.4 South Atlantic segmentation: a comparison.

The southern MAR is spreading at 34-38 mm yr^{-1}(full rate), which falls within a transitional range between intermediate and slow spreading rates (Carbotte et al., 1991). In recent years it has been the location of a number of bathymetry, magnetic, and sampling studies (Batiza et al., 1989; Carbotte et al., op. cit; Grindlay et al., 1992). Interest has particularly focused on the 26°S segment which was the location of a detailed sampling program (Niu & Batiza, 1994) and so is particularly suitable for a comparative study with the MARNOK area.

7.4.1 Along-axis variations in magnetization

In the south Atlantic, magnetization highs at the intersection of the MAR with both large and small offsets between 25°00'S-27°30'S and 31°00'S-34°30'S (Carbotte et al., 1991; Grindlay et al., 1992) are predicted to be the result of geochemical variations along-axis. This suggests that the systematic variations in fractionation similar to those identified in the MARNOK area may be a relatively common occurrence on slow spreading ridges.

7.4.2 Comparison with the 26°S segment

The 26°S segment (figure 7.5) is bounded at one end by a transform (right lateral offset of 42km) and at the other end by a NTO (left lateral offset of 9.5km) (Grindlay et al., 1992). About 30km south of the axial-high at the segment centre, a right lateral offset of about 2.5km, known as the Midway Discontinuity, is apparent in the magnetics, but has virtually no bathymetric or petrological expression at present, although it was a transform in the past (Grindlay et al., op.cit.; Niu & Batiza, 1994).

Like the MARNOK area, the 26°S segment can be used to assess the relative impact of both transform and non-transform segmentation. Blackman and Forsyth (1991) found that a large amplitude mantle Bouguer low of 35mgals, centred over the axial-high of the segment, was best modelled by assuming 100m crustal thickening plus a decrease in both the upper and lower crustal densities.

The sampling survey of Niu and Batiza (1994) has 15 dredges spaced about 7km apart, so the resolution of the survey is similar to that of the MARNOK segments. Tables 7.1, 7.2 and 7.3 respectively compare the morphological, petrological and geochemical features of the MARNOK segments with the 26°S segment.

7.4.2.1 Morphological features

The 26°S segment is longer than the two MARNOK segments put together, although it should be noted that if the Midway Discontinuity had a larger offset, the present 26°S segment would be divided into two segments, approximately the same size as the MARNOK area. The second feature that is immediately obvious from the bathymetry is that the 26°S segment has a very prominent axial-high which virtually fills the centre of the median valley. Hence the variation in relief is greater over the 26°S segment than it is over the MARNOK segments. Hence the 26°S segment seems more robust in terms of axial volcanism and shows a stronger degree of magmatic focusing (manifest as the prominent central bulge) than the MARNOK segments (figure 7.5).

The morphological effect of the transform is less prominent on the 26°S segment than for the MARNOK segment 1. This is probably because the Rio Grande has a much smaller offset than the Kane. The plunge in the axial bathymetry towards the RTI is less dramatic and the median valley asymmetry is less well-developed. However, MARNOK segment 1 and the 26°S segment show a similar development of median valley asymmetry towards the NTO, and both are symmetrical at the segment centre.

7.4.2.2 Petrological features

The mineral phases and mineral compositions of the MARNOK and 26°S segment are remarkably similar. There are two main differences between the two areas. Firstly, the plagioclase megacrysts are rarer in the 26°S segment suggesting that the magma chamber might have a higher proportion of melt in the mush of the magma chamber. Secondly, the 26°S segment has two petrographic groups with differing orders of crystallisation. The early fractionation of plagioclase in the type I petrological group is a reflection of the higher Ca in the parents of these lavas (see table 7.3).

	26°S segment on MAR	Segment 1, MARNOK	Segment 2, MARNOK
Length	100km	57km	35km
Depth of axial-high	2600m	3950m	3550m
Depth at end of NVR	4100m at N end 4100m at S end	4600m at N end 5000m at S end	4000m at N end 4500m at S end
Width of inner valley floor	17km in north filled with axial swell in centre 10km in south	8.5km in north 8 km at centre 15km at RTI	Lies within an oblique portion of MAR in north 13km in south
Relief over rift valley walls	1500m at N end (asymmetric) ~200m at centre (symmetric) 1500m at s end (slightly asymmetric)	1600m at NE end (slightly asymmetric) 500m minimum in centre (symmetric) 3000m at inside corner (strongly asymmetric)	500m over NW wall 1000m over E curving boundary fault (asymmetric) 2500m at S (asymmetric)
General morphology **(segment group of Sempéré et al., 1993)**	Group 1 "robust narrowgate" well-developed rift valley at ends of segment; gently rifted axial swell at centre	Group 1 "narrowgate" with bathymetric saddle at segment centre	Group 2, robust NVR, 400-600m high, flanked by marginal basins
Spreading rate	19.3 mm yr^{-1} to W 16.3 mm yr^{-1} to E	13.0 mm yr^{-1} to W 13.0 mm yr^{-1} to E at segment centre 8.0 mm yr^{-1} to E at transform	13.0 mm yr^{-1} to W 13.0 mm yr^{-1} to E
Discontinuities	Rio Grande transform to north; Midway Discontinuity (see text) 30km south of axial-high; Moore Discontinuity to south (2nd order NTO)	3rd order NTO to north Kane transform to south	2nd order NTO to north 3rd order NTO to south

Table 7.1 Comparison of physical features of 26°S and the MARNOK segments. Information for 26°S segment is taken from Grindlay et al. (1992).

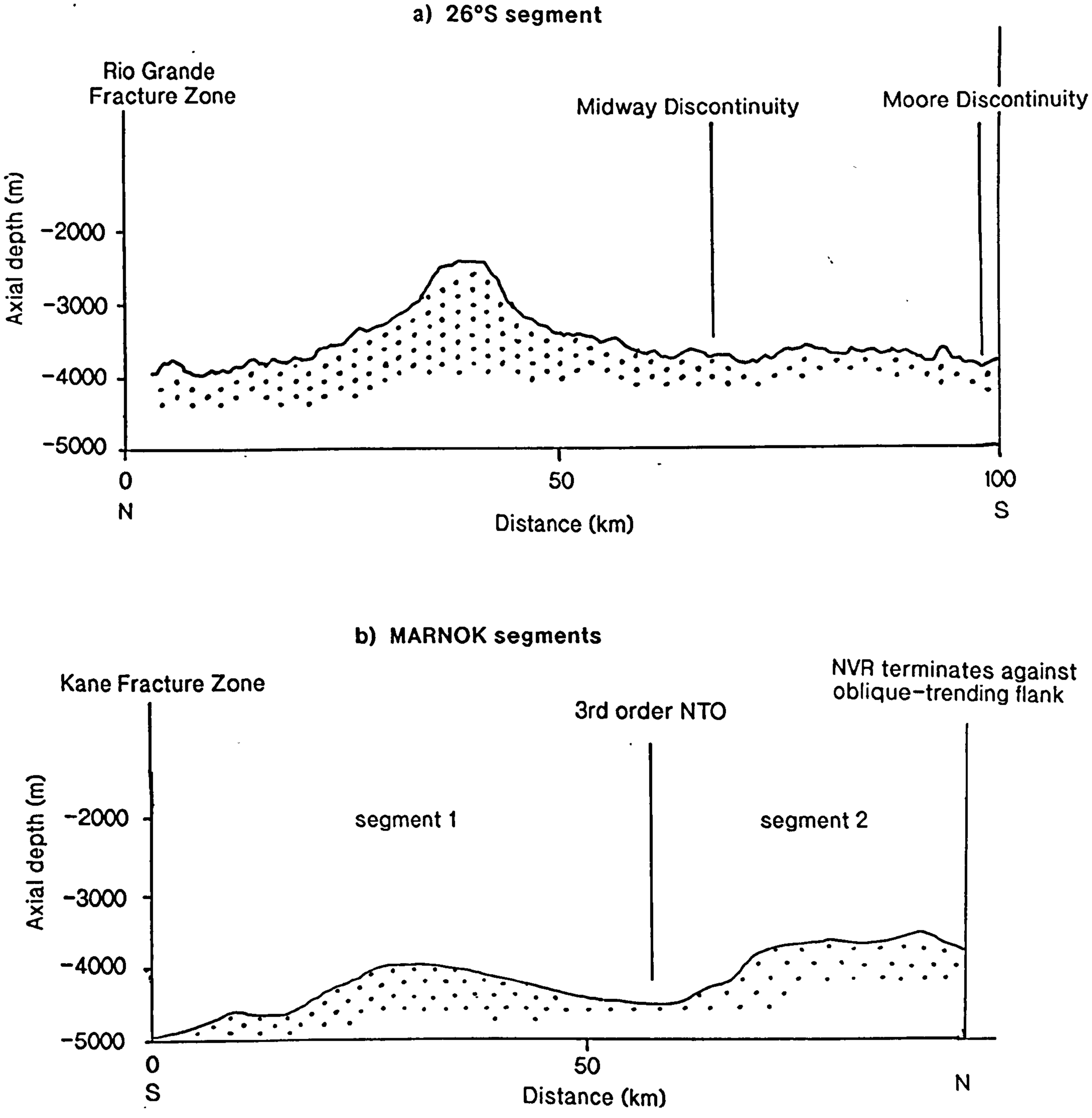

Figure 7.5 Comparison between axial depth of a) the 26°S segment and b) the MARNOK segments. Vertical exaggeration is ~10. Profile for the 26°S segment is adapted from Grindlay et al. (1992).

	26°S segment	MARNOK
Mineral phases	Low pressure assemblages: ol., plag. and rare cpx.	Low pressure assemblages: ol., plag. and rare cpx.
Order of crystallisation	Two petrographic types. Type I: plag. →plag. + ol. (mainly from segment centre) Type II: ol. →ol. + plag. (mainly from segment ends)	ol. →ol. + plag. (i.e. only type II of Niu & Batiza, 1994)
Megacrysts	Calcic plagioclase megacrysts, no reported along-axis variation	Calcic plagioclase megacrysts occur throughout area, but are more common in the TD and near the NTO.
Xenoliths	Crystalline clot, course-grained aggregate of plag. with minor ol. and cpx.	Crystalline clot, course-grained aggregate of plag. in active disequilibrium with host melt

Table 7.2 Comparison of petrography between the 26°S segment and MARNOK. Information on the 26°S segment is from Niu & Batiza (1994).

7.4.2.3 Geochemical features

Transform-related variations in the degree of mantle melting are not detected in the 26°S segment, in agreement with the result from the MARNOK area. Again, the geochemical systematics of the second-order segmentation are dominant. One of the most important contrasts between the two areas is the difference in the degree of melting and the along-axis melting systematics. The average degree of melting in the MARNOK area is less than in the 26°S segment, and whereas the MARNOK melting profile was uniform along-axis, the 26°S segment has higher degrees of melting in the segment centre than at the ends. Hence, whereas I attributed the along-axis variation in melt supply to melt migration processes in the MARNOK area, the 26°S segment requires a degree of focused adiabatic upwelling along-axis to explain the greater melt proportions in the centre of the segment. I will return to this issue later in the discussion.

There is an along-axis variation in fractionation within the type I lavas of the 26°S segment in the same manner as seen in MARNOK. However, this breaks down at the ends of the segment where more primitive type II lavas occur. The ranges of MgO values for the two segments are virtually identical, but the major element liquid-lines-

	26°S segment	MARNOK
Fo (mol %)	81.5 - 88.0	80.5 - 87.5
An (mol %) (phenocrysts)	65.0 - 87.0	58.0 - 91.0 (some megacrysts may be wrongly identified as phen.)
An (mol %) (megacrysts)	81.5 - 93.0	83.0 - 92.0
MgO (glass)	8.62 - 6.55 wt.%	8.7 - 6.5 wt.%
Liquid-line-of-decent and range of parental magmas	Type I have relatively well-defined LLD, with wide range in fractionation, but still show evidence of diverse parental compositions. Type II have poorly-defined LLD, small range in fractionation (mostly primitive) and have greater diversity in parental compositions than type I. (Type I have higher Ca and lower Fe, Ti and Na than type II, but same Al.)	Well-defined LLD; very little evidence for diverse parental magmas in major element chemistry. MARNOK samples have lower fractionation-corrected Ca and Fe and higher Na than the 26°S lavas.
Fractionation systematics along-axis	Type I is primitive at the centre, and fractionated at the ends. Type II is restricted to the ends and is relatively primitive. Combination of type 1 and type II produces "W" and "M" patterns along-axis.	Primitive lavas at the centre. Fractionated lavas at the ends.
Degree of melting[2]	15% -18% higher in centre of segment.	15.5% uniform along-axis.
[La/Sm]N[3]	0.468 - 0.596	0.547 - 0.800
Mantle isotopic diversity	Isotopic ratios within the range of NMORB. Small significant variations in Sr and Nd isotopes correlate with trace element ratios indicating a small scale mantle heterogeneity.	Isotopic ratios within the range of NMORB. Very small significant variations in Sr and Pb isotopes do not correlate with trace elements.

Table 7.3 Comparison of mineral chemistry and geochemistry between the 26°S segment and MARNOK. Information on the 26°S segment is from Niu & Batiza (1994).

---

[2] % melting is calculated using equations of Niu & Batiza (1991) because the 26°S data is thought to contain anomalous amounts of Na and Al in the mantle source and therefore Niu & Batiza (1994) are are unable to use the method of Plank & Langmuir (1992). Instead they adapt the equations of Nui & Batiza (1991) to exclude Na and Al. Note that the method of Niu & Batiza (1991) produces systematically higher values of batch melting than Plank & Langmuir (1992). For explanation of reason for this see Niu & Batiza (1994).

[3] [La/Sm]N: chondrite-normalised REE ratio that reflects the gradient of the left hand side of a chondrite-normalised trend. Values are from whole-rock analyses.

of-decent show a much greater diversity in parental compositions at 26°S. A greater diversity of parental lavas is a consequence of the variations in the degree of partial melting mentioned earlier, but as most of the scatter is from the type II samples at the end of the segment there must be some other factor operating. Niu and Batiza (1994) suggest the type II lavas are erupted from small chambers with short residence times at the end of the segment.

In my MARNOK model I suggest that the upper crustal chambers at the ends of the segment have *longer* residence times and generate more fractionated lavas, because of the low replenishment rate and the generally cooler environment. However, localities like the nested seamounts, which are relatively primitive and have diverse parental compositions, erupt where there is little or no ponded magma in the crust. I suggest that the type II samples result from a similar plumbing system to the nested seamounts, implying that there is little or no ponded magma for 10km from the Rio Grande Fracture Zone and 20km from the Moore Discontinuity. Correspondingly the type I samples are equivalent to the majority of samples in MARNOK area, which I hypothesise are erupted from a steady-state, mush-filled chamber. The type I samples do have a different order of crystallisation from the MARNOK suite, but this can be explained by the higher Ca_8 in the 26°S lavas, which is a consequence of their higher degrees of partial melting.

The MARNOK samples also have lower Fe_8 than the 26°S data. Hence, in addition to the melt fraction being greater, the average melt depth at 26°S is also deeper (Klein & Langmuir, 1987). These aspects of the geochemistry imply that there are greater mantle potential temperatures for the 26°S area of the South Atlantic.

Both MARNOK and the 26°S segment have small significant variations in radiogenic isotopes, but whereas these can not be correlated with any trace element variations in the MARNOK area, they can in the 26°S segment. This implies that the variations in highly incompatible elements at 26°S are caused by small-scale mantle heterogeneity. In the MARNOK area the diversity in incompatible elements is attributed to variable mixing with small degree melts from the base of the melting column. It is interesting that the MARNOK rocks show a greater range in incompatible elements than 26°S despite the variable source in the South Atlantic segment (see range of [La/Sm]N in Table 7.3). It seems that the diversity in parental compositions in the MARNOK area is reflected by the highly incompatible trace element chemistry, while the diversity at 26°S is reflected by the major element chemistry. This may be the result of some fundamental contrast in the melting regimes, as will be discussed below.

7.4.3 Summary and implications

The differences in axial topography, petrology and geochemistry between the 26°S segment and the MARNOK segments are consistent with the former having greater degrees of mantle melting resulting from deeper mantle upwelling, probably because of a slightly higher mantle potential temperature. Not only is the degree of mantle melting higher for the 26°S segment, but the melt-flux is also more focused, as indicated by the very prominent axial-high and the inferred lack of a steady-state, mushy magma chamber at the end of the segment. The variation in extent of melting across the 26°S segment implies that the underlying mantle is focusing along-axis as it upwells. It seems that focused upwelling acts to homogenise small degree melts from the base of the melting column but produces more variation in terms of the accumulated melts at the top of the melt column. In contrast, focused melt migration preserves the signature of subtle variations in small-degree melt accumulation from the base of the melting column, but accumulation of incremental melts throughout the bulk of the melt column is relatively uniform.

In my review of segmentation models in chapter 1, I explained that a 2D pattern of mantle upwelling, common at fast spreading rates, is expected to break down to a 3D pattern at slower spreading rates where the buoyancy forces become more important (Parmentier & Phipps Morgan, 1990; Sparks & Parmentier, 1990; Jha et al., 1994.) Hence it is not particularly surprising to find the variation in degree of partial melting along-axis in the 26°S segment. The interesting result of this study is that the slower-spreading MARNOK area does not show a similar variation, but instead appears to have essentially 2D mantle upwelling with focused melt migration towards the centre of the segment. This implies that the initiation of a 3D mantle flow is not entirely dependent on the spreading rate. The greater degree of partial melting in the 26°S segment should enhance the buoyancy forces and may well be the root cause of the focused mantle upwelling, which in turn, has governed the morphology, petrology and geochemistry of this segment.

In fact the three segments discussed here (26°S, segment 1, MARNOK and segment 2, MARNOK) define a progression from high melt-flux and high degrees of focusing to low melt-flux and low degrees of focusing. To conclude, I suggest that at slow spreading rates, second order variations in crustal thickness are achieved primarily by melt migration which is not controlled by the focusing of mantle upwelling. There is likely to be a degree of feedback in the melt migration mechanism so that larger melt-fluxes result in higher degrees of focusing. I suggest that the transition between essentially 2D mantle flow and 3D mantle flow occurs just above the degree of melting for MARNOK, and just below the average degree of melting at 26°S (see

table 7.3). Hence, if the degree of melting increases above about 13% (using the method of Plank and Langmuir [1992]) or 15.5% (using the method of Niu and Batiza [1991]) then the additional buoyancy forces provided by the increased melt fraction initiate 3D focused mantle upwelling, which in turn results in even greater melt focusing. This positive feedback is consistent with melt retention buoyancy acting to a small degree in areas of high melt-flux.

BLANK IN ORIGINAL

Chapter 8

Conclusions

Of the making of books there is no end, and much study wearies the soul.
Now all has been heard;
Here is the conclusion of the matter:
Ecclesiastes 12 vs 12b-13a.

8.1 Geological interpretation of TOBI sidescan sonar

I establish a basis for the geological interpretation of TOBI sidescan sonar, by identifying a wide range of textural terrains of volcanic and tectonic origin. These are later modified by sedimentation and mass-wasting. The geological significance of these textural terrains is established by correlation with deep-tow camera traverses, submersible dives, dredge localities and the 7.5kHz profiler. Volcanic terrains include hummocky ridges and mounds (comprising pillow flows), flat-topped seamounts, cratered cones, areas of tumescence, smooth textured sheet flows and pillow fields. Tectonic terrains include fissures and different scales of faulting. Aligned hummocky ridges are often related to underlying faults or eruption through a fault plane. The mass wasting of fault scarps can produce talus fans, erosional gullies, landslides, sediment slumps, and debris flows. Very steep-sided mounds may be of hydrothermal origin, but there is little evidence to back this claim.

8.2 Volcanic morphologies and magmatic plumbing

Hummocky ridges are structurally controlled eruptions which have undergone a small degree of flow focusing. Lavas sampled along a single hummocky ridge are all related to a common parent, but can show a variation in the degree of fractionation along their length, which may result from the tapping of a density-stratified magma chamber, ponded at the brittle-ductile transition. A small degree of lateral dyke propagation probably occurs, but is unlikely to be responsible for the variations in degree of fractionation.

Thatcher's Nose is a chain of composite hummocky seamounts with steep summit cones. It is formed from a relatively primitive magma which has entrained 40% modal plagioclase megacrysts. The high viscosity of this highly phyric lava is responsible for the distinctive shape of the edifice.

The flat-topped seamounts are preferentially located at the ends of segments, although they are not any taller than adjacent hummocky mounds. They are often located over faults and next to the median valley walls. Their parental magmas are distinct from nearby hummocky terrain. The petrography indicates little crustal ponding or interaction with other melts, but a relatively long period of time spent in an eruptive conduit.

The hackly/jumbled sheet flow type is analogous to transitional pahoehoe. It is indicative of high viscosities as well as the high flow rates predicted by Griffiths and Fink (1992a). After the consideration of many factors, I conclude that rapid quenching under high hydrostatic pressure accounts for the differing characteristics of hackly deep-sea flows and mature subaerial aa. I suggest that rapid quenching may also be a primary factor in producing the differences between deep-sea and subaerial volcanic morphologies.

Flat-topped seamounts have similar petrological and geochemical characteristics to shield volcanoes in Iceland. Their morphologies are especially akin to the subglacial seamounts which may be a consequence of the common presence of water in the two eruptive environments. Hummocky ridges are correspondingly analogous to fissure swarms. The steep flanks of the flat-topped seamounts may form by the stacking of exogenous low relief flows around a vent. These flows are shortened compared with the subaerial shields as a result of rapid quenching and thus pile up around the vent promoting the growth of a steep flank. I reject the hypothesis that the flat top is produced by a limiting magmatic head, because it is inconsistent with the variation in seamount height and morphology along-axis in the MARNOK area. I tentatively suggest that the low relief of the summit plateaux is a result of rapid flow rates. These may be maintained by enhanced CO_2 exsolution during eruption from relatively high pressures (e.g. at the base of the crust).

Drawing on a comparison with Iceland, I suggest a model for crustal plumbing at accretionary plate boundaries. In this model, melt reaching the base of the crust usually percolates relatively slowly upwards, into a mush-filled magma chamber, similar to that proposed by Sinton and Detrick (1992). This magma chamber is the source of the hummocky pillow flows that dominate the ridge crest. If there is a rifting event, magma is drawn more rapidly into the magma chamber, entraining some of the plagioclase megacrysts from the lower parts of the mush zone to produce features such as Thatcher's Nose. If there is no upper crustal magma chamber, then a rifting event may allow the magma body to pass through the entire thickness of the crust to erupt as a shield-like, flat-topped seamount. The relatively low ambient temperature of the crust and the large vertical extent of the conduit promote early fissure focusing

into a pipe to produce a circular edifice. Thus seamount eruption should be characteristic of rifting in a relatively low magma-flux environment (e.g. segment ends), or after a period of magmatic starvation.

8.3 Features relating to the transform

The TD extends along most of the southern half of segment 1, up to 26km from the transform valley. There is no decrease in the degree of bulk mantle melting towards the transform. Instead, the magmatic transform effect manifests itself by a reduction in the magma supply over the TD, reflected by unfocused, small, discrete volcanic episodes, which are probably from individual magma bodies separated in space and time. The relative lack of a magmatic transform effect leads to the conclusion that transform segmentation is primarily of a tectonic origin.

The orientation of fissure ridges in the RTI is probably controlled by flexural downbending of the lithosphere in response to the formation of the nodal basin and the increasing throw on the inside corner towards the transform. For flexural processes to be operating the lithosphere at the MARNOK RTI must be thick enough to act as a coherent 'plate'. The observation is also consistent with a high degree of coupling between the brittle plate and ductile flow (Chen and Morgan, 1990a) as a result of the enhanced hydrothermal circulation associated with the fracture zone (Chen and Morgan, 1990b).

The median ridge in the transform probably comprises a sheared fault block and is bounded to the north by the PTDZ. In the west, near the RTI, this sheared fault block shows evidence for increasing serpentinite diapirism. The low shear strengths of the serpentinite protrusions are thought to initiate slope failure, which leads to the widening and flattening of the median ridge. The initiation of serpentinite diapirism may be related to the transtensional stress regime in this area, or may be a consequence of the close proximity of the large inside corner wall fault, as both these features may allow seawater penetration to great depths.

8.4 Segmentation and melting systematics

The two second order segments in the MARNOK area have contrasting volcanic morphology, valley asymmetry, temporal variations and hydrothermal features.

Segment 1, adjacent to the transform, is a narrowgate-type segment, with a symmetrical median valley at the centre, which becomes increasingly asymmetric towards the ends. The northern half of segment 1 has a very uniform low relief NVR (~100m high), which is flanked by a narrow zone of unsedimented, fissured terrain and continuous ridge-parallel narrow fault terraces. The bathymetric saddle is

characterised by short-lived eruptive episodes with high effusion rates, which subsequently are rapidly dismembered by tectonism, preventing the formation of a mature volcano. This segment shows little evidence of hydrothermal activity.

With the exception of the RTI area, the inner valley of segment 2 is slightly wider than that of segment 1. It has a robust NVR, 400-600m high, which is characterised by syn-tectonic magmatism. The older crust in the marginal basins reflects a large time gap between ridge-constructing episodes. The northern half of the segment lies within a NE trending oblique portion of the MAR. The valley floor located within this oblique zone and in the marginal basin to the NE of the NVR comprises relative young, but slightly tectonised crust, reflecting the changing orientation of the NVZ to the NE of segment 2. Rocks recovered from this segment have hydrothermal precipitates.

The second order segmentation dominates the magmatic systematics. I report a variation in the degree of fractionation along-axis in segment 1, with primitive lavas at the centre of the segment and more fractionated compositions at the ends. A trend of increasing MgO content towards the axial-high of segment 2 is also apparent, but has more scatter than that of segment 1. The ends of the segments also have a greater variation in parental compositions.

Variations in magnetization along-axis are controlled by variations in the geochemistry of the lavas. The higher proportion of magnetic minerals associated with the fractionated lavas produce highs in the crustal magnetization at the end of the segment.

There is no variation in the bulk degree of melting along-axis, favouring melt migration rather than mantle upwelling as the primary control on the variation in crustal supply along-axis in the MARNOK area. The differential enrichments in highly incompatible trace elements are attributed to derivation from mantle sources with varying degrees of short-lived enrichment. This is equivalent to the selective tapping of small melt-fractions from the base of a melting column during the melting of an adiabatically upwelling source.

The scale of petrological segmentation ranges from 3-6km in the RTI up to 11km in the north of segment 1. It tends to correlate with distinct volcanic constructions on the sidescan, especially in the TD. Petrological segmentation has a length scale which precludes extensive mixing and along-axis transport in the crust. The variations in parental lavas along the ridge crest will also be the result of temporal changes in the magma chamber.

A model is proposed that relates the morphological and petrogenetic variations in second order segmentation to aspects of the melt supply. Regular, focused injections of magma associated with a relatively large overall melt-flux maintain a shallow brittle-ductile transition in the centre of the segment. This results in symmetrical valley wall faulting according to the hypothesis of Harper (1985). These magmatic conditions will also promote the development of a relatively continuous, well-mixed magma chamber with low crustal residence times in the segment centre, and thus account for the primitive compositions erupted at the axial-highs. With decreasing magmatic input, the brittle-ductile transition is lowered, the valley wall faulting becomes asymmetric, the median valley widens, the residence time of magma within the crust increases and more fractionated compositions erupt. These variations in melt supply can account for variations within and between ridge segments.

Focused mantle upwelling acts to homogenise small degree melts from the base of the melting column but produces more variation in terms of the accumulated melts at the top of the melt column. In contrast, focused melt migration preserves the signature of subtle variations in small-degree melt accumulation from the base of the melting column, but accumulation of incremental melts throughout the bulk of the melt column is relatively uniform.

At slow spreading rates, second order variations in crustal thickness are achieved primarily by melt migration with no along-axis focusing in mantle upwelling. If the degree of melting increases above about 13-15% then the increased melt fraction provides sufficient additional buoyancy to initiate 3D focused mantle upwelling. There is likely to be a degree of feedback in the melt migration mechanism so that larger melt-fluxes result in higher degrees of focusing. Hence the degree and distribution of partial melt *can* influence the mantle flow at moderately high degrees of partial melting.

8.5 Suggested future work.

8.5.1 Within MARNOK area

The main data deficiencies in my study of the MARNOK area are gravity and seismics, although a gravity survey has recently been completed (Fujimoto et al. 1994). These can be used to constrain crustal thickness variations, which can be compared with those predicted from the segmentation model. A microseismicity study may confirm variations in the brittle-ductile transition along-axis.

Detailed magnetic modelling and direct magnetisation measurement are required to confirm that the geochemical variations are sufficient to cause the along-axis variations in magnetization.

U-Th disequilibria studies will provide information on temporal aspects of melting and segregation processes. This may reveal a difference in the plumbing system between the hummocky ridges and the flat-topped seamounts.

Ion probe measurements on the glasses and melt inclusions should help to constrain the nature of the small melt fractions in the melting column and the refractory melts from which the plagioclase megacrysts form.

Detailed modelling of magma chamber processes, including assimilation-fractional crystallisation and boundary-layer fractionation should confirm and quantify variations in crustal residence time along-axis.

8.5.2 Regional studies

Groundtruthing of sidescan textures off-axis may help to evaluate models predicting large detachment faults at ridge discontinuities. More rigorous groundtruthing of the flat-topped seamounts is required to confirm whether they are indeed formed from exogenous piles of lavas with higher flow rates than hummocky mounds.

With the wealth of SeaBeam and TOBI data now available, a systematic study should be made of the relationship between the volcanic morphologies on the ridge crest, the degree of asymmetry of the median valley and the cumulative strain across a segment This information should enable my segmentation and magmatic plumbing models to be tested on a regional scale. Additional information from microseismicity studies on correlations with the brittle-ductile transition and the locations and proportions of ponded magma would also be highly beneficial.

An investigation of a range of segments at slow spreading rates should confirm whether increasing degrees of partial melting are accompanied by increased melt focusing and buoyant mantle flow.

BLANK IN ORIGINAL

References

ABRAMS, L. J., DETRICK, R. S. & FOX, P. J. 1988. Morphology and crustal structure of the Kane Fracture Zone Transverse Ridge. *Journal of Geophysical Research,* **93,** 3,195-3,210.

AHERN, J. L & TURCOTTE, D. L. 1979. Magma migration beneath an ocean ridge, *Earth and Planetary Science Letters,* **45**, 115-122.

ALLERTON, S., MURTON, B. J., SEARLE, R. C. & JONES, M. 1995. Extensional faulting and segmentation of the Mid-Atlantic Ridge North of the Kane Fracture Zone (24°00' to 24°40'). *Marine Geophysical Researches,* **17,** 37-61.

ANDERSON, E. M. 1936. The dynamics of the formation of cone-sheets, ring-dykes, and cauldron subsidences. *Proceedings of the Royal Society of Edinburgh,* **56**, 128-157.

ANDERSON, E. M. 1938. The dynamics of sheet intrusion. *Proceedings of the Royal Society of Edinburgh,* **58**, 242-251.

APPELGATE, B. T. 1990. Volcanic and structural morphology of the south flank of Axial Volcano. *Journal of Geophysical Research,* **95,** 12,765-12,783.

APPELGATE, B. T. & EMBLEY, R. W. 1992. Submarine tumuli and inflated tube-fed flows on Axial Volcano, Juan Fuca Ridge. *Bulletin of Volcanology,* **54,** 447-458.

APPELGATE, B. T. & SHOR, A. N. 1994. The northern Mid-Atlantic and Reykjanes Ridges: Spreading center morphology between 55°50'N and 63°00'N. *Journal of Geophysical Research,* **99,** 17,935-17,956.

ARCYANA, 1975. Transform Fault and Rift Valley from Bathyscape and Diving Saucer. *Science,* **190**, 108-115.

ARGUS, D. F., GORDON, R. G., DEMETS, C. & STEIN, S. 1989. Closure of the Africa-Eurasia-North America plate motion circuit and tectonics of the Gloria fault. *Journal of Geophysical Research,* **94,** 5,585-5,603.

ATWATER, T. M. 1979. Constraints from the FAMOUS area concerning the structure of the oceanic section. *In*: TALWANI, M., HARRISON, C. G. & HAYES, D. E. (eds) *Deep Drilling Results in the Atlantic Ocean: Ocean crust.* Maurice

Ewing Series, **2,** American Geophysical Union, Washington D.C., 33-42.

AUMENTO, F. 1968. The Mid-Atlantic Ridge near 45°N. II. Basalts from the area of Confederation Peak. *Canadian Journal of Earth Science*, **5**, 1-21.

BALLARD, R. D. & MOORE, J. G. 1977. *Photographic Atlas of the Mid-Atlantic Ridge Rift Valley*. Springer-Verlag, New York.

BALLARD, R. D., BRYAN, W. B., HEIRTZLER, J. R., KELLER, G., MOORE, J. G. & VAN ANDEL, T. J. 1975. Manned submersible observations in the FAMOUS Area: Mid-Atlantic Ridge. *Science,* **190,** 103-108.

BALLARD, R. D., FRANCHETEAU, J., JUTEAU, T., RANGAN, C. & NORMARK, W. 1981. East Pacific Rise at 21°N: The volcanic, tectonic and hydrothermal processes of the central axis. *Earth and Planetary Science Letters*, **55**, 1-10.

BALLARD, R. D., HOLCOMB, R. T. & VAN ANDEL, T. H. 1979. The Galapagos Rift at 86°W: Sheet Flows, Collapse Pits and Lava Lakes of the Rift Valley. *Journal of Geophysical Research,* **84,** 5,407-5,422.

BALLARD, R. D. & VAN ANDEL, T. H. 1977. Morphology and tectonics of the inner rift valley at latitude 36°50'N on the Mid-Atlantic Ridge. *Geological Society of America Bulletin,* **88,** 507-530.

BARONE, A. M. & RYAN, W. B. F. 1988. Along-axis variations within the plate boundary zone of the southern segment of the Endeavour Ridge. *Journal of Geophysical Research,* **93,** 7,856-7,868.

BARONE, A. M. & RYAN, W. B. F. 1990. Single plume model for Asynchronous formation of the Lamont seamounts and adjacent East Pacific Rise terrains. *Journal of Geophysical Research,* **95,** 10,801-10,827.

BARTH, G. A., KASTENS, K A & KLEIN, E. M., 1994. The Origin of Bathymetric Highs at Ridge-Transform Intersections: A Multi-Disciplinary Case Study at the Clipperton Fracture Zone. *Marine Geophysical Researches,* **16,** 1-50.

BATIZA, R. 1982. Abundances, distribution and sizes of volcanoes in the Pacific Ocean and implications for the origin of non-hotspot volcanoes. *Earth and Planetary Science Letters,* **60,** 195-206.

BATIZA, R. & NIU, Y. 1992. Petrology and magma chamber processes at the East Pacific Rise ~ 9° 30' N. *Journal of Geophysical Research,* **97,** 6,779-6,797.

BATIZA, R. & VANKO, D. 1983. Volcanic development of small conic central volcanoes on the flanks of the East Pacific Rise : inferred from narrow beam echo sounder surveys. *Marine Geology,* **54**, 53-90.

BATIZA, R. & VANKO, D. 1984. Petrology of young pacific seamounts. *Journal of Geophysical Research,* **89**, 11,235-11,260.

BATIZA, R., FORNARI, D. J., VANKO, D. A. & LONSDALE, P. 1984. Craters, calderas,

and hyaloclastites on young Pacific seamounts. *Journal of Geophysical Research,* **89,** 8,371-8,390.

BATIZA, R, FOX, P. J, VOGT, P. R., CANDE, S. C., GRINDLAY, N. R., MELSON, W. G. & O'HEARN, T. 1989. Morphology, abundance, and chemistry of near-ridge seamounts in the vicinity of the Mid-Atlantic Ridge~26°S. *Journal of Geology,* **97,** 209-220.

BELLAICHE, G., CHEMINEE, J. L. & FRANCHETEAU, J. 1974. Inner floor of the Rift Valley: first submersible study. *Nature,* **250,** 558-560.

BENDER, J. F., LANGMUIR, C. H. & HANSON, G. N. 1984. Petrogenesis of basalt glasses from the Tamayo Region, East Pacific Rise. *Journal of Petrology,* **25,** 213-254.

BERCOVICI, D., DICK, H. J. B. & WAGNER, T. P. 1992. Non-linear viscoelasticity and the formation of Transverse Ridges. *Journal of Geophysical Research,* **97,** 14,195-14,206.

BIENVENU, P., BOUGAULT, H., JORON, J. L., TREUIL, M. & DMITRIEV, L. 1990. MORB alteration: Rare earth element / non-rare earth element hygromagaphile element fractionation. *Chemical Geology,* **82,** 1-14.

BJÖRNSSON, A. 1985. Dynamics of crustal rifting in NE Iceland. *Journal of Geophysical Research,* **90,** 10,151-10162.

BJÖRNSSON, A., JOHNSEN, G., SIGURDSSON, S., THORBERGSSON, G. & TRYGGVASON, E. 1977. Current rifting episode in North Iceland. *Nature,* **266**, 318-323.

BJÖRNSSON, A., JOHNSEN, G., SIGURDSSON, S., THORBERGSSON, G. & TRYGGVASON, E. 1979. Rifting of the plate boundary in northern Iceland 1975-78. *Journal of Geophysical Research,* **84**, 3,029-3,038.

BLACKMAN, D. K. & FORSYTH, D. W. 1991. The effects of plate thickening on three-dimensional, passive flow of the mantle beneath mid-ocean ridges. *In*: PHIPPS MORGAN, J., BLACKMAN, D. K. & SINTON, J. M. (eds) *Mantle flow and melt generation beneath mid-ocean ridges.* Geophysical Monograph Series, American Geophysical Union, Washington D.C., **71,** 311-326.

BLONDEL, P. & PARSON, L. 1994. Sonar Processing in the U.K. - A short review of existing potential & new developments for the BRIDGE Community. *Institute of Oceanographic Sciences, Bridge publication.*

BONATTI, E. 1976. Serpentinite protrusions in the oceanic crust. *Earth and Planetary Science Letters,* **32,** 107-113.

BONATTI, E. & HARRISON, C. G. A. 1988. Eruption styles of basalt in oceanic spreading ridges and seamounts: effect of magma temperature and viscosity. *Journal of Geophysical Research,* **93**, 2,967-2,980.

BOTTINGA, Y. & JAVOY, M. 1990. Mid-ocean ridge basalt degassing: bubble

nucleation. *Journal of Geophysical Research,* **95,** 5,125-5,131.

BOUGAULT, H. & TREUIL, M. 1980. Mid-Atlantic Ridge: zero-age geochemical varations between Azores and 22°N. *Nature*, **286**, 209-212.

BOWEN, N. L. 1928. *The evolution of the igneous rocks.* Princeton University Press, New Jersey.

BOYNTON, W. V. 1984. Cosmochemistry of the rare earth elements: meteorite studies. *In*: HENDERSON, P. (ed.) *Rare earth element geochemistry.* Elsevier, Amsterdam, pp.63-114.

BRANDSDOTTIR, B. & EINARSSON, P. 1979. Seismic activity associated with the September deflation of the Krafla Central Volcano in N.E.-Iceland. *Journal of Volcanology and Geothermal Research,* **6**, 197-212.

BRIAIS, A., SLOAN, H., PARSON, L. M. & MURTON, B. L. 1994. Tectonic and volcanic processes in the axial valley of the Mid-Atlantic Ridge 27°-30°N from TOBI images. *EOS Transactions, American Geophysical Union,* **75**, 660.

BROWN, J. R. & KARSON, J. A. 1988. Variation in axial processes on the Mid-Atlantic Ridge: The Median valley of the MARK area. *Marine Geophysical Researches*, **10**, 109-138.

BRUCE, P. M. & HUPPERT, H. E. 1989. Thermal control of basalt fissure eruptions. *Nature,* **342,** 665-666.

BRUCE, P. M. & HUPPERT, H. E. 1990. Solidification and melting along dykes by the laminar flow of basaltic magma. *In*: RYAN, M. P.(ed.) *Magma Transport and Storage.* John Wiley and Sons, London & New York, 87-101.

BRYAN, W. B. 1983. Systematics of modal phenocryst assemblages in submarine basalts: petrologic implications. *Contributions to Mineralogy and Petrology,* **83,** 62-74.

BRYAN, W. B. & MOORE, J. G. 1977. Compositional variations of young basalts in the Mid-Atlantic Ridge rift valley near lat. 36°49'N. *Geological Society of America Bulletin,* **88,** 556-570.

BRYAN, W. B., HUMPHRIS, S. E., THOMPSON, G. & CASEY, J. F. 1994. Comparative volcanology of small axial eruptive centers in the MARK area. *Journal of Geophysical Research,* **99**, 2,973-2,984.

BRYAN, W. B., THOMPSON, G. & LUDDEN, J. N. 1981. Compositional variation in normal MORB from 22°-25°N; Mid-Atlantic Ridge and Kane Fracture Zone. *Journal of Geophysical Research,* **86,** 11,815-11,836.

BUCK W. R. & SU, W. 1989. Focused mantle upwelling below mid-ocean ridges due to feedback between viscosity and melting. *Geophysical Research Letters,* **16,** 641-644.

BURNETT, M. S., CARESS, D. W. & ORCUTT, J. A. 1989. Tomographic image of the East Pacific Rise at 12°50'N. *Nature*, **339**, 206-208.

CANN, J. R. 1974. A model for oceanic crustal structure developed. *Geophysical Journal of the Royal Astronomical Society,* **39**, 169-187.

CANN, J. R., SMITH, D. K., BROOKS, B., DOUGHERTY, M. E., GARLAND, S., KEETON, J., LIN, J., MCALLISTER, E., MACLEOD, C., PASCOE, R., & SPENCER, S. 1992b. Building the crust at the Mid Atlantic Ridge. *RRS Charles Darwin Cruise 65 Report, University of Leeds, U.K.*

CANN, J. R., SMITH, D. K., DOUGHERTY, M. E., LIN, J., BROOKS, B., SPENCER, S., MACLEOD, C., KEETON, J., MCALLISTER, E., PASCOE, R. & GARLAND, S.C. 1992a. Major landslides in the MAK Median Valley, 25°-30°N: Their role in crustal construction and plutonic exposure. *Abstract: BRIDGE Open Science Meeting 1992*, 11.

CARBOTTE, S. M. & MACDONALD, K. C. 1994. The axial topographic high at intermediate and fast spreading ridges. *Earth and Planetary Science Letters,* **128,** 85-97.

CARBOTTE, S. M., WELCH, S. M. & MACDONALD, K. C. 1991. Spreading rates, rift propagation, and fracture zone offset histories during the past 5 my on the Mid-Atlantic Ridge; 25°-27°'S and 31°-34°30'S. *Marine Geophysical Researches,* **13,** 51-80.

CARESS, D. W., BURNETT, M. S. & ORCUTT, J. A. 1992. Tomographic image of the axial low velocity zone at 12°50'N on the East Pacific Rise. *Journal of Geophysical Research,* **97,** 9,243-9,263.

CHALMERS, B. 1964. *Principles of Solidification.* John Wiley and Sons, London & New York.

CHEN, Y. & MORGAN, W. J. 1990a. A nonlinear rheology model for mid-ocean ridge axis topography. *Journal of Geophysical Research,* **95**, 17,583-17,604.

CHEN, Y. & MORGAN, W. J. 1990b. Rift valley / no rift valley transition at Mid-ocean ridges. *Journal of Geophysical Research,* **95**, 17,571-17,581.

CHRISTIE, D. M. & SINTON J. M. 1981. Evolution of abyssal lavas along propogating segments of the Galapagos spreading center. *Earth and Planetary Science Letters,* **56**, 321-335.

COLLETTE, B. J. 1974. Thermal contraction joints in a spreading seafloor as origin of fracture zones. *Nature,* **251,** 299-300.

COLLETTE, B. J. 1986. Fracture Zones in the North Atlantic: Morphology and a model. *Journal of the Geological Society, London,* **143,** 763-774.

COOPER, R. F. & KOHLSTEDT, D. L. 1984. Solution-precipitation enhanced diffusional

creep of partially molten olivine-basalt aggregates during hot-pressing, *Tectonophysics,* **107,** 207-233.

COOPER, R. F. & KOHLSTEDT, D. L. 1986. Rheology and structure of olivine - Basalt partial melts. *Journal of Geophysical Research*, **91,** 9,315-9,323.

CORDERY, M. J. & PHIPPS MORGAN, J. 1992. Melting and mantle flow beneath a mid-ocean spreading center. *Earth and Planetary Science Letters*, **111**, 493-516.

CORMIER, M.-H., DETRICK, R. S. & PURDY, G. M. 1984. Anomalously thin crust in oceanic fracture zones: new seismic constraints from the Kane Fracture Zone. *Journal of Geophysical Research*, **89,** 10,249-10,266.

COX, K. G., BELL, J. D. & PANKHURST, R. J. 1979. *The interpretation of igneous rocks.* Allen and Unwin, London.

CRANE, K. 1985. The spacing of rift axis highs: dependence upon diapiric processes in the underlying athenosphere. *Earth and Planetary Science Letters*, **72**, 405-414.

CRISP, J. A. & BALOGA, S. M. 1990. A model for lava flows with two thermal components. *Journal of Geophysical Research,* **95,** 1,255-1,270.

DAINES, M. J. & RICHTER, F. M. 1989. An experimental method for directly determining the interconnectivity of melt in a partially molten system. *Geophysical Research Letters,* **15,** 1,459-1,462.

DAMUTH, J. E. 1980. Migrating sediment waves created by turbidity cuirrents in the northern South China Basin. *Geology,* **7,** 520-523.

DECKER, R. W. 1987. Dynamics of Hawaiian volcanoes: an overview. *U.S. Geological Survey Professional Papers,* **1350,** 997-1018.

DELANY, P. & POLLARD, D. D. 1982. Solidification of basaltic magma during flow in a dike. *American Journal of Science,* **282**, 856-885.

DELANY, P., POLLARD, D. D., ZIONY, J. I. & MCKEE, E. H. 1986. Field relations between dykes and joints: emplacement processes and paleostress analysis. *Journal of Geophysical Research,* **91,** 4,920-4,938.

DEMETS, C., GORDON, R. G., ARGUS, D. F. & STEIN, S. 1990. Current plate motions. *Geophysical Journal International,* **101,** 425-478.

DEPLUS, C., MAIA, M., ASLANIAN, D. & GENTE, P. 1992. Segmentation of the Mid-Atlantic Ridge south of the Kane Fracture Zone revealed by gravity anomalies. *EOS Transactions, American Geophysical Union,* **73,** 568.

DETRICK, R. S. & PURDY G. M. 1980. The crustal structure of the Kane Fracture Zone. *Journal of Geophysical Research,* **85,** 3,759-3,778.

DETRICK, R. S., BUHL, P., VERA, E., MUTTER, J., ORCUTT, J., MADSEN, J. &

BROCHER, T. 1987. Multichannel seismic imaging of crustal magma chamber along the East Pacific Rise. *Nature*, **326**, 35-41.

DETRICK, R. S., FOX, P. J., SCHULZ, N., POCKALNY, R., KONG, L., MAYER, L. & RYAN, W. B. F. 1990. Geological and tectonic setting of the MARK area. *Initial Reports of the Deep Sea Drilling Project*, **109**, U.S. Government Printing Office, Washington D.C., 15-22.

DETRICK, R. S., NEEDHAM, D. & RENARD, V. 1992. Variations in gravity, crustal thickness and morphology along the MAR between the Oceanographer and Hayes FZs. *EOS Transactions, American Geophysical Union,* **73,** 568.

DETRICK, R. S., NEEDHAM, D., RENARD, V. & LANGMUIR, C. 1991. Variations in gravity, anomalies on the Mid-Atlantic Ridge from the Hayes Fracture Zone to the Azores Platform. *EOS Transactions, American Geophysical Union,* **72,** 470.

DETRICK, R. S., HONNOREZ, J., BRYAN, W. B., JUTEAU, T. ET AL. 1988. Introduction and explanatory notes. *Proceedings of the Ocean Drilling Program, Initial Reports,* (Pt. A), **106/109:** College Station, Texas, U.S.A.

DEVEY, X. W., GARBE-SCHONBERG, C. D., STOFFERS, P., CHAUVEL, C. & MERTZ, D. F. 1994. Geochemical effects of dynamic melting beneath ridges: Reconciling major and trace element variations in Kolbeinsey (and global) mid-ocean ridge basalt. *Journal of Geophysical Research,* **99,** 9,077-9,095.

DIXON, J. E. STOLPER, E. & DELANEY, J. R. 1988. Infrared spectroscopic measurements of CO_2 and H_2O in Juan de Fuca Ridge basaltic glasses. *Earth and Planetary Science Letters,* **90,** 87-104.

DMITRIEV, L., HEIRTZLER, J., ET AL. 1978. *Initial reports of the Deep Sea Drilling Project,* **45,** U.S. Government Printing Office,Washington D.C.

DONALDSON, C. H. 1976. An experimental investigation of olivine morphology. *Contributions to Mineralogy and Petrology,* **57,** 187-213.

DONALDSON, C. H. & BROWN, R. W. 1977. Refractory megacrysts and magnesium rich melt inclusions within spinel in oceanic tholeiites: Indicators of magma mixing and parental magma composition. *Contributions to Mineralogy and Petrology,* **37,** 81-89.

DOWTY, E. 1980. Crystal growth and nucleation theory and the numerical simulation of igneous crystallisation. *In*: HARGRAVES, R. B. (ed.) *Physics of magmatic processes.* Princetown University Press, New Jersey, 419-485.

DRAGONI, M. 1993. Modelling the rheology and cooling of lava flows. *In*: KILBURN, C. R. J. & LUONGO, G. (eds) *Active Lavas: monitoring and modelling.* UCL Press, London. 235-261.

DRAGONI, M. & TALLARICO, A. 1994. The effects of crystallisation on the rheology and dynamics of lava flows. *Journal of Volcanology and Geothermal*

Research, **59**, 241-252.

DUNCAN, R. A. & GREEN, D. H. 1980. Role of multistage melting in the formation of oceanic crust. *Geology,* **8**, 22-26.

DUNGAN, M. A. & RHODES, J. M. 1978. Residual glasses and melt inclusions in basalts from DSDP legs 45 and 46: evidence for magma mixing. *Contributions to Mineralogy and Petrology,* **67**, 417-431.

EATON, J. P. & MURATA, K. J. 1960. How Volcanoes Grow. *Science,* **132,** 925-938.

EBERHART G. L., RONA, P. A. & HONNOREZ, J. 1988. Geologic controls of hydrothermal activity in the Mid-Atlantic Ridge Rift Valley: Tectonics and volcanics. *Marine Geophysical Researches,* **10,** 233-259.

EINARSSON, P. & BRANDSDOTTIR, B. 1980. Seismological evidence for lateral magma intrusion during the July 1978 deflation of the Krafla Central Volcano in N.E. Iceland. *Journal of Geophysics,* **47**, 160-165.

ELLIOT, T. R., HAWKESWORTH, C. J. & GRONVOLD, K. 1991. Dynamic melting of the Iceland Plume. *Nature,* **351,** 201-206.

EMBLEY, R. W. 1975. Studies in deep-sea sedimentation processes using high-frequency seismic data. *Ph.D. Thesis, Colombia University, New York,* 334pp.

EMBLEY, R. W. 1976. New evidence for occurence of debris-flow deposits in the deep sea. *Geology* **4**, 371-374.

EMBLEY, R. W. 1980. The role of mass transport in the distribution and transport of deep-sea sediments with special referance to the North Atlantic. *Marine Geology*, **38,** 23-50.

EMBLEY, R. W. & CHADWICK, W. W. 1994. Volcanic and hydrothermal processes associated with a recent phase of seafloor spreading at the northern Cleft segment: Juan de Fuca Ridge. *Journal of Geophysical Research,* **99,** 4,741-4,760.

EMBLEY, R .W., MURPHY, K. M. & FOX, C. G. 1990. High-resolution studies of the summit of Axial Volcano. *Journal of Geophysical Research,* **95,** 12,785-12,812.

ESCARTÍN, J. & LIN, J. 1995. Ridge offsets, normal faulting, and gravity anomalies of slow spreading ridges. *Journal of Geophysical Research,* **100,** 6,163-6,177.

FINK, J. H. & FLETCHER, R. C. 1978. Ropy pahoehoe: surface folding of viscous fluid. *Journal of Volcanology and Geothermal Research,* **4**, 151-170.

FINK, J. H. & GRIFFITHS, R. W. 1990. Radial spreading of viscous-gravity currents with solidifying crusts. *Journal of Fluid Mechanics*, **221,** 485-509.

FLEWELLEN, C., MILLARD, N. & ROUSE, I. 1993. TOBI, a vehicle for deep ocean

survey. *Electronics and Communication Engineering Journal,* April, 85-93.

FLOOD, R. D. 1980. Deep-sea sedementary morphology: modelling and interpretation of echo-sounding profiles. *Marine Geology*, **38**, 77-92.

FORNARI, D. J. 1986. Submarine lava tubes and channels. *Bulletin of Volcanology,* **48**, 291-298.

FORNARI, D. J., BATIZA R. & ALLAN, J. F. 1987a. Irregularly shaped seamounts near the East Pacific Rise: implications for seamount origin and rise axis processes. *In*: KEATING, B. H., FRYER, P., BATIZA, R. & BOEHLERT, G. W. (eds) *Seamounts, Islands and Atolls.* Geophysical Monograph Series, **43**, American Geophysical Union, Washington D.C., 35-47.

FORNARI, D. J., BATIZA R. & LUCKMAN, M. A. 1987b. Seamount abundances and distribution near the East Pacific Rise 0-24°N based on SeaBeam data. *In*: KEATING, B. H., FRYER, P., BATIZA, R. & BOEHLERT, G. W. (eds) *Seamounts, Islands and Atolls.* Geophysical Monograph Series, **43**, American Geophysical Union, Washington D.C., 13-21.

FORNARI , D. J., PERFIT, M. R., ALLAN, J. F., & BATIZA, R. 1988a. Small-scale heterogeneities in depleted mantle sources: near-ridge seamount lava geochemistry and implications for mid-ocean-ridge magmatic processes . *Nature,* **331,** 511-513.

FORNARI, D. J., PERFIT, M .R., ALLAN, J. F., BATIZA, R., HAYNON, R., BARONE, A., RYAN, W.B.F., SMITH, T., SIMKIN, T. & LUCKMAN, A.M. 1988b. Geochemical and structural studies of the Lamont seamounts: seamounts as indicators of mantle processes. *Earth and Planetary Science Letters,* **89,** 63-83.

FORNARI, D. J., RYAN, W. B. F. & FOX, P. J. 1984. The evolution of craters and calderas on young seamounts: Insights from Sea MARC I and SeaBeam sonar surveys of a small group near the axis of the East Pacific Rise at ~ 10°N. *Journal of Geophysical Research,* **89,** 11,069-11,083.

FORSYTH, D. W. 1992. Geophysical constraints on mantle flow and melt generation beneath mid-ocean ridges. *In*: PHIPPS MORGAN, J., BLACKMAN, D. K. & SINTON, J. M. (eds) *Mantle flow and melt generation beneath mid-ocean ridges.* Geophysical Monograph Series, **71**, American Geophysical Union, Washington D.C., 1-65.

FORSYTH, D. W. & WILSON, B. 1984. Three-dimensional temperature structure of a ridge-transform-ridge system. *Earth and Planetary Science Letters,* **70**, 355-362.

FOULGER, G. R. & TOOMEY, D. R. 1989. Structure and evolution of the Hengill-Grensdalur volcanic complex, Iceland: Geology, geophysics and seismic tomography. *Journal of Geophysical Research,* **94,** 17,511-17,522.

FOX, P. J. & GALLO, D. G. 1984. A tectonic model for ridge-transform-ridge plate boundaries; implications for the structure of oceanic lithosphere.

Tectonophysics, **104,** 205-242.

FOX, P. J. & GALLO, D. G. 1986. The Geology of the North Atlantic Transform Plate Boundaries and their aseismic extentions. *In*: VOGT, P. R. & TUCHOLKE, B. E. (eds.) *The Geology of North America, Volume M: The western North Atlantic Region.* Geological Society of America, Boulder, Colorado, U.S.A., 157-162.

FOX, P. J., DETRICK, R. S. & PURDY, G. M. 1980. Evidence for crustal thinning near fracture zones: Implications for ophiolites. *In*: PANAYIOTOU, A. (ed.) *Ophiolites.* Proceedings of the International Ophiolite Symposium, Cyprus, 1979, 161-168.

FOX, P. J., GRINDLAY, N. R. & MACDONALD, K.C. 1991. The Mid-Atlantic Ridge (31°-34°S): Temporal and spatial variations of accretionary processes. *Marine Geophysical Researches,* **13**, 1-20.

FOX, C. G., MURPHY, K. M. & EMBLEY, R. W. 1987. Automated display and statistical analysis of interpreted deep-sea bottom photographs. *Marine Geology,* **78,** 199-216.

FRANCHETEAU, J. & BALLARD, R. D. 1983. The East Pacific Rise near 21°N & 13°N & 20°S: inferences for along-strike variability of axial processes of the mid-ocean ridge. *Earth and Planetary Science Letters,* **64**, 93-116.

FRANCIS, T. J. G. 1977. A bathymetric survey of the eastern end of the St. Paul's Fracture Zone. *In*: ANGEL, A. (ed.) *A Voyage of Discovery.* Pergamon Press, Oxford, 637-645.

FREY, F. A., WALKER, N., STAKES, D., HART, S. R. & NIELSEN, R. L. 1993. Geochemical characteristics of basaltic glasses from the AMAR and FAMOUS axial valleys, Mid-Atlantic Ridge (36^0-37^0N): Petrogenetic implications. *Earth and Planetary Science Letters,* **115**, 117-136.

FUJIMOTO, H., BRYAN, B., KOBAYASHI, K., KINOSHITA, H., TIVEY, M., KELEMEN, P., TAKEUCHI, A., MATSUMOTO, T., ISHIZUKA, H., FURUTA, T., FUJIWARA, T., LIN, J., HOTTA, H. & PURDY, M. 1994. Diving and surface surveys of the western part of the Kane Transform Fault. *InterRidge News,* **3,** 20.

GASS, I. G. & SMEWING, J. D. 1981. Ophiolites: Obducted ocean lithosphere. *In*: EMALIANI, (ed.) *The Oceanic Lithosphere - The Sea,* **7,** John Wiley and Sons, London & New York, 339-362.

GAST, P. W. 1968. Trace element fractionation and the origin of tholeiitic and alkaline magma types. *Geochimica et Cosmochimica Acta,* **32,** 1,057-1,086.

GAUTNEB, H. & GUDMUNDSSON, A. 1992. Effect of local and regional stress field on sheet emplacement in west Iceland. *Journal of Volcanology and Geothermal Research,* **51,** 339-356.

GENTE, P., POCKALNY, R. A., DURAND, C., DEPLUS, C., MAIA, M., CEULENEER, G., MEVEL, C., CANNAT, M. & LAVERNE, C. 1995. Characteristics and evolution

of the segmentation of the Mid-Atlantic Ridge between 20°N and 24°N during the last 10 million years. *Earth and Planetary Science Letters,* **129,** 55-71.

GERLACH, T. M. 1989. Degassing of carbon dioxide from basaltic magma at spreading centers; II. Mid-ocean ridge basalts. *Journal of Volcanology and Geothermal Research,* **39,** 221-232.

GOLDBERG, E. D. & KOIDE, M. 1962. Geochronological studies of deep-sea sediments by the Ionium/Thorium method. *Geochimica et Cosmochimica Acta,* **26,** 417-450.

GOVINDARAJU, K. 1989. *Special issue of the Geostandards Newsletter,* **8**.

GREGG, T. K. P. & FINK, J. H. 1994. Quantification of primary submarine lava flow morphologies. *Ridge Events,* **5** (No. 2),1,2,9.

GREGG, T. K. P & FINK, J. H. 1995. Quantification of submarine lava-flow morphology through analog experiments. *Geology,* **23,** 73-76.

GRIFFITHS, R. W. & FINK, J. H. 1992a. Solidification and morphology of submarine lavas: A dependence on extrusion rate. *Journal of Geophysical Research,* **97,** 19,729-19,737.

GRIFFITHS, R. W. & FINK, J. H. 1992b. The morphology of lava flows in planetary environments: predictions from analogue experiments. *Journal of Geophysical Research,* **97,** 19,739-19,748.

GRINDLAY, N. R., FOX, P. R. & VOGT, P. R. 1992. Morphology and tectonics of the Mid-Atlantic Ridge (25°-27°30'S) from SeaBeam and magnetic data. *Journal of Geophysical Research,* **97,** 6,983-7,010 (abst., disc. & conc.).

GUDMUNDSSON, A. 1984. Formation of crustal magma chambers in Iceland. *Bulletin of Volcanological Research,* **46**, 537-550.

GUDMUNDSSON, A. 1990. Dyke emplacement at divergent plate boundaries. *In*: PARKER, A. J., RICKWOOD, P. C. & TUCKER, D. H. (eds) *Mafic dykes and emplacement mechanisms,* Balkema, Rotterdam, 47-62.

GUEST, J. E., WOOD, C. & GREERLY, R. 1984. Lava tubes, terraces, and megatumuli on the 1614-24 pahoehoe lava flow field, Mount Etna, Sicily. *Bulletin of Volcanology,* **47**, 635-648.

GUSPI, F. 1987. Frequency-domain reduction of potential field measurements to a horizontal plane. *Geoexploration,* **24**, 87-98.

HALL, J. M. 1979. A model for the structural state of the upper half kilometer of north Atlantic ocean layer 1. *In*: TALWANI, M., HARRISON, C. G. & HAYES, D. E. (eds) *Deep Drilling Results in the Atlantic Ocean: Ocean crust.* Maurice Ewing Series, **2,** American Geophysical Union, Washington D.C., 166-168.

HAMILTON, D. L., BURNHAM, C. W. & OSBORN, E. F. 1964. The solubility of water

and effects of oxygen fugacity and water contents on crystallization in mafic magmas. *Journal of Petrology,* **5,** 21-39.

HARDING, A. J., ORCUTT, J. A., KAPPUS, M. E., VERA, E. E., MUTTER, J. C., BUHL, P., DETRICK, R. S. & BROCHER, T. M. 1989. Structure of young oceanic crust at 13°N on the East Pacific Rise from expanding spread profiles. *Journal of Geophysical Research,* **94,** 12,163-12,196.

HARPER, G. D. 1985. Tectonics of slow spreading mid-ocean ridges and consequences of a variable depth to the brittle/ductile transition. *Tectonics,* **4,** 395-409.

HAXBY, W. F. & PARMENTIER, E. M. 1988. Thermal contraction and the state of stress in the oceanic lithosphere. *Journal of Geophysical Research,* **93,** 6,419-6,429.

HAYMON, R. M., FORNARI, D. J., EDWARDS, M. H., CARBOTTE, S., WRIGHT, D. & MACDONALD, K. C. 1991. Hydrothermal vent distribution along the East Pacific Rise crest (9° 09-54'N) and its relationship to magmatic and tectonic processes on fast-spreading mid-ocean ridges. *Earth and Planetary Science Letters,* **104,** 513-534.

HEEZEN, B. C. & THARP, M. 1965. Tectonic fabric of the Atlantic and Indian oceans and continental drift. *Philosophical Transactions of the Royal Society, London,* **A258,** 90-106.

HEIRTZLER, J. R. & LE PICHON, X. 1974. FAMOUS: A plate tectonics study of the genesis of the lithosphere. *Geology,* **2(6)** 273-278.

HEKINIAN, R. & THOMPSON, G. 1976 Comparative Geochemistry of volcanics from rift valleys, transform faults and aseismic ridges. *Contributions to Mineralogy and Petrology,* **57,** 145-162.

HEKINIAN, R., AUZENDE, J.-M., FRANCHETEAU, J., GENTE, P., RYAN, W. B. F.& KAPPEL, E. S. 1985. Offset spreading centres near 12°53'N on the East Pacific Rise: submersible observations and composition of the volcanics. *Marine Geophysical Researches,* **7,** 359-377.

HESS, H. H. 1962. History of the ocean basins. *In*: ENGEL, A. E. J., JAMES, H. L. & LEONARD, B. F. (eds) *Petrologic Studies: A volume in honor of A. F. Buddington.* Geological Society of America, Boulder, Colorado, U.S.A., 599-620.

HILTERMAN, F. J. 1975. Amplitudes of seismic waves - a quick look. *Geophysics,* **40,** 745-762.

HOFTON, M. A. 1995. Anelastic deformation in Iceland studied using GPS with special reference to post-tectonic motion following the 1975-1985 Krafla rifting episode, and isostatic rebound. *Ph.D. thesis, University of Durham.*

HOLCOMB, R. T., PETERSON, D. W. & TILLING, R. I. 1974. Recent landforms at the Kilauea volcano. *In*: *Geological guide to the island of Hawaii.* NASA CR **152416,** 20-58.

HOUSEMAN, G. & MCKENZIE, D. P. 1982. Numerical experiments on the onset of convective instability in the Earth's mantle. *Geophysical Research of the Royal Astronomical Society*, **68**, 133-164.

HUMPHRIS, S. E. 1984.The mobility of rare earth elements in the crust. *In*: HENDERSON, P. (ed.) *Rare earth element geochemistry.* Elsevier, Amsterdam, pp.317-342.

HUMPHRIS, S. E. & THOMPSON, G. 1978a. Hydrothermal alteration of oceanic basalts by seawater. *Geochimica et Cosmochimica Acta,* **42,** 107-125.

HUMPHRIS, S. E. & THOMPSON, G. 1978b. Trace element mobility during hydrothermal alteration of oceanic basalts. *Geochimica et Cosmochimica Acta,* **42,** 127-136.

HUMPHRIS, S. E., BRYAN, W. B., THOMPSON, P. & AUTIO, L. K. 1990. Morphology, geochemistry, and evolution of Serocki volcano. *In*: DETRICK, R. (ed.) *Proceedings of the ODP, Scientific Results Report,* **106/109**.

HUNTER, A. G. & KEMPTON, P. D. 1995. Radiogenic and stable isotope investigations of mantle heterogeneities at MARK, 23ºN. *In*: *Tectonic, Magmatic, Hydrothermal, & Biological Segmentation at Mid-ocean Ridges.* Geological Society of London Special Publication (in press).

HUSSENOEDER, S. A., TIVEY, M. A. & SCHOUTEN, H. 1995. Direct inversion of potential fields from an uneven track with application to the Mid-Atlantic Ridge. *Geophysical Research Letters,* **22,** 3,131-3,134.

HUSSENOEDER, S., TIVEY, M. A. & SCHOUTEN, H. Deep tow magnetics near the Kane Fracture Zone (in prep., 1995).

IRVING, E., PARK, J. K., HAGGERTY, S. E., AUMENTO, F. & LONCAREVIC, B. 1970. Magnetism and opaque mineralogy of basalts from the Mid-Atlantic Ridge at 45ºN, *Nature,* **228,** 874-976.

JAEGAR, J. C. & COOK, G. W. 1979. *Fundamentals of rock mechanics.* Chapman & Hall, London.

JAGGAR, T. A. 1947. Origin and development of craters. *Geological Society of America Memoir,* **21,** 508.

JAKOBSSON, S. P., JONSSON, J. & SHIDO, F. 1978. Petrology of the Western Reykjanes Peninsula, Iceland. *Journal of Petrology,* **19,** 669-705.

JHA, K., PARMENTIER, E. M. & PHIPPS MORGAN, J. 1994. The role of mantle depletion and melt retention buoyancy in spreading center segmentation. *Earth and Planetary Science Letters,* **125**, 221-234.

JOHNSON, G. L. & VOGT, P. R. 1973. Mid-Atlantic Ridge from 47º to 51ºN. *Geological Society of America,* **84,** 3,443-3,462.

JOHNSON, H. P. & ATWATER, T. 1977. Magnetic study of basalts from the Mid-Atlantic Ridge, lat. 37°N. *Geological Society of America Bulletin,* **88,** 637-647.

JOHNSON, H. P. & HELFERTY, M. 1990. The geological interpretation of sidescan sonar. *Reviews of Geophysics,* **28,** 357-380.

JOHNSON, K. T. M., DICK, H. J. B. & SHIMIZU, N. 1990. Melting in the oceanic upper mantle: an ion microprobe study of diopside in abyssal peridotites. *Journal of Geophysical Research,* **95,** 2,661-2,678.

JONES, A. C. 1993. The cooling rates of pahoehoe flows: the importance of lava porosity. *Lunar Planetary Science Abstracts*, **25,** 731-732.

JONES, J. G. 1970. Intraglacial volcanoes of the Laugarvatn region, Southwest Iceland, II. *Journal of Geology,* **78,** 127-140.

JORDAN, T. H., MENARD, W. H. & SMITH, D. K. 1983. Density and size distribution of seamounts in the Eastern Pacific inferred from wide-beam sounding data. *Journal of Geophysical Research*, **88,** 10,508-10,518.

KAPPEL, E. S. & NORMARK, W. R. 1987. Morphometric variability within the axial zone of the southern Juan de Fuca Ridge: Interpretation from SeaMARC II, SeaMARC I, and deep-sea photography. *Journal of Geophysical Research,* **92,** 11,291-11,302.

KARSON, J. A. 1990. Seafloor spreading on the Mid-Atlantic ridge: implications for the structure of ophiolites and ocean lithosphere produced in slow-spreading environments. *In*: MALPAS, J., MOORSE, E. M., PANAYIOTOU, C. & XANOPONTOS, C. (eds) *Proceedings of the symposium on ophiolites and oceanic lithosphere.* - Troodos '87, Geological Survey Department, Nicosia, Cyprus, 547-555.

KARSON, J. A. & BROWN, J. R. 1988. Geologic Setting of the Snake Pit Hydrothermal Site: An Active Vent Field on the Mid-Atlantic Ridge. *Marine Geophysical Researches,* **10**, 91-107.

KARSON, J. A. & DICK, H. J. B. 1983. Tectonics at ridge-transform intersections at the Kane Fracture Zone. *Marine Geophysical Researches,* **6,** 51-98.

KARSON, J. A. & DICK, H. J. B. 1984. Deformed and metamorphosed oceanic crust on the Mid-Atlantic Ridge. *Ofioliti,* **9**, 279-302.

KARSON, J. A., THOMPSON, G., HUMPHRIS, S. E., EDMOND, J. M., BRYAN, W. B., BROWN, J. R., WINTERS, A. T., POCKALNY, R. A., CASEY, J. F., CAMPBELL, A. C., KLINKHAMMER, G., PALMER, M. R., KINZLER, R. J. & SULANOWSKA, M. M. 1987. Along-axis variations in seafloor spreading in the MARK area. *Nature,* **328,** 681-685.

KASTENS, K. A., MACDONALD, K. C. & MILLER, S. P. 1986. Deep Tow Studies of the Vema Fracture Zone 2. Evidence for Tectonism and bottom currents in the

Sediments of the Transform Valley Floor. *Journal of Geophysical Research,* **91,** 3,355-3,367.

KASTENS, K. A., RYAN, W. B. F. & FOX, P. J. 1986. Structural and volcanic expression of a fast slipping ridge-transform-ridge-plate boundary SeaMARC I and photographic surveys at the Clipperton Transform Fault. *Journal of Geophysical Research,* **91,** 3,469-3,488.

KENT, G. M., HARDING, A. J. & ORCUTT, J. A. 1990. Evidence for a smaller magma chamber beneath the EPR at 9°30'N. *Nature*, **344**, 650-653.

KERR, A. C. 1993. The Geochemistry and Petrogenesis of the Mull and Morvern Tertiary Lava Succession, Argyll, Scotland. *Ph.D. thesis, University of Durham,* 357pp.

KESZTHELYI, L. 1994. Calculated effect of vesicles on the thermal properties of cooling basaltic lava flows. *Journal of Volcanology and Geothermal Research,* **63,** 257-266.

KILBURN, C. R. J. 1990. Surfaces of aa flow-field on Mount Etna, Sicily: morphology, rheology, crystallization and scaling phenomena. *In*: FINK, J. H. (ed.) *IAVCEI Proceedings in Volcanology. Vol.2. Lava flows and domes: emplacement mechanisms and hazard implications.* Springer, Berlin, 129-156.

KILBURN, C. R. J. 1993. Lava crust, aa flow lengthening and pahoehoe - aa transition. *In*: KILBURN, C. R. J. & LUONGO, G. (eds) *Active Lavas: monitoring and modelling.* UCL Press, London, 263-280.

KILBURN, C. R. J. & GUEST, J. E. 1993. Aa lavas of Mount Etna, Sicily. *In*: KILBURN, C. R. J. & LUONGO, G. (eds) *Active Lavas: monitoring and modelling.* UCL Press, London, 73-106.

KILBURN, C. R. J. & LOPES, R. M. C. 1991. General patterns of flow field growth: aa and blocky lavas. *Journal of Geophysical Research,* **96,** 19,721-19,732.

KIRKPATRICK, R. J. 1976. Towards a kinetic model for the crystallisation of magma bodies. *Journal of Geophysical Research,* **81,** 2,565-2,571.

KLEIN, E. M. 1991. Ocean ridge magmatic and hydrothermal geochemical processes. *Reviews of Geophysics, Supplement*, **29**, 532-541.

KLEIN, E. M. & LANGMUIR, C. H. 1987. Global correlations of ocean ridge basalt chemistry with axial depth & crustal thickness. *Journal of Geophysical Research,* **92,** 8,089-8,115.

KOKELAAR, P. 1986. Magma-water interactions in subaqueous and emergent basaltic volcanism. *Bulletin of Volcanology,* **48,** 275-289.

KONG, L. S. L., DETRICK, R. S., FOX, P. J., MAYER, L. A. & RYAN, W. B. F. 1988. The Morphology and Tectonics of the MARK area from SeaBeam and SeaMARC I observations (Mid-Atlantic Ridge 23°N.) *Marine Geophysical*

Researches, **10,** 59-90.

KONG, L. S. L., SOLOMON, S. C. & PURDY, G. M. 1992. Microearthquake characteristics of a mid-ocean ridge along-axis high. *Journal of Geophysical Research,* **97,** 1,659-1,685.

KRIENS, B. & WERNICKE, B. 1987. Characteristics of a continental margin magmatic arc with depth: The Skagit-Methow crustal section. *Abstract: Geological Society of America Abstracts with Programs,* **19,** 733.

KUO, B.-Y. & FORSYTH, D. W. 1988. Gravity anomalies of the Ridge-Transform system in the South Atlantic between 31° and 34.5°S; Upwelling centers and variations in crustal thickness. *Marine Geophysical Researches,* **10,** 205-232.

KUO, L.-C. & KIRKPATRICK, R. J. 1982. Pre-eruption history of phyric basalts from DSDP legs 45 and 46: Evidence from Morphology and zoning patterns in Plagioclase. *Contributions to Mineralogy and Petrology,* **79,**13-27.

LACHENBRUCH, A. H. 1973. A simple mechanical model for oceanic spreading centres. *Journal of Geophysical Research,* **78,** 3,395-3,410.

LANGMUIR, C. H. & BENDER, J. F. 1984. The geochemistry of ocean basalts in the vicinity of transform faults: observations and implications. *Earth and Planetary Science Letters,* **69,** 107-127.

LANGMUIR, C. H., BENDER, J. F. & BATIZA, R. 1986. Petrological and tectonic segmentation of the East Pacific Rise, 5°30'-14°30'N. *Nature,* **322,** 422-429.

LAUGHTON, A. S. & RUSBY, J. S. M. 1975. Long-range sonar and photographic studies of the median valley in the FAMOUS area of the Mid-Atlantic Ridge near 37°N. *Deep Sea Research,* **22,** 279-298.

LAUGHTON, A. S. & SEARLE, R. C. 1979. Tectonic processes on slow spreading ridges. *In*: TALWANI, M., HARRISON, C. G. & HAYES, D. E. (eds) *Deep Drilling Results in the Atlantic Ocean: Ocean crust.* Maurice Ewing Series, **2,** American Geophysical Union, Washington D.C., 15-32.

LE BAS, T. P. 1993. TOBI, sidescan processing with edge segmentation. *Proceedings of the Institute of Acoustics,* **15,** Part 2, 65-73.

LE BAS, T. P., MASON, D. C. & MILLARD, N. C. 1995. TOBI image processing: The state of the art. *IEEE Journal of Oceanic Engineering,* **20,** 85-93.

LEENHARDT, O. 1974. Side-scanning sonar - a theoretical study. *International Hydrographic Review Monaco,* **51,** 61-80.

LE ROEX, A. P., DICK, H. J. B. & FISHER, R. L. 1989. Petrology and geochemistry of MORB from 25°E to 46°E along the Southwest Indian Ridge: Evidence for contrasting styles of mantle enrichment. *Journal of Petrology,* **30,** 947-986.

LICHTMAN, G. S., NORMARK, W. R. & SPIESS, F. N. 1984. Photogeologic study of a

segment of the East Pacific Rise axis near 21°N latitude. *Geological Society of America Bulletin*, **95**, 743-752.

LILWALL, R. C., FRANCIS, T. T. G. & PORTER, I. T. 1978. Ocean-bottom seismographic observations on the MAR near 45°N - further results. *Geophysical Journal of the Royal Astronomical Society*, **55**, 255-262.

LIN, J. & PARMENTIER, E. M. 1990. A finite element necking model of extension in brittle lithosphere. *Journal of Geophysical Research*, **95**, 4,909-4,923.

LIN, J. & PHIPPS MORGAN, J. 1992. The spreading rate dependence of three-dimensional mid-ocean ridge gravity structure. *Geophysical Research Letters*, **19**, 13-16.

LIN, J., PURDY, G. M., SCHOUTEN, H., SEMPERE, J.-C. & ZERVAS, C. 1990. Evidence from gravity data for focused magmatic accretion along the Mid-Atlantic Ridge. *Nature*, **344**, 627-632.

LIPMAN, P. W., BANKS, N. G. & RHODES, J. M. 1985. Gas release induced crystallization of 1984 Mauna Loa magma, Hawaii and effects on lava rheology. *Nature*, **317**, 604-607.

LISTER, J. R. & KERR, R. C. 1991. Fluid mechanical models of crack propagation and their application to magma transport in dykes. *Journal of Geophysical Research*, **96**, 10,049-10,077.

LONSDALE, P. & BATIZA, R. 1980. Submersible study of haloclastite and lava flows on young seamounts at the mantle of the Gulf of California. *Geological Society of America Bulletin*, **91**, 545-554.

LONSDALE, P. & SPIESS, F. N. 1980. Deep-Tow observations at the East Pacific Rise 8°45'N and some interpretations. *Initial Reports of the Deep Sea Drilling Project*, **54**, U.S. Government Printing Office, Washington D.C., 43-62.

LOOMIS, T. P. 1982. Numerical solutions of crystallisation processes of plagioclase in complex melts: the origin of major and minor oscillatory zoning in plagioclase. *Contributions to Mineralogy and Petrology*, **81**, 219-229.

LOUDEN, K. E. & FORSYTH, D. W. 1982. Crustal structure and isostatic compensation near the Kane fracture zone from topography and gravity measurements, 1. Spectral analysis approach. *Geophysical Journal of the Royal Astronomical Society*, **68**, 725-750.

LOUDEN, K. E., WHITE, R. S., POTTS, C. G. & FORSYTH, D. W. 1986. Structure and seismotectonics of the Vema fracture zone, Atlantic Ocean. *Journal of the Geological Society, London*, **143**, 795-805.

LUYENDYK, B. P. & MACDONALD, K. C. 1977. Physiography & structure of the inner floor of the FAMOUS rift valley: Observations with a deep-towed instrument package. *Geological Society of America Bulletin*, **88**, 648-663.

LUYENDYK, B. P. & MACDONALD K. C. 1985. A geological transect across the crest of the East Pacific Rise at 21°N latitude made from the deep submersible ALVIN. *Marine Geophysical Researches,* **7,** 467-488.

MACDONALD, G. A. 1953. Pahoehoe, aa and block lava. *American Journal of Science,* **251,** 169-191.

MACDONALD, G. A. 1972. *Volcanoes.* Englewood Cliffs: Prentice-Hall, London.

MACDONALD, G. A. & ABBOTT, A. T. 1970. *Volcanoes In The Sea.* University of Hawaii Press, Honalulu.

MACDONALD, K. C. 1977. Near-bottom magnetic anomalies, asymmetric spreading, oblique spreading, and tectonics of the Mid-Atlantic Ridge near lat. 37°N. *Geological Society of America Bulletin,* **88,** 541-555.

MACDONALD, K. C. 1986. The crest of the Mid-Atlantic Ridge: Models for crustal generation processes and tectonics. *In*: VOGT, P. R. & TUCHOLKE, B. E. (eds) *The Geology of North America, Vol. M, The Western North Atlantic Region.* Geological Society of America, Boulder, Colorado, U.S.A., 51-68.

MACDONALD, K. C & LUYENDYK, B. P. 1977. Deep-tow studies of the structure of the Mid-Atlantic Ridge near lat. 37°N. *Geological Society of America Bulletin,* **88,** 621-636.

MACDONALD, K. C., FOX, P. J., PERRAM, L. J., EISEN, M. F., HAYMON, R. M., MILLER, S. P., CARBOTTE, S. M., CORMIER, M. H. & SHOR, A. N. 1988. A new view of the mid-ocean ridge from the behaviour of ridge-axis discontinuities. *Nature,* **335,** 217-225.

MACDONALD, K. C., LUYENDYK, B. P., MUDIE, J. D. & SPIESS, F. N. 1975. Near-bottom geophysical study of the Mid-Atlantic Ridge median valley near latitude 37°N: Preliminary observations. *Geology,* **3,** 211-215.

MACHADO, N., LUDDEN, J. N. & BROOKS, C. 1982. Fine scale isotopic heterogeneity in the sub-Atlantic mantle. *Nature,* **295,** 226-228.

MACLEOD, C. J., ALLERTON, S., GASS, I. G., XENOPHONTOS, C. 1990. Structure of a fossil ridge transform intersection in the Troodos ophiolite. *Nature,* **348,** 717-720.

MAGDE, L. S. & SMITH, D. K. 1995. Seamount volcanism at the Reykjanes Ridge: Relationship to the Iceland hot spot. *Journal of Geophysical Research,* **100,** 8,449-8,468.

MARKS, S. N. 1981. Sedimentation on new ocean crust: The Mid-Atlantic Ridge at 37°N. *Marine Geology,* **43,** 65-82.

MARSH, B. D. 1989. Magma chambers. *Annual Review of Earth and Planetary Sciences,* **17,** 439-474.

MATHEWS, W. H. 1947. "Tuyas", flat-topped volcanoes in northern British Columbia. *American Journal of Science,* **245,** 560-570.

MCALLISTER, E. & CANN, J. R. 1995. Tectonic anatomy of a slow-spreading segment. *Geological Society of London Special Publication.* (in press).

MCALLISTER, E., SPENCER, S. & DOUGHERTY, M. 1993. Observations of mass-wasting in the crestal mountains of the MAR: implications for the seismic life of a crestal mountain fault. *Bridge Newsletter,* **4,** Leeds University, 7-8.

MCBIRNEY, A. R. 1963. Factors governing the nature of submarine volcanism. *Bulletin Volcanolique,* **26,** 455-469.

MCBIRNEY, A. R. & MURASE, T. 1984. Rheological properties of magmas. *Annual Review of Earth and Planetary Sciences,* **12,** 337-357.

MCKENZIE, D. P. 1984. The generation and compaction of partially molten rock. *Journal of Petrology,* **25,** 713-765.

MCKENZIE, D. P. 1985a. ^{230}Th-^{238}U disequilibrium and the melting processes beneath ridge axes. *Earth and Planetary Science Letters,* **72,** 149-157.

MCKENZIE, D. P. 1985b. The extraction of magma from the crust and mantle. *Earth and Planetary Science Letters,* **74,** 81-91.

MCKENZIE, D. P. & BICKLE, M. J. 1988. The volume and composition of melt generation by extention of the lithosphere. *Journal of Petrology,* **29,** 625-679.

MCKENZIE, D. P. & O'NIONS, R. K. 1991. Partial melt distributions from inversion of rare earth element concentrations. *Journal of Petrology,* **32,** 1,021-1,091.

MCKENZIE, D. P. & RICHTER, F. M. 1976. Convection currents in the earth's mantle. *Scientific American,* **235,** no5, 101-109.

MELSON, W. G. & O'HEARN, T. 1986. Zero age variations in the composition of abyssal volcanic rocks along the axial zone of the Mid-Atlantic Ridge. *In*: VOGT, P. R. & TUCHOLKE, B. E. (eds) *The Geology of North America, Volume M: The Western North Atlantic.* Geology Society of America, Boulder, Colorado, U.S.A., 51-68.

MELSON, W. G. & THOMPSON, G. 1971. Petrology of a transform fault zone and adjacent ridge segments. *Philosophical Transactions of the Royal Society, London,* A. **268,** 423-441.

MELSON, W. G., RABINOWICZ, P. D. ET AL. 1978. *Initial Reports of the Deep Sea Drilling Project,* **45,** U.S. Government Printing Office, Washington D.C.

MENARD, H. W. & CHASE, T. E. 1970. Fracture zones. *In*: MAXWELL, A. E. (ed.) *New Concepts of Sea Floor Evolution - The Sea,* **4,** John Wiley and Sons, London & New York, 321-443.

MICHAEL, P. J. & CHASE, R. L. 1987. The influence of primary magma composition, water and pressure on mid-ocean ridge basalt differentiation. *Contributions to Mineralogy and Petrology,* **96,** 245-263.

MICHAEL, P. J., FORSYTH, D. W., BLACKMAN, D. K., FOX, P. J., HANAN, B. B., HARDING, A. J., MACDONALD, K. C., NEUNMANN, G. A., ORCUTT, J. A., TOLSTOY, M. & WEILAND, C. M. 1994. Mantle control of a dynamically evolving spreading center: Mid-Atlantic Ridge 31-34°S. *Earth and Planetary Science Letters,* **121,** 451-468.

MILLS, A. A. 1984. Pillow lavas and the Leidenfrost effect. *Journal of the Geological Society, London,* **141,** 183-186.

MINSHULL, T. A., WHITE, R. S., MUTTER, J. C., BUHL, P., DETRICK, R. S., WILLIAMS, C. A. & MORRIS, E. 1991. Crustal structures at the Blake Spur Fracture Zone from expanding spread profiles. *Journal of Geophysical Research,* **96,** 9,955-9,984.

MINSTER, J. B. & JORDAN, T. H. 1978. Present-day plate motions. *Journal of Geophysical Research,* **83,** 5,331-5,354.

MITCHELL, N. 1993. A model for attenuation of backscatter due to sediment accumulations and its application to determine sediment thickness with GLORIA sidescan sonar. *Journal of Geophysical Research,* **98,** 22,477-22,493.

MIYASHIRO, A., FUMIKO, S. & EWING, M. 1969. Diversity and origin of abyssal tholeiite from the Mid-Atlantic Ridge near 24° and 30° North latitude. *Contributions to Mineralogy and Petrology,* **23,** 38-52.

MOORE, J. G. 1965. Petrology of deep-sea basalt near Hawaii. *Journal of the Geological Society of America,* **263,** 40-52.

MOORE, J. G. 1975. Mechanism of formation of pillow lava. *American Scientist,* **63,** 269-277.

MOORE J. G & LOCKWOOD, J. R. 1978. Spreading cracks on pillow lava. *Journal of Geology,* **86,** 661-671.

MORRIS, E. & DETRICK, R. S. 1991. Three-dimensional analysis of gravity anomalies in the MARK area, Mid-Atlantic Ridge, 23°N. *Journal of Geophysical Research,* **96,** 4,355-4,366.

MORRISON, M. A. & THOMPSON, R. N. 1983. Alteration of basalt: Deep Sea Drilling Project Legs 64 and 65. *In*: LEWIS, B. T. R. (ed.) *Initial Reports of the Deep Sea Drilling Project,* **65,** U.S. Government Printing Office, Washington D.C., 643-660.

MULLER, O. H. & POLLARD, D. D. 1977. The stress state near the Spanish Peaks, Colorado, determined from pyke pattern. *Pure and Applied Geophysics,* **115,** 69-86.

MURTON, B. J. & GERMAN, C. R. 1992. Hydrothermal supermounds. *Nature,* **358,** 629.

MURTON, B. J. & PARSON, L. M. 1993. Segmentation, volcanism and deformation of oblique spreading centres: a quantitative study of the Reykjanes Ridge, 1992. *Tectonophysics,* **222,** 237-257.

MURTON, B. J., KLINKHAMMER, G., VAN DOVER, C. L., BECKER, K., BRIAIS, A., EDGE, D., MILLARD, N., MITCHELL, I., ROUSE, I., PARSON, L., HAYWARD, N., SAYANAGI, K. & SLOAN, H. 1993. Direct measurement of the distribution and occurrence of hydrothermal activity between 27°N and 30°N on the Mid-Atlantic Ridge. *EOS Transactions, American Geophysical Union,* **74,** 99.

MURTON, B. J., ROUSE, I. P., MILLARD, N. W. & FLEWELLEN, C. G. 1992. Multisensor, deep-towed instrument explores ocean floor. *EOS Transactions, American Geophysical Union,* **73,** 225-228.

MUTTER, J. C. 1985. Multichannel seismic images of the oceanic crust's internal structure: Evidence for a magma chamber beneath the Mesozoic Mid-Atlantic Ridge. *Geology,* **13,** 629-632.

MUTTER, C. Z. & MUTTER, J. C. 1993. Variations in thickness of layer 3 dominate oceanic crustal structure. *Earth and Planetary Science Letters,* **117,** 295-317.

MUTTER, J. C. & DETRICK, R. S. 1984. Multichannel seismic evidence for anomolously thin crust at Blake Spur fracture zone. *Geology,* **12,** 534-537.

MUTTER, J. C. & KARSON, J. A. 1992. Structure processes at slow-spreading ridges. *Science,* **257,** 627-634.

NAAR, D. F. & HEY, R. N. 1989. Speed limit for oceanic transform faults. *Geology,* **17,** 420-422.

NAKAMURA, K. 1977. Volcanoes as possible indicators of tectonic stress orientations. *Journal of Volcanology and Geothermal Research,* **2,** 1-16.

NATLAND, J. H. 1980. Effect of axial magma chambers beneath spreading centers on the compositions of basaltic rocks. *In*: ROSENDAHL, B. R. ET AL. (eds) *Initial Reports of the Deep Sea Drilling Project,* **54,** U.S. Government Printing Office, Washington D.C., 833-850.

NEEDHAM, H. D. & FRANCHETEAU, J. 1974. Some characteristics of the rift valley in the Atlantic ocean near 36°48'N. *Earth and Planetary Science Letters,* **22,** 29.

NICOLAS, A. & BOUDIER, F. 1995. Mapping oceanic ridge segments in Oman ophiolite. *Journal of Geophysical Research,* **100,** 6,179-6,197.

NICOLAS, A., REUBER, I. & BENN, K. 1988. A new magma chamber model based on structural studies in the Oman ophiolite. *Tectonophysics,* **151,** 87-105.

NISBET, E. G. & FOWLER, C. M. R. 1978. The Mid-Atlantic Ridge at 37 and 45°N:

Some geophysical and petrological constraints. *Geophysical Journal of the Royal Astronomical Society,* **54,** 631-660.

NIU, Y. & BATIZA, R. 1991. An empirical method for calculating melt compositions produced beneath mid-ocean ridges: Application for axis and off-axis (seamounts) melting. *Journal of Geophysical Research,* **96,** 21,753-21,777.

NIU, Y. & BATIZA, R. 1994. Magmatic processes at a slow spreading ridge segment: 26°S Mid-Atlantic Ridge. *Journal of Geophysical Research,* **99,** 19,719-19,740.

ODE, H. 1957. Mechanical analysis of the dyke patterns in the Spanish Peaks area, Colorado. *Geological Society of America Bulletin,* **68,** 567-576.

PARMENTIER, E. M. & FORSYTH, D. W. 1985. Three-dimensional flow beneath a slow spreading ridge axis; a dynamic contribution to the deepening of the median valley towards fracture zones. *Journal of Geophysical Research,* **90,** 678-684.

PARMENTIER, E. M. & PHIPPS MORGAN, J. 1990. Spreading rate dependence of 3D structure in oceanic spreading centres. *Nature,* **348,** 325-328.

PARSON, L. M., MURTON, B. J., SEARLE, R. C., BOOTH, D., EVANS, J., FIELD, P., KEETON, J., LAUGHTON, A., MCALLISTER, E., MILLARD, N., REDBOURNE, L., ROUSE, I., SHOR, A., SMITH, D., SPENCER, S., SUMMERHAYES, C. & WALKER, C. 1993. En-echelon volcanic ridges at the Reykjanes Ridge: a life cycle of volcanism and tectonics. *Earth and Planetary Science Letters,* **117,** 73-87.

PARSONS, B. & RICHTER, F. M. 1981. Mantle convection and the oceanic lithosphere. *In*: EMALIANI, (ed.) *The Oceanic Lithosphere - The Sea*, **7,** John Wiley and Sons, London & New York, 73-113.

PARSONS, B. & SCLATER, J. G. 1977. Analysis of the variation of ocean floor bathymetry and heat flow with age. *Journal of Geophysical Research,* **82,** 803-827.

PEARCE, J. A. 1976. Statistical analysis of major element patterns in basalts. *Journal of Petrology,* **17,** 15-43.

PEARCE, J. A. 1983. Role of the sub-continental lithosphere in magma genesis at active continental margins. *In*: HAWKESWORTH, C. J. & NORRY, M. J. (eds) *Continental basalts and mantle xenoliths.* Shiva, Nantwich, 230-249.

PEARCE, J. A., BROWNING, P., KEMPTON, P., LAWSON, K. & MEVEL, C. 1993. Tectonic, volcanic and petrological studies of the Mid-Atlantic Ridge near the Kane Fracture Zone (GR3/7340). *NERC Final Report,* 17pp.

PERFIT, M. R., FORNARI, D. J., MALAHOFF, A. & EMBLEY, R. W. 1983. Geochemical studies of abyssal lavas recovered by DSRV *Alvin* from Eastern Galapagos Rift, Inca Tranform, and Ecuador Rift 3. Trace element abundances and petrogenesis. *Journal of Geophysical Research,* **88,** 10,551-10,572.

PETERSON, D. W. & SWANSON, D. A. 1974. Observed formation of lava tubes during 1970-71 at Kilauea Volcano, Hawaii. *Studies in Speleology,* **2,** 209-222.

PETERSON, D. W. & TILLING, R. I. 1980. Transition of basaltic lava from pahoehoe to aa, Kilauea volcano, Hawaii: field observations and key factors. *Journal of Volcanology and Geothermal Research,* **7,** 271-293.

PETERSON, D. W., HOLCOMB, R. T., TILLING, R. I., & CHRISTIANSEN, R. L. 1994. Development of lava tubes in the light of observations at Mauna Ulu, Kilauea Volcano, Hawaii. *Bulletin of Volcanology,* **56,** 343-360.

PHILIPS, J. D. & FLEMING, H. S. 1978. Multi-beam sonar study of the Mid-Atlantic rift valley 36°-37°N FAMOUS. *Geological Society of America,* MC-19.

PHIPPS MORGAN, J. 1987. Melt migration beneath mid-ocean spreading centers. *Geophysical Research Letters,* **14,** 1,238-1,241.

PHIPPS MORGAN, J. 1991. Mid-Ocean Ridge dynamics: Observations and theory. *Reviews of Geophysics, Supplement,* **29,** 807-822.

PHIPPS MORGAN, J. & FORSYTH, D. W. 1988. Three-dimensional flow and temperature perturbations due to a transform offset: Effects on oceanic crustal and upper mantle structure. *Journal of Geophysical Research,* **93,** 2,955-2,966.

PHIPPS MORGAN, J., PARMENTIER, E. M. & LIN, J. 1987. Mechanisms for mid-ocean ridge axial topography: Implications for the thermal and mechanical structure at accreting plate boundaries. *Journal of Geophysical Research,* **92,** 12,823-12,836.

PILKINGTON, M. & URQUHART, W. E. S. 1990. Reduction of potential field data to a horizontal plane. *Geophysics,* **55,** 549-555.

PINKERTON, H. 1993. Measuring the properties of flowing lavas. *In*: KILBURN, C. R. J. & LUONGO, G. (eds) *Active Lavas: monitoring and modelling.* UCL Press, London, 175-192.

PLANK, T. & LANGMUIR, C. H. 1992. Effects of the melting regime on the composition of the oceanic crust. *Journal of Geophysical Research,* **97,** 19,770-19,794.

POCKALNY, R. A., DETRICK, R. S. & FOX , P. J. 1988. Morphology and tectonics of the Kane Transform from SeaBeam bathymetry data. *Journal of Geophysical Research,* **93,** 3,179-3,193.

POCKALNY, R. A., FOX, P. J. & MACDONALD, K. C. 1991. Generation of volcanic transverse ridges along the Siqueiros fracture zone. *EOS Transactions, American Geophysical Union,* **72,** 491.

POTTS, P. J., TINDLE, A. G. & WEBB, P. C. 1992. *Geochemical reference material compositions.* Whittles Publishing, Caithness.

PREVOT, M., LECAILLE, A. & HEKINIAN, R. 1979. Magnetism of the Mid-Atlantic Ridge crest near 37°N from FAMOUS and DSDP results: A review. *In:* TALWANI, M., HARRISON, C. G. & HAYES, D. E. (eds) *Deep Drilling Results in the Atlantic Ocean: Ocean crust.* Maurice Ewing Series, **2,** American Geophysical Union, Washington D.C., 210-229.

PURDY, G. M. & DETRICK, R. S. 1986. Crustal structure of the Mid-Atlantic Ridge at 23°N from seismic refraction studies. *Journal of Geophysical Research,* **91,** 3,739-3,762.

PURDY, G. M., RABINOWICZ, P. D. & VELTROP, J. J. A. 1979. The Kane Fracture Zone in the central North Atlantic. *Earth and Planetary Science Letters*, **45,** 429-434.

PURDY, G. M., SEMPERE, J.-C., SCHOUTEN, H., DUBOIS, D. L. & GOLDSMITH, R. 1990. Bathymetry of the Mid-Atlantic Ridge, 24°-31°N: A map series. *Marine Geophysical Researches,* **12,** 247-252.

RABINOWICZ, M., CEULENEER, G., MONNEREAU, M. & ROSEMBERG, C. 1987. Melt segregation and flow in mantle diapirs below spreading centres: Evidence from the Oman ophiolite. *Journal of Geophysical Research*, **92**, 3,475-3,486.

RABINOWICZ, M., ROUZO, S., SEMPERE, J.-C. & ROSEMBERG, C. 1993. Three-dimensional mantle flow beneath mid-ocean ridges. *Journal of Geophysical Research,* **98,** 7,851-7,869.

REED, T. B. 1987. Digital image processing and analysis techniques for SeaMARC II side-scan sonar imagery. *Ph.D. University of Hawaii, Honolulu.*

REED, T. B. & HUSSONG, D. 1989. Digital image processing and analysis techniques for Enhancement and classification of SeaMARC II side-scan sonar imagery. *Journal of Geophysical Research,* **94**, 7,469-7,490.

RENARD, V., HEKINIAN, R., FRANCHETEAU, J., BALLARD, R. D. & BACKER, H. 1985. Submersible observations at the axis of the ultra-fast spreading East Pacific Rise (17°30' to 21°30'S). *Earth and Planetary Science Letters*, **75,** 339-353.

REYNOLDS, J. R. & LANGMUIR, C. H. 1995. Petrological systematics of the Mid-Atlantic Ridge south of Kane: Implications for models of ocean crust formation. *Journal of Geophysical Research* (in press).

REYNOLDS, J. R., LANGMUIR, C. H., BENDER, J. F., KASTENS, K. A. & RYAN, W. B. F. 1992. Spatial and temporal variability in the geochemistry of basalts from the East Pacific Rise. *Nature,* **359,** 493-499.

RIBE, N. M. 1985a. The deformation and compaction of partial molten zones. *Geophysical Journal of the Royal Astronomical Society,* **83,** 487-501.

RIBE, N. M. 1985b. The generation and composition of partial melts in the earth's mantle. *Earth and Planetary Science Letters*, **73,** 361-376.

RICHTER, D. H. & PARSONS, B. 1975. On the interaction of two scales of convection in the mantle. *Journal of Geophysical Research*, **80**, 2,529-2,541.

RICHTER, D. H., EATON, J. P., MURATA, K. J., AULT, W. A. & KRIVOY, H. L. 1970. Chronological narrative of the 1955-60 eruption of the Kilauea volcano, Hawaii. *United States Geological Survey Professional Paper* **537-E**, 1-73.

RICKWOOD, P.C. 1990. The anatomy of a dyke and the determination of proportion and magma flow directions. *In*: PARKER, A. J., RICKWOOD, P. C. & TUCKER, D. H. (eds) *Mafic dykes and emplacement mechanisms,* Balkema, Rotterdam, 81-100.

RINEHART, E. J., SANFORD, A. R. & WARD, R. M. 1979. Geographic extent and shape of an extensive magma body at mid-crustal depths in the Rio Grande Rift near Socorro, New Mexico. *In*: RIECKER, R. E. (ed.) *Rio Grande Rift: Tectonics and Magmatism.* American Geophysical Union, Washington D.C., 237-251.

ROBB, J. M. & KANE, M. F. 1975. Structure of the VEMA fracture zone from gravity and magnetic intensity profiles. *Journal of Geophysical Research,* **80,** 4,441-4,445.

ROEST, W. R., SEARLE, R. C. & COLLETTE, B. J. 1984. Fanning of fracture zones and a three-dimensional model of the Mid-Atlantic Ridge. *Nature,* **308,** 527-531.

ROLLINSON, H. 1993. *Using geochemical data: evaluation, presentation, interpretation.* Longman Scientific & Technical, Harlow, Essex.

ROMMEVAUX, C., DEPLUS, C., PATRIAT, PH. & SEMPERE, J.-C. 1994. Three-dimensional gravity study of the Mid-Atlantic Ridge: Evolution of the segmentation between 28° and 29°N during the last 10 m.y. *Journal of Geophysical Research,* **99,** 3,015-3,029.

RONA, P. A. 1980. TAG hydrothermal field: Mid-Atlantic Ridge crest at latitude 26°N. *Journal of the Geological Society, London*, **137,** 385-402.

ROSENDAHL, B. R. 1987. Architecture of continental rifts with special reference to East Africa. *Annual Review of Earth and Planetary Sciences*, **15,** 445-503.

ROUZO, S., RABINOWICZ, M. & BRIAIS, A. 1995. Segmentation of mid-ocean ridges with an axial valley induced by small-scale mantle convection. *Nature,* **374,** 795-798.

RUTTEN, M. G. 1964. Formation of plateau basalt series (from the example of Iceland). *Bulletin of Volcanology,* **27,** 93-111.

RYAN, M. P. 1987. Neutral buoyancy and the mechanical evolution of magmatic systems. *In*: MYSEN, B. O. (ed.) *Magmatic Processes: Physical Chemical Principles.* Geochemistry Society Special Publication, **1,** 259-305.

RYAN, M. P., KOYANAGI, R. Y. & FISKE, R. 1981. Modeling the three-dimensional structure of macroscopic magma transport systems: Applications to Kilauea,

Hawaii. *Journal of Geophysical Research,* **86**, 7,111-7,129.

SAEMUNDSSON, K. 1979. Outline of the geology of Iceland. *Jökull,* **29**, 7-28.

SANDERSON, D. J. & MARCHINI, W. R. D. 1984. Transpression. *Journal of Structural Geology,* **6**, 449-458.

SANDWELL, D. T. 1986. Thermal stress and the spacings of transform faults. *Journal of Geophysical Research,* **91**, 6,402-6,417.

SARDA, P. & GRAHAM, D. 1990. Mid-ocean ridge popping rocks: implications for degassing at ridge crests. *Earth and Planetary Science Letters,* **97**, 268-289.

SAUNDERS, P. M. 1981. Practical conversion of pressure to depth. *Journal of Physical Oceanography,* **11**, 573-574.

SCANDONE, R. 1979. Effusion rate and energy balance of Paricutin eruption (1943-1952) Michoacan, Mexico. *Journal of Volcanology and Geothermal Research,* **6**, 49-59.

SCARFE, C. M. 1973. Viscosity of basic magmas at varying pressure. *Nature,* **241**, 101-102.

SCHEIRER, D. S. & MACDONALD, K. C. 1995. Near-axis seamounts on the flanks of the East Pacific Rise, 8°N to 17°N. *Journal of Geophysical Research,* **100**, 2,239-2,259.

SCHILLING, J.-G. 1986. Geochemical and isotopic variation along the Mid-Atlantic Ridge axis from 79°N to 0°N. *In*: VOGT, P. R. & TUCHOLKE, B. E. (eds) *The Geology of North America, Volume M: The Western North Atlantic.* Geology Society of America, Boulder, Colorado, U.S.A., 51-68.

SCHMINCKE, H.-U. & BEDNARZ, U. 1990. Pillow, sheet flow and breccia flow volcanoes and volcano-tectonic hydrothermal cycles in the Extrusive Series of the northeastern Troodos Ophiolite (Cyprus). *In*: MALPAS, J. ET AL. (eds) *Ophiolites: oceanic crustal analogues.* Proceedings of the Symposium "Troodos 1987", Geological Survey Department, Nicosia, Cyprus, 185-206.

SCHMINCKE, H.-U. & RAUTENSCHLEIN, M. 1987. Troodos Extrusive Series (Akasi River Canyon) and the Sheeted Diabase. Part 1: Volcanology along the Akaki River. *In*: XENOPHONTOS, C. & MALPAS, J. (eds) *Troodos '87 Ophiolites & Oceanic Lithosphere.* Field Excursion Guidebook. Geological Survey Department, Nicosia, Cyprus, 36-80.

SCHMINCKE, H.-U., RAUTENSCHLEIN, M., ROBINSON, P. T. & MEHEGAN, J. M. 1983. Troodos extrusive series of Cyprus: A comparison with oceanic crust. *Geology,* **11**, 405-409.

SCHOUTEN, H. & KLITGORD, K. D. 1982. The memory of accreting plate boundary and the continuity of fracture zones. *Earth and Planetary Science Letters,* **59**, 255-266.

SCHOUTEN, H. & WHITE, R. S. 1980. Zero-offset fracture zones. *Geology,* **8,** 175-179.

SCHOUTEN, H., KLITGORD, K. D. & WHITEHEAD J. A. 1985. Segmentation of mid-ocean ridges. *Nature,* **317,** 225-229.

SCHULZ, N. J., DETRICK, R. S. & MILLER, S. P. 1988. Two and three dimensional inversions of magnetic anomalies in the MARK area (Mid-Atlantic Ridge 23° N). *Marine Geophysical Researches,* **10,** 41-57.

SCOTT, D. R. & STEVENSON, D. T. 1986. Magma ascent by porous flow. *Journal of Geophysical Research,* **91,** 9,283-9,296.

SCOTT, D. R. & STEVENSON, D. T. 1989. A self-consistent model of melting, magma migration and buoyancy-driven circulation beneath Mid-Ocean Ridges. *Journal of Geophysical Research,* **94,** 2,973-2,988.

SCOTT, R. B., RONA, P. A., MCGREGOR, B. A. & SCOTT, M. R. 1974. The TAG hydrothermal field. *Nature,* **251,** 301-302.

SEARLE, R. C. 1983. Submarine central volcanoes on the Nazca plate - high resolution sonar observations. *Marine Geology,* **53,** 77-102.

SEARLE, R. C. 1986. GLORIA investigations of oceanic fracture zones: comparative study of the transform fault zone. *Journal of the Geological Society, London,* **143,** 743-756.

SEARLE, R. C. 1992. The volcano-tectonic setting of oceanic lithosphere generation. *In*: PARSONS, L. M. & BROWNING, P. (eds) *Ophiolites and their modern oceanic analogues.* Geological Society of London Special Publications, **60,** 65-79.

SEARLE, R. C. 1995. Tectonic, volcanic and petrological studies on the Mid-Atlantic Ridge near the Kane Fracture Zone (GR3/7702'A'). *NERC Final Report,* 27pp.

SEARLE, R. C. & LAUGHTON, A. S. 1977. Sonar studies of the Mid-Atlantic Ridge and Kurchatov Fracture Zone: *Journal of Geophysical Research,* **82,** 5,313-5,328.

SEARLE, R. C., KEETON, J. A., PARSONS, B. A., OWENS, R. B., MECKLENBURGH, R., WHITE, R. S., HEPBURN, C. & ROBINSON, C. 1994. A detailed sonar, gravity and magnetic study of the oblique spreading Reykjanes Ridge, 57°30'N-62°05'N. *EOS Transactions, American Geophysical Union,* **75,** 589.

SEEWALD, J. S. & SEYFRIED, W. E. 1990. The effect of temperature on metal mobility in subseafloor hydrothermal systems: constraints from basalt alteration experiments. *Earth and Planetary Science Letters,* **101,** 388-403.

SEMPERE, J.-C. & MACDONALD, K. C. 1987. Marine tectonics: processes at Mid-Ocean ridges. *Reviews of Geophysics,* **25,** 1,313-1,347.

SEMPERE, J.-C., BLONDEL, P., BRIAIS, A., FUJIWARA, T., GELI, L., ISEZAKI, N., PARISO, J. E., PARSON, L., PATRIAT, PH. & ROMMEVAUX, C. 1995. The Mid-Atlantic Ridge between 29°N and 31°N in the last ten Ma. *Earth and Planetary Science Letters,* **130,** 45-55.

SEMPERE, J.-C., LIN, J., BROWN, H. S., SCHOUTEN, H. & PURDY, G. M. 1993. Segmentation and Morphotectonic Variations Along a Slow Spreading Centre: The Mid-Atlantic Ridge (24°00'N–30°40'N). *Marine Geophysical Researches,* **15,** 153-200.

SEMPERE, J.-C., PURDY, G. M. & SCHOUTEN, H. 1990. Segmentation of the MAR between 24°N and 30°40'N. *Nature*, **344**, 427-431.

SEVERINGHAUS, J. P. & MACDONALD, K. C. 1988. High inside corners at ridge-transform intersections. *Marine Geophysical Researches,* **9**, 353-367.

SHAW, D. M. 1970. Trace element fractionation during anatexis. *Geochimica et Cosmochimica Acta,* **34,** 237-243.

SHAW, H. R. 1969. Rheology of basalt in the melting range. *Journal of Petrology,* **10,** 510-535.

SHAW, H. R. 1980. The fracture mechanism of magma transport from the mantle to the surface. *In*: HARGREAVES, R. B. (ed.) *Physics of Magmatic Processes.* Princeton University Press, Princeton, New Jersey, U.S.A.

SHAW, P. R. 1992. Ridge segmentation, faulting and crustal thickness in the Atlantic Ocean. *Nature,* **358**, 490-493.

SHAW, H. R. & SWANSON, D. A. 1969. Eruption and flow rates of flood basalts. *In*: GILMOUR, E. H. & STRADLING, D. (eds) *Proceedings of the 2nd Columbia River Basalt Symposium.* Cheney, Eastern Washington University, 271-299.

SHAW, P. R. & LIN, J. 1993. Causes and consequences of variations in faulting style at the Mid-Atlantic Ridge. *Journal of Geophysical Research,* **98**, 21,819-21,851.

SHEN, Y. & FORSYTH, D. W. 1992. The effects of temperature- and pressure-dependant viscosity on three-dimensional passive flow of the mantle beneath a ridge-transform system. *Journal of Geophysical Research,* **97**, 19,717-19,728.

SHERIFF, R. E. 1977. Limitations in resolution of seismic reflections and geological detail derivable from them. *American Association of Petroleum Geology Memoir,* **26**, 3-14.

SIGURDSSON, H. 1981. First-order major element variation in basalt glasses from the Mid-Atlantic Ridge: 29° to 73°N. *Journal of Geophysical Research*, **86**, 9,483-9,502.

SIGURDSSON, H. 1987. Dyke injection in Iceland: a review. *In*: HALLS, H. C. & FAHRIG, W. F. (eds) *Mafic dyke swarms.* Geological Association of Canada Special Paper, **34,** 55-64.

SIGURDSSON, H. & SPARKS, R. S. J. 1978. Lateral magma flow within rifted Icelandic crust. *Nature*, **274**, 126-130.

SIMKIN, T. 1972. Origin of some flat-topped volcanoes and guyots. *Geological Society of America Memoir*, **132**, 183-193.

SINTON, J. M. & DETRICK, R. S. 1992. Mid-ocean ridge magma chambers. *Journal of Geophysical Research*, **97**, 197-216.

SINTON, J. M., WILSON, D. S., CHRISTIE, D. M., HEY, R. N. & DELANEY, J. R. 1983. Petrologic consequences of rift propagation on oceanic spreading ridges. *Earth and Planetary Science Letters*, **62**, 193-207.

SLEEP, N. H. 1969. Sensitivity of heat flow and gravity to the mechanisms of sea-floor spreading. *Journal of Geophysical Research*, **74**, 542-549.

SLEEP, N. H. 1975. Formation of oceanic crust: Some thermal constraints. *Journal of Geophysical Research*, **80**, 4,037-4,042.

SLEEP, N. H. 1978. Thermal structure and kinematics of mid-ocean ridge axis: some implications to basaltic volcanism. *Geophysical Research Letters*, **5**, 426-428.

SLEEP, N. H. & BIEHLER, S. 1970. Topography and tectonics at the intersections of Fracture Zones with Central Rifts. *Journal of Geophysical Research*, **75**, 2,748-2,752.

SLEEP, N. H. & ROSENDAHL, B. P. 1979. Topography and tectonics of mid-ocean ridge axes. *Journal of Geophysical Reearch*, **84**, 6,831-6,839.

SMITH, D. K. & CANN, J. R. 1990. Hundreds of small volcanoes on the median valley floor of the Mid-Atlantic Ridge at 24-30°N. *Nature*, **348**, 152.

SMITH, D. K. & CANN, J. R. 1992. The role of seamount volcanism in crustal construction at the Mid-Atlantic Ridge (24°-30°N). *Journal of Geophysical Research*, **97**, 1,645-1,658.

SMITH, D. K. & CANN, J. R. 1993. Building the crust at the Mid-Atlantic Ridge. *Nature*, **365**, 707-715.

SMITH, M. C., PERFIT, M. R. & JONASSON, I. R. 1994. Petrology and geochemistry of basalts from the southern Juan de Fuca Ridge: Controls on the spatial and temporal evolution of mid-ocean ridge basalt. *Journal of Geophysical Research*, **99**, 4,787-4,812.

SOTIN, C. & PARMENTIER, E. M. 1989. Dynamical consequences of compositional and thermal density stratification beneath spreading centers. *Geophysical Research Letters*, **16**, 835-838.

SPARKS, D. W. & PARMENTIER, E. M. 1990. Buoyant flow beneath ridge-transform systems and long axis variations in gravity and crustal thickness. *EOS Transactions, American Geophysical Union*, **71**, 627.

SPARKS, D. W. & PARMENTIER, E. M. 1991. Melt extraction from the mantle beneath spreading centers. *Earth and Planetary Science Letters,* **105**, 368-377.

SPARKS, R. S. J. & PINKERTON, H. 1978. Effects of degassing on rheology of basaltic lava. *Nature,* **276**, 385-386.

SPARKS, R. S. J., HUPPERT, H. E., KOYAGUCHI, T. & HALLWORTH, M. A. 1993 Origin of modal and rhythmic igneous layering by sedimentation in a convecting magma chamber. *Nature,* **361,** 246-249.

SPENCE, D. A. & TURCOTTE, D. L. 1990. Buoyancy-driven magma fracture: A mechanism for ascent through the lithosphere and the emplacement of diamonds. *Journal of Geophysical Research,* **95**, 5,133-5,139.

SPIEGELMAN, M. & MCKENZIE, D. 1987. Simple 2D models for melt extraction at MOR's and island arcs. *Earth and Planetary Science Letters,* **83,** 137-152.

SPOONER, E. C. T. & GALE, N. H. 1982. Pb isotopic composition of ophiolitic volcanogenic sulphide deposits, Troodos complex, Cyprus. *Nature,* **296**, 239-242.

STAKES, D. S., SHERVAIS, J. W. & HOPSON, C. A. 1984. The volcanic-tectonic cycle of FAMOUS & AMAR valleys; Mid-Atlantic Ridge (36°47'N): Evidence from basaltic glass and phenocryst compositional variations for a steady state magma chamber beneath the valley midsections, AMARC 3. *Journal of Geophysical Research*, **89,** 6,995-7,028.

STASIUK, M. V., JAUPART, C. & SPARKS, R. S. J. 1993. On the variations of flow rate in non-explosive lava eruptions. *Earth and Planetary Science Letters*, **114**, 505-516.

STEARNS, H. T. & MACDONALD, G. A. 1942. Geology and groundwater resources of the island of Hawaii. *Hawaii Division Hydrological Bulletin,* **9**, 363.

STOLPER, E. & HOLLOWAY, J. R. 1988. Experimental determination of the solubility of carbon dioxide in molten basalt at low pressure. *Earth and Planetary Science Letters,* **87,** 397-408.

SUN, S. S. & MCDONOUGH, W. F. 1989. Chemical and isotopic systematics of oceanic basalts: implications for mantle composition and processes. *In*: SAUNDERS, A. D. & NORRY, M. J. (eds) *Magmatism in the Ocean Basins.* Geological Society of London Special Publications, **42**, 313-345.

SUN, S. S., NESBITT, R. & SHARASKIN, A. 1979. Geochemical characteristics of MORB. *Earth and Planetary Science Letters*, **44**, 119-138.

TAPPONNIER, P. & FRANCHETEAU, J. 1978. Necking of the lithosphere and the mechanics of slowly accreting plate boundaries. *Journal of Geophysical Research,* **83,** 3,955-3,969.

TAZIEFF, H., 1972. About deep sea volcanism. *Geologische Rundschau*, **61,** 470-480.

TEPLEY, L. & MOORE, J. G. 1974. Fire under the sea: the origin of the pillow lava (16mm motion picture). Mountain View, California, Moonlight Productions.

THOMPSON, G. B., BRYAN, W. B., BALLARD, R., HAMURO, K. & MELSON, W. G. 1985. Axial processes along a segment of the East Pacific Rise, 10°-12°N. *Nature*, **318**, 429-433.

THOMPSON, G., HUMPHRIS, S. E., SCHROEDER, B., SULANOWSKA, M. & RONA, P. A. 1988. Active vents and massive sulfides at 26°N (TAG) and 23°N (Snakepit) on the Mid-Atlantic Ridge. *Canadian Mineralogist,* **26,** 697-711.

THORARINSSON, S. 1969. The Lakagigar eruption of 1783. *Bulletin of Volcanology,* **33**, 910-929.

THORARINSSON, S. & SIGVALDASON, G. E. 1972. The Hekla eruption of 1970. *Bulletin of Volcanology,* **36**, 1-20.

THORARINSSON, S., STEINTHORSSON, S., EINARSSON, T. H., KRISTMANNSDOTTIR, H. & OSKARSSON, N. 1973. The eruption on Heimay, Iceland. *Nature,* **241**, 372-75.

TIVEY, M. A., RONA, P. A. & SCHOUTEN, H. 1993. Reduced crustal magnetization beneath the active sulfide mound, TAG hydrothermal field, Mid-Atlantic Ridge at 26°N. *Earth and Planetary Science Letters,* **115,** 101-115.

TODT, W., CLIFF, R. A., HANSER, A. & HOFMANN, A. W. 1984. ^{202}Pb and ^{205}Pb double spike for lead isotopic analyses. *Terra Cognita,* **4**, 209.

TOOMEY, D. R., SOLOMON, S. C., PURDY, G. M. & MURRAY, M. H. 1985. Microearthquakes beneath the median valley of the Mid-Atlantic Ridge near 23°N: Hypocentres and focal mechanisms. *Journal of Geophysical Research,* **90**, 5,443-5,458.

TORMEY, D. R., GROVE, T. L. & BRYAN, W. B. 1987. Experimental petrology of normal MORB near the Kane Fracture Zone: 22°-25°N Mid-Atlantic Ridge. *Contributions to Mineralogy and Petrology,* **96,** 121-139.

TUCHOLKE, B. E. 1992. Massive submarine rockslide in the rift-valley wall of the mid-Atlantic Ridge. *Geology*, **20,** 129-132.

TUCHOLKE, B. E. & LIN, J. 1994. A geological model for the structure of ridge segments in slow spreading ocean crust. *Journal of Geophysical Research,* **99**, 11,937-11, 958.

TUCHOLKE, B. E. & SCHOUTEN, H. 1988. Kane Fracture Zone. *Marine Geophysical Researches,* **10,** 1-39.

TURCOTTE, D. L. 1974. Are transform faults thermal contraction cracks? *Journal of Geophysical Research,* **79**, 2,573-2,577.

TYCE, R. C. 1986. Deep seafloor mapping systems - A review, *MTS Journal,* **20,** 4-16.

UPTON, B. G. J. & THOMAS, J. E. 1980. The Tugtutoq Younger Giant Dyke Complex, South Greenland: fractional crystallization of transitional olivine basalt magma. *Journal of Petrology,* **21,** 167-198.

URICK, R. J. 1979. Sound propagation in the sea. *Doc 008-051-000071-2, U.S. Government Printing Office, Washington D.C.*

VAN ANDEL, T. & KOMAR, P. D. 1969. Ponded sediments of the Mid-Atlantic Ridge between 22° and 23° North latitude. *Geological Society of Americia Bulletin,* **80,** 1,163-1,190.

VAN WAGONER, N. A. & JOHNSON, H. P. 1983. Magnetic properties of three segments of the Mid-Atlantic Ridge at 37°N: FAMOUS, Narrowgate, and AMAR: AMAR 2. *Journal of Geophysical Research,* **88,** 5,065-5,082.

VERA, E. E., MUTTER, J. C., BUHL, P., ORCUTT, J. A., HARDING, A. J., KAPPUS, M. E., DETRICK, R. S. & BROCHER, T. M. 1990. The structure of 0 to 0.2-m.y. old oceanic crust at 9°N on the East Pacific Rise from expanded spread profiles. *Journal of Geophysical Research,* **95,** 15,529-15,556.

VIDAL, P. & CLAUER, N. 1981. Pb and Sr isotopic systematics of some basalts and sulfides from the East Pacific Rise at 21°N (project RITA). *Earth and Planetary Science Letters,* **55,** 237-246.

VINE, F. J. & MATTHEWS, D. H. 1963. Magnetic anomalies over oceanic ridges, *Nature,* **199,** 947-949.

VOGT, P. R. 1971. Asthenosphere motion recorded by the ocean floor south of Iceland. *Earth and Planetary Science Letters,* **13,** 153-160.

VOGT, P. R. 1974a. Volcano height and plate thickness. *Earth and Planetary Science Letters,* **23,** 337-348.

VOGT, P. R. 1974b. Volcano spacing, fractures and thickness of the lithosphere. *Earth and Planetary Science Letters,* **21,** 235-252.

VOGT, P. R. 1979. Amplitude of oceanic magnetic anomalies and the chemistry of oceanic crust: Synthesis and review of "magnetic telechemistry" *Canadian Journal of Earth Science,* **16,** 2,236-2,262.

VOGT, P. R. 1986. The present plate boundary configuration. *In*: VOGT, P. R. & TUCHOLKE, B. E. (eds) *The Geology of North America, Vol. M, The Western North Atlantic Region.* Geological Society of America, Boulder, Colorado, U.S.A., 189-204.

VOGT, P. R. & AVERY, O. E. 1976. Plumes, subaxial pipe flow and topography along the mid-Atlantic Ridge. *Earth and Planetary Science Letters,* **29,** 309-325.

VOGT, P. R. & BYERLY, G. 1976. Magnetic anomalies and basalt composition in the

Juan de Fuca-Gorda Ridge area. *Earth and Planetary Science Letters*, **33**, 185-207.

VOGT, P. R. & DE BOER, J. 1976. Morphology, magnetic anomalies and magnetization at the ends of the Galapagos high-amplitude zone. *Earth and Planetary Science Letters*, **33**, 145-163.

VOGT, P. R. & JOHNSON, G. L. 1973. Magnetic telechemistry of oceanic crust? *Nature*, **245**, 373-375.

WADGE, G. 1981. The variation of magma discharge during basaltic eruptions. *Journal of Volcanology and Geothermal Research*, **11**, 139-168.

WALKER, C. 1992a. The volcanic history and geochemical evolution of the Hveragerdi region, S. W. Iceland. *Ph.D. Thesis, University of Durham.*

WALKER, G. P. L. 1971. Compound and simple lava flows and flood basalts. *Bulletin of Volcanology*, **35**, 1-12.

WALKER, G. P. L. 1992b. Morphometric study of pillow-size spectrum among pillow lavas *Bulletin of Volcanology*, **54**, 459-474.

WEAVER, J. S. & LANGMUIR, C. H. 1990. Calculation of phase equilibrium in mineral-melt systems. *Computers and Geosciences*, **16**, 1-19.

WESSEL, P. & SMITH, W. H. F. 1992. Generic mapping tools (GMT) for manipulating multidimensional datasets (version 2.1.2). Available via ftp from kiawe.soest.hawaii.edu (Internet address 128.171.151.16).

WHITE, R. S., DETRICK, R. S., SINHA, M. C. & CORMIER, M. H. 1984. Anomalous seismic crustal structure of oceanic fracture zones. *Geophysical Journal of the Royal Astronomical Society*, **79**, 779-798.

WHITEHEAD, J. A. 1986. Buoyancy-driven instabilities of low-viscosity zones as models of magma-rich zones. *Journal of Geophysical Research*, **91**, 9,303-9,314.

WHITEHEAD, J. A., DICK, H. J. B. & SCHOUTEN, H. 1984. A mechanism for magmatic accretion under spreading centres. *Nature*, **312**, 146-148.

WHITMARSH, R. B. & LAUGHTON, A. S. 1976. A long-range sonar study of the Mid-Atlantic crest near 37°N (Famous area) and its tectonic implications. *Deep-Sea Research*, **23**, 1,005-1,023.

WILCOCK, W. S. D., PURDY, G. M. & SOLOMON, S. C. 1990. Microearthquake evidence for extension across the Kane Transform Fault. *Journal of Geophysical Research*, **95**, 15,439-15,462.

WILKINSON, J. F. G. 1982. The genesis of mid-ocean ridge basalt. *Earth Science Reviews*, **18**, 1-57.

WILLIAMS, H. & MCBIRNEY, A. R. 1979. *Volcanology.* Freeman and Cooper Publishing Co., San Francisco, California.

WILSON, D. S. 1992. Focused mantle upwelling beneath mid-ocean ridges: evidence from seamount formation and isostatic compensation of topography. *Earth and Planetary Science Letters,* **113,** 41-55.

WILSON, J. T. 1965. A new class of faults and their bearing on continental drift. *Nature,* **207,** 343-347.

WILSON, M. 1989. *Igneous petrogenesis: A global tectonic approach.* Unwin Hyman, London.

WOODCOCK, N. H. & FISCHER, M. 1986. Strike-slip duplexes. *Journal of Structural Geology,* **8** (no.7), 725-735.

WRIGHT, T. L. & DOHERTY, P. C. 1970. A linear programming and least squares computer method for solving petrologic mixing problems. *Geological Society of America Bulletin,* **81,** 1,995-2,008.

YAMAGISHI, H. 1985. Growth of pillow lobes - evidence from pillow lavas of Hokkaido, Japan and North Island, New Zealand. *Geology,* **13,** 499-502.

YODER. H. S. JR. & TILLEY, C. E. 1962. Origin of basalt magmas: an experimental study of natural and synthetic rock systems: *Journal of Petrology,* **3,** 342-532.

ZONENSHAIN, L. P., KUZMIN, M. I., LISITSIN, A. P., BOGDANOV, YU. A. & BARANOV, B. V. 1989. Tectonics of the Mid-Atlantic rift valley between the TAG and MARK areas (26-24°N): evidence for vertical tectonism. *Tectonophysics,* **159,** 1-23.

BLANK IN ORIGINAL

Appendix 1

Generation of bathymetric maps.

Examples of typical shell scripts used to generate figures using GMT (Wessel & Smith, 1992).

```
#!/bin/csh
# shell script used to generate figure 2.6 -colour bathymetry map
# and two cross section profiles
unalias rm
rm track.xy, track.dz
rm wmap.grd wfine.grd
rm fig26.ps
GMT
grdcut marnok.grd -Gwmap.grd -R-46:14/-46:08/24:33/24:38
grdsample wmap.grd -Gwfine.grd -N445/371
grdimage wfine.grd -Clay.cpt -Jm50 -Ba1mf1mg1m -X2.0 -Y6.3 -P -K > fig26.ps
grdcontour wfine.grd -C50. -A100f6 -Jm50 -Wc0.5 -Wa1.2 -T -V -P -O -K >> fig26.ps
psxy layov.1 -Jm -R -W2 -O -V -K >> fig26.ps
psxy layov.2 -Jm -R -W2 -O -V -K >> fig26.ps
#
# Now generate first section
#
sampleld layov.2 -I0.0001 -L | awk '{printf("%f %f\n",$1-360.0,$2)}' > track.xy
grdtrack track.xy -Gwfine.grd -V |\
 awk '{printf("%f %f\n",-(sqrt($1*$1+$2*$2)-52.291084),$3)}'  > track.dz
psxy track.dz -R-0.057476/0.0000/-5000./-3000. -Bg0.06/a500g100 -JX5.4/1.8 -W2 -X-0.2 -Y-2
rm track.xy, track.dz
#
# Now generate second section
#
sampleld layov.1 -I0.0001 -L | awk '{printf("%f %f\n",$1-360.0,$2)}' > track.xy
grdtrack track.xy -Gwfine.grd -V |\
 awk '{printf("%f %f\n",-(sqrt($1*$1+$2*$2)-52.291676),$3)}'  > track.dz
psxy track.dz -R-0.058640/0.0000/-5000./-3000. -Bg0.06/a500g100 -JX5.4/1.8 -W1 -X0.0 -Y-2.
exit(0)
```

```
#!/bin/csh
# shell to generate figure 2.7
unalias rm
rm map.grd fine.grd
rm fig27.ps
GMT
grdcut marnok.grd -Gmap.grd -R-46:04/-46:00/23:47/23:50.31
grdsample map.grd -Gfine.grd -I0.000444444
grdimage fine.grd -Cshad.cpt -Jm80 -Ba1mf1mg1m -P -X1.8 -Y6.3 -V -K >   fig27.ps
grdcontour fine.grd -C5Q. -A100f8 -Jm80 -Wc0 \
-Wa1 -P -T -V -O -K >> fig27.ps
rm map.grd fine.grd
grdcut marnok.grd -Gmap.grd -R-46:23/-46:19/23:48.611/23:51.58
grdsample map.grd -Gfine.grd -I0.000444444
grdimage fine.grd -Cshad.cpt -Jm80 -Ba1mf1mg1m -P -O -X0.0 -Y-5.1 -V -K >> fig27.p
grdcontour fine.grd -C50. -A100f8 -Jm80 -Wc0 \
 -Wa1 -P -T -V -O >> fig27.ps
```

```
#!/bin/csh
# Script to create a colour scale .  It utilises the GMT command
#rainbow which creates a colour scale but in reverse.  It then breaks the file
# up reversing the colour scale and pastes it back together.
#
rainbow -Z-6000/-1800/20 -C -G3.0 > rain2.col
cat rain2.col | awk '{print $1}' > cont1
cat rain2.col | awk '{print $5}' > cont2
sort -o colsrev rain2.col
cat colsrev | awk '{print $2, $3, $4}' > cols1
cat colsrev | awk '{print $6, $7, $8}' > cols2
paste cont1 cols2 cont2 cols1 > rainbow1.cpt
rm rain2.col cont1 cont2 cols1 cols2 colsrev
```

```
#!/bin/csh
#typical shell used to generate bathymetry overlays
#this is for the median ridge east of 46 degrees W
unalias rm
rm medridmap2.grd medridfine2.grd
rm medridmap2.ps
GMT
grdcut transform.grd -Gmedridmap2.grd -R-46:00/-45:53/23:44.5/23:49
grdsample medridmap2.grd -Gmedridfine2.grd -N351/226
grdcontour medridfine2.grd -C20 -Jm80 -A100/f8 -Wa2/0/0/0 -Wc1/0/0/0
-T -Ba1mg1m -X1.2 -V > medridmap2.ps
exit(0)
```

RGB colour scales used to generate output on various printers.

```
# RGB colour scale used on colour bathymetric overlay
# colours are chosen for colour laser printer
#
-4550   245     0       255     -4500   245     0       255
-4500   230     0       255     -4450   230     0       255
-4450   190     0       255     -4400   190     0       255
-4400   150     0       255     -4350   150     0       255
-4350   120     0       255     -4300   120     0       255
-4300   0       130     255     -4250   0       130     255
-4250   0       160     255     -4200   0       160     255
-4200   0       190     255     -4150   0       190     255
-4150   0       231     255     -4100   0       231     255
-4100   0       255     255     -4050   0       255     255
-4050   0       255     219     -4000   0       255     219
-4000   0       255     158     -3950   0       255     158
-3950   0       255     97      -3900   0       255     97
-3900   85      255     0       -3850   85      255     0
-3850   146     255     0       -3800   146     255     0
-3800   207     255     0       -3750   207     255     0
-3750   230     255     0       -3700   230     255     0
-3700   255     255     0       -3650   255     255     0
-3650   255     230     0       -3600   255     230     0
-3600   255     210     0       -3550   255     210     0
-3550   255     190     0       -3500   255     190     0
-3500   255     170     0       -3450   255     170     0
-3450   255     150     0       -3400   255     150     0
-3400   255     130     30      -3350   255     130     30
-3350   255     120     60      -3300   255     120     60
-3300   255     130     90      -3250   255     130     90
-3250   255     150     120     -3200   255     150     120
-3200   255     180     150     -3150   255     180     150
-3150   255     200     170     -3100   255     220     170
-3100   255     220     200     -3050   255     220     200
-3050   255     240     220     -3000   255     240     220
B       0       0       0
F       255     255     255

# RGB colour table for MARNOK bathymetry
# colours best for output on the colour versatec
-6000   150     0       150     -5800   150     0       150
-5800   200     0       200     -5600   200     0       200
-5600   190     0       255     -5400   190     0       255
-5400   150     0       255     -5200   150     0       255
-5200   100     0       255     -5000   100     0       255
-5000   0       0       255     -4800   0       0       255
-4800   0       190     255     -4600   0       190     255
-4600   0       255     255     -4400   0       255     255
-4400   0       255     190     -4200   0       255     190
-4200   0       255     150     -4000   0       255     150
-4000   0       255     0       -3800   0       255     0
-3800   75      255     75      -3600   75      255     75
-3600   150     255     0       -3400   150     255     0
-3400   190     255     0       -3200   190     255     0
-3200   255     255     0       -3000   255     255     0
-3000   255     190     0       -2800   255     190     0
-2800   255     150     0       -2600   255     150     0
-2600   255     120     0       -2400   255     120     0
-2400   255     75      0       -2200   255     75      0
-2200   255     75      75      -2000   255     75      75
-2000   255     100     100     -1800   255     100     100
-1800   255     150     150     -1600   255     150     150
-1600   255     175     175     -1400   255     175     175
B       0       0       0
F       255     255     255
```

```
# RGB colour scale used for MARNOK bathymetry
# colours best for output on the thermal wax
-6000   150     0       150     -5800   150     0       150
-5800   200     0       200     -5600   200     0       200
-5600   190     0       255     -5400   190     0       255
-5400   150     0       255     -5200   150     0       255
-5200   100     0       255     -5000   100     0       255
-5000   0       0       255     -4800   0       0       255
-4800   0       100     255     -4600   0       100     255
-4600   0       190     255     -4400   0       190     255
-4400   0       225     255     -4200   0       225     255
-4200   0       255     255     -4000   0       255     255
-4000   0       255     190     -3800   0       255     190
-3800   0       255     150     -3600   0       255     150
-3600   0       255     0       -3400   0       255     0
-3400   75      255     75      -3200   75      255     75
-3200   150     255     0       -3000   150     255     0
-3000   190     255     0       -2800   190     255     0
-2800   255     255     0       -2600   255     255     0
-2600   255     190     0       -2400   255     190     0
-2400   255     150     0       -2200   255     150     0
-2200   255     120     0       -2000   255     120     0
-2000   255     75      0       -1800   255     75      0
-1800   255     75      75      -1600   255     75      75
-1600   255     100     100     -1400   255     100     100
-1400   255     150     150     -1200   255     150     150
-1200   255     175     175     -1000   255     175     175
B       0       0       0
F       255     255     255
```

BLANK IN ORIGINAL

Appendix 2

Construction of high resolution profiles from WASP traverses.

A2.1 Aims and Theory.

The WASP deep tow-camera system carries a pressure sensor and a 35.5kHz near bottom echo sounder. Although the primary function of these monitors is to aid the operators to fly the camera at an optimum height above the seafloor, the readings can also be used to construct a high resolution depth vs. time profile. The hard copy trace of the signal from the pressure transducer gives a value of 'metres delay' which is then converted to 'true pressure' using a pressure transducer calibration. The empirical equation for a standard ocean (T = 0°C, salinity = 35 ppm) of Saunders (1981) stated in [1] below was used to convert pressure to depth of vehicle.

$$Z = (1-c_1)p - c_2p^2 \qquad [1]$$

(Where Z is the depth in metres, p is the pressure in decibars,

$c_1 = (5.92 + 5.25\sin^2\phi) \times 10^{-3}\ mdb^{-1}$, *$\phi$ being the latitude in degrees*

and $c_2 = 2.21 \times 10^{-6}\ mdb^{-2}$ *)*

The echo sounder trace is used to calculate the altitude of the vehicle above the seafloor and this is added to the vehicle depth to give a value for seafloor depth. The high resolution profiles can be correlated with the SeaBeam bathymetry to constrain the position of the camera during the runs. It is also used during the interpretation of the photographs in the frame description log.

A2.2 Digitising the Waverley linescan hard copies.

The Waverley linescan hard copies were the only available records of the measurements from the WASP monitoring instruments. The hard copies were digitised on the digitising table using the program **'dig'** (D. L. Stevenson). This returns x,y positions of the mouse crosswires and a flag (1, 2 or 3) when the respective button on the mouse is pressed.

The hard copy is a continuous paper output, aspects of which are illustrated in figure A2.1. The long axis of the paper has regular time intervals marked in the x direction (every 6 mins for 26W & 10 mins for 28W). There are 4 traces of interest: the baseline reference trace; the phase calibration trace; the pressure trace; and the near bottom echo sounder (NBES). The y direction is divided into 15 arbitrary sonar units. The NBES is calibrated so that each one of these sonar units is 10m of altitude when the altitude is less than 80m. The altitude is obtained by measuring the difference between the NBES trace and the baseline and applying the above calibration. When the altitude is greater than the maximum range of 80m the NBES trace runs parallel to the reference trace at a spacing of 8 sonar units. The hard copies were only digitised over the area where the NBES is within range.

The difference between the pressure trace and the baseline reference trace is the 'metres delay', measured so that a complete sweep of 15 arbitrary sonar units is 1500m delay. The phase calibration trace runs parallel to the baseline trace with the distance between them indicating the phase of the pressure calibration. There is no calibration trace for the 1st phase which is for a signal of 0-1volts from the transducer representing 0-1000 meters delay. The 2nd phase (1-2V, 1000-2000m delay) is flagged by the presence of the calibration trace 2cm below the reference line. For the 3rd phase (2-3V, 2000-3000m delay) the calibration trace is 1.5cm below the reference. The trend continues for the 4th and 5th phases where the calibration markings are at 1cm and 0.5cm respectively.

The recorder is set to wrap-round mode so as a trace rises above the limit of the top edge of the paper it continues from the bottom edge vertically below the point where it overshot the top. Where this happens the trace should be regarded as continuous with the same y coordinate at top and bottom edges. This wrap-round leads to a situation where the digitised pressure or NBES traces are below the reference trace instead of above it. The program **xtotime.c** tests for this and adds on a page width (corresponding to 15 arbitrary sonar units) to make the y coordinates continuous. At several places during the recording of the data, all the traces are offset by a constant value in the y direction. As the pressure and altitude measurements are all relative to the reference line, such jumps do not need to be corrected for during processing.

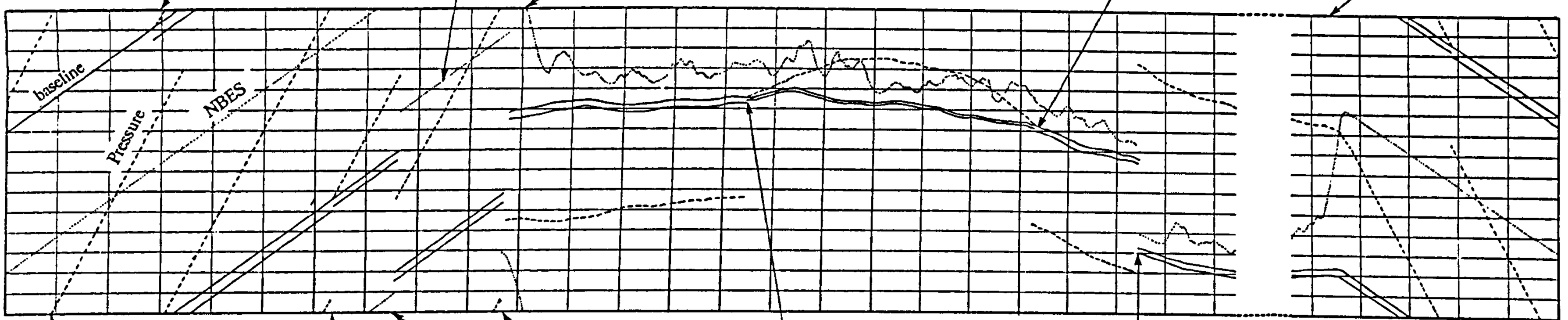

direction divided into 15 arbitrary sonar units (=1500m delay)

Calibration changes from 1st to 2nd phase. The 2nd phase is marked by the phase calibration trace which runs 2cm below the reference baseline.

NBES trace runs parallel to the baseline, 8 sonar units above when it is out of range.

When the NBES comes into range (altitude < 80m) the decreasing altitude causes the trace to fall abruptly.

Calibration changes down from 4th to 3rd phase. Distance between baseline and calibration trace changes from 1.0cm to 1.5cm.

Hauling starts, so camera moves away from bottom. The NBES locks on 80m as it moves out of range.

Paying out the wire

Traces wrap-round (i.e. when a trace rises above the top edge it continues vertically below from the bottom edge).

Calibration changes from 2nd to 3rd phase. (Phase change occurs every 1000m delay.)

Recording moved manually to keep interesting traces clear of chart edge. All the traces are offset by a constant amount in the y-direction.

Calibration changes from 3rd to 4th phase. (Phase calibration trace moves 0.5cm closer to the baseline as the phase increases)

x-direction marked in time intervals (6mins for 26W; 10mins for 28W).

Recording is moved again.

Hauling in wire.

Records are about 6 hour long in all.

Key to Traces.

- Baseline reference trace
- Phase calibration trace runs parallel below.
- Pressure trace
- Near Bottom Echo Sounder - altitude trace.

Figure A2.1 Illustration of WASP hard copy output, showing features of the digitised traces.

As the hard copy for a whole station is too long to be digitised in a continuous stream, it is divided into sections of about one hour in length. The section to be digitised is taped down on the table within the limits in which the digitiser operates, with the edges as near to colinear with the x and y axes of the digitiser as possible. As the WASP frames were taken every 30 seconds, it was decided to digitise the traces at the same time interval. A 30 second grid was placed over the relevant section and for each time increment the positions of the 4 traces were digitised as follows:

phase calibration trace :	flag 1
baseline reference trace :	flag 1
pressure trace :	flag 2
NBES trace :	flag 3

Once a section has been digitised the file is edited by adding the start and end times (in decimal hours, separated by a tab) as a first line header. Each file is then input into the program **xtotime.c** which checks the data input is in sets with the correct flags and calculates the time using an average of the x coordinates for each set of 4 traces and the start and end times in the header. Before any calculation is made it would be possible to correct for a deviation of the section from alignment with the axes of the digitiser, but this was deemed unnecessary, partly due to the ability to align the paper sections accurately but mostly because the natural distortion of the paper caused a greater error which was too complex to correct for. This program also outputs (in digitised units) values for the phase calibration, pressure and altitude which are calculated by subtracting the respective y-values from that of the reference baseline.

The output files from all the sections of a complete WASP run are concatenated together and run through the program **convert.c** which outputs values of time (in decimal hours), pressure of the instrument (in bars), altitude and sea depth (in metres). The pressure transducer calibrations used in **convert.c** are described below.

A2.3 Pressure transducer calibration.

Each transducer is calibrated to give 5V for its maximum output and 1V produces 4/3sec offset of the ping. The line recorder is set so that a full sweep is 1500m delay (2 seconds), so 1V (equivalent to 1000m delay at 1500 ms^{-1}) is 2/3 sweep. The phase on the recorder changes every 2/3 sweep, so the first phase is 0-1V, the second is 1-2V etc. The 700 bar transducer was fitted during the two CD57 WASP runs. Hence, in theory, one phase is 140 bars, so:

$$\mathbf{p = 0.14m} \qquad \mathbf{[2]}$$

(where p is pressure in bars, and m is 'metres delay', so that the full paper width of 15 sonar units is 1500 meters delay)

When equation [2] was used as the calibration, a considerable discrepancy was found between the depths on the high resolution profile and those along the ship's track from the SeaBeam bathymetry. In fact, the 700bar transducer had been calibrated on a previous occasion to give a slightly different equation:

$$\mathbf{p = 0.1414m - 17.7788} \qquad \mathbf{[3]}$$

This calibration gives a better, but still imperfect fit to the SeaBeam bathymetry data. The issue of which calibration to use was further confused by the marking of the hard copies by two other alternatives. 26W was marked with one sweep being equivalent to 120atm. pressure, while 28W had 100m delay labelled as 100dbar. The calibration in equation [3] remained the closest fit to the SeaBeam data.

A2.4 Creation of the bathymetric profiles.

The program **convert.c** calculates several values for the sea depth using the different calibrations and a short shell script is used to generate a profile of depth vs. time. The command:

awk '{printf("%f %f\n", $1 $7)}'

is used to create a new x,y file of time and depth values. (The output of **convert.c** has time in field 1 and 'best' depth in field 7) A postscript file of the profile is then created using the GMT command **psxy** with the following command line arguments:

psxy *file.xy* **-R***start/endtime/lower/upperdepth* **-Ba***xintg**xint*/**a***yintg**yint* **-JX***x/ysize*

-W*pen_attributes*

The shell script **wprof** uses GMT to generate a cross-section and a map marking the position of the section from SeaBeam bathymetry datafiles in grd format. Several

sections are generated to find the best fit to the wasp profile. The shell requires an input file of the x,y coordinates of the start and end points of the profile in decimal degrees. The shell uses a linear interpolation at a specified x interval to generate a file of x,y coordinates along the section line. The grided data-set is sampled at each of these x,y positions to give x,y,z values. Before the section can be plotted the x,y coordinates must be converted to a horizontal distance using Pythagoras' theorem within the **awk** command. The horizontal distance between the origin and start point is subtracted from each of the calculated horizontal distances to ensure that the section is measured from a starting point at zero distance. The program **caldist.c** calculates the horizontal distance between the start point and the origin, the end point and the origin, and the difference between them. These values are then used to edit the shell script before it is run on each new coordinate set. The boundaries and scale of the map and section should also be edited with the shell. Further explanations of the GMT commands used and the relevant places to edit can be found as comments within the shell which is included with the other programs at the end of this appendix.
The best matches between the SeaBeam cross-sections and the high resolution profiles are shown in figures A2.2 and A2.3.

A2.5 Instrument position and navigational accuracy.

The best match of the SeaBeam cross-sections with the high resolution profiles should provide an additional navigational constraint on the position of the deep-tow camera relative to the bottom.

A2.5.1 The northern traverse (26W)

Figure A2.2 shows the comparison between the cross-section generated from the SeaBeam data-set and the high resolution profile for 26W. Two comparisons are shown: (a) is the line of the ship's track; and (b) is the 'best match' which flows a parallel trajectory about 400m to the south (figure 4.1). Although the profile directly under the ship's track is a reasonable fit, profile (b) is better as the western crest is less rounded, the undulations of the western flank are better defined and the eastern flank dips less steeply towards the end of the traverse. Hence, it is reasonable to assume that the camera followed a similar trajectory to the ship but its position was offset to the south by currents acting on the cable and the instrument sledge. However, there is a problem with this hypothesis in that the wireout readings over 26W do not allow for an offset of 400m between instrument and ship. In fact, for most of the traverse, the wireout measurements follow the depth of the high resolution profile to within 10m, the maximum discrepancy being 30m. Clearly, this suggests that camera sledge was directly beneath the ship during the traverse.

(a) Fit of bathymetry along ship's track.

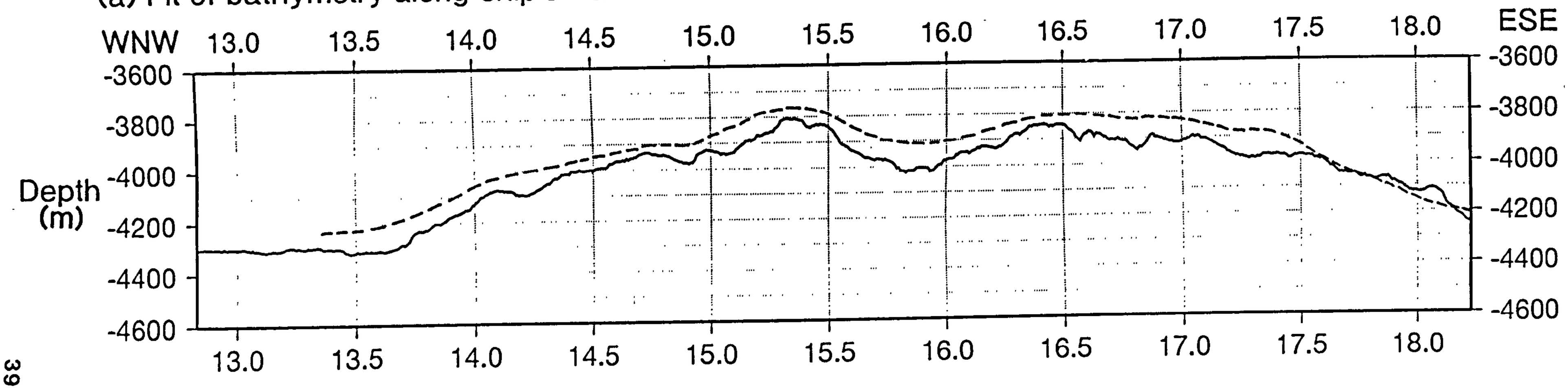

(b) Fit of section 400m south of ship's track.

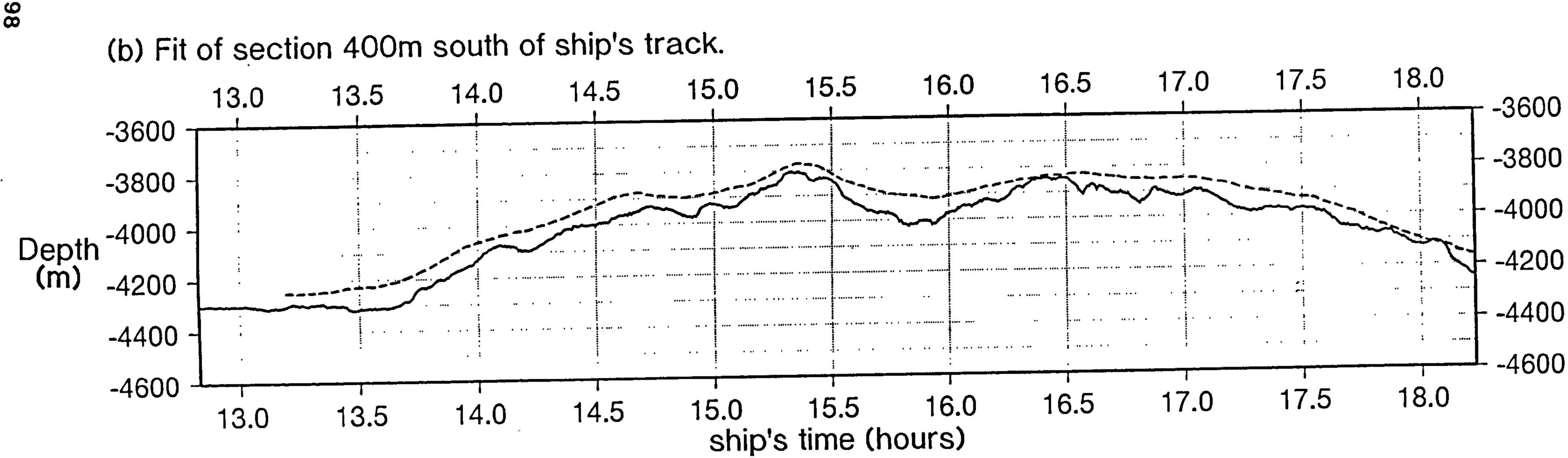

Figure A2.2 The high resolution profile of 26W obtained from WASP altimeter and instrument depth matched with SeaBeam bathymetry. See figure 4.1 for the location of the two profiles. The best fit profile occurs 400m south of the ship's track and can be used to constrain the navigation of the phototraverse. See text for a discussion on the accuracy of the SeaBeam data used to obtain the map and these profiles.

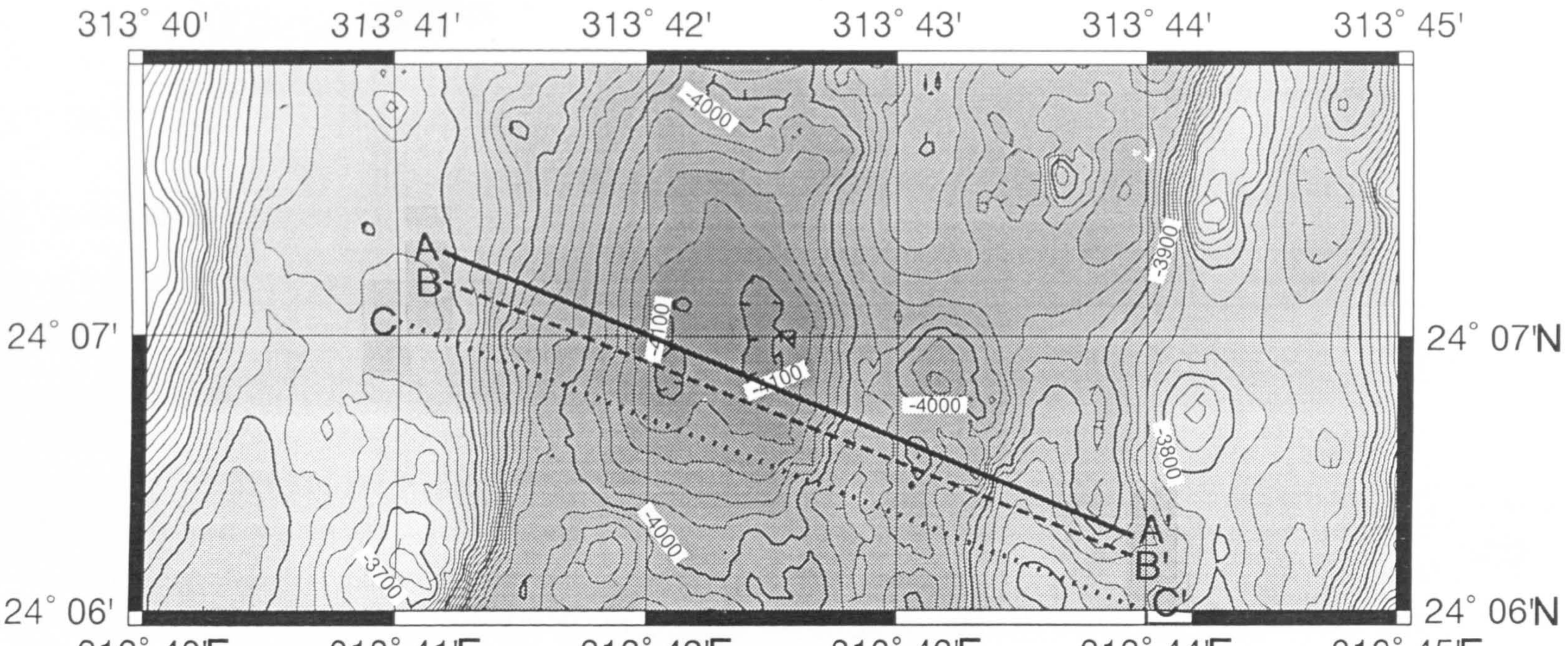

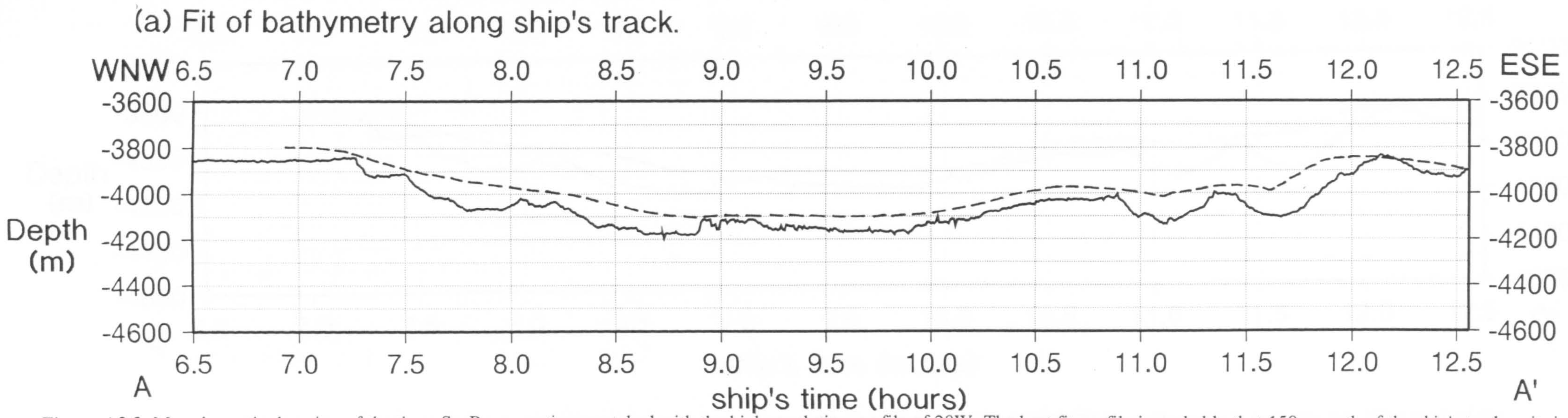

Figure A2.3 Map shows the location of the three SeaBeam sections matched with the high resolution profile of 28W. The best fit profile is probably that 150m south of the ship's track as it rises slightly higher over the crest at the end of the traverse than the section under the ship's track. As the profiles are so similar the navigational constrain of 28W is not as tight as that for 26W.

(b) Fit of section 500m south of ship's track.

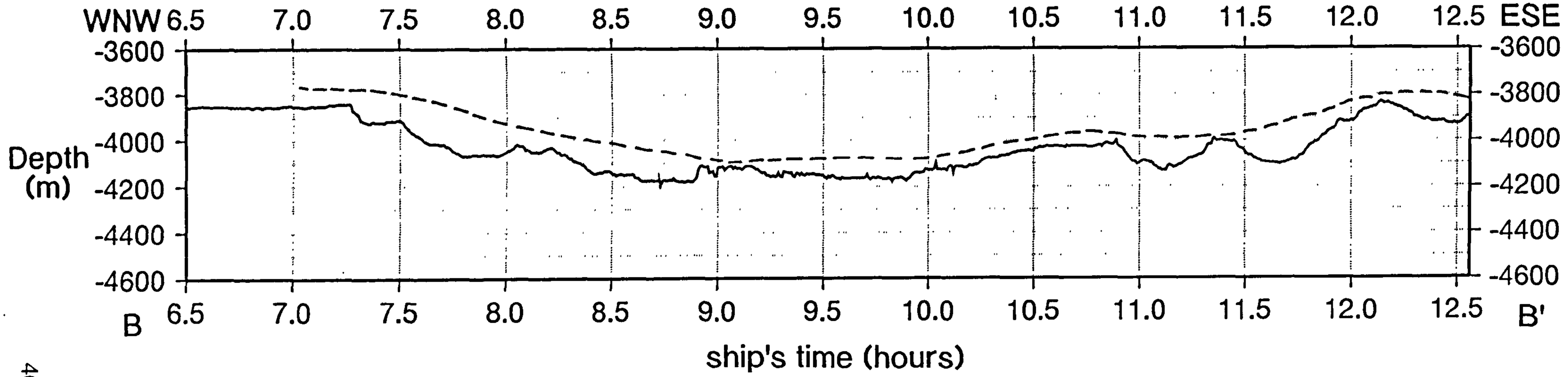

(c) Fit of section 150m south of ship's track.

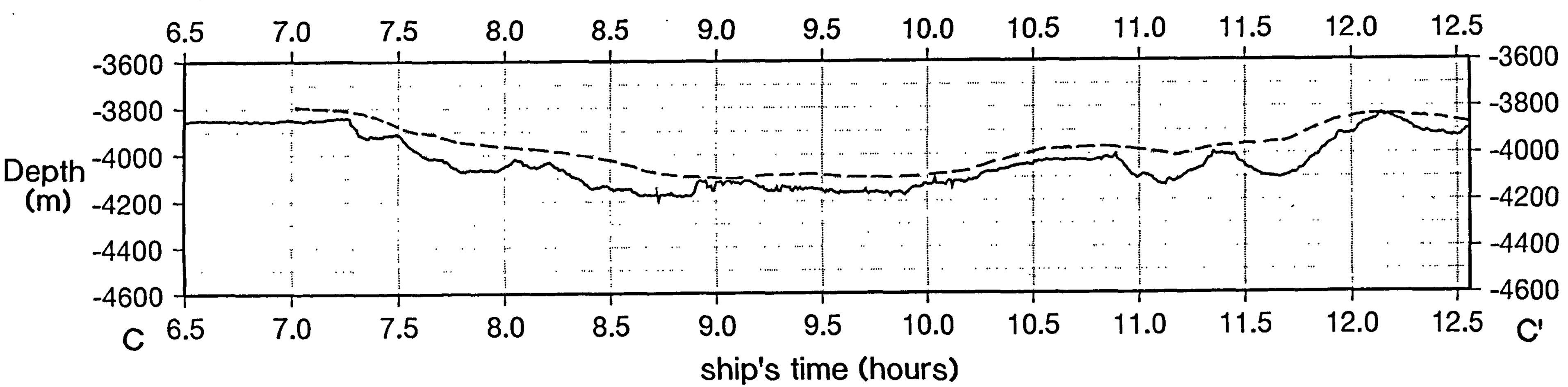

Figure A2.3 Map shows the location of the three SeaBeam sections matched with the high resolution profile of 28W. The best fit profile is probably that 150m south of the ship's track as it rises slightly higher over the crest at the end of the traverse than the section under the ship's track. As the profiles are so similar the navigational constrain of 28W is not as tight as that for 26W.

This problem is resolved by considering the navigational accuracy of the SeaBeam maps. A comparison of the SeaBeam maps printed in 1991 at WHOI (which were originally used on the cruise), with those generated in Durham using the grided data-set obtained from WHOI in 1993, shows offsets in the bathymetry with respect to the lines of latitude and longitude of the two maps. At the site of the W26 traverse, the lines of latitude of the 1991 maps are offset about 400m to the south and the longitude 100m to the east compared to the map in figure 2.1 which was generated using GMT in Durham. Consequently if the coordinates for the ship's track are plotted on the 1991 maps, the line coincides with that of the best fit profile of figure A2.2b. The offset between the two maps does not vary systematically, and in general there is a larger discrepancy between the latitude than the longitude. Such a mismatch can only be explained by a difference in the gridding of the two data-sets. The coincidence of the high resolution profile from the CD57 cruise (which was navigated with GPS) with the 1991 map suggests that the gridding of the 1991 data-set is the more accurate, at least over this small area.

During the SeaBeam survey, the strategy was to collect the majority of the data in tracks oriented perpendicular to the axis at spacings of about 3km. This produced overlapping swaths within the rift valley, while a pair of along-axis tracks provided the crossing points used to constrain the navigation. This strategy will tend to reduce the errors in longitude more than those in latitude, as the fixes for longitude of the crossing points are more consistent than those for the latitude. A consistent error in the latitude of a swath, or a number of swaths, is easily introduced if there is a discrepancy in the latitude measurements at the crossover points. This explains the observation that the divergence between the latitudes of the supposed track and the actual track is more pronounced than the offsets in longitude. It seems reasonable to conclude that the discrepancies between the 1991 and 1993 maps have resulted from different navigational adjustments of the data-set. There is a navigational uncertainty of about 925m in the SeaBeam maps (Purdy et al., 1990). The 400m discrepancy between the 1991 and 1993 data-sets at the site of 26W falls well within this error.

A2.5.2 The southern traverse (28W)

The measurements of wireout for 28W are consistently less then the depths from the high resolution profile. The divergence between wireout and depth is greater than in 26W. Over some of the faults, the depth varies more quickly than the winch team can respond, and the wire out becomes as much as 70m less than the corresponding depth on the high resolution profile. This was obvious in the photoanalysis where the camera auto-shutoff or the quality of the exposures decreased dramatically when there was a sharp drop in relief. As for 26W, this implies that the camera sledge must be

nearly vertically below the ship.

The correspondence of SeaBeam cross-sections with the high resolution profiles (figure A2.3) are not as close as that achieved for 26W. The fit over the grabens at the eastern end of the traverse is particularly poor as the SeaBeam resolution is not fine enough to pick up the rapid variations in relief at this point. Consequently, it is also harder to pinpoint a best fit for 28W, and so the constraint on the navigation is less well fixed. From three profiles matched and shown in figure A2.3 the best fit is that just to the south of the ship's track. The offset in the gridding between the 1991 and the 1993 maps are less for this area than for 26W. The 1991 latitude lines are only a 100m to the south of those of 1993, while the longitude lines are offset 150m to the east. Once again the best fit plots under the ship's track of the 1991 data-set.

A2.5.3 Strategy to maximise navigational accuracy

The navigational accuracy is a crucial factor in this study where there has been an attempt to relate the sidescan imagery and bathymetry to the dredging program. A strategy for towing the dredge and the camera were adopted to try to ensure the minimum deviation from the ship's track. At the starting location the ship would stop and maintain position while the instrument was lowered. The wireout was used to assess the deviation of the instrument from vertically below the ship. Once the instrument was at the required depth from the bottom, the ship made way along the decided course and the wireout was adjusted to maintain the required altitude.

The profile matching from the WASP surveys suggests that this strategy works, in that the camera follows the ship's track near vertically below the ship. The main source of error seems to be the accuracy of location of the SeaBeam maps themselves. This is important as the SeaBeam maps were used as the basis of all the work carried out on this and other cruises. In this, and subsequent BRIDGE cruises, the need for accurate sampling has been emphasised. In CD78, piston coring was used, not only because of its speed, but because it samples a more precise area of seafloor. It must be emphasised that without a GPS-navigated bathymetric survey the location accuracy is limited by the errors within the data-set used to select the station localities.

A2.6 WASP frame description logs.

Descriptions and interpretations of individual frames were systematically recorded on the WASP frame logs. For each frame the time and altitude were noted, although for 26W where the clock battery failed, the frame number was recorded instead of the time. The altitude measurements recorded in the data chamber seem to be unreliable as frames with the same altitude values look as if they have been taken from different heights. The log also contains a description of the rock morphologies, any structure

present and an estimate of the amount of pelagic sediment in terms of the relative age (see figure 2.1). The difficulties and errors involved in making relative age estimates are discussed in section 2.3.8. Some examples of the different flow morphologies, flow contacts and tectonic features are shown in figures A2.4, A2.5, A2.6, A2,7, and A2.8.

The final column in the frame logs is for any other comments that might help with the positioning on the high resolution profile. The direction of flow estimated from a lava surface, or the variation in relief across a frame are recorded in this section. Adjacent frames are compared to assess any overlap. This can be used to estimate the orientation of the frame relative to the general direction of motion of the camera. It is also useful for assessing the relative dimensions of the frames, especially given that the altitude readings in the data window are so unreliable. Sometimes the altitude can vary considerably between adjacent frames so that one frame can be identified as a close up of an area in another frame.

A2.7 Expanded high resolution profiles.

When the frame logs were completed the information was summarised in the expanded high resolution plots contained in this appendix. The different kinds of lava morphologies are represented by symbols, a key to which is shown below. The relative ages estimates are recorded at the top of the profile. The contacts between flows are denoted by vertical lines through the sections. A solid line indicates that the contact is observed - either a frontal talus downlaps onto the back of an older flow, there is a dramatic change in sediment cover which cannot be related to the local topography or there is an obvious contact between flows of different morphologies. A dot-dashed line indicates that the contact is not observed, but is inferred by dramatic changes in the lava morphology, variation in the bathymetry and/or the direction of flow of the lava. A dashed line is used where a contact is uncertain. There may be changes in the lava morphology or a flow contact may be suggested by the relief of the high resolution profile. There are also usually small variations in the extent of sediment cover, but these are also inconclusive.

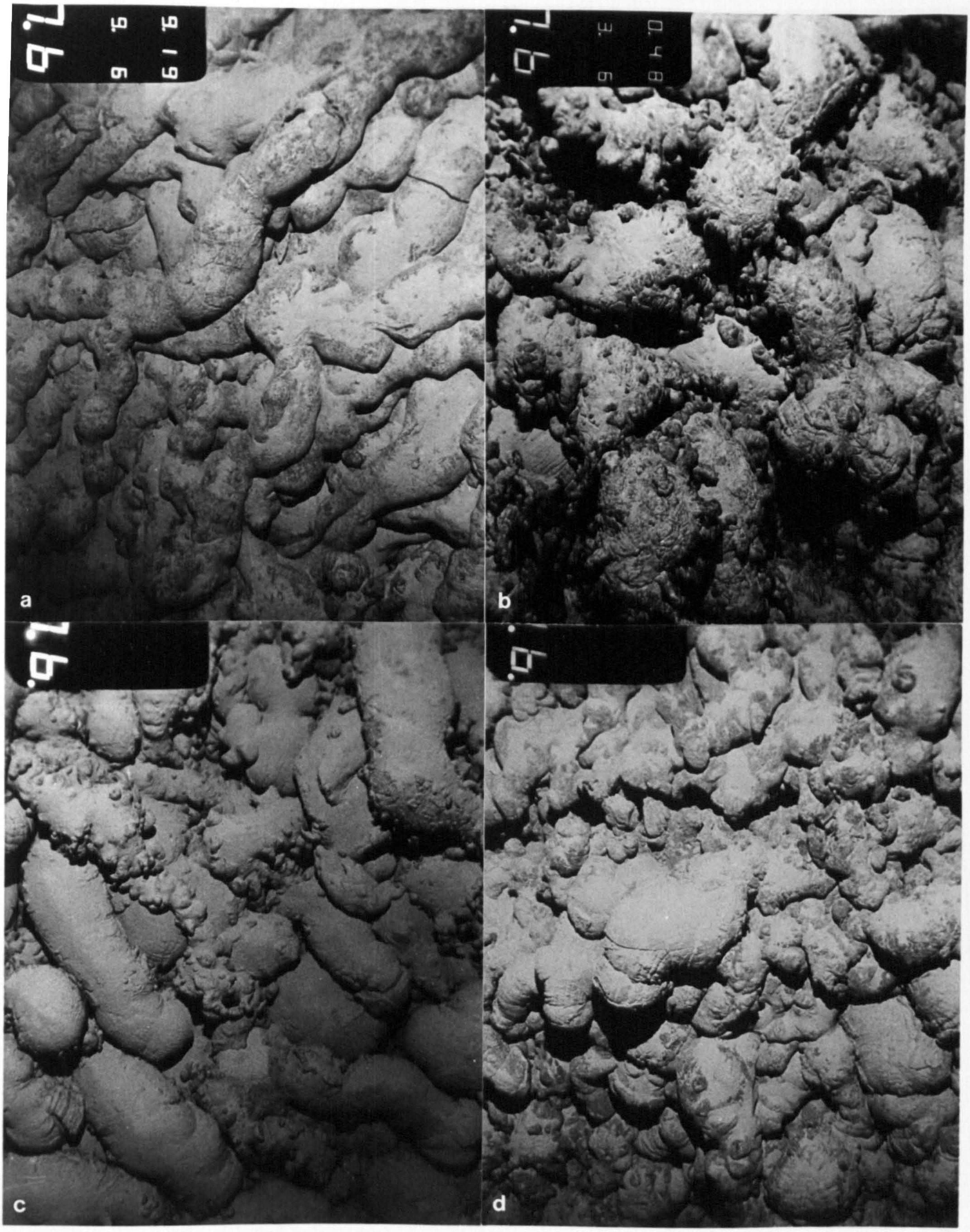

Plate A2.4 (a) Well developed lava tubes from flow 11 of the narrowgate traverse. (b) Highly knobby pillows from recent eruption, showing fingers and buds of various shapes and sizes. (c) Elongated pillows with blunt round terminations indicating flow direction. Some pillows are extremely knobby while others lack buds and have more strongly developed crenulations. (d) Transition in lava morphology from lobate character to knobby and more elongate as the flow surface steepens. A crenulated bulbous pillow and an elongated trapdoor pillow perch above the main body of the flow. The linear shadow which exends across the frame possibly marks the presence of a narrow fissure Note how all the frames have the same altitude measurement (7.6) yet it is clear that frame (b) was taken closer to the seafloor than the others. As the altitude readings are untrustworthy it is impossible to give an accurate scale bar for the WASP photographs.

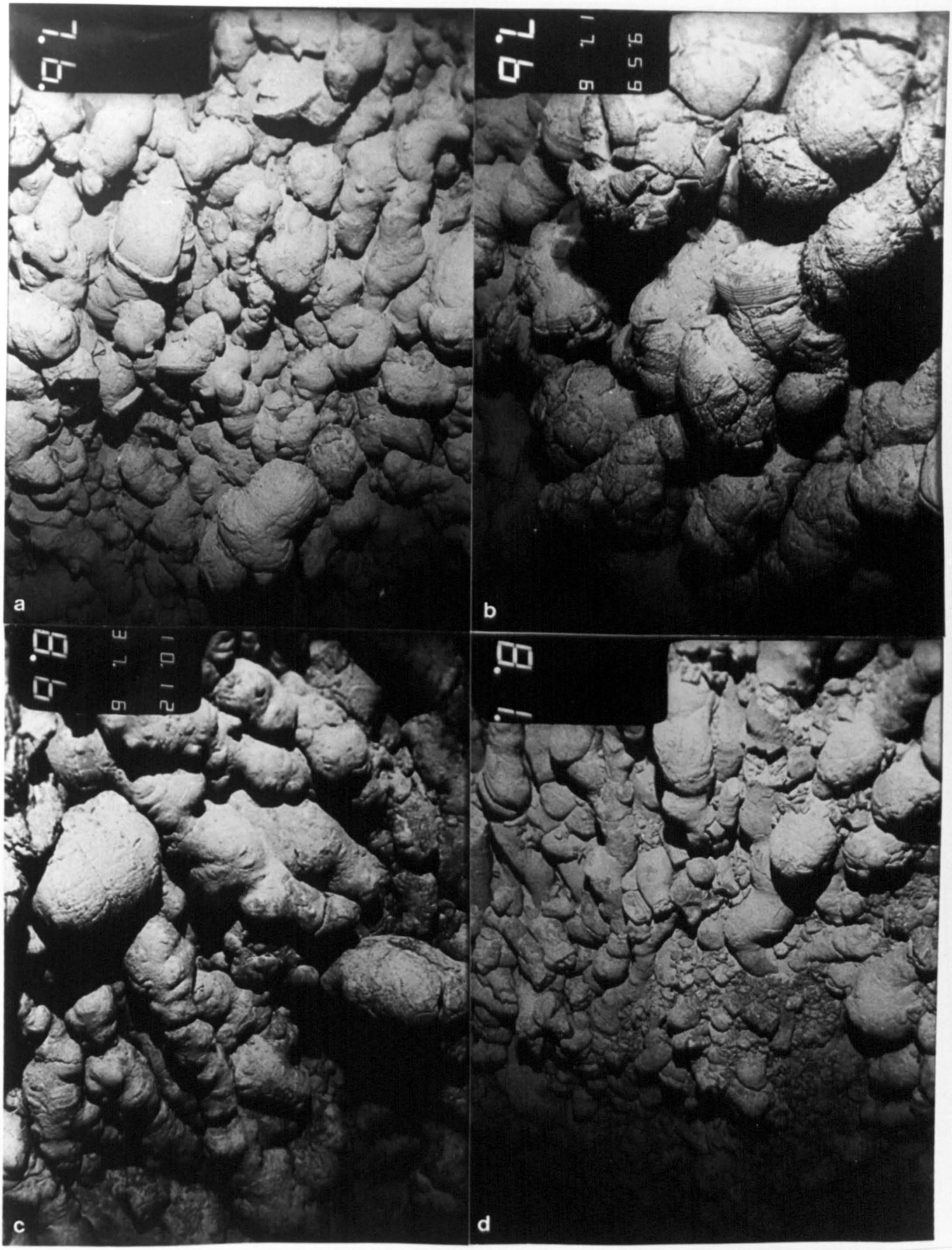

Plate A2.5 (a) Flow with a wide variety of pillow morphologies: a long thin knobby pillow is in the centre of the frame; a slightly crenulated phallic pillow is to the left of this with a number of small trapdoor pillows below; a stubby angular toothpaste pillow occurs in the shadow to the bottom right. (b) Breadcrust cracks and strongly crenulated textures indicative of slow pillow growth rates and/or more viscous lavas. (c) Elongated pillows at steep step in a knobby flow. Note how bud formation is suppressed but surface bulges are present. Although the pillows are strongly elongated here, there is no frontal breccia. This is probably not a flow front, but rather the response of the pillow morphology to the underlying topography. (d) Foreset bedded elongated pillows at a flow front, with poorly sorted breccia below forming the top of the frontal talus ramp.

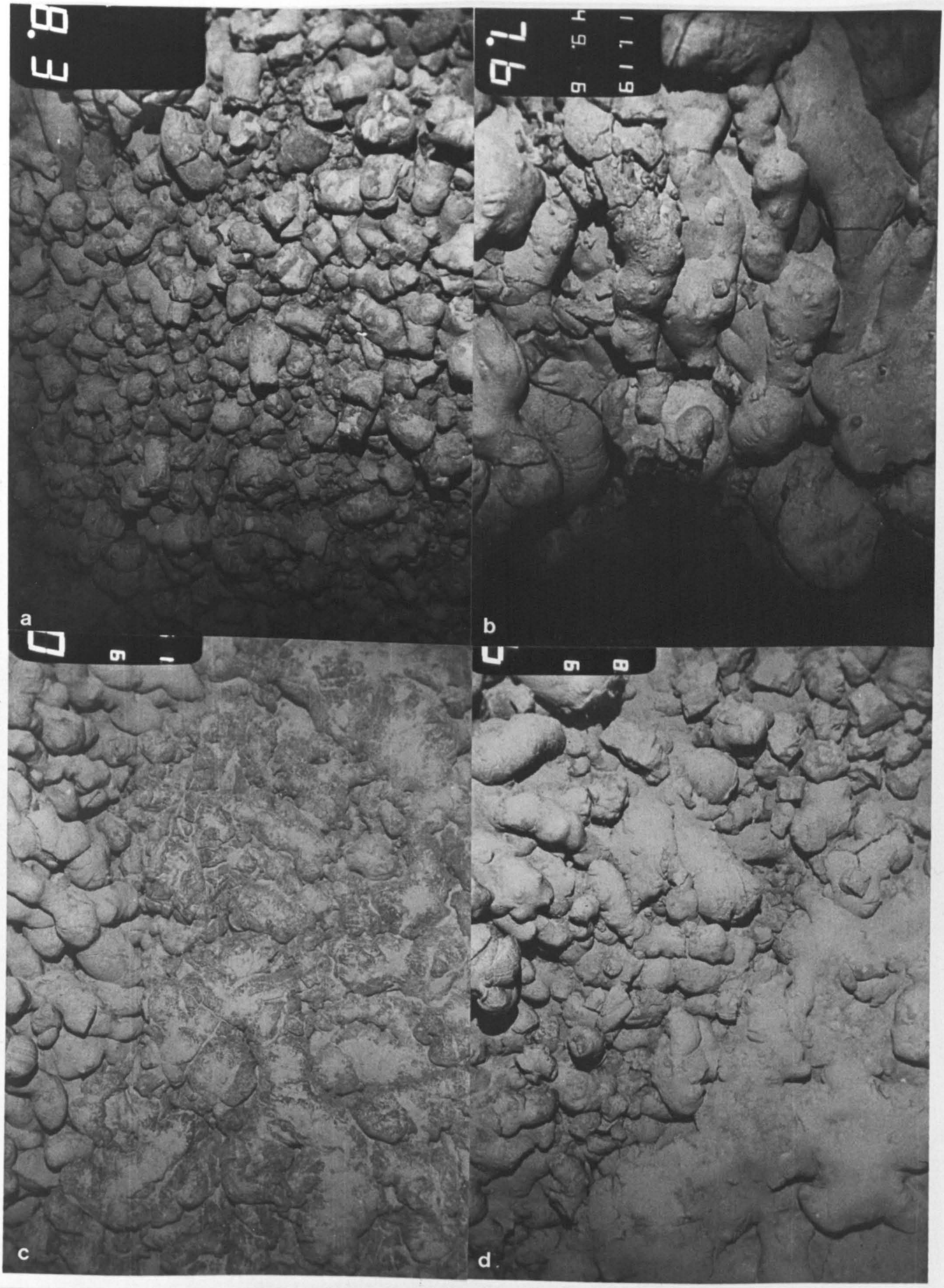

Plate A2.6 (a) Flow front breccia with a large number of cylindrical shaped cobbles from broken elongated pillows. (b) Faulted elongated pillows indicate that steep flow fronts may sometimes be associated with fault scarps. (c) Lobate sheet flow onlaps against an older pillow front, possibly burying any frontal breccia. Note how the sediment cover on the sheet flow seems greater than that on the pillows, although the contact relationship proves it is younger. (d) Striking change in sediment cover used to identify flow contacts where no steep flow front is present. The broken blocks in the top right of the frame are part of a talus ramp associated with a nearby fault.

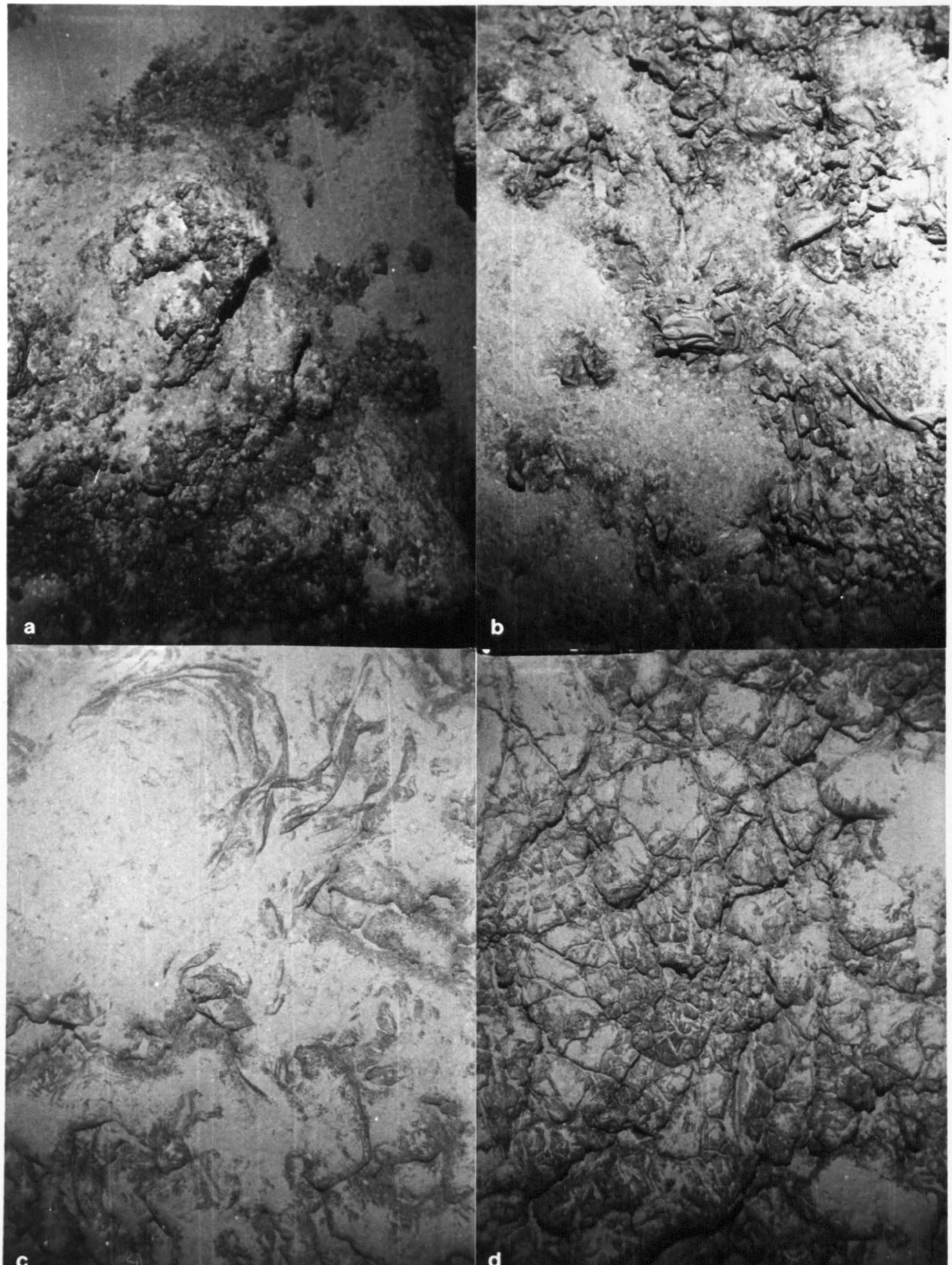

Plate A2.7 Sheet flow morphologies. (a) Granular hackly flow surface covered in gravel to pebble sized rubble. The jagged lumps create roughness on two scales, the mm/cm scale of the hackly texture and the decimetre/metre scale of the irregular topography. (b) Flow surface is rumpled with thin-skinned folding. The chaotically broken blades (bottom right) which are a feature of the jumbled flow perhaps result from intense thin skinned folding. (c) Loosely folded ropy pahoehoe transforms into a lobate flow. (d) Planar surface with irregular pattern of fractures into polygonal blocks. The morphology is similar to the pavingstone lava, which is thought to form by partial fragmentation on eruption. There is a strong relation between this and the lobate lava type as seen in the upper right of the frame.

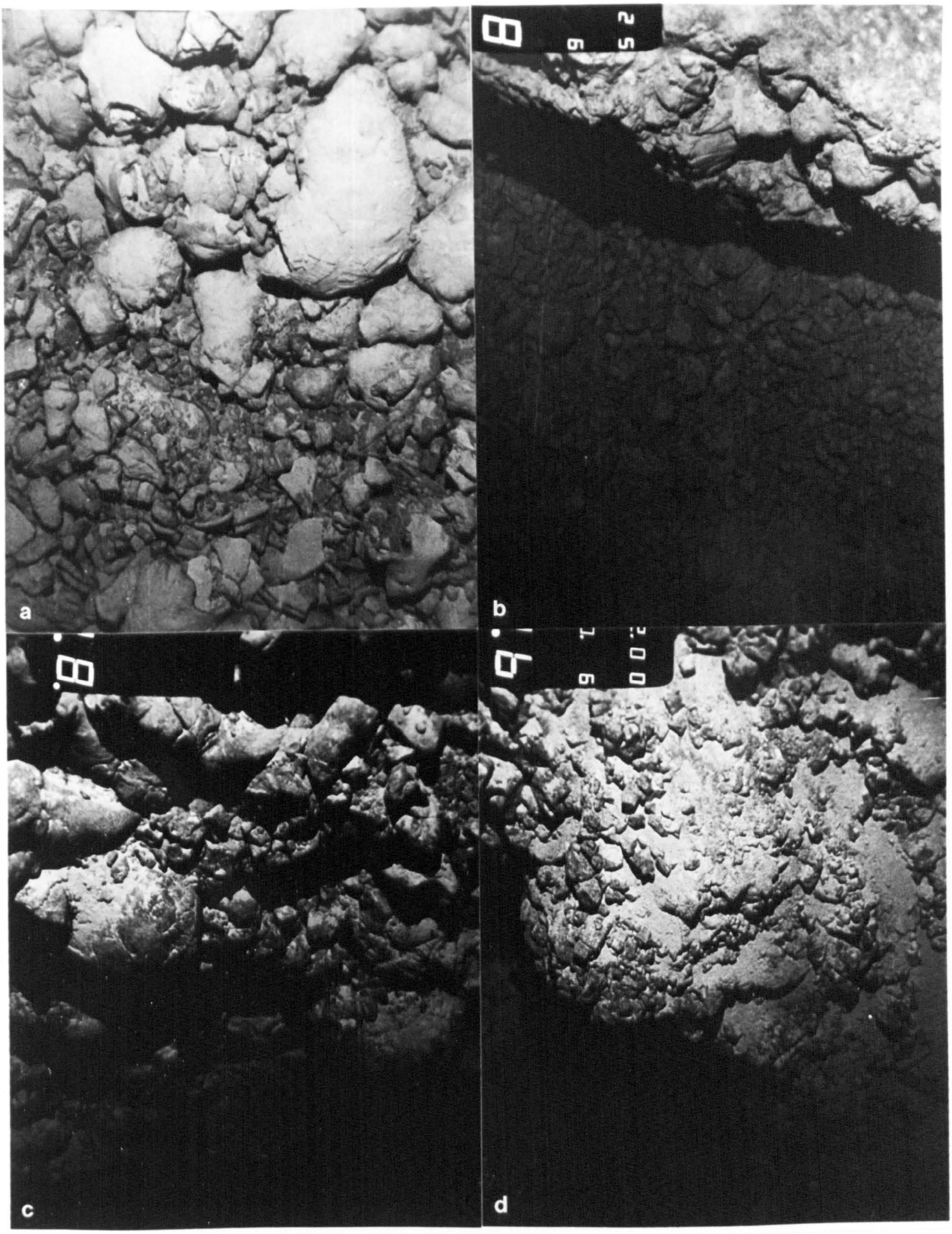

Plate A2.8 (a) A pillow flow with relatively little sedimentation, but considerable degradation is probably an indication of proximal tectonic activity. Several pillows are broken with fragments lying in situ (top left). The rims of bulbous pillows fracture in a conchoidal manner to produce slightly curved platy spall, while bread crust texture produces blocky rubble. (b) One side of a wide fissure in sedimented pillow flow (other side occurs on next frame). The scarp reveals the morphology of the underlying flow and the sediment thickness. The lack of sediment cover on the infilling breccia is an indication that the fissure was active recently compared to other fissures which are almost completely infilled with hemipelagics. (c) View down the large fault scarp on flow 15 of 26W. The fractured pillow surface is steep, but non-vertical allowing a little loose rubble and sediment to collect. (d) Near the base of one of the older and larger faults of 28W, where the scarp is almost entirely obscured by sediment and breccia. The breccia tends to be finer grained than that of flow fronts.

Key to symbols on the high resolution profiles.

bulbous pillows (with crenulations and fault slivers)

bulbous pillows with breadcrust cracks

knobby pillows

elongate pillows (elongated approximately down to the E, W, N, or S respectively indicating flow is moving in these directions)

knobby elongate pillows (orientation as above)

indistinct pillow surface

toothpaste pillows

trap-door pillows

broken pillows

hollow pillows

lobate surface

ropy sheet flow

flat cracked 'pavingstone' sheet surface

crinkled sheet flow, jumbled in places

hackly sheet flow, jumbled in places

pillow breccia blocks (usually flow front breccia or fault talus)

degraded pillow surface

hemipelagic sediment

feeding trails in sediment

narrow fissure (<50cm)

wide fissure (>50cm)

fault with relative displacement directions

direction of flow of lava

Figure A2.9 High resolution profile: 26W

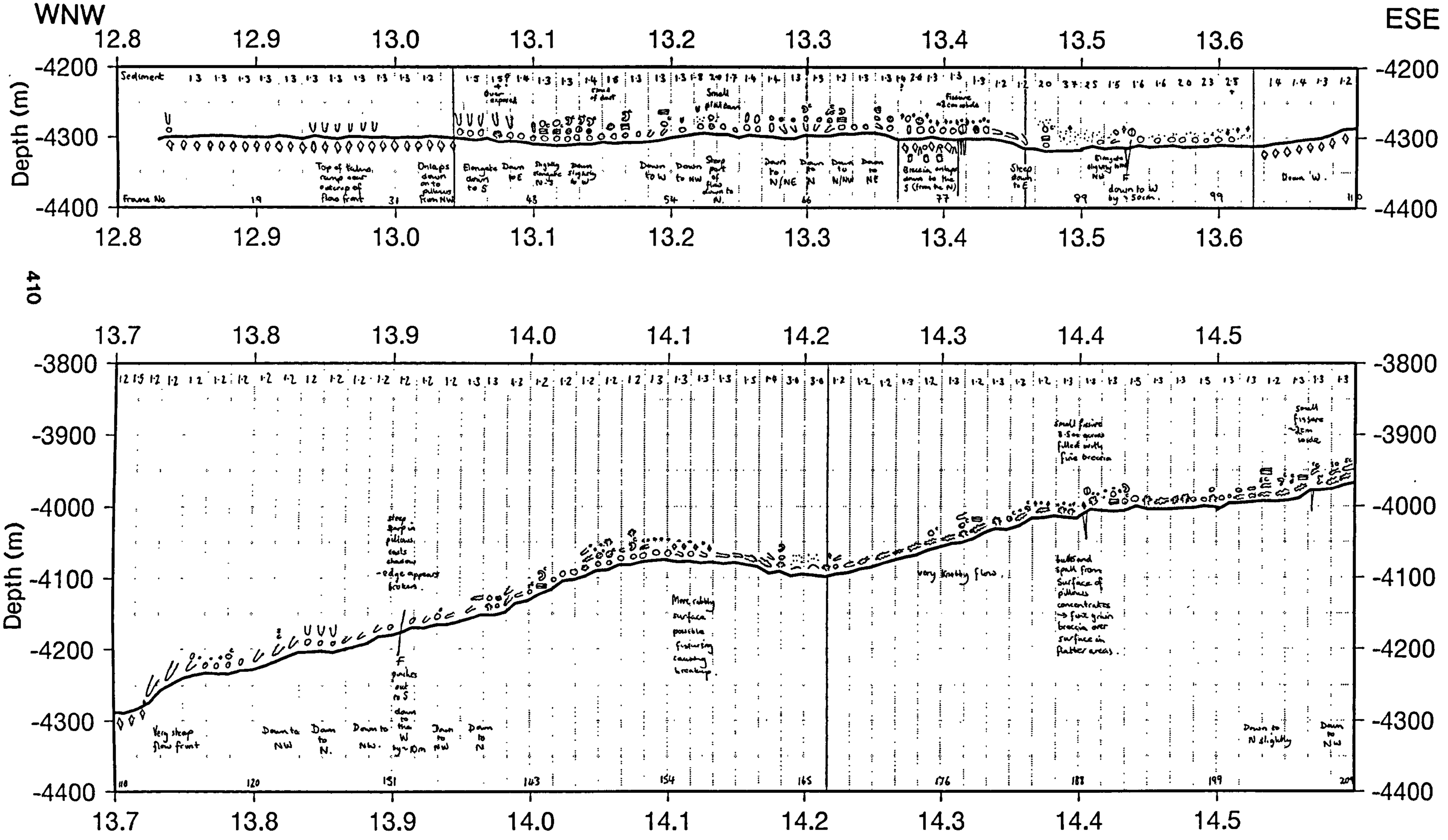

Figure A2.9 High resolution profile: 26W (continued)

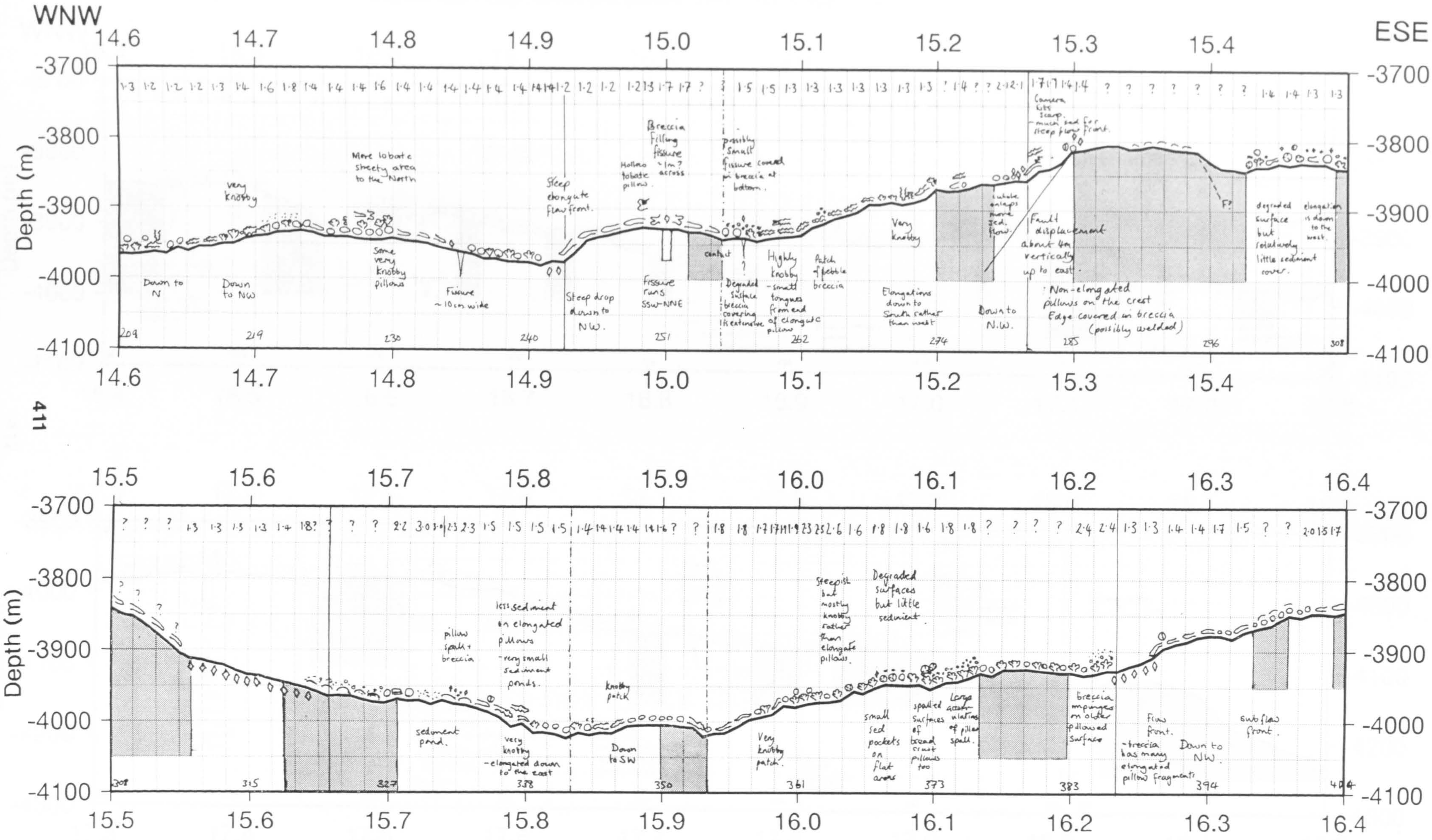

Figure A2.9 High resolution profile: 26W (continued)

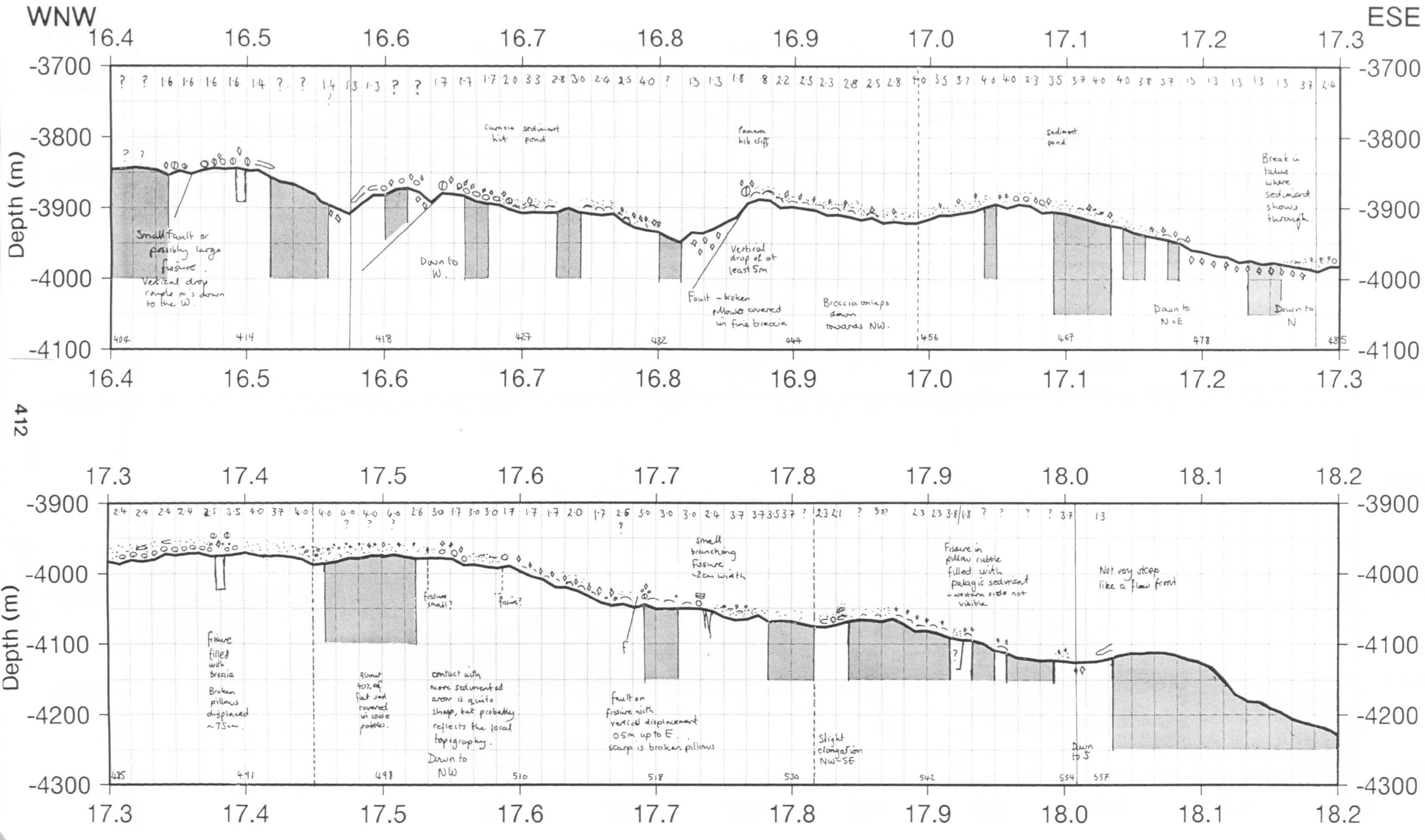

Figure A2.10 High resolution profile: 28W

Figure A2.10 High resolution profile: 28W (continued)

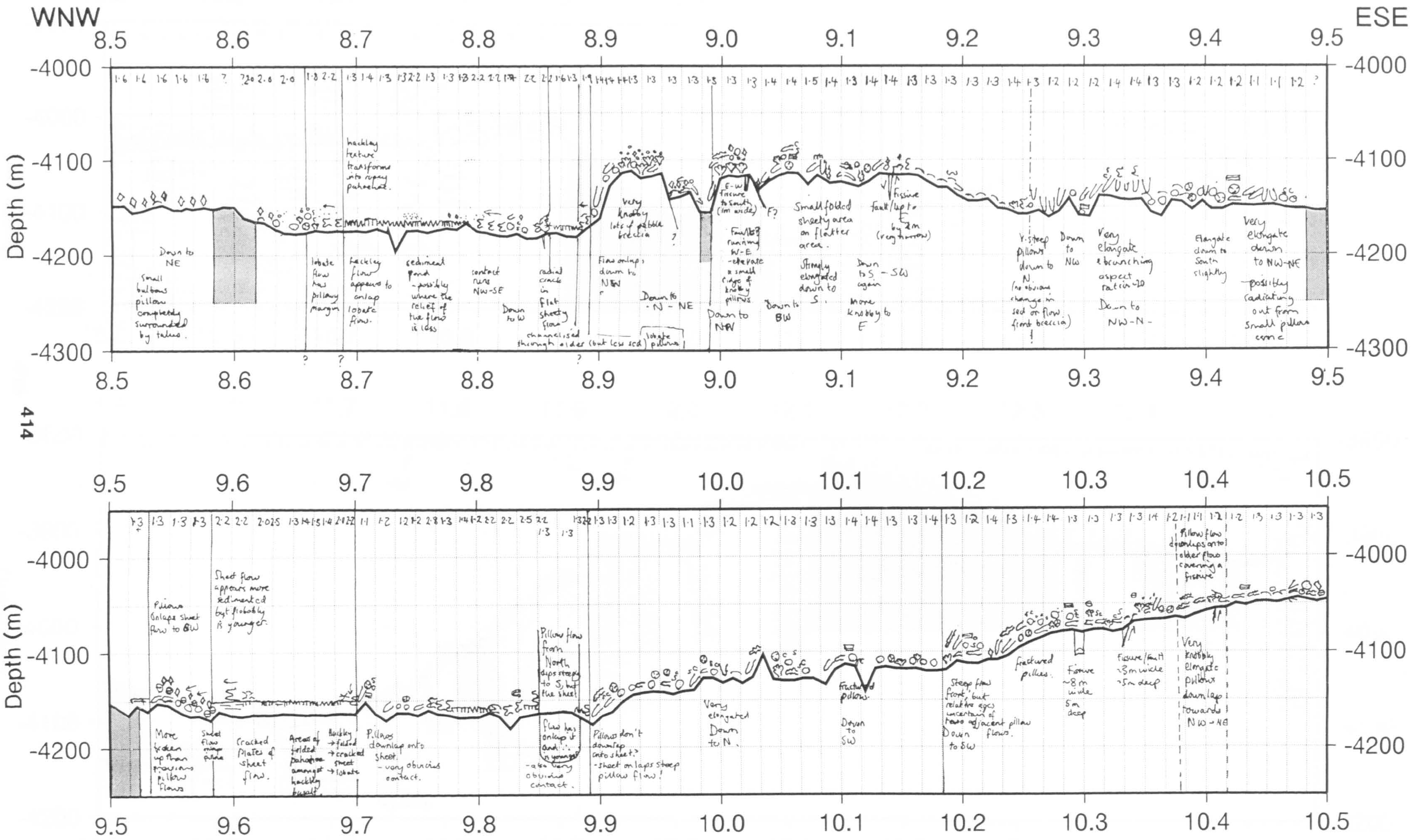

Figure A2.10 High resolution profile: 28W (continued)

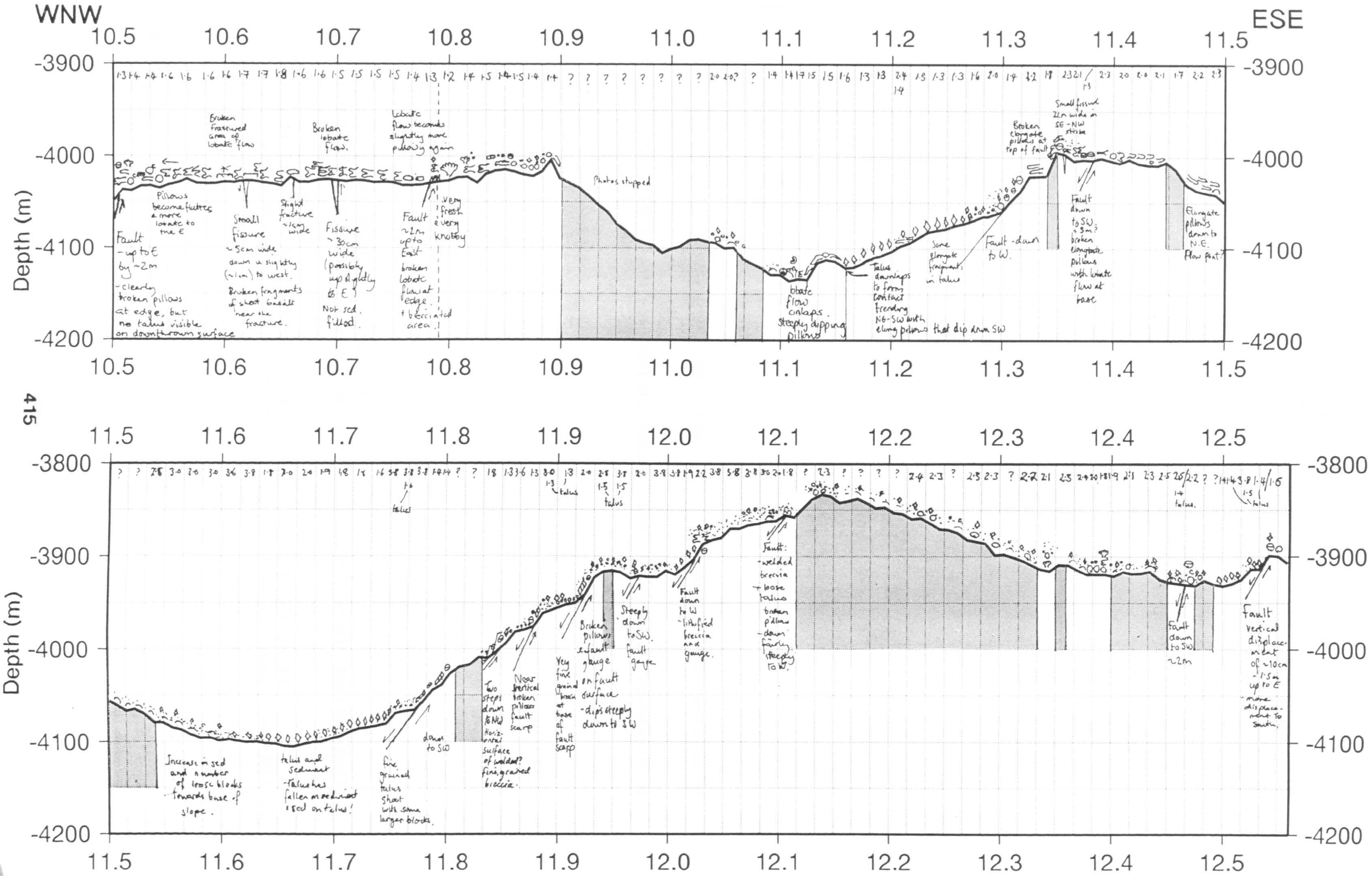

```
/*-----------------------------------------------------------------
 * convert.c : a program which outputs values for the wasp pressure and
 *             sea depth for each time interval using the output
 *             generated by program x2time.c
 *             Three different methods are used to calculate sea depth.
 *-----------------------------------------------------------------*/

#include <stdio.h>
#include <math.h>


#define MAX 2000
#define PAGE 480.0
#define ATMBAR 1.013250
float   time[MAX],
        caldiff[MAX],
        height[MAX],
        pressure[MAX],
        delay_pressure[MAX],
        delay_height[MAX],
        total_delay[MAX],
        total_pressure[MAX],
        alt_wasp_p[MAX],
        wasp_pressure[MAX],
        wasp_depth[MAX],
        total_deptha[MAX],
        total_depthb[MAX],
        total_depthc[MAX];



main ()
{  register int  stop = 0 ;
   register int  n= 0 ;

/* reading in data, 4 numbers per line: time, flag, height (mm), pressure(mm)*/
    while (!stop)
      {
        if (scanf("%f%f%f%f\n", &time[n], &caldiff[n], &height[n], &pressure[n])\
 == EOF)
        { stop=1;
        goto  stopit ; }
        else n++;
      }

stopit:
    do_cal (n) ;
}

void print_out_results (n)
        int n;
 { int i;

/*      printf("Final Results : \n\n");*/
/*      printf("no wasp_pressure wasp_depth alt_wasp_p del_height deptha  depthb
 *      depthc \n\n"); */
        for (i=0; i<n ; i++) {
        printf("%f %f %f %f %f %f %f %f\n", time[i],wasp_pressure[i],\
-wasp_depth[i],alt_wasp_p[i], delay_height[i],-total_deptha[i],-total_depthb[i],\
-total_depthc[i]);
        }
}


int do_cal (n)
        int n ;
```

```
{
int i;

for (i=0; i<n; i++) {
        delay_height[i] = height[i]*(150.0/PAGE);
        delay_pressure[i] = pressure[i]*(1500.0/PAGE);
        if ((8.0 < caldiff[i]) && (caldiff[i] < 12.0)) {
                delay_pressure[i] += 3000;
                alt_wasp_p[i] = pressure[i]*130*ATMBAR*1.5/PAGE + 3*130*ATMBAR; }
        else if ((13.0 < caldiff[i] ) && (17.0 > caldiff[i])) {
                delay_pressure[i] += 2000;
                alt_wasp_p[i] = pressure[i]*130*ATMBAR*1.5/PAGE + 2*130*ATMBAR; }
        else if (caldiff[i] < 7.0) {
                delay_pressure[i] += 4000;
                alt_wasp_p[i] = pressure[i]*130*ATMBAR*1.5/PAGE + 4*130*ATMBAR; }
        else error(n);
        total_delay[i] = delay_height[i] + delay_pressure[i];
        wasp_pressure[i] = delay_pressure[i]*0.1414 - 17.7788;
        wasp_depth[i] = wasp_pressure[i]*9.93214 \
-0.000221*wasp_pressure[i]*wasp_pressure[i];
        total_pressure[i] = total_delay[i]*0.1414 -17.7788;
        total_deptha[i] = total_pressure[i]*9.93214 \
-0.000221*total_pressure[i]*total_pressure[i];
        total_depthb[i] = wasp_depth[i] + delay_height[i];
        total_depthc[i] = (alt_wasp_p[i]*9.93214 \
-0.000221*alt_wasp_p[i]*alt_wasp_p[i] + delay_height[i]);
        if (height[i] == 0.000000) {
        total_pressure[i] = '/0';
        total_deptha[i] = '/0';
        total_depthb[i] = '/0';
        total_depthc[i] = '/0'; }
        }
print_out_results(n);

}
```

```
int error (n)
  int n;
{ fprintf (stderr, "baseline fault line %d\n", n) ;
}
```

```
/*-------------------------------------------------------------------
 * x2time.c : checks file of digitised data, averages x-values for each time
 *            interval and calculates the time-value from the start and end
 *            times in the header on the first line. Adds a pagewidth to the
 *            y-value if wrap-round has occured.
 *            The phase calibration, (in digitised units) is calculated as
 *            the difference between the two baselines.
 *            Values of altitude and pressure (also in digitised units) are
 *            calculated by subtracting the baseline value.
 *-------------------------------------------------------------------*/
#include <stdio.h>
#include <math.h>


#define MAX 2000
#define PAGE 19172.0
float   x[MAX],
        cal1[MAX],
        cal2[MAX],
        caldiff[MAX],
        height[MAX],
        pressure[MAX],
        time[MAX];

float x1,x2,x3,x4,start,endtime ;

int  flag ;

main ()
{  register int  stop = 0 ;
   register int  n = 0 ;

/* read in start and endtime */
        scanf ("%f%f\n", &start, &endtime);

/* reading in data, 3 numbers per line = x,y,f with 3 or 4 lines per time
 * interval */
/* cal1=calibration baseline, cal2=baseline, pressure, altitude(optional)*/
    while (!stop)
      {
        if (scanf ("%f%f%d\n", &x1, &cal1[n], &flag) == EOF)
            goto  stopit ;
        if (flag != 1)
                fault(n);
noalt:  scanf ("%f%f%d\n", &x2, &cal2[n], &flag) ;
        if (flag != 1)
                fault(n);
        caldiff [n]  =  cal2[n]-cal1[n] ;
        scanf ("%f%f%d\n", &x3, &pressure[n], &flag) ;
        if (flag != 2)
                fault(n);
        if (scanf ("%f%f%d\n", &x4, &height[n], &flag) == EOF)
                goto doneall ;
/* if there is no altitude goto no_alt */
if (flag==1)
        goto no_alt ;
if (flag!=3)
        goto no_alt ;

x[n]  =  (x1+x2+x3+x4)/4.0 ;
pressure[n] -= cal2[n] ;
if (pressure[n] < 0.0) pressure[n] += PAGE;
height[n] -= cal2 [n] ;
if (height[n] < 0.0) height[n] += PAGE;
goto next ;
```

```
doneall: stop = 1 ;
no_alt: x[n]  =  (x1+x2+x3)/3.0 ;
        call [n+1]  =  height[n];
        height[n]  =  0.0 ;
        x1  =  x4 ;
        pressure[n]-=cal2[n] ;
        if (pressure[n] < 0.0) pressure[n] += PAGE;
        if (!stop)
        { n++ ;
          goto noalt ;
        }
next:   n++;
      }
stopit:
    do_time (n) ;
}
```

```
void print_out_results (n)
        int n;
 { int i;
        for (i=0; i<n ; i++) {
        printf("%f %f %f %f\n", time[i], caldiff[i], height[i], pressure[i]);
        }
}


int do_time (n)
        int n ;
{
float timediff,ydist;
int i;
timediff = endtime-start;
ydist = timediff/(x[n-1]-x[0]);
/*printf("%f %f %f %f\n", timediff, ydist, x[n-1], x[0]);*/
for (i=0; i<n; i++) {
        time[i] = (x[i]-x[0])*ydist + start; }
print_out_results (n);
}

int error (n)
  int n;
{ fprintf (stderr, "baseline fault line %d\n", n) ;
}

int fault (n)
  int n;
{ fprintf (stderr, "fault line %d\n", n) ;
}
```

```
/*-------------------------------------------------------------
 * caldist.c : The input file contains the coordinate sets of the start
 *             and end points (long  lat) in 360 degree notation.
 *             Output : distance from origin start point, distance from
 *             origin to end point and difference between them.
 *             These are used in shell wprof when generating a X-section
 *-------------------------------------------------------------

#include <stdio.h>
#include <math.h>

#define MAX 10
float x[MAX],y[MAX], d[MAX], diff[MAX];
int i,j;

main ()
{ register int stop = 0;
  register int n=0;

/* read in data */
while (!stop)
        {
        if (scanf ("%f%f\n", &x[n],&y[n])==EOF)
          goto readall;
        n++;
        }
readall: stop=1;
for (i=0; i<n; i++){
        printf ("%f %f\n", x[i],y[i]);
        d[i] =sqrt((x[i]-360)*(x[i]-360)+y[i]*y[i]) ;
        }
for (j=0; j<(n-1); j++){
        diff[j]=d[j+1]-d[j];
        printf ("%f %f %f\n", d[j+1], d[j], diff[j]);
        }
}
```

```
#!/bin/csh
#
# Shell to generate map and cross section from seabeam bathymetry
#
unalias rm
rm track.xy, track.dz
rm w26map.grd w26fine.grd
rm w26map.ps 26wprof.ps
GMT
grdcut marnok.grd -Gw26map.grd -R-46:12/-46:08/24:34/24:36
grdsample w26map.grd -Gw26fine.grd -N151/76
grdimage w26fine.grd -Cwasp50.cpt -Jm80 -Ba1mf1mg1m -K >w26map.ps
grdcontour w26fine.grd -C50. -A100f8 -Jm80 -Wc1 \
 -Wa3  -T -V -O -K >> w26map.ps
psxy prof26w1.xy -Jm -R -W10 -O -V >> w26map.ps
#
# Now generate section
#
sampleld prof26w1.xy -I0.0005 -L | awk '{printf("%f %f\n",$1-360.0,$2)}' \
 > track.xy
grdtrack track.xy -Gw26fine.grd -V |\
 awk '{printf("%f %f\n",-(sqrt($1*$1+$2*$2)-52.276),$3)}'  > track.dz
psxy track.dz -R-0.045/0.000/-5000./-3000. -Bg0.045/a200g100 \
 -JX8/4 -W6 -X1.6 -Y2.1 > 26wprof.ps
exit(0)
```

BLANK IN ORIGINAL

Appendix 3

Analytical methods and error analysis

A3.1 Sample selection and preparation.

The dredged rocks from cruise CD57 were initially sampled on board ship. Rocks were washed and scrubbed to remove pelagic ooze and brine and sorted into units based on extent of alteration, morphology and phenocryst content. At least one sample was taken from each of these units, the remainder being stored in hessian bags in the cold store of the hold (Igor Browning, pers. comm.). Larger boulders were broken by hammering to obtain pieces of suitable size for sawing. Alteration fronts were clearly visible penetrating in from cracks and exposed surfaces, so in many cases it was possible to trim the sample to optimise the freshness. With the exception of the smallest pebbles and most pristine glasses on any exposed surfaces were removed. Although it was desirable to sample the glassey rim of a sample (as this represents the basaltic melt on eruption), it was noted that such surfaces were the most vulnerable to alteration with the onset of palagonitization and consequently, were avoided. The samples for analysis were generally 20-50cm^3 with two slices cut from them for thin and probe sections. The freshest glass chips and pebbles were selected for isotope analysis. Samples were then labelled and bagged for transport to the UK.

Once in Durham the samples were washed with distilled water and more critically inspected for alteration. A diamond saw and grinder were used to remove the more subtley altered areas and oxidised patches of glass. It was at this stage that each hand specimen was described in terms of phenocryst content (size, shape and mode), vesicularity and alteration. This data was combined with information on original morphology and extent of sediment recovered in the dredge to form the table of appendix 3.

A3.2 Crushing and powdering.

The prepared samples were crushed on the finest setting of a *Fritsch Pulverisette* jaw crusher *(type 01-704)*. The crushed rock was briefly inspected and any visible zeolites or altered material was removed. The equipment was extensively cleaned at the beginning of each crushing session to avoid contamination with rocks of diverse geochemical affinity. It was found that rock dust and fragments had accumulated to a worrying extent on the struts beside the plates and on a shelf behind the back plate - both areas which are not easily accessable for cleaning and yet situated directly above

the collecting tub. The extent to which this material could cause cross contamination was demonstrated by switching on the machine for a period of time with an empty collecting bin in place. The subsequent vibration would frequently cause some of this potential contaminent to be dislodged into the bin. Hence, a considerable effort was made to clean even the most inaccessible areas of the machine, and a check was kept during the crushing proceedure that there was no fallout onto an emtpy bin. A wire brush, absolute alcohol and tissue were used to clean the plates of the jaw crusher between each sample preparation and absolute alcohol was also used to clean the collecting bin. For the phyric samples, some of this crush (which consisted of fragments <1cm in size) was retained for future mineral and/or basalt separates. The remainder was then reduced to a fine powder, using a *Fritsch* Agate Ball Mill Tema.

The agate pots and balls were washed out with water and scrubbed with a bristle brush between sucessive samples. For more altered rocks, this was not sufficient to remove all trace of the powder, but powdering quartzite or quartz sand proved a successful cleaning agent.

A3.3 X-Ray Fluorescence (XRF)

All of the samples listed in appendix 4 have been analysed by XRF at the University of Durham, using fusion discs and pressed powder pellets.

A3.3.1 Fusion disc preparation.

4-5g of rock powder was accurately weighed out and heated in porcelain crucibles at 900 °C for 2 hours. On removal the ignited powders were re-weighed to determine the loss on ignition (LOI). This powder was then stored in a glass sample valve ready for fusion disk preparation. 0.45g (+/- 0.0010g) of ignited rock powder was accurately weighed out, along with 2.25g +/- 0.0010g of dried lithium metaborate and lithium tetraborate flux (Johnson Mattey "Spectroflux 100B") into a platinum crucible. After thorough mixing with a glass rod, taking care to avoid any powder spillages, this 1:5 rock-to-flux mixture was placed in a furnace at 1050 °C. The crucible was covered with a lid and left for 20 minutes, a time sufficient to ensure complete melting, but not long enough to cause Na loss. The molten mixture was then removed from the furnace, swirled briefly in the platinum crucible to ensure complete mixing and poured onto a graphite moulds surrounded with a stainless steel ring sitting on a hot-plate set at 250 °C. The disc was formed by immediately flattening the molten blob with a stainless steel plunger. The steel plunger and ring were removed and the bead covered with a heated glass beaker to prevent quench fragmentation. Following slow cooling for 20 minutes the disc was removed from the hot plate until it was cool enough to be labelled, sealed in air-tight plastic bags and stored in a dessicator. Care was taken to ensure that the analytical surface of the disc did not come into contact

with the surface of the skin as this can cause considerable contamination with Na_2O, P_2O_5 and K_2O (R. Hardy, pers. comm.). The used crucibles were placed in a boiling solution of hydrochloric acid to remove any remaining glass and then rinsed with distilled water ready for the next batch. Two fusion disks were made of each of the CD57 samples to provide a cross check as errors can be introduced by insufficient mixing during this method of preparation.

A3.3.2 Pressed powder pellet preparation

Approximately 5g (a slightly heaped teaspoon) of rock powder was added with ~10 drops of PVA "Mowiol" organic binding solution, (4% solution) to a small beaker and mixed thoroughly. The mixture was then subjected to ~10 tonnes of pressure for half a minute, between two polished disks within a steel mould. Some of the more altered Troodos samples were unable to take more than 5 tonnes of pressure, the high clay content of these powders making them weak and allowing them to penetrate round the edges of the disk mould. The pellets were dried in an oven at 100 °C overnight, labelled and bagged.

A3.3.3 XRF analysis

During this study the elements have been analysed using a *Philips PW 1400*, fitted with a *PW1500/10* automatic sample changer. A Rh tube was used to provide the X-ray source (accelerating potential = 80kV, 35mA or, = 55kV, 50mA when analysing REEs). *Philips X40* software has been used to process the raw count rates of the peaks and backgrounds. International reference standards used in the calibration and for monitoring accuracy were taken from Govindaraju (1989). Some of the features of this software are as follows: (Walker, 1992; R. Hardy, pers. comm.)

1. There is good user control with a variety of options available within the package. These include options to incorporate a monitor and the LOI values into the calculations, and to normalise the results to 100wt%;
2. The dectection limits for all the elements on an individual run can be calculated;
3. The calibration can be manipulated before the data is acquired. Standards in the calibration can be deleted if they fall far from the regression line or if they cause the line to deviate off the best fit in the area of interest. The calibration can then be tested by running International reference material as unknowns. The calibration for each element can be manipulated independently of the others;
4. Any combination of elements can be run at any one time; and
5. The proximity of the 'Total' to 100wt% is a good measure of the quality of the major element oxide data. This data is very sensitive to the method of preparation, so if the disks are incorrectly made then this can be demonstrated by poor totals.

A3.3.4 Data accuracy and precision

A3.3.4.1 Major elements

The CD57 major elements were run in three batches separated by seven or eight months. Careful monitoring had to be employed to ensure coherence of the data set both within and between runs. Duplicate beads of all samples were made and 21 samples were run on at least two calibrations. Any data with totals deviating from 100wt% by more than 0.8wt% was excluded from the final averages. It was found that the precision was optimized by normalising the results to 100%. Precision was estimated from 17 samples which were analysised three or more times and also from the standard BOB-1 which was analysed 4 times during one run. Table A3.1 documents the maximum and average values of the 2σ precision estimates from the 17 samples and compares estimates with those of other recent studies based on Durham XRF data.

Element	Original Totals		Normalized Totals		BOB-1	Walker	Kerr	
	Max	Mean	Max	Mean			Max	Mean
SiO2	0.58	0.28	0.44	0.18	0.28	0.53	0.47	0.34
TiO2	0.02	0.01	0.03	0.01	0.01	0.03	0.07	0.03
Al2O3	0.29	0.18	0.25	0.15	0.1	0.14	0.22	0.21
Fe2O3*	0.27	0.10	0.29	0.11	0.04	0.16	0.19	0.14
MnO	0.01	0.00	0.01	0.00	0.00	0.01	0.01	0.00
MgO	0.20	0.09	0.17	0.07	0.06	0.23	0.25	0.12
CaO	0.29	0.17	0.34	0.15	0.12	0.21	0.13	0.09
Na2O	0.39	0.23	0.39	0.21	0.11	0.25	0.11	0.07
K2O	0.05	0.02	0.05	0.02	0.01	0.00	0.02	0.01
P2O5	0.03	0.01	0.03	0.01	0.01	0.02	0.01	0.01

Table A3.1 2σ weight % precision estimates based on repeat analyses on 17 samples (where n>=3) and BOB-1 (n=4). Also included are 2σ weight % precision estimates of Walker (1992) (n=28) and similar estimates calculated from Kerr (1993), from the range of values obtained on samples BR1, BR2 & BR6.

Eight reference standards (BR, W-2, BHVO-1, DNC-1, BE-N, AGV-1, G-1 & BOB-1) were analysed as unknowns one or more times during the major element runs. Accuracy was assessed by comparing the measured values to standard compositions from Potts et al. (1992), with anhydrous majors normalised to 100%. The accuracy in

terms of these difference measurements does not appear to vary with the composition af the standard analysed (ie accuracy for granite G-1 is not significantly different from those of more basaltic compositions like BHVO-1 & W2). This demonstrates that the quality of calibrations were uniform for a data range considerably greater than that required for the data set in this study. Table A3.2 gives the maximum and minimum differences (standard value - measured value) in wt% from 11 of these accuracy assessments. The average and twice the standard deviation (for n=11) are also recorded. These are compared to an accuracy assessment of Kerr (1993) where the average Durham XRF values of QUB-S3 (a basaltic dyke from the BTVP) are compared with the average composition of QUB-S3, as analysed by British universities[1].

	SiO2	Al2O3	Fe2O3	MgO	CaO	Na2O	K2O	TiO2	MnO	P2O5
Max diff	0.36	0.03	0.32	0.13	0.01	0.39	0.33	0.02	0.00	0.02
Min diff	-0.45	-0.04	-0.18	-0.09	-0.01	-0.11	-0.09	-0.76	-0.06	-0.01
Average	-0.04	-0.01	0.05	0.02	0.00	0.08	0.04	-0.12	-0.02	0.00
2σ	0.56	0.04	0.33	0.15	0.01	0.34	0.23	0.47	0.05	0.02
QUB-S3[2]	-0.02	0.01	-0.16	0.04	0.00	0.11	0.02	0.01	-0.01	-0.01

Table A3.2a Accuracy is calculated as (standard wt%-measured wt%). 11 accuracy measurements were made from 8 different standards. The maximum, minimum, average and 2σ deviation of these are tabulated above.

A3.3.4.2 Trace Elements

The trace elements measured by XRF include Ti, Sc, V, Cr, Ni, Cu, Zn, Ga, Rb, Sr, Y, Zr, Nb, Ba, La, Ce & Nd. They were measured in four batches, separated by time periods ranging from about a week to five months. The calibrations of each run were checked to ensure they were comparable to avoid systematic errors in the data set. Corrections were made to the data if the standard analyses suggested that there were systematic differences between to runs. Each sample was run at least twice (some up to four times) and the final values were an average of these runs. Table A3.3 shows

[1] Compiled by Dr I. Meighan, Queens University, Belfast.

[2] wt% major element differences for QUB-S3: UK-Average[1] - Durham XRF average, from Kerr (1993).

Table A3.3 Standards run during XRF trace element analyses

(Standard values are taken from Potts, Tindle & Webb*)

Ident	Nb std	Nb ppm	Zr std	Zr ppm	Y std	Y ppm	Sr std	Sr ppm	Ga std	Ga ppm	Ni std	Ni ppm	Cr std	Cr ppm	V std	V ppm	Rb std	Rb ppm	Sc std	Sc ppm	Date std
Batch 1																					
$BEN	97	100	**255.40**	265.00	**30.70**	30.00	**1370**	1370	18.20	17.00	**279**	267	**338**	360	**250**	235	**47**	47	**28**	22	92/02/28
$BIR	3	2	20.00	22.00	**15.60**	16.00	**107**	108	19.10	16.00	**169**	166	**350**	382	**337**	313	*-1*	*1*	**40**	44	92/02/28
$BIR	3	1	*20.00*	12.10	**15.60**	16.80	**107**	109	19.10	16.00	**169**	166	**350**	382	**337**	313	-1	0	**40**	44	92/02/28
$BCR-1	11	14	**188.30**	190.00	**36.80**	38.00	**330**	330	**22.20**	22.00	12	13	18	16	**416**	407	**48**	47	**34**	33	92/02/28
$MRG-1	18	20	**104.10**	108.00	15.50	14.00	**267**	266	18.90	17.00	**195**	193	385	430	**557**	526	7	9	**60**	55	92/02/28
$MRG-1	18	18	**104.10**	107.00	15.50	14.00	**267**	266	18.90	17.00	**195**	193	385	430	**557**	526	7	9	**60**	55	92/02/28
BR4	4	4	**73.20**	77.00	**20.30**	20.60	**521**	527	18.00	17.10	212	205	**428**	456	**274**	248	4	6	**31**	32	92/02/28
BR5	5	5	**98.60**	101.00	**21.00**	20.90	**312**	310	19.40	17.20	373	360	**608**	645	**293**	278	6	8	**35**	31	92/02/28
BR6	5	5	**77.00**	80.00	**19.40**	18.20	**507**	506	18.80	16.70	353	344	**914**	980	**243**	229	4	6	**31**	26	92/02/28
$DR-N	9	8	**117.50**	125.00	**26.30**	28.00	**387**	400	**19.80**	22.00	14	15	28	42	**245**	220	71	73	**35**	28	92/02/28
$AGV-1	15	15	**220.00**	227.00	**19.30**	20.00	**658**	662	**22.10**	20.00	16	16	13	10	**136**	121	**67**	67	**18**	12	92/02/28
$AGV-1	15	16	**220.00**	242.00	**19.30**	20.00	**658**	662	**22.10**	20.00	16	16	13	10	**136**	121	**67**	67	**18**	12	92/02/28
$W-2	8	8	**91.20**	179.00	**21.20**	24.00	**193**	194	**21.70**	20.00	**75**	70	**81**	93	**280**	262	**21**	20	**37**	35	92/02/28
$W-2	8	8	**91.20**	102.00	**21.20**	24.00	**193**	194	**21.70**	20.00	**75**	70	**81**	93	**280**	262	**21**	20	**37**	35	92/02/28
$DNC-1	2	3	**37.20**	41.00	**16.00**	18.00	**142**	145	16.60	15.00	**250**	247	**268**	285	**162**	148	*4*	*5*	**34**	31	92/02/28
$DNC-1	2	2	**37.20**	40.00	**16.00**	17.40	**142**	145	16.60	15.00	**250**	247	**268**	285	**162**	148	4	4	**34**	31	92/02/28
$BR	97	98	**259.30**	250.00	**29.90**	30.00	**1351**	1320	**17.00**	19.00	**262**	260	**331**	380	**244**	235	46	47	**24**	25	92/02/28
BR1	8	8	**169.40**	167.00	**28.00**	27.80	**384**	379	19.80	19.20	108	110	**121**	132	**225**	221	1	3	**26**	21	92/02/28
QUBS3	5	4	**155.10**	160.00	**21.20**	23.00	**423**	430	19.90	20.00	318	310	**517**	516	**302**	302	4	5	**30**	30	92/02/28
BR2	7	8	**167.80**	168.00	**25.90**	27.50	**390**	378	21.50	18.70	104	107	**129**	140	**233**	226	4	3	**25**	20	92/02/28
BE-N	97	100	**252.70**	265.00	**29.50**	30.00	**1376**	1370	19.30	17.00	**276**	267	**331**	360	**253**	235	**48**	47	**25**	22	92/02/28
Batch 2																					
BR1	8	8	**169.80**	167.00	**28.10**	27.80	**390**	379	19.80	19.20	109	110	**123**	132	**235**	221	2	3	**24**	21	92/03/16
BR2	8	8	**170.00**	168.00	**28.60**	27.50	**387**	378	21.40	18.70	104	107	**125**	140	**225**	226	1	3	**27**	20	92/03/17
BR3	8	8	**168.60**	166.00	**25.90**	26.20	**771**	756	18.40	17.60	92	98	**108**	113	**209**	200	12	12	**22**	19	92/03/17
BR4	5	4	**71.70**	77.00	**19.80**	20.60	**527**	527	18.50	17.10	215	205	**429**	456	**275**	248	5	6	**35**	32	92/03/17
BR5	5	5	**100.90**	101.00	**20.70**	20.90	**309**	310	16.40	17.20	338	360	**596**	645	**282**	278	8	8	**33**	31	92/03/18
BR6	4	5	**78.40**	80.00	**17.90**	18.20	**501**	506	18.30	16.70	348	344	**912**	980	**245**	229	7	6	**31**	26	92/03/18

Table A3.3 Standards run during XRF trace element analyses (continued)

(Standard values are taken from Potts, Tindle & Webb*)

Ident	**Nb**	Nb	**Zr**	Zr	**Y**	Y	**Sr**	Sr	**Ga**	Ga	**Ni**	Ni	**Cr**	Cr	**V**	V	**Rb**	Rb	**Sc**	Sc	Date
Batch 3																					
BR1	8	8	**167.70**	167.00	**27.90**	27.80	**384**	379	24.70	19.20	107	110	**123**	132	**230**	221	2	3	**23**	21	92/03/24
BR2	7	8	**168.70**	168.00	**28.10**	27.50	**387**	378	22.50	18.70	108	107	**131**	140	**229**	226	-2	3	**25**	20	92/03/25
BR1	7	8	**168.20**	167.00	**27.90**	27.80	**384**	379	20.70	19.20	106	110	**120**	132	**236**	221	1	3	**27**	21	92/03/25
BR2	7	8	**169.00**	168.00	**26.80**	27.50	**383**	378	20.80	18.70	105	107	**131**	140	**227**	226	2	3	**21**	20	92/03/25
BR3	8	8	**166.80**	166.00	**26.10**	26.20	**771**	756	18.60	17.60	97	98	**108**	113	**213**	200	10	12	**22**	19	92/03/26
BR4	4	4	**71.90**	77.00	**19.70**	20.60	**519**	527	20.60	17.10	208	205	**423**	456	**273**	248	5	6	**34**	32	92/03/26
BR5	5	5	**102.10**	101.00	**21.80**	20.90	**311**	310	16.50	17.20	363	360	**615**	645	**289**	278	8	8	**35**	31	92/03/26
Batch 4																					
BR1	10	8	**175.40**	167.00	**30.20**	27.80	**371**	379	21.00	19.20	129	110	**141**	132	**263**	221	2	3	**25**	21	92/08/12
BOB-1	7	4	**116.00**	100.76	**28.10**	25.29	**203**	194	14.70	14.05	**111**	112	**306**	280	**240**	254	5	5	**33**	31	92/08/12
BOB-1	7	4	**116.00**	100.76	**28.10**	25.29	**203**	194	14.70	14.05	**111**	112	**306**	280	**240**	254	5	5	**33**	32	92/08/12
BOB-1	7	6	**116.00**	102.00	**28.10**	26.30	**203**	200	14.70	16.70	**111**	113	**306**	262	**240**	241	5	5	**33**	32	92/08/12
2 sigma for BOB-1		**1.4**		**1.4**		**1.2**		**6.8**		**3.1**		**1.6**		**20.8**		**14.9**		**0.2**		**1.2**	

*Confidence limits of standard values are distinguised by type face

bold typeface - precision of compiled data establihed to be better then 10% relative (2 sigma), normally based on 5 or more results from two or more independent techniques.

plain typeface - other compiled data

the standards run as unknowns during each batch and international standard values taken from Potts et al. (1992). BOB-1 is a Leicester standard and BR1 - BR6 are internal standards which have been developed at Durham. Two sigma is calculated for BOB-1 which was run 3 times during the final batch.

A3.4 Inductively Coupled Plasma - Mass Spectrometry (ICP-MS).

A subset of trace and rare-earth elements including Rb, Sr, Y, Zr, Nb, Cs, Ba, La, Ce, Pr, Nd, Sm, Eu, Gd, Tb, Dy, Ho, Er, Tm, Yb, Lu, Hf, Ta, W, Pb, Th and U was analysed by Inductively Coupled Plasma Mass Spectrometry (ICP-MS) on VG Elemental Plasma Quad device at Industrial Research Laboratories of the University of Durham (UDIRL).

A3.4.1 ICP-MS Sample preparation

Small amounts of powdered rock samples were put into the labelled glass containers in an oven at 105°C overnight to dry. Savillex teflon capsules were cleaned by rinsing with deionised water and then leaving them filled with 2 ml Aristar concentrated HNO_3 on the hot plate at 140°C for at least two hours. After following the same procedure twice, capsules were dried in the oven at 100°C and then numbered. A powder aliquot of 0.1 ± 0.001g was weighed out from each sample and transferred into the capsule. Special care was taken, using the anti-static gun to prevent powder sticking to the sides of the capsules and subsequent spillage. In addition to the samples, six international standards and also two blanks were prepared. After that, 1ml Aristar HNO_3 and 4ml 48% HF were added into the capsules respectively, their caps were closed tightly and the samples were left in the acid on the hot plate at about 130°C for about two days for complete digestion. At the end of this period the samples were evaporated on the hot plate to dryness in order to remove the HF from the system and to allow the formation of nitrate salts. After completing evaporation, 1ml HNO_3 was added to the capsules and evaporated again. This procedure was followed twice. Then 2.5ml HNO_3 and 20ml deionised water were put into the capsules, their lids were closed and the solution was boiled for over one hour to dissolve the salts. The solutions were allowed to cool, checked for any solid residue and spiked with 1.25ml of 2 ppm Rh, Re and Bi internal standard spike solution when they were still in the capsules. After this stage they were transferred into the 50ml polypropylene volumetric flasks and made up accurately to 50ml with deionised water. In this case internal standard element concentrations in the sample solution became 50 ppb. Finally all the solutions were transferred into the polypropylene containers and kept in a cool and dark place prior to analysis. Two reagent blank samples were prepared with each batch of sample.

The machine was calibrated using solutions of known elemental concentrations. Correction for drift was achieved by analysing a drift monitor every six samples.

A3.4.2 ICP-MS accuracy and precision

The ICP-MS data was compiled during three runs. The first (JP35) and the third (JP37) analysed mass range 82-185. During JP35 and JP37 the machine was set to complete 200 sweeps with a dwell time of 160µs; so with 2048 channels this gave an aquisition time of 65.5s. The second run (JP36) analysed mass range 43 - 104 with 200 sweeps, a dwell time of 160µs and 1024 channels to give an aquisition time of 32.7s.

Table A3.4 shows the final data values for a "cocktail" mixture of solutions that was run 6 times during the period of data collection to gain an analytical precision (2 sigma standard deviation) and Table A3.5 shows the values obtained for international geostandard BHVO-1 for an accuracy comparison. The final values were compared with the XRF values and Nb XRF values were recalibrated to the more accurate ICP values (see appendix 5). The final data table uses mostly ICP measurements when available but with averages of ICP and XRF for Sc, V, Cr, Ni, Cu, Zn Y and Zr.

A3.5 Isotope analysis.

The CD57 isotope analyses were done by Pamela Kempton from the NERC Isotope Geosciences Laboratory (NIGL) in Keyworth. Pb, Sr and Nd were extracted on the same dissolution using approximately 100-200 mg of powder from the rock samples. Many of the samples were run once with no leaching and once after leaching in hot 6M HCl for approximately 30 minutes, after which the leachate was decanted off and stored for analysis if appropriate. After dissolution using approximately 1ml of HNO_3 combined with 3 to 5 mls of HF, residues were converted to nitrate and finally chloride. 1 ml of 1M HBr was then added to the residue. Pb was separated by passing the sample through columns prepared from PVP disposable pipette tips fitted with a 2 mm diameter polyethylene frit and containing Dowex 1 x 8 200-400 mesh resin; completely new columns were prepared for each sample to minimise the Pb blank. The Sr and Nd fractions were collected in 2 mls of 1M HBr and Pb collected in 1 ml of 6M HCl, Sr and Nd were purified using standard one- and two-column cation exchange techniques respectively.

Table A3.4 Precision (two standard deviations) for runs JP35, JP36 and JP37

Run JP35

Sample	Rb	Sr	Y	Zr	Nb	Mo	Cs	Ba	La	Ce	Pr	Nd	Sm	Eu	Gd	Tb	Dy	Ho	Er	Tm	Yb	Lu	Hf	Ta	Pb	Th	U
1	1.44	142.92	28.51	82.15	2.57	1.57	0.024	13.15	3.24	9.60	1.61	8.68	2.95	1.10	3.80	0.69	4.64	1.02	3.10	0.43	2.85	0.41	2.22	0.17	0.60	0.174	0.085
2	1.45	142.92	28.47	82.25	2.54	1.64	0.022	13.16	3.24	9.47	1.66	8.68	3.00	1.06	3.72	0.65	4.60	1.00	3.15	0.42	2.81	0.45	2.22	0.18	0.60	0.181	0.069
3	1.52	142.86	28.25	82.73	2.53	1.51	0.021	13.16	3.26	9.61	1.56	8.76	2.73	1.13	3.84	0.69	4.59	1.00	3.04	0.43	2.92	0.46	2.13	0.16	0.64	0.151	0.068
4	1.54	142.86	28.35	82.09	2.72	1.62	0.020	13.10	3.17	9.47	1.71	8.62	3.06	1.06	3.76	0.70	4.73	1.01	3.04	0.43	2.71	0.41	2.14	0.13	0.61	0.191	0.057
5	1.51	142.87	28.24	82.20	2.75	1.66	0.027	13.20	3.21	9.64	1.63	8.63	2.85	1.13	4.09	0.63	4.73	0.99	3.03	0.39	2.88	0.36	2.01	0.15	0.60	0.176	0.066
6	1.53	142.85	27.98	82.74	2.70	1.77	0.039	13.12	3.31	9.36	1.59	8.82	2.94	1.14	3.61	0.72	4.57	1.00	2.97	0.43	2.94	0.43	2.06	0.12	0.56	0.199	0.091
7	1.47	142.90	27.92	82.97	2.69	1.55	0.028	13.15	3.13	9.68	1.65	8.66	2.95	1.08	3.90	0.66	4.80	0.95	2.97	0.43	2.83	0.40	2.24	0.15	0.59	0.187	0.071
Average	1.48	142.68	28.24	82.36	2.64	1.48	0.010	12.45	3.22	9.54	1.62	8.67	2.91	1.10	3.80	0.67	4.65	0.99	3.03	0.42	2.83	0.41	2.12	0.15	0.41	0.175	0.068
2 sigma	**0.0723**	**0.1548**	**0.4212**	**0.6572**	**0.1708**	**0.1868**	**0.0162**	**0.4974**	**0.1066**	**0.215**	**0.0909**	**0.1298**	**0.1981**	**0.0649**	**0.2783**	**0.0597**	**0.1609**	**0.0417**	**0.116**	**0.0288**	**0.1451**	**0.0631**	**0.1625**	**0.0364**	**0.142**	**0.0285**	**0.0219**

Run JP37

1	1.53	144.97	28.16	86.13	2.54	0.02	13.57	3.10	9.54	1.52	8.93	2.90	1.06	3.76	0.72	4.54	0.91	2.66	0.41	2.84	0.45	2.21	0.17	0.71	0.14	0.07
2	1.56	144.78	27.83	86.80	2.45	0.04	13.89	3.05	9.71	1.54	8.84	2.89	1.07	3.76	0.67	4.51	0.94	2.82	0.42	2.96	0.44	2.48	0.16	0.84	0.12	0.06
3	1.56	144.47	27.95	86.51	2.50	0.02	13.53	2.99	9.53	1.55	9.11	2.88	1.07	3.89	0.70	4.48	0.89	2.69	0.43	2.78	0.45	2.30	0.13	0.72	0.15	0.06
4	1.47	144.46	27.67	86.98	2.47	0.04	13.92	2.97	9.69	1.55	8.92	2.85	1.09	3.65	0.76	4.58	0.90	2.71	0.43	2.79	0.44	2.37	0.17	0.84	0.12	0.05
5	1.57	144.78	27.57	87.24	2.41	0.04	13.93	2.99	9.64	1.59	8.97	2.90	1.06	3.75	0.71	4.59	0.90	2.66	0.46	2.89	0.44	2.27	0.16	0.80	0.15	0.07
6	1.23	145.28	28.18	86.85	2.12	0.06	14.04	3.12	9.00	1.60	9.41	2.81	1.12	3.63	0.77	4.48	1.00	2.88	0.43	2.86	0.47	2.55	0.17	0.81	0.14	0.06
Average	1.49	144.79	27.89	86.75	2.41	0.04	13.81	3.04	9.52	1.56	9.03	2.87	1.08	3.74	0.72	4.53	0.92	2.74	0.43	2.85	0.45	2.36	0.16	0.79	0.14	0.06
2 sigma	**0.2644**	**0.6216**	**0.4998**	**0.772**	**0.3047**	**0.0265**	**0.422**	**0.1293**	**0.5316**	**0.0564**	**0.4146**	**0.0675**	**0.0471**	**0.188**	**0.0764**	**0.0977**	**0.0805**	**0.1796**	**0.0331**	**0.1341**	**0.0272**	**0.2612**	**0.0309**	**0.1204**	**0.0239**	**0.0141**

JP36

	Sc	Ti	V	Cr	Co	Ni	Cu	Zn	Ga	Rb	Sr	Y	Zr	Nb	Mo
1	35.39	1.32	249	321	41.05	109.61	72.35	69.48	14.92	1.47	142.50	29.85	85.21	2.62	1.33
2	35.39	1.32	248	317	42.68	108.57	70.45	65.84	14.56	1.51	142.47	29.77	85.50	2.50	1.44
3	35.70	1.33	247	310	42.74	107.23	70.81	65.47	14.34	1.68	142.35	30.37	84.64	2.51	1.44
4	35.75	1.33	250	313	43.67	108.53	68.88	64.99	14.00	1.47	142.50	30.27	84.46	2.66	1.39
5	34.58	1.34	247	308	42.35	111.21	70.02	64.57	13.65	1.30	142.62	30.14	85.00	2.49	1.31
6	36.30	1.34	244	306	39.90	113.72	73.09	68.25	14.87	1.45	142.51	30.02	85.11	2.51	1.38
7	35.68	1.31	250	323	38.43	117.00	73.99	67.53	12.72	1.41	142.54	29.95	85.90	2.18	1.13
Average	35.52	1.33	248	314	41.78	110.45	71.15	66.49	14.15	1.47	142.50	30.06	85.12	2.49	1.34
2 sigma	**1.04**	**0.02**	**4**	**13**	**3.70**	**6.90**	**3.65**	**3.69**	**1.55**	**0.23**	**0.16**	**0.44**	**0.98**	**0.31**	**0.22**

Table A3.5 Accuracy for international standard BHVO-1

element		Rb	Sr	Y	Zr	Nb	Mo	Cs	Ba	La	Ce	Pr	Nd	Sm	Eu	Gd	Tb	Dy	Ho	Er	Tm	Yb	Lu	Hf	Ta	Pb	Th	U
JP35	Bhvo-1	9.38	396.78	27.96	179.66	19.76	1.09	0.118	139.69	16.19	38.70	5.44	25.14	6.22	2.09	6.49	1.01	5.40	0.97	2.59	0.40	2.03	0.30	4.55	1.20	2.23	1.408	0.449
JP37	Bhvo-1	9.82	400.68	28.78	175.99	19.12		0.11	123.52	15.71	38.69	5.23	25.01	6.14	2.01	6.02	0.95	5.20	0.89	2.37	0.33	1.93	0.29	4.45	1.27	2.62	1.33	0.46
JP37	Bhvo-1	9.94	389.46	27.27	174.00	19.36		0.11	123.72	15.61	39.01	5.28	25.16	6.19	2.04	6.74	0.99	5.36	0.93	2.25	0.32	2.11	0.27	4.34	1.20	2.71	1.13	0.42
Geostandards		11.00	403.00	27.60	179.00	19.00	1.02	*0.13*	139.00	15.80	39.00	5.70	25.20	6.20	2.06	6.40	0.96	5.20	0.99	2.40	0.33	2.02	0.29	4.38	1.23	2.60	1.08	0.42

element		Sc	Tl	V	Cr	Mn	Co	Ni	Cu	Zn	Ga	Rb	Sr	Y	Zr	Nb	Mo
Jp36		32.85	2.82	342.33	352.21	0.18	47.66	124.03	145.57	114.65	22.72	9.77	412.54	28.00	181.13	20.54	1.19
BHVO1	geostds	31.80	2.710	317.00	289.00	0.168	45.00	121.00	136.00	105.00	21.00	11.00	403.00	27.60	179.00	19.00	1.02

Sr and Pb were run as the metal species on single Ta and single Re filaments, respectively using a Finnegan MAT 262 multicollector mass spectrometer at the NIGL; Nd was run as the metal species on double/triple Re-Ta filament assemblies using either a VG354 or a Finnegan MAT 262 multicollector mass spectrometer, also located at NIGL. Blanks ranged from 0.3 to 1.4 ng for Sr, 106 to 233 pg for Nd and 103 to 256 pg for Pb. Reference standards throughout the course of analysis averaged values of $^{87}Sr/^{86}Sr = 0.710218 \pm 38$ (2σ) for the NBS987 standard, $^{143}Nd/^{144}Nd = 0.511110 \pm 22$ (2σ) for the Johnson Matthey Nd standard on the VG 354 and 0.511146 ± 18 (2σ) on the Finnegan MAT 262. Finnegan $^{143}Nd/^{144}Nd$ data have been normalized assuming a value of 0.511110 for the J&M standard in order to make the data comparable between the two machines. $^{87}Sr/^{86}Sr$ was normalised to $^{86}Sr/^{88}Sr = 0.1194$; $^{143}Nd/^{144}Nd$ was normalised to a value of $^{146}Nd/^{144}Nd = 0.7219$. Pb isotopic ratios were corrected relative to the average standard Pb isotopic compositions of Todt et al. (1984). Pb mass fractionation was 0.10% per a.m.u. Total analytical uncertainties for Pb are ±0.02 for 206Pb/204Pb, ±0.02 for 207Pb/204Pb and ±0.04 for 208Pb/204Pb. Internal errors on individual isotope measurements were always much smaller than the standard reproducibility reported here and, therefore, the ability to reproduce the standards should be taken as the limiting factor in interpreting the uncertainty of any given analysis

A3.6 Electon Microprobe.

Major element oxides were measured on glasses and phenocrysts by Paul Browning on a JEOL electron probe, at Bristol university. During analysis the accelerating voltage was 15kV, sample current 15nA and beam size 10microns. A mixture of silicate and metal oxide standards were used for calibration. A MORB basaltic glass for which wet chemistry was available was used as a secondary standard. Repeat analysis on the secondary standard suggest that errors are ±1% on all oxides in excess of 10 wt% and ±10% relative for all minor constituents.

BLANK IN ORIGINAL

Appendix 4

Station results and hand-specimen descriptions

Explanation of hand specimen description table.

Figures in columns D, E, F, G are laid out thus:

α ; β
γ ; λ

Column D
figures are for plagioclase phenocryst percentages as follows:

α represents the % of microphenocrysts

β represents the % of phenocrysts or megacrysts

γ represents the % of microphenocrysts in the unit as a whole

λ represents the % of phenocrysts and megacrysts in the unit as a whole

Column E
figures are for plagioclase phenocryst sizes

Column F
figures are for olivine phenocryst percentages

Column G
figures are for olivine phenocryst sizes,
in this column figures in square brackets [ ] indicate that they are for clinopyroxene

TABLE A4.1: SUMMARY OF STATION RESULTS

Number	Type	Location (1a= south segment 1 1b=north segment 1)	Result
CD57/1D	Dredge	Foot of transform S wall	Mylonitic, deformed, massive, chlorite- and talc-rich ultramafics; deformed gabbros; dolerites; brownstones; plagiogranite.
CD57/2D	Dredge	Foot of transform S wall	Dolerites; deformed, mylonitic, and talc-rich ultramafics; massive serpentinite; ultramafic breccia.
CD57/3D	Dredge	RTI NVR,slightly tectonized, seg. 1a	Plagioclase phyric basalt, probably pillow and tube fragments.
CD57/4D	Dredge	RTI seamount, W of NVR	Sparsely plagioclase phyric basalt. Pillow and pahoehoe (sheet flow) fragments.
CD57/5D	Dredge	RTI NVR, fissure seamounts, seg. 1a	Aphyric to very sparsely plagioclase phyric basalt. Pillow fragments, one highly vesicular, with zeolite amygdales.
CD57/6D	Dredge	RTI NVR, fissure seamounts, seg 1a	Plagioclase phyric basalt with glassy rims and highly vesicular interior; older plagioclase and olivine phyric basalt.
CD57/7D	Dredge	Old ridge, W flank of nodal basin	Sparsely plagioclase phyric (olivine microphyric) pillow basalt fragments.
CD57/8D	Dredge	S. tip of NVR in RTI, segment 1a	Plagioclase phyric basalt glass fragments; older plagioclase (plus minor olivine) phyric basalt. Pillow and lava tube fragments.
CD57/9D	Dredge	Slightly oblique NVR, segment 1a	Plagioclase phyric pillow basalt fragments; plagioclase and olivine phyric pahoeoe textured sheet flow.
CD57/10D	Dredge	Volcano on NW edge of nodal basin	Palagonitised basaltic glass fragments; pelagic ooze.
CD57/11D	Dredge	Flat area W of NVZ, segment 1a	Plagioclase phyric pillow basalt fragments.
CD57/12D	Dredge	Large seamount, centre of seg.1a	Younger and older units of plagioclase phyric sheet flow, pillow basalt and glass. Oldest unit is of aphyric pillow. Ooze
CD57/13D	Dredge	Seg.1a axial smt (Thatcher's Nose')	Highly plagioclase phyric olivine-bearing basalt, (>40% phenocrysts), possibly sheet flow. Glassy rims slightly palagonitized.
CD57/14D	Dredge	NVR axial graben, segment 1a	Sparsely plagioclase phyric pillow basalt fragments.
CD57/15D	Dredge	Segment 1a NVZ, fissure seamounts	Aphyric pillow and possibly sheet flow basalt fragments; fresh glassy basalt tubules.
CD57/16D	Dredge	N. tip of segment 1a, oblique ridge	Plagioclase phyric pillow basalt and lava tubules from very recent eruption.
CD57/17D	Dredge	S. tip of seg.1b, slightly tectonized	Aphyric basalt with glassy rims (prob. sheet flow); scoriaceous aphyric basalt; plagioclase phyric pillow basalt fragments.
CD57/18D	Dredge	SE margin of seg. 1b	Plagioclase phyric pillow and possibly sheet flow basalts, some with olivine microphenocrysts; fairly glassy.
CD57/19D	Dredge	Centre of segment 1b, broad NVR	Aphyric basalt glass and very fine-grained basalt -- pillow selvedges. Older, very sparsely plagioclase phyric pillow basalt fragments.
CD57/20D	Dredge	N end of segment 1b, broad NVR	Sparsely plagioclase phyric (olivine microphyric) pillow basalt. One boulder has twisted pahoehoe texture.
CD57/21D	Dredge	N tip of segment 1b, NVR	Sparsely plagioclase phyric basalt; plagioclase and olivine phyric basalt; probably pillow fragments of three different ages.
CD57/22D	Dredge	Major scarp on W MV wall, seg. 2.	Aphyric basalt (old pillows); plagioclase-olivine-clinopyroxene phyric, weathered basalt; olivine phyric basalt; variolitic pillows; basalt fragments with secondary mineralisation (zeolites, celadonite?); massive basalt (thick flow);aphyric basalt glass; rounded basalt pebbles; basaltic breccias and hyaloclastite; tectonic breccias.
CD57/23D	Dredge	S end of segment 2, broad NVR	Aphyric basalt (old pillows); highly plagioclase (sparsely olivine) phyric pillow basalt fragments with powdery black MnO_2 coating; very sparsely plagioclase phyric (possibly sheet flow) basalt; aphyric glassy to very fine-grained basalt; assorted glassy pillow rinds.
CD57/24D	Dredge	Centre of segment 2, broad NVR	Plagioclase phyric basalt, prob. sheet flow; aphyric pillow basalt with powdery black MnO_2 coating; highly weathered aphyric pillow basalts.
CD57/25D	Dredge	Segment 2 axis	Plagioclase phyric glass and basalt.
CD57/26W	WASP	Across segment 2 NVR	500 frames exposed. Mostly pillows and tubes, pillow breccias and talus. No sheet flows or sediment ponds. Few faults or fissures.
CD57/27D	Dredge	S wall of W FZ limb	Highly plagioclase phyric olivine-bearing basalt; sparsely plagioclase phyric (olivine-microphyric) basalt; greenschist facies cataclasites; hydrothermal veins.
CD57/28W	WASP	Across 'narrowgate'	800 frames. Highly variable terrain: mostly pillows , tubes, some sheets; some areas of heavy faulting/fissuring, some sed. ponds.
CD57/29D	Dredge	Nested smts at N tip of segment 1b	Sparsely plagioclase phyric old pillow basalt; highly plagioclase (olivine-bearing) phyric pillow basalt; very sparsely plagioclase-phyric old pillow basalt; pelagic ooze.
CD57/30D	Dredge	Between segments 1b and 2	Sparsely plagioclase phyric olivine-bearing basalt -- bolster pillows -- not fresh, with powdery black MnO_2 coating;
CD57/31D	Dredge	Centre of segment 2, broad NVR	Highly plagioclase phyric basalt -- very fresh sheet flow.
CD57/32D	Dredge	NVR and smt at N end of segment 2	Very sparsely plagioclase phyric variolitic pillow basalt fragments with glassy rim; aphyric pillow, bud or sheet basalt,some with powdery black MnO_2. coating; aphyric basalt, possibly sheet flow.

Microphenocrysts (%)

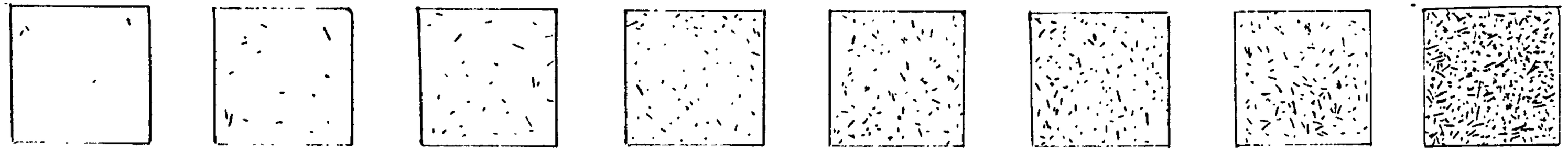

Phenocrysts and glomerocrysts (%)

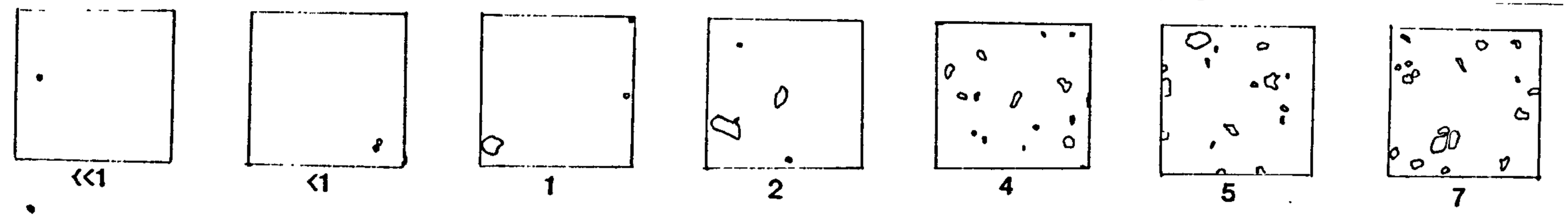

Vesicularity (%)

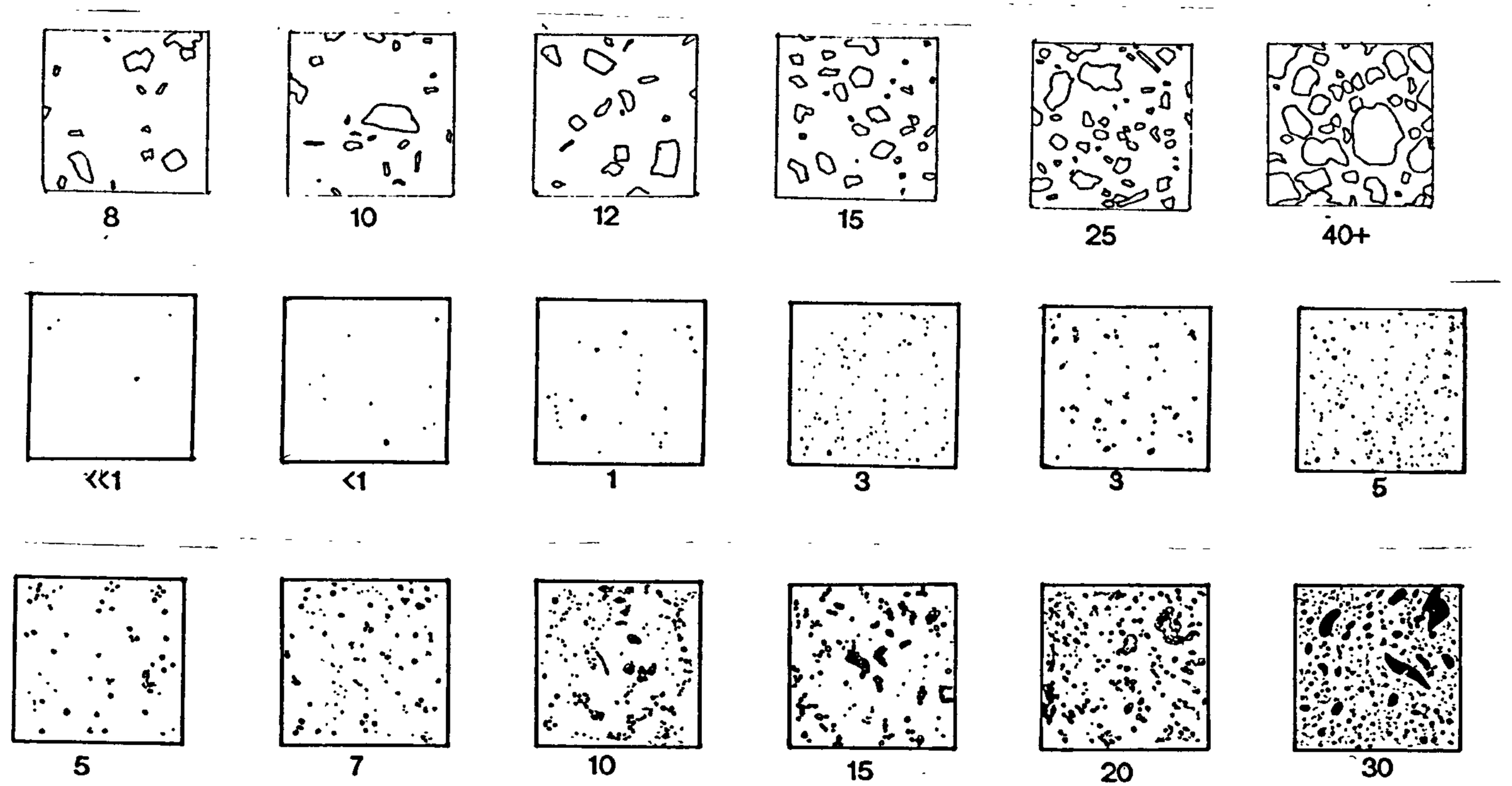

Fig. A4.1 Percentage estimation diagram of (a) microphenocryst content, (b) phenocryst and glomerocryst content, and (c) vesicularity

A Sample No.	B Description	C Type of phenocrysts	D % plag. phenocrysts	E size of plag. phenocrysts(mm)	F % ol. phenocrysts	G size of ol. phenocrysts(mm)	H % vesicularity	I Alteration	J Ooze?
1D-3-1b	Dolerite boulder with slickensides on surface	Practically aphyric; Euhedral/subhedral plagioclase	<<1	2.00	----	----	none	No glass; brown oxidised exterior; not pervasive into sample.	none
3D-1-1b	Boulder of plagioclase phyric pillow basalt	Plag:Acicular microphenocrysts & eu/subhedral phenocrysts; olivine microphenocrysts	<1 ; 7 *(– ; 10 - 20)*	0.25 - 2.00 ; 1.00 - 5.00 *(---- ; 1.00 - 15.00)*	---- *(? <<1)*	----	2 - 10	Palagonite rim? oxidation in vesicles	in pipe
3D-1-2b	Cobble of pillow tube	Plag:Subhedral and euhedral phenocrysts & glomerocrysts; olivine in glomerocryst?	– ; 10 *(– ; 10 - 20)*	---- ; 1.00 - 8.00 *(---- ; 1.00 - 15.00)*	---- *(? <<1)*	----	10	Palagonite rim, minor oxidation in vesicles	in pipe
4D-1-1b	Cobble of pillow basalt with glassy rind (from interior)	Plag:Acicular microphenocrysts & subhedral glomerocrysts; olivine in glomerocryst?	4 ; 1	0.25 - 1.00 ; 1.00 - 3.00 *(---- ; 2.00 - 7.00)*	----	----	10 - 1	Glassy rind. Yellow weathered surface and concentric alteration fronts	none
4D-1-2b	Cobble of pillow basalt with glassy rind (from interior)	Plag:Acicular microphenocrysts & subhedral glomerocrysts	2 ; 2	0.25 - 1.00 ; 2.00 - 4.00 *(---- ; 2.00 - 7.00)*	----	----	2	Glassy rind. Yellow weathered surface and concentric alteration fronts	none
4D-1-3b	Fine grained interior of glassy basalt tubule	Plag Acicular microphenocrysts & subhedral glomerocrysts; olivine in glomerocryst?	4 ; 2	0.25 - 2.00 ; 4.00 - 6.00 *(---- ; 2.00 - 7.00)*	----	----	2 - 20	Glassy rind beginning to alter yellow; oxidation in vesicles; cracks	none
5D-1-2b	Boulder of plagioclase phyric pillow basalt	Plag.Acicular microphenocrysts & anhedral glomerocrysts. Phenocrysts tend to concentrate in quenched rims	4 ; 1	0.25 - 1.50 ; 1.00 - 3.00 *(---- ; 2.00 - 5.00)*	----	----	2	Glassy rind beginning to alter yellow with most of the glass spawled off, pale weathered surface; minor alteration front in the fine grained analysis slab.	none
6D-1-1b	Edge of pillow; glassy rim; vesicular interior	Plag.Acicular microphenocrysts & sparse subhedral glom/phenocrysts tend to concentrate in quenched rims and interior with less phyric layer 2 - 3 cm layer below glassy rind	4 ; <1 *(– ; 2 - 30)*	0.25 - 1.50 ; 1.00 - 2.00 *(---- ; 2.00 - 13.00)*	----	----	1 - 15 vesicular interior	Glass rim 1-3mm; little palagonite; oxidation in vesicles	none
6D-1-2b	Edge of pillow; glassy rim; vesicular interior	Plag:Acicular and subhedral microphenocrysts & sparse subhedral xenocrysts(dark cores with inclusions) tend to concentrate in quenched rims and interior with less phyric layer 2 - 3 cm layer below glassy rind.	5 ; 1 *(– ; 2 - 30)*	0.25 - 2.00 ; 4.00 - 5.00 *(---- ; 2.00 - 13.00)*	----	----	2 - 20 vesicular interior	Glass rim 1mm; very little palagonite; rim retained in analysis	none
6D-1-3b	Edge of pillow; glassy rim; vesicular interior	Plag:Acicular microphenocrysts & sparse subhedral glom/phenocrysts tend to concentrate in quenched rims and interior with less phyric layer 2 - 3 cm layer below glassy rind	5 ; 1 *(– ; 2 - 30)*	0.25 - 2.50 ; 2.00 - 3.00 *(---- ; 2.00 - 13.00)*	----	----	2 - 3 vesicular interior	More weathered than 6D-1-2b; orange/yellow weathered surface	none
6D-2-1b	Older pillow; plag. & olivine phyric	Plag.Acicular microphenocrysts & eu/subhedral pheno/glomerocrysts (poss xenocrysts cos of dark cores) ; olivine in glomerocryst	5 ; 20 *(– ; 10 - 20)*	0.25 - 1.00 ; 1.00 - 8.00 *(---- ; 2.00 - 15.00)*	2 *(1)*	0.50 - 4.00 *(0.50 - 4.00)*	2 - 5 *(1 - 3)*	Older than 6D-1; slight orange/brown surface oxidation; very minor alteration front in sample. Vesicles concentrated in layer parallel to rim. *(Dark and pale grey weathered surface.)*	none
6D-2-2b	Older pillow; less olivine, more vesicular than 6D-2-1b	Plag:Acicular microphenocrysts & eu/subhedral pheno/glomerocrysts (poss xenocrysts cos of dark cores) ; olivine in glomerocryst	4 ; 15 *(– ; 10 - 20)*	0.25 - 1.00 ; 1.00 - 5.00 *(---- ; 2.00 - 15.00)*	<1 *(1)*	0.5 *(0.50 - 4.00)*	2 - 20 *(1 - 3)*	Older than 6D-1; slight orange/brown surface oxidation; very minor alteration front in sample. Vesicles concentrated in layer parallel to rim. *(Dark and pale grey weathered surface.)*	none
7D-1-1b	Boulder of plag (+olivine?) phyric pillow basalt	Plag:Acicular microphenocrysts & subhedral pheno/glomerocrysts (possibly xenocrysts cos of dark cores) Inclusions possibly melt spinel and cpx.	8 ; 2 *(– ; 1 - 5)*	0.25 - 1.75 ; 1.00 - 3.00 *(---- ; 2.00 - 10.00)*	----	---- *(<1.00)*	4	Palagonite rind; cracks alter yellow and alteration penetrates a few cm in, but interior is fresh	none
7D-1-2b	Boulder of plag (+olivine?) phyric pillow basalt	Plag:Acicular microphenocrysts & subhedral phenocrysts	5 ; <1 *(– ; 1 - 5)*	0.25 - 1.00 ; 1.00 - 2.00 *(---- ; 2.00 - 10.00)*	----	---- *(<1.00)*	2 - 5	Palagonite rind; cracks alter yellow; alteration fronts in sample.	none
7D-1-3b	Boulder of plag (+olivine?) phyric pillow basalt	Plag:Acicular microphenocrysts & subhedral pheno/glomerocrysts (poss xenocrysts cos of dark cores); olivine microphenocrysts in groundmass.	10 ; 4 *(– ; 1 - 5)*	0.25 - 2.50 ; 2.00 - 4.00 *(---- ; 2.00 - 10.00)*	<1	0.5 *(<1.00)*	3	Palagonite rind; cracks alter yellow; minor alteration front in sample.	none
8D-1-1b	Boulder of plagioclase phyric pillow basalt	Plag:Acicular microphenocrysts & euhedral phenocrysts/subhedral glomerocrysts. *(Olivine microphenocrysts in glomerocrysts with plagioclase)*	7 ;13 *(– ; 15 - 20)*	0.25 - 1.50 ; 1.00 - 9.00 *(---- ; <10.00)*	---- *(1)*	---- *(1.00 - 2.00)*	2 - 6	Thin glassy rind; weathered surface white-brown; fresh interior	none
9D-1-1b	Plag. phyric basalt with pahoehoe surface texture	Plag.Acicular microphenocrysts & eu/anhedral phenocrysts;subhedral glomerocrysts; olivine: subhedral phenocrysts	<1 ; 4 *(– ; 5)*	0.50 - 1.50 ; 0.50 - 4.00 *(---- ; <3.00)*	<1 *(1)*	0.50 - 3.00 *(<2.00)*	2	Fresh interior; pale grey and yellow surface alteration	none

A Sample No.	B Description	C Type of phenocrysts	D % plag. phenocrysts	E size of plag. phenocrysts(mm)	F % ol. phenocrysts	G size of ol. phenocrysts(mm)	H % vesicularity	I Alteration	J Ooze?
9D-1-2b	Olivine bearing; plag phyric cobble with glassy rim	Plag.Acicular microphenocrysts & eu/subhedral phenocrysts;subhedral glomerocrysts,some with black inclusions; olivine in glomerocryst. High concentration of plag in rim; low conc in interior	1 ; 5 *(– ; <5 - 20)*	0.25 - 1.50 ; 1.00 - 4.00 *(---- ; <10.00)*	<<1	0.5	2 - 4 increases into core	1mm glassy rim partly palagonitised; pale surface alteration; fresh interior with minimal alteration	none
9D-1-3b	Glassy rimmed fresh basalt pillow bud	Plag:Acicular microphenocrysts & eu/subhedral phenocrysts;subhedral glomerocrysts;some with black inclusions;some with darker cores - xenocrysts; olivine microphenocryst in rim? High concentration of plag in rim; low conc in interior	<1 ; 5 *(– ; <5 - 20)*	0.50 - 1.50 ; 1.00 - 4.00 *(---- ; <10.00)*	<<1	0.75	<1 increases into core	1mm glassy rim; fresh interior	none
11D-1-1b	Representative plagioclase phyric basalt	Plag.Acicular microphenocrysts & sub/anhedral phenocrysts and glomerocrysts; some with black inclusion or dark cores - xenocrysts? *(Possible olivine present)*	2 ; 8 *(– ; 10)*	0.50 - 2.00 ; 1.50 - 9.00 *(---- ; <10.00)*	----	----	3 microvesicular cores	Yellow surface alteration; some alteration down cracks in sample *(Partly palagonitized glassy rims)*	none
12D-1-1b	Plagioclase phyric cobble with glassy top (tabular). Fresh sheet flow.	Plag.Acicular microphenocrysts & eu/subhedral phenocrysts; an/subhedral glomerocrysts; some with black inclusions. Phenocrysts tend to be concentrated in upper glassy layer.	1 ; 5 (3 -5 in glass; <5 in interior)	0.25 - 2.00 ; 1.50 - 6.00 *(---- ; 2.00 - 10.00)*	----	----	<1 conc towards lower margin	Glassy rim: upper 10mm; lower 1mm (removed for isotopes). Glass generally fresh but slightly palagonitized; fresh interior	none
12D-1-2c	Plagioclase phyric cobble with glassy top (tabular). Fresh sheet flow.	Plag Acicular microphenocrysts & sub/euhedral phenocrysts; sub/anhedral glomerocrysts some with red/brown and black inclusions. Phenocrysts tend to be concentrated in upper glassy layer.	<1 ; 5 (3 -5 in glass; <5 in interior)	0.25 - 2.00 ; 0.75 - 6 00 *(---- ; 2.00 - 10.00)*	----	----	<1 - 3 conc towards lower margin	Glassy rim: upper 5mm (max); lower 1mm with very slight yellow alteration - generally fresh; fresh interior	none
12D-3-1c	Cobble of plagioclase phyric pillow basalt related to 12D-1?	Plag.Acicular microphenocrysts & sub/euhedral phenocrysts; sub/anhedral glomerocrysts; some with black inclusions that weather red/brown. Phenocrysts tend to be concentrated in upper glassy layer.	<1 ; 5 (3 -5 in glass; <5 in interior)	0.25 - 3 00 ; 1.00 - 7.00 *(---- ; 2.00 - 10.00)*	----	----	<1 - 10 conc towards interior	Yellow alteration fronts on cracked surfaces moderately pervasive; red/brown alteration/ inclusions in plag on slightly altered quench surface.	none
12D-4-1c	Representative plagioclase phyric basalt cobble	Plag:Acicular microphenocrysts & eu/subhedral phenocrysts; sub/anhedral glomerocrysts; minor olivine? and spinel (black) inclusions in plag. Phenocrysts concentrate towards glassy rim.	<1 ; 5 *(---- ; <5.00 - 15 00)*	0.50 - 2.00 ; 0.50 - 7.00 *(---- ; <5.00 - 15 00)*	----	----	1 *(1 - 5)* 1 - 3 mm diam	Palagonitized glass; black Mn coating,minor alteration front across half the sample. Vesicles homogeneously distributed.	none
12D-5-1c	Representative plagioclase phyric basalt cobble. Related to 12D-4.	Plag:Acicular microphenocrysts & sub/euhedral phenocrysts sub/anhedral glomerocrysts; some with inclusions; some with dark cores - xenocrysts?	<1 ; 7 *(– ; 10 - 15)*	0.25 - 2.50 ; 0.50 - 5.00 *(---- ; 5.00)*	----	----	<1 - 2 *(<5)*	Considerable pervasive alteration fronts in sample (concentric with cracks), phenocrysts partly altered and there is orange alteration in vesicles; exterior heavily coated by white (hydrothermal?) alteration - possibly carbonate.	none
12D-5-2b	Sparsely plagioclase phyric basalt cobble	Plag:Acicular microphenocrysts & sub/anhedral phenocrysts	<<1 ; <1	0.75 - 1.50 ; 1.00 - 1.50 *(---- ; 5.00)*	----	----	<1 *(<5)*	Thin Mn coating; major alteration fronts removed, but minor ones remain.	none
12D-6-1b	Representative aphyric basalt pebble. Oldest unit of 12D	None; possibly minor plagioclase microphenocrysts	----	----	----	----	1 up to 1mm	Slab for analysis has possible fine grained pervasive alterationand slight oxidation in some vesicles; yellow altered exterior with Mn coating thicker than 12D-5.	none
13D-1-1b	Cobble of very plagioclase phyric basalt	Plag & ol: subhedral phenocrysts most packed with inclusions	– ; 40	---- ; 1.00 - 12.00 *(---- ; <5.00 - 20 00)*	3 *(<1)*	1.00 - 7.00 *(<3.00)*	1	Slab for analysis looks fresh; glassy rim is a few mm thick and slightly palagonitized.	none
13D-1-2a	Cobble of very plagioclase phyric basalt	Plag & ol: subhedral phenocrysts most packed with inclusions; some plag have dark cores	– ; 40	---- ; 1.00 - 12.00 *(---- ; <5.00 - 20.00)*	3 *(<1)*	0.50 - 3.00 *(<3.00)*	1	Some of the plag is beginning to alter in the slab for analysis; glassy rim is a few mm thick and slightly palagonitized.	none
14D-1-1b	Representative sparsely plagioclase phyric basalt	Plag.Acicular microphenocrysts & sub/anhedral phenocrysts, some with inclusions & darker cores; concentrate towards glassy rim. Cpx : black eu/subhedral elongate tabular phenocrysts with 1 good and 1 parting cleavage.	– ; 3 *(– ; 5)*	0.25 - 2.50 ; 1.00 - 5.00 *(---- ; <6.00 in rim)* *(---- ; <3.00 in interior)*	[1]	[6.00]	4 *(5)* *(<0.5 mm)*	Thin selvage of glass 1 - 2mm thick palagonitized along cracks and on some surfaces; considerable yellow/orange oxidation and black Mn coating on the weathered surface. Alteration fronts penetrate approx 1cm into the sample. The interior looks fresh.	none
15D-1-2b	Fine grained aphyric basalt	Plag Acicular microphenocrysts & anhedral microphenocrysts	<1 ;<<1	0.25 - 2.00 ; 0.25 - 1.50	----	----	<1 - 5 slightly vesic. cores	No glass. Weathered surface darker with occasional rusty patches.	none
15D-1-3b	Fine grained aphyric basalt	Plag:Acicular microphenocrysts & anhedral microphenocrysts	<1 ;<<1	0.25 - 1.50 ; 0.25 - 1.00	----	----	<1 - 10	Fresh glassy rind 5mm thick with only very slight pale brown alteration. Outer edges of	none

A Sample No.	B Description	C Type of phenocrysts	D % plag. phenocrysts	E size of plag. phenocrysts(mm)	F % ol. phenocrysts	G size of ol. phenocrysts(mm)	H % vesicularity	I Alteration	J Ooze?
	with glassy rind						slightly vesic. cores	analysis slab have a greenish tinge and some spots of rusty alteration.	
15D-1-4c	Fine grained aphyric basalt tubule with glassy rind	Plag:Acicular microphenocrysts & anhedral microphenocrysts	<1 ;<<1	0.25 - 1.00 ; 0.25 - 2.00	----	----	2 slightly vesic. cores	Unpalagonitized glassy rind 1 - 3mm thick. Untrimmed edges of sample for analysis weather white/yellow with an occasional rusty spot. Plag phenocrysts in glass starting to turn yellow.	none
15D-1-5c	Fine grained aphyric pillow basalt or tubule with thick glassy layer	Plag Acicular microphenocrysts & an/sub/euhedral microphenocrysts, some with inclusions	<1 ;<<1	0.25 - 1.00 ; 0.25 - 2.00	----	----	1 slightly vesic. cores	Unaltered glassy rim (max thickness 10mm) Green tinge on broken surface of analysis slab (previously a crack in the rock)	none
16D-1-1b	Representative cobble of plagioclase phyric basalt	Plag: sub/anhedral phenocrysts some with inclusions and dark cores. They are unevenly distributed and tend to concentrate in margins.	--; 6 *(--; 1 - 10)*	---- ; 1.00 - 7.00 *(---- ; <15.00)*	----	----	3	Pale yellow weathered surface Interior of slab highly cracked but looks fairly fresh. *(Thick fresh glass upto 15mm thick with some incipient palagonite)*	none
16D-1-2b	Representative cobble of plagioclase phyric basalt	Plag. sub/anhedral pheno/glomerocrysts some with inclusions and dark cores. Plag is unevenly distributed and tend to concentrate in margins.	--; 8 *(--; 1 - 10)*	---- ; 1.00 - 9.00 *(---- ; <15.00)*	----	----	1 - 15	Very thin but unpalagonitized glassy rim (most of glass spawled off). Weathering is pale; orange alteration concentrates in vesicles. Slight alteration on broken edge of the anal. slab. *(Thick fresh glass upto 15mm thick with some incipient palagonite)*	none
16D-1-3c	Boulder of plagioclase phyric basalt with glassy rind	Plag: sub/anhedral pheno/glomerocrysts some with inclusions and dark cores.	--; 4	---- ; 1.00 - 6.00	----	----	2	Rusty spots trimmed off otherwise fresh analysis slab. Glassy rind; some incipient palagonitization, but generally very fresh.	none
17D-1-2a	Very fine grained aphyric basalt pebble with thin (<1mm) glassy rind	Aphyric *(Sparse acicular plagioclase microphenocrysts)*	----	---- *(---- ; <2.00)*	----	----	<<1	Glassy unpalagonitized rim up to 2mm thick. Interior is fine-grained and looks fresh.	none
17D-1-2b	Very fine grained aphyric basalt pebble with thin (<1mm) glassy rind (for T.S.)	Aphyric *(Sparse acicular plagioclase microphenocrysts)*	----	---- *(---- ; <2.00)*	----	----	<<1	Glassy unpalagonitized rim up to 2mm thick. Interior is fine-grained and looks fresh.	none
17D-1-3a	Very fine grained aphyric basalt pebble with 0.5cm glassy rim on one side and tabular morphology.	Plag subhedral phenocrysts packed with black inclusions *(Sparse acicular plagioclase microphenocrysts)*	--; <<1	---- ; 1.00 - 4.00 *(---- ; <2.00)*	----	----	1	Glassy unpalagonitized rim mostly 2mm (up to 4mm) thick beginning to deteriorate into fine-grained white alteration mineral (ie. not shiney fresh). Rusty weathering spots and streaks along side; underneath has orange/brown weathering surface.	none
17D-1-3b	Very fine grained aphyric basalt pebble with 0.5cm glassy rim on one side and tabular morphology (for T.S.)	Plag: subhedral phenocrysts packed with black inclusions *(Sparse acicular plagioclase microphenocrysts)*	--; <<1	---- ; 1.00 - 4.00 *(---- ; <2.00)*	----	----	1	Glassy unpalagonitized rim mostly 2mm (up to 4mm) thick beginning to deteriorate into fine-grained white alteration mineral (ie. not shiney fresh). Rusty weathering spots and streaks along side; underneath has orange/brown weathering surface.	none
17D-2-1a	Vesicular aphyric basalt; partially altered	Aphyric	----	----	----	----	30	Fine-grained brown/orange alteration in some of the vesicles in the analysis slab.	none
18D-1-3b	Plag & ol phyric basalt pebble; tabular morphology, quenched upper & lower surfaces	Plag. sub/anhedral pheno/glomerocrysts some with inclusions. *(Unevenly distributed phenocrysts, possibly of 2 generations- first large crystals with inclusions and later smaller more translucent and subhedral. Olivine microphenocrysts in the groundmass.)*	5 *(--; 2 - 6)*	---- ; 1.00 - 7.00 *(---- ; 3.00 - 10.00)*	---- *(1)*	---- *(0.50)*	1 - 2 *(larger cavities in interior)*	Some palagonite on rim, though glass on T.S. looks very fresh. Sample for analysis had 2mm of glass which was trimmed off. It is quite cracked with possible faint alteration right through: otherwise looks fresh. *(Weathered surface is pale grey / yellow orange some with black Mn coating)*	none
18D-1-4b	Pebble of plag phyric basalt; very thin rim of glass on curved upper surface	Plag: sub/anhedral pheno/glomerocrysts some with inclusions. *(Unevenly distributed phenocrysts, possibly of 2 generations- first large crystals with inclusions and later smaller more translucent and subhedral. Olivine microphenocrysts in the groundmass.)*	4 *(--; 2 - 6)*	---- ; 0.50 - 9.00 *(---- ; 3.00 - 10.00)*	---- *(1)*	---- *(0.50)*	3 *(larger cavities in interior)*	Glass rim of 1mm was trimmed off sample for analysis which is cracked but looks fresh. One plag has some yellow alteration *(Weathered surface is pale grey / yellow orange some with black Mn coating)*	none
19D-1-2a	Very fine grained aphyric basalt pebble with thin glassy selvage (probably a lava bud)	Aphyric *(Two fragments show euhedral plagioclase phenocrysts)*	---- *(<5)*	----	----	----	2	Max glass thickness 3mm, some palagonite ie. glass just starting to alter pale yellow.	none
19D-2-1b	Representative very sparsely	Plag: acicular and anhedral microphenocrysts & anhedral phenocrysts	<<1 ; <<1	0.25 - 1.00 ; 1.00 - 1.50	<<1	0.50	2	Thin rim of glass (1mm) with patchy palagonitization in fractures; yellow/orange weathered	none

A Sample No.	B Description	C Type of phenocrysts	D % plag. phenocrysts *(- ; < 2)*	E size of plag. phenocrysts(mm) *(--- ; <5.00)*	F % ol. phenocrysts	G size of ol. phenocrysts(mm)	H % vesicularity Vesicular cores	I Alteration	J Ooze?
	phyric basalt from small boulder.	with inclusions. Olivine microphenocrysts						surface with some Mn coating. Interior and analysis slab look fresh.	
20D-1-1b	Boulder of plagioclase phyric pillow basalt	Plag: subhedral phenocrysts with possibly some black inclusions Large plags concentrated in the rim *(Olivine microphenocrysts)*	- ; 1 *(- ; 1 - 3)*	--- ; 1.00 - 4.00 *(--- ; 2.00 - 12.00)*	--- *(1)*	--- *(1.00 - 2.00)*	2 (1 - 5)	Thin glassy rind; white/yellow surface alteration, fairly pervasive. In analysis slab, one plagioclase is slightly yellow, otherwise it looks fresh. *(Vesicles 1mm in diameter and evenly distributed.)*	none
20D-1-2b	Boulder of sparsely plag phyric basalt.	Plag: sub/anhedral phenocrysts; fairly course grained groundmass:- possible plag laths visible. olivine: anhedral microphenocrysts; most phenocrysts with inclusions Large plags concentrated in the rim	- ; 2 *(- ; 1 - 3)*	--- ; 1.00 - 4.00 *(--- ; 2.00 - 12.00)*	<1 *(1)*	2.00 *(1.00 - 2.00)*	4 (1 - 5)	No glass; surface alteration pale yellow with Mn coating. Interior looks fresh *(Vesicles 1mm in diameter and evenly distributed.)*	none
20D-1-3b	Small plag phyric basalt boulder with a pahoehoe-like glassy structure on surface.	Plag: *sub/an/euhedral* phenocrysts; inclusions rare. Large plags concentrated in the rim *(Olivine microphenocrysts)*	- ; 1 *(- ; 1 - 3)*	--- ; 0.50 - 5.00 *(--- ; 2.00 - 12.00)*	--- *(1)*	--- *(1.00 - 2.00)*	4 (1 - 5)	Pale yellow and rusty weathering surface with some dark Mn coating; alteration fronts penetrate into the rock but were avoided in sampling. In the slab for analysis there are one or two slightly altered plags. *(Vesicles 1mm in diameter and evenly distributed.)*	none
21D-1-1b	Plag phyric pillow basalt cobble.	Plag: anhedral phenocrysts with inclusions.	- ; <1 *(- ; 2 - 5)*	--- ; 1.00 - 4 00 *(--- ; 2.00 - 5.00)*	---	---	1	Quenched on 2 sides; upper: *max* glass thickness is 3mm; lower: 1mm max. Some glass still looks shiney but there are patches of yellow alteration. Analysis slab is cracked and may have some alteration on the edges.	none
21D-2-1b	Plag phyric pillow basalt older than unit 1.	Plag:Acicular microphenocrysts & an/sub/euhedral pheno/glomerocrysts. Olivine. anhedral phenocrysts some in glomerophyric clusters with plag. Most phenocrysts have inclusions.	<1 ; 8	0.25 - 3.00 ; 0.50 - 10.00	1	1.50 - 5.00	3 - 5	Considerable alteration (pale yellow) on weathered surfaces and deep cracks. Analysis slab seems fresh as alteration fronts don't penetrate deep.	none
21D-3-1b	Aphyric pillow basalt.	Plag:Acicular microphenocrysts & anhedral phenocrysts, some with inclusions	<<1 ; <1	0.25 - 1.50 ; 0.50 - 4.00	---	---	2 - 6	Considerable alteration front in analysis slab. Altered part is darker with orange alteration in some vesicles.	none
22D-1-1b	Representative old aphyric pillow basalt cobble.	Plag: anhedral phenocrysts	- ; << 1	--- ; 1.00 - 2.00	---	---	2 *(5)*	Very thin glassy selvage is highly palagonitized. Weathered surface has grey mottled Mn coating and yellow oxidation; some alteration is penetrative.Some of the vesicles have pale infil. The only plag in the analysis slab is yellow and altered.	On weathered surface.
22D-2-1b	Small boulder of plag and ol phyric basalt.	Plag.Acicular microphenocrysts & subhedral pheno/glomerocrysts.	<1 ; 3 *(5)*	0.25 - 2.00 ; 0.50 - 7.00 *(--- ; <4.00)*	--- *(1 - 2)*	--- *(< 1.00)*	2 *(5)* homogeneous	Glassy selvage on one side up to 1cm thick and is palagonitized. weathered surface has partial Mn coating. Pale alteration round many of the vesicles on the analysis slab. Many of the plags show yellow alteration too.	On glassy surface. In pipe.
22D-2-2b	Boulder of plag, ol and cpx phyric basalt.	Plag: subhedral, anhedral (+ a few euhedral and acicular) phenocrysts & euhedral phenocrysts, some with inclusions. Olivine microphenocryst inclusion in plag.	- ; 5 *(- ; 5 - 15)*	--- ; 1.00 - 10.00 *(--- ; 1.00 - 10.00)*	<< 1 *(< 2)*	0.50 - 1.00	1 *(5)* homogeneous	No glass. Weathered surface has partial Mn coating. Strong alteration fronts with orange weathering plag. Analysis slab trimmed down to fresh interior	On glassy surface. In pipe.
22D-3-1b	Small cobble of olivine phyric basalt, older than 22D-2	Plag Acicular and subhedral microphenocrysts, sometimes in clusters about 3mm in diameter. Anhedral olivine microphenocrysts?	<1 ; -	0.25 - 1.00 ; --- *(1.00 - 2.00 ; ---)*	1	0.50 - 1.50 *(< 1.00)*	3	Most of the plag appears slightly yellow and altered. Faint alteration front across half of the analysis slab which has orange/pale yellow alteration in some vesicles. *(Weathered surface has thin Mn coating.)*	In pipe.
22D-3-2b	Small cobble of olivine phyric basalt, older than 22D-2	Plag.Acicular microphenocrysts & *sub/anhedral* (+ a few euhedral and acicular phenocrysts), some packed with inclusions (possibly some cpx). Subhedral olivine (or maybe just altered plagioclase?)	1 ; 4 *(1 - 2)*	0.25 - 3.00 ; 1.00 - 5.00	--- [<1] *(5)*	--- [0.50 - 1.50] (1.00 - 3.00)	<1	A pervasive alteration front has passed through most of the analysis slab leaving it with a speckled rusty tinge. Most of the plags are quite badly altered and orange in colour. *(Weathered surface has thin Mn coating.)*	In pipe.
22D-6-1b	Large cobble of massive fine-grained basalt. Thick flow.	Plag.Acicular microphenocrysts & eu/sub/anhedral phenocrysts, most with inclusions. Olivine microphenocrysts	<1 ; 1 *(1)*	0.25 - 1.00 ; 1.00 - 6.00 *(--- ; <10 00)*	<< 1	0.25	1	Weathered surface has thin partial Mn coating. Minor alteration fronts penetrate 1 - 2cm into the rock but have nearly all been cut out of the analysis slab which looks fresh apart from one half mm diameter rusty spot.	In pipe.
22D-6-2b	Boulder of massive basalt more coarse grained than 22D-6-1.	Plag:Acicular microphenocrysts & anhedral phenocrysts.	2 ; <<1 *(1)*	0.25 - 2.00 ; 0.25 - 2.00 *(--- ; <10.00)*	---	---	<1	Thin partial Mn coating and penetrative alteration 1 - 2cm into rock (at least). Analysis slab has no alteration fronts as it has been trimmed but a slight yellowish tinge and some vesicles have a pale coat. The plags are pale yellow-green.	In pipe.
23D-1-1b	Aphytic basalt; quite an old pillow.	Plag:Acicular microphenocrysts & anhedral phenocrysts.	<1 ; <<1	0.25 - 2.00 ; 0.50 - 2.00	---	---	5 homogeneous	Very thin rind of glass1 - 2mm thick, partly palagonitized. Orange-yellow weathered surface. Alteration down crack in the analysis slab.	none

A Sample No.	B Description	C Type of phenocrysts	D % plag. phenocrysts	E size of plag. phenocrysts(mm)	F % ol. phenocrysts	G size of ol. phenocrysts(mm)	H % vesicularity	I Alteration	J Ooze?
23D-2-2b	Representative highly plag and ol phyric basalt with tabular morphology and a glassy top.	Plag.Acicular microphenocrysts & eu/sub/anhedral pheno/glomerocrysts, some with dark cores. Olivine subhedral phenocryst and in glomerocryst with plag. (Possibly just altered plag). Some phenocrysts have inclusions.	1 ; 15 - 20 *(– ; 20)*	0.25 - 2.00 ; 0.50 - 14.00 *(---- ; <15.00)*	1 *(<1)*	1.50 - 3.00 *(2.00 - 3.00)*	1	Top glassy margin (up to 1cm thick) is palagonitized. Black powdery Mn coating. Plags in the analysis slab have yellow altered patches and there are orange flecks in a cavity. It is quite cracked; some parts are slightly altered.	In cracks; in pipe
23D-3-1b	Representative very sparsely plag phyric basalt with glassy upper and lower surfaces. Has tabular morphology 3cm thick.	Plag:Acicular microphenocrysts & eu/subhedral phenocrysts	<1 ; <1 *(<1)*	0.25 - 1.00 ; 0.50 - 3.00 *(---- ; <3.00)*	----	----	1	Remnant of palagonitized glass rim on top and bottom of tabular sample, both with 5mm chilled margin.Slabs for analysis have yellow alteration on none cut surfaces. Some orange palagonite left entrained in glass cracks. Fine-grained interior looks fairly fresh.	*none*
23D-4	Pebble of fine grained aphyric basalt; no alteration/oxidation. Recovered from dredge bag.	Plag:Acicular microphenocrysts & eu/subhedral phenocrysts	<1 ; <1	0.25 - 1.00 ; 0.25 - 3.00	----	----	1	Very slightly palagonitized glassy rim with minor orange alteration in the cracks and 2mm chilled margin. All the fresh shiney glass has spawled off. Uncut surfaces have minor spots of brown alteration. One plag has a rusty patch.	none
24D-1-1b	Representative plag phyric basalt. Thick sheet flow.	Plag: sub/anhedral pheno/glomerocrysts, some with inclusions. *(Large phenocrysts have xenocrystic dark cores)*	– ; 4 *(<10)*	---- ; 0.50 - 9.00 *(---- ; <10.00)*	----	----	1 - 3 *(<1)*	Black Mn coat and rusty weathering on surface.Some palagonitized glass remaining, but nearly all spawled off.Pale alteration along major cracks. Analysis slab will be quite fresh if all the altered surfaces are removed. Youngest unit in 24D.	In cracks on quench surface.
24D-2-1b	Representative cobble with glassy rind. Pillow basalt older than 24D-1.	Plag.Acicular microphenocrysts & sub/anhedral phenocrysts, occasionally with inclusions.	<1 ; <1	0.25 - 2.00 ; 1.00 - 4.00	----	----	5 *(none)*	Glassy margins <3mm thick, moderately palagonitized. Weathered surface has black Mn coat and patches of pale alteration; fractures have orange alteration. Interior looks fresh apart from a few pale yellow patches in the phenocrysts. Older than 24D-1.	In pits on surfaces
24D-3-1b	Representative aphyric basalt older than unit 2.	Aphyric	----	----	----	----	3 - 7	No glass. Black Mn coat and patches of pale alteration on the surface. Analysis slab looks fresh apart from a few small alteration fronts on the edge and a small crack with alteration front in the middle.	none
27D-1-1b	Representative boulder of highly plag phyric pillow basalt.	Plag Acicular microphenocrysts & subhedral phenocrysts *(Subhedral ol microphenocrysts some containing spinel inclusions; cpx?)*	1 ; 5 *(20 - 30)*	0.25 - 3.00 ; 0.50 - 8.00 *(---- ; 0.50 - 5.00)*	---- *(0.5)*	---- *(0.20 - 0.80)*	1 - 3	Glassy rim palagonitized and eroded away; slight Mn coating; silicified margins removed from sample. Alteration fronts and yellow/orange alteration in vesicles in analysis slab. *(Most samples have black halo type of alteration around margins and cracks, penetrating a few cm. Some have a coating of celadonite)*	Slight coating
27D-2-1b	Representative boulder of sparsely plag phyric basalt.	Plag.Acicular microphenocrysts & eu/sub/anhedral phenocrysts, some with inclusions. subhedral olivine microphenocrysts?? Clinopyroxene: black laths	1 ; 5 *(0.5 - 1)*	0.25 - 2.00 ; 0.50 - 9.00 *(---- ; 0.50 - 1.00)*	<<1 ; [<1] *(0.5 - 1)*	1.00 : [2.00 - 2.50] *(0.20 - 0.50)*	1 microvesic.	Palagonitized glass 2 -5mm thick, most eroded away. Slight Mn coating and silicified margins removed. also orange/brown weathered surface penetrates quite deeply as black halo type alteration. There are some alteration fronts in the analysis slab but may be able to cut these down to fresh centre. Brown specks -a *mineral*?	Slight coating
29D-1-1c	Small representative boulder of sparsely plag phyric basalt.	Plag Acicular microphenocrysts & subhedral phenocrysts, the larger ones with inclusions. Olivine: anhedral microphenocrysts??	1 ; 3 *(2)*	0.25 - 2.00 ; 0.50 - 8.00 *(---- ; <4.00)*	-??-	-??-	1 - 5 lined with black - Mn?	Glassy margins up to 5mm thick are largely palagonitized. Pervasive alteration along fine cracks in interior - dark halos of alteration about 1cm wide. Broken surfaces stained green; weathered have Mn coating. Slight pale alteration around larger clumps of vesicles. Analysis slab has an inhomogeneous colour with darker finer grained (less altered?) patches	none
29D-2-1c	Coble of representative plag and ol phyric pillow basalt with palagonitized glassy rim.	Plag Acicular microphenocrysts & eu/sub/anhedral phenocrysts, a few with inclusions. Olivine: one anhedral microphenocrysts *(Larger plags have dark cores.)*	1 ; 7 *(– ; 10 - 20)*	0.25 - 2.00 ; 0.25 - 10.00 *(---- ; <20.00)*	<<1 *(<1)*	1 00 *(<2)*	1	Palagonitized rim with up to 1mm chilled margin. Mn coat quite well developed; rusty coloured staining on broken surfaces.Analysis slab is quite cracked and some of the plags are beginning to alter pale yellow/green.	none
29D-3-1c	Boulder of representative very sparsely plag phyric pillow basalt.	Plag.Acicular microphenocrysts & sub/anhedral pheno/glomerocrysts.	2 ; 1	0.25 - 2.50 ; 1.00 - 6.00	----	----	1 - 10 *(<1)*	Glass highly palagonitized and eroded away; max thickness 1 - 2mm. Weathered exterior pale with extensive infiltration of alteration into interior. There is thin Mn coating on outer surfaces and Mn spots on interior fractures. Some minor pale alteration in vesicles. In the analysis slab very few vesicles have alteration but there is a minor alteration rim round one glomerophyric clusters, otherwise fairly fresh.	In pipe & embedded in cracks.
29D-3-2c	Small pillow bud.	Plag.Acicular & subhedral microphenocrysts, some with inclusions, sometimes in glomerophyric clusters .	3 ; <1	0.25 - 3 00 ; 0.25 - 2.50	----	----	<1	Analysis slab has glassy rind up to 1.5mm thick; most glass has spawled off and there are some patches of pale slight alteration; chilled margin 8mm. Interior is fresh apart from occasional rusty spot. Cracked/weathered surfaces have yellow/green tinge. Finer grained and less altered than 29D-3-1.	In pipe & embedded in cracks.
30D-1-2c	Representative boulder of	Plag.Acicular microphenocrysts & an/sub/euhedral phenocrysts, most	<<1 ; 3	0.25 - 1.50 ; 0.25 - 7.00	<1	1.00 - 2.50	5	Glassy selvages extensively palagonitized - max fresh glass thickness is 2mm. Rusty	Traces in

A Sample No.	B Description	C Type of phenocrysts	D % plag. phenocrysts *(3)*	E size of plag. phenocrysts(mm) *(---- ; 3.00 - 8.00)*	F % ol. phenocrysts *(<1)*	G size of ol. phenocrysts(mm) *(1.00 - 2.00)*	H % vesicularity	I Alteration	J Ooze?
	sparsely plag phyric pillow basalt.	with inclusions. Olivine: sub/anhedral phenocrysts commonly in glomerophyric clusters with plag.					conc in core	weathered surface with sooty Mn coating. Interior of the sample looks fresh.	cracks.
31D-1-2b	Representative cobble of highly plag phyric basalt sheet flow?	Plag: sub/anhedral phenocrysts, a few with inclusions, two with dark cores - one contains a black elongate crystal...cpx? Large phenocryst in rim has brown 0.5mm inclusion - Al spinel? Olivine: microphenocrysts often in clusters with plag.	12 *(20 - 30)*	---- ; 0.25 - 11.00 *(---- ; <5.00)*	<<1 [<<1]	0.75 [3.00]	2 *(1)*	Thin glassy rind mostly <1mm thick but up to 2mm, speckled with pale alteration; chilled margin 5mm. Weathered surface is pale yellow/ blue grey. Interior and the analysis slab seem fresh with only a few slightly yellowing plags.	none
32D-1-1b	Representative cobble of variolitic pillow basalt. Sample from pillow interior.	Plag: sub/anhedral phenocrysts, some with inclusions. (One particularly large 1mm melt or spinel inclusion.)	1	---- ; 0.50 - 10.00 *(---- ; 3.00 - 10.00)*	----	----	3 homogeneous *(2 - 10)*	Small amount of glass remaining, fairly fresh, but most eroded; variolitic texture for several cm adjacent to glass rim. Rusty weathered surface. Interior and analysis slab looks fresh with a few small brown/orange spots. Small alteration front was trimmed from the slab *(Mn coating on most weathered faces; pale yellow/orange alteration on fractured surfaces)*	none
32D-1-2c	Representative cobble of variolitic pillow basalt. Anal. sample from pillow interior. T.S. and glass from rim.	Plag: anhedral phenocrysts	1	---- ; 0.50 - 3.50 *(---- ; 3.00 - 10.00)*	----	----	1	0.5mm of glass remaining, fairly fresh but most eroded.Yellow/green alteration down pervasive cracks in rock Alteration fronts have been cut off the analysis slab. Where a front has penetrated there is alteration in vesicles, down microcracks and brown spots on surface *(Mn coating on most weathered faces; pale yellow/orange alteration on fractured surfaces)*	none
32D-2-1c	Representative aphyric pillow basalt cobble. Has glass on one whole surface & a stripe of glass at 90 degrees, suggesting a flow fold.	Plag: an/subhedral microphenocrysts, occasionally in clusters. *(Olivine microphenocrysts)*	<1	0.25 - 1.00 ; ---- *(---- ; <1.00)*	----	---- *(<<1.00)*	3	Palagonitized glass upto 2mm thick; parts still shiney but oxidation is extensive especially in the cracks; chilled margin 5mm. Weather surfaces and fractures are pale with some mottled Mn coat. Analysis slab has faint brown spots but otherwise looks fresh. *(Some samples have sooty Mn coating)*	In cracks in glass?
32D-3-1b	Representative aphyric pillow basalt cobble. Has tabular blocky shape - from massive flow?	Plag: sub/anhedral microphenocrysts; possibly olivine???	<1	0.25 - 1.50 ; ---- *(---- ; <1.00)*	----	----	3 *(<2 - 3)*	No glass. Mottled Mn coating and dark orange patches on the weathered surface. Analysis slab has dark alteration fronts with greenish tinge, rusty alteration in vesicles and some paler alteration of microvesicles and groundmass.	In cavities

BLANK IN ORIGINAL

Appendix 5

Whole-rock data set

Sample		1D-3-1b	3D-1-1c	3D-1-2b	4D-1-1b	4D-1-2b	4D-1-3b	4D-1-3bR	5D-1-2b	6D-1-1c	6D-1-2c	6D-1-3c
latitude		23.64	23.88	23.88	23.89	23.89	23.89	23.89	23.86	23.85	23.85	23.85
SiO2	%	50.52	50.51	49.68	49.55	50.11	50.10	50.10	49.74	49.80	49.90	49.93
Al2O3	%	15.43	16.84	17.91	15.63	15.75	15.84	15.84	15.69	15.44	15.59	15.38
Fe2O3	%	10.61	9.56	8.79	9.90	9.98	9.91	9.91	10.36	10.38	10.46	10.81
MgO	%	7.82	7.07	6.43	7.99	7.94	8.16	8.16	7.85	7.91	7.91	7.48
CaO	%	10.40	11.79	12.15	11.25	11.18	11.25	11.25	11.53	11.49	11.52	11.03
Na2O	%	3.14	2.75	2.77	2.86	2.88	2.85	2.85	2.80	2.81	2.89	3.06
K2O	%	0.08	0.19	0.17	0.14	0.12	0.11	0.11	0.12	0.15	0.11	0.20
TiO2	%	1.56	1.32	1.20	1.36	1.40	1.36	1.36	1.37	1.37	1.38	1.69
MnO	%	0.17	0.16	0.15	0.17	0.17	0.17	0.17	0.17	0.17	0.17	0.18
P2O5	%	0.15	0.12	0.13	0.13	0.14	0.12	0.12	0.12	0.13	0.11	0.16
TOTAL	%	99.86	100.31	99.34	98.96	99.63	99.87	99.87	99.73	99.64	100.04	99.89
Nb	ppm	2.19	2.33	5.00	2.80	4.58	4.05	4.00	2.43	4.45	4.65	4.50
Zr	ppm	92.76	87.75	83.05	95.00	99.00	95.97	93.49	92.03	92.19	92.69	119.23
Y	ppm	34.14	29.68	28.56	30.41	31.61	30.47	31.02	32.81	33.35	32.77	39.67
Sr	ppm	152.88	132.95	135.20	139.58	133.50	134.08	137.85	123.25	117.95	116.53	126.25
Ga	ppm	16.39	15.17	16.17	14.85	16.46	15.95	15.49	16.26	16.52	15.11	17.84
Zn	ppm	64.42	69.11		67.43				72.32			
Cu	ppm	95.70	65.68		65.31				88.01			
Ni	ppm	71.19	83.30	75.45	125.24	122.20	126.71	123.82	71.44	72.81	74.74	99.65
Co	ppm	39.51	39.91		43.85				46.70			
Cr	ppm	147.46	231.89	231.76	298.92	302.21	301.02	291.37	349.49	349.99	356.29	274.08
V	ppm	292.36	248.31	246.01	261.29	288.12	283.37	272.58	265.27	257.62	280.27	311.86
Rb	ppm	0.21	1.68	3.31	1.11	2.62	1.69	1.86	1.25	2.01	2.96	2.57
Ba	ppm	20.55	11.33	10.85	12.32	18.88	19.43	21.21	10.75	18.31	17.78	20.45
Sc	ppm	40.23	34.71	32.20	36.67	37.00	37.05	37.89	40.73	35.20	41.17	37.77
Cs	ppm	0.02	0.05		0.01				0.02			
La	ppm	3.34	3.14	0.48	3.50	0.41	1.22	1.57	3.13	0.10	0.99	3.06
Ce	ppm	10.85	9.73	3.95	10.57	13.80	9.29	8.68	9.37	11.76	7.20	14.32
Pr	ppm	1.82	1.65		1.73				1.60			
Nd	ppm	10.31	8.89	5.56	9.40	7.08	6.85	8.88	8.84	3.95	6.45	12.84
Sm	ppm	3.32	2.94		3.02				2.98			
Eu	ppm	1.19	1.11		1.13				1.10			
Gd	ppm	4.41	3.96		3.86				3.98			
Tb	ppm	0.82	0.73		0.75				0.73			
Dy	ppm	5.30	4.75		4.72				5.02			
Ho	ppm	1.13	1.02		1.00				1.12			
Er	ppm	3.34	3.00		2.90				3.16			
Tm	ppm	0.48	0.43		0.44				0.48			
Yb	ppm	3.19	2.95		2.91				3.29			
Lu	ppm	0.47	0.44		0.43				0.49			
Hf	ppm	2.55	2.33		2.37				2.42			
Ta	ppm	0.14	0.14		0.17				0.14			
Mo	ppm	10.93	2.63		0.70				1.51			
W	ppm	0.05	0.02		0.06				0.07			
Tl	ppm	0.01	0.07		0.02				0.06			
Pb	ppm	0.95	0.80		1.23				0.83			
Th	ppm	0.09	0.19		0.16				0.17			
U	ppm	0.05	0.11		0.08				0.08			
Chondrite Normalised												
La		10.16	9.55		10.16				9.52			
Ce		13.43	12.04		13.09				11.59			
Pr		14.93	13.49		14.15				13.13			
Nd		17.18	14.82		15.67				14.74			
Sm		17.02	15.09		15.49				15.28			
Eu		16.18	15.20		15.36				15.04			
Gd		17.04	15.29		14.90				15.37			
Tb		17.22	15.35		15.84				15.38			
Dy		16.46	14.76		14.66				15.58			
Ho		15.69	14.18		13.96				15.55			
Er		15.88	14.26		13.81				15.05			
Tm		14.89	13.36		13.43				14.86			
Yb		15.25	14.12		13.92				15.75			
Lu		14.51	13.68		13.46				15.21			
recal Nb for xrf		2.19	2.33	3.45	2.40	2.87	2.15	2.08	2.43	2.70	2.97	2.77
Nb	ppm	2.19	2.33	5.00	2.40	4.58	4.05	4.00	2.43	4.45	4.65	4.50

Sample		6D-2-1c	6D-2-2e	6D-2-2eR	7D-1-1c	7D-1-2c	7D-1-3c	8D-1-1b	9D-1-1b	9D-1-2b	9D-1-2bR	11D-1-1b
latitude		23.85	23.85	23.85	23.85	23.85	23.85	23.85	23.90	23.90	23.90	23.93
SiO2	%	49.63	50.08	50.08	49.84	50.07	49.74	49.74	50.01	49.97	49.97	49.89
Al2O3	%	17.68	16.92	16.92	16.27	16.15	16.36	17.22	16.38	16.51	16.51	16.16
Fe2O3	%	9.42	10.01	10.01	9.17	9.33	9.35	9.83	9.39	9.40	9.40	10.74
MgO	%	6.39	6.48	6.48	8.62	8.69	8.58	6.75	8.12	8.12	8.12	6.96
CaO	%	11.71	11.41	11.41	11.73	11.66	11.65	11.43	11.71	11.69	11.69	11.05
Na2O	%	2.90	2.91	2.91	2.65	2.73	2.58	2.91	2.71	2.73	2.73	2.89
K2O	%	0.18	0.24	0.24	0.16	0.18	0.13	0.21	0.18	0.09	0.09	0.19
TiO2	%	1.42	1.54	1.54	1.16	1.18	1.20	1.54	1.28	1.26	1.26	1.67
MnO	%	0.16	0.17	0.17	0.15	0.16	0.16	0.16	0.16	0.16	0.16	0.18
P2O5	%	0.15	0.16	0.16	0.12	0.11	0.12	0.14	0.12	0.11	0.11	0.16
TOTAL	%	99.62	99.90	99.90	99.86	100.25	99.86	99.94	100.04	100.02	100.02	99.89
Nb	ppm	2.79	4.23	4.70	4.90	4.45	2.83	2.88	3.75	1.85	3.93	3.25
Zr	ppm	99.87	108.02	112.02	78.17	79.45	78.86	111.99	85.46	82.83	85.68	117.69
Y	ppm	32.39	35.86	37.78	26.61	26.82	27.10	35.34	29.31	29.06	29.19	38.52
Sr	ppm	138.31	130.53	129.65	117.10	121.38	123.65	136.47	120.70	125.05	120.25	130.17
Ga	ppm	15.86	16.37	18.07	15.46	15.57	14.17	16.19	15.68	14.78	14.55	16.28
Zn	ppm	79.12					61.99	72.32		74.27		83.26
Cu	ppm	51.23					73.90	54.31		71.67		64.28
Ni	ppm	66.60	75.00	76.06	114.26	101.68	113.87	76.28	128.40	131.04	123.45	82.27
Co	ppm	35.92					44.20	37.75		40.79		40.60
Cr	ppm	197.46	190.70	194.62	380.83	375.73	368.02	234.04	339.84	344.49	351.24	224.04
V	ppm	245.40	288.46	298.85	250.45	247.70	241.28	264.63	256.06	248.86	260.52	296.56
Rb	ppm	1.56	5.17	2.50	2.50	2.35	1.41	1.79	2.72	0.85	1.91	1.55
Ba	ppm	12.88	21.32	21.56	25.44	23.91	13.67	13.16	14.82	8.67	11.58	14.15
Sc	ppm	30.84	34.29	36.12	33.24	32.94	33.87	33.44	33.08	35.69	33.90	38.43
Cs	ppm	0.02					0.02	0.02		0.01		0.03
La	ppm	3.64	3.25	0.80	0.74	-0.08	3.01	3.90	0.31	2.84	0.04	3.98
Ce	ppm	11.29	17.34	13.04	11.99	9.75	9.00	12.24	11.66	8.93	10.84	12.08
Pr	ppm	1.83					1.44	2.02		1.48		2.05
Nd	ppm	10.20	11.49	12.42	7.26	8.93	7.85	11.02	9.16	8.15	7.48	11.16
Sm	ppm	3.48					2.60	3.68		2.78		3.81
Eu	ppm	1.22					0.96	1.27		1.05		1.35
Gd	ppm	4.29					3.45	4.77		3.71		5.06
Tb	ppm	0.81					0.66	0.86		0.69		0.90
Dy	ppm	5.38					4.14	5.75		4.43		6.03
Ho	ppm	1.16					0.87	1.20		1.01		1.27
Er	ppm	3.30					2.58	3.59		2.79		3.77
Tm	ppm	0.50					0.41	0.52		0.46		0.60
Yb	ppm	3.39					2.58	3.61		2.86		3.80
Lu	ppm	0.50					0.37	0.54		0.43		0.60
Hf	ppm	2.64					1.93	2.94		2.19		3.13
Ta	ppm	0.17					0.16	0.19		0.12		0.22
Mo	ppm	0.49					0.42	0.38		0.31		0.66
W	ppm	0.12					0.03	0.03		0.02		0.02
Tl	ppm	0.01					0.04	0.04		0.02		0.03
Pb	ppm	0.58					0.53	0.57		0.48		0.64
Th	ppm	0.17					0.17	0.19		0.13		0.22
U	ppm	0.09					0.08	0.07		0.06		0.10
Chondrite Norm												
La		11.05					9.16	11.87		8.62		12.20
Ce		13.98					11.14	15.15		11.05		15.25
Pr		14.98					11.81	16.60		12.11		17.32
Nd		16.99					13.09	18.37		13.58		18.72
Sm		17.85					13.31	18.89		14.27		19.84
Eu		16.71					13.08	17.27		14.29		18.56
Gd		16.58					13.31	18.42		14.33		20.11
Tb		17.15					13.97	18.14		14.66		19.00
Dy		16.71					12.85	17.86		13.75		18.43
Ho		16.10					12.18	16.76		14.04		17.51
Er		15.69					12.29	17.07		13.29		17.71
Tm		15.52					12.68	16.18		14.27		18.73
Yb		16.24					12.32	17.29		13.69		17.65
Lu		15.65					11.43	16.77		13.47		18.65
recal Nb for xrf		2.79	2.39	3.04	3.31	2.70	2.83	2.88	1.74	1.85	1.98	3.25
Nb	ppm	2.79	4.23	4.70	4.90	4.45	2.83	2.88	3.75	1.85	3.93	3.25

Sample		11D-1-1bR	12D-1-1b	12D-1-2c	12D-3-1c	12D-4-1c	12D-5-1c	12D-5-2b	12D-6-1b	13D-1-1b	14D-1-1b	15D-1-2b
latitude		23.93	23.96	23.96	23.96	23.96	23.96	23.96	23.96	24.01	24.01	24.05
SiO2	%	49.89	50.00	49.93	50.04	49.91	50.03	50.35	50.41	47.96	50.42	49.70
Al2O3	%	16.16	16.26	16.17	16.40	16.41	16.48	15.68	15.65	23.86	15.83	16.12
Fe2O3	%	10.74	9.65	9.66	9.67	9.70	9.52	10.07	10.09	5.28	9.59	9.45
MgO	%	6.96	7.91	7.90	7.98	7.90	7.68	7.78	7.81	5.89	7.72	8.73
CaO	%	11.05	11.51	11.37	11.51	11.52	11.49	11.50	11.47	13.56	11.53	11.59
Na2O	%	2.89	2.94	2.93	2.98	2.99	3.00	2.98	3.05	2.00	2.91	2.68
K2O	%	0.19	0.09	0.08	0.09	0.11	0.12	0.17	0.11	0.08	0.24	0.06
TiO2	%	1.67	1.33	1.34	1.33	1.34	1.33	1.43	1.44	0.69	1.31	1.20
MnO	%	0.18	0.17	0.17	0.16	0.16	0.16	0.17	0.17	0.09	0.16	0.16
P2O5	%	0.16	0.12	0.12	0.11	0.12	0.12	0.13	0.13	0.08	0.13	0.10
TOTAL	%	99.89	99.96	99.66	100.24	100.14	99.90	100.25	100.31	99.48	99.83	99.76
Nb	ppm	5.10	1.90	4.18	4.08	3.78	3.90	3.95	4.50	2.28	3.09	1.65
Zr	ppm	117.58	89.09	92.47	92.57	92.67	91.99	99.03	98.80	47.83	91.54	74.29
Y	ppm	39.34	29.93	30.93	30.75	30.79	31.24	33.68	32.72	15.98	28.75	27.85
Sr	ppm	125.75	133.02	128.60	128.35	129.10	131.28	127.03	126.53	151.34	145.35	111.85
Ga	ppm	16.84	15.53	15.37	17.13	14.73	16.70	17.16	16.36	13.30	14.80	14.58
Zn	ppm		65.89							34.14	62.89	71.74
Cu	ppm		69.78							39.64	68.65	73.67
Ni	ppm	83.49	114.24	126.54	115.71	117.27	121.89	115.44	106.55	107.39	88.26	133.69
Co	ppm		42.36							32.51	41.03	46.30
Cr	ppm	228.98	316.09	322.06	317.33	310.99	315.58	320.61	321.45	290.25	300.72	385.70
V	ppm	302.98	261.33	276.45	267.18	271.84	272.32	291.00	284.94	121.36	246.93	247.91
Rb	ppm	3.09	0.83	1.37	2.10	1.96	2.89	3.01	2.40	1.07	2.09	0.61
Ba	ppm	23.58	8.71	20.29	17.47	17.28	14.78	18.58	15.49	12.91	15.21	6.61
Sc	ppm	37.47	35.99	36.83	36.48	35.56	34.85	38.09	37.24	17.23	36.72	34.50
Cs	ppm		0.01							0.02	0.03	0.01
La	ppm	2.45	2.92	1.80	0.95	1.43	0.64	1.34	1.51	2.16	3.57	2.46
Ce	ppm	11.71	9.70	8.55	6.74	7.29	10.39	9.20	10.48	5.88	10.65	7.71
Pr	ppm		1.63							0.95	1.68	1.36
Nd	ppm	10.12	9.00	8.32	7.86	8.51	7.73	9.64	9.02	5.07	9.16	7.38
Sm	ppm		3.06							1.60	2.88	2.57
Eu	ppm		1.13							0.68	1.10	1.00
Gd	ppm		3.91							2.20	3.79	3.44
Tb	ppm		0.73							0.40	0.69	0.62
Dy	ppm		4.72							2.63	4.56	4.29
Ho	ppm		1.04							0.58	0.97	0.95
Er	ppm		2.94							1.63	2.77	2.65
Tm	ppm		0.44							0.24	0.44	0.40
Yb	ppm		3.01							1.64	2.70	2.71
Lu	ppm		0.44							0.26	0.47	0.40
Hf	ppm		2.38							1.33	2.23	1.92
Ta	ppm		0.13							0.14	0.19	0.11
Mo	ppm		0.38							0.41	0.41	0.29
W	ppm		0.05							0.04	0.05	0.04
Tl	ppm		0.02							0.00	0.04	0.04
Pb	ppm		0.54							0.33	0.52	0.42
Th	ppm		0.11							0.15	0.16	0.08
U	ppm		0.05							0.05	0.08	0.04
Chondrite Norm												
La			8.88							6.56	10.86	7.47
Ce			12.00							7.28	13.18	9.54
Pr			13.35							7.81	13.75	11.13
Nd			15.01							8.45	15.27	12.31
Sm			15.68							8.23	14.79	13.17
Eu			15.36							9.23	14.96	13.68
Gd			15.09							8.48	14.65	13.28
Tb			15.48							8.51	14.57	12.70
Dy			14.66							8.18	14.17	13.32
Ho			14.53							8.13	13.54	13.25
Er			14.00							7.74	13.19	12.62
Tm			13.60							7.30	13.73	11.49
Yb			14.39							7.86	12.91	12.95
Lu			13.70							7.96	14.66	11.10
recal Nb for xrf		3.59	1.90	2.32	2.18	1.77	1.94	2.01	2.77	2.28	3.09	1.65
Nb	ppm	5.10	1.90	4.18	4.08	3.78	3.90	3.95	4.50	2.28	3.09	1.65

Sample		15D-1-3b	15D-1-3bR	15D-1-4c	15D-1-5c	16D-1-1b	16D-1-1bR	16D-1-2b	16D-1-2bR	16D-1-3c	17D-1-2a
latitude		24.05	24.05	24.05	24.05	24.08	24.08	24.08	24.08	24.08	24.12
SiO2	%	49.66	49.70	49.88	49.99	49.93	49.93	50.01	50.01	49.98	49.86
Al2O3	%	16.09	16.11	16.06	16.41	17.58	17.58	17.09	17.09	16.59	15.52
Fe2O3	%	9.45	9.43	9.60	9.50	9.19	9.19	9.47	9.47	9.59	9.51
MgO	%	8.73	8.66	8.64	8.72	7.44	7.44	7.67	7.67	7.72	8.20
CaO	%	11.62	11.60	11.58	11.64	11.76	11.76	11.63	11.63	11.54	11.88
Na2O	%	2.65	2.67	2.70	2.62	2.82	2.82	2.89	2.89	3.00	2.65
K2O	%	0.05	0.05	0.07	0.05	0.07	0.07	0.07	0.07	0.12	0.08
TiO2	%	1.20	1.19	1.23	1.20	1.29	1.29	1.34	1.34	1.35	1.17
MnO	%	0.16	0.16	0.16	0.16	0.16	0.16	0.16	0.16	0.16	0.16
P2O5	%	0.11	0.10	0.11	0.11	0.11	0.11	0.12	0.12	0.12	0.11
TOTAL	%	99.69	99.65	100.20	100.39	100.34	100.34	100.43	100.43	100.15	99.12
Nb	ppm	3.60	3.85	3.70	3.70	1.97	3.95	3.80	3.80	3.90	2.16
Zr	ppm	76.40	76.65	79.50	75.55	83.56	87.15	86.80	88.70	87.33	73.94
Y	ppm	28.00	27.45	28.65	27.05	29.71	30.00	30.45	31.40	31.17	26.84
Sr	ppm	107.10	106.95	109.35	106.55	129.66	122.80	123.70	121.80	123.97	116.38
Ga	ppm	16.92	17.11	16.87	16.03	15.62	16.83	16.64	18.33	16.42	14.87
Zn	ppm					69.41					68.83
Cu	ppm					67.50					91.90
Ni	ppm	139.45	143.20	124.15	125.95	105.70	113.90	115.15	124.10	114.27	100.60
Co	ppm					40.77					44.46
Cr	ppm	373.19	374.53	362.38	375.44	268.51	319.71	275.74	274.23	273.62	425.01
V	ppm	266.04	266.27	260.23	249.90	248.33	276.60	277.13	278.46	254.85	258.09
Rb	ppm	2.77	2.57	3.09	2.53	0.87	2.53	1.93	3.61	1.53	1.03
Ba	ppm	13.05	18.53	8.64	12.79	9.61	12.75	14.84	8.24	14.69	11.84
Sc	ppm	34.36	34.45	34.19	33.66	33.21	35.68	31.94	36.17	30.68	38.03
Cs	ppm					0.02					0.02
La	ppm	-0.48	0.93	-0.07	1.00	2.79	1.39	1.14	0.87	-0.18	2.74
Ce	ppm	6.76	9.39	9.38	10.54	8.98	8.62	8.12	-0.63	4.48	8.46
Pr	ppm					1.52					1.42
Nd	ppm	3.23	5.43	6.91	7.14	8.64	4.90	7.16	2.34	3.86	7.74
Sm	ppm					2.96					2.74
Eu	ppm					1.10					1.01
Gd	ppm					3.92					3.68
Tb	ppm					0.72					0.68
Dy	ppm					4.64					4.32
Ho	ppm					1.02					0.90
Er	ppm					2.97					2.76
Tm	ppm					0.45					0.39
Yb	ppm					3.04					2.68
Lu	ppm					0.46					0.42
Hf	ppm					2.37					2.05
Ta	ppm					0.13					0.14
Mo	ppm					5.33					1.42
W	ppm					0.02					0.04
Tl	ppm					0.01					0.01
Pb	ppm					0.54					0.49
Th	ppm					0.12					0.14
U	ppm					0.04					0.04
Chondrite Norm											
La						8.47					8.32
Ce						11.12					10.47
Pr						12.46					11.66
Nd						14.40					12.90
Sm						15.16					14.06
Eu						15.03					13.74
Gd						15.13					14.19
Tb						15.78					14.75
Dy						14.41					13.41
Ho						14.24					12.58
Er						14.12					13.12
Tm						12.93					12.17
Yb						14.54					12.81
Lu						14.21					12.91
recal Nb for xrf		1.53	1.87	1.67	1.67	1.97	2.01	1.81	1.81	1.94	2.16
Nb	ppm	3.60	3.85	3.70	3.70	1.97	3.95	3.80	3.80	3.90	2.16

Sample		17D-1-2aR	17D-1-2b	17D-1-3a	17D-2-1a	18D-1-3b	18D-1-4b	19D-1-2a	19D-2-1b	20D-1-1b	20D-1-2b
latitude		24.12	24.12	24.12	24.12	24.14	24.14	24.19	24.19	24.25	24.25
SiO2	%	49.86	49.86	50.14	49.96	50.08	49.90	**49.46**	50.61	**50.18**	49.86
Al2O3	%	15.52	15.52	15.54	15.66	16.73	16.47	**15.68**	15.22	**15.14**	15.24
Fe2O3	%	9.51	9.51	9.54	9.52	9.74	9.90	**10.34**	10.54	**10.81**	10.70
MgO	%	8.20	8.20	8.29	8.28	7.36	7.52	**8.10**	7.80	**7.72**	7.68
CaO	%	11.88	11.88	11.94	11.96	11.56	11.49	**11.05**	11.37	**10.98**	11.00
Na2O	%	2.65	2.65	2.82	2.82	2.97	2.82	**3.00**	2.89	**3.06**	3.08
K2O	%	0.08	0.08	0.10	0.27	0.11	0.09	**0.10**	0.17	**0.16**	0.16
TiO2	%	1.17	1.17	1.17	1.17	1.38	1.40	**1.47**	1.44	**1.59**	1.58
MnO	%	0.16	0.16	0.16	0.16	0.16	0.17	**0.17**	0.18	**0.18**	0.18
P2O5	%	0.11	0.11	0.11	0.11	0.13	0.14	**0.14**	0.12	**0.14**	0.15
TOTAL	%	99.12	99.12	99.79	99.90	100.19	99.88	**99.72**	100.33	**99.96**	99.59
Nb	ppm	4.60	4.60	4.15	4.10	4.70	4.65	**2.15**	4.15	**2.68**	4.90
Zr	ppm	72.50	75.20	75.40	75.00	92.40	93.10	**101.68**	93.95	**109.80**	106.50
Y	ppm	26.50	27.00	27.65	27.60	31.30	32.65	**32.87**	32.20	**36.63**	36.80
Sr	ppm	107.80	108.90	111.75	115.95	124.15	124.55	**139.47**	119.05	**130.17**	127.85
Ga	ppm	15.32	17.01	15.56	17.63	16.36	17.77	**14.67**	18.19	**16.35**	17.01
Zn	ppm							**71.66**		**79.66**	
Cu	ppm							**63.16**		**65.38**	
Ni	ppm	101.00	97.00	90.35	96.75	100.50	100.70	**117.55**	98.75	**111.45**	107.30
Co	ppm							**39.33**		**44.64**	
Cr	ppm	408.07	417.10	446.99	424.09	295.03	304.12	**339.15**	319.22	**251.40**	243.06
V	ppm	266.56	274.65	271.18	265.32	279.22	277.98	**253.42**	295.17	**288.85**	292.98
Rb	ppm	3.29	3.21	2.45	4.41	2.29	2.93	**0.83**	3.33	**1.22**	2.45
Ba	ppm	20.65	16.64	24.18	21.38	17.45	20.49	**9.48**	17.42	**11.59**	16.71
Sc	ppm	34.50	35.73	35.86	37.62	33.53	32.43	**36.07**	35.24	**38.66**	33.48
Cs	ppm							**0.02**		**0.01**	
La	ppm	1.03	2.08	4.14	-0.13	3.05	0.99	**3.38**	1.78	**3.69**	2.22
Ce	ppm	12.71	7.23	11.53	6.31	12.31	11.24	**10.90**	12.89	**11.57**	13.05
Pr	ppm							**1.78**		**1.90**	
Nd	ppm	4.02	3.52	8.15	6.74	12.90	9.11	**9.78**	9.70	**10.50**	9.13
Sm	ppm							**3.33**		**3.52**	
Eu	ppm							**1.23**		**1.30**	
Gd	ppm							**4.22**		**4.75**	
Tb	ppm							**0.78**		**0.87**	
Dy	ppm							**5.09**		**5.80**	
Ho	ppm							**1.11**		**1.21**	
Er	ppm							**3.27**		**3.53**	
Tm	ppm							**0.47**		**0.56**	
Yb	ppm							**3.26**		**3.62**	
Lu	ppm							**0.47**		**0.53**	
Hf	ppm							**2.63**		**2.88**	
Ta	ppm							**0.14**		**0.16**	
Mo	ppm							**2.06**		**0.43**	
W	ppm							**0.04**		**0.04**	
Tl	ppm							**0.06**		**0.04**	
Pb	ppm							**0.68**		**0.53**	
Th	ppm							**0.14**		**0.16**	
U	ppm							**0.05**		**0.09**	
Chondrite Norm											
La								**10.29**		**11.21**	
Ce								**13.49**		**14.32**	
Pr								**14.57**		**15.53**	
Nd								**16.30**		**17.50**	
Sm								**17.08**		**18.03**	
Eu								**16.84**		**16.78**	
Gd								**16.31**		**18.36**	
Tb								**16.53**		**19.56**	
Dy								**15.81**		**18.02**	
Ho								**15.41**		**16.80**	
Er								**15.57**		**16.79**	
Tm								**14.58**		**17.24**	
Yb								**15.59**		**17.31**	
Lu								**14.73**		**16.38**	
recal Nb for xrf		2.90	2.90	2.29	2.22	3.04	2.97	2.15	2.29	2.68	3.31
Nb	ppm	4.60	4.60	4.15	4.10	4.70	4.65	**2.15**	4.15	**2.68**	4.90

Sample		20D-1-3b	21D-1-1b	21D-1-1bR	21D-2-1b	21D-2-1bRI	D-3-1bFre:	21D-3-1b	22D-1-1b	22D-2-1b	22D-2-1bR	22D-2-2b
latitude		24.25	24.31	24.31	24.31	24.31	24.31	24.31	24.33	24.33	24.33	24.33
SiO2	%	50.40	50.33	50.33	50.17	50.17	50.54	50.09	49.72	50.48	50.48	50.39
Al2O3	%	15.43	15.46	15.46	16.20	16.20	15.75	15.44	15.29	16.87	16.87	17.64
Fe2O3	%	10.73	10.71	10.71	10.13	10.13	10.54	10.75	10.83	8.86	8.86	8.47
MgO	%	7.68	7.66	7.66	7.46	7.46	7.68	7.61	8.38	8.07	8.07	7.20
CaO	%	10.99	10.79	10.79	11.11	11.11	10.87	10.82	10.88	11.86	11.86	11.91
Na2O	%	3.04	3.13	3.13	3.05	3.05	3.12	3.13	2.81	2.62	2.62	2.72
K2O	%	0.11	0.13	0.13	0.24	0.24	0.24	0.22	0.19	0.16	0.16	0.27
TiO2	%	1.57	1.63	1.63	1.54	1.54	1.62	1.64	1.48	1.19	1.19	1.29
MnO	%	0.18	0.18	0.18	0.17	0.17	0.18	0.19	0.18	0.15	0.15	0.14
P2O5	%	0.15	0.16	0.16	0.16	0.16	0.16	0.16	0.15	0.11	0.11	0.13
TOTAL	%	100.28	100.17	100.17	100.22	100.22	100.68	100.02	99.88	100.36	100.36	100.15
Nb	ppm	4.85	3.28	5.20	5.27	4.95	4.90	4.25	4.90	2.60	4.30	5.77
Zr	ppm	106.10	116.56	116.70	107.40	107.15	115.80	115.80	101.70	78.25	79.80	92.93
Y	ppm	36.85	36.26	36.00	33.93	33.65	35.70	36.95	34.80	26.87	27.00	28.10
Sr	ppm	127.35	140.75	136.40	138.33	138.40	136.40	139.00	120.67	126.23	120.30	139.53
Ga	ppm	17.30	15.49	16.54	17.92	17.48	16.83	18.00	17.11	14.36	14.57	16.29
Zn	ppm		77.92							65.21		
Cu	ppm		65.85							62.66		
Ni	ppm	111.95	116.33	118.60	112.27	116.40	117.00	112.55	157.27	123.85	125.40	126.80
Co	ppm		46.89							36.41		
Cr	ppm	247.84	282.64	305.52	274.45	266.17	270.15	264.67	311.18	387.26	385.93	339.27
V	ppm	303.88	301.36	316.25	289.76	296.41	300.83	296.21	278.21	244.15	265.80	265.77
Rb	ppm	3.01	1.45	8.99	3.67	4.37	3.85	3.93	3.40	2.10	4.17	4.44
Ba	ppm	19.78	14.94	24.51	28.36	24.42	26.06	19.79	21.36	13.64	24.29	30.90
Sc	ppm	37.84	39.00	40.83	34.61	35.07	36.26	33.97	38.81	33.61	33.18	30.68
Cs	ppm		0.02							0.04		
La	ppm	1.77	4.20	3.73	1.13	2.72	4.10	1.34	2.26	3.08	-0.78	0.73
Ce	ppm	11.68	13.19	13.98	13.29	12.49	13.96	17.33	12.65	8.71	4.90	10.28
Pr	ppm		2.08							1.43		
Nd	ppm	6.19	11.40	14.83	6.15	10.46	14.04	12.72	9.23	7.91	5.50	3.87
Sm	ppm		3.61							2.63		
Eu	ppm		1.31							0.97		
Gd	ppm		4.77							3.51		
Tb	ppm		0.89							0.67		
Dy	ppm		5.74							4.10		
Ho	ppm		1.21							0.86		
Er	ppm		3.50							2.59		
Tm	ppm		0.52							0.37		
Yb	ppm		3.47							2.63		
Lu	ppm		0.54							0.40		
Hf	ppm		2.91							2.07		
Ta	ppm		0.20							0.16		
Mo	ppm		0.30							0.60		
W	ppm		0.04							0.02		
Tl	ppm		0.04							0.05		
Pb	ppm		0.60							0.53		
Th	ppm		0.22							0.19		
U	ppm		0.07							0.07		
Chondrite Norm												
La			12.75							9.37		
Ce			16.33							10.78		
Pr			17.03							11.74		
Nd			19.01							13.19		
Sm			18.51							13.51		
Eu			17.93							13.19		
Gd			18.42							13.53		
Tb			18.86							14.15		
Dy			17.82							12.72		
Ho			16.86							11.97		
Er			16.65							12.33		
Tm			16.04							11.50		
Yb			16.60							12.59		
Lu			16.92							12.57		
recal Nb for xrf		3.25	3.28	3.73	3.82	3.38	3.31	2.42	3.31	2.60	2.49	4.50
Nb	ppm	4.85	3.28	5.20	5.27	4.95	4.90	4.25	4.90	2.60	4.30	5.77

Sample		22D-2-2bR	22D-3-1b	22D-3-2b	22D-6-1b	22D-6-2b	23D-1-1b	23D-2-2b	23D-3-1b	23D-4	24D-1-1b	24D-2-1b
latitude		24.33	24.33	24.33	24.33	24.33	24.41	24.41	24.41	24.41	24.55	24.55
SiO2	%	50.75	50.36	50.00	50.45	49.95	50.90	**49.58**	50.54	50.50	**49.72**	50.39
Al2O3	%	17.45	15.42	15.65	15.89	15.43	15.37	**17.82**	15.19	15.21	**16.39**	15.36
Fe2O3	%	8.58	9.76	9.95	9.72	10.14	10.19	**9.31**	10.31	10.26	**9.68**	10.20
MgO	%	7.60	7.81	8.11	7.77	9.32	7.63	**7.13**	7.63	7.64	**8.14**	8.17
CaO	%	11.74	11.74	11.28	11.26	10.90	11.24	**11.87**	11.15	11.15	**11.49**	11.27
Na2O	%	2.64	2.73	2.99	3.06	2.82	3.04	**2.73**	2.98	2.97	**2.61**	2.83
K2O	%	0.24	0.29	0.14	0.21	0.10	0.23	**0.07**	0.13	0.13	**0.07**	0.09
TiO2	%	1.30	1.32	1.49	1.50	1.45	1.53	**1.17**	1.54	1.53	**1.27**	1.39
MnO	%	0.14	0.16	0.16	0.16	0.16	0.18	**0.16**	0.18	0.17	**0.16**	0.17
P2O5	%	0.14	0.14	0.14	0.15	0.14	0.16	**0.10**	0.16	0.16	**0.11**	0.13
TOTAL	%	100.53	99.72	99.89	100.16	100.40	100.46	**99.93**	99.77	99.69	**99.62**	99.98
Nb	ppm	5.87	5.47	4.23	5.13	4.57	5.50	**1.83**	5.17	5.10	**1.97**	4.06
Zr	ppm	92.90	89.33	96.63	104.50	99.80	112.27	**71.98**	112.00	111.03	**79.05**	92.23
Y	ppm	28.97	30.07	34.23	33.00	32.50	34.20	**28.29**	33.50	33.57	**28.72**	30.47
Sr	ppm	140.80	129.27	125.50	134.73	124.23	149.50	**119.25**	147.27	146.83	**115.85**	125.04
Ga	ppm	15.43	16.49	17.34	17.78	14.34	15.08	**15.20**	15.37	15.58	**15.00**	16.83
Zn	ppm							**64.85**			**70.05**	77.59
Cu	ppm							**62.62**			**67.19**	66.07
Ni	ppm	141.23	103.00	251.30	136.73	199.17	85.17	**122.20**	90.07	92.63	**157.30**	119.95
Co	ppm							**39.96**			**45.00**	43.82
Cr	ppm	345.09	327.99	425.25	323.60	434.05	255.36	**315.50**	254.72	270.73	**372.50**	299.68
V	ppm	270.08	278.35	306.87	297.90	279.55	298.57	**229.39**	313.10	308.30	**262.16**	292.17
Rb	ppm	3.82	5.78	2.28	2.70	2.28	1.88	**0.89**	1.75	1.52	**0.81**	1.86
Ba	ppm	27.45	33.91	19.90	22.01	15.44	19.51	**9.54**	27.50	26.51	**8.98**	13.95
Sc	ppm	31.52	34.80	34.80	34.34	31.90	36.98	**32.71**	39.70	38.77	**35.57**	37.27
Cs	ppm							**0.02**			**0.01**	
La	ppm	1.06	0.79	1.41	2.43	2.56	3.08	**2.42**	2.85	2.79	**2.71**	
Ce	ppm	7.72	12.36	10.14	10.62	9.72	16.95	**7.84**	12.64	18.06	**8.47**	
Pr	ppm							**1.34**			**1.39**	
Nd	ppm	8.22	7.49	7.51	10.08	9.03	10.79	**7.49**	9.86	10.15	**8.03**	
Sm	ppm							**2.63**			**2.75**	
Eu	ppm							**0.96**			**0.99**	
Gd	ppm							**3.53**			**3.87**	
Tb	ppm							**0.67**			**0.71**	
Dy	ppm							**4.52**			**4.63**	
Ho	ppm							**0.95**			**0.97**	
Er	ppm							**2.90**			**2.89**	
Tm	ppm							**0.42**			**0.46**	
Yb	ppm							**2.86**			**2.87**	
Lu	ppm							**0.45**			**0.45**	
Hf	ppm							**1.98**			**2.12**	
Ta	ppm							**0.13**			**0.13**	
Mo	ppm							**0.25**			**0.20**	
W	ppm							**0.03**			**0.02**	
Tl	ppm							**0.00**			**0.03**	
Pb	ppm							**0.39**			**0.43**	
Th	ppm							**0.12**			**0.13**	
U	ppm							**0.03**			**0.05**	
Chondrite Norm												
La								**7.36**			**8.22**	
Ce								**9.70**			**10.49**	
Pr								**11.01**			**11.41**	
Nd								**12.48**			**13.39**	
Sm								**13.47**			**14.12**	
Eu								**13.08**			**13.56**	
Gd								**13.62**			**14.95**	
Tb								**14.23**			**15.02**	
Dy								**14.04**			**14.38**	
Ho								**13.23**			**13.53**	
Er								**13.79**			**13.74**	
Tm								**12.85**			**14.07**	
Yb								**13.67**			**13.71**	
Lu								**13.91**			**14.12**	
recal Nb for xrf		4.64	4.09	2.40	3.63	2.86	4.14	**1.83**	3.68	3.59	1.97	2.16
Nb	ppm	5.87	5.47	4.23	5.13	4.57	5.50	1.83	5.17	5.10	1.97	4.06

Sample		24D-2-1bR	24D-3-1b	27D-1-1b	27D-1-1bMf	27D-1-1bR	27D-2-1b	27D-2-1bMf	27D-2-1bR	29D-1-1c	29D-2-1c
latitude		24.55	24.55	23.84	23.84	23.84	23.84	23.84	23.84	24.35	24.35
SiO2	%	50.40	50.53	**50.17**	50.17	50.35	50.47	50.47	50.47	50.15	49.85
Al2O3	%	15.35	15.13	**16.58**	16.58	16.15	15.92	15.92	15.92	16.22	17.21
Fe2O3	%	10.20	10.27	**9.92**	9.92	10.23	10.33	10.33	10.33	9.71	9.02
MgO	%	8.17	7.48	**7.12**	7.12	7.02	7.34	7.34	7.34	8.03	7.87
CaO	%	11.26	11.23	**11.40**	11.40	11.30	11.20	11.20	11.20	11.27	11.59
Na2O	%	2.81	3.05	**2.86**	2.86	2.91	2.89	2.89	2.89	2.90	2.77
K2O	%	0.09	0.26	**0.27**	0.27	0.29	0.23	0.23	0.23	0.22	0.10
TiO2	%	1.39	1.54	**1.57**	1.57	1.61	1.63	1.63	1.63	1.40	1.26
MnO	%	0.17	0.17	**0.17**	0.17	0.17	0.17	0.17	0.17	0.17	0.15
P2O5	%	0.12	0.14	**0.16**	0.16	0.16	0.16	0.16	0.16	0.14	0.12
TOTAL	%	99.96	99.80	**100.21**	100.21	100.18	100.31	100.31	100.31	100.18	99.94
Nb	ppm	4.23	4.94	**3.45**	5.25	5.27	5.97	5.11	4.79	4.61	4.00
Zr	ppm	92.48	111.87	**114.09**	118.53	120.63	121.85	117.05	116.87	101.53	90.82
Y	ppm	30.39	32.09	**35.74**	34.93	35.64	35.98	35.06	34.51	29.51	27.33
Sr	ppm	124.86	147.57	**130.38**	132.85	131.90	128.37	129.50	128.90	137.64	138.80
Ga	ppm	16.33	16.31	**15.85**	16.85	17.29	16.51	17.31	16.85	15.77	15.45
Zn	ppm	77.64	78.91	**75.67**	81.30	81.73	81.44	80.40	79.73	70.14	69.13
Cu	ppm	70.74	71.91	**64.28**	69.69	70.54	68.64	67.36	65.15	67.66	67.82
Ni	ppm	122.17	84.02	**111.81**	120.27	111.40	109.31	110.93	109.24	129.21	136.95
Co	ppm	45.49	40.71	**40.87**	43.20	40.53	43.72	43.41	40.52	40.30	39.58
Cr	ppm	311.79	221.36	**266.65**	261.90	261.91	288.66	274.00	273.29	304.08	324.93
V	ppm	288.50	306.68	**279.17**	296.78	307.18	306.44	299.91	300.68	280.74	262.61
Rb	ppm	1.92	2.26	**2.48**	3.25	4.07	3.12	3.14	3.14	2.74	1.54
Ba	ppm	13.34	19.96	**15.77**	21.27	19.98	16.00	16.47	21.48	18.51	17.06
Sc	ppm	39.95	38.22	**35.06**	34.39	37.15	37.17	37.26	36.93	36.98	33.34
Cs	ppm			**0.03**							
La	ppm			**4.08**							
Ce	ppm			**12.59**							
Pr	ppm			**2.01**							
Nd	ppm			**10.98**							
Sm	ppm			**3.63**							
Eu	ppm			**1.32**							
Gd	ppm			**4.79**							
Tb	ppm			**0.96**							
Dy	ppm			**5.80**							
Ho	ppm			**1.26**							
Er	ppm			**3.56**							
Tm	ppm			**0.56**							
Yb	ppm			**3.62**							
Lu	ppm			**0.51**							
Hf	ppm			**2.95**							
Ta	ppm			**0.21**							
Mo	ppm			**0.43**							
W	ppm			**0.05**							
Tl	ppm			**0.14**							
Pb	ppm			**0.53**							
Th	ppm			**0.20**							
U	ppm			**0.27**							
Chondrite Norm											
La				**12.40**							
Ce				**15.58**							
Pr				**16.45**							
Nd				**18.29**							
Sm				**18.63**							
Eu				**18.00**							
Gd				**18.48**							
Tb				**20.17**							
Dy				**18.00**							
Ho				**17.50**							
Er				**16.95**							
Tm				**17.35**							
Yb				**17.31**							
Lu				**15.88**							
recal Nb for xrf		2.40	3.36	**3.45**	3.80	3.82	4.79	3.60	3.17	2.92	2.08
Nb	ppm	4.23	4.94	**3.45**	5.25	5.27	5.97	5.11	4.79	4.61	4.00

Sample		29D-3-1c	29D-3-2c	30D-1-2c	31D-1-2b	31D-1-2bR	32D-1-1b	32D-1-2c	32D-2-1c	32D-3-1b
latitude		24.35	24.35	24.35	24.50	24.50	24.62	24.62	24.62	24.62
SiO2	%	50.45	50.38	50.64	50.17	50.17	49.86	49.56	49.73	49.38
Al2O3	%	15.88	15.53	15.32	18.39	18.39	15.91	15.70	15.76	15.46
Fe2O3	%	9.97	10.40	11.03	9.03	9.03	10.18	10.21	10.14	10.21
MgO	%	7.97	8.06	7.25	6.40	6.40	8.69	8.72	9.13	9.15
CaO	%	11.21	10.93	10.70	11.85	11.85	11.07	11.04	11.10	11.06
Na2O	%	2.94	2.94	3.10	2.90	2.90	2.86	2.77	2.73	2.74
K2O	%	0.25	0.18	0.25	0.09	0.09	0.14	0.13	0.10	0.12
TiO2	%	1.46	1.52	1.67	1.36	1.36	1.37	1.37	1.22	1.25
MnO	%	0.17	0.17	0.18	0.15	0.15	0.17	0.17	0.17	0.17
P2O5	%	0.14	0.16	0.14	0.14	0.14	0.13	0.12	0.12	0.12
TOTAL	%	100.42	100.26	100.30	100.45	100.45	100.36	99.76	100.15	99.65
Nb	ppm	4.46	5.12	3.08	2.50	4.33	4.22	2.65	3.53	3.72
Zr	ppm	106.05	105.06	115.04	94.69	104.15	94.54	92.97	83.37	85.51
Y	ppm	31.42	32.91	36.07	30.26	31.09	29.16	29.89	26.95	27.75
Sr	ppm	138.22	143.38	138.96	141.82	136.94	132.33	135.47	131.53	131.38
Ga	ppm	16.15	15.69	17.36	15.61	17.61	17.40	15.29	15.76	15.16
Zn	ppm	74.38	78.22	85.07	68.17	73.35	74.74	72.75	75.47	74.14
Cu	ppm	73.59	62.40	65.79	60.43	61.83	70.79	68.06	76.51	77.28
Ni	ppm	125.73	135.29	97.23	86.34	88.97	171.03	180.37	193.55	201.79
Co	ppm	42.48	44.30	44.83	36.41	38.69	47.50	44.76	47.46	50.15
Cr	ppm	312.71	334.10	172.79	247.01	255.14	347.81	353.01	439.13	445.41
V	ppm	295.13	285.79	313.64	247.28	279.27	269.87	262.61	254.08	261.70
Rb	ppm	2.46	2.60	1.90	1.07	1.87	1.87	1.19	1.64	1.71
Ba	ppm	16.71	25.91	14.49	12.39	17.49	13.06	11.55	12.42	12.73
Sc	ppm	36.35	38.06	40.06	33.63	34.58	35.61	35.98	38.88	36.80
Cs	ppm		0.03	0.02	0.02			0.01		
La	ppm		4.56	3.97	3.23			3.33		
Ce	ppm		12.89	12.23	10.04			10.36		
Pr	ppm		1.97	2.01	1.71			1.71		
Nd	ppm		10.50	10.94	9.45			9.27		
Sm	ppm		3.38	3.56	3.09			3.12		
Eu	ppm		1.23	1.31	1.13			1.18		
Gd	ppm		4.32	4.70	4.20			3.98		
Tb	ppm		0.85	0.86	0.78			0.74		
Dy	ppm		5.20	5.66	4.80			4.88		
Ho	ppm		1.13	1.20	1.06			1.03		
Er	ppm		3.35	3.57	3.06			3.02		
Tm	ppm		0.49	0.52	0.45			0.45		
Yb	ppm		3.35	3.56	3.12			3.08		
Lu	ppm		0.49	0.56	0.45			0.46		
Hf	ppm		2.70	2.77	2.53			2.44		
Ta	ppm		0.30	0.18	0.14			0.16		
Mo	ppm		0.36	6.75	1.22			0.42		
W	ppm		0.04	0.05	0.01			0.05		
Tl	ppm		0.05	0.03	0.05			0.01		
Pb	ppm		0.84	1.75	0.78			0.52		
Th	ppm		0.34	0.19	0.18			0.16		
U	ppm		0.12	0.08	0.06			0.11		
Chondrite Norm										
La			13.88	12.08	9.83			10.12		
Ce			15.96	15.13	12.43			12.83		
Pr			16.14	16.51	13.98			13.99		
Nd			17.50	18.24	15.75			15.44		
Sm			17.35	18.25	15.84			16.02		
Eu			16.79	17.90	15.39			16.14		
Gd			16.67	18.17	16.23			15.38		
Tb			17.85	18.21	17.89			15.69		
Dy			16.14	17.59	14.90			15.15		
Ho			15.80	16.69	14.79			14.41		
Er			15.95	17.00	14.57			14.36		
Tm			15.23	15.90	14.01			13.82		
Yb			16.03	17.03	14.91			14.75		
Lu			15.20	17.30	14.09			14.23		
recal Nb for xrf		2.71	5.12	3.08	2.50	2.53	2.38	2.65	1.44	1.69
Nb	ppm	4.46	5.12	3.08	2.50	4.33	4.22	2.65	3.53	3.72

BLANK IN ORIGINAL

Appendix 6

Melt modelling

The equations of Gast (1968) and Shaw (1970) are used to calculate the non-modal batch melting of a depleted lherzolite source. The EXCEL™ spreadsheet **MELTEQ.XLS** (below) shows the partition coefficients and compositional parameters used in the melting calculations. This spreadsheet is accessed by the EXCEL™ macro **EQUILIB** (seen overleaf) to obtain the melting parameters used in the generation of chondrite normalised REE patterns. The patterns show the changing REE patterns for progressive degrees of partial melting. The numerical results of these calculations are returned to this spreadsheet during the running of the macro.

MELTEQ.XLS

Dist coeff	La	Ce	Nd	Sm	Eu	Dy	Er	Yb
ol	0.0005	0.001	0.002	0.003	0.003	0.012	0.025	0.059
opx	0.002	0.005	0.01	0.02	0.03	0.045	0.06	0.075
cpx	0.05	0.1	0.19	0.3	0.42	0.5	0.51	0.5
sp								
init conc	1	1.2	1.6	2	2	2	2	2
/ chond								
	%ol	%opx	%cpx	%sp	% melt	ol	opx	cpx
starting%	60	25	15	0	0	60	25	15
cpx out %	70	30	0	0	25	52.5	22.5	0
opx out %	100	0	0	0	65	35	0	0
melt fract	ol	opx	cpx	% ol	% opx	% cpx		

Excel macro to calculate REE spidergrams for progressive degrees of batch melting.

EQUILIB	
=SELECT("R16C1:R117C23")	
=CLEAR(1)	
=SELECT("R16C2:R117C7")	
=FORMAT.NUMBER("0.0")	
=SELECT("R16C8.R117C15")	
=FORMAT.NUMBER("0.0000")	
=SELECT("R16C16:R117C23")	
=FORMAT.NUMBER("0.00")	
=SELECT("R16C1")	
=FORMULA("=R10C6")	
=SELECT("R[+1]C")	
=FORMULA("=R[-1]C+1")	
=SELECT("R[+1]C")	
=FORMULA("=R[-1]C+4")	
=FOR("melt",10,100,5)	PLOTS MELT FRACT 10 TO 100, STEP 5
=SELECT("R[+1]C")	
=FORMULA("=R[-1]C+5")	
=NEXT()	
=SELECT("R16C2")	
=FOR("phase",0,100,5)	CALC PHASE % IN SYSTEM SOLID + MELT UNTIL CPX OUT
=FORMULA("=R10C7+(RC[-1]*(R11C7-R10C7)/R11C6)")	
=SELECT("RC[+1]")	
=FORMULA("=R10C8+(RC[-2]*(R11C8-R10C8)/R11C6)")	
=SELECT("RC[+1]")	
=FORMULA("=R10C9+(RC[-3]*(R11C9-R10C9)/R11C6)")	
=SELECT("R[+1]C[-2]")	
=IF(phase='K:\THESIS\NEWTHES\APPEND\CHP2MELT.XLS'!$F$11,GOTO(A30))	
=NEXT()	
=FOR("cpxout",5,100,5)	CALC PHASE % IN SYSTEM SOLID + MELT BETWEEN CPX OUT & OPX OUT
=FORMULA("=R11C7+((R12C7-R11C7)*(RC[-1]-R11C6)/(R12C6-R11C6))")	
=SELECT("RC[+1]")	
=FORMULA("=R11C8+((R12C8-R11C8)*(RC[-2]-R11C6)/(R12C6-R11C6))")	
=SELECT("RC[+1]")	
=FORMULA("=R11C9+((R12C9-R11C9)*(RC[-3]-R11C6)/(R12C6-R11C6))")	
=SELECT("R[+1]C[-2]")	
=IF(cpxout=('K:\THESIS\NEWTHES\APPEND\CHP2MELT.XLS'!$F$12-'K:\THESIS\NEWTHES\APPEND\CHP2I	
=NEXT()	
=FOR("opxout",0,100,5)	CALC PHASE % IN SYSTEM SOLID + MELT BETWEEN OPX OUT &100% MELT
=FORMULA("=R12C7+(0-R12C7)*(RC[-1]-R12C6)/(100-R12C6)")	
=SELECT("RC[+1]")	
=FORMULA("=R12C8+(0-R12C8)*(RC[-2]-R12C6)/(100-R12C6)")	
=SELECT("RC[+1]")	
=FORMULA("=R12C9+(0-R12C9)*(RC[-3]-R12C6)/(100-R12C6)")	
=IF(opxout=(100-'K:\THESIS\NEWTHES\APPEND\CHP2MELT.XLS'!$F$12),GOTO(A48))	
=SELECT("R[+1]C[-2]")	
=NEXT()	
=SELECT("R16C5")	
=FOR("solid",0,20,1)	CALC % OF PHASE IN REMAINING SOLID
=FORMULA("=100*RC[-3]/(100-RC[-4])")	
=SELECT("RC[+1]")	
=FORMULA("=100*RC[-3]/(100-RC[-5])")	
=SELECT("RC[+1]")	
=FORMULA("=100*RC[-3]/(100-RC[-6])")	
=SELECT("R[+1]C[-2]")	

Excel macro to calculate REE spidergrams for progressive degrees of batch melting.

=NEXT()	
=SELECT("R16C16")	
=FOR("start",1,8,1)	SETS CI TO ZERO FOR 0% MELTING
=FORMULA("=0")	
=SELECT("RC[+1]")	
=NEXT()	
=SELECT("R16C8")	
=FOR("kd",0,20,1)	CALCS kd FOR THE REE'S
=FORMULA("=RC[-3]/100*R2C2+RC[-2]/100*R3C2+RC[-1]/100*R4C2")	
=SELECT("RC[+1]")	
=FORMULA("=RC[-4]/100*R2C3+RC[-3]/100*R3C3+RC[-2]/100*R4C3")	
=SELECT("RC[+1]")	
=FORMULA("=RC[-5]/100*R2C4+RC[-4]/100*R3C4+RC[-3]/100*R4C4")	
=SELECT("RC[+1]")	
=FORMULA("=RC[-6]/100*R2C5+RC[-5]/100*R3C5+RC[-4]/100*R4C5")	
=SELECT("RC[+1]")	
=FORMULA("=RC[-7]/100*R2C6+RC[-6]/100*R3C6+RC[-5]/100*R4C6")	
=SELECT("RC[+1]")	
=FORMULA("=RC[-8]/100*R2C7+RC[-7]/100*R3C7+RC[-6]/100*R4C7")	
=SELECT("RC[+1]")	
=FORMULA("=RC[-9]/100*R2C8+RC[-8]/100*R3C8+RC[-7]/100*R4C8")	
=SELECT("RC[+1]")	
=FORMULA("=RC[-10]/100*R2C9+RC[-9]/100*R3C9+RC[-8]/100*R4C9")	
=SELECT("R[+1]C[+1]")	
=FORMULA("=R7C2/(R[-1]C[-8]*(1-(RC[-15]/100))+RC[-15]/100)")	CALCS CI FOR THE REE'S
=SELECT("RC[+1]")	
=FORMULA("=R7C3/(R[-1]C[-8]*(1-(RC[-16]/100))+RC[-16]/100)")	
=SELECT("RC[+1]")	
=FORMULA("=R7C4/(R[-1]C[-8]*(1-(RC[-17]/100))+RC[-17]/100)")	
=SELECT("RC[+1]")	
=FORMULA("=R7C5/(R[-1]C[-8]*(1-(RC[-18]/100))+RC[-18]/100)")	
=SELECT("RC[+1]")	
=FORMULA("=R7C6/(R[-1]C[-8]*(1-(RC[-19]/100))+RC[-19]/100)")	
=SELECT("RC[+1]")	
=FORMULA("=R7C7/(R[-1]C[-8]*(1-(RC[-20]/100))+RC[-20]/100)")	
=SELECT("RC[+1]")	
=FORMULA("=R7C8/(R[-1]C[-8]*(1-(RC[-21]/100))+RC[-21]/100)")	
=SELECT("RC[+1]")	
=FORMULA("=R7C9/(R[-1]C[-8]*(1-(RC[-22]/100))+RC[-22]/100)")	
=SELECT("RC[-15]")	
=NEXT()	
=REEPLOT()	PLOTS SPIDER GRAPH
=RETURN()	
REEPLOT	
=ACTIVATE("EQFIVE.XLM")	
=HIDE()	
=OPEN("spider5.xlc")	
=OPEN("charteq5.xlc")	
=OPEN("charteq6.xlc")	
=ARRANGE.ALL()	
=RETURN()	

BLANK IN ORIGINAL

Appendix 7

Thatcher's Nose